Technische Universität München
TUM School of Natural Sciences

Optimization of Aqueous Alkaline and Alkaline Earth Metal-Ion Batteries for Sustainable Energy Storage

Raphael Louis Streng

Vollständiger Abdruck der von der TUM School of Natural Sciences der Technischen Universität München zur Erlangung eines

Doktors der Naturwissenschaften (Dr. rer. nat.)

genehmigten Dissertation.

Vorsitz: Prof. Dr. Alejandro Ibarra

Prüfende der Dissertation:

1. Prof. Dr. Aliaksandr S. Bandarenka
2. Prof. Dr. Peter Müller-Buschbaum

Die Dissertation wurde am 01.07.2025 bei der Technischen Universität München eingereicht und durch die TUM School of Natural Sciences am 25.09.2025 angenommen.

Abstract

The ongoing transformation of the global energy landscape towards renewable energy sources such as solar and wind necessitates the development of robust, scalable, and sustainable energy storage technologies. Batteries are envisaged to play a central role in this transition. However, the widespread use of lithium-ion batteries (LIBs) is increasingly limited by concerns regarding safety, resource availability, and environmental sustainability. In this context, this dissertation explores the development of Li-free aqueous batteries (LFABs) as an alternative solution, focusing on systems consisting of abundant, non-toxic, and inexpensive materials.

This work presents a novel LFAB design strategy based on the integration of polyimide (PI) organic anodes with Prussian Blue Analog (PBA) cathodes, namely copper hexacyanoferrate (CuHCF) and a manganese-rich iron-manganese hexacyanoferrate (FeMnHCF-C), in combination with neutral or mildly acidic mixed-salt 1.8 mol kg^{-1} KCl + 1.8 mol kg^{-1} $MgCl_2$ (KMC) and 2.5 M $Ca(NO_3)_2$ + 1.5 M KNO_3 (CKN) aqueous electrolytes. These electrolytes combine the advantages of monovalent and divalent ions, enabling high cell voltages and good cycling stability without relying on expensive water-in-salt electrolytes (WiSEs). The CuHCF/KMC/PI full cell exhibits excellent fast-charging performance, delivering energy densities up to 48 Wh kg^{-1} and power densities exceeding 10 kW kg^{-1}, with ≈90 % capacity retention over 700 cycles. The stabilizing effects of divalent cations (Mg^{2+}, Ca^{2+}) are attributed to reduced free water content and pH shifts that mitigate parasitic degradation reactions. Building on these results, the FeMnHCF-C/CKN/PI battery extends the design strategy to a high-capacity, Mn-based cathode stabilized by Fe-substitution and controlled crystallinity. Electrochemical and structural analyses confirm improved phase stability and reduced degradation linked to the Jahn-Teller effect. The optimized full cell achieves a high specific capacity (~110 mAh kg^{-1}) and energy density of ≈72 Wh kg^{-1}, which are among the highest reported for LFABs, while maintaining good rate capability and cyclability. A conceptual upscaling study confirms the practical potential of the developed systems for stationary applications such as home energy storage, offering promising advantages in terms of safety, cost, and environmental impact. The results of this work demonstrate the viability of LFABs for stationary energy storage and represent an important step towards their practical application.

Zusammenfassung

Die fortschreitende Umgestaltung der globalen Energielandschaft hin zu erneuerbaren Energiequellen wie Solar- und Windenergie erfordert die Entwicklung robuster, skalierbarer und nachhaltiger Energiespeichertechnologien. Batterien sind dazu prädestiniert, eine zentrale Rolle in diesem Übergang zu spielen. Der weitverbreitete Einsatz von Lithium-Ionen-Batterien (LIBs) wird jedoch zunehmend durch Bedenken hinsichtlich Sicherheit, Ressourcenverfügbarkeit und ökologischer Nachhaltigkeit eingeschränkt. Vor diesem Hintergrund untersucht diese Dissertation die Entwicklung von lithiumfreien wässrigen Batterien (LFABs) als alternative Lösung, mit Fokus auf Systeme, die aus reichlich vorhandenen, ungiftigen und kostengünstigen Materialien bestehen.

Diese Arbeit stellt eine neuartige LFAB-Designstrategie vor, die auf der Kombination von organischen Polyimid Anoden (PNFE) mit Kathoden auf Basis von den Preußisch Blau-Analoga (PBA) Kupferhexacyanoferrat (CuHCF) und Eisen-Mangan-Hexacyanoferrat (FeMnHCF-C), in Verbindung mit neutralen oder schwach sauren Mischsalz-Elektrolyten, beruht. Als Elektrolyte dienen 1,8 mol kg^{-1} KCl + 1,8 mol kg^{-1} $MgCl_2$ (KMC) sowie 2,5 M $Ca(NO_3)_2$ + 1,5 M KNO_3 (CKN). Diese Elektrolyte vereinen die Vorteile von ein- und zweiwertigen Ionen und ermöglichen hohe Zellspannungen sowie eine gute Zyklenstabilität, ohne auf teure „Wasser-in-Salz“-Elektrolyte (WiSEs) angewiesen zu sein. Die CuHCF/KMC/PNFE-Vollzelle zeigt eine ausgezeichnete Schnellladefähigkeit mit Energiedichten von bis zu 48 Wh kg^{-1} und Leistungsdichten über 10 kW kg^{-1} sowie einer Kapazitätserhaltung von ≈90 % über 700 Zyklen. Die stabilisierende Wirkung zweiwertiger Kationen (Mg^{2+}, Ca^{2+}) wird auf den reduzierten Gehalt an freiem Wasser und pH-Verschiebungen zurückgeführt, die parasitäre Abbaureaktionen mindern. Aufbauend auf diesen Ergebnissen erweitert die FeMnHCF-C/CKN/PNFE-Batterie die Designstrategie auf eine hochkapazitive, manganbasierte Kathode, die durch Eisensubstitution und kontrollierte Kristallinität stabilisiert ist. Elektrochemische und strukturelle Analysen bestätigen eine verbesserte Phasenstabilität und eine verringerte Degradation im Zusammenhang mit dem Jahn-Teller-Effekt. Die optimierte Vollzelle erreicht eine hohe spezifische Kapazität (~110 mAh kg^{-1}) und eine Energiedichte von ≈72 Wh kg^{-1}, die eine der höchsten bislang für LFABs berichteten darstellt, bei gleichzeitig guter Leistungsfähigkeit und Zyklenstabilität. Eine konzeptionelle Hochskalierungsstudie bestätigt das praktische Potenzial der entwickelten Systeme für stationäre Anwendungen wie die Heimspeicherung von Energie und bietet vielversprechende Vorteile in Bezug auf Sicherheit, Kosten und Umweltverträglichkeit. Die Ergebnisse dieser Arbeit belegen die Anwendbarkeit von LFABs für die stationäre Energiespeicherung und stellen einen wichtigen Schritt hin zu ihrer praktischen Nutzung dar.

Acknowledgments

I would like to express my heartfelt gratitude to the following people, without whom this work would not have been possible:

- **Prof. Aliaksandr Bandarenka** for giving me the opportunity to work in his group, starting with my MSc thesis and continuing during my PhD project. I am particularly grateful for the invaluable scientific input provided throughout the last years, as well as the productive working atmosphere, allowing me to work on exciting research directions with great creative freedom.
- **Prof. Peter Müller-Buschbaum** for agreeing to be my second examiner and for taking the time to evaluate this dissertation, as well as for originally introducing me to the field of battery research during my Bachelor's project.
- Our external collaborators**, Dr. Anatoliy Senyshyn, Dr. Sergei Vagin, Christine Benning, Bernardo Miller Naranjo, David Gryc, Dr. Mian Zahid Hussain, Prof. Oliver Lieleg,** and **Prof. Martin Elsner,** for their important contributions to this research and our collaborative publications. I would like to express special gratitude to **Dr. Anatoliy Senyshyn** and **Dr. Sergei Vagin** for their extended support with XRD data interpretation and organic synthesis, respectively. It was their expertise that made many important findings of this work possible.
- **Siegfried Schreier** for his assistance in taking SEM images and designing new setup components. I highly appreciate his technical expertise and support, which are essential to the whole group.
- **Tim Steeger and Johannes Sterzinger**, who joined our group as PhD students after finishing their MSc projects, which I advised. Besides the hard work during their MSc thesis phases, they supported me in many projects and contributed to multiple publications. I am proud and grateful that they continue our group's research on aqueous batteries.

- The many students I had the pleasure of advising for their BSc and MSc theses. Many thanks to the master students **Johannes Sterzinger, Yuejie Guo, Samuel Reiser, Aria Lozano Mojica, Tim Steeger, Felicia Weißbach, Prameswara Diposeno Hanggoro, Muhammad Haris Razaq Vance,** and **Muhammad Basil Minjai,** as well as the bachelor students **Luis Pretsch, Jeanette Plechinger, Sabrina Wager, Nykola Pommer, Tobias Grebien, Patrick Richter, Johannes Heiter, Andre Scholz, Steffen Abel,** and **Elisa Fill.** They carried out countless measurements and invested a lot of effort into the success of our joint projects.
- **Dr. Elena Gubanova** for guidance and mentoring during my whole time at the chair.
- **Dr. Xaver Lamprecht** for introducing me to the topic of aqueous batteries during my MSc thesis and for helping me get started as a PhD student.
- **Manuela Ritter** for taking care of all administrative issues and keeping the group running at all times.
- All other former and current ECS colleagues for their scientific contributions, for creating a great working environment, for countless fruitful discussions, and last but not least for their support with proofreading this thesis. I enjoyed every day in and outside the lab with them. Thus, I would like to express my deep gratitude to **Dr. Theophilus Kobina Sarpey, Dr. Kun-Ting Song, Dr. Felix Haimerl, Dr. Göktug Yesilbas, Dr. Thorsten Schmidt, Dr. Katarina Cicvaric, Peter Schneider, Rainer Götz, Christian Schott, Haiting Yu, Lewin Deville, Qingdian Liao, Susana Suttor, Huiyu Gai, Jian Zhou, Yixiao Zhang, Dima Blum, Wang Hu, Jinyang Li, Shuai Chen, Lilly Steil, and Da Lei.**
- Finally, I would like to thank my family, namely my parents Martina and Klaus, and my siblings Philipp and Fiona, as well as my partner, Maxi, for their unconditional love and support. I am forever grateful to them for enabling me to have all the opportunities and freedom to pursue my goals.

Related Publications

1. R.L. Streng, S. Vagin, Y. Guo, B. Rieger, A.S. Bandarenka. Identifying the charge storage mechanism in polyimide anodes for Na-ion aqueous batteries by impedance spectroscopy. *RSC Energy Advances* **2024**, 3, 874-882
2. R. Götz*, R.L. Streng*, J. Sterzinger*, T. Steeger, M.M. Kaye, M. Vitort, A.S. Bandarenka. All-solid-state Li-ion batteries with commercially available electrolytes: A feasibility review. *InfoMat* **2024**, 6, e12627
3. R.L. Streng, S. Reiser, S. Wager, N. Pommer, A.S. Bandarenka. A fast and highly stable aqueous calcium-ion battery for sustainable energy storage. *ChemSusChem* **2025**, 18, e202401469
4. R.L. Streng, T. Steeger, A. Senyshyn, S. Abel, P. Schneider, C. Benning, B. Miller Naranjo, D. Gryc, M.Z. Hussain, O. Lieleg, M. Elsner, A.S. Bandarenka, K. Cicvarić. A low-cost and high-energy aqueous potassium-ion battery. *Journal of Energy Chemistry* **2025**, 106, 523-531.
5. J. Sterzinger, R.L. Streng, S. Chen, R. Götz, W. Hu, J. Li, A.S. Bandarenka. Degradation mechanisms of Prussian blue analogs and state-of-the-art approaches for stability optimization: A review. *J. Phys. Chem. C* **2025**, 129, 7135-7153.
6. T. Steeger,* R.L. Streng,* A. Senyshyn, V. Dyadkin, X. Lamprecht, R. List, A. S. Bandarenka. Controlling the morphology and electrochemical properties of electrodeposited nickel hexacyanoferrate thin films. *ChemElectroChem* **2025**, 12, 2500073.
7. R.L. Streng, S. Reiser, A. Senyshyn, S. Wager, J. Sterzinger, P. Schneider, D. Gryc, M.Z. Hussain, A.S. Bandarenka. Sustainable high-performance aqueous batteries enabled by optimizing electrolyte composition. *Advanced Science* **2025**, 12, 2417587.

* The authors contributed equally to this work.

Conference Contributions

1. R.L. Streng, A.S. Bandarenka. High-performance aqueous batteries utilizing low-cost and sustainable bisalt electrolytes. *8th Baltic Electrochemistry Conference*. April 14-16, 2024, Tartu, Estonia. *Oral Presentation*
2. R.L. Streng, A.S. Bandarenka. Bisalt electrolytes for stable high-energy and high-power aqueous batteries. *GDCh Electrochemistry 2024*. September 16-19, 2024, Braunschweig, Germany. *Poster Presentation*
3. R.L. Streng, A.S. Bandarenka. Bisalt electrolytes for stable high-energy and high-power aqueous batteries. *ECS Student Chapter Munich, Energizing the Future – Battery and Hydrogen Research at TUM*. 24 September 2024, Garching, Germany. *Poster Presentation*

Advised Student Projects

Bachelor's Theses:

1. L. Pretsch. Characterization of Slurry-Coated Copper Hexacyanoferrate Cathodes for Aqueous Sodium-Ion Batteries. **2023**
2. J. Plechinger. Optimization of Copper Hexacyanoferrate Electrodes for Aqueous Sodium-Ion Batteries. **2023**
3. S. Wager. Optimizing Electrolyte Design for High-Performance Aqueous Batteries with Organic Anodes. **2023**
4. N. Pommer. Performance and Stability of Prussian Blue Analogue Based Cathodes for Aqueous Potassium-Ion Batteries. **2023**
5. T. Grebien. Organic Cathode Materials for Aqueous Sodium-Ion Batteries. **2023**
6. P. Richter. Sustainable and Hydrophilic Binder Materials for High-Performance Aqueous Sodium-Ion Batteries. **2024**
7. J. Heiter. Electrolyte Effects on the Performance of Model Aqueous Na-Ion Batteries. **2024**
8. A. Scholz. Investigating the Intercalation in Aqueous Electrolytes with the Quartz Crystal Microbalance. **2024**
9. S. Abel. Characterization of Manganese-Based PBA Electrodes in Aqueous Batteries. **2024**
10. E. Fill. Design Strategies for an Upscaled Na-Ion Aqueous Battery Prototype. **2025**

Master's Theses:

1. J. Sterzinger. Development and Optimization of a Prototype Aqueous Sodium-Ion Battery. **2023**
2. Y. Guo. Novel Organic Anode Materials for Aqueous Sodium-Ion batteries. **2023**
3. S. Reiser. Investigating the Performance of Aqueous Batteries Utilizing Various Metal Ions. **2024**

4. A. Lozano Mojica. A study of Organic and Organically Modified Cathode Materials for Aqueous Sodium-Ion Batteries. **2024**
5. T. Steeger. Exploring the Scalability of Electrodeposited Electrodes for Aqueous Na-Ion Batteries. **2024**
6. Felicia Weißbach. Developing an Upscaled Aqueous K-Ion Battery Prototype (working title). **Ongoing**
7. Prameswara Diposeno Hanggoro. Modeling the Impedance of Aqueous Alkaline and Alkaline Earth Metal-Ion Batteries. **Ongoing**
8. Muhammad Haris Razaq Vance. Synthesis and Optimization of Mn-rich Prussian Blue Analog Cathode Materials (working title). **Ongoing**
9. Muhammad Basil Minjai. Aqueous Batteries based on Mn-rich Prussian Blue Analog Cathodes and Organic Polyimide Anodes. **Ongoing**

Table of Contents

Abstract ... 2
Zusammenfassung ... 3
Acknowledgments ... 4
Related Publications ... 6
Conference Contributions ... 7
Advised Student Projects ... 8
Table of Contents ... 10
1. Introduction ... 13
1.1 The Sustainable Energy Transition ... 13
1.2 The Role of Energy Storage ... 15
1.3 Li-Free Aqueous Batteries (LFABs) ... 17
1.4 Materials for LFABs ... 20
1.4.1 Prussian Blue Analogs (PBAs) ... 20
1.4.2 Polyimides (PIs) ... 22
1.5 Motivation and Objectives of this Work ... 23
2. Theoretical Background ... 25
2.1 Underlying Electrochemical Principles ... 25
2.1.1 The Electrical Double Layer ... 26
2.1.2 Thermodynamic Background: Electrode Potentials ... 28
2.1.3 Charge Transfer Kinetics ... 31
2.2 Batteries ... 33
2.2.1 Components and Working Principle ... 33
2.2.2 Battery Electrolytes ... 34
2.2.3 Important Terms and Performance Metrics ... 38
2.2.4 Charge Storage Mechanisms ... 41
2.2.5 Battery Polarization Losses ... 44
3. Methods ... 49
3.1 Electrochemical Techniques ... 49
3.1.1 Cyclic Voltammetry ... 49
3.1.2. Galvanostatic Charging and Discharging ... 52
3.1.3 Electrochemical Impedance Spectroscopy ... 54
3.2 Structural Characterization Techniques ... 59
3.2.1 Scanning Electron Microscopy ... 59
3.2.2 X-Ray Diffraction ... 61

3.2.3 Fourier Transform Infrared Spectroscopy 62
3.2.4 X-Ray Photoelectron Spectroscopy 63
3.2.5 Inductively Coupled Plasma Mass Spectrometry 64
3.2.6 Brunauer-Emmet-Teller Surface Area Measurements 65
3.2.7 Shear Rheometry 65
4. Experimental 67
4.1 List of Chemicals 67
4.2 List of Materials 68
4.3 List of Software 68
4.4 List of Devices 69
4.5 Synthesis 70
4.5.1 PBA Cathode Materials 70
4.5.2 Poly(Naphthalene-4-Formyl-Ethylenediamine) Anode Material 71
4.6 Electrode Preparation 72
4.7 Electrochemical Measurements 73
4.7.1 Single-Electrode Measurements (Three-Electrode Setup) 73
4.7.2 Full Cells (Two-Electrode Setup) 74
4.7.3 Applied Techniques 75
5. Results and Discussion 76
5.1 Developing High-Performance Aqueous Batteries Based on Sustainable Materials by Electrolyte Optimization 76
5.1.1 Structural Characterizations 77
5.1.2 Cation Effect on the Performance of the CuHCF Cathode 83
5.1.3 Cation Effect on the Performance of the PNFE Anode 95
5.1.4 The CuHCF/KMC/PNFE Full Cell 105
5.2 Stabilizing Mn-Rich PBAs for Low-Cost and High-Energy Aqueous Batteries 112
5.2.1 Jahn-Teller Effect on MnHCF 112
5.2.2 Structure and Morphology of the Mn-rich PBA cathodes 114
5.2.3 Stabilizing the MnHCF Cathode 118
5.2.4 Electrochemical Performance of the Optimized FeMnHCF-C cathode in the CKN Electrolyte. 122
5.2.5 The FeMnHCF-C/CKN/PNFE Full Cell 123
5.3 Benchmarking the Performance of the Proposed Aqueous Batteries 126
6. Conclusion and Outlook 130
List of Abbreviations 136
Attached Publications 139
1. Identifying the Charge Storage Mechanism in Polyimide Anodes for Na-ion Aqueous Batteries by Impedance Spectroscopy. 139

2. All-Solid-State Li-ion Batteries with Commercially Available Electrolytes: A Feasibility Review. 148

3. A Fast and Highly Stable Aqueous Calcium-Ion Battery for Sustainable Energy Storage. 168

4. A Low-Cost and High-Energy Aqueous Potassium-Ion Battery. 180

5. Degradation Mechanisms of Prussian Blue Analogs and State-of-the-Art Approaches for Stability Optimization: A Review. 189

6. Controlling the Morphology and Electrochemical Properties of Electrodeposited Nickel Hexacyanoferrate Thin Films. 208

7. Sustainable High-Performance Aqueous Batteries Enabled by Optimizing Electrolyte Composition. 218

References 231

1. Introduction

1.1 The Sustainable Energy Transition

Fossil fuels have dominated the global energy economy since the first industrial revolution in the late 18th century.[1,2] Over the last 200-250 years, coal, natural gas, and oil have provided the necessary energy to power industrialization and rapid economic growth.[3] However, the strong reliance on these sources has resulted in significant environmental, economic, and geopolitical issues.[4] One of the main concerns linked to the burning of fossil fuels is the anthropogenic climate change driven by rising greenhouse gas emissions.[5] Overwhelming scientific evidence points towards a strong correlation between these emissions and rising global temperatures, extreme weather events, and other disruptions of ecological systems.[6,7,8] Consequences include rising sea levels, loss of biodiversity, increased frequency of droughts, storms, and wildfires, and severe impacts on agriculture and water resources.[9,10,11,12]

Besides climate and environmental impacts, the depletion of fossil fuel resources also presents a pressing challenge to energy supply security, with current forecasts predicting that oil production will become resource-limited by 2019 (already past) for conventional oil and by 2040 for all types of deposits.[13] As these resources are non-renewable, their extraction becomes increasingly costly and destructive.[14,15] In addition, the dependence on fossil fuels has contributed to volatile energy prices due to the uneven distribution of natural gas and oil deposits and geopolitical conflicts, as seen in recent fluctuations caused by the Russian-Ukrainian conflict.[16,17] Transitioning to renewable energy sources promises to mitigate these risks by providing a more stable, decentralized, and sustainable energy supply.

Another major concern associated with the burning of fossil fuels is air pollution. The combustion of coal, oil, and gas releases pollutants such as CO, carbon-containing aromatic carcinogens, sulfur dioxide, nitrogen oxides, and particulates, contributing to respiratory diseases, cardiovascular conditions, and premature deaths.[18,19] According to the World Health Organization (WHO), air pollution is responsible for millions of deaths each year, with a

significant portion linked to fossil fuel use.[20] By shifting to emission-free alternatives, public health and healthcare costs associated with pollution-related illnesses can be significantly reduced.[21]

Accordingly, global energy production has significantly transformed in recent years, rapidly shifting towards renewable and low-carbon energy sources. Driven by technological advances and supportive policies, renewable energy generation has become economically competitive with conventional fossil fuel-based power generation in many regions.[22] Countries worldwide have implemented programs to subsidize renewables, carbon pricing mechanisms, and strict emission regulations to encourage the adoption of green energy. Hence, the global share of renewable energy in electricity generation has steadily increased. Renewables account for around 70 % of electricity generation in Germany in 2025, with wind and solar as the leading technologies. **Fig. 1.1** shows the development of the net installed power of different sources in Germany, according to the Fraunhofer-Institute for Solar Energy Systems (ISE).[23]

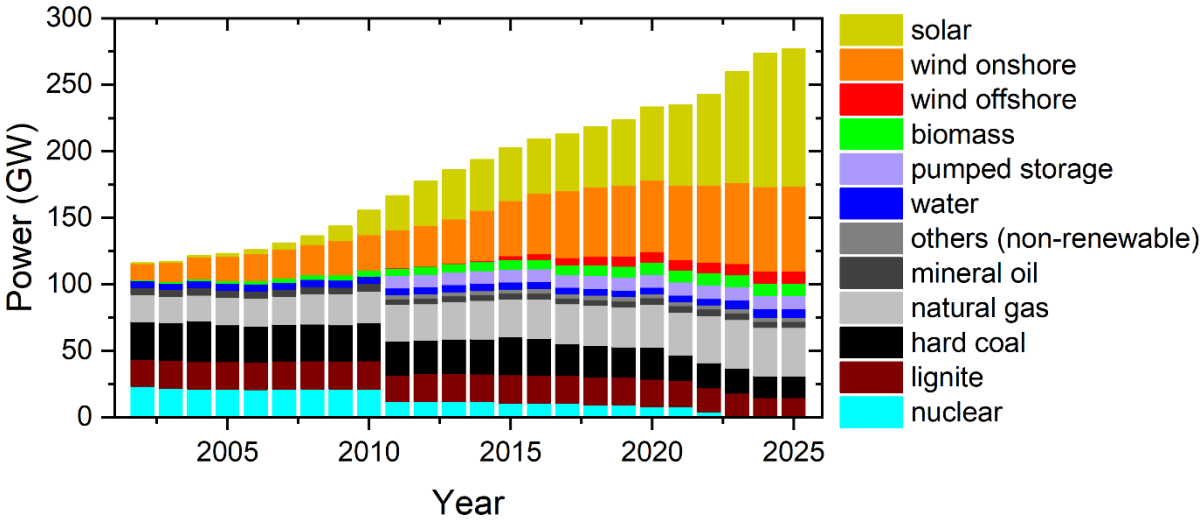


Fig. 1.1. *Installed power of different energy sources in Germany since 2002. Data taken from Fraunhofer ISE.*[23]

While nuclear power has vanished due to political decisions, the absolute power generation from lignite, hard coal, mineral oil, and other non-renewable sources has only declined slightly. In contrast, the relative share of renewable energy sources has increased drastically since 2002.

With 102.8 GW and 74.1 GW, respectively, solar and wind energy comprise over 65 % of the total installed power today, whereas biomass and water play a relatively minor role.

1.2 The Role of Energy Storage

As global energy generation shifts towards renewable sources to combat climate change, reduce the dependence on fossil fuels, and mitigate air pollution, energy storage is emerging as a critical component of the sustainable energy transition.[24] The primary renewable energy sources, namely wind and solar, are inherently intermittent, meaning they do not produce power continuously due to natural fluctuations.[25] Hence, the generation does not always align with the concurrent consumption. To illustrate this mismatch, **Fig. 1.2** shows Germany's public power generation and consumption during a representative week in 2025 according to data from the Fraunhofer ISE.[26]

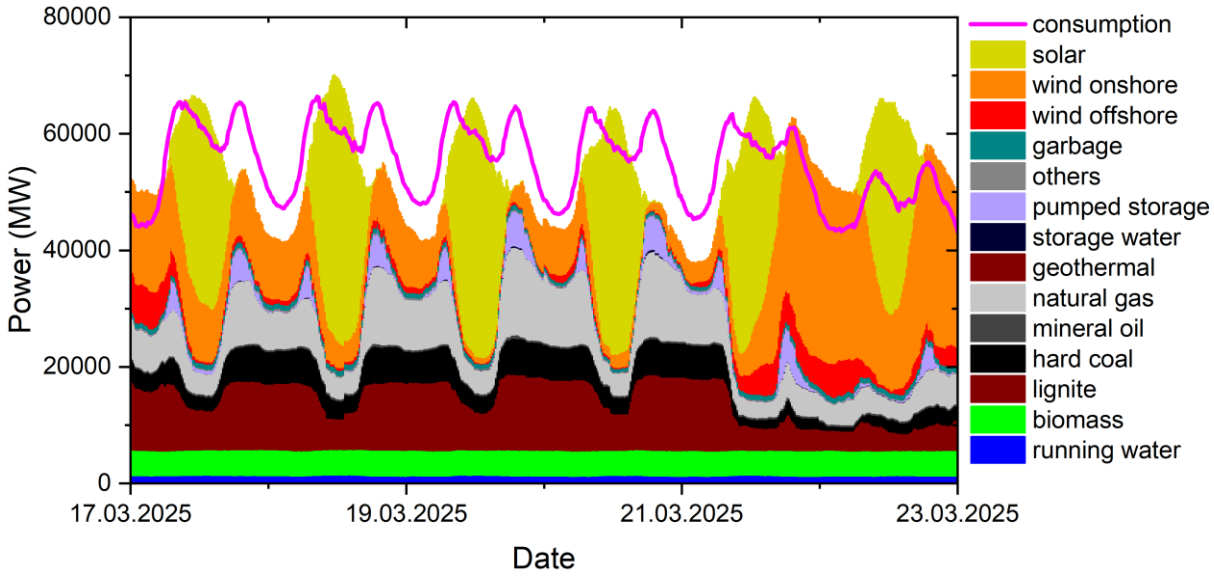


Fig. 1.2. *Public power generation from all sources and power consumption in Germany in week 12 of 2025. Date taken from Fraunhofer-ISE.*[26]

Solar power generation, in particular, experienced daily fluctuations of up to 45 GW between peak production at midday and zero production at night. Similarly, the power output from wind farms varied between around 2 GW and 40 GW throughout the week. Therefore, the power demand indicated by the magenta line in **Fig. 1.2** can often not be met by domestic generation

and needs to be compensated by cross-border electricity trade.[26,27] However, during peak production hours, generation regularly exceeds consumption by multiple GW.

Enhancing the efficiency of renewable energy technologies by storing and redistributing this excess energy is one of the key challenges of the energy transition. Large-scale energy storage solutions can maximize the utilization of installed power, reducing waste and costs.[28] Currently, the most established utility-scale electricity storage system is pumped hydroelectric storage (PHES).[29,30] Although it offers high capacities and scalability, as well as low operation and maintenance costs, there are several significant drawbacks to PHES. Most importantly, PHES power plants require suitable terrains with natural elevations and water resources. In addition, the high upfront capital investment and long construction times limit the expansion of this technology.[29,31] In Germany, the total installed pumped hydro-storage power output has stagnated at around 9-10 GW since 2011, as apparent from **Fig. 1.1.** However, calculations from the Fraunhofer-ISE show that 142 GW of electricity storage will be required by 2045.[32]

In recent years, large-scale stationary batteries have gained traction as one of the most promising energy storage technologies due to their exceptional efficiency, flexibility, and compactness.[33,34] Between 2014 and 2024, the net power capacity of public battery storage systems in Germany increased from 0.06 GW to 12.37 GW, corresponding to energy storage capacities of 0.08 GWh and 18.05 GWh, respectively.[23] Additionally, photovoltaic (PV) home-storage systems have been increasingly widely adopted to increase the self-consumption of private solar energy generation, with more than 85000 devices installed in Germany since 2013.[35] Besides balancing fluctuations in energy generation, batteries serve another essential purpose in the energy transition. Renewable electricity is generally produced in stationary power plants, such as wind and solar farms, whereas internal combustion engines enable mobile energy generation from fossil fuels. Batteries have been a key technology for providing electrical power to mobile applications, including personal vehicles, public transport, and transport of goods for many years.[36,37] As part of the energy transition, the global market share

of battery electric vehicles has been rising steadily, underlining the central role of batteries in the modern energy landscape.[38,39]

1.3 Li-Free Aqueous Batteries (LFABs)

Today's leading battery technology is the lithium-ion battery (LIB), based on Li^+ intercalation materials and organic electrolytes. This system dominates the markets for consumer electronics, electric vehicles, home storage, and large-scale storage.[40,41,42] With their high gravimetric and volumetric energy densities of 200-300 Wh kg^{-1} and 500-700 Wh L^{-1}, respectively, LIBs offer attractive properties for mobile applications.[43] Hence, nearly all state-of-the-art electric mobile devices and battery-electric vehicles employ them.[44] Technological maturity and falling retail prices have also allowed them to take a leading role among stationary storage systems.[45] Lead-acid batteries, which in 2013 held a market share of around 60 % for PV home-storage systems in Germany, have been almost entirely pushed out of the market by LIBs.[35] However, further adoption of LIBs for large-scale storage has sparked safety, supply, and sustainability concerns.[46,47] Various causes, such as internal short circuits, overcharging, overheating, mechanical damage, heat exposure, or manufacturing defects, can trigger a thermal runaway, leading to excessive heat, which ignites the flammable organic electrolyte.[48] Once the thermal runaway is initiated, the decomposition of typical cathode materials, like lithium cobalt oxide (LCO) or lithium nickel cobalt manganese oxide (NCM), releases oxygen, further fueling the fire and complicating extinction.[49]

Besides safety concerns, lithium resources are unevenly distributed across the globe, with major deposits located in Chile, Australia, Argentina, and China.[50] Hence, the reliance on lithium is associated with geopolitical dependencies and unsustainable mining, leading to market instabilities and temporary price surges.[51] The electric vehicle boom and the growing adoption of LIB-powered consumer electronics have amplified the competition for available lithium resources, further impacting the market.[52,53,54] As shown in **Fig. 1.3** (a), lithium production has increased by a factor of 8 since 2010 to meet the rising demand,[55] and although the price of

lithium carbonate has fallen in the last 3 years, the extreme surge in 2022 demonstrates its volatility (**Fig. 1.3** (b)).[56] Taking into account high insurance costs due to the aforementioned safety risks, the economic viability of expanding the capacity of large-scale LIBs for stationary storage by a factor of 10 or higher is likely limited. Accordingly, research into novel battery technologies has received growing attention in recent years since established alternatives, such as lead-acid, nickel-metal hydride, or sodium-sulfur batteries, suffer from their inherent drawbacks.[57,58,59]

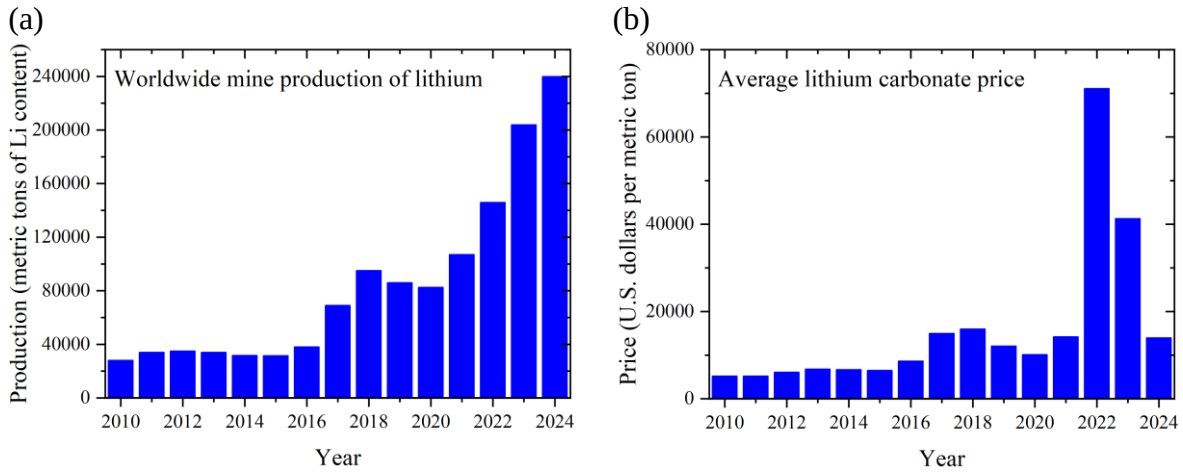


Fig. 1.3. *Development of the lithium market since 2010. (a) Worldwide mine production of lithium from 2010 to 2024. (b) The average price for battery-grade lithium carbonate from 2010 to 2024.*

Lithium-free aqueous batteries (LFABs), such as aqueous sodium-ion batteries (ASIB),[60] aqueous potassium-ion batteries (AKIB),[61] aqueous magnesium-ion batteries (AMIB),[62] aqueous calcium-ion batteries (ACIB),[63] or aqueous zinc-ion batteries (AZIB),[64] are among the most promising candidates to replace LIBs for large-scale applications. Na, K, Mg, and Ca are highly abundant in the Earth's crust and well distributed worldwide in the form of salt water (Na and Mg) and mineral rocks.[65] Therefore, their use is generally associated with fewer geopolitical dependencies and more sustainable mining than for Li. Furthermore, employing aqueous instead of organic electrolytes eliminates flammability and environmental risks, enabling safer battery production and operation.[60,61,62,63,66] Owing to these characteristics, aqueous batteries based on abundant alkali and alkaline earth metal ions hold great potential to

be economically competitive without the safety and sustainability concerns of LIBs or non-aqueous Li-based supercapacitors.[66,67] To fully realize this potential, these devices must meet relative manufacturing and operating costs similar to competing technologies. Since water electrolysis limits their typical operating cell voltage (1-2 V) and, thus, energy density (30-60 Wh kg^{-1}), the price per kWh and cycle must be minimized by employing inexpensive electrode and electrolyte materials and improving their cycle life.[68] At the same time, energy densities should be maximized within these inherent limitations. While stationary systems do not require the same compactness as personal electric vehicles or mobile devices, power plant installation and construction costs are still impacted by space requirements.[69] Here, established technologies like lead-acid batteries and supercapacitors can serve as benchmarks for desirable energy densities. State-of-the-art devices for both systems typically reach energy densities in the 20-40 Wh kg^{-1} range.[76,70,71]

Although aqueous batteries are mostly considered for stationary storage, their inherent characteristics also allow for other applications. The high ionic conductivity of water-based electrolytes and fast charge storage kinetics of typical electrode materials enable ultra-high rate capabilities, rendering LFABs a viable option for fast-response or high-power systems.[72] Research has demonstrated charging times of a few minutes to even seconds for aqueous batteries.[60,61,62,63,73,74] Typical applications requiring short charging times and moderate energy densities include public transport and grid stabilization. Currently, these systems mostly employ supercapacitors based on organic electrolytes and Li-ions.[75,76] For example, the successful implementation of a 32 Wh kg^{-1} supercapacitor by *Aowei* in *Chariot Motors* city buses demonstrates the feasibility of using lower-energy-density, high-power-density systems for public transport applications.[77,78] However, organic Li-ion supercapacitors have the same inherent drawbacks as LIBs. Based on these considerations, aqueous batteries featuring fast charging capability, long cyclability, and cost efficiency can be a viable alternative to existing energy storage technologies.[67,72,73] Accordingly, the choice and optimization of electrode and electrolyte materials should adhere to the outlined principles for LFAB design.

1.4 Materials for LFABs

1.4.1 Prussian Blue Analogs (PBAs)

Prussian Blue Analogs (PBAs) are a group of materials that have received growing attention for their capability to fulfill these requirements and their suitability for use in electrodes, particularly cathodes, for LFABs.[79,80,81,82,83] PBAs derive their name from the pigment iron hexacyanoferrate (FeHCF), commonly known as Prussian Blue (PB). They are generally represented by the chemical formula $A_xM_A[M_B(CN)_6]_y\square_{1-y}\cdot zH_2O$, where A is the guest cation, M_A and M_B are transition metals such as Mn, Fe, Co, Ni, or Cu (M_B is commonly Fe), and □ denotes a $Fe(CN)_6$ vacancy.[83] **Fig. 1.4** shows the typical structure of a PBA consisting of octahedral transition metal complexes. Most PBAs crystallize in the shown cubic *fcc* structure, but depending on the constituent transition metals and the guest ion content, other phases, including monoclinic, tetragonal, and rhombohedral, are possible.[84] M_A and M_B are interconnected by -C≡N- ligands, forming an open-framework structure with large interstitial sites, allowing for the intercalation of large guest ions from an electrolyte and fast ion insertion and transport kinetics.[79]

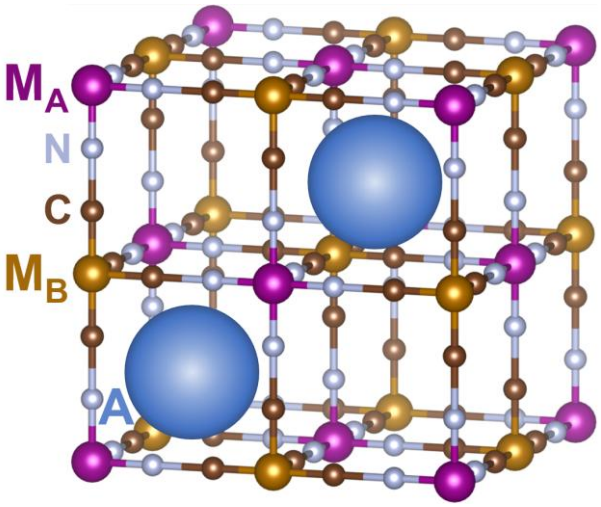


Fig. 1.4. *Typical open-framework crystal structure of Prussian Blue Analogs (PBAs). M_A and M_B are transition metals (M_B is commonly Fe) connected by -C≡N- linkers. A is the intercalated guest cation.*

As PBAs can be synthesized via a facile co-precipitation reaction from abundant precursor materials like carbon, nitrogen, iron, manganese, copper, and nickel, they are particularly well-suited for the specific requirements of LFABs.[85] Furthermore, their structural and electrochemical properties can be easily tuned due to their exceptional compositional flexibility.[79,80,82,85] PBAs are commonly categorized into two sub-groups based on their composition. The first group consists of materials like nickel hexacyanoferrate (NiHCF) and copper hexacyanoferrate (CuHCF), where M_A is electrochemically inactive, and only Fe (M_B) participates in redox reactions. The second group includes materials such as FeHCF, manganese hexacyanoferrate (MnHCF), and cobalt hexacyanoferrate (CoHCF), which can undergo two electrochemical transitions, utilizing both transition metal centers M_A and M_B.[79,80,81,82,83,85] NiHCF and CuHCF were first investigated as electrodes for aqueous batteries by Wessels et al. in 2011 and have since been used in various LFABs.[86,87,88,89,90,91] CuHCF, in particular, is commonly employed as a cathode material due to its favorable intercalation potential close to the upper limit of the electrochemical stability window (ESW) of water.[89,90] Both materials typically feature specific charge storage capacities of around 60 mAh g^{-1}.[86,87] However, optimized synthesis procedures have enabled higher capacities of 70-80 mAh g^{-1} by controlling the precipitation rate, defect density, and water content.[91,92] The main advantages of PBAs with only one active transition metal center are their high structural stability and exceptionally fast charge transfer kinetics, as they only undergo minimal lattice distortions upon reduction and oxidation.[93,94]

Nevertheless, the focus of research has shifted towards PBAs that can undergo two electrochemical transitions due to their higher specific capacities.[95,96] FeHCF, CoHCF, and MnHCF typically reach specific capacities of 100-140 mAh g^{-1}, about twice that of NiHCF and CuHCF.[97,98,99,100] It should be noted that despite its superior electrochemical properties, CoHCF can not be regarded as a suitable material for sustainable LFABs due to the relative scarcity of Co and the humanitarian and ecological concerns linked to Co-mining in the D.R. Congo.[101,102] Since Mn is comparatively abundant and MnHCF features a significantly higher redox potential

than FeHCF, it is considered one of the most promising PBA cathode materials for high-energy-density LFABs.[65,100,103,104,105,106] However, the limited cycle life caused by Mn dissolution in aqueous electrolytes and structural instability resulting from Mn^{III}-induced Jahn-Teller distortions (see **section 5.2.1**) remain significant challenges for this material.[107] Considerable progress in LFAB development was achieved by combining ion-doped MnHCF with highly concentrated water-in-salt electrolytes (WiSE). Mn substitution stabilizes the structure by suppressing harmful phase transitions, while a low free-water content in the electrolyte helps to reduce Mn dissolution. [105,108,109] However, the practicality of this approach is limited by the high cost of the salts used in WiSEs.[108] Therefore, finding alternative pathways to stabilize PBAs and integrating them into LFAB full cells is one of the main focuses of this work.

1.4.2 Polyimides (PIs)

Although the PBA manganese hexacyanomanganate (MnHCM) can be used as an anode material, PBAs are generally employed as cathodes due to their high intercalation potentials.[82,83,84,85] In fact, only a few suitable anode materials have been reported for LFABs besides NASICON-type titanium phosphates, which suffer from low intrinsic electronic conductivity and fast degradation.[110,111,112] Redox-active organic materials have emerged as promising anode materials for aqueous metal-ion batteries. Their key advantages include structural tunability, high theoretical capacities, and environmental friendliness.[113,114,115,116] Unlike metal-based anodes, most organic electrode materials do not contain any scarce or polluting elements, making them particularly attractive for developing sustainable and cost-effective batteries.[113,114,115,116] Among various organic anode materials, polyimides (PIs) have gained significant attention due to their excellent electrochemical stability, high redox activity, and reversible multi-electron transfer capabilities.[117,118] Polyimides are characterized by imide (-CO-N-CO-) functional groups integrated into an aromatic or conjugated polymer backbone, which provides robust structural integrity and enhances electronic conductivity.[117,118,119] Their redox activity arises from the reversible enolization of carbonyl groups (**Fig. 1.5**), enabling efficient charge storage and fast ion transport in aqueous electrolytes.

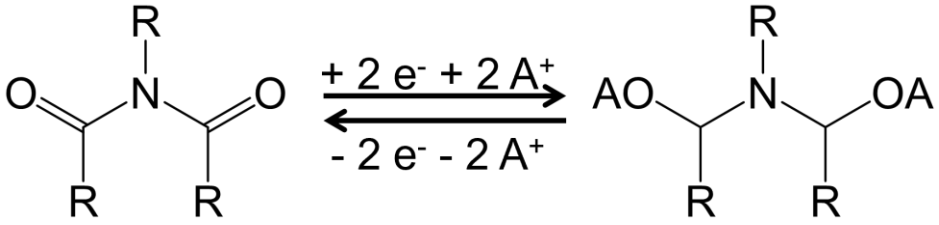


Fig. 1.5. *Structure and enolization mechanism of the characteristic imide group of polyimides. A is a monovalent guest cation (e.g., Na^+, K^+). In the case of divalent guest cations (e.g., Mg^{2+}, Ca^{2+}), the carbonyl groups of two neighboring imide units participate in the charge storage.*

A key advantage of polyimides is their ability to accommodate various alkali and alkaline earth metal ions, such as Na^+, K^+, Mg^{2+}, and Ca^{2+}, making them highly versatile for different aqueous battery chemistries.[120,121,122,123] Additionally, polyimides exhibit superior chemical and mechanical stability in aqueous environments, preventing degradation over extended cycling.[117,118] With their combination of sustainability, electrochemical performance, and cost-effectiveness, they are among the most promising LFAB anode materials. Hence, multiple PIs have been proposed as anode active materials for aqueous batteries. Particularly, poly(naphthalene-four-formyl-ethylenediamine) (PNFE) has been shown to provide high specific capacities of up to 130-150 mAh g^{-1}, long cyclability, and exceptional rate capability.[123,124,125] Since being first reported by Deng et al. in 2015, it has successfully been incorporated in various aqueous batteries based on Na^+, K^+, Mg^{2+}, and Ca^{2+} ions, underlining its great versatility.[120,121,122,123,124,125,126]

1.5 Motivation and Objectives of this Work

Accordingly, various high-performance LFABs combining PBA cathodes and (poly-)imide anodes have been reported in recent years.[108,120,121,124,125] One of the best-performing cells is an 80 Wh kg^{-1} AKIB consisting of a Fe-doped MnHCF cathode, a 22 mol kg^{-1} KCF_3SO_3, and a 3,4,9,10-perylene tetracarboxylic diimide (PTCDI) anode reported by Jiang et al. in 2019.[108] Other notable examples include an AMIB reported by Xia et al.,[120] an ACIB reported by Yao et al.,[121] and AKIBs reported by Du et al.[124] and Li et al.,[125] which all feature energy densities

in the 30-50 Wh kg^{-1} range. However, most high-performance LFABs rely on WiSEs like 22 mol kg^{-1} KCF_3SO_3, 30 mol kg^{-1} $KN(SO_2F)_2$, or 17 mol kg^{-1} $NaClO_4$.[68,108,124,125,126] While this approach is highly effective at stabilizing the electrode active materials and widening the ESW of the aqueous electrolyte, it employs high amounts of expensive and potentially harmful salts. Hence, the WiSE strategy often contradicts the core principles of LFAB design, which comprise sustainability, safety, and cost-efficiency.

Therefore, this work aims to develop high-performance LFABs using inexpensive materials with low environmental impact. By combining multiple optimization steps ranging from synthesis procedure to electrolyte composition, we propose new strategies for designing sustainable aqueous batteries. As mentioned above, PBAs and PIs can host various alkali and alkaline earth metal ions. We develop novel mixed-salt electrolytes by probing the influence of the guest cation species on the electrode potential, cycling stability, and charge storage mechanism of the anode and cathode. After discussing the underlying degradation and stabilization mechanisms, the electrochemical performance of both electrodes in the optimized electrolytes is investigated. Based on these results, two high-performance LFABs were assembled. **Section 5.1** focuses on a CuHCF/PNFE-based battery, which delivers ultra-high power densities, good cyclability, and competitive energy densities using a mixed-salt electrolyte based on KCl and $MgCl_2$. **Section 5.2** introduces a second LFAB optimized for high energy densities using a Mn-rich PBA cathode and a PNFE anode. After multiple strategies to mitigate the degradation of MnHCF due to the Jahn-Teller effect are explored, the electrodes are combined with a mixed-salt $Ca(NO_3)_2$ + KNO_3 electrolyte, and the resulting full cell is characterized. Finally, the batteries proposed in this work are benchmarked against state-of-the-art LFABs reported in the literature and other electrochemical energy storage devices.

2. Theoretical Background

This chapter provides the underlying theoretical principles required to understand the content of this work. It covers fundamental concepts of electrochemistry and batteries. After introducing the electrical double layer, the thermodynamic and kinetic basics of electrochemical systems are explained. This is followed by a description of components and operating principles of a battery, as well as key concepts like cell voltage, capacity, energy, (dis-)charge, and electrolyte considerations. Unless specifically noted otherwise, the primary references for this chapter will be the following standard textbooks on electrochemistry and batteries: C. H. Hamann and W. Vielstich, “Electrochemistry”[127], T. B. Reddy and D. Linden, "Linden’s Handbook of Batteries"[128], C. Daniel and J. O. Besenhard, "Handbook of Battery Materials".[129]

2.1 Underlying Electrochemical Principles

Electrochemistry describes the charge transfer between reactants, which are brought into contact with separated ionic and electronic conduction pathways. In most cases, this involves interfacial processes between a solid electron conductor and a liquid ion conductor, commonly denoted as the electrode and electrolyte. Electrochemical processes are characterized by converting electrical energy into chemical energy and vice versa, which is the underlying principle of all electrochemical energy storage and conversion. Generally, an electrochemical cell (EC) consists of two electrodes immersed in an electrolyte and connected by an external circuit. Batteries are a type of EC that converts energy by electrochemical oxidation and reduction (redox) reactions occurring at the electrodes. In this type of reaction, electrons travel through an external circuit as they transfer from one electrode to another. The electrode at which oxidation occurs is called the anode, while reduction occurs at the cathode. It should be noted that in rechargeable batteries, the designation of anode and cathode would thus change upon charging and is conventionally based on the discharge direction. In contrast to non-electrochemical spontaneous redox reactions, where the electron transfer occurs directly and only heat is produced, electrochemical devices are not subject to the thermodynamic limitations

of the Carnot cycle. Therefore, ECs, like batteries, typically have higher energy conversion efficiencies than, e.g., combustion and heat engines. ECs are classified into galvanic (or voltaic) cells and electrolytic cells. Galvanic cells generate energy through spontaneous redox reactions, whereas electrolytic cells rely on non-spontaneous reactions and require an external power source to drive the process. This section covers the phenomena and processes occurring at electrode-electrolyte interfaces in ECs.

2.1.1 The Electrical Double Layer

The electrical double layer (EDL) plays a central role in all electrochemical systems as it forms at the boundary between the electrode and the electrolyte, where the reactions occur. A polarized metal electrode distributes its excess charge evenly over its surface as the electric field inside the electronically conducting electrode vanishes. When it is immersed in an electrolyte, ions of opposite charge are attracted, and solvent dipoles are oriented to compensate for the imbalance. If interfacial charge transfer is omitted, a layer of charge forms in the metal and another in the electrolyte. This separation of accumulated charges establishes the so-called "electrical double layer", which is present in all electrochemical systems regardless of other processes.

Several models have been proposed since the initial description by Hermann von Helmholtz in 1853 to describe the structure of the EDL.[130] The Gouy-Chapman model was introduced in 1910 and is one of the earliest theories. It focuses on the diffuse layer, where ions are assumed to follow the Boltzmann distribution. According to this model, the electric potential decreases exponentially with the distance from the charged surface.[131,132] As the model treats the ions as point charges, they can be arbitrarily close to the electrode. Building on this, the Stern model introduced by Otto Stern in 1924 incorporates a more realistic approach by recognizing the compact Stern layer.[133] In this model, ions closest to the surface are tightly bound and form a rigid layer, while the ions in the diffuse layer behave as described in the Gouy-Chapman theory. The Stern model thus provides a more accurate representation of ion adsorption and the

potential decay within the EDL by explicitly separating the compact region from the diffuse one. This model was further modified by Grahame in 1947[134] and Bockris, Devanathan, and Müller in 1963,[135] taking into account the role of the solvent and specific adsorption. Building on this, contemporary models divide the EDL into three regions as shown in **Fig. 2.1.**

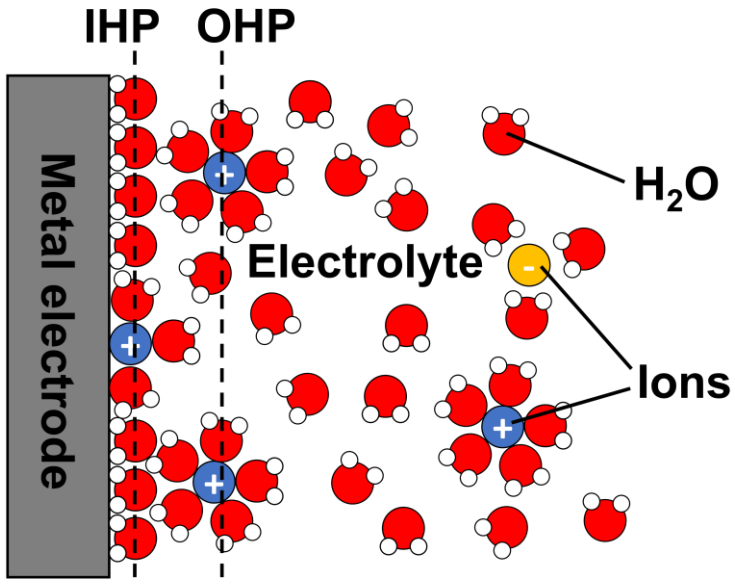


Fig. 2.1. *Schematic representation of the EDL at the electrode-electrolyte interface. The inner Helmholtz plane (IHP) marks the centers of specifically adsorbed ions or the oriented solvent molecules (in this case, H_2O). The outer Helmholtz plane (OHP) passes through the centers of non-specifically adsorbed ions that retain their solvation shells. Beyond the OHP lies the diffuse layer.*

The inner Helmholtz plane (IHP) passes through the centers of specifically adsorbed, (partially) desolvated ions or adsorbed solvent molecules in direct contact with the electrode surface. It lies closer to the electrode than the Outer Helmholtz Plane (OHP), which marks the closest approach of fully solvated ions. The IHP and the OHP define the boundaries of the Helmholtz layer toward the solid and the liquid phase, respectively. Beyond the OHP lies the diffuse layer as described by the Stern model. The potential displays two different linear drops from the electrode surface to the IHP and from the IHP to the OHP, and then drops exponentially in the diffuse layer, approaching the potential of the bulk electrolyte.

2.1.2 Thermodynamic Background: Electrode Potentials

The behavior of ions and electrons in ECs is governed by thermodynamics. Non-ionic solutions are described by the chemical potential μ_i, which is defined as the partial molar Gibbs free energy of the species *i*:

$$\mu_i = \left(\frac{\partial G}{\partial n_i}\right)_{T,P,j\neq i} = \mu_i^0 + R \cdot T \cdot \ln a_i \qquad \textbf{Eq. 2.1}$$

Here, μ_i^0 is the standard chemical potential and a_i is the activity of the species *i*. This expression represents the change in the Gibbs free energy *G* of a system when an infinitesimal amount of species *i* is added, keeping temperature *T*, pressure *P*, and the amounts of all other species constant. The chemical potential drives mass transport and chemical reactions, determining the direction in which these processes occur spontaneously. However, in electrochemical systems, the movement of charge carriers is typically influenced by concentration gradients and electric fields. Therefore, the Galvani potential Φ, which describes the inner electric potential of a phase, must also be considered. Φ denotes the electrostatic potential within the bulk of the phase, where it has a constant value, in contrast to the phase boundary, where it can vary as described in **section 2.1.1**. While the absolute value of Φ is practically not measurable, potential differences between phases play a critical role in ECs. The Galvani potential difference between two phases in electrochemical equilibrium, for example, a metal electrode (*s*) and a liquid electrolyte (*l*), is defined as

$$\Delta\Phi := \Phi^{(s)} - \Phi^{(l)}. \qquad \textbf{Eq. 2.2}$$

The electrical energy necessary to transfer 1 mol of ions or electrons of the species *i* with the charge $z_i \cdot e$ from an infinite distance into the bulk of a phase yields

$$\mu_{i,el} = z_i \cdot F \cdot \Phi, \qquad \textbf{Eq. 2.3}$$

with the Faraday constant F = 96485 C mol^{-1}. To account for both chemical and electrical contributions to the energy of a charged species, the electrochemical potential $\tilde{\mu}_i$ is defined as

$$\tilde{\mu}_i = \mu_i + \mu_{i,el} = \mu_i + z_i \cdot F \cdot \Phi \qquad \textbf{Eq. 2.4}$$

At thermodynamic equilibrium, the electrochemical potential of each mobile species must be the same in both phases:

$$\tilde{\mu}_i^{(s)} = \tilde{\mu}_i^{(l)} \qquad \textbf{Eq. 2.5}$$

If this condition is not met, a net flux of species *i* will occur from the phase with higher electrochemical potential to the phase with lower electrochemical potential. By combining **Eq. 2.1**, **Eq. 2.2**, and **Eq. 2.4**, the Galvani potential difference between two phases *s* and *l* can be written as

$$\Delta\Phi = \Phi^{(s)} - \Phi^{(l)} = \frac{1}{z_i \cdot F} \cdot \left[\left(\mu_i^{0,(s)} - \mu_i^{0,(l)}\right) + R \cdot T \cdot \ln\left(\frac{a_i^{(s)}}{a_i^{(l)}}\right)\right] \qquad \textbf{Eq. 2.6}$$

The Galvani potential difference between a solid and a liquid phase can not be measured directly. It would require an additional electrode in with a solid-electrolyte interface, where an EDL and an electrochemical equilibrium would form, impacting the potential. However, the reversible cell voltage *E* of an EC consisting of two half-cells at the anode and cathode sides, denoted as *A* and *C*, is a measurable quantity. It can be written as

$$E = \Delta\Phi_C - \Delta\Phi_A = E_C - E_A, \qquad \textbf{Eq. 2.7}$$

with the electrode potentials E_C and E_A of the cathode and anode, respectively. In electrochemical devices such as batteries or fuel cells, redox reactions take place at both electrodes. In generalized terms, the oxidation reaction at the anode, the reduction reaction at the cathode, and the overall redox reaction can be represented by the following equations.

$$\begin{aligned} &\text{Oxidation reaction:} && A \longrightarrow C + ze^- \qquad \textbf{Eq. 2.8} \\ &\text{Reduction reaction:} && B + ze^- \longrightarrow D \\ &\text{Redox reaction:} && A + B \longrightarrow C + D \end{aligned}$$

The change of the standard Gibbs free energy ΔG_0 of the overall redox reaction is directly related to the difference in their standard electrode potentials ΔE_0, which corresponds to the standard cell voltage of the EC.

$$\Delta G_0 = -z \cdot F \cdot \Delta E_0 = -z \cdot F \cdot (E_{C,0} - E_{A,0}) \qquad \textbf{Eq. 2.9}$$

Using **Eq. 2.6,** the so-called Nernst equation is obtained, which gives the equilibrium cell voltage ΔE_{eq} for non-standard conditions,

$$\Delta E_{eq} = \Delta E_0 + \frac{R \cdot T}{z \cdot F} \cdot \ln\left(\frac{a_C a_D}{a_A a_B}\right), \qquad \textbf{Eq. 2.10}$$

where a_i is the activity of the respective species, R is the universal gas constant, T is the absolute temperature in K, F is the Faraday constant, and ΔE_0 is the difference in standard electrode potential.

Table 2.1 shows the values for the standard electrode potentials of selected reactions. As the direct measurement of single absolute electrode potentials is considered practically impossible, they are measured against a reference. The most common reference potential is defined by the standard hydrogen electrode (SHE). 0 V vs. SHE corresponds to the potential at which the hydrogen evolution reaction (HER) occurs on Pt under a specific set of standard conditions ($c(H^+)$ = 1 M or pH = 1, $P(H_2)$ = 1 bar, T = 298.15 K). In real-world experiments, other more practical reference electrodes are employed. However, using the Nernst equation (**Eq. 2.10**), measured potentials can be transferred to any reference scale if the electrode potential of the used reference electrode is known.

Table 2.1. *Standard reduction potentials of selected electrode reactions at 25 °C in aqueous solution.*[127]

Reaction	E_0 **vs. SHE**
$F_2 + 2e^- \rightleftharpoons 2F^-$	2.89 V
$Cl_2 + 2e^- \rightleftharpoons 2Cl^-$	1.36 V
$O_2 + 4H^+ + 4e^- \rightleftharpoons 2H_2O$	1.23 V
$O_2 + 2H_2O + 4e^- \rightleftharpoons 4OH^-$	0.40 V
$AgCl + e^- \rightleftharpoons Ag + Cl^-$ (SSC)	0.22 V
$2H^+ + 2e^- \rightleftharpoons H_2$ (SHE)	0.00 V
$Zn^{2+} + 2e^- \rightleftharpoons Zn$	-0.76 V
$Mg^{2+} + 2e^- \rightleftharpoons Mg$	-2.36 V
$Na^+ + e^- \rightleftharpoons Na$	-2.71 V
$Ca^{2+} + 2e^- \rightleftharpoons Ca$	-2.87 V
$K^+ + e^- \rightleftharpoons K$	-2.94 V
$Li^+ + e^- \rightleftharpoons Li$	-3.04 V

2.1.3 Charge Transfer Kinetics

Thermodynamic considerations describe electrochemical systems under equilibrium conditions, but do not account for non-equilibrium states with current flow. In ECs, current flow is typically induced by external electrode polarization, forcing the system to adapt to a potential different from the equilibrium potential. The amount of charge ΔQ that is exchanged due to this so-called Faradaic current is directly linked to the transferred mass Δm via Faraday's law, where *M* is the molar mass of the transferred species.

$$\Delta Q = \frac{zF}{M}\Delta m \qquad \textbf{Eq. 2.11}$$

According to the Nernst equation (**Eq. 2.10),** this is achieved by changing the activities and, thus, concentrations of the educts and products of the redox reaction. Although electrode reactions can be as simple as the reduction of a metal ion and its incorporation into an electrode structure, these processes often include multiple steps, such as mass transport, adsorption, and

chemical reactions. The rate of an electrochemical process is often determined by the slowest step. The relationship between the current *I* and the overpotential η is described by the empirical Tafel equation

$$\eta = a \pm b \cdot \log(I) \qquad \textbf{Eq. 2.12}$$

where *a* and *b* are constants, and *b* is often referred to as the Tafel slope. Although the Tafel equation does not hold at very low overpotentials, it is applicable for various important electrochemical systems. It describes the current-voltage relationship of a unidirectional process. However, for a general electrode process, both the forward and backward directions have to be considered. Both are characterized by rate constants k_f and k_b, which can be expressed as

$$k_f = k_f^0 \cdot \exp\left(\frac{-\alpha z F E}{RT}\right) \qquad \textbf{Eq. 2.13}$$

$$k_b = k_b^0 \cdot \exp\left(\frac{(1-\alpha) z F E}{RT}\right) \qquad \textbf{Eq. 2.14}$$

with the transfer coefficient α and the electrode potential *E*. The rates of the forward and backward reactions can then be expressed as currents i_f and i_b,

$$i_{f/b} = z \cdot F \cdot A \cdot k_{f/b} \cdot C_{O/R}, \qquad \textbf{Eq. 2.15}$$

where *A* is the area of the electrode and C_O and C_R are the concentrations of the oxidized or reduced species, respectively. Under equilibrium conditions, the backward and forward currents are equal. In this case, the Nernst equation can be expressed as

$$E_{eq} = \frac{RT}{zF} \ln\left(\frac{k_f^0}{k_b^0}\right) + \frac{RT}{zF} \ln\left(\frac{C_O}{C_R}\right) = E_0' + \frac{RT}{zF} \ln\left(\frac{C_O}{C_R}\right) \qquad \textbf{Eq. 2.16}$$

where E_0' is defined as the so-called formal standard potential. In reversible systems E_0' is often used as a reference point and can be determined experimentally when $\frac{C_O}{C_R} = 1$. For battery electrodes, this normally corresponds to the equilibrium condition at 50 % state-of-charge (SOC). Furthermore, by combining **Eq. 2.13, Eq. 2.14,** and **Eq. 2.15,** the so-called Butler-

Volmer (**Eq. 2.17**) equation can be derived, which can describe the dependency of the electrical current *i* on the overpotential η.

$$i = i_0 \left\{ \exp\left[\frac{\alpha z F \eta}{RT}\right] - \exp\left[-\frac{(1-\alpha) z F \eta}{RT}\right] \right\} \qquad \textbf{Eq. 2.17}$$

where $i_0 = i_f$ is the exchange current, which corresponds to the rate of exchange of charge between oxidized and reduced species at zero net current.

2.2 Batteries

2.2.1 Components and Working Principle

As electrochemical devices, batteries convert chemical energy stored in the electrode active materials into electric energy using spatially separated redox reactions. Strictly speaking, batteries consist of one or more cells. However, the term "battery" is often used to describe either a single cell or a whole device. Generally, they are categorized into primary and secondary batteries. Primary batteries are assembled in a charged state and can only be discharged once. This work focuses on secondary batteries, which, in contrast, can be charged and discharged multiple times before they reach their end of life. While primary batteries still play a significant role in consumer electronics, only secondary cells are suitable for charge storage applications like electric vehicles, large-scale storage, and rechargeable mobile devices.[136,137,138,139,140,141] This section provides an overview of the active components of battery cells, as well as their working principle.

Every cell consists of three major components: The anode or negative electrode is oxidized during discharge and releases electrons into the external circuit. The cathode or positive electrode is reduced during discharge and takes up electrons from the external circuit. Both electrodes are immersed in the ionically conducting electrolyte, which transports the charge inside the cell. By separating the ionic and electronic conduction ways, the generated electric energy can be harvested by connecting a device to an external circuit. In the case of rechargeable batteries, the directions of the charge transfer processes can be reversed by applying an external

voltage. This drives electrons from the cathode to the anode, reducing the anode active material and oxidizing the cathode active material. By standard convention, the terms anode and cathode always refer to the role of the respective electrode during discharge and are not exchanged for recharging. **Fig. 2.2** shows a simple galvanic cell during both battery operation modes. The discharge process is shown in **Fig. 2.2 (a)**, and the charge process is shown in **Fig. 2.2 (b)**.

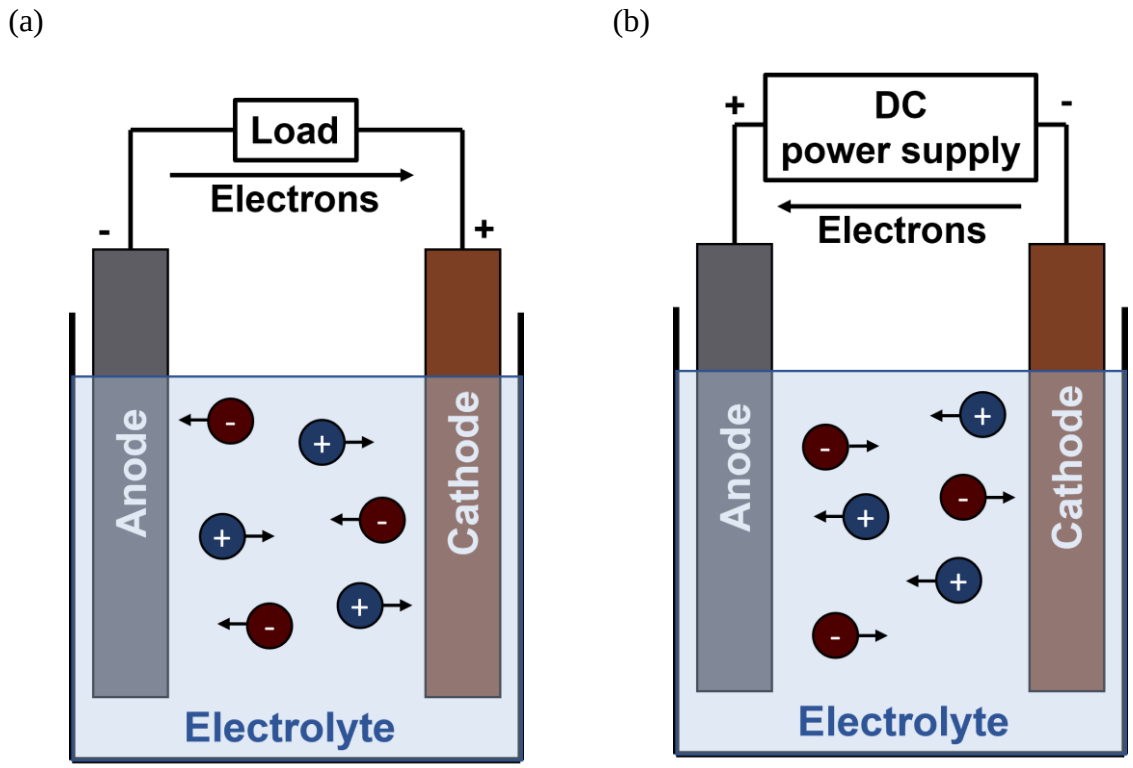


Fig. 2.2. *A simple galvanic cell during different modes of operation. (a) Discharge. (b) Charge.*

Besides anode, cathode, and electrolyte, batteries require further components. Due to the compact design of real cells, the anode and cathode are generally separated by a membrane soaked in electrolyte, which is referred to as the separator. Furthermore, the anode and cathode active materials are usually immobilized on electron-conducting substrates, called current collectors. Typical current collector materials include aluminum, copper, or other metal foils as well as carbon-based substrates.[142,143]

2.2.2 Battery Electrolytes

Electrolytes, serving as ionic conductors and electronic insulators, are a critical component of every battery system. Their properties determine the internal resistance, efficiency, and stability

of batteries. This section gives a short overview of the most relevant types of electrolytes used in state-of-the-art batteries, focusing mostly on aqueous electrolytes, which are the central component of the cells investigated in this work.

Organic non-aqueous electrolytes comprise organic solvents, such as cyclic carbonates (e.g., propylene carbonate, ethylene carbonate), linear carbonates (e.g., dimethyl carbonate, diethyl carbonate), or ethers (e.g., tetrahydrofuran, diglyme), and dissolved salts.[144,145,146] These electrolytes are essential to high-voltage LIBs and primary lithium metal batteries, offering a wide ESW (up to 4-5 V) and enabling high-energy-density cell compositions. However, as mentioned in the introduction, they pose challenges related to flammability, thermal instability, and moisture sensitivity. Continuous research into solvents, salts, and additives seeks to address these safety and performance issues.[147,148,149] The ionic conductivities of organic electrolytes typically range from 8 to 12 mS cm^{-2} at room temperature.[150]

Ionic liquids are a promising class of electrolytes due to their negligible vapor pressure, wide ESW, and non-flammability.[151] They consist of salts that are liquid at or near room temperature and are primarily used in high-temperature and high-voltage LIBs and lithium metal batteries.[152] Typical examples include imidazolium-based, pyrrolidinium-based, or piperidinium-based salts. Despite their thermal and chemical advantages, limitations such as high viscosity, high costs, and low ionic conductivity at moderate temperatures (≈1-10 mS cm^{-2}) have hindered widespread commercialization.[153]

Solid-state electrolytes (SSEs) have recently received rapidly growing attention as the primary component of all-solid-state lithium-ion batteries (ASSBs). The concept of ASSBs is still relatively novel, but it promises higher energy densities and better safety than conventional LIBs based on organic electrolytes. For a detailed discussion of the research progress and future of SSEs, the reader is referred to our review entitled "All-solid-state Li-ion batteries with commercially available electrolytes: A feasibility review".[154] However, a short overview is given below. SSEs can be classified into three types: Polymers, oxides, and halides (including

sulfides). Polymer electrolytes, typically polyethylene oxide (PEO) complexes, offer mechanical flexibility and high safety.[155] Oxide electrolytes, such as NASICON-type materials, perovskites, and garnets, are more rigid and brittle, while showing higher ionic conductivities.[156] Halides and particularly sulfides, such as LPSCl and LGPS, exhibit the highest ionic conductivities among the solid electrolytes but suffer from electrochemical instability.[157] However, the ionic conductivities of SSEs are generally low compared to their liquid counterparts, with the highest reported values in the range of 0.1 to 1 mS cm^{-2}.[154] In addition, interfacial challenges such as dendrite growth and ionic conduction need to be addressed to advance their adaptation into commercial devices.[158,159]

Aqueous electrolytes have been part of some of the earliest battery designs. They are classified by pH into alkaline, neutral/mildly acidic, and acidic. All aqueous electrolytes display high ionic conductivities compared to their non-aqueous counterparts. However, they suffer from the relatively narrow ESW of water, potentially leading to water splitting, which is associated with gas production (hydrogen and oxygen) and water loss.[66,67,68,160]

Alkaline electrolytes, typically concentrated NaOH or KOH, are frequently used in Zn-MnO_2, Ni-Cd, Ni-MH, Zn-air, and Ni-Zn batteries and are the most widely employed types of aqueous electrolytes.[161,162] It should be noted that KOH is often preferred over NaOH for the higher mobility of K^+ compared to Na^+ and the lower freezing point.[163] Alkaline electrolytes offer ionic conductivities of up to 800 mS cm^{-2} due to the enhanced cation conductance in high pH (close to 14) solutions.[164] Nevertheless, the charge and discharge kinetics of alkaline batteries are often limited by the relatively slow charge transfer kinetics of the electrode materials that are compatible with the high pH environment (e.g., Zn, Ni). Furthermore, the highly caustic nature of concentrated KOH requires corrosion-resistant materials to avoid harmful interactions between the electrolyte and metal parts of the battery, such as current collectors or casings.

The most relevant acidic electrolyte is sulfuric acid, which has a long history in battery technology and is still the standard electrolyte for lead-acid batteries.[70,71] At 300-500 mS cm^{-2},

depending on the concentration (typically 20 - 40 %), the ionic conductivity of acid electrolytes is slightly lower than for alkaline electrolytes, but still much higher than for non-aqueous solutions.[164] Acidic electrolytes are well-established, cost-effective, and offer a broad operation range regarding temperature and discharge rate. However, like alkaline electrolytes, their corrosive nature comes with material constraints and poses environmental and safety risks.

Therefore, aqueous batteries with neutral or mildly acidic electrolytes have received growing attention. As mentioned in the introduction, systems based on different alkali metal and alkaline earth metal cations are being explored.[61,62,63,64] Neutral electrolytes rely on salts such as chlorides, sulfates, nitrates, or perchlorates and are characterized by moderate conductivities (typically 100-300 mS cm^{-2}) compared to alkaline and acidic electrolytes.[165] Generally, the pH of these solutions is shifted to mildly acidic due to the presence of dissolved carbon dioxide in aqueous media. In addition, multivalent ions like Mg^{2+} and Ca^{2+} decrease the activity of OH^- ions in the electrolyte by undergoing a hydrolysis reaction with water (**Eq. 2.18**), further lowering the pH.[166]

$$M(H_2O)_n^{2+} \leftrightharpoons MOH(H_2O)_{n-1}^{+} + H^+ \text{ (with M = Mg or Ca)} \qquad \textbf{Eq. 2.18}$$

Currently, the main commercially available type of battery based on slightly acidic electrolytes is the Leclanché battery, which combines zinc chloride and ammonium chloride.[167] However, research has proposed a wide range of novel aqueous battery systems. So far, the practical adaptation of these batteries is impeded by the trade-off between performance and cost-efficiency.[67,68] WiSEs enable wider electrolyte ESWs, higher cell voltages, and improved cyclability by suppressing hydrogen and oxygen evolution reactions and the hydrolysis of electrode active materials due to the absence of free water in the electrolyte. However, they rely on high concentrations of expensive, often fluorinated, salts.[68,108,124,125,126] In contrast, conventional salt-in-water electrolytes with moderate concentrations of less expensive salts come at a lower cost, but without the beneficial effects on electrolyte and electrode stability.[67] One strategy to circumvent this trade-off is to use organic and inorganic electrolyte additives,

including sugar and metal oxides, as low-cost molecular crowding agents, mitigating side reactions and degradation.[168,169] However, the insulating nature of these additives generally lowers the electrolyte conductivity. Hence, this work explores novel pathways for high-performance and low-cost electrolyte design.

2.2.3 Important Terms and Performance Metrics

This section introduces the most essential terms and metrics that define battery performance. These metrics will be used throughout this work to evaluate and compare the assembled batteries with state-of-the-art devices.

Theoretical cell voltage and open-circuit voltage

The electrode active materials and electrolyte composition determine the theoretical cell voltage. It corresponds to the difference in standard electrode potential ΔE_0 between the anode and the cathode and is thus directly related to their difference in Gibbs free energy ΔG_0, as described in **section 2.1.2**. Experimentally, the theoretical cell voltage can be closely approximated by measuring the open-circuit voltage U_{OC} of the cell, which corresponds to the voltage across the EC when no current flows through the circuit.

$$U_{OC} \approx E_{0,Cathode} - E_{0,Anode} = -\frac{\Delta G_0}{zF} \qquad \textbf{Eq. 2.19}$$

Working voltage

When a load is applied, the cell voltage deviates from the open-circuit voltage. During discharge, the working voltage is lower than the theoretical cell voltage due to overpotentials caused by various polarization mechanisms, which are explained in detail in **section 2.2.5**. As the working voltage changes during discharging, batteries are commonly compared based on their average discharge voltage.

Specific Capacity

The capacity of a battery is defined as the amount of charge that can be obtained from the active materials during discharge. It is calculated by integrating the current $I(t)$ over the discharge time.

$$C = \int I(t) \cdot dt \qquad \textbf{Eq. 2.20}$$

For comparison, capacities are normalized to the mass of the full cell or the active material's mass. This so-called specific capacity is determined by the employed active materials. The theoretical specific capacity of an electrode material is given by the number of electrons *z* involved in the reaction per formula unit and the molar mass *M* of the formula unit.

$$c_{spec,theo} = \frac{z \cdot F}{M} \qquad \textbf{Eq. 2.21}$$

C-rate

The (dis)charge current is often given as a C-rate to compare the rate performance of different cells. For constant current (dis-)charging, the C-rate is defined as the current *I* normalized to the maximum capacity C_{max} of the electrode (**Eq. 2.22**). A C-rate of 1 C corresponds to a (dis-)charging time of 1 h.

$$C\text{-}rate = \frac{I}{C_{max}} \qquad \textbf{Eq. 2.22}$$

Due to mass transport limitations (see **section 2.2.5**), the capacity drops at higher C-rates (e.g., higher currents). The capacity retention at increasing rates is described by the so-called rate capability.

Energy and power density

The energy density, or specific energy, E_{spec} of a cell corresponds to the released electric energy normalized to the mass of either the full battery or the active materials. The energy, E_{dis}, released by discharging the battery with the current *I(t)* at the voltage *V(t)* is calculated by integrating the discharge curve.

$$E_{dis} = \int V(t) \cdot I(t)\, dt;$$

$$E_{dis} = \int V(C) dC \text{ (for constant current conditions)} \qquad \textbf{Eq. 2.23}$$

Energy density is one of the most important performance indicators for batteries since it takes into account both specific capacity and working voltage. Power density also plays a significant role. The power density P_{spec} at a specific C-rate is obtained by multiplying the average discharge voltage, $\bar{V}$, by the gravimetric current density, *i*:

$$P_{spec} = \bar{V} \cdot i \qquad \textbf{Eq. 2.24}$$

Energy storage devices are commonly compared in so-called Ragone plots, which show the energy density versus the power density on a double logarithmic scale. **Fig. 2.3** shows a Ragone plot with typical energy and power densities for different electrochemical energy storage devices, namely lead-acid batteries,[70,71] nickel-cadmium batteries (Ni-Cd),[170,171] nickel-metal-hydride batteries (Ni-MH),[172,173] Li-ion batteries,[37,41,42] supercapacitors,[174,175] and fuel cells.[176,177] These values refer to the mass of the whole device, including electrode additives, current collectors, contacts, separator, electrolyte, casing, and other battery components. However, as these mass contributions are difficult to quantify on a lab scale, it is common practice to report energy and power densities with regard to only the electrode active materials. Since the active materials make up around 40-60 % of the battery weight in real devices, the practically achievable values are significantly lower.[178]

Coulombic and Energetic Efficiency

The Coulombic efficiency (CE) is the ratio of discharge and charge capacity (C_{dis} and C_{charge}) for a specific cycle. Therefore, it is affected by parasitic currents stemming from side reactions between the electrode and the electrolyte or other cell components.

$$CE = \frac{C_{dis}}{C_{charge}} \qquad \textbf{Eq. 2.25}$$

In contrast, energy efficiency (EE) is determined by the ratio of discharge and charge energy (E_{dis} and E_{charge}), also taking the working voltage into account. It is, thus, additionally affected by voltage polarization due to charge transfer or mass transport losses.

$$EE = \frac{E_{dis}}{E_{charge}} \qquad \textbf{Eq. 2.26}$$

The CE and EE can be calculated for full cells or single electrodes. For cathodes, charging corresponds to oxidation, and discharging corresponds to reduction. For anodes, the directions are reversed.

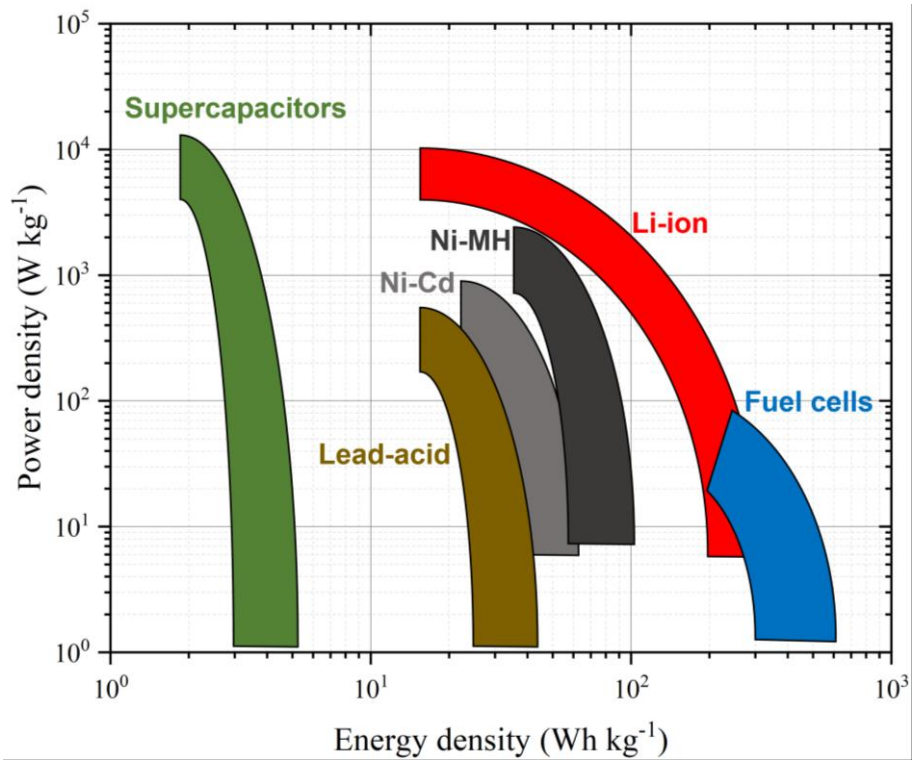


Fig. 2.3. *Ragone plot comparing typical energy and power densities for different electrochemical energy storage devices, including lead-acid batteries,*[70,71] *nickel-cadmium batteries (Ni-Cd),*[170,171] *nickel-metal-hydride batteries (Ni-MH),*[172,173] *Li-ion batteries,*[37,41,42] *supercapacitors,*[174,175] *and fuel cells.*[176,177]

2.2.4 Charge Storage Mechanisms

Although all batteries are based on the same general working principle, the underlying mechanisms governing charge transfer and storage differ significantly between materials. Most active materials store charge utilizing either intercalation,[179,180] conversion,[181,182] alloying,[183,184] double-layer capacitance,[185] pseudocapacitance,[186,187] or a redox flow mechanism.[188] The cells investigated in this thesis rely primarily on intercalation and pseudocapacitance, which are explained in more detail in this section.

2.2.4.1 Intercalation

PBAs belong to the class of intercalation-type materials.[79,80,81,82,83] In the intercalation mechanism, guest ions are reversibly inserted into the crystal lattice of a host electrode material without significantly disrupting its structure.[189] The host provides interstitial sites (e.g., layers

or tunnels in the lattice) that accommodate the ions with only minimal lattice expansion or bonding changes. The most famous example is the graphite anode commonly used in LIBs, where Li-ions are reversibly intercalated into the layered structure of graphite, which can be represented by **Eq. 2.27.**[190] During reduction, positively charged Li-ions from the electrolyte are inserted into the host structure, while electrons travel through the external circuit to reduce the host material, maintaining charge neutrality:

$$C_6 + x\mathrm{Li}^+ + x\mathrm{e}^- \rightleftharpoons \mathrm{Li}_x\mathrm{C}_6 \qquad \textbf{Eq. 2.27}$$

x ranges from 0 to 1 and corresponds to the relative occupation of available intercalation spaces. It is linked to the state of charge (SOC) and state of discharge (SOD), with $x = SOC = 1 - SOD$ for anodes and $x = SOD$ for cathodes. In generalized terms, the relative occupation *x* is represented by the ratio of occupied and available interstitial sites, which is analogous to the concentration of reduced and oxidized species in the host lattice. Therefore, the equilibrium electrode potential can be expressed in analogy to the Nernst equation (**Eq. 2.16**) by the Langmuir adsorption isotherm:[191]

$$E_{eq} = E_0' + \frac{RT}{zF}\ln\left(\frac{1-x}{x}\right), \qquad \textbf{Eq. 2.28}$$

where E_0' is the equilibrium potential at $x = 0.5$. The Langmuir adsorption isotherm describes the potential vs. charge curve for an ideal intercalation electrode at infinitesimal constant current (**Fig.2.4 (a)**).

In PBAs, one or both transition metal ions in the lattice structure can be reduced depending on the composition, while the open-framework structure with large interstitial sites shown in **Fig. 1.4** allows for hosting cations. **Eq. 2.29** gives a simplified representation of the intercalation of Na-ions into CuHCF, a PBA where only Fe-ions are active:[87]

$$\mathrm{Na}_1\mathrm{Cu}^{\mathrm{II}}[\mathrm{Fe}^{\mathrm{III}}(\mathrm{CN})_6] + \mathrm{Na}^+ + \mathrm{e}^- \rightleftharpoons \mathrm{Na}_2\mathrm{Cu}^{\mathrm{II}}[\mathrm{Fe}^{\mathrm{II}}(\mathrm{CN}_6)] \qquad \textbf{Eq. 2.29}$$

For PBAs with two active transition metal centers, such as MnHCF, an additional cation can be intercalated upon reducing both transition metal ions in the unit cell. The intercalation mechanism generally enables high reversibility and is governed by ion diffusion within the host lattice.[189]

2.2.4.2 Pseudocapacitance

Like most redox-active polymers, PIs store ions from an electrolyte reversibly.[192,193] Pseudocapacitive effects associated with this involve fast, reversible Faradaic charge transfer occurring at or near the polymer-electrolyte interface. It is enabled by the redox activity of functional groups like quinones, imides, or amines covalently bound to a polymer backbone, which undergo rapid oxidation and reduction without significant structural or phase changes.[194,195] Unlike intercalation, where charge is stored via bulk ion diffusion and often phase transitions, pseudocapacitive polymers store charge through **s**urface-confined or near-surface redox reactions, enabling high-rate performance.[196] Counter-ions from the electrolyte migrate into the polymer matrix to maintain electroneutrality during reduction or oxidation. This results in a quasi-linear potential vs charge relationship and capacitor-like behavior, as shown in **Fig. 2.4 (b)**, even though the process is Faradaic.[197] However, for crystalline and layered polymers, like most PIs, ion transport must occur throughout the bulk, and they show partially intercalation-like characteristics. Thus, the pseudocapacitive behavior in redox-active polymers often combines capacitive and battery-type charge storage properties. Hence, PIs display both fast kinetics and high specific capacities.[117,118,119]

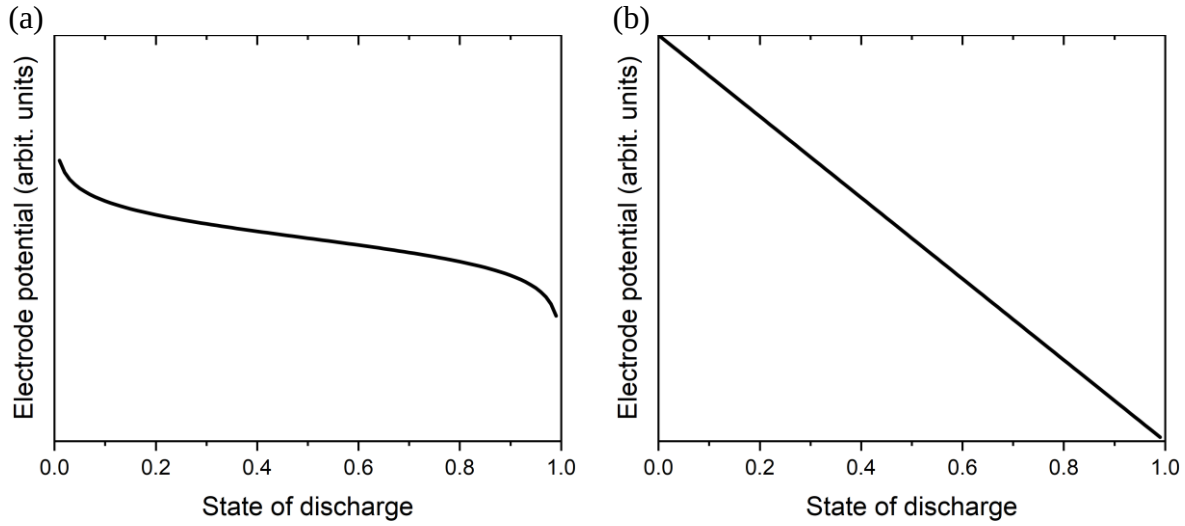


Fig. 2.4. *Discharge curves for ideal electrodes. (a) Intercalation-type behavior. (b) Capacitive behavior with linear potential vs. charge relationship.*

2.2.5 Battery Polarization Losses

2.2.5.1 Diffusion Polarization

In the above sections, the thermodynamics of electrode potentials, the kinetics of charge transfer, and the general working principle and charge storage mechanisms of batteries were introduced. We have discussed overpotentials caused by charge transfer limitations, which are described by the Butler-Volmer equation (**Eq. 2.17**). However, these considerations do not take the transport of charged ions to or from the electrode surface into account. The reaction rate and, thus, the current density is limited by the amount of mass that can be transported towards the surface within a certain time. Mass transport in electrolytes occurs through three different mechanisms: Convection, migration, and diffusion.[198] Convectional movement follows a mechanical flow field caused by an external stimulus, such as stirring or pumping. While this mechanism plays an important role in rotating electrode experiments and redox flow batteries, it is not relevant to this work.[199,200] When solid electrodes and a stagnant electrolyte are employed, convectional mass transport is not present. Migration is driven by electrostatic forces caused by electric potential gradients. Mobile ions in the electrolyte will migrate to compensate for electric fields.[201] This contribution vanishes for sufficiently high ion concentrations, as the

electric potential gradient in the bulk electrolyte is reduced to near zero since it is compensated close to the phase boundary.

Accordingly, the primary mass transport mechanism in batteries is diffusion. It occurs when concentration gradients are present in the electrolyte or the electrode. In intercalation-type electrodes, ions must move into the bulk of the active material film or particle after intercalation into an interstitial site close to the phase boundary. Since intercalation only occurs at the electrode-electrolyte interface, the ion concentration varies within the electrode. The movement of ions caused by the induced gradient in chemical potential follows Fick's law, which describes the particle flux J_i through a plane at a distance x and time t. It is proportional to the concentration gradient as represented by **Eq. 2.30**.[202]

$$J_i = -D\frac{\delta c_i}{\delta x} \qquad \textbf{Eq. 2.30}$$

where D is the diffusion coefficient, and c_i is the concentration of the species i. The solution of **Eq. 2.30** requires boundary conditions to be imposed, which depend on the specific battery composition and electrochemical techniques. The current i transported by diffusion of charged particles is given by **Eq. 2.31**.

$$i = zFD\left(\frac{\partial c}{\partial x}\right)_{x=0} = zFD\frac{c_{bulk}-c_{x=0}}{\delta_D} \qquad \textbf{Eq. 2.31}$$

where $\left(\frac{\partial c}{\partial x}\right)$ is the potential gradient between the interface region and the distance x. At $x = 0$, this term corresponds to the difference between the bulk concentration c_{bulk} and the concentration at the phase boundary $c_{x=0}$ divided by the thickness δ_D of the so-called diffusion layer. At high charge transfer rates, the concentration at the phase boundary approaches zero, and the diffusion current reaches its maximum. In this case, the overall electrochemical current is solely limited by the mass transport rate. The overpotential caused by mass transport η_{diff} can be expressed as a Nernstian term as it is linked to the ratio of $c_{x=0}$ and c_{bulk}.

$$\eta_{diff} = \frac{RT}{F}\ln\left(\frac{c_{x=0}}{c_{bulk}}\right) \qquad \textbf{Eq. 2.32}$$

Hence, the contribution of diffusion overpotentials increases drastically at high currents, whereas it can be neglected at low currents. Diffusion limitations can occur on both sides of the electrode-electrolyte interface within a battery. In the bulk electrolyte, the diffusivity and concentration of ions are generally too high to significantly limit the electrochemical current, since mass transport to the electrode surface is faster than the consumption. However, in the case of porous electrodes, as used in this work, local ion deficiencies can occur within the pores of the electrode film, where the diffusivity is much lower. Battery electrodes typically consist of porous matrices of solid constituents, including the active material, a conductive additive, and a binder. To maximize material utilization, a high specific surface area is required, which allows the electrolyte to contact as many active material particles as possible. However, the mass transport behavior in the pores and void spaces within these matrices differs significantly from the bulk electrolyte and is very complicated. As different pore sizes and positions are present in one electrode, current densities vary for different locations and depend on the physical structure of the electrode.[203,204]

Additionally, diffusion in the solid phase is usually significantly slower and can, therefore, lead to the build-up of depletion or excess regions close to the phase boundary. If the rate of the redox reaction is faster than the diffusion of ions from or to the interface, their surface concentration will significantly decrease or increase, depending on the direction of the reaction. Considering the case of reduction, the electrode potential will appear lower than the equilibrium potential as the concentration of intercalates rises close to the surface while the concentration of empty interstitial sites decreases. This leads to the build-up of a concentration gradient within the active material particle or film. If this concentration gradient reaches the center of the particle, the diffusion can be considered finite. In contrast, if the concentration gradient only expands through the outer layers of the particle, the diffusion is semi-infinite. The behavior of concentration gradients depends on the rate of concentration changes, which is expressed by Fick's second law.

$$\frac{\delta c}{\delta t} = D\frac{\delta^2 c}{\delta x^2} \qquad \textbf{Eq. 2.33}$$

The solution of **Eq. 2.33** requires a set of boundary conditions, which are determined by the measuring technique used and the expected discharge behavior of the electrode.

2.2.5.2 Ohmic Losses

In addition to concentration and charge transfer overpotentials, ohmic resistances must be considered for any current flow. In batteries, internal resistance mainly stems from the ionic conductivity of the electrolyte, contact resistances, and electron transport within the porous electrodes. The overpotential induced by the internal ohmic resistance R_U within the cell at the current I follows Ohm's law:

$$\eta_{ohm} = R_U \cdot I \qquad \textbf{Eq. 2.34}$$

2.2.5.3 Effect on (Dis)Charging Characteristics

The effect of each loss mechanism on the cell voltage and on the charge-discharge characteristics of the battery is schematically illustrated in **Fig. 2.5**.

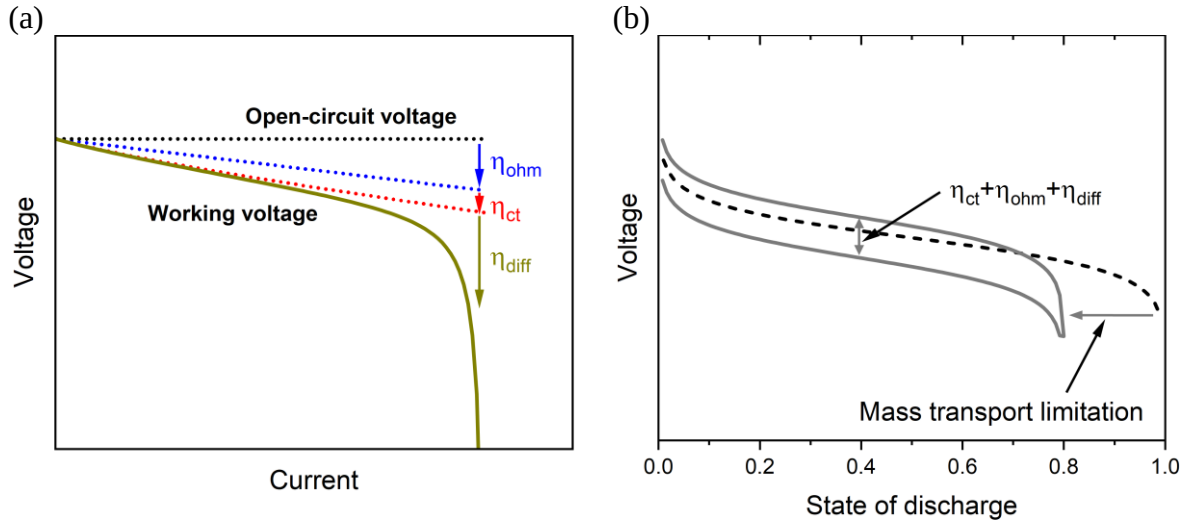


Fig. 2.5. *Effect of different loss mechanisms on battery discharge characteristics. (a) Current dependency of the contributions of the ohmic drop (η_{ohm}), charge transfer polarization (η_{ct}), and diffusion polarization. (b) Effect of the loss mechanisms on the charge and discharge characteristics. The dashed line represents an approximation based on the Langmuir isotherm for infinitesimal currents.*

As shown in **Fig. 2.5 (a)**, the ohmic polarization scales linearly with the current, while the charge transfer or activation polarization increases logarithmically. The mass transfer or

diffusion polarization rises sharply as the current approaches the limiting current. **Fig. 2.5 (b)** shows schematic charge and discharge curves of a cell at constant non-zero current conditions. The dashed line corresponds to an approximation based on the Langmuir isotherm for infinitesimal current. The total deviation of the working voltage from the equilibrium voltage is the sum of all overpotentials arising at the anode, cathode, and electrolyte.

$$\eta = \eta_{ct} + \eta_{ohm} + \eta_{diff}$$

$$= \eta_{ct,cathode} + \eta_{ct,anode} + \eta_{diff,cathode} + \eta_{diff,anode} + \eta_{ohm} \qquad \textbf{Eq. 2.35}$$

Additionally, mass transport limitations decrease the available capacity if mass transport from or to the electrode surface is too slow for the reaction to continue. For example, suppose intercalating ions occupy all interstitial sites close to the interface and are not transported fast enough. In that case, the potential will drop drastically as further intercalation is blocked.

3. Methods

This chapter covers the methods used to investigate the electrode materials and batteries in this work. First, an overview of the employed electrochemical techniques is given, while the second section focuses on structural characterizations.

3.1 Electrochemical Techniques

Electrochemical measurements are usually conducted in either two-electrode or three-electrode setups. If only two electrodes are used, i.e., in full cells, the measured current or voltage response is a combination of the anode and cathode contributions, which cannot be easily distinguished. In the three-electrode setup, one of the electrodes is effectively split into a reference electrode (RE) and a counter electrode (CE). This configuration allows for measuring and controlling the potential of the working electrode (WE) with regard to a constant reference. Accordingly, electrode potentials are reported against the used reference electrode or a standard scale such as SHE or RHE. While the voltage is measured between WE and RE, nearly all current runs between WE and CE. All techniques introduced in this section can be used to characterize either single electrodes in a three-electrode half-cell or full batteries. Like chapter 2, this section is primarily based on the following standard textbooks: C. H. Hamann and W. Vielstich, “Electrochemistry”,[127] T. B. Reddy and D. Linden, "Linden’s Handbook of Batteries",[128] C. Daniel and J. O. Besenhard, "Handbook of Battery Materials".[129]

3.1.1 Cyclic Voltammetry

Cyclic voltammetry (CV) is one of the most versatile electrochemical techniques, commonly used to gain information on redox processes, reaction mechanisms, and electrochemical kinetics. In a CV scan, the voltage that is applied to the electrode is linearly changed between two potential limits at a constant sweep rate. Typically, the chosen potential window is centered around the equilibrium potential of the investigated electrode. By varying the scan rate, CV can also be used to study the mass and charge transfer kinetics of the electrode reaction. The initial potential sweep is described by

$$E = E_i + \nu \cdot t, \qquad \textbf{Eq. 3.1}$$

where $\nu = \frac{dE}{dt}$ is the scan rate, t is the time, and E_i is the initial potential. For the reverse scan, the sign of ν is negative. CV scans are conventionally represented by plotting the current response i against the potential E in a cyclic voltammogram. When the potential is increased (anodic scan), a positive current is observed corresponding to an oxidation process, whereas a negative current occurs when the potential is subsequently decreased (cathodic scan). A typical CV curve with its most important features is shown in **Fig. 3.1.** As the applied potential approaches the equilibrium potential of a reversible out-of-sphere reaction from the left, the current starts to increase rapidly. After the peak current i_p^{ox} is reached at a potential E_p^{ox} that is slightly higher than the standard electrode potential, the current becomes limited by the depletion of reactants at the phase boundary and starts to decrease. During the cathodic scan, a rising negative current is observed as the potential approaches the equilibrium potential from the right. The negative peak current i_p^{red} is reached at a potential E_p^{red} that is slightly lower than the standard potential.

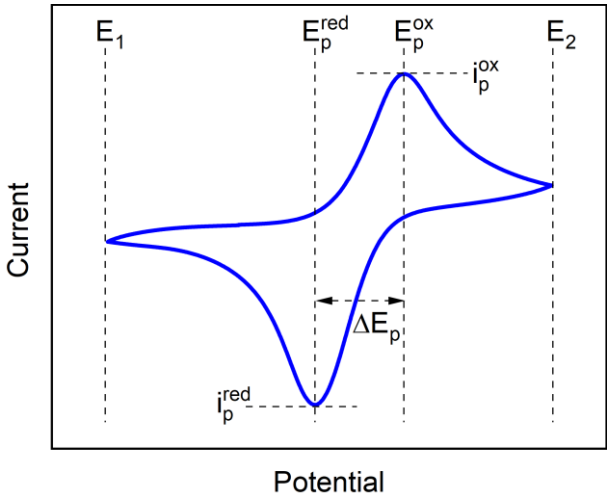


Fig. 3.1*. Typical cyclic voltammogram of a working electrode for an out-of-sphere reversible electrochemical reaction showing the current response to a potential sweep.*

If the selected potential window is sufficiently wide and no other reactions occur, the current approaches zero towards the potential boundaries E_1 and E_2 due to mass transport limitations. The depletion of reactants at the electrode-electrolyte interface leads to concentration gradients spreading into the electrolyte. Therefore, the diffusion rate at the interface decreases, limiting the observed current. The flux of ions to the electrode surface during CV can be described by combining **Eq. 3.1**, the Nernst equation (**Eq. 2.10**), and Fick's laws (**Eq. 2.30** and **Eq. 2.33**). The solution of the resulting complex differential equation is explained in detail by Ševčík[205] and T. Berzins[206] and will not be discussed further.

Cyclic voltammograms provide a rapid and informative assessment of the electrochemical processes occurring between the electrode and the electrolyte. However, they reflect the cumulative response of all Faradaic and non-Faradaic processes occurring within the system. This includes not only redox reactions but also capacitive currents associated with the formation of the electrochemical double layer. Moreover, CV can not distinguish between different redox processes that occur at overlapping potentials. Nevertheless, important features can be derived from a cyclic voltammogram. For battery electrodes, the peak potentials E_p^{ox} and E_p^{red} are centered around the half-charge potential $E_{1/2,}$ which serves as an experimental approximation of the standard electrode potential. The peak-to-peak separation ΔE_p allows for insights into overpotentials and kinetics, with a higher voltage polarization corresponding to higher losses. Furthermore, evaluation of the peak currents i_p^{ox} and i_p^{red} at different scan rates reveals important information on the kinetics of a specific electrode reaction. The relationship between the peak current i_p and the scan rate ν can be represented by **Eq. 3.2**, with the constant parameters *b* and *a*.[207]

$$i_p = b \cdot \nu^a \qquad \textbf{Eq. 3.2}$$

For fully surface-limited processes like adsorption, the value of parameter a is 1.0, meaning that the peak current scales linearly with the scan rate. This describes the ideal case in which the rate of the reaction is only limited by charge transfer. For mass-transport-limited reactions, like in various intercalation electrodes, a is closer to 0.5, and the linear relationship between

peak current and scan rate becomes weaker. For fully reversible, diffusion-controlled reactions, the cyclic voltammogram exhibits a symmetrical pair of peaks with constant peak-to-peak separation independent of the scan rate. In contrast, quasi-reversible processes yield more separated, less sharp peaks, with increasing peak-to-peak separation at higher scan rates.

3.1.2. Galvanostatic Charging and Discharging

Galvanostatic cycling (GC) is a standard electrochemical technique used to characterize the charge storage behavior of electrode materials, particularly in the context of batteries and supercapacitors. In this method, a constant current, commonly expressed as the corresponding C-rate, is applied to the half-cell or battery during the charging and discharging steps (**Fig. 3.2 (a)**), while the resulting potential or voltage response is recorded as a function of time (**Fig. 3.2 (b)**). The charge and discharge time can also be correlated with the exchanged charge, often expressed as capacity, by multiplying it by the current (**Fig. 3.2 (c)**). A positive current is applied until a pre-selected upper potential boundary is reached. Subsequently, a negative current of typically the same magnitude is applied until the lower potential limit is reached. This controlled-current approach allows for evaluating key performance metrics such as specific capacity, energy and power density, Coulombic efficiency, and cycling stability. Commercial systems usually employ a constant-current-constant-voltage (CCCV) (dis-)charging protocol, where the voltage is held at the upper limit until the current drops to a predefined value.

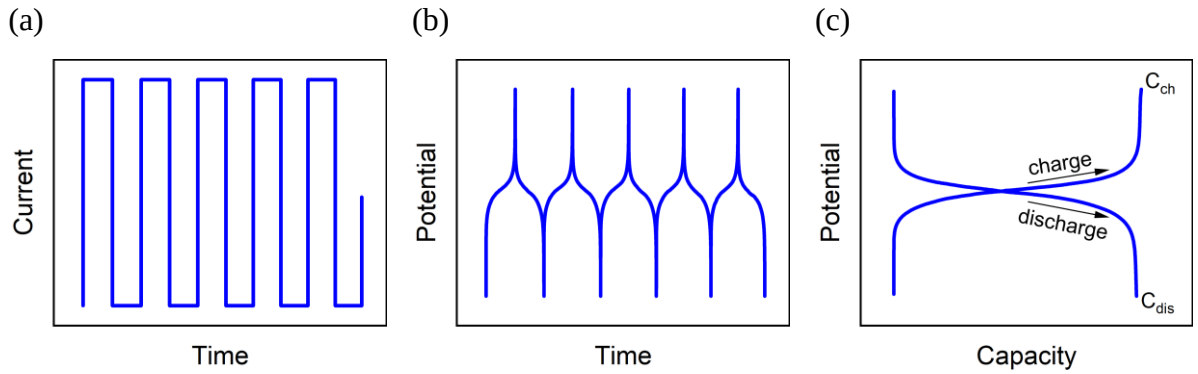


Fig. 3.2. *Schematic representation of galvanostatic cycling. (a) Applied current vs. time. (b) Resulting potential response vs. time. (c) Resulting charge-discharge curve for a typical galvanostatic cycle of a cathode (for an anode, the terms of charge and discharge would be reversed).*

The voltage–time profiles generated during GC provide insight into the underlying electrochemical processes. In battery-type materials, the discharge curve often resembles the Langmuir isotherm (**Eq. 2.28**), and distinct voltage plateaus appear as shown in **Fig. 2.4 (a)**, corresponding to two-phase reactions or well-defined redox couples. These plateaus are associated with the intercalation or conversion reactions of the active material and indicate stable potential regions where redox processes occur at constant voltage. In contrast, materials exhibiting capacitive or pseudocapacitive behavior typically produce sloped voltage profiles without clear plateaus, as shown in **Fig. 2.4 (b)**. This is characteristic of surface-controlled charge storage processes or fast, reversible redox reactions occurring over a range of potentials. The shape and symmetry of the charge–discharge curves can also reveal important information about the kinetics and reversibility of the electrochemical processes. Ideal capacitive systems display nearly linear and symmetric voltage profiles between the charge and discharge steps, while deviations can indicate polarization effects, resistive losses, or degradation phenomena. Repeated GC over many cycles is used to assess the long-term stability and capacity retention of electrode materials under realistic operating conditions.

3.1.3 Electrochemical Impedance Spectroscopy

The current response to a potential sweep that is measured in CV and the potential response to constant current conditions that is measured in GC are governed by the properties of the electrolyte and the electrode-electrolyte interface. Whereas resistance corresponds to the opposition of a system to a direct current, impedance describes the opposition to an alternating current. The impedance of an electrochemical cell can be probed directly via electrochemical impedance spectroscopy (EIS). By evaluating the impedance over a wide frequency range, typically from mHz to MHz, EIS can be used to distinguish processes occurring on different time scales. This allows for isolating different steps of an electrode reaction, like double layer charging, diffusion, adsorption, and charge transfer.[208,209,210,211] In an EIS measurement, a small sinusoidal voltage or current signal superimposed on a constant bias potential or current is applied to the system. As only potentiostatic EIS is used in this work, the following introduction, based on the textbooks by A. Lasia[208] and M.E. Orazem,[211] will focus on this method, in which the current response to a voltage signal is measured. The applied sinusoidal potential signal is represented by

$$E(t) = E_0 \cdot \sin(\omega \cdot t), \qquad \textbf{Eq. 3.3}$$

where E_0 is the amplitude (typically 5 mV to 10 mV), ω is the frequency in radians/s ($\omega = 2\pi f$, with the frequency f), and *t* is the time. The resulting current wave is also sinusoidal, but has a different amplitude I_0 and a phase shift ϕ as shown in **Fig. 3.3 (a)**.

$$I(t) = I_0 \cdot \sin(\omega \cdot t + \phi) \qquad \textbf{Eq. 3.4}$$

The impedance *Z* of the system corresponds to the ratio of the current response and the potential perturbation, similar to Ohm's law. Using Euler's formula, it can be expressed as a complex function of the phase shift.

$$Z(\omega) = \frac{E(t)}{I(t)} = Z_0 \exp(j \cdot \phi) = Z_0(\cos\phi + j \cdot \sin\phi) = \mathrm{Re}(Z) + j \cdot \mathrm{Im}(Z) \qquad \textbf{Eq. 3.5}$$

with $j^2 = -1$ and $Z_0 = \frac{E_0}{I_0}$

Hence, the overall impedance can be split into a real part, Re(Z), and an imaginary part, Im(*Z*). By plotting -Im(Z) against Re(Z), the so-called Nyquist plot (**Fig. 3.3 (b)**) is obtained.

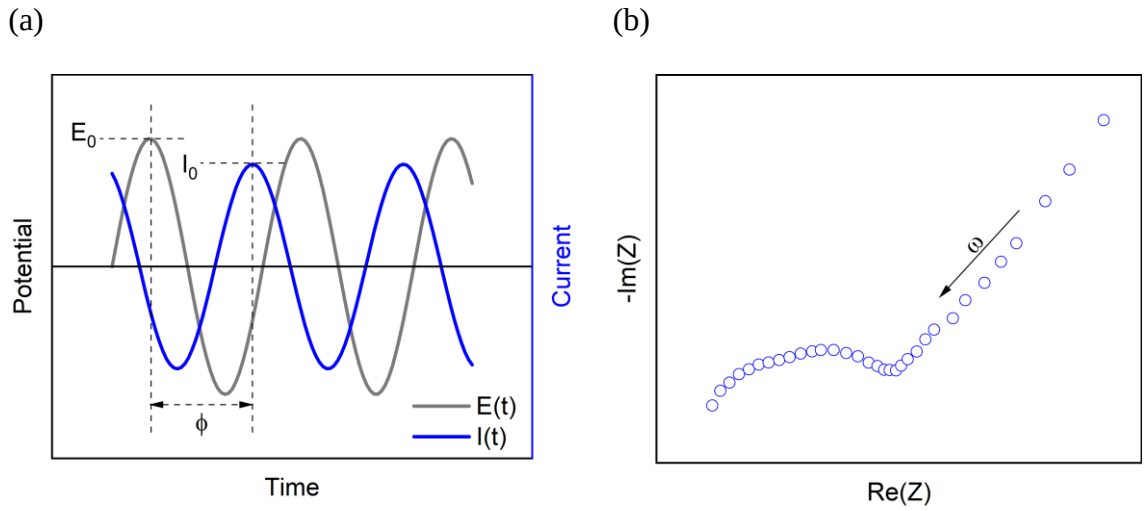


Fig. 3.3. *Electrochemical impedance spectroscopy. (a) Waveforms of the sinusoidal potential signal and current response. (b) Nyquist plot showing a typical impedance spectrum of a complex electrochemical system.*

Purely resistive systems lead to a single point on the x-axis of the Nyquist plot corresponding to their ohmic resistance. However, both resistive and reactive loads are involved in electrochemical cells, and the recorded spectrum becomes more complex. Accordingly, interpreting the impedance response requires fitting the data to an electrical equivalent circuit (EEC) consisting of classical electrical network passive elements and representing the electrode processes in a physical way. In an EEC, different impedance elements accounting for resistance, kinetics, and capacitances are combined in series or parallel configurations. As for DC resistances, the total impedance for multiple elements connected in series corresponds to their sum, while the inverse of the total impedance of elements connected in parallel is given by the sum of their inverse values. **Table 3.1** lists the most important circuit elements and their respective impedances. The behavior of each element in a Nyquist plot is shown in **Fig. 3.4.**

Table 3.1. *Important equivalent circuit elements and their respective impedances.*

Circuit element	**Impedance**
Resistance, *R*	$Z_R = R$
Capacitance, *C*	$Z_C = \frac{1}{Cj\omega}$
Constant phase element, *CPE*	$Z_{CPE} = \frac{1}{P(j\omega)^n}$
Warburg, *W* (semi-infinite diffusion)	$Z_W = \frac{\sigma}{(j\omega)^{1/2}}$
Warburg short, W_s (finite diffusion, transmissive boundary)	$Z_{W_s} = \frac{\sigma}{(j\omega)^{1/2}} \tanh(B(j\omega)^{1/2})$
Warburg open, W_o (finite diffusion, reflective boundary)	$Z_{W_o} = \frac{\sigma}{(j\omega)^{1/2}} \coth(B(j\omega)^{1/2})$
Inductance, *L*	$Z_L = j\omega L$

The Nyquist plot of a capacitance C is a vertical line along the imaginary axis approaching the real axis at high frequencies. Capacitances are commonly used to model the electrical double layer introduced in **section 2.1.1.** In many electrochemical systems, the double layer does not behave like an ideal capacitor for various reasons, which are still under debate in the literature. In these cases, the EDL is often modeled using a constant phase element, *CPE*, with an adjustable parameter $n \leq 1$, which indicates how close the CPE is to an ideal capacitor. For $n = 1$, the CPE behaves like a pure capacitor, while for $n = 0$, the CPE acts as a pure resistor. Typically, *n* assumes values between 0.8 and 1.0, leading to a sloped line in the Nyquist plot.

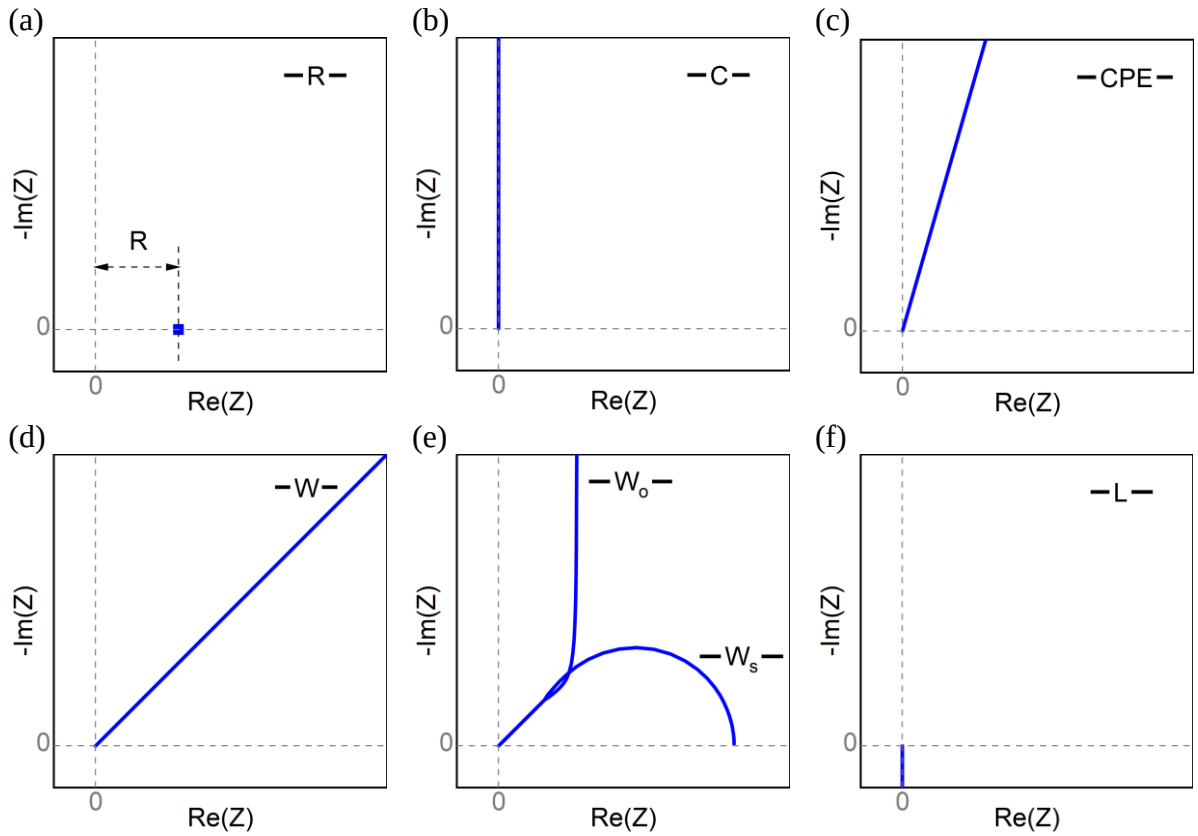


Fig. 3.4. *Nyquist plots of the passive equivalent circuit elements. (a) Resistance. (b) Capacitance. (c) Constant phase element. (d) Warburg impedance for semi-infinite diffusion. (e) Warburg impedance for finite-length diffusion with a transmissive boundary (Warburg short, W_s) and a reflective boundary (Warburg open, W_o). (f) Inductance.*

The Warburg impedance describes diffusion behavior. As introduced in **section 2.2.5**, there are two types of diffusion based on the thickness of the diffusion layer: Semi-infinite and finite-length diffusion. Semi-infinite diffusion is represented by the Warburg element *W*, with the Warburg coefficient σ. In the Nyquist plot, the Warburg impedance for semi-infinite diffusion corresponds to a diagonal line forming a 45° angle with the x-axis. Finite-length diffusion is either modeled by a Warburg short W_s or a Warburg open W_o element, with $B = \frac{\delta}{D^{1/2}}$, where δ is the thickness of the diffusion layer and *D* is the diffusion coefficient. W_s describes finite-length diffusion with a transmissive boundary, whereas W_o refers to a reflective boundary. Inductances are not commonly observed in electrochemical cells, but their impedance contribution is listed for completeness. Generally, any impedance spectrum can be fitted by

combining the equivalent circuit elements listed above in more than one arrangement. Therefore, the selected models must have a clear physical meaning.

The general equivalent circuit model for an electrochemical cell consisting of an electrode immersed in a liquid electrolyte was proposed by Randles in 1947 and is still used today.[212] The impedance of the ionically conducting electrolyte is purely resistive and is therefore described by an ohmic uncompensated resistance R_U. Assuming that no Faradaic processes occur, the current signal at the interface will be entirely governed by the electrical double layer. As the ideal EDL behaves like a plate capacitor, it can be described by the double layer capacitance C_{dl}, which is connected in series with the electrolyte resistance. In this case, the Nyquist plot would yield a vertical line, which is shifted to the right by the magnitude of R_U. A CPE is used instead of a simple capacitor for the non-ideal behavior of the EDL. However, in electrochemical systems, redox reactions occur, causing a Faradaic current *i* to occur in parallel to the capacitive charging of the double layer. This current is affected by the electrode potential, the concentration of reduced and oxidized species at the surface, and the coverage of adsorbents at the electrode surface. Hence, the contribution of this "leaking" of charge in the double layer is generally complex, depending on the boundary conditions imposed by the specific reaction. In the simplest case, where only the effect of the kinetics and the mass transport play a significant role, a charge transfer resistance $R_{ct} = \frac{\partial i}{\partial E}$ to account for the contribution of the potential and a Warburg element to account for the contribution of diffusion are added to the model. This yields the Randles equivalent circuit shown in **Fig. 3.5 (a).** The resulting Nyquist plot is depicted in **Fig. 3.5 (b)**. The parallel combination of the double layer capacitance and the charge transfer resistance leads to a semicircle, which is shifted to the right by the uncompensated resistance and has a diameter equal to the magnitude of the charge transfer resistance. At lower frequencies, the 45° tail corresponding to the Warburg impedance is observed.

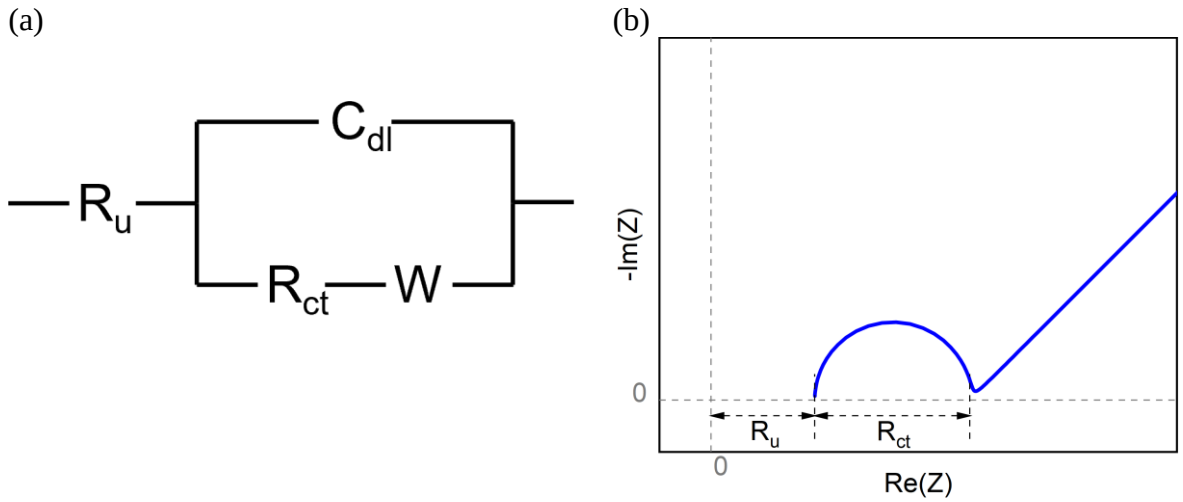


Fig. 3.5. *Typical impedance behavior of an electrochemical cell. (a) The Randles equivalent circuit for an electrode-electrolyte interface, including the uncompensated electrolyte resistance R_u, the double layer capacitance C_{dl}, the charge transfer resistance R_{ct}, and the Warburg impedance W. (b) Nyquist plot of the schematic impedance spectrum of the Randles circuit.*

Various battery electrodes display this type of behavior. However, the impedance associated with the Faradaic processes usually consists of a combination of several circuit elements connected in series or parallel, as most electrode reactions feature additional adsorption and desolvation steps. In this case, multiple overlapping semicircles are observed in the Nyquist plot as shown in the exemplary spectrum in **Fig. 3.3 (b).** Therefore, finding a physical electrical equivalent circuit model is essential for interpreting the data meaningfully. In summary, EIS is a non-destructive electrochemical method that enables the investigation of reaction mechanisms, degradation, and other processes.

3.2 Structural Characterization Techniques

3.2.1 Scanning Electron Microscopy

Scanning electron microscopy (SEM) is a powerful characterization technique widely used for investigating the surface morphology, microstructure, and compositional properties of materials at high spatial resolution.[213] This section briefly introduces the working principle and

application of SEM based on the textbooks by J.I. Goldstein et al.[214], L. Reimer,[215] and A. Ul-Hamid.[216]

As shown in **Fig. 3.6**, SEM operates by directing a focused beam of high-energy electrons, typically in the range of 1–30 keV, onto the surface of a sample. As the electron beam is moved over the surface of the sample in a raster, it interacts with the atoms in the sample, generating different signals that can be detected and analyzed. The primary signals used for imaging are secondary electrons and backscattered electrons. Secondary electrons are low-energy electrons ejected from the outer shells of atoms due to inelastic scattering. Because they originate from the topmost surface layers, secondary electrons are highly sensitive to surface topography, allowing for the generation of detailed images that reveal fine structural features at the nanometer scale. On the other hand, backscattered electrons result from elastic scattering of the incident beam and are reflected back from deeper within the material. Back-scattered electron imaging provides compositional contrast because heavier elements backscatter electrons more efficiently, appearing brighter in the image.

In addition to imaging, SEM can be coupled with energy-dispersive X-ray spectroscopy (EDS or EDX) for elemental analysis. When the incident electron beam excites electrons in the sample atoms, it can lead to the emission of characteristic X-rays specific to each element. By detecting and analyzing these X-rays, EDX enables both qualitative and quantitative compositional analysis of selected areas. It should be noted that SEM requires the samples to be electrically conductive. Hence, non-conductive specimens are typically coated with a thin layer of conductive material to prevent charging and improve imaging quality. However, for battery electrodes containing conductive additives, this is usually not necessary.

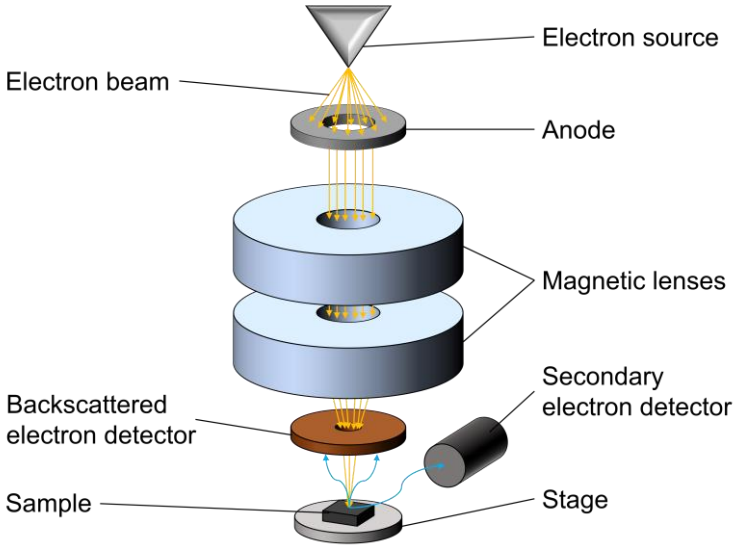


***Fig. 3.6**. Schematic illustration of the working principle of a scanning electron microscope.*

The technique operates under high vacuum conditions, although variable pressure or environmental SEM systems allow for imaging of hydrated or insulating samples without extensive preparation.[217] Due to its high spatial resolution, significant depth of field, and compositional sensitivity, SEM is frequently employed to image and investigate the structure and morphology of electrodes and other cell components.

3.2.2 X-Ray Diffraction

X-ray diffraction (XRD) is the most important non-destructive technique used to analyze the crystalline structure of materials. It exploits the interaction between incident X-rays and the periodically arranged crystal lattice. For detailed explanations of the methods, applications, and interpretation of XRD, the reader is referred to the extensive literature.[218,219,220,221,222] The following short introduction is based on the standard textbook by B.E. Warren.[218] When a beam of monochromatic X-rays strikes a crystalline sample, the atoms act as scattering centers, and the waves diffracted from different atomic planes can interfere constructively under specific geometric conditions. This condition is described by Bragg's Law, as shown in **Fig. 3.7:**

$$n\lambda = 2d \sin\theta \qquad \textbf{Eq. 3.6}$$

where λ is the X-ray wavelength, d is the spacing between the crystallographic planes, θ is the incident angle, and n is the order of the reflection.

By measuring the angles 2θ at which diffraction occurs and the corresponding intensities, a diffraction pattern is produced. This pattern consists of a series of peaks, each corresponding to diffraction from specific sets of lattice planes within the crystal. The positions of these peaks are directly related to the crystal's unit cell dimensions and symmetry, while the intensities provide information about the arrangement and types of atoms within those planes. Interpreting an XRD pattern involves comparing the observed peak positions and intensities with reference patterns from databases such as the powder diffraction file (PDF).[223] This allows for phase identification, enabling determination of the material's crystal structure and any secondary or impurity phases present.

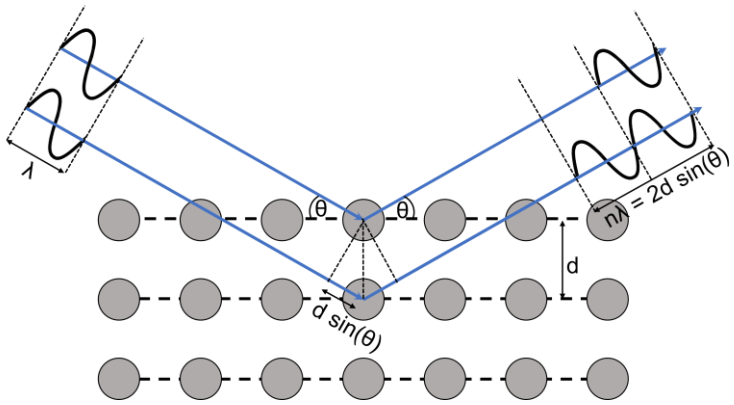


Fig. 3.7*. Schematic illustration of XRD based on X-ray scattering and Bragg's law.*

In addition to phase identification, careful analysis of the width and shape of the diffraction peaks can reveal microstructural details. For instance, broader peaks may indicate small crystallite sizes or the presence of lattice strain. Shifts in peak positions can suggest changes in lattice parameters due to doping, thermal expansion, or mechanical stress. Overall, XRD provides a powerful, non-destructive method of investigating the structural characteristics of crystalline materials and is therefore used to analyze electrode materials, synthesis methods, and degradation mechanisms.

3.2.3 Fourier Transform Infrared Spectroscopy

Fourier transform infrared spectroscopy (FTIR) is a versatile analytical technique used to identify molecular structures and functional groups by measuring the absorption of infrared (IR) light. This section gives a short explanation based on the books by N. Jaggi[224] and B.C.

Smith.[225] The working principle is schematically illustrated in **Fig. 3.8**. When IR rays interact with a material, certain frequencies are absorbed, corresponding to the vibrational modes of chemical bonds within the molecules. These vibrations, such as stretching, bending, or twisting, occur at characteristic frequencies specific to particular bond types and molecular structures. FTIR works by passing a broad spectrum of IR radiation through the sample. An interferometer modulates the light, and the resulting signal is mathematically transformed into an IR spectrum using the Fourier transform. The resulting spectrum plots transmittance as a function of wavenumber, typically ranging from around 4000 to 400 cm^{-1}. Each peak in the FTIR spectrum corresponds to a specific vibrational mode and provides information about the chemical bonds in the material. For example, a sharp peak near 1700 cm^{-1} often indicates a carbonyl (C=O) group, while broad peaks around 3200–3600 cm^{-1} are characteristic of O–H or N–H stretching. Because every compound has a unique IR absorption pattern, FTIR is especially useful for qualitative identification and verification of chemical structures of organic compounds.

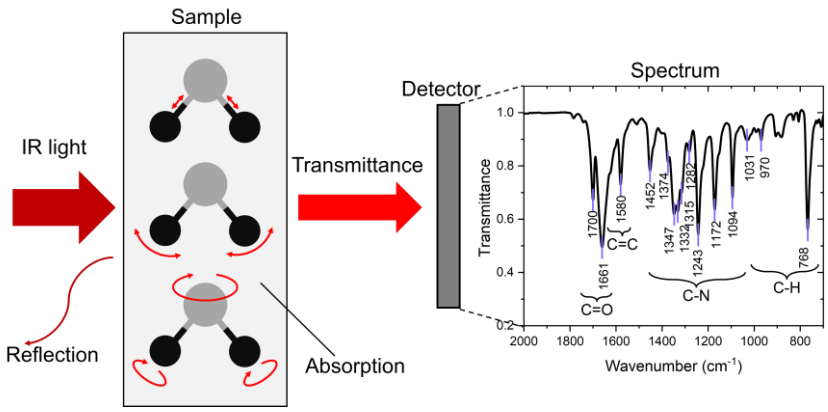


Fig. 3.8. *Schematic illustration of the working principle of FTIR.*

3.2.4 X-Ray Photoelectron Spectroscopy

X-ray photoelectron spectroscopy (XPS) is a surface-sensitive analytical technique used to determine the elemental composition, chemical state, and electronic environment of atoms within the top few nanometers of a material. It is particularly valuable for studying thin films, coatings, and surface modifications. XPS works by irradiating a sample with monochromatic X-rays, typically Al Kα or Mg Kα radiation.[226] The energy from the X-rays causes photoemission of core-level electrons from atoms in the sample. By measuring the kinetic

energy of the emitted electrons, the binding energy E_B of each electron can be calculated using the photoelectric equation.

$$E_B = h\nu - E_K - \Phi \qquad \textbf{Eq. 3.7}$$

where $h\nu$ is the energy of the x-rays, E_K is the measured kinetic energy, and Φ is a correction term accounting for the work function of the sample and the spectrometer.[226] The binding energies are characteristic of specific elements and chemical environments, allowing for detailed surface chemical analysis. An XPS spectrum plots photoelectron intensity versus binding energy. Peaks in the spectrum correspond to specific core-level electrons, and their positions and shapes provide information about the chemical state of the element. For instance, shifts in binding energy can indicate oxidation states or the presence of different chemical bonds (e.g., distinguishing between C–C, C–O, and C=O in the C 1s region). XPS is a quantitative technique capable of determining atomic concentrations with good accuracy and can therefore be used to investigate the composition of electrode materials or films.[227]

3.2.5 Inductively Coupled Plasma Mass Spectrometry

Inductively coupled plasma mass spectrometry (ICP-MS) is a highly sensitive analytical technique used to detect and quantify the elemental composition of a sample. It combines a high-temperature ionization source with mass spectrometric detection, enabling fast analysis at extremely low detection limits, often in the parts-per-trillion (ppt) range.[228] In an ICP-MS measurement, the dissolved sample is introduced into a plasma generated by an argon gas flow sustained by an inductively coupled radiofrequency field. The high temperatures (6000–10,000 K) of the plasma atomize and ionize the elements present in the sample. These ions are then directed into a mass spectrometer, where they are separated and detected based on their mass-to-charge (m/z) ratios. The resulting mass spectrum displays ion intensities as a function of m/z values, allowing for the simultaneous identification and quantification of multiple elements. Therefore, it can be used to determine the exact ratios of different elements present in a sample. ICP-MS is also capable of distinguishing between isotopes of the same element.[229]

3.2.6 Brunauer-Emmet-Teller Surface Area Measurements

The Brunauer–Emmett–Teller (BET) method is a widely used technique for determining the specific surface area of porous and powder samples based on gas adsorption. It extends the Langmuir theory of monolayer adsorption to multilayer adsorption, providing a more accurate description of how gases interact with solid surfaces. Nitrogen gas at liquid nitrogen temperature (77 K) is most commonly used as the adsorbate. In a typical BET measurement, the sample is first degassed under vacuum or inert gas flow to remove contaminants and pre-adsorbed species. The material is then exposed to nitrogen at varying relative pressures, and the volume of gas adsorbed at each pressure point is recorded, forming an adsorption isotherm.[230] The monolayer adsorption capacity is then calculated from the linear region of the isotherm. From this value, the total surface area can be determined, using the known cross-sectional area of a nitrogen molecule. BET analysis is particularly important for characterizing materials with high surface areas, such as catalysts, adsorbents, porous solids, and nanopowders. Surface area plays a crucial role in properties like chemical reactivity, catalytic efficiency, and adsorption performance. Because of its simplicity, reproducibility, and broad applicability, the BET surface area measurement is also a standard technique to analyze the pore structure of battery electrodes.[231]

3.2.7 Shear Rheometry

Shear rheometry is a rheology method used to study the flow properties of liquids, gels, suspensions, and other complex fluids. A shear rheometer applies a controlled shear force or shear rate to a material and measures its response, allowing for the precise determination of viscosity under varying flow conditions. In a typical measurement, the sample is placed between two geometries, such as parallel plates or a cone-and-plate system. One geometry remains stationary while the other one rotates, creating a controlled shear deformation.[232] The rheometer records the shear stress (force per unit area) and the shear rate (the rate of deformation), from which the viscosity, defined as the ratio of shear stress to shear rate, is calculated. Rheometers allow for both steady-shear and dynamic measurements, making it

possible to study Newtonian fluids, whose viscosity remains constant, as well as non-Newtonian fluids, whose viscosity changes with the shear rate. By varying the shear conditions, additional properties such as yield stress, thixotropy, and viscoelasticity can also be analyzed. In battery research, rheometry is mainly used to study the viscosity of liquid or gel electrolytes.[233]

4. Experimental

4.1 List of Chemicals

Table 4.1. *List of chemicals used for the synthesis of active materials and electrode and electrolyte preparation, including suppliers and grades.*

Chemical	Formula	Supplier	Grade
Copper chloride dihydrate	$CuCl_2 \cdot 2\ H_2O$	Sigma-Aldrich	≥99.0 %
Sodium pyrophosphate decahydrate	$Na_4P_2O_7 \cdot 10\ H_2O$	Sigma-Aldrich	≥99.0 %
Sodium ferrocyanide decahydrate	$Na_4Fe(CN)_6 \cdot 10\ H_2O$	Sigma-Aldrich	≥99.0 %
Polyvinylpyrrolidone (PVP)	C_6H_9NO	Sigma-Aldrich	N.A.
Sodium chloride	NaCl	Sigma-Aldrich	≥99.5 %
Manganese sulfate monohydrate	$MnSO_4 \cdot H_2O$	Sigma-Aldrich	≥98.0 %
Iron sulfate heptahydrate	$FeSO_4 \cdot 7\ H_2O$	Sigma-Aldrich	≥99.0 %
Potassium ferricyanide	$K_3Fe(CN)_6$	Sigma-Aldrich	≥99.0 %
Potassium ferrocyanide trihydrate	$K_4Fe(CN)_6 \cdot 3\ H_2O$	Sigma-Aldrich	≥98.5 %
Sodium citrate dihydrate	$C_6H_5Na_3O_7 \cdot 2\ H_2O$	Sigma-Aldrich	≥99.0 %
1,4,5,8-naphthalene tetracarboxylic dianhydride	$C_{14}H_4O_6$	BLDpharm	≥98.0 %
Ethylenediamine	$C_2H_8N_2$	Sigma-Aldrich	≥99.0 %
N-Methyl-2-pyrrolidone (NMP)	C_5H_9NO	Sigma-Aldrich	≥99.5 %
Carbon black (Super C65)	C	MTI Corp.	≥99.5 %
Polyvinylidene fluoride (PVDF)	$(C_2H_2F_2)_n$	MTI Corp.	≥99.5 %
Nafion^{TM} (5wt% dispersion)	$C_7HF_{13}O_5S \cdot C_2F_4$	Sigma-Aldrich	N.A.
Potassium chloride	KCl	Sigma-Aldrich	≥99.0 %
Potassium nitrate	KNO_3	Sigma-Aldrich	≥99.6 %
Magnesium chloride hexahydrate	$MgCl_2 \cdot 6\ H_2O$	Sigma-Aldrich	≥99.0 %
Calcium chloride dihydrate	$CaCl_2 \cdot 2\ H_2O$	Sigma-Aldrich	≥99.0 %
Calcium nitrate tetrahydrate	$Ca(NO_3)_2 \cdot 4\ H_2O$	Sigma-Aldrich	≥99.0 %
Sodium perchlorate monohydrate	$NaClO_4 \cdot H_2O$	Sigma-Aldrich	≥98.0 %

4.2 List of Materials

Table 4.2. *List of materials used for electrode preparation, cell setups, and measurements.*

Material	Product specifications	Supplier
Pyrolytic graphite sheet	Thickness 40 μm, supported on a removable PET foil, carbon content ≥99.7 %	ProGraphite GmbH
Pt wire	99.9 % Pt	MaTeck
Argon gas	Ar 5.0	Westfalen
Nitrogen gas	N 5.0	Westfalen
3D printing filament	Polylactide 2.85 mm	Filamentworld
Separator	BS 17–25 separator for alkaline batteries	Mativ Inc.

4.3 List of Software

Table 4.3. *List of software used for instrument control, data acquisition, data analysis, and figure preparation*

Application	Software, version	Supplier
Potentiostat control and data acquisition	EC-Lab®, version 11.60 and earlier versions	Bio-Logic
EIS data analysis	EIS Data Analysis, version 2.1	A.S. Bandarenka[234]
XPS data analysis	Casa XPS, version 2.3.24	Casa Software Ltd.
General data analysis and plotting	Origin Pro 2023	OriginLab
FTIR data analysis	SpectraGryph, version 1.2	Spectroscopy Ninja
Crystal drawings	Vesta, version 3.5.8	K. Momma and F. Izumi[235]
Chemical drawings	ChemDraw, version 22.2.0	Revvity Signals
Figure preparation	PowerPoint	Microsoft
3D-CAD	SolidWorks 2022	SolidWorks
3D slicer	Ultimaker Cura, version 5.3.0	Ultimaker

4.4 List of Devices

Table 4.4. *List of devices and equipment used for electrochemical measurements, full cell preparation, and material characterizations*

Device	Device specifications	Supplier
Water purification system	Milli-Q EQ 7000, $\sigma \leq 0.055$ $\mu S\ cm^{-1}$	Merck
Potentiostat	VSP-300	Bio-Logic
Reference electrode	SSC, 3 M KCl, B3420+	SI Analytics
Planetary ball mill	XQM-0.4A	TENCAN
Film applicator	AOT-FCM-100-B	AOTelec
SEM	Gemini NVision40	Zeiss
XRD	MiniFlex 600-C, Cu-Kα source (λ = 1.5406 Å), integrated Ni-based filter	Rigaku
FTIR	Vertex-70	Bruker
XPS	Monochromatized Al Kα source (1486.7 eV), XR50 X-ray source, PHOIBOS 150 hemispherical analyzer	SPECS
BET	3Flex analyzer	Micrometrics
Shear rheometer	MCR 302, cone-shaped measuring head (CP50-1, 79040), air-cooled bottom plate (P-PTD 200/56/Air)	Anton Paar GmbH
TGA	TGA/DSC 2 (STARe system)	Mettler Toledo
3D printer	Ultimaker 2+	Ultimaker

4.5 Synthesis

4.5.1 PBA Cathode Materials

The PBAs used in this work were synthesized using a simple single-step aqueous coprecipitation method as schematically depicted in **Fig. 4.1**. The details of each synthesis procedure are listed below.

CuHCF

CuHCF nanosheets were synthesized from two aqueous precursor solutions according to the method reported by Xu et al.[92] Solution A was prepared by dissolving 1 mmol $CuCl_2 \cdot 2\ H_2O$ and 1 mmol $Na_4P_2O_7 \cdot 10\ H_2O$ in 20 mL deionized (DI) water. For solution B, 1 mmol $Na_4Fe(CN)_6 \cdot 10\ H_2O$, 0.58 g NaCl, and 0.3 g polyvinylpyrrolidone (PVP) were dissolved in 50 mL DI water. Subsequently, solution A was slowly dropped into solution B under vigorous stirring at room temperature as schematically illustrated in **Fig. 4.1 (a)**. The mixture was left for aging for 5 days, before the precipitate was collected by centrifugation at 10000 rpm for 10 min. Finally, the product was washed twice with water and once with ethanol and dried overnight at 70 °C.

MnHCF and FeMnHCF-A

MnHCF and iron-doped FeMnHCF-A were also synthesized from two aqueous precursor solutions. For MnHCF, 8 mmol $MnSO_4 \cdot H_2O$ was dissolved in 200 mL DI water to form solution A, while 5.2 mmol $MnSO_4 \cdot H_2O$ and 2.8 mmol $FeSO_4 \cdot 7\ H_2O$ in 200 mL DI water were used for FeMnHCF-A. In both cases, solution B was prepared by dissolving 8 mmol of $K_3Fe(CN)_6$ in 200 mL DI water. Subsequently, both solutions were simultaneously added to a beaker containing 100 mL DI water, which was kept at 60 °C, under vigorous stirring (**Fig. 4.1 (b)**). As for CuHCF, the precipitate was collected by centrifugation at 10000 rpm for 10 min, washed twice with water and once with ethanol, and dried overnight at 70 °C.

FeMnHCF-C

Morphology-controlled FeMnHCF-C was synthesized similarly. For solution A, 5.2 mmol $MnSO_4 \cdot H_2O$, 2.8 mmol $FeSO_4 \cdot 7\ H_2O$, as well as 8 mmol $C_6H_5Na_3O_7 \cdot 2\ H_2O$ as a chelating

agent, were dissolved in 200 mL DI water. Solution B consisted of 4 mmol $K_4Fe(CN)_6 \cdot 3\ H_2O$ dissolved in 200 mL DI water. Subsequently, the synthesis was carried out the same way as for MnHCF and FeMnHCF-A.

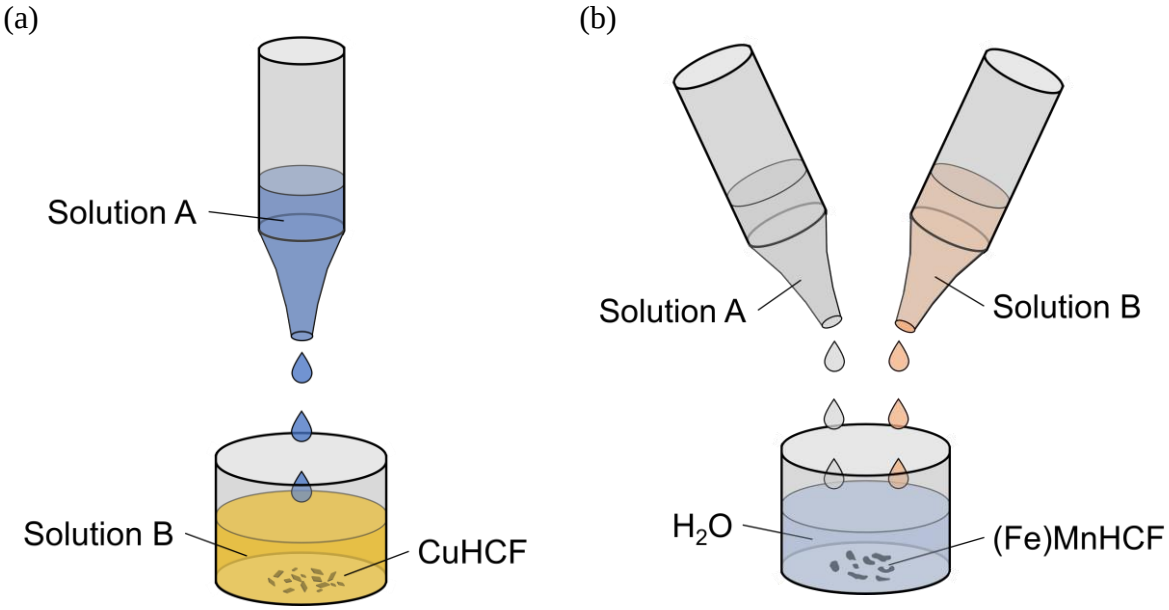


Figure 4.1. *Schematic illustration of the synthesis process of PBA materials by coprecipitation from aqueous precursor solutions. (a) Synthesis of CuHCF. (b) Synthesis of (Fe)MnHCF.*

4.5.2 Poly(Naphthalene-4-Formyl-Ethylenediamine) Anode Material

Poly(naphthalene-four-formyl-ethylenediamine) (PNFE) was synthesized based on the procedure reported by Deng et al.[123] with minor modifications. Briefly, 1,4,5,8-naphthalene tetracarboxylic dianhydride (NTCDA, 2.68 g, 10 mmol) and ethylenediamine (EDA, 0.60 g, 10 mmol) were mixed in 20 mL of degassed N-methyl-2-pyrrolidone (NMP) within a Schlenk flask. The flask was equipped with an air-cooled condenser and an overpressure valve, and the reaction mixture was heated overnight in a sand bath maintained at 215 °C.

After cooling to room temperature, the resulting dark precipitate was collected by filtration and washed thoroughly with NMP, followed by extensive washing with water. The solid was dried under reduced pressure (0.08 mbar) with a stepwise increase in drying temperature (room temperature, 120 °C, and finally 210 °C), yielding 2.7 g (92%) of a grey-brown powder.

Elemental analysis (calculated for an infinite polyimide, $C_{16}H_8N_2O_4$): C 65.76%, H 2.76%, N 9.59%; (calculated for an octamer): C 65.10%, H 3.03%, N 10.52%; found: C 65.13%, H 2.91%, N 10.32%.

4.6 Electrode Preparation

Composite electrodes were prepared using the slurry casting method. For the cathodes, 80 wt. % of the respective PBA (CuHCF, MnHCF, FeMnHCF-A/C), 10 wt. % of carbon black Super C65, and 10 wt. % of PVDF were ground and mixed together in a planetary ball mill at 800 rpm for 20 min using Y-stabilized ZrO_2 balls. Subsequently, NMP was added as a solvent until a homogeneous slurry with a honey-like texture was formed.

The anode slurries consisted of 80 wt. % of PNFE, 10 wt. % of carbon black super C65, and 10 wt. % of Nafion^{TM} binder (5 wt.% dispersion in lower aliphatic alcohols and water), which were also mixed in the planetary ball mill at 800 rpm for 20 min. For the anodes, water and isopropyl alcohol in a 1:1 ratio were used as dispersing agents.

All slurries were cast onto pyrolytic graphite sheets using a film applicator and a doctor blade with variable height. The NMP-based PBA cathodes were dried at 70 °C, and the water-based PNFE anodes were dried at room temperature overnight. All electrodes in this work had mass loadings in the range of 2-5 mg cm^{-2}.

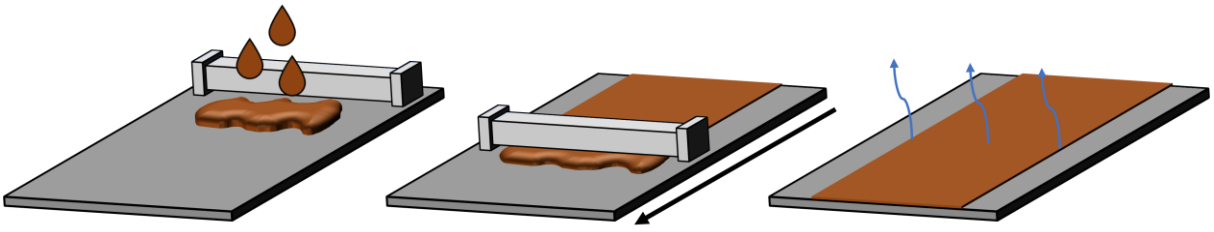


Figure 4.2. *Schematic illustration of the electrode casting process. The slurry is dropped onto the pyrolytic graphite sheet and spread using a doctor blade. Finally, the electrode is dried to evaporate the solvent.*

4.7 Electrochemical Measurements

4.7.1 Single-Electrode Measurements (Three-Electrode Setup)

Single-electrode measurements were carried out in a custom setup shown in **Fig. 4.3**. It consists of a main and preconditioning cells. The airtight main cell contains a three-electrode setup, including a working electrode (WE), reference electrode (RE), and counter electrode (CE). The WE is the anode or cathode investigated in the specific experiment. Typically, circular electrodes held by an alligator clip, which was fixed to a stainless steel rod, were used. To avoid contact between the electrolyte and the alligator clip, only half of the electrode area was coated with the slurry, and the empty half was not submerged in the electrolyte. An Ag/AgCl (SSC, 3 M KCl) electrode was used for the RE.

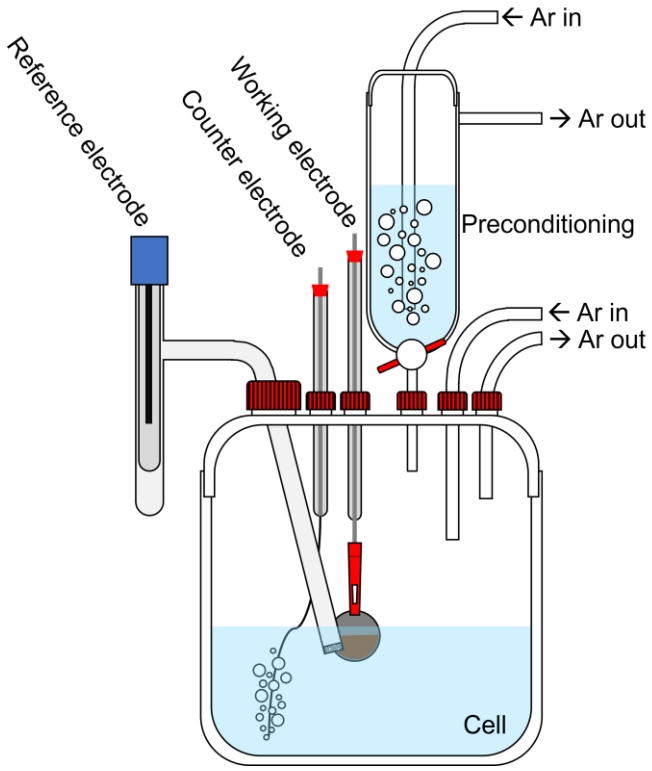


Fig. 4.3. *Schematic illustration of the custom three-electrode setup used in this work.*

To minimize the ohmic drop associated with the electrolyte resistance, the RE was connected to the main cell by a Luggin capillary with the opening as close as possible to the WE. A platinum wire, which provides and sinks electrons through either the HER or the OER, served

as the CE. The electrode terminals were connected to a potentiostat to control the measurements and record the voltage or current response.

The main glass cell was continuously purged with Ar to maintain an inert atmosphere during the measurements. In addition, the electrolyte was flushed with Ar for at least 10 min inside the preconditioning cell before being run into the cell to remove residual oxygen. For the unlikely case of HCN evolution from the decomposition of hexacyanoferrates, the gas outlets were connected to gas traps.

4.7.2 Full Cells (Two-Electrode Setup)

Full cell measurements were typically carried out in stainless steel coin cells. However, due to the corrosive nature of aqueous electrolytes, particularly Cl-based solutions, custom metal-free 3D-printed cells, as shown in **Fig. 4.4,** were used. The cathode and anode caps were printed from a PLA filament and sealed by screws and a rubber O-ring. Carbon contacts connect the electrodes inside the cell with the potentiostat. The anode is placed on the bottom contact, with the separator soaked in electrolyte and the cathode on top. The cathode is connected to the second contact by a piece of carbon paper fixed to the cathode cap. The full batteries were assembled inside a nitrogen-filled glovebox to avoid dissolved oxygen in the electrolyte.

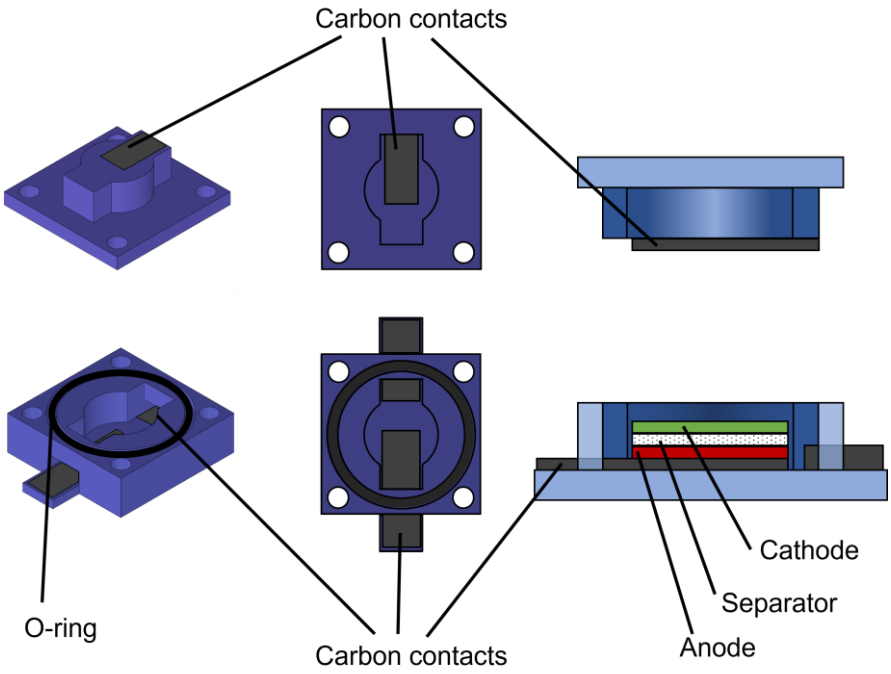


Fig. 4.4. *Schematic illustration of the custom 3D-printed coin cells.*

4.7.3 Applied Techniques

All investigated electrodes and full cells were characterized by CV and GC. For CV, scan rates between 1 mV s^{-1} and 50 mV s^{-1} were applied. The potential or voltage boundaries were selected based on the observed electrode potentials. GC at different C-rates ranging from 1 C to 100 C or 300 C within the same potential or voltage boundaries was carried out to assess the rate capabilities. Theoretically, a C-rate of 60 C corresponds to a (dis-)charging time of 1 min. However, as the capacity retention decreases at higher C-rates, the real (dis-)charging time will be shorter. Furthermore, the cycling stabilities were tested by constant current cycling at 10 C (cathodes and full cells) and 100 C (anode). A higher rate, allowing for recording more cycles within the same time, was used for the polyimide anodes, as they displayed very fast charge storage kinetics.

The charge storage mechanisms were further investigated by potentiostatic EIS. A potential close to the half-charge potential was selected to record single spectra. This potential was held for 10 min before recording the impedance spectrum to ensure equilibrium conditions. The AC amplitude of the probing signal was set to 10 mV, and the frequency was varied between 1.00 MHz and 250 mHz in logarithmic steps with 25 points per decade. Before fitting, the validity of the data was verified by Kramers-Kronig analysis.

5. Results and Discussion

5.1 Developing High-Performance Aqueous Batteries Based on Sustainable Materials by Electrolyte Optimization

As explained in **Chapter 1**, Li-free aqueous batteries (LFABs) can be a promising alternative to conventional Li-ion batteries (LIBs) for stationary energy storage, due to their inherent safety and the abundance of their constituent materials. They can also replace Li-based supercapacitors in public transport or similar applications, if sufficiently high energy and power densities, as well as long cyclability, are achieved. The practical implementation of LFABs will require optimization of these properties while keeping material and manufacturing costs as low as possible. Hence, the viability of the typical strategy of using high-concentration water-in-salt electrolytes (WiSEs) based on expensive and hazardous salts to mitigate side reactions and active material degradation is limited. In this section, a novel, cost-effective electrolyte design is proposed. It relies on safe and low-cost salts at moderate concentrations to achieve battery performance similar to WiSE-based cells. By systematically investigating the effects of the cation species on the most important performance metrics of the CuHCF cathode and the PNFE anode, an optimized mixed-salt electrolyte is developed. The proposed battery delivers a competitive energy density and exceptional fast-charging capabilities, advancing the practical viability of LFABs for stationary and mobile energy storage. The results presented in this section are primarily based on the following published article, which was written with contributions from all listed co-authors:

R.L. Streng, S. Reiser, A. Senyshyn, S. Wager, J. Sterzinger, P. Schneider, D. Gryc, M.Z. Hussain, A.S. Bandarenka. Sustainable high-performance aqueous batteries enabled by optimizing electrolyte composition. *Advanced Science* 2025, 12, 2417587.

5.1.1 Structural Characterizations

CuHCF and PNFE were used as the cathode and anode active materials, respectively. This section analyzes their structural properties before discussing their electrochemical performance. This includes XRD results on the crystal structure of CuHCF, FTIR analysis of the chemical structure of PNFE, and structural and morphological investigations of the composite electrodes using BET, SEM, and XPS.

5.1.1.1 Structure and Morphology of the CuHCF Cathode

CuHCF was synthesized by coprecipitation from aqueous solutions of $CuCl_2$ and $Na_4Fe(CN)_6$, providing the Cu cations and $Fe(CN)_6$ anions, respectively, which combine to form the PBA lattice. Generally, the formation of PBA crystals is a rapid process, often leading to irregular structures with high defect and water contents, impairing their ion storage capacity and structural stability.[82,83,84,85,236,237] Therefore, chelating agents are often employed to slow down the reaction and minimize $Fe(CN)_6$ vacancies and interstitial water inclusions.[106,107,112,238,239] The synthesis method used in this work was developed by Xu et al. and employs sodium citrate and PVP as chelating additives.[92] Furthermore, NaCl is added to the reaction bath, as the presence of alkali metal ions during the formation of PBAs has been shown to improve their crystallinity and lower the water content.[240,241] Accordingly, Xu et al. found that their optimized synthesis method yields highly crystalline CuHCF with improved cation storage capacity compared to conventional synthesis processes.[92] The crystal structure of the CuHCF particles prepared in this study was investigated using XRD. **Fig. 5.1 (a)** shows the fitted XRD pattern, which is in good accordance with the pattern reported by Xu et al. Under these conditions, CuHCF crystallizes in a monoclinic crystal structure with lattice parameters a = 11.22 Å, b = 7.30 Å, and c = 6.95 Å. Typically, PBAs like CuHCF or NiHCF, where only Fe-ions are the active redox centers, assume cubic phases. However, previous studies have shown that they can be shifted towards pseudo-cubic monoclinic phases at higher intercalated alkali metal ion contents.[86,87,242] As $Na_4Fe(CN)_6$ was used as the precursor salt, the as-prepared CuHCF is fully reduced upon synthesis and therefore contains high amounts of intercalated Na^+, leading to the

observed monoclinic structure. Nevertheless, the phase can be regarded as pseudo-cubic, since the monoclinic angle is relatively close to 90° (β = 92.93°). **Fig. 5.1 (b)** shows a schematic illustration of the structure of CuHCF synthesized for this work as extracted from the XRD pattern.

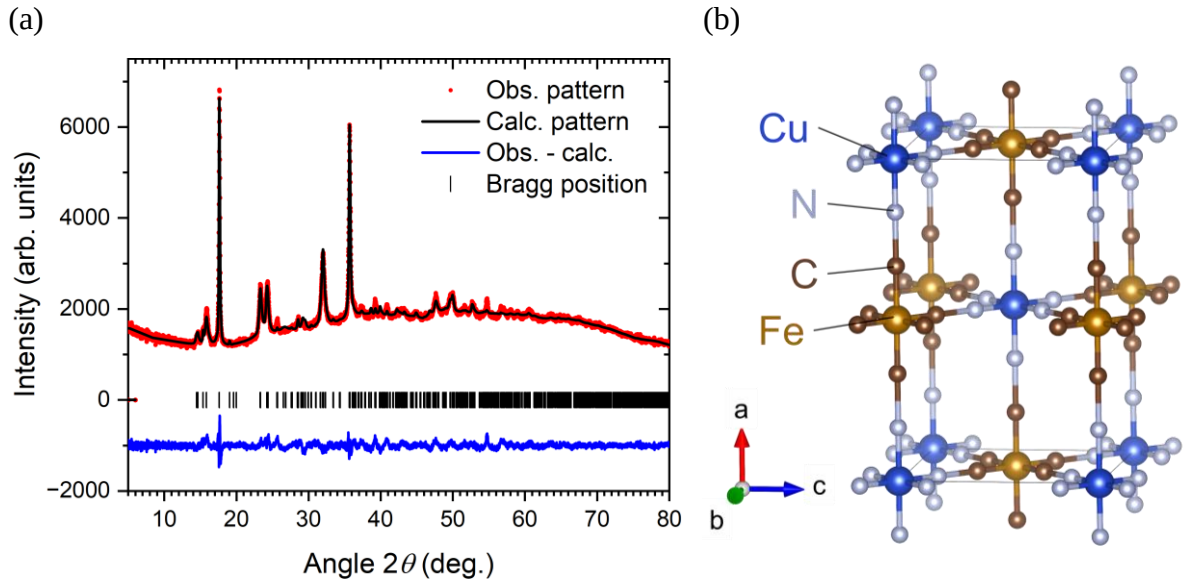


Fig. 5.1. *XRD analysis of the CuHCF particles synthesized for this work. (a) Fitted XRD pattern corresponding to a pseudo-cubic monoclinic phase. (b) Schematic illustration of the extracted crystal structure. Redrawn from ref. 243 (own work).*

After incorporating the CuHCF particles into composite electrodes, their morphology was investigated using SEM. **Fig. 5.2 (a)-(c)** show SEM images of the CuHCF cathodes at different magnifications. The active material appears evenly distributed, forming a macroporous structure. The bright spheres can be identified as carbon black nanoparticles. Unlike conventional synthesis routines, the method using sodium pyrophosphate and PVP additives does not result in cubic particles.[87,88] Instead, the CuHCF crystals possess a sheet-like morphology with particle sizes in the 200 nm – 800 nm range. The pore structure was investigated using BET measurements to analyze the morphology of the cathode further. As shown in **Fig. 5.2 (d)**, the N_2 adsorption displays a so-called Type II isotherm, suggesting that the sample is predominantly macroporous with negligible micro- or mesoporous contributions. This is confirmed by the minimal adsorption volume at relative pressures below 0.2, indicating

weak interactions between the nitrogen molecules and the surface. For intermediate relative pressures between 0.2 and 0.8, the behavior is dominated by multilayer adsorption. The steep rise in N_2 uptake at high relative pressures (>0.9) is attributed to the condensation of nitrogen in the macropores or on the external electrode surface. The BET specific surface area (SSA) of the cathode is relatively low at 1.9 $m^2\ g^{-1}$, further indicating the absence of micropores or low accessibility. For comparison, the pyrolytic graphite exhibited a negligible SSA of around 0.5 $m^2\ g^{-1}$ under the same conditions.

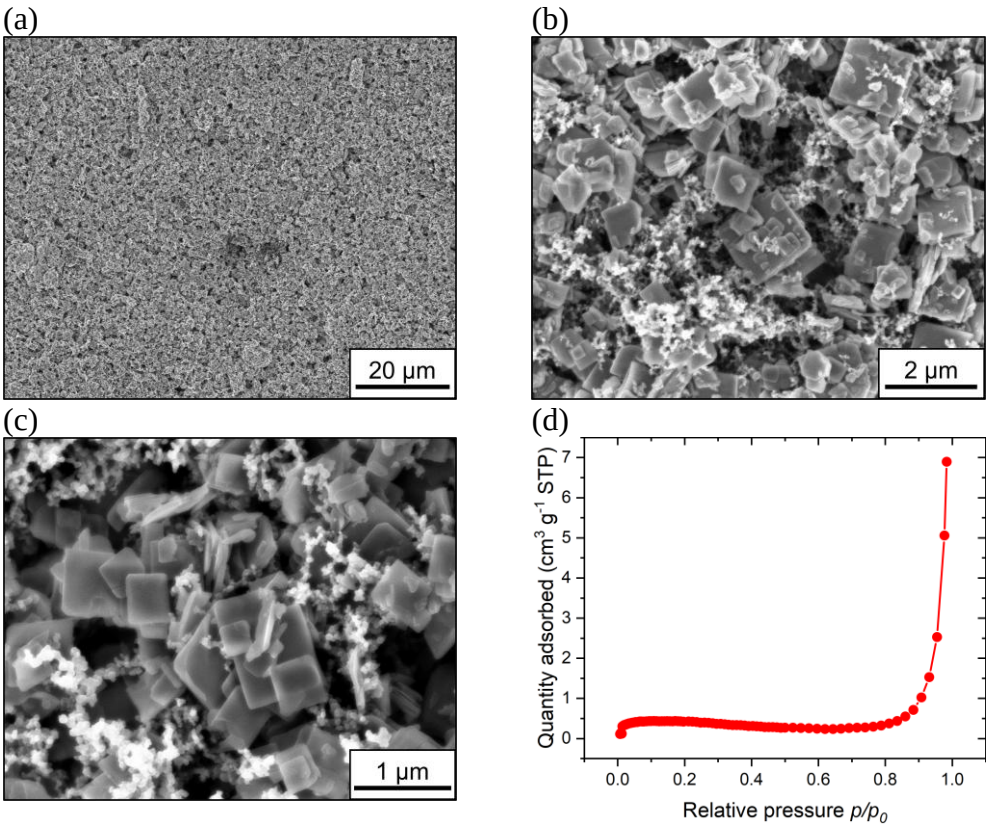


***Fig. 5.2**. Morphology of the CuHCF cathode. (a)-(c) SEM images at various magnifications, showing the sheet-like CuHCF particles. (d) BET analysis: N_2 adsorption isotherm obtained at 77 K. Redrawn from ref. 243 (own work).*

5.1.1.2 Structure and Morphology of the PNFE Anode

PNFE was synthesized in a simple one-step dehydration condensation reaction in NMP from the NTCDA and EDA precursors. This method is established in the literature and reliably produces high yields of the desired polyimide.[117,118,119] As shown in **Fig. 5.3**, PNFE features

two imide groups connected by aromatic rings per polymer unit. The four carbonyl groups theoretically allow for reduction by up to four electrons, enabling high specific capacities.

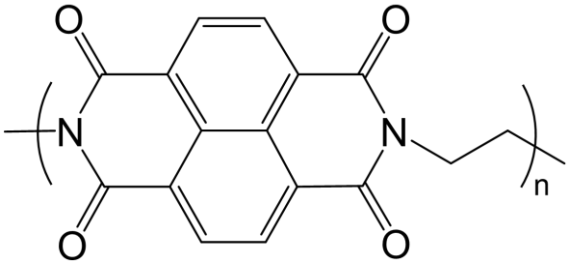


Fig. 5.3 *Chemical structure of the polyimide PNFE, which was used as an anode active material in this work.*

The successful synthesis of PNFE was confirmed by FTIR spectroscopy. **Fig. 5.4 (a)** shows the observed FTIR spectrum of the synthesized material, which is in good accordance with the expected structure. The peaks at 1700 cm^{-1} and 1661 cm^{-1} can be associated with characteristic stretching vibrations of the C=O bonds in the redox-active carbonyl groups. The shoulder peak at 1626 cm^{-1} and the peak at 1580 cm^{-1} correspond to stretching vibrations of the aromatic C=C double bonds. Furthermore, various stretching, bending, and twisting vibrations of aromatic and non-aromatic C-N bonds are indicated by the bands between 1452 cm^{-1} and 1094 cm^{-1}. The remaining peaks are attributed to vibrations of C-H bonds in the aromatic and non-aromatic parts of the polymer. Polyimides are typically characterized by exceptional thermal stability.[114,115,116,244,245] Thermogravimetric analysis (TGA) was carried out to evaluate the thermal decomposition behavior of the active material (**Fig. 5.4 (b)**). While the evaporation of residual water or solvent causes a small initial mass loss below 100 °C, no polymer decomposition is observed until approximately 500 °C, which is in good accordance with previously reported TGA results for this material.[123]

After preparing the composite electrodes, XPS was performed to investigate the surface composition. The survey spectrum in **Fig. 5.4 (c)** shows characteristic peaks corresponding to F1s, O1s, N1s, and C1s. While carbon and oxygen can be attributed to both PNFE and

Nafion™, the nitrogen and fluorine peaks confirm the presence of the active material and the binder on the surface, respectively.

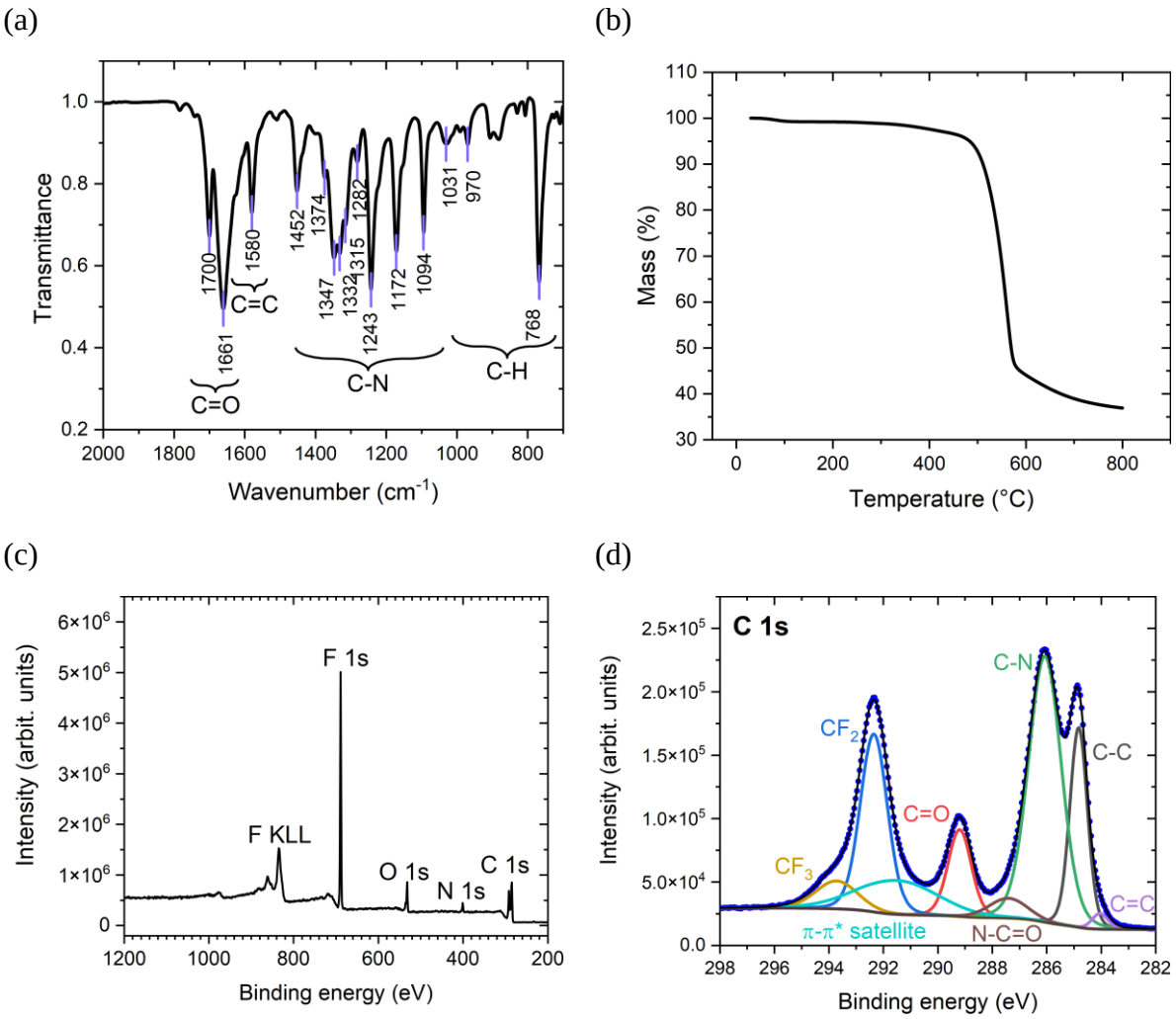


Fig. 5.4. *Structure of the PNFE anode. (a) FTIR spectrum of the PNFE powder. (b) TGA curve at a heating rate of 10 °C min^{-1} under Ar atmosphere. (c) XPS survey spectrum of the composite electrode. (d) Fitted high-resolution XPS spectrum in the C 1s region. Redrawn from ref. 246 (own work).*

Fig. 5.4 (d) shows the fitted XPS spectrum of the anode in the C 1s region. The observed peaks are attributed to various carbon chemical states. The sharpest peaks at 284.5 eV, 286.1 eV, 293.8 eV, and 292.4 eV correspond to C-C, C-N, C=O, and CF_2 bonds. Weaker peaks linked to C=C, N-C=O, and CF_3 appear at 284.3 eV, 287.4 eV, and 293.8 eV, respectively. Furthermore, at 291.5 eV, a broad π–π* satellite peak originating from the extended delocalized electrons in the aromatic rings of PNFE is found. The characteristic peaks attributed to C-C, C-N, C=O,

C=C, and N-C=O bonds confirm the structure of the polyimide shown in **Fig. 5.3**, while the carbon-fluorine bonds are an integral part of the Nafion™ binder.

Fig. 5.5 (a)-(c) show SEM images of the PNFE anode at various magnifications. Although the electrode film has some larger cracks, it mainly consists of evenly distributed crystalline polymer particles in the 100 nm to 500 nm range. Together with the conductive additive and the binder, these particles form a porous structure with pore sizes ranging from around 100 nm to 1 µm.

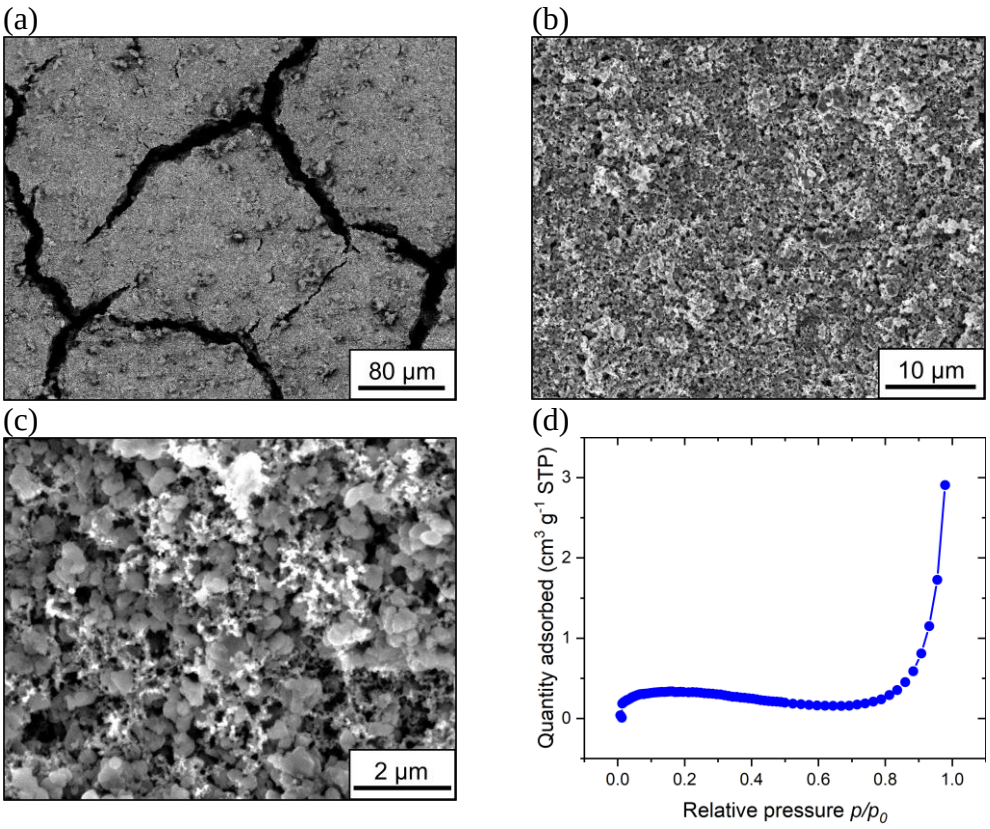


***Fig. 5.5**. Morphology of the PNFE anode. (a)-(c) SEM images at various magnifications, showing the morphology of the anode. (d) BET analysis: N_2 adsorption isotherm obtained at 77 K. Redrawn from ref. 243 (own work).*

The macroporous structure of the anode was confirmed by BET analysis. As shown in **Fig. 5.5 (d)**, the nitrogen adsorption is characterized by a Type II isotherm similar to the CuHCF cathode, typical for the absence of micropores. Hence, the SSA of the anode is also relatively low (1.5 m^2 g^{-1}).

5.1.2 Cation Effect on the Performance of the CuHCF Cathode

As mentioned in **chapter 1**, PBAs can host various cations, including alkali metal ions such as Li^+, Na^+, K^+, and Cs^+, as well as multivalent ions such as Mg^{2+}, Ca^{2+}, and Al^{3+}. Among them, Na^+, K^+, Mg^{2+}, and Ca^{2+} are considered the most suitable for sustainable batteries due to their high abundance in the Earth's crust and stability in aqueous electrolytes, i.e., hydrolysis can be efficiently suppressed. In this section, the influence of the electrolyte cation species on the most important electrochemical properties of CuHCF. is investigated, and an optimized mixed-salt electrolyte is proposed.

5.1.2.1 Electrode Potential

For the cathode, high electrode potentials are generally desirable to maximize the cell voltage of the full battery. Therefore, the electrode potentials of the CuHCF electrode in different electrolytes were assessed by CV to identify the effect of the cation species on this parameter. **Fig. 5.6** shows the corresponding CV curves of CuHCF in 4 mol kg^{-1} (denoted as 4 m) NaCl, KCl, $MgCl_2$, and $CaCl_2$ aqueous electrolytes. In contrast to all other studied electrolytes, the CV curve in NaCl (**Fig. 5.6 (a)**) shows a double peak structure. Generally, the cathode displays sharper and less separated peaks in the electrolytes based on monovalent cations. As divalent ions are characterized by higher charge densities, Coulombic interactions between the guest cation and the host lattice are stronger, leading to more sluggish diffusion and charge transfer kinetics.[124] The half-charge potential of the cathode in each electrolyte was evaluated from the midpoint between the anodic and the cathodic peak of the CV curve, as described in **section 3.1.1.** The electrode potential is found to be strongly dependent on the guest cation, increasing from around 0.63 V for Na^+ to around 0.78 V for K^+. Overall, the trend $Na^+ < Mg^{2+} < Ca^{2+} < K^+$ is observed, with a relatively small difference between Mg^{2+} and Ca^{2+}.

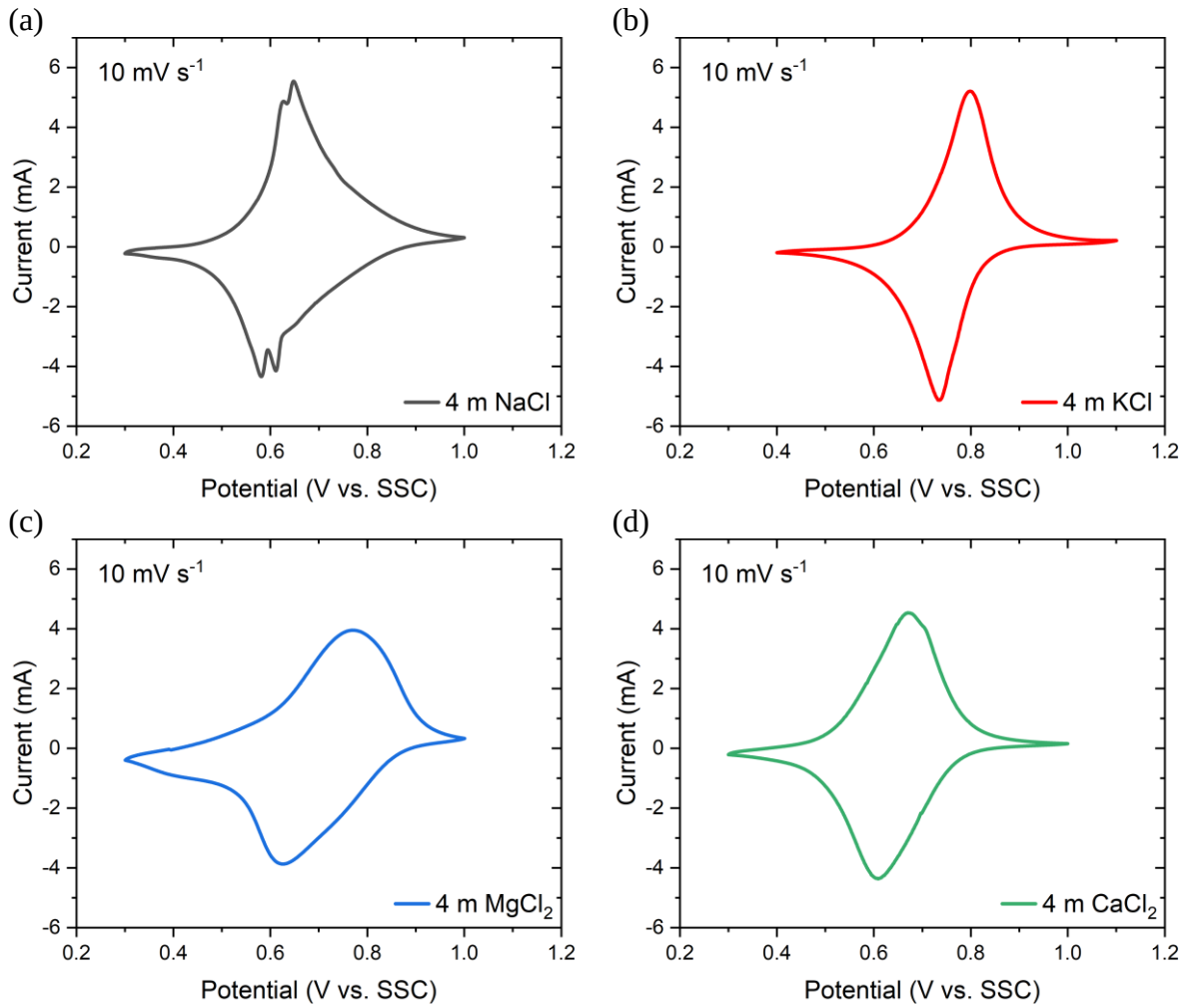


Fig. 5.6. *CV curves of the CuHCF cathode in different aqueous 4 mol kg^{-1} (m) MCl_x electrolytes (M=Na, K, Mg, Ca). (a) NaCl. (b) KCl. (c) $MgCl_2$. (d) $CaCl_2$.*

For the alkali metal ions Na^+ and K^+, this correlation has frequently been reported in previous studies.[247,248,249] Larger alkali metal cations are characterized by less negative hydration enthalpies and smaller hydration shells, facilitating intercalation into the host lattice. This raises the reduction potential, as less energy is needed to insert the guest ion into the lattice. Based on this observation, Mg^{2+} and Ca^{2+} intercalation should occur at lower potentials, as their hydration enthalpies are significantly lower and their hydration shells are much larger than those of monovalent ions. However, they intercalate at higher potentials than Na^+, as shown in **Fig. 5.6 (c)** and **(d),** and confirmed by previous literature.[250,251] According to Mizuno et al., the similar potentials for intercalation of Na^+ and Mg^{2+} into PBAs can be explained by the observation that Mg^{2+} only partially sheds its hydration shell upon intercalation. In contrast to aqueous electrolytes, Mg^{2+} insertion into the cathode is blocked in an organic propylene carbonate (PC)

electrolyte. Since the PC molecule is too large to co-intercalate, the cations must completely shed their solvation shell to intercalate, resulting in strong Coulombic repulsion between the PBA surface and the bare Mg^{2+}. In the case of aqueous electrolytes, the solvent molecules are significantly smaller, allowing some of them to co-intercalate together with the cation, such that the solvation shell is only partly shed. Hence, the energy demand for intercalation becomes significantly lower, promoting the reduction of the PBA and raising the electrode potential.[251] Among the tested electrolytes, the most positive electrode intercalation potential for CuHCF is observed in potassium-based solutions. Accordingly, using potassium-ion electrolytes enables the highest energy densities regarding the cathode.

5.1.2.2 Cycling Stability

Besides energy density, cycling stability is one of the most important parameters determining battery performance. Therefore, the cyclability of the CuHCF cathode in the mentioned electrolytes was assessed by GC at 10 C for 100 cycles. Since the results of these tests are subject to statistical fluctuations, all measurements were repeated at least five times. The average capacity retention after 100 cycles in each electrolyte is shown in **Fig. 5.7**.

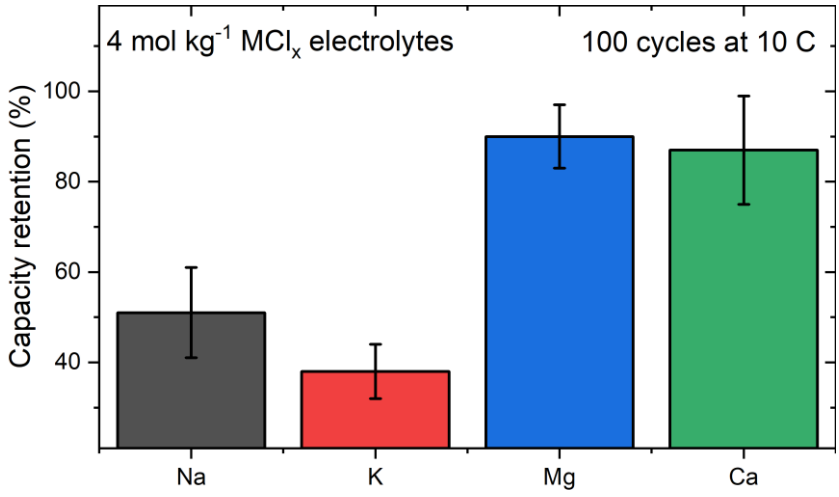


***Fig. 5.7**. Capacity retention of CuHCF in different aqueous 4 mol kg^{-1} MCl_x electrolytes (M=Na, K, Mg, Ca) after 100 GC cycles at 10 C. Data presented as mean ± SD, n=5. Redrawn from ref. 243 (own work).*

Evidently, the cathode active material degrades severely in the alkali metal-ion electrolytes, with less than 40 % of the initial capacity remaining after cycling in KCl. To explain this

behavior, multiple degradation mechanisms that have previously been identified as impacting PBAs need to be considered. We have discussed the existing literature on PBA degradation in a dedicated review. For a more detailed overview, the reader is referred to this publication:

J. Sterzinger, R.L. Streng, S. Chen, R. Götz, W. Hu, J. Li, A.S. Bandarenka. Degradation mechanisms of prussian blue analogs and state-of-the-art approaches for stability optimization: A review. *J. Phys. Chem. C* 2025, 129, 7135-7153.

In short, the three primary processes responsible for transition metal dissolution in CuHCF can be described as follows. First, any PBA inevitably features lattice defects caused by $Fe(CN)_6$ vacancies introduced by imperfect crystal growth during synthesis. These defects have been demonstrated to promote structural collapse upon intercalation and deintercalation of guest cations.[252,253,254] Secondly, water inclusions forming alongside $Fe(CN)_6$ vacancies during crystallization contribute to the degradation of CuHCF by hydrolyzing the framework or blocking ion channels. Although a sodium pyrophosphate chelating agent was used to minimize the amount of H_2O inclusions, the presence of a certain amount of interstitial water is inevitable in PBAs.[254,255,256] Lastly, OH^- anions have been shown to contribute to the degradation of PBAs by driving transition metal dissolution and passivation. Since H_3O^+ and OH^- are generally present in any aqueous solution, their effect can play a role even in neutral electrolytes like NaCl and KCl. Furthermore, operating potentials close to or beyond the OER onset potential lead to specific adsorption of OH^- on the PBA surface, increasing the local pH value. Since the cathodes are cycled to potentials well above 1.23 V vs. RHE, this effect can promote the well-understood alkaline degradation pathway for PBAs.[254,257] While the first effect can be assumed to only play a minor role in this case due to the high crystallinity of the CuHCF nanosheets, the latter two are likely responsible for the severe capacity losses in KCl and NaCl. In contrast, these mechanisms appear to be suppressed by divalent cations, as the capacity decay in $MgCl_2$ and $CaCl_2$ is only minimal.

To gain further insight into the degradation during cycling in electrolytes based on monovalent and divalent ions, post-cycling structural changes were analyzed using SEM and XRD. **Fig. 5.8**

(a) and **(b)** show the XRD patterns of the fully reduced CuHCF cathode before and after cycling in 4 mol kg^{-1} KCl and 4 mol kg^{-1} $MgCl_2$ electrolytes. The initial diffraction pattern exhibits the expected superposition of reflections from the monoclinic CuHCF and the graphite-based current collector. However, following cycling in either electrolyte, most of the characteristic reflections associated with the monoclinic CuHCF phase are no longer observed, and the pattern becomes dominated by signals from the substrate.

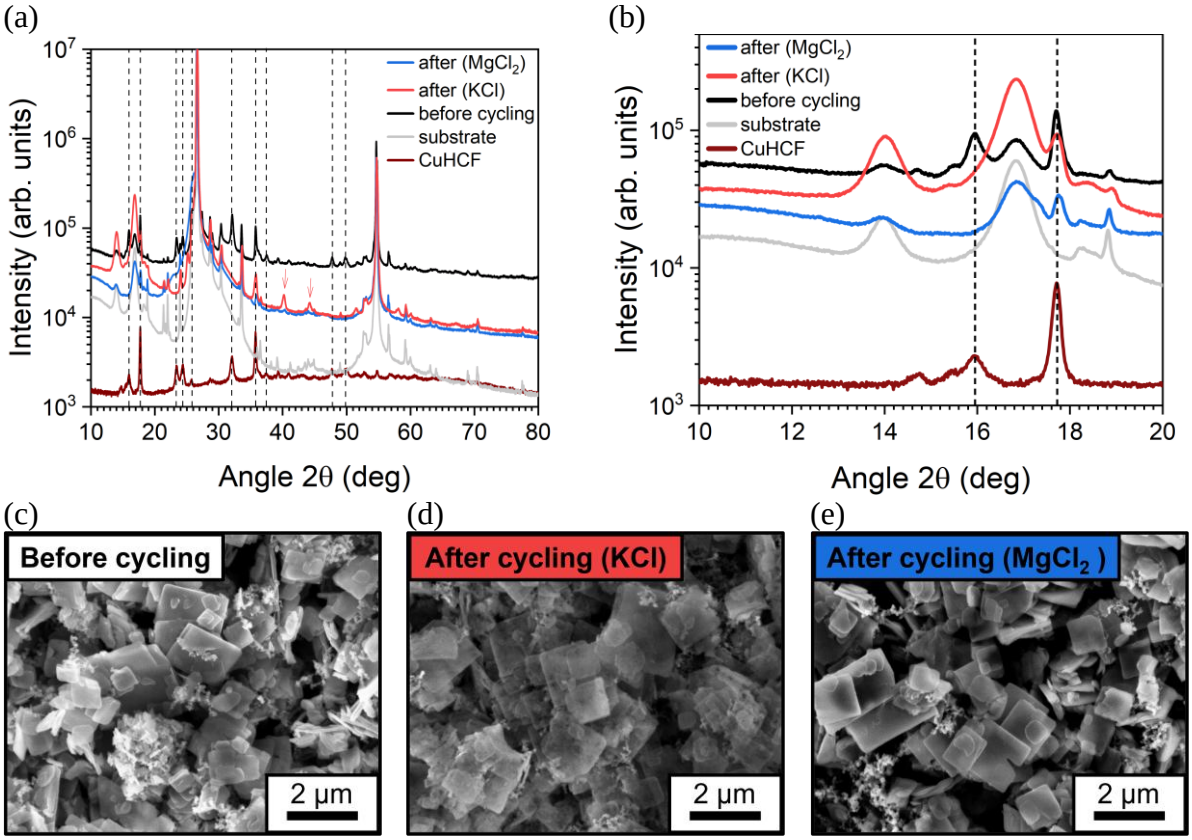


Fig. 5.8. *Structural evolution of the CuHCF cathode during cycling. (a) XRD patterns of CuHCF powder, the composite CuHCF cathode, the graphite-based substrate, and the cathode after 100 cycles at 10 C in KCl and in $MgCl_2$. The arrows mark two new superstructural peaks for the sample cycled in KCl. (b) Zoom in on the monoclinic (011) (pseudo-cubic (200)) reflection. (c) SEM image of the cathode before cycling. (d) SEM image after cycling in KCl. (E) SEM image after cycling in $MgCl_2$. Redrawn from ref. 243 (own work).*

Notably, the monoclinic (011) reflection equivalent to the pseudo-cubic (200) peak remains detectable at 2θ = 17.7°, corresponding to a pseudo-cubic unit cell volume of approximately

1000 $Å^3$ across all samples (**Fig. 5.8 (b)**). The position and full width at half maximum (FWHM) of this reflection remain essentially unchanged after cycling, indicating that the average coherent scattering domain and local chemical composition are mostly preserved. Nonetheless, the disappearance of other characteristic reflections suggests significant peak broadening at higher diffraction angles, most likely caused by increased microstrain. This strain is attributed to an inhomogeneous distribution of intercalated species within the active material. Additionally, two unidentified peaks appear in the XRD pattern of the severely degraded sample cycled in KCl, suggesting the formation of secondary phases and structural changes. To fully elucidate the structural degradation pathways, operando or in situ studies tracking the evolution of the CuHCF framework during electrochemical cycling will be necessary in the future.

The SEM analysis further confirms the strong structural degradation in the KCl electrolyte. As shown in **Fig. 5.8 (d)**, the CuHCF nanosheets exhibit substantial morphological changes after cycling. Although the overall particle morphology is unchanged, the surfaces display etched holes and pores, indicating significant transition metal dissolution, which is consistent with the observed electrochemical performance. In contrast, the sample cycled in 4 mol kg^{-1} $MgCl_2$ (**Fig. 5.8 (e)**) does not show such surface damage, suggesting that the Mg^{2+}-based electrolyte more effectively suppresses material dissolution.

This stabilization can be explained by the stronger interaction between divalent ions and water. Due to their high charge density and much more negative hydration enthalpy, Mg^{2+} and Ca^{2+} form larger and more strongly bound hydration shells than Na^+ and K^+. For example, Mg^{2+} typically coordinates with six water molecules in its stable and well-ordered primary hydration shell, also allowing for a second shell.[258,259] Whereas the hydrated Mg^{2+}-ion complex is very stable, K^+ only forms a single relatively unstable hydration shell with a coordination number between 6 and 8.[260] Thus, the free water content in electrolytes based on divalent ions is lower than in electrolytes using monovalent ions, promoting stabilization through molecular crowding similar to highly concentrated WiSEs. In addition, multivalent ions can capture detrimental interstitial water in the PBA framework after intercalation, as they partially shed their hydration

shell upon insertion. This observation was previously reported by Xie et al., who significantly enhanced the cyclability of a PBA cathode by using $AlCl_3$ as an electrolyte additive. They demonstrated that detrimental side reactions were suppressed by Al^{3+} ions binding to interstitial water molecules.[261] For Mg^{2+} and Ca^{2+}, a similar effect can be assumed as their high charge densities lead to strong interactions with water. In addition to their water-binding capabilities, divalent ions tend to undergo a hydrolysis reaction with water, decreasing the activity of OH^- anions in aqueous electrolytes, as described in **section 2.2.2**.[262] Hence, Mg^{2+} and Ca^{2+} can mitigate the alkaline degradation pathway by capturing OH^- species at the electrode surface or within the crystal structure. In summary, divalent ions can stabilize the CuHCF cathode during cycling since water molecules and hydroxide ions are more likely to coordinate with the electrolyte cations than the PBA framework, suppressing detrimental hydrolytic reactions between water and the active material. Therefore, CuHCF displays largely improved cycling stability in divalent-ion-based electrolytes, making them the ideal choice for batteries with long cycle life.

5.1.2.3 Charge Storage Mechanism

To analyze the charge storage mechanism of the CuHCF cathode in electrolytes based on monovalent and divalent ions, potentiostatic EIS was performed in KCl and $CaCl_2$. These investigations were published in the following article, which will serve as the basis for this section:

R.L. Streng, S. Reiser, S. Wager, N. Pommer, A.S. Bandarenka. A fast and highly stable aqueous calcium-ion battery for sustainable energy storage. *ChemSusChem* 2025, 18, e202401469.

For the EIS measurements, the bias potential was set to 700 mV vs. SSC for $CaCl_2$ and 800 mV vs. SSC for KCl to account for the different electrode potentials of CuHCF in the two electrolytes. The fitted impedance spectra and the EEC model used to fit the data are shown in **Fig. 5.9**. The presented model for cation (de)intercalation, which represents a three-step mechanism and is based on the Randles analysis approach introduced in **section 3.1.3**, was adapted from Yun et al.[263] They identified three distinct stages: First, Fe^{II} is oxidized to Fe^{III} in the fast-proceeding electroactive step represented by the charge transfer resistance R_{ct}. Due to the significantly slower kinetics of cation de-intercalation, this leads to a temporary excess positive charge, which is compensated for by specific adsorption of electrolyte anions in the second step ($C_{a,1}$ and $R_{a,1}$). Finally, the charged ions leave the surface in the non-electroactive step ($C_{a,2}$ and $R_{a,2}$). Since the original model is limited to thin film electrodes, it is expanded by a semi-infinite Warburg element (W) to account for the diffusion limitations in porous composite electrodes, as described in **section 2.2.5.** The impedance spectra can be accurately fitted using this model regardless of the cation species. That fact indicates that the charge storage mechanism is the same for monovalent and divalent electrolyte cations.

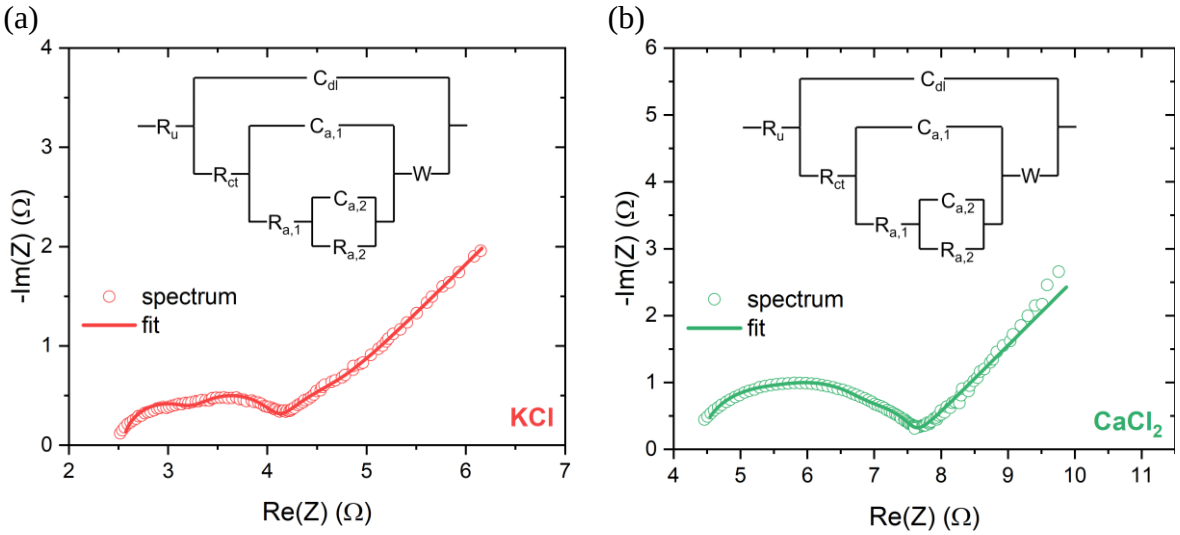


Fig. 5.9. *EIS of CuHCF in different electrolytes. (a) An example of a fitted impedance spectrum for a CuHCF cathode in an aqueous KCl electrolyte at 800 mV vs. SSC and EEC model used to fit the data. (b)) An example of a fitted impedance spectrum taken in an aqueous $CaCl_2$ electrolyte at 700 mV vs. SSC and EEC model used to fit the data. Redrawn from ref. 264 (own work).*

In addition, most fitting parameters are in the same range for both configurations. However, the resistances representing adsorption and the non-electroactive desorption step are significantly higher in $CaCl_2$ due to the higher temporary charge density in the presence of divalent cations at the electrode surface during the slow deintercalation step.

5.1.2.4 An Optimized Mixed-Salt Electrolyte

As demonstrated in sections 5.1.2.1 and 5.1.2.2, CuHCF exhibits the highest intercalation potentials in potassium-based electrolytes and the best cycling stability in divalent-ion-based electrolytes. Since the stabilization mechanism is linked to the interaction of multivalent ions with the water molecules and hydroxide ions, using them as electrolyte additives is expected to have a similar effect. Therefore, the electrochemical performance of the CuHCF cathode in a mixed 1.8 mol kg^{-1} KCl + 1.8 mol kg^{-1} $MgCl_2$ (denoted as KMC) electrolyte was investigated (**Fig. 5.10**).

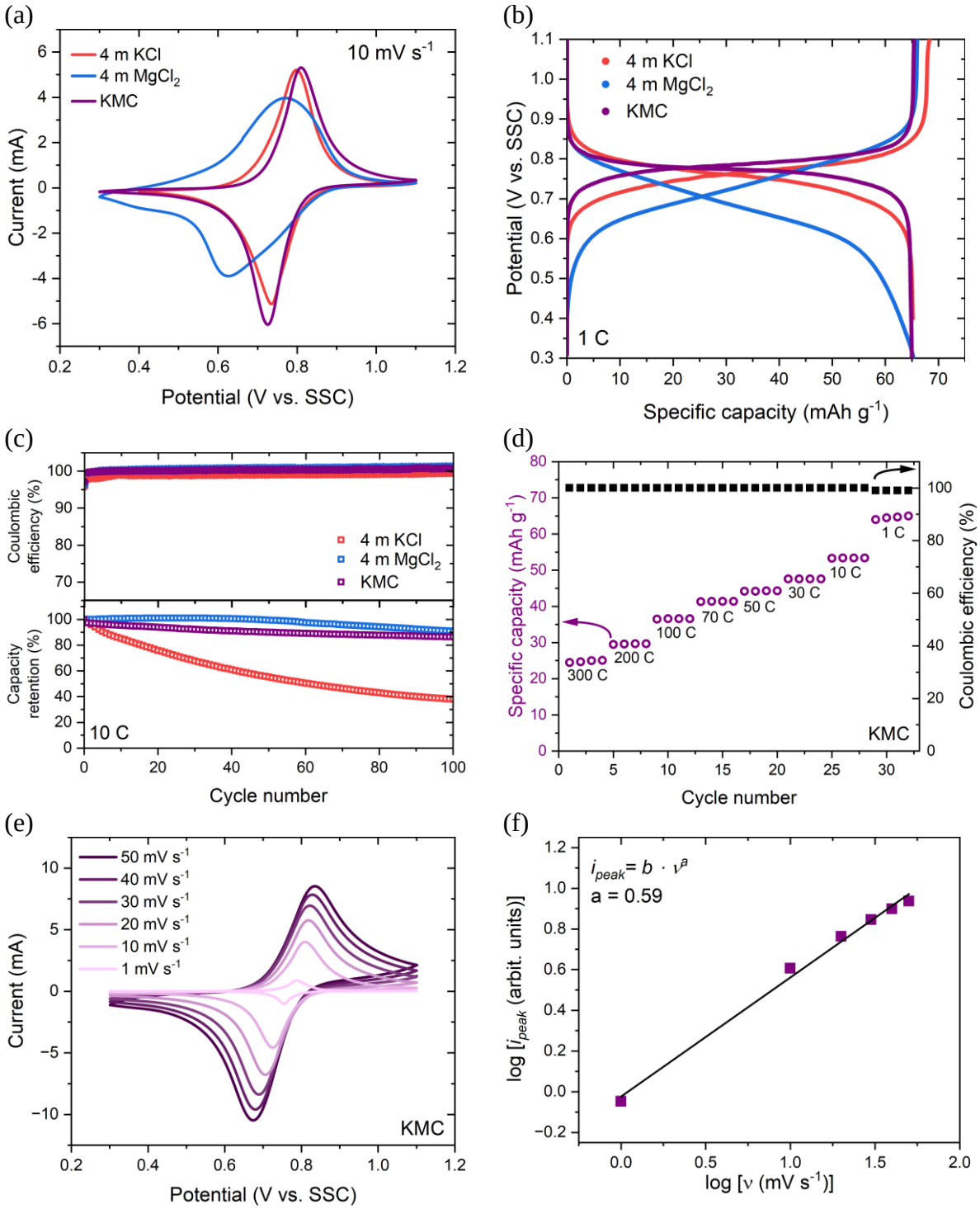


Fig. 5.10. *Electrochemical performance of the CuHCF cathode in the mixed 1.8 mol kg^{-1} KCl + 1.8 mol kg^{-1} $MgCl_2$ (KMC) electrolyte. (a) CV curves, (b) galvanostatic (dis)charge curves, and (c) cycling stability in 4 mol kg^{-1} KCl and $MgCl_2$, as well as the KMC electrolyte. (d) The specific discharge capacity of CuHCF in KMC at different C-rates. (e) CV curves of CuHCF in KMC at various scan rates. (f) Peak current vs. scan rate extracted from graph (e). Redrawn from ref. 243 (own work).*

Fig. 5.10 (a) shows the CV curves of CuHCF in pure KCl and $MgCl_2$ electrolytes and the mixed-salt electrolyte. As mentioned previously, the peak positions and shapes vary significantly between the potassium-based and magnesium-based electrolytes due to the more sluggish charge transfer and diffusion kinetics of the high-charge-density Mg^{2+} cations. In KMC, the CV shape closely resembles the curve recorded in pure KCl, indicating that the potassium ions primarily influence the intercalation characteristics. However, since the peaks representing Mg^{2+} and K^+ insertion overlap, co-intercalation of both cations may occur. As shown in **Fig. 5.11,** energy dispersive x-ray spectrometry (EDX) reveals that both magnesium and potassium are present in the electrode after complete reduction in the mixed electrolyte. Nonetheless, the overall ion transfer kinetics are the same as in pure KCl, although both cations intercalate simultaneously.

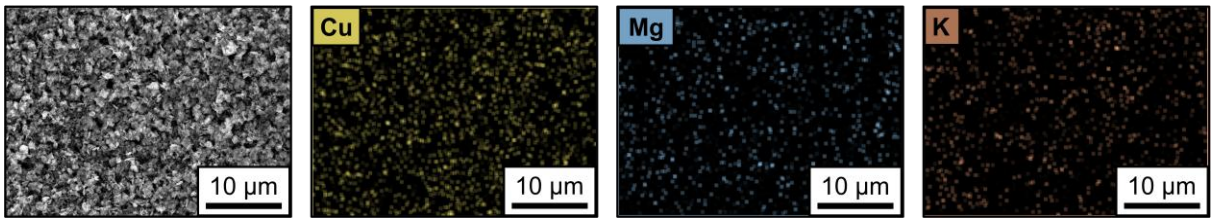


***Fig. 5.11**. SEM-EDX analysis of a CuHCF cathode after complete reduction in the mixed KMC electrolyte.*

That is also confirmed by the GC curves shown in **Fig. 5.10 (b).** While CuHCF displays flat charge and discharge profiles in KCl, the plateaus are significantly more sloped in the magnesium-based electrolyte, which also leads to a lower average operating potential for the electrode. In the mixed-salt electrolyte containing K^+ and Mg^{2+}, the curves nearly match the pure KCl electrolyte, retaining the high electrode potential. At the same time, the Coulombic efficiency at 1 C is improved from ≈95 % to ≈99 % due to the increased incorporation of water molecules in the Mg-ion solvation shell and the acidification of the electrolyte by the Lewis acid. These results suggest that the favorable redox behavior of CuHCF in potassium-based electrolytes is preserved when Mg^{2+} ions are added, while other important electrode properties are enhanced.

To test the effect of the mixed electrolyte on the cycling stability of the cathode, GC was performed for 100 cycles at 10 C. The resulting capacity retention per cycle in pure KCl and $MgCl_2$ and the mixed-salt KMC electrolyte is depicted in **Fig. 5.10 (c).** As explained in **section 5.1.2.2**, the cyclability of CuHCF is largely improved in divalent-ion-based electrolytes. The capacity retention also increases from ≈40 % in KCl to ≈90 % when a mixed-salt electrolyte is used, indicating that the stabilizing effect of divalent ions is also achieved by using them as an additive to alkali-metal-ion electrolytes. Since Mg^{2+} co-intercalates together with K^+, it can stabilize the PBA framework by binding water and reducing the activity of OH^- at the electrode surface and within the interstitial sites. Therefore, the same stabilization mechanism as that of the pure magnesium-based electrolyte can be assumed for the KMC electrolyte. That demonstrates that using mixed-salt electrolytes can combine the beneficial effects of both cations by retaining the favorable electrode potentials and flat discharge profile associated with the potassium-based electrolyte while providing the enhanced cyclability observed in the magnesium-based electrolyte.

To evaluate the rate capability of the CuHCF cathode in the KMC electrolyte, GC was conducted at different C-rates ranging from 1 C (65 mA g^{-1}) to 300 C (19.5 A g^{-1}) with four cycles at each rate. The specific capacity and Coulombic efficiency for each cycle are shown in **Fig. 5.10 (d).** At 1 C, a maximum specific capacity of 65 mAh g^{-1} is observed, exceeding the values commonly reported for CuHCF synthesized by conventional coprecipitation. That is associated with the low water and defect content achieved by using sodium pyrophosphate as an effective chelating agent during the crystal formation.[92] Furthermore, the cathode exhibits exceptional rate performance, retaining ≈85 % of its maximum capacity at 10 C. Even at an ultra-high rate of 300 C, corresponding to charging and discharging times of only a few seconds, around 40 % of the maximum capacity is retained. The rate-limiting process was identified from the peak currents of CV curves recorded at different scan rates ranging from 1 mV s^{-1} to 50 mV s^{-1} (**Fig. 5.10 (e)**). As described in section **3.1.1**, the peak current i_p can be related to the scan rate v by **Eq. 3.2**, where parameter a indicates which mechanism limits the reaction rate.

By plotting i_p against v on a double-logarithmic scale, a can be extracted from a linear fit (**Fig. 5.10 (f)**). For the CuHCF cathode, it lies at 0.59, indicating that the process is mostly mass transport limited, as expected for intercalation-type active materials in composite electrodes (see **section 2.2.5**).

5.1.3 Cation Effect on the Performance of the PNFE Anode

Similar to CuHCF, polyimides can host various monovalent and divalent metal cations. This section analyzes the influence of the electrolyte cation species on the electrochemical properties of the PNFE anode. Subsequently, the anode performance is investigated in the mixed-salt KMC electrolyte, which previously achieved the best performance for the cathode.

5.1.3.1 Electrode Potential

Fig. 5.12 shows the CV curves of the PNFE anode recorded at a scan rate of 10 mV s^{-1} in 4 mol kg^{-1} NaCl, KCl, $MgCl_2$, and $CaCl_2$. Two distinct pairs of peaks can be observed in the alkali metal-ion electrolytes, with the cathodic peaks partly overlapping in NaCl. Each peak is associated with the reduction or oxidation of one of the four carbonyl groups of the naphthalene diimide polymer units. The double-peak structure supports the generally accepted two-electron enolization process commonly reported for PNFE and similar materials, illustrated in **Fig. 5.13**.[123,124,125] Initially, a radical anion is formed, which is subsequently reduced to a dianion upon acceptance of a second electron, allowing for the coordination of two cations. A more detailed analysis of this charge storage mechanism by EIS is presented in **section 5.1.3.3**. It should be noted that further reduction of all four carbonyl groups is generally possible. However, the remaining two groups can only be reduced at significantly lower potentials beyond the onset of the HER, rendering them inaccessible in aqueous battery systems.[265] In the divalent-ion-based electrolytes, the reduction peaks overlap and can no longer be distinguished. This overlapping of the reduction potentials likely arises from the cooperative interaction of multiple polymer units that host a single multivalent ion. As several neighboring monomers simultaneously coordinate with the divalent cation, the two reduction steps no longer appear as distinct peaks but instead merge into a single, broadened feature. Two naphthalene diimide

groups may each participate in binding the same cation while being in different oxidation states, which further contributes to the merging of the redox signals.

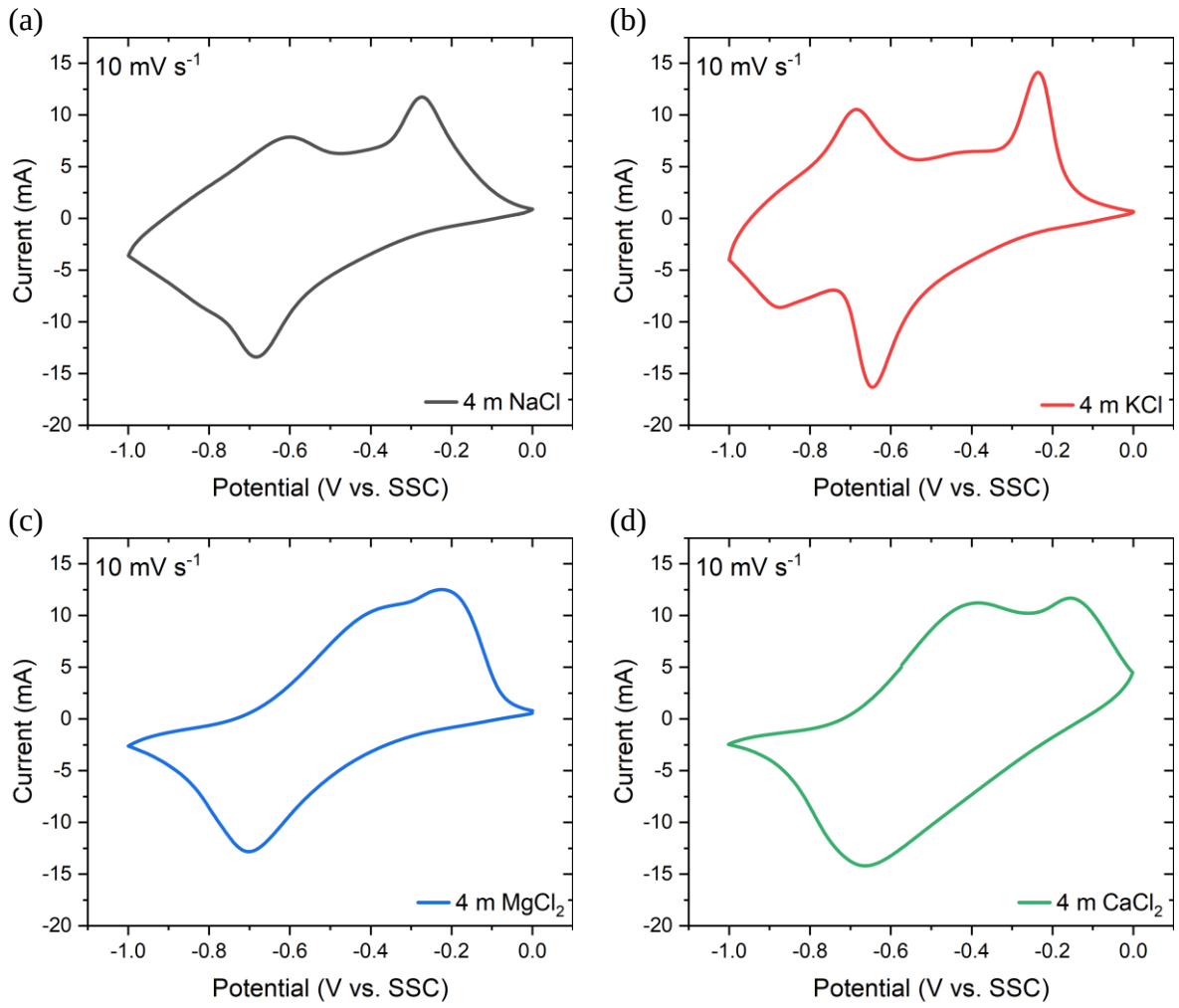


Fig. 5.12. *Typical CV curves of the PNFE anode in different aqueous 4 mol kg^{-1} (m) MCl_x electrolytes (M=Na, K, Mg, Ca). (a) NaCl. (b) KCl. (c) $MgCl_2$. (d) $CaCl_2$.*

When a reduced carbonyl group attracts a Mg^{2+} or Ca^{2+} ion, the ion's electron-withdrawing effect promotes the reduction of adjacent carbonyl groups. This process increases the conjugation of redox events across the polymer chain and alters the shape of the CV curve.[266] In addition, repulsive electrostatic interactions between closely spaced redox centers broaden the peaks and reduce the resolution between individual redox steps.[267,268] In addition to influencing the CV shape, the nature of the cation markedly affects the peak positions and, thereby, the electrode potential and reaction reversibility. The half-charge potential is the lowest in the potassium-based electrolyte and follows the trend $K^+<Na^+<Mg^{2+}/Ca^{2+}$, with no significant difference between the divalent cations. Based on this result, the redox potential can

be related to the charge density of the cation, implying that the electron-drawing nature of the high-charge-density divalent cations facilitates the enolization process.

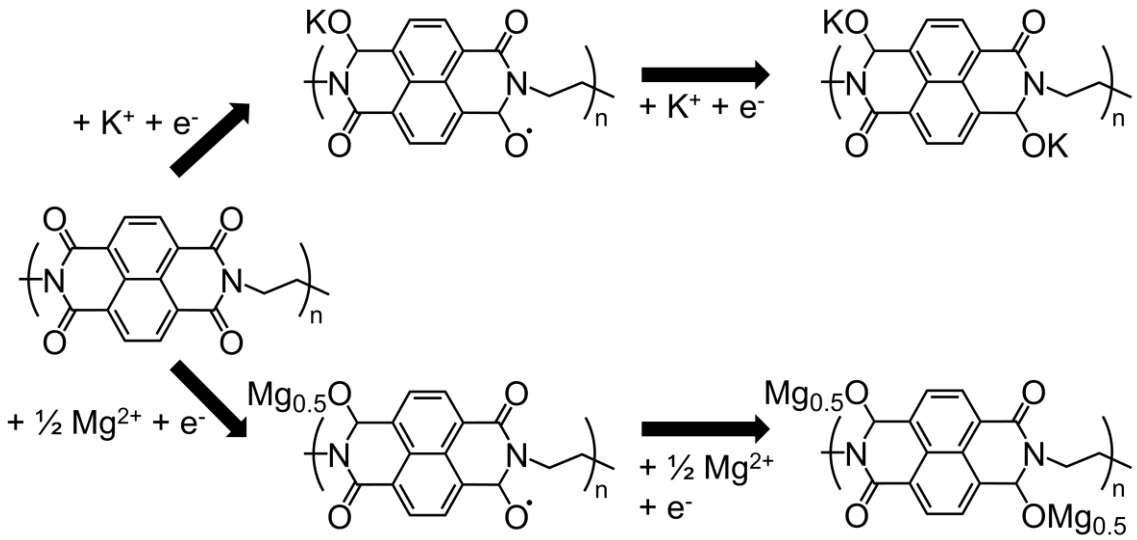


***Fig. 5.13**. The charge storage mechanism of PNFE with monovalent and divalent guest cations.*

In contrast, the low charge densities of Na^+ and K^+ increase the energy barrier for reduction, yielding more negative electrode potentials. Since the pseudo-capacitive charge storage mechanism does not involve the intercalation of a guest cation into an interstitial site of limited size, the extension of the hydration shell does not appear to play a role. Hence, using a potassium-based electrolyte, which also enables the highest cathode potentials, should achieve the highest cell voltages and energy densities in the full battery.

5.1.3.2 Cycling Stability

The cation effect on the cycling stability of PNFE was assessed by GC over 1000 cycles at 100 C. The faster cycling rate was chosen due to the high fast-charging capabilities of the anode material. As shown in **Fig. 5.14**., the capacity losses are generally small compared to the cathode across all tested electrolytes. Nonetheless, slightly higher capacity fading is observed in NaCl and KCl, with the lowest stability observed in the potassium-based electrolyte. Hence, it follows a similar trend to that of the cathode, as almost no degradation occurs in the electrolytes based on Mg^{2+} and Ca^{2+}.

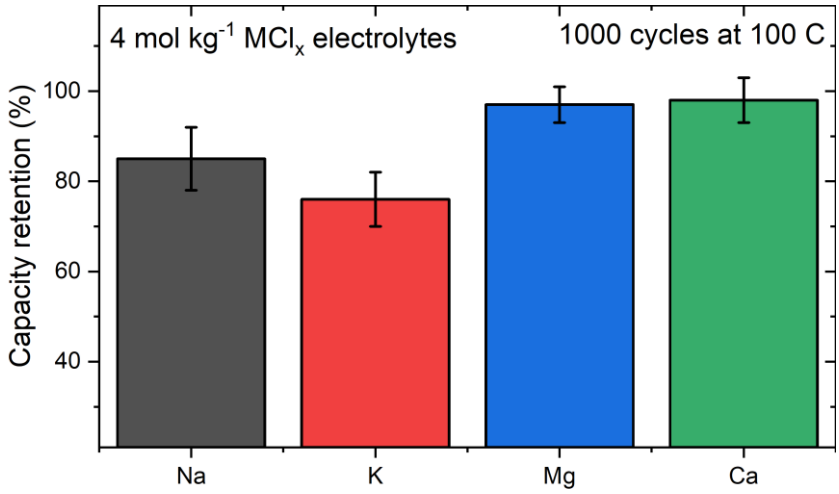


***Fig. 5.14**. The capacity retention of PNFE in different aqueous 4 mol kg^{-1} MCl_x electrolytes (M=Na, K, Mg, Ca) after 1000 cycles at 100 C. Data presented as mean ± SD, n=5. Redrawn from ref. 243 (own work).*

The minor capacity losses are likely linked to material detachment from the current collector since no degradation mechanisms have been reported for PNFE. This hypothesis is supported by SEM images taken before and after cycling the anode in KCl for 1000 cycles at 100 C (**Fig. 5.15**). After cycling, the cracks in the electrode film are significantly enlarged, and flakes have detached in various areas, as seen in the bottom left corner of **Fig. 5.15. (c)**. The detached material was observed floating in the electrolyte as small flakes, suggesting that this is the main reason for the capacity decay.

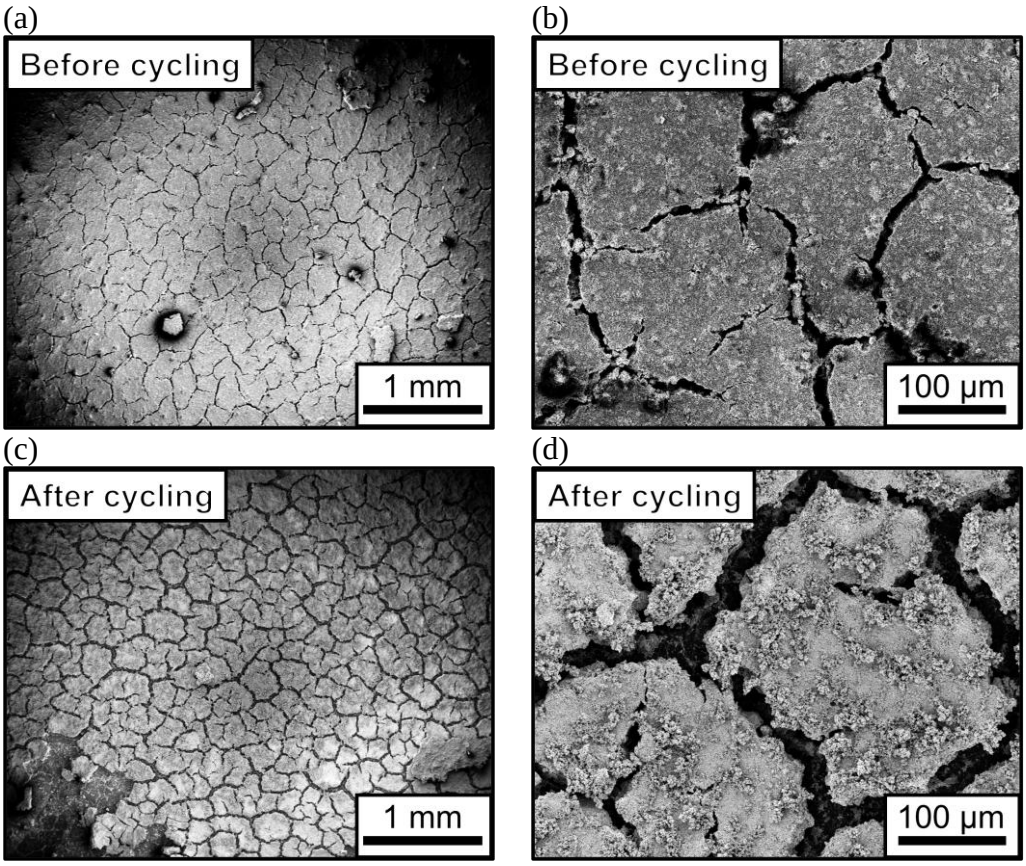


Fig. 5.15. *SEM images of the PNFE anode before and after cycling in 4 mol kg $^{-1}$ KCl. (a) Low magnification image before cycling. (b) Higher magnification image before cycling. (c) Low magnification and (d) higher magnification images after cycling for 1000 cycles at 100 C. Redrawn from ref. 243 (own work).*

In contrast, no such loss could be observed in the $MgCl_2$ and $CaCl_2$ electrolytes, implying that the material detachment is suppressed in these electrolytes. This effect is most likely related to the higher viscosity of these solutions, which prevents the transport of dissolution products away from the electrode. To compare the viscosity of alkali metal-ion-based and divalent-ion-based electrolytes, shear rheometry measurements of 4 mol kg^{-1} KCl and $MgCl_2$ were conducted. As shown in **Fig. 5.16**, the $MgCl_2$ solution exhibits a viscosity approximately ten times higher than that of the KCl solution at the same concentration, which is attributed to the stronger degree of water coordination in the cation hydration shells and the higher anion concentration.[269,270] Therefore, the Mg-ion and Ca-ion electrolytes enable enhanced cyclability of the anode compared to the K-ion and Na-ion electrolytes. However, since the capacity losses are generally small and material detachment should be suppressed in realistic full cell setups

with much smaller volumes of electrolyte, the cycling stability of the full battery will mostly depend on the CuHCF cathode.

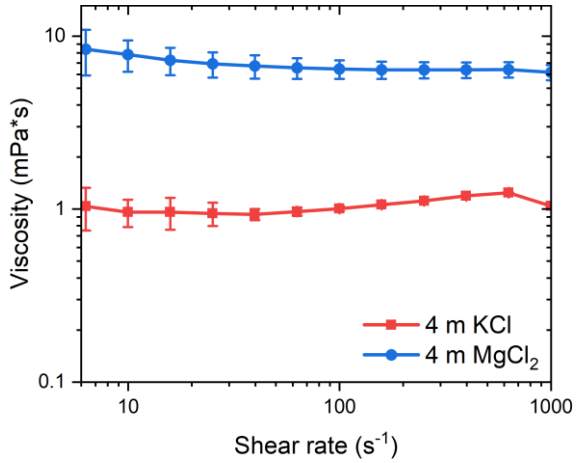


***Fig. 5.16**. Viscosities of 4 mol kg^{-1} (m) KCl and $MgCl_2$. The viscosity was measured over a range of shear rates following a logarithmic ramp. Newtonian behavior is observed for all solutions as expected. Data presented as mean ± SD, n=3. Redrawn from ref. 243 (own work).*

5.1.3.3 Charge Storage Mechanism

To analyze the effect of the cation species on the charge storage mechanism of the PNFE anode, potentiostatic EIS was conducted at -500 mV vs. SSC in KCl and $CaCl_2$ electrolytes. The fitted spectra and the used equivalent circuit are shown in **Fig. 5.17**. We first reported this EEC model and demonstrated its capability of accurately describing the charge transfer mechanism of PNFE in the following published article:

R.L. Streng, S. Vagin, Y. Guo, B. Rieger, A.S. Bandarenka. Identifying the charge storage mechanism in polyimide anodes for Na-ion aqueous batteries by impedance spectroscopy. *RSC Energy Advances* 2024, 3, 874-882.

The analysis below is based on this model and was carried out for ref. 264, which will serve as the basis for this section. As all equivalent circuits used in this work, the EEC is derived from the Randles analysis described in **section 3.1.3**. Accordingly, R_U and C_{dl} represent the uncompensated electrolyte resistance and the double layer capacity, respectively. Generally, a CPE may be used instead of a capacitor to model the double-layer behavior. However, since

that does not significantly improve the already high fit quality (R^2 < 1 %) and the resulting exponent is very close to 1.0, the use of a CPE was omitted.

The EEC also includes the charge transfer resistances $R_{ct,1}$ and $R_{ct,2}$, as well as a semi-infinite Warburg element (*W)* to account for pore diffusion and mass transport limitations due to charge delocalization over the conjugated polymer structure.

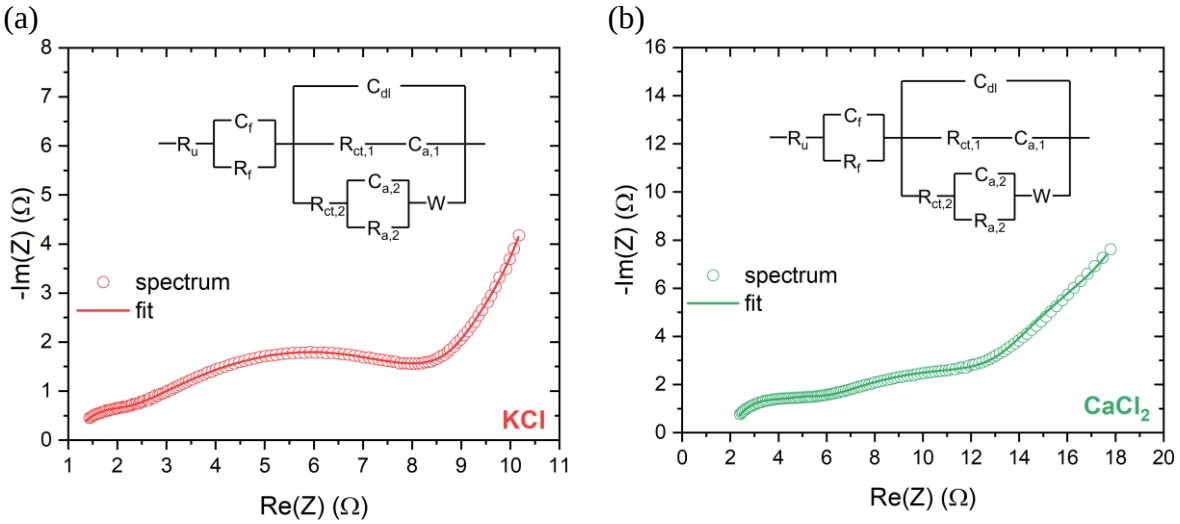


Fig. 5.17. *EIS of PNFE in different electrolytes. (a) An example of the fitted impedance spectrum of a PNFE anode in an aqueous KCl electrolyte at -500 mV vs. SSC, and the EEC model used to fit the data. (b) An example of the fitted impedance spectrum in an aqueous $CaCl_2$ electrolyte at -500 mV vs. SSC, and the EEC model used to fit the data. Redrawn from ref. 264 (own work).*

C_f and R_f represent the impedance contribution of the polymer film on the graphite substrate to the overall impedance of the system. For PNFE, a two-stage charge transfer mechanism is expected as each monomer unit is reduced by two electrons. This mechanism is modeled by the arrangement of $R_{ct,2}$, $C_{a,2}$, and $R_{a,2}$, reflecting that the reduction of the first carbonyl group and the subsequent formation of the radical anion determine the second reduction step, which can only take place after the first enolization process is completed. Accordingly, the bottom branch of the EEC describes a conjugated two-electron transfer with reversible stages. In addition to the expected two-step mechanism, a secondary single-step pathway was identified, which takes place simultaneously and is represented by $R_{ct,2}$ and $C_{a,2}$. This process is likely associated with the stabilization of the radical species via interactions with the substrate or other nearby radicals

after the first reduction step, thereby inhibiting further reduction. The experimental specific capacity of PNFE is commonly observed to be lower than the theoretical capacity, implying that not all parts of the polymer accept two electrons, which serves as a verification of this EEC.[123,124,271]

For both KCl and $CaCl_2$, the described model can be used to fit the spectra with high accuracy, suggesting that the charge transfer mechanism remains unaffected by the valency of the inserted cation. Moreover, the single-stage pathway is significantly suppressed compared to the dominating two-stage mechanism in both electrolytes, as $R_{ct,1}$ is ≈10 times and ≈15 times higher than $R_{ct,2}$ for $CaCl_2$ and KCl, respectively. This also confirms that the single cathodic peak in the CV curves of PNFE in the divalent-ion electrolytes represents the merging of two distinct reduction steps.

5.1.3.4 Performance of the Anode in the Optimized Electrolyte

As shown above, the cation effect on the electrochemical properties of the cathode is significantly more pronounced than for the anode. Therefore, the performance of the anode was also investigated in the KMC electrolyte, which yields an optimal electrode potential and cycling stability for the cathode.

Fig. 5.18 (a) shows the CV curves of the PNFE anode recorded at 10 mV s^{-1} in pure 4 mol kg^{-1} KCl and $MgCl_2$, as well as the mixed-salt KMC electrolyte. In KMC, the shape and position of the redox peaks closely resemble the magnesium-based electrolyte, indicating that the charge transfer is dominated by the kinetics of Mg^{2+} insertion. While the half-charge potential in KMC is slightly higher than in KCl, the peak-to-peak separation is lower, indicating enhanced reversibility.

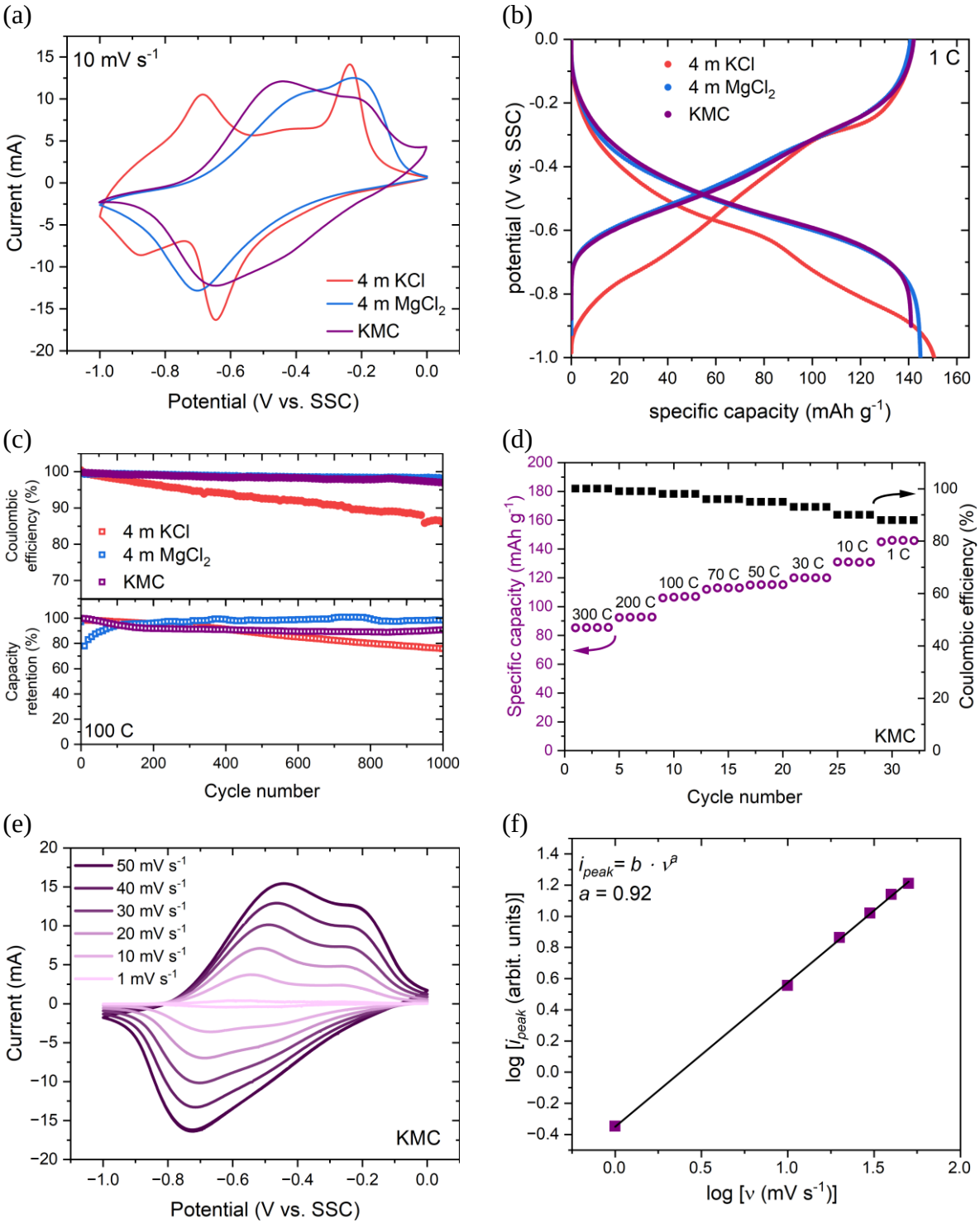


Fig. 5.18. *Electrochemical performance of the PNFE anode in the mixed 1.8 mol kg^{-1} KCl + 1.8 mol kg^{-1} $MgCl_2$ (KMC) electrolyte. (a) CV curves, (b) galvanostatic (dis)charge curves, and (c) cycling stability in 4 mol kg^{-1} KCl and $MgCl_2$, as well as the KMC electrolyte. (d) Specific discharge capacity of PNFE in KMC at different C-rates. (e) CV curves of PNFE in KMC at different scan rates. (f) Peak current vs. scan rate extracted from graph (e). Redrawn from ref. 243 (own work).*

This is confirmed by the galvanostatic (dis)charge curves shown in **Fig. 5.18 (b)**, as the profiles are less sloped and separated for KMC and $MgCl_2$ compared to KCl. Moreover, PNFE exhibits a slightly improved Coulombic efficiency, and the curves are nearly identical for the two magnesium-containing electrolytes. Hence, although the potassium-based electrolyte enables higher cell voltages, the mixed electrolyte leads to flatter discharge profiles and suppresses side reactions.

Fig. 5.18 (c) shows the capacity retention of the anode in 4 mol kg^{-1} KCl and MgCl, as well as the mixed salt electrolyte during 1000 cycles at 100 C. In KCl, a slow but continuous capacity decay accompanied by a gradual decrease in Coulombic efficiency can be observed, as discussed in detail in **section 5.1.3.2**. In contrast, PNFE only exhibits minor capacity losses and remains stable after the initial cycles in the magnesium-containing electrolytes. The high Coulombic efficiencies indicate effective suppression of parasitic HER at this rate, attributed to molecular crowding despite the shift towards a more acidic pH value due to hydrolysis of Mg^{2+}. An initial increase in capacity in the pure $MgCl_2$ electrolyte can be attributed to the slow wetting of the electrode surface due to the high viscosity. Overall, using the KMC electrolyte enhances the cycling stability of the anode, compared to the potassium-based electrolyte. Nonetheless, the effect is less pronounced than for the cathode, as PNFE is generally more stable. Accordingly, the full cell stability is expected to be primarily governed by the degradation rate of CuHCF in the employed electrolyte.

The rate performance of PNFE in the KMC electrolyte was investigated by GC at different rates ranging from 1 C (150 mA g^{-1}) to 300 C (45 A g^{-1}). As shown in **Fig. 5.18 (d)**, PNFE displays a maximum specific discharge capacity of ≈148 mAh g^{-1} at 1C, underlining the promising potential of organic anode materials for LFABs. Moreover, it exhibits exceptional fast-charging capabilities, retaining ≈90 % of its maximum capacity at 10 C and ≈60 % at 300 C. The decreasing Coulombic efficiency at lower rates indicates parasitic HER, which starts to play a role at lower current densities. However, this effect is usually more pronounced in the flooded cell setup compared to practical batteries with minimal electrolyte volumes.

As the fast-charging capabilities are linked to the charge transfer kinetics, the rate-limiting process was identified using CV at different scan rates (**Fig. 5.18 (e)**). From the fit in **Fig. 5.18 (f)**, which plots the peak current against the scan rate, the extracted parameter *a* yields a value of 0.92. In contrast to the cathode, this indicates mainly surface-limited charge transfer kinetics, confirming the expected pseudo-capacitive nature of the charge storage mechanism. As mass transport is not a primary limiting factor, this translates to fast charge transfer kinetics and good fast-charging capabilities.

5.1.4 The CuHCF/KMC/PNFE Full Cell

The results above show that the two electrodes exhibit different fast-charging capabilities and have important implications for the design of the full battery. If the cell is to be optimized for high fast-charging, the cathode capacity should be higher than the anode capacity by adjusting the mass balance. To maximize energy density, the capacities should be the same for both electrodes. For this work, the latter approach was chosen, and a cathode-to-anode active material ratio of 1:2 was used, which corresponds to the ratio of specific capacities at 1 C. The electrodes were combined with the KMC electrolyte, which showed promising results in the previous analyses. **Fig. 5.19 (a)** shows the combined CV curves of the CuHCF cathode and the PNFE anode in the KMC electrolyte. From the single-electrode measurements, the full battery can be expected to operate between cell voltages of 0.8 V and 1.7 V without strong HER or OER side reactions. Indeed, the CV curve of the full cell exhibits reversible oxidation and reduction peaks within this range, as shown in **Fig. 5.19 (b).** As for the single electrodes, the fitting parameter a (**Eq. 3.2**), which indicates the rate-limiting process, was extracted from the peak currents of the CV curves recorded at different scan rates (**Fig. 5.19(c)**). For the full cell, it lies at 0.82, suggesting mixed charge transfer kinetics. As the anode processes are surface-limited and the cathode processes are diffusion-limited, the full battery exhibits partially mass-transport-limited kinetics. Due to the fast kinetics of the pseudo-capacitive charge storage of the anode, the fast-charging capabilities of the battery are primarily limited by the diffusion at the cathode.

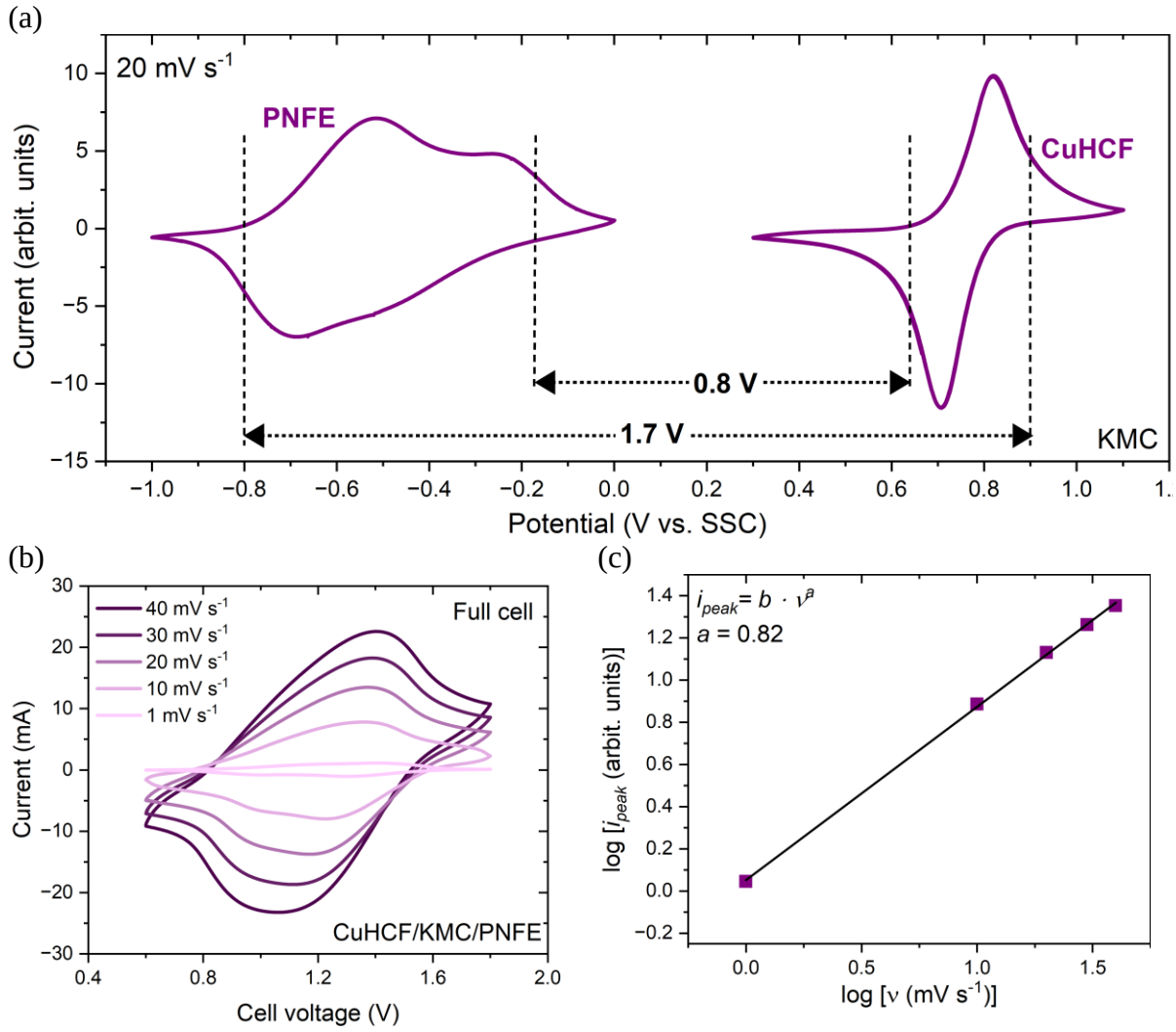


***Fig. 5.19**. CV characterisation of the CuHCF/KMC/PNFE batteries. (a) CV curves of the single electrodes in the KMC electrolyte. The dotted lines indicate the expected voltage range of the full cell. (b) CV curves of the full cell at different scan rates. (c) Peak current vs. scan rate extracted from graph (b). Redrawn from ref. 243 (own work).*

To analyze the rate performance, GC was carried out at different C-rates ranging from 1 C (42 mA g^{-1}) to 300 C (12.6 A g^{-1}). The resulting (dis-)charge profiles are shown in **Fig. 5.20 (a).** Due to the pseudo-capacitive properties of the anode, the discharge displays a sloping plateau between 1.6 V and 0.8 V at 1C, corresponding to an average discharge voltage of ≈1.22 V. The maximum discharge capacity is ca 42 mAh g^{-1} normalized to the combined mass of the anode and cathode active materials. Considering the specific capacities of the anode (148 mAh g^{-1})

and cathode (65 mAh g^{-1}), the experimental specific capacity of the full cell is only slightly lower than the calculated value (43.3 mAh g^{-1}).

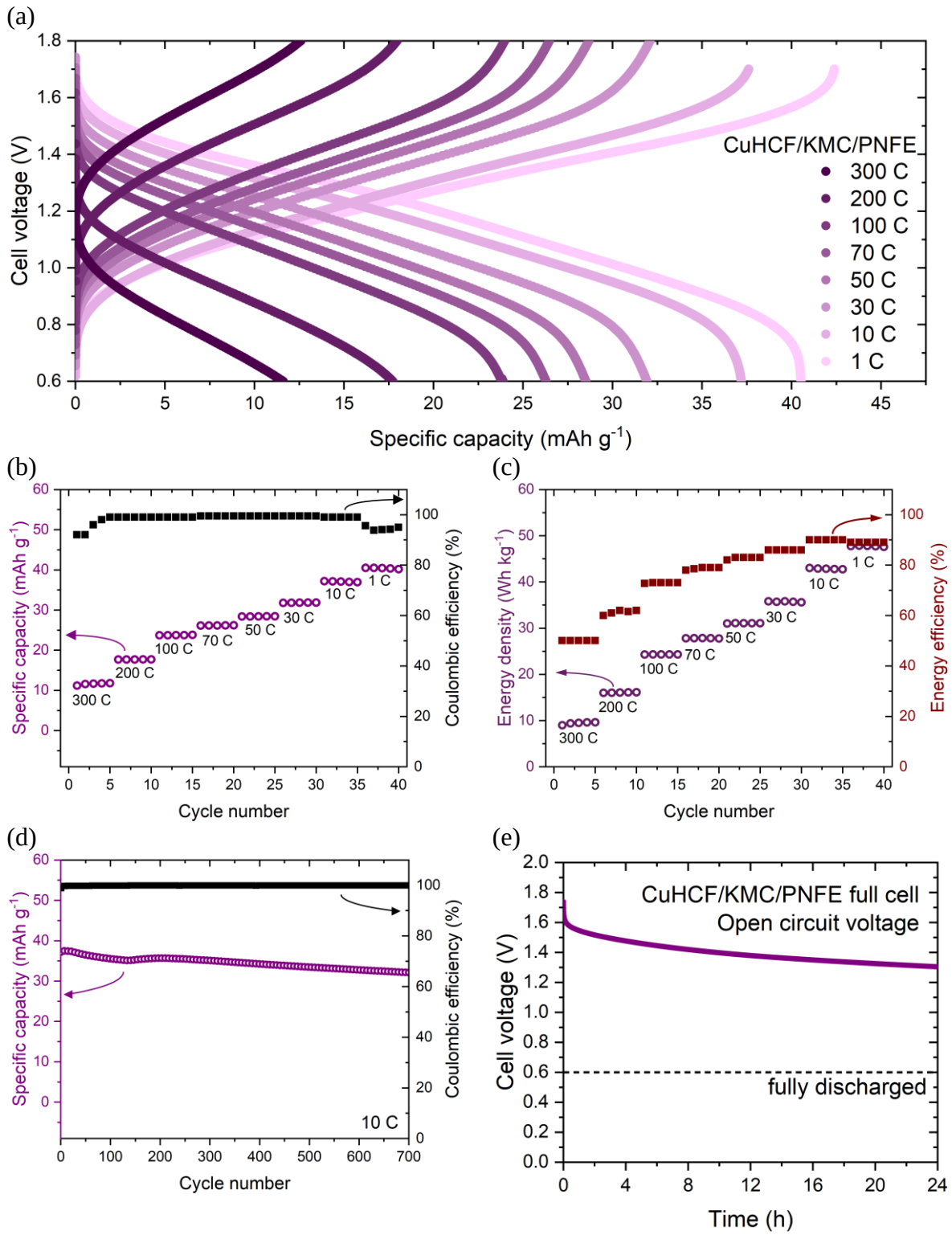


Fig. 5.20. *Electrochemical performance of the CuHCF/KMC/PNFE aqueous battery. (a) Galvanostatic (dis-)charge profiles at different rates. (b) Specific capacity and Coulombic efficiency at different C-rates. (c) Energy density and energy efficiency at different C-rates. (d) Capacity retention during 700 cycles at*

10 C. (e) Open circuit voltage measured over 24 hours. Redrawn from ref. 243 (own work).

Moreover, the battery retains the fast-charging capabilities of the single electrodes, as ≈90% of the maximum capacity can still be delivered at 10 C (6 min charging time). Even when charged in less than one minute, the battery remains functional, retaining ≈57 % and ≈30 % of its maximum capacity at 100 C and 300 C, respectively. Since mass transport at the cathode was identified as the main rate-limiting process of the battery, the exceptionally high rate capability can be attributed to the high mobility of K^+ due to its small hydration shell and low charge density. Furthermore, the battery performance remains stable over all tested cycles and exhibits high Coulombic efficiencies exceeding 95 % at every rate (**Fig. 5.20 (b)**). The slightly lower CE at 1 C can be linked to water splitting. Cl^- oxidation, which can occur in Cl-containing electrolytes, likely plays a minor role, as it is characterized by a higher onset potential than the OER (see **section 2.1.2**).

The energy density for each cycle and C-rate was evaluated by integrating the discharge profiles, as described in **section 2.2.3**, and is shown in **Fig. 5.20 (c)**. Thereby, a maximum energy density of ca 48 Wh kg^{-1} is obtained at 1 C. This value is similar to state-of-the-art lead acid batteries, although the mass contribution of other cell components, such as current collectors, electrode additives, electrolyte, and casing, needs to be taken into account for a full device. At higher currents, the voltage polarization increases, leading to a stronger rate dependence of the energy density compared to the specific capacity and lower energy efficiencies. This effect is explained in detail in **section 2.2.5**. The highest energy efficiency is obtained at 10 C (≈90 %), since lower Coulombic efficiencies decrease the energy efficiency at 1 C. Nonetheless, ca 43 Wh kg^{-1} are retained at 10 C, meaning that the battery can be nearly fully charged in less than 10 min. Even at ultra-high rates of 100 C to 300 C the battery can still operate effectively, and can thus be considered a hybrid battery/supercapacitor, combining intermediate energy densities with short charging times. It is therefore suitable for high-power applications, such as public transport or grid stabilization. The power densities can be calculated

from the discharge current density and the average discharge voltage at each rate, as explained in **section 2.2.3**. A C-rate of 1 C corresponds to a gravimetric current density of 42 mA g^{-1} and leads to an average discharge voltage of 1.22 V, resulting in a power density of ~51.2 W kg^{-1}. At 300 C (12.6 A g^{-1}), an average discharge voltage of 0.85 V is obtained, and a high maximum power density of ca 10.7 kW kg^{-1} is obtained.

The cycling stability of the CuHCF/KMC/PNFE aqueous battery was investigated by GC for 700 cycles at 10 C. **Fig. 5.20 (d)** shows the remaining capacity and Coulombic efficiency for each cycle. Over the course of 700 charge and discharge cycles, the cell retains ≈90 % of its initial capacity, confirming the good cyclability expected from the half-cell measurements. Moreover, the high Coulombic efficiency of nearly 100 % throughout the measurement indicates successful suppression of parasitic side reactions in the KMC electrolyte. Accordingly, the battery does not exhibit significant self-discharge, as demonstrated by measuring the open circuit voltage over 24 h (**Fig. 5.20 (e)**). After disconnecting the fully charged battery from the power source, the cell voltage remains relatively stable following an initial drop from 1.7 V to 1.5 V.

The performance of the CuHCF/KMC/PNFE battery was compared to similar cells with different electrolytes and to other aqueous Mg-ion and K-ion batteries previously reported in the literature. First, to demonstrate the advantages of the mixed-salt electrolyte, various cells were assembled with the same electrode materials and different single-salt and mixed-salt electrolytes. As the specific capacity of the electrode material combination is independent of the used electrolyte, the average discharge voltage serves as a good indicator for energy density, and was thus assessed for each battery. Furthermore, the cycling stability was tested by GC for 700 cycles at 10 C (**Fig. 5.21 (a)**). Saturated solutions of all electrolytes were used to maximize molecular crowding, which improves capacity retention during cycling. As expected from the results presented above, the battery based on saturated (4.5 mol kg^{-1}) KCl features the highest cell voltage, but suffers from severe degradation, with only ≈60 % of the initial capacity remaining after 700 cycles. In contrast, batteries using saturated (6.7 mol kg^{-1}) $CaCl_2$ exhibit

almost no capacity losses during the measurement. This can be attributed to the high solubility of $CaCl_2$, leading to high viscosity and a low free water content in the electrolyte. We have discussed the performance of this battery in more detail in a dedicated published article.[264] Like the cell based on pure $MgCl_2$, the calcium-ion battery is characterized by a significantly lower operating voltage than the potassium-ion battery. Therefore, it is particularly suitable for long-term applications that require long cycle life and minimal maintenance.

Mixed-salt electrolytes are capable of combining the high energy densities of K-based systems and the cyclability of Mg or Ca-based systems. Batteries using the KMC electrolyte discussed above or a mixed 2 mol kg^{-1} KCl + 2 mol kg^{-1} $CaCl_2$ electrolyte exhibit significantly enhanced capacity retention compared to pure KCl, as well as higher cell voltages than the Ca-ion and Mg-ion cells.

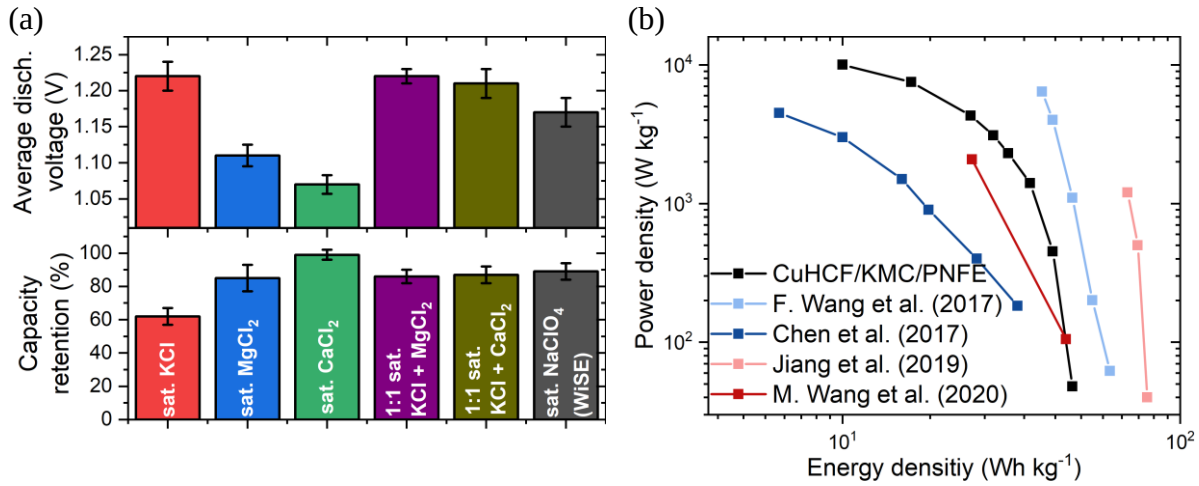


Fig. 5.21. *Comparing the performance of the CuHCF/KMC/PNFE full cell. (a) Average discharge voltage and capacity retention over 700 cycles at 10 C for CuHCF/PNFE batteries based on different aqueous electrolytes. Data presented as mean ± SD, n = 5. (b) Ragone plot comparing the performance of the cell with AKIBs and AMIBs reported in previous literature. (refs. 108,272, 273,274). Redrawn from ref. 243 (own work).*

To further demonstrate the competitive performance of mixed-salt electrolytes, a benchmark cell using a commonly used saturated $NaClO_4$ WiSE was assembled for comparison.[275,276,277,278] Due to the low intercalation potential of Na^+ into CuHCF, this battery features a lower average

discharge voltage than the mixed-salt systems, while achieving similar cyclability, confirming the promising properties of the KMC electrolyte.

Fig. 5.21 (b) shows a Ragone plot comparing the energy density and power density of the LFAB proposed in this chapter with other AKIBs and AMIBs reported in the literature. While the batteries developed by Wang et al.[272] and Jiang et al.[108] demonstrate higher energy densities, their systems rely on expensive fluorinated salts, specifically $Mg(TFSI)_2$ and KCF_3SO_3, respectively. It is worth noting that Jiang et al. employ highly concentrated electrolytes to achieve stable cycling of the Mn-based Prussian Blue Analogue (PBA) cathode, whereas Wang et al. use a comparatively dilute electrolyte. However, the $Li_3V_2(PO_4)_3$ cathode used in the latter contains both lithium and vanadium, which could significantly increase the overall cost of the cell. Despite this, the high energy densities of those systems make them well-suited for applications where minimizing cell weight is critical. In comparison, the energy density achieved in this work surpasses typical values reported for aqueous batteries that use F-free, dilute electrolytes, such as the aqueous K-ion and Mg-ion batteries described by Chen et al.[273] and Wang et al.,[274] respectively. Furthermore, the power density of our system exceeds 10 kW kg^{-1}, outperforming all of the above-mentioned designs. To our knowledge, such high power outputs have rarely been reported for aqueous batteries to date. A more extensive comparison, including a wider range of LFABs and other energy storage devices, can be found at the end of **section 5.2**.

Overall, the results presented above demonstrate the tunability of battery performance by optimizing the electrolyte composition. While potassium ions enable the highest cell voltages and energy densities, divalent cations such as Mg^{2+} and Ca^{2+} help to stabilize electrode materials and enhance cycling stability. Both advantages can be combined by using mixed-salt electrolytes containing both K^+ and Mg^{2+}, which allow for both high energy densities and long cycle lives. In addition, the so-prepared batteries exhibit exceptional fast-charging capabilities and power densities.

5.2 Stabilizing Mn-Rich PBAs for Low-Cost and High-Energy Aqueous Batteries

In **section 5.1**, a novel aqueous battery using a PNFE anode, a mixed 1.8 mol kg^{-1} KCl + 1.8 mol kg^{-1} $MgCl_2$ electrolyte, and a CuHCF cathode was introduced. Since the specific capacity of CuHCF is considerably lower than that of PNFE, using an alternative cathode active material with higher ion storage capacity is the most promising approach to enhance energy density further. In contrast to CuHCF, MnHCF features a two-electron redox reaction allowing for significantly higher capacities, as explained in the introduction. However, its practical application is impaired by severe degradation upon cycling, due to lattice distortions.[103,104,105,106] In this section, three strategies for mitigating capacity decay in Mn-based PBAs are investigated and combined to stabilize these materials. Subsequently, a second full cell consisting entirely of low-cost and sustainable materials with a high energy density is proposed. The results presented below are primarily based on the following article, which was published with contributions from all listed co-authors:

R.L. Streng, T. Steeger, A. Senyshyn, S. Abel, P. Schneider, C. Benning, B. Miller Naranjo, D. Gryc, M.Z. Hussain, O. Lieleg, M. Elsner, A.S. Bandarenka, K. Cicvarić. A low-cost and high-energy aqueous potassium-ion battery. *Journal of Energy Chemistry* 2025, 106, 523-531.

5.2.1 Jahn-Teller Effect on MnHCF

The following section briefly introduces the main degradation mechanism of MnHCF to help understand the results discussed below. **Eq. 5.1** gives a simplified representation of the two reduction steps of MnHCF with K^+ as the guest cation.

$$\mathrm{Mn^{III}[Fe^{III}(CN)_6] + K^+ + e^- \rightleftharpoons K_1Mn^{II}[Fe^{III}(CN_6)]}$$

$$\mathrm{K_1Mn^{II}[Fe^{III}(CN)_6] + K^+ + e^- \rightleftharpoons K_2Mn^{II}[Fe^{II}(CN_6)]} \qquad \textbf{Eq. 5.1}$$

The additional $Mn^{II/III}$ transition doubles the theoretical specific capacity compared to PBAs using a single-electron reaction. However, it also causes rapid degradation due to structural collapse induced by so-called Jahn-Teller distortions upon oxidation.[107] A schematic illustration of this effect is given in **Fig. 5.22**. In the fully oxidized state of FeMnHCF, the manganese ion

adopts a +3 oxidation state, yielding a $3d^4$ electronic configuration. The cyanide (CN^-) ligands impose a crystal field splitting that stabilizes a high-spin d^4 electron configuration. Under this ligand field, the 3d electrons of Mn(III) populate the lower-energy $t_{2}g$ orbitals first, followed by the e_g orbitals, resulting in a $t_{2}g^3e_g^1$ configuration. The presence of a single electron in the degenerate e_g orbitals, which comprise the d_{z^2} and $d_{x^2-y^2}$ orbitals, creates an electronically unstable condition. According to the Jahn-Teller theorem, this degeneracy will be compensated by structural distortion. Indeed, Mn^{III} in this complex exhibits axial elongation along the z-axis, leading to a splitting of the e_g orbitals.[279] Therefore, the d_{z^2} orbital, which is aligned along the elongated z-axis, is stabilized as the energy is lowered. This distortion reduces the overall symmetry of the complex from ideal octahedral to a lower symmetry, resulting in a more stable electronic configuration.[280,281,282] During complete oxidation, the Jahn-Teller distortions cause an irreversible phase transition from cubic to tetragonal upon removal of the second guest cation, leading to rapid degradation.[283] It should be noted that another phase transition from monoclinic to cubic occurs during the first oxidation step. However, this reversible distortion does not impair the stability of the PBA.[283]

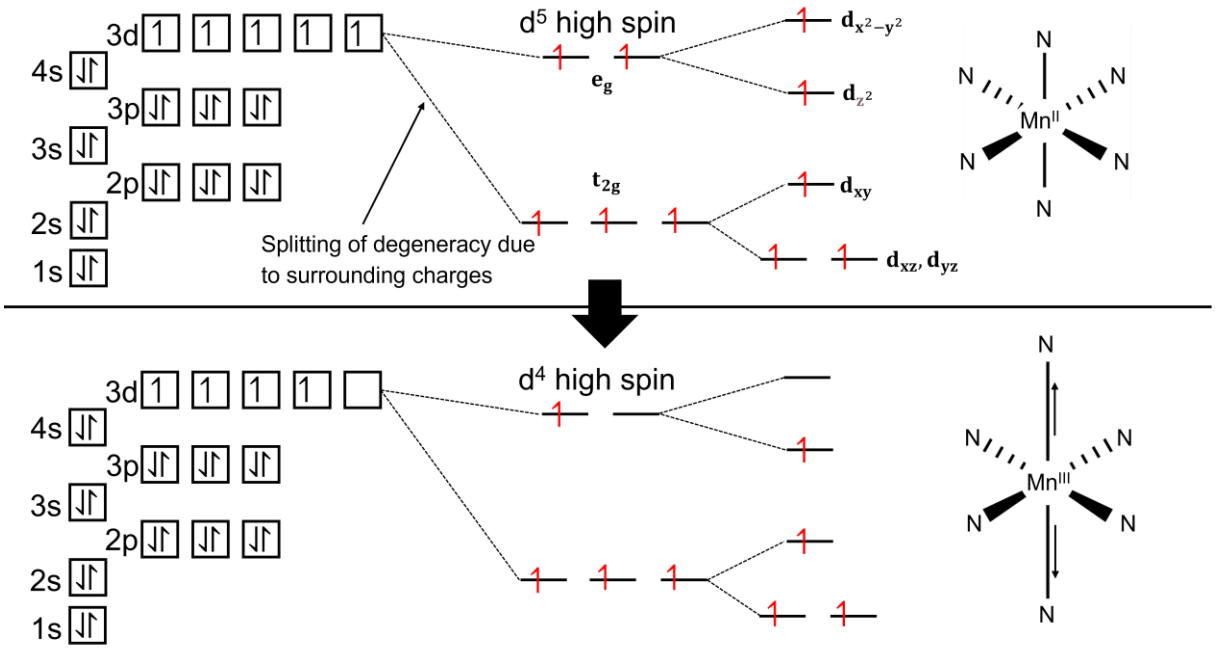


***Fig. 5.22**. Schematic illustration of the Jahn-Teller effect responsible for the rapid degradation of MnHCF upon oxidation.*

5.2.2 Structure and Morphology of the Mn-rich PBA cathodes

As described in **section 4.5.1,** three different Mn-rich PBA active materials were synthesized by coprecipitation from aqueous precursor solutions. Besides pure MnHCF, Fe-doped FeMnHCF-A and FeMnHCF-C were prepared by adding $FeSO_4$ to the Mn-containing precursor solution. While the procedure for FeMnHCF-A was the same as for MnHCF, sodium citrate was used as a chelating agent to control the crystallinity of FeMnHCF-C. The structure of all three materials was investigated using XRD, ICP-MS, and SEM. **Fig. 5.23** shows the fitted XRD patterns. The instrumental resolution function was estimated using data from a Si reference measurement. The X-ray diffraction pattern of MnHCF reveals sharp, well-defined peaks with slight splitting and the presence of additional low-intensity reflections beneath the dominant ones. This suggests a highly ordered structure with near-cubic symmetry.[218] The primary features of the pattern are consistent with a face-centered cubic lattice from the *Fm*-3*m* space group with a lattice constant of 10.504 Å, as shown in **Fig. 5.23 (a)**.[284] However, the weak splitting of certain reflections points to a minor deviation from ideal cubic symmetry. This deviation can be more accurately described using a tetragonal model with a primitive unit cell, characterized by a similar *a* lattice parameter and a doubled *c* parameter (a = 10.530 Å and c = 20.991 Å), depicted in **Fig. 5.23 (b)**. The calculated tetragonal distortion is relatively small, approximately 0.3%, indicating only a slight structural anisotropy.

The XRD pattern of the Fe-doped FeMnHCF-A displays well-isolated, broad peaks, as shown in **Fig. 5.23 (c)**. Similarly to MnHCF, these reflections are associated with a cubic lattice from the *Fm-3m* space group with a lattice parameter of a = 10.188 Å. However, two sharp reflections are observed, which belong to an unidentified secondary phase, as they are not associated with a tetragonal distortion like for MnHCF.

In contrast to MnHCF and FeMnHCF-A, the XRD pattern of FeMnHCF-C can be associated with a monoclinic phase from the $P2_1/c$ space group, since it was synthesized using $K_4Fe(CN)_6$, resulting in the formation of a fully reduced PBA. Most notably, this phase is indicated by a characteristic triplet at 2θ = 25°. FeMnHCF-C is characterized by a highly crystalline structure

with lattice parameters a = 6.983 Å, b = 7.304 Å, c = 12.305 Å, and β = 124.79°, indicating that the crystal formation process was successfully controlled by the chelating agent. By analyzing the peak broadening, a slight micro-strain of isotropic character was identified, suggesting local chemical inhomogeneities due to uneven distribution of the intercalated potassium ions.

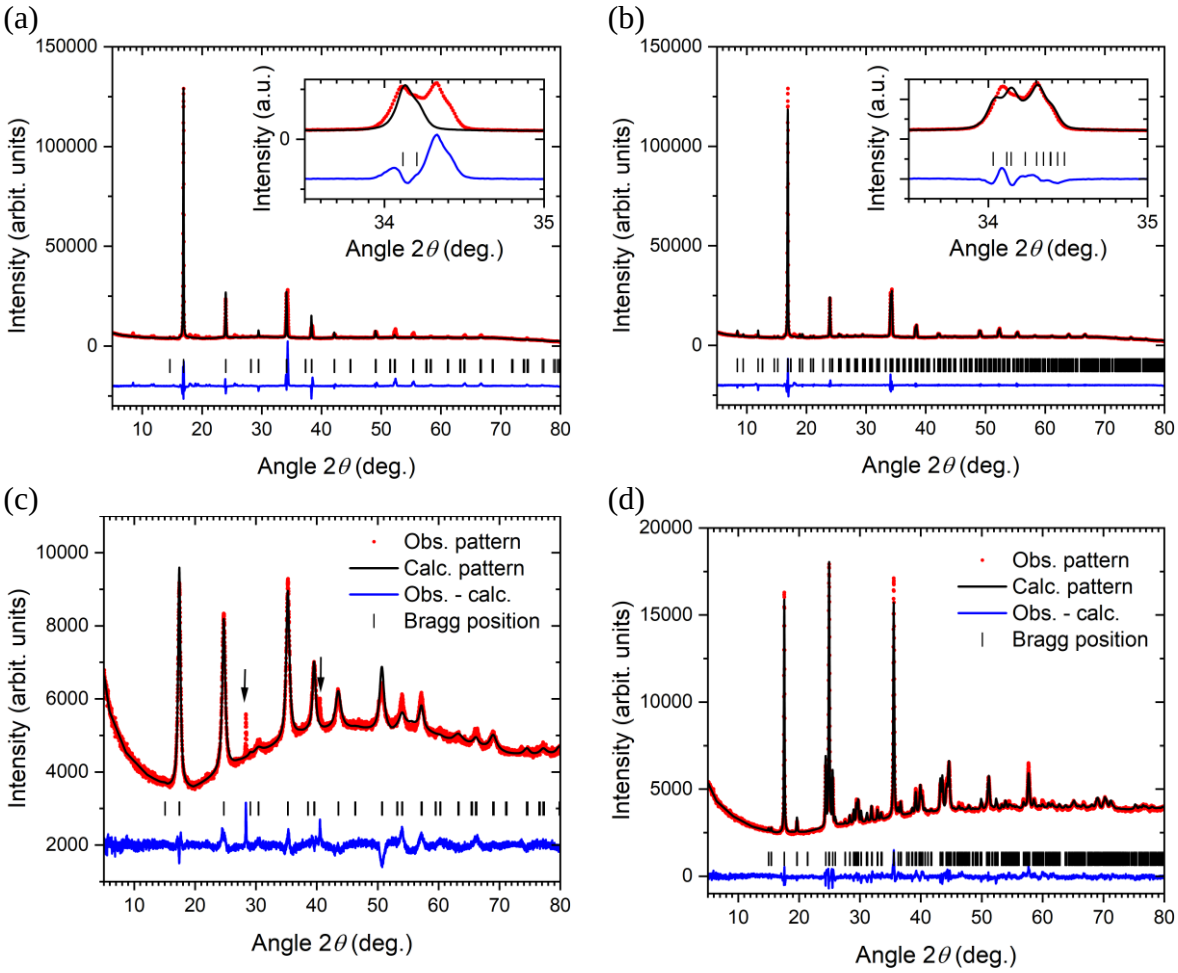


***Fig. 5.23**. Fitted XRD patterns of Mn-rich PBAs. (a) MnHCF, dominant cubic phase. (b) MnHCF, weak tetragonal distortion. (c) FeMnHCF, cubic. (d) FeMnHCF-C, monoclinic. Redrawn from ref. 285 (own work).*

ICP-MS analysis was carried out to confirm the successful substitution of Mn by Fe in the doped samples (**Table 5.1**). For MnHCF, a Fe/Mn molar ratio of merely 0.83 is observed, indicating a high number of $Fe(CN)_6$ vacancies. In contrast, FeMnHCF-A and FeMnHCF-C exhibit Fe/Mn ratios significantly larger than 1, revealing decreased Mn content in the Fe-doped samples. It is worth noting that for these samples, the vacancy content can not be determined from the ICP-MS data, as it can not discriminate between C-coordinated and N-coordinated Fe.

Nonetheless, these results indicate the presence of N-coordinated iron, confirming the partial replacement of manganese.

***Table 5.1**. ICP-MS results for the different Mn-rich PBAs*

Sample	Mn mol ratio	Fe mol ratio
MnHCF	1	0.83
FeMnHCF-A	1	1.68
FeMnHCF-C	1	1.37

After preparing composite cathodes comprising the respective active material, carbon black, and a PVDF binder, the morphology of the PBAs was investigated by SEM (**Fig. 5.24**). The SEM image of MnHCF shown in **Fig. 5.24 (a)** reveals a non-uniform morphology and inconsistent particle sizes of up to ≈7 μm, indicating uncontrolled and uneven crystallization. Similarly, the FeMnHCF-A cathode (**Fig. 5.24 (a)**) consists of irregularly shaped particles of highly varying sizes (up to ≈3 μm).

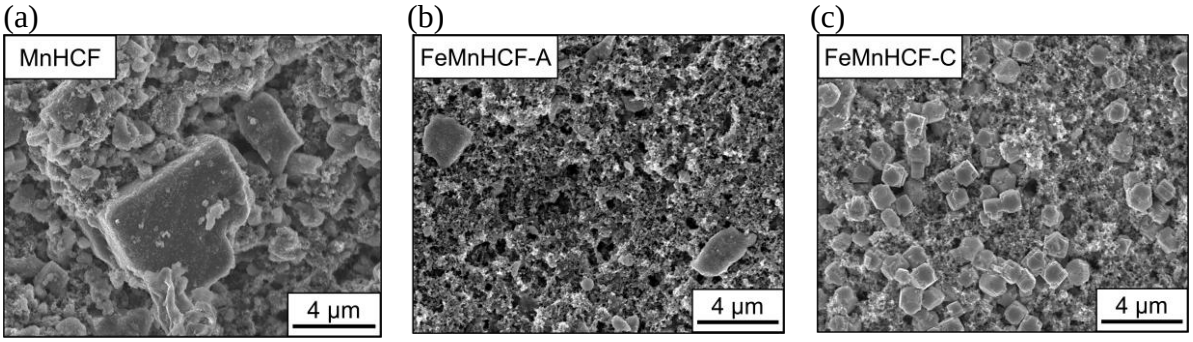


***Fig. 5.24.** SEM images of the Mn-rich PBA cathodes. (a) MnHCF. (b) FeMnHCF-A. (c) FeMnHCF-C. Redrawn from ref. 285 (own work).*

In contrast, FeMnHCF-C displays regular and highly crystalline cube-shaped particles mostly in the 700-900 nm range. Hence, the largest particles are significantly smaller than for the other samples, suggesting a more controlled crystal formation process. These observations are consistent with the high crystallinity revealed by the XRD measurements and can be attributed to the chelating effect of sodium citrate used in the synthesis. Citrate anions have been shown to effectively slow down the crystallization rate and reduce the defect content in the resulting structure by binding to the transition metal cations.[100,286]

BET analysis was carried out to evaluate the specific surface area and pore size distribution of all three samples (**Fig. 5.25**). The nitrogen adsorption–desorption isotherms reveal a significant reduction in overall porosity upon iron doping. As shown in **Fig. 5.25 (a)**, pristine MnHCF exhibits a type-I isotherm characteristic of microporous materials, with an SSA of 81 m^2 g^{-1}. In contrast, the iron-doped FeMnHCF-A and FeMnHCF-C show substantially lower SSAs of 5.6 and 2 m^2 g^{-1}, respectively. For reference, the graphite substrate displayed an almost negligible surface area of 0.5 m^2 g^{-1} under the same conditions. Notably, FeMnHCF-A shows a pronounced hysteresis loop between relative pressures of 0.4 and 0.8 and displays a type-IV isotherm, indicating mesoporous character.

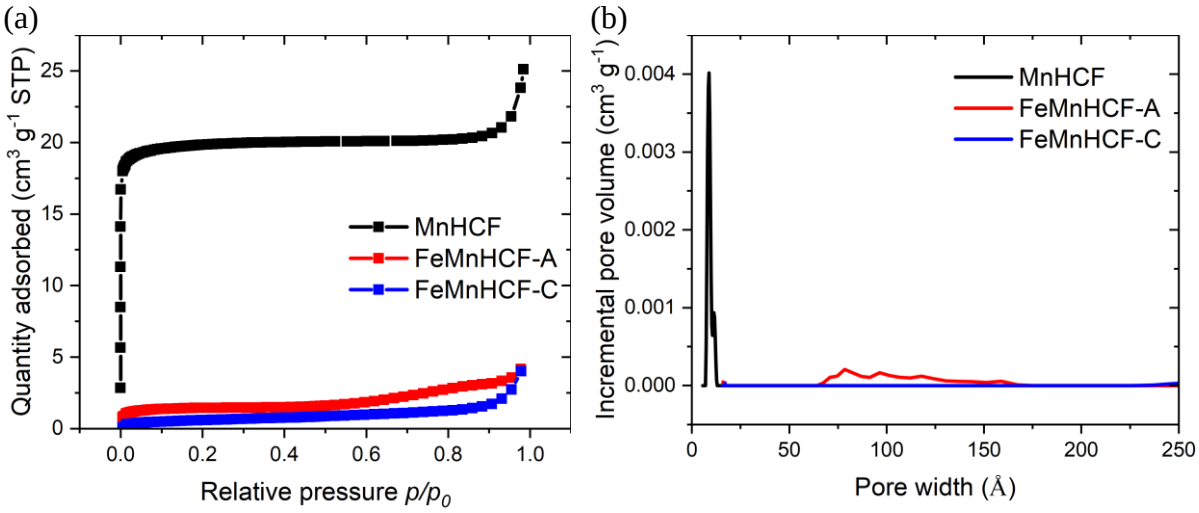


***Fig. 5.25**. BET analysis of the Mn-rich PBA cathodes. (a) N_2 adsorption isotherms obtained at 77 K. (b) Pore size distributions obtained from NLDFT calculations. Redrawn from ref. 285 (own work).*

Pore size distribution obtained via Non-Local Density Functional Theory (NLDFT) analysis (**Fig. 5.25 (b)**) confirms that MnHCF contains primarily micropores centered at 0.9 and 1.1 nm, while FeMnHCF-A and FeMnHCF-C exhibit a lower volume of more broadly distributed mesopores ranging from 6 to 20 nm. These results suggest that the large MnHCF agglomerates observed in SEM images are not dense, crystalline structures but rather highly porous frameworks with a substantial microporous network, likely due to a high defect content. In comparison, FeMnHCF-A and especially FeMnHCF-C consist of more uniformly distributed

and crystalline particles, as supported by SEM and XRD data, resulting in predominantly mesoporous morphologies and consequently lower specific surface areas.

5.2.3 Stabilizing the MnHCF Cathode

To screen the electrochemical behavior and stability of the different Mn-based PBA compounds, CV was carried out at 20 mV s^{-1} over multiple cycles. **Fig. 5.26** shows the 1st, 10th, and 50th cycles and the capacity retention over 100 cycles for each material in three different electrolytes. In cases where a pre-cycling phase with growing peak currents was observed, the 1st cycle refers to the first cycle that displayed maximum currents to allow for comparison of the degradation rate. The CV curves of pure MnHCF display two distinct pairs of peaks, especially in saturated 3 M KNO_3 (corresponding to a molality of 3.7 mol kg^{-1}). As they are centered around half charge potentials of ≈0.64 V and ≈1.09 V vs. SSC, respectively, MnHCF cathodes can enable higher cell voltages than CuHCF. The dominant left peaks are linked to the $Fe^{II/III}$ transition, whereas the weaker peaks at higher potentials correspond to the $Mn^{II/III}$ transition. However, as discussed in **section 5.2.1**, complete oxidation to Mn^{III} leads to detrimental Jahn-Teller distortions, causing rapid degradation.[279,281,282,287,288,289] Accordingly, MnHCF suffers from significant capacity decay within the first few cycles, as shown in Fig. **5.26 (a)** and **(j).** In addition, the increase in current towards the upper potential boundary indicates parasitic oxygen evolution reactions. Therefore, modifications to the material and electrolyte composition are required to enable the practical application of MnHCF. Mn substitution with different transition metal ions is one of the most promising approaches to mitigate degradation caused by the Jahn-Teller effect. For example, doping with Fe, Ni, or Co has been shown to significantly enhance the cyclability of Mn-rich PBAs.[105,108,290,291] As shown in **Fig. 5.26 (b)** and **(j),** the Fe-doped FeMnHCF-A exhibits improved stability, especially within the first cycles. Jiang et al. attributed this effect to an asymmetry in the $Mn^{II/III}$ reaction induced by the Fe doping, which significantly alters the charge transfer mechanism and suppresses distortions.

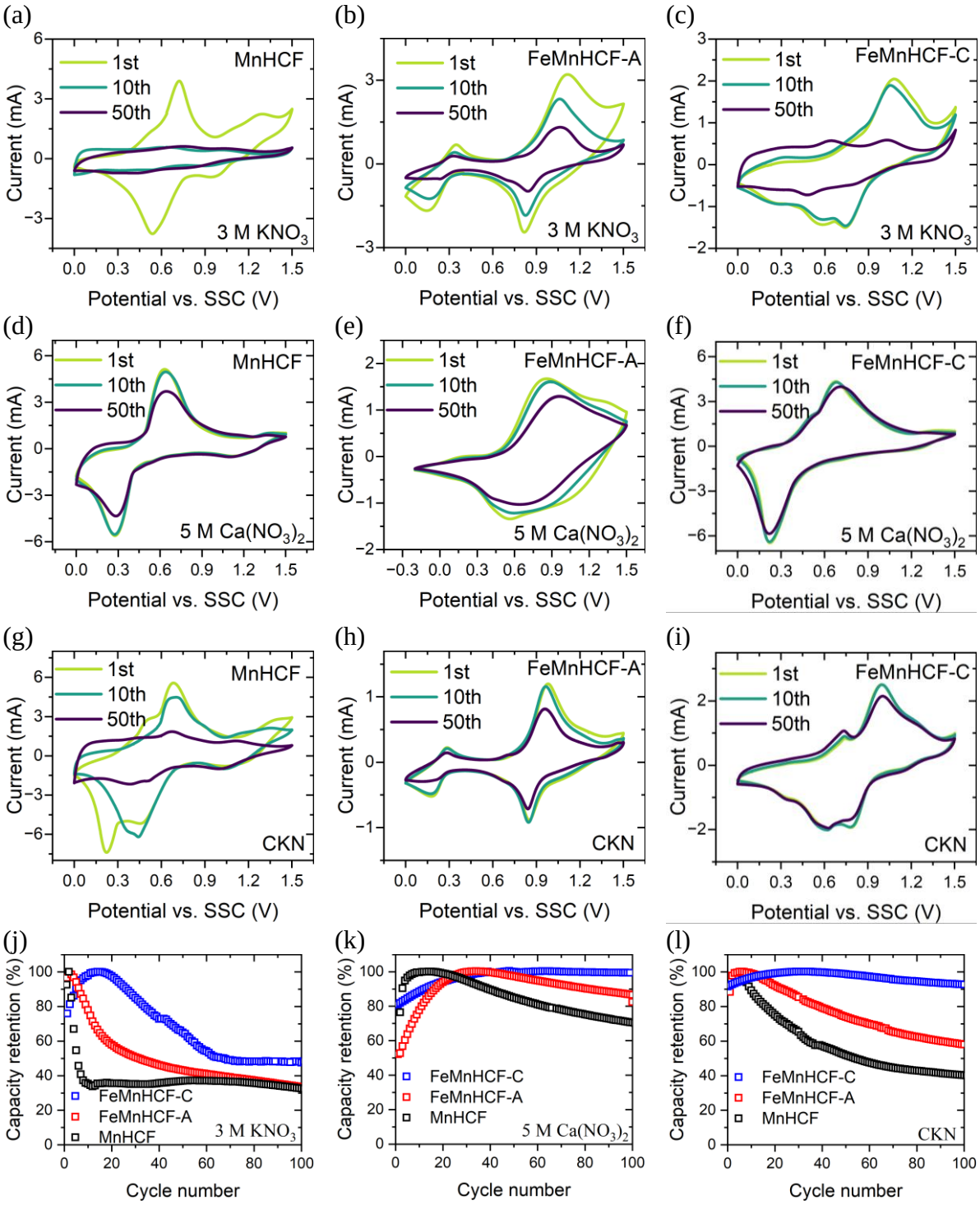


Fig. 5.26. *Stabilization of Mn-rich PBAs. CV curves of the 1st, 10th, and 50th cycles at 20 mV* s^{-1} *of (a) MnHCF in 3 M* KNO_3*, (b) FeMnHCF-A in 3 M* KNO_3*, (c) FeMnHCF-C in 3 M* KNO_3*, (d) MnHCF in 5 M* $Ca(NO_3)_2$*, (e) FeMnHCF-A in 5 M* $Ca(NO_3)_2$*, (f) FeMnHCF-C in 5 M* $Ca(NO_3)_2$ *(denoted as CKN). (g) MnHCF in CKN, (h) FeMnHCF-A in CKN, (i) FeMnHCF-C in CKN. Cycling performance of the three electrode materials in (j) 3 M* KNO_3*, (k) 5 M* $Ca(NO_3)_2$*, (l) CKN. Redrawn from ref. 285 (own work).*

While the $Mn^{II/III}$ and the $Fe^{II/III}$ transitions are completely independent in pure MnHCF, the $Fe^{II/III}$ redox couple is active over the whole potential range in FeMnHCF, mitigating the irreversible cubic-to-tetragonal transition. Thus, instead of two phase transitions from monoclinic to cubic to tetragonal, Fe-doped MnHCF undergoes a more reversible solid solution reaction with a single transition from monoclinic to cubic.[108] Besides the stability improvements, the high-potential peaks become more dominant, enabling higher capacity utilization at higher cell voltages. For the highly crystalline FeMnHCF-C, the potentials at which the $Fe^{II/III}$ and $Mn^{II/III}$ transitions occur overlap even more, resulting in a single major oxidation and reduction peak centered around a half charge potential of ≈0.91 V vs. SSC (**Fig. 5.26 (c)**). Moreover, the higher crystallinity further enhances the cycling stability compared to FeMnHCF-A, indicating that the lower defect content facilitates the compensation of lattice distortions during cycling, impeding structural collapse. Nonetheless, all three materials degrade severely in 3 M KNO_3. In **section 5.1**, electrolytes based on divalent cations were demonstrated as an alternative to WiSEs for stabilizing PBAs in aqueous batteries. To avoid Cl^- oxidation at the high oxidation potentials of the Mn-rich PBAs, the stability of MnHCF, FeMnHCF-A, and FeMnHCF-C was assessed in saturated 5 M $Ca(NO_3)_2$ (corresponding to a molality of 6.7 mol kg^{-1}). Saturated solutions were used to further reduce the amount of free water, which is linked to the suppression of detrimental side reactions and the hydrolysis of the transition metals. Accordingly, all three materials exhibit significantly improved stability in this electrolyte, as shown in **Fig. 5.26 (d-f)** and **(k)**. The highly crystalline Fe-doped FeMnHCF-C retains nearly 100 % of its maximum capacity after 100 cycles (**Fig. 5.26 (k)**), indicating that transition metal dissolution is mitigated by this electrolyte. Furthermore, the calcium-based electrolyte is characterized by a significantly higher viscosity than saturated KNO_3, as shown in **Fig. 5.27**. The viscous electrolyte likely hinders the transport of dissolution products away from the electrode, shifting the reaction equilibrium and hindering further degradation. In a previous study, Zhao et al. also demonstrated the ultrafast re-nucleation of PBAs from dissolved transition metal ions confined in the close vicinity of the electrode surface in the presence of

$Fe(CN)_6$ anions.[292] A similar effect is utilized in the electrochemical synthesis of PBAs, which we investigated in detail in a dedicated article.[293] Thus, sluggish transport of dissolved transition metal ions in the bulk electrolyte is generally linked to improved cycling stability of PBAs.[294]

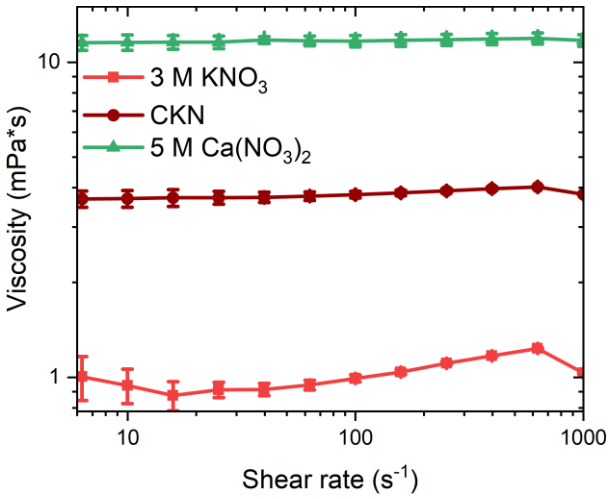


Fig. 5.27. *Viscosities of saturated KNO_3, saturated $Ca(NO_3)_2$, and the mixed-salt CKN electrolyte. The viscosity was measured over a range of shear rates following a logarithmic ramp. Newtonian behavior is observed for all solutions as expected. Data presented as mean ± SD, n=3. Redrawn from ref. 285 (own work).*

However, the Ca-ion electrolyte also affects the electrode potentials of the cathode materials. For all three materials, the reduction and oxidation peaks are shifted in the negative direction and exhibit increased peak-to-peak separation, suggesting lower reversibility of the electrochemical reactions. Both effects negatively impact the overall cell performance by reducing efficiency, lowering the operating voltage, and ultimately diminishing the energy density of the full cell.

Based on the promising results discussed in **section 5.1**, a mixed-salt 2.5 M $Ca(NO_3)_2$ + 1. 5 M KNO_3 (CKN) electrolyte was prepared by mixing saturated $Ca(NO_3)_2$ and KNO_3 in a 1:1 volumetric ratio, taking advantage of the high co-solubility of the two salts without crystallization. As shown in **Fig. 5.26 (g-i)**, the CVs of all materials in this electrolyte display similar peak shapes and positions to the pure potassium-based electrolyte. For MnHCF, the peaks corresponding to Ca^{2+} (de-)intercalation can be observed in the first few cycles but vanish rapidly, leaving only the peaks associated with K^+. Similarly, the redox peak positions of

FeMnHCF-A and FeMnHCF-C are the same as in the pure potassium-ion electrolyte, indicating that the charge transfer kinetics are dominated by K^+, as was also observed for CuHCF in mixed-salt electrolytes (**section 5.1.2**). Although not as pronounced as in 5 M $Ca(NO_3)_2$, the mixed electrolyte achieves significant stability improvements compared to 3 M KNO_3, especially for the Fe-doped samples. FeMnHCF-C is the most stable in all tested electrolytes, confirming the effective stabilization by Mn substitution and morphology control. As for CuHCF, the mixed electrolyte combines the favorable intercalation kinetics of K^+ and the stabilizing effect of Ca^{2+}.

5.2.4 Electrochemical Performance of the Optimized FeMnHCF-C cathode in the CKN Electrolyte.

In the previous section, the stability of the Mn-rich PBA cathode was optimized by partially substituting Mn with Fe, controlling the crystallinity with a chelating agent, and tuning the electrolyte composition. The electrochemical performance of this configuration was evaluated by GC and CV at different C-rates and scan rates, respectively. **Fig. 5.28 (a)** shows the constant current (dis)charge profiles of the FeMnHCF-C cathode in the CKN electrolyte recorded at various rates ranging from 1 C (110 mA g^{-1}) to 100 C (11 A g^{-1}). The resulting specific discharge capacity and Coulombic efficiency for each cycle are displayed in **Fig. 5.28 (b).** At 1 C, the discharge curve exhibits multiple different slopes between 0.95 and 0.60 V vs. SSC, corresponding to various transitions of Mn and Fe. FeMnHCF-C displays a maximum specific capacity of ≈109 mAh g^{-1}, of which ≈91 % is retained at 10 C. With ≈55 % capacity retention at 100 C, the fast-charging capabilities are slightly inferior to CuHCF, due to the more sluggish kinetics of the $Mn^{II/III}$ transition.[108] Nonetheless, the FeMnHCF-C cathode can be nearly fully charged within minutes. Moreover, the high Coulombic efficiencies, especially at rates above 10 C indicate high ion storage reversibility.

The charge transfer kinetics were further investigated by CV at different scan rates ranging from 1 mV s^{-1} to 50 mV s^{-1}. As shown in **Fig. 5.28 (c)**, the peak-to-peak separation decreases to ≈20 and ≈120 mV for the left and right redox couple, respectively, at 1 mV s^{-1}, suggesting

reversible kinetics. The rate-limiting process was identified by relating the peak current to the scan rate, as described in **section 3.1.1.** For FeMnHCF-C, the fitting parameter *a* lies at 0.56, corresponding to mostly mass-transport-limited kinetics. As for the CuHCF cathode, this can be attributed to the diffusion of the intercalates toward the center of the PBA particles and the porous structure of the composite electrode, as described in **section 2.2.5**.

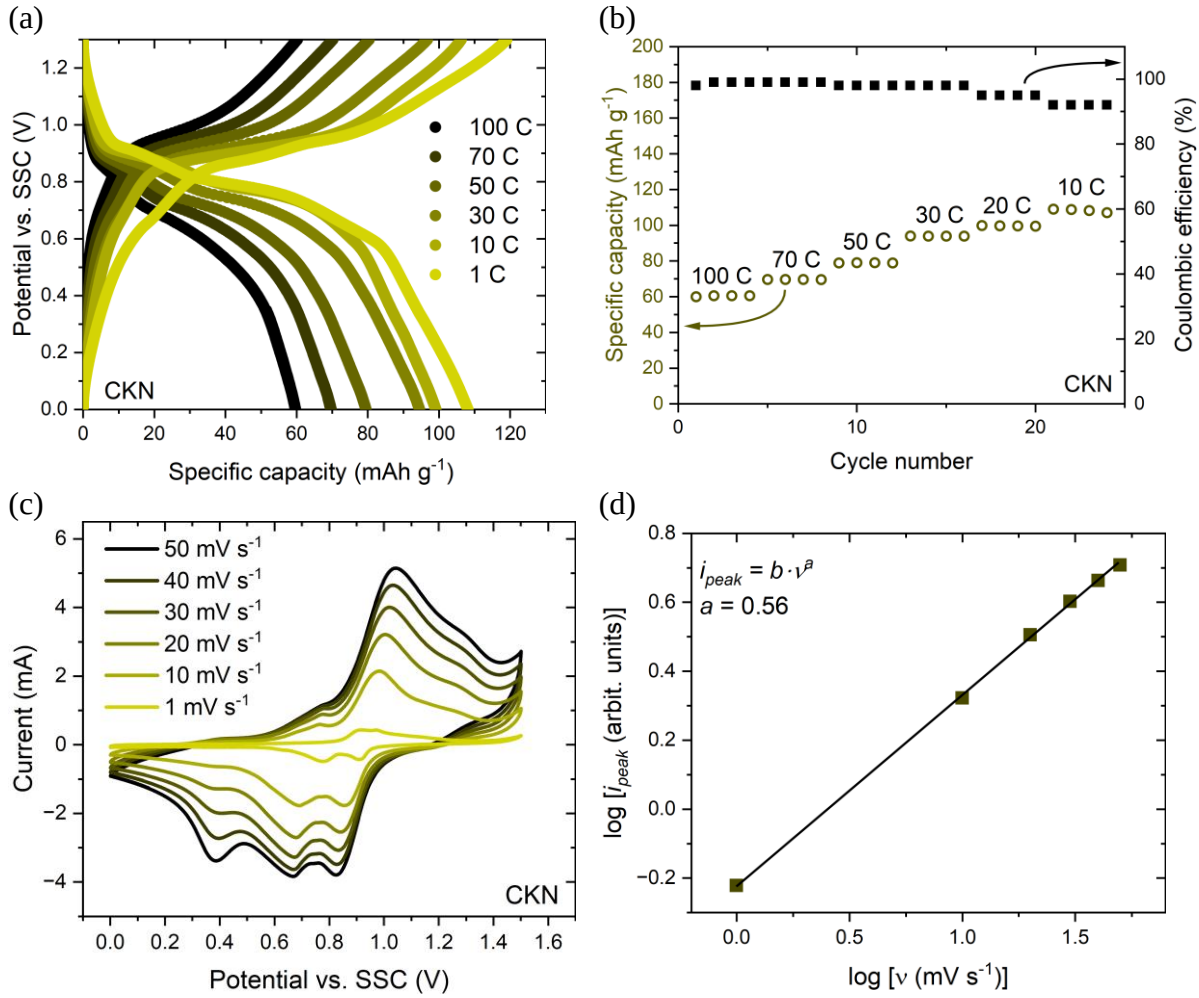


Fig. 5.28. Electrochemical performance of the FeMnHCF-C cathode in the mixed-salt CKN electrolyte. (a) Galvanostatic (dis)charge curves at different C-rates. (b) Specific capacity and Coulombic efficiency for each cycle and rate. (c) CV curves at different scan rates. (d) Peak current vs. scan rate extracted from graph (c). Redrawn from ref. 285 (own work).

5.2.5 The FeMnHCF-C/CKN/PNFE Full Cell

The promising FeMnHCF-C cathode was combined with a PNFE anode and the CKN electrolyte in an aqueous battery. Due to the high specific capacity and electrode potential of

the Mn-rich PBA, this cell should exhibit a significantly higher energy density than the cell introduced in **section 5.1.4**. Based on the specific capacities at 1 C, a cathode-to-anode active material mass ratio of 1.4:1 was selected to account for the difference in specific capacity between FeMnHCF-C and PNFE and maximize material utilization. **Fig. 5.29 (a)** shows the (dis)charge profiles at different C-rates ranging from 1 C (62 mA g^{-1}) to 100 C (6.2 A g^{-1}).

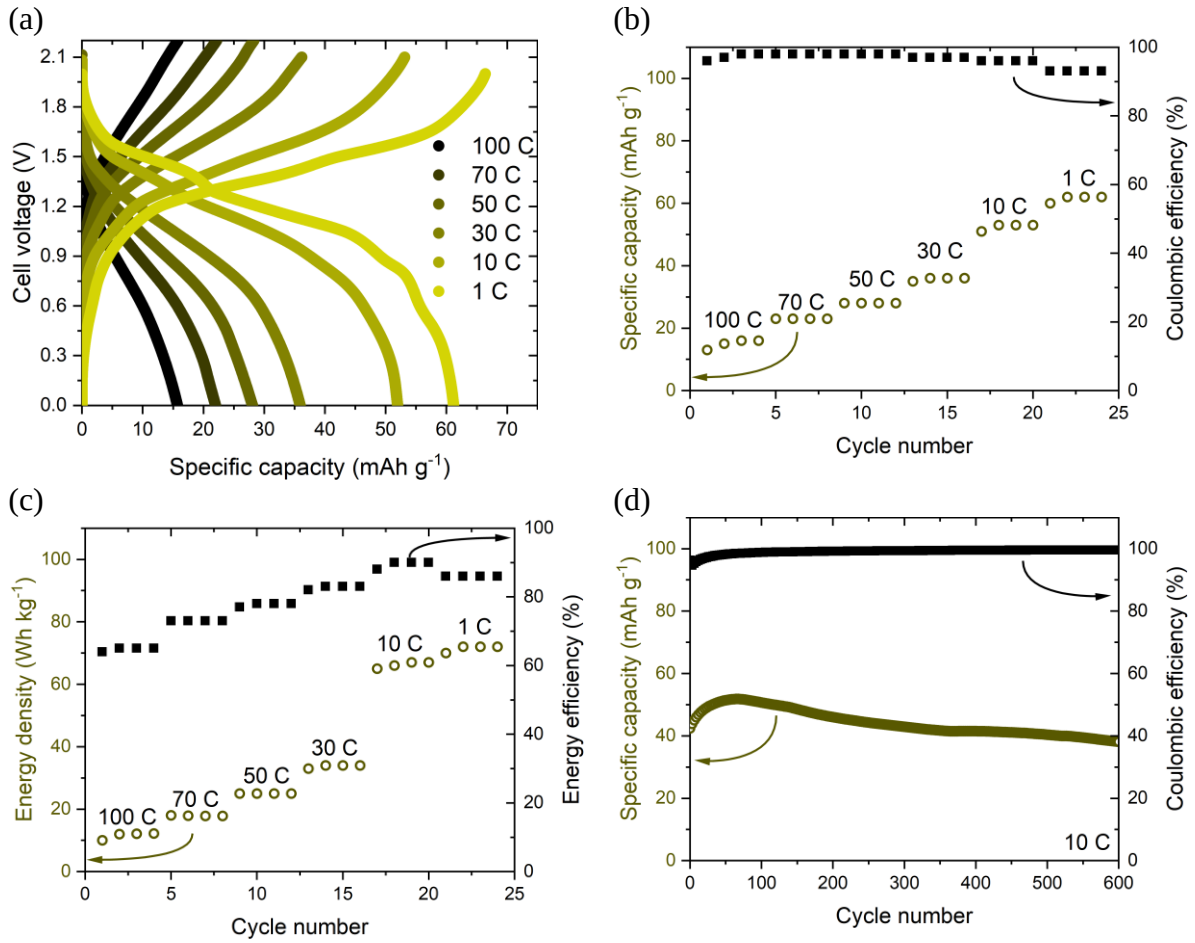


***Fig. 5.29**. Electrochemical performance of the FeMnHCF-C/CKN/PNFE full cell. (a) (Dis)charge profiles at different C-rates. (b) Specific discharge capacity and Coulombic efficiency per cycle and C-rate. (c) discharge energy density and energy efficiency per cycle and C-rate. (d) Capacity retention during 600 cycles at 10 C. Redrawn from ref. 285 (own work).*

At 1 C, the battery exhibits a sloping discharge plateau between 1.8 V and 1.0 V, with an average operating voltage of 1.16 V. While the discharge profiles are slightly more sloped than for the CuHCF-based cell, a significantly higher maximum specific capacity of ≈62 mAh g^{-1} is observed when using the Mn-rich PBA cathode. The battery also shows good

fast-charging capabilities, retaining ≈85 % of its maximum capacity at 10 C (**Fig. 5.29 (b)**). At very high rates of 30 C and above, the performance deteriorates more significantly than for the CuHCF battery due to the more sluggish kinetics of the $Mn^{II/III}$ transition (≈25 % retention at 100 C). Nonetheless, the battery can be effectively charged within less than ten minutes. Furthermore, high Coulombic efficiencies imply that the CKN electrolyte is electrochemically stable within the operating voltage window of the cell. **Fig. 5.29 (c)** shows the corresponding discharge energy densities and energy efficiencies for each cycle and C-rate. The battery exhibits a maximum reversible energy density of ≈72 Wh kg^{-1}, of which up to 67 Wh kg^{-1} can be retained at 10 C. The energy efficiency peaks at ≈92 % at 10 C and declines towards lower currents due to Coulombic losses. At higher currents, the energy density and efficiency decline due to rising overpotentials caused by mass transport and charge transfer limitations. The corresponding power densities range from ≈70 W kg^{-1} at 1 C to ≈5 kW kg^{-1} at 100 C.

The cycling stability was assessed by repeatedly charging and discharging the battery for 600 cycles at 10 C. As shown in **Fig. 5.29 (d)**, it retains around 80 % of its maximum capacity over the course of the measurement, confirming the stability improvements achieved by the synthesis and electrolyte modifications. The initial increase in capacity is linked to electrolyte penetration into the pores of the composite electrode. Overall, the full cell using a FeMnHCF-C cathode degrades more rapidly than the one using CuHCF, but exhibits higher specific capacities and energy densities. A comprehensive comparison of the most important performance metrics is given in the next section.

5.3 Benchmarking the Performance of the Proposed Aqueous Batteries

To benchmark the electrochemical performance of the CuHCF/KMC/PNFE and the FeMnHCF-C/CKN/PNFE batteries, their energy and power densities are compared with state-of-the-art aqueous batteries reported in the literature and other energy storage devices in this section.

Fig. 5.30 shows a Ragone plot visualizing the performance of the two batteries proposed in this work, together with some of the most relevant designs from previous literature. The FeMnHCF-C/CKN/PNFE cell ranks among the highest energy densities reported. Only a few groups, such as Jiang et al.[108] and Liang et al.,[295] have reported slightly higher energy densities for aqueous K-ion batteries. While Jiang et al. carried out pioneering work on Fe-doped MnHCF, Liang et al. relied on a KVO_x cathode. Both groups used a 3,4,9,10-perylene tetracarboxylic diimide (PTCDI) anode, belonging to the same group of materials as PNFE, confirming the great potential of organic anode materials for LFABs.

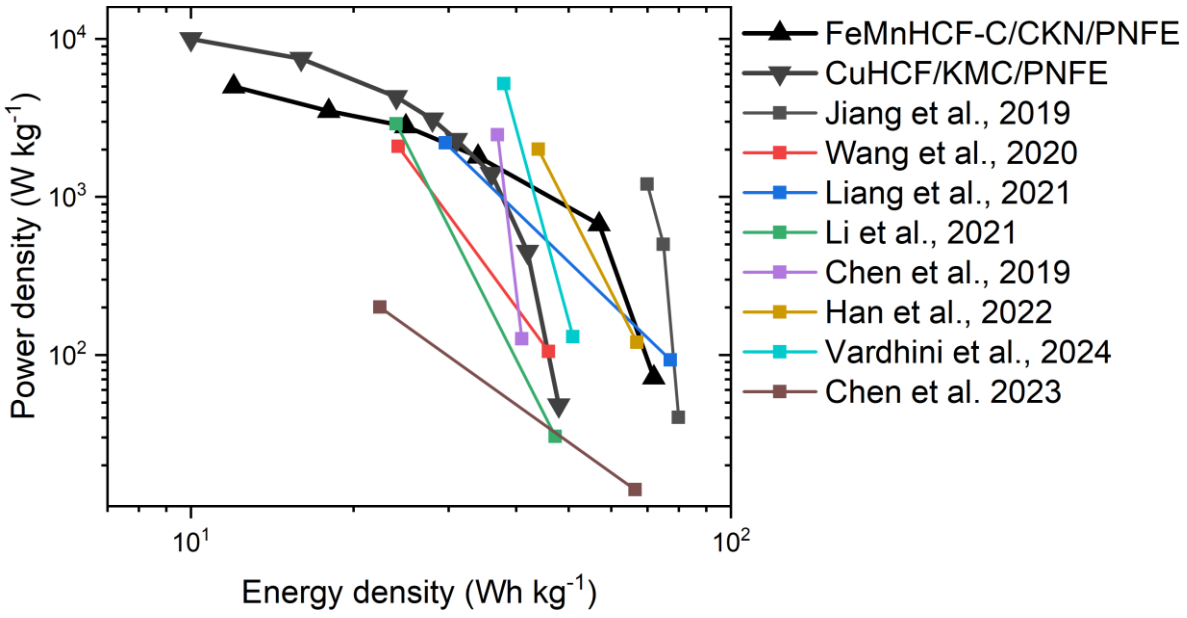


***Fig. 5.30**. Ragone plot comparing the performance of the batteries in this work with other state-of-the-art AKIBs reported by Jiang et al.,[108] Wang et al.,[125] Liang et al.,[295] Li et al.,[296] Chen et al. [124], Han et al.,[297] Vardhini et al.,[298] and Chen et al.[299] Redrawn from ref. 285 (own work).*

The CuHCF/KMC/PNFE battery delivers a comparable energy density to the batteries proposed by Wang et al.,[125] Li et al.,[296] Chen et al.,[124] and Vardhini et al.[298] However, except for the FeHCF/ saturated KNO_3/PNFE cell by Wang et al., all other designs employ expensive WiSEs. Although this strategy allows for long cyclability, it is linked to high material costs for the electrolyte. While the used electrode materials are typically abundant and cost-effective, the electrolyte can become the limiting factor for the practical application of these compositions. In contrast, the mixed-salt KMC and CKN electrolytes proposed in this work are based on highly available and low-cost materials, enabling economically viable battery production. Furthermore, the power density of the CuHCF/KMC/PNFE battery is among the highest reported so far due to its superior fast-charging capabilities. Therefore, the CuHCF or FeMnHCF-C-based cells are optimized for applications requiring high power densities or high energy densities, respectively.

Fig. 5.31 compares the performance of the LFABs with other electrochemical energy storage technologies based on the Ragone plot in **Fig. 2.3**. The lower borders of the bar representing LFABs correspond to the energy and power densities that could be achieved taking into account other cell components besides the active materials, which typically make up around 50-70 % of the total battery weight.[154,300] Based on these considerations, a realistic CuHCF/KMC/PNFE battery should reach energy densities between 25 Wh kg^{-1} and 35 Wh kg^{-1}, while values of up to 50 Wh kg^{-1} appear feasible when using a FeMnHCF-C cathode. Hence, LFABs are capable of much higher energy densities than most supercapacitors, achieving values similar to those of lead-acid and Ni-Cd batteries.[70,71,144,145,148,149] At the same time, their good fast-charging capabilities allow for high power densities in the same range as high-power LIBs and supercapacitors.

Moreover, the proposed LFABs are superior to lead-acid, Ni-Cd, Ni-MH, and Li-ion batteries in terms of safety and material abundance, suggesting that they are a promising alternative for large-scale applications.

To put these results into perspective, the hypothetical weight of a home-storage battery using the LFABs discussed in this work is calculated in the following. Typically, these devices are sold with energy capacities between 10 and 20 kWh. For example, BYD offers 10.24 kWh and 16.56 kWh batteries weighing 167 kg and 243 kg, respectively.[301] Similar devices by Huawei, which can store up to 10 kWh and 15 kWh, weigh 114 kg and 164 kg, respectively.[302]

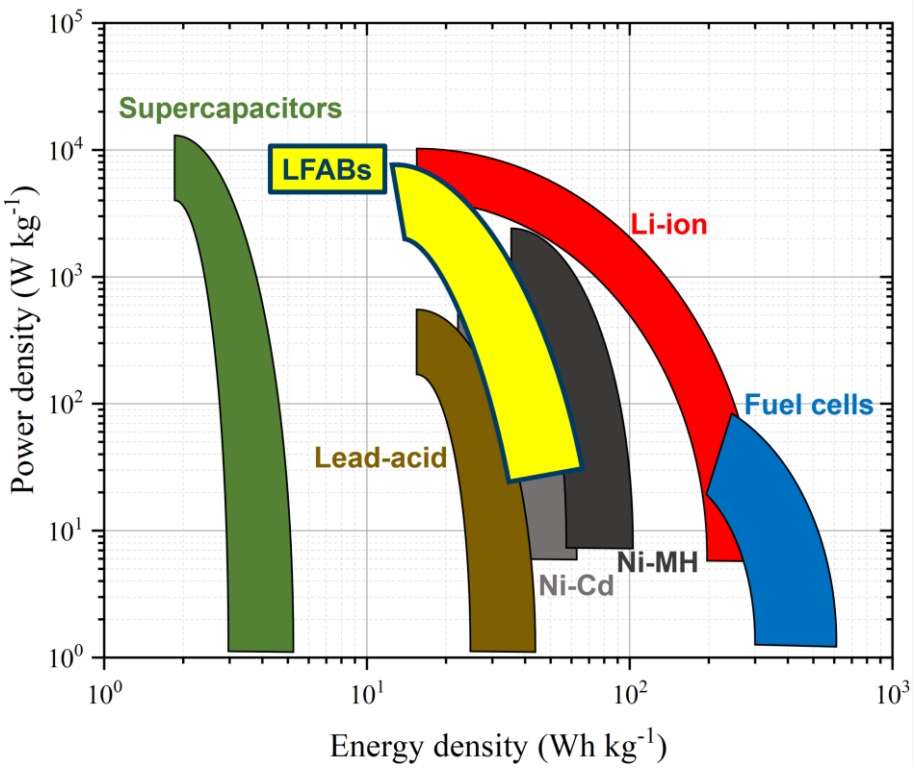


Fig. 5.31. *Modified Ragone plot based on* ***Fig. 2.3*** *comparing the energy and power density of electrochemical energy storage devices, including the LFABs developed in this work. The lower limits of the bar take into account a typical active material share of 50-70 % of the total mass of the battery.*

Assuming realistic energy densities of around 35 Wh kg^{-1}, a 10 kWh battery based on LFABs would weigh around 280-300 kg, which can be feasible for a stationary device. Since an average German household consumes around 3400 kWh of electric energy per year (9.3 kWh per day), a 10 kWh battery could supply energy for approximately one day.[303] Larger households of 3 persons or more typically consume around 5400 kWh per year, or 15 kWh per day, and could be supplied by an LFAB weighing around 430-500 kg. Although LFAB-based devices would hence be about twice as heavy as state-of-the-

art home-storage batteries, they offer significantly enhanced safety and sustainability, and could be produced using less expensive raw materials. However, the successful upscaling from lab scale to larger devices needs to be demonstrated first to confirm these hypotheses.

6. Conclusion and Outlook

The global energy landscape is undergoing a rapid and essential transformation toward renewable energy generation. As fossil fuel-based systems are replaced by solar and wind power, the supporting infrastructure must evolve in parallel. Among the most important components of a renewable-based energy grid is robust and scalable energy storage capable of balancing generation vs. consumption discrepancies, compensating natural fluctuations, and supporting decentralized power systems. Batteries, in particular, are expected to play a critical role not only in grid storage but also in mobile and private energy storage applications. However, LIBs, which are the predominant battery technology today, are increasingly linked to safety, cost, resource, and sustainability concerns.

Therefore, aqueous battery systems using abundant, non-toxic, and inexpensive materials have gained considerable attention as a promising alternative. This work contributes to the rapidly growing field of research on sustainable LFABs by proposing a novel design strategy combining advanced electrode materials with optimized mixed-salt electrolytes. The feasibility of this approach is demonstrated by the successful development of two high-performance full cells using the PBAs CuHCF or FeMnHCF-C as the cathode material and the polyimide PNFE as the organic anode. The full batteries use neutral or mildly acidic electrolytes consisting of two inexpensive and environmentally benign salts. In particular, potassium and magnesium chloride were used for the KMC electrolyte, and potassium and calcium nitrate were combined in the CKN electrolyte. Both systems display exceptional rate capabilities, high energy and power densities, and good cycling stabilities, and they outperform the majority of comparable aqueous battery designs reported in the literature.

In the first part, an LFAB based on a CuHCF cathode and a PNFE anode was developed. Structural analyses based on SEM and XRD showed that the CuHCF cathode active material consisted of highly crystalline, nanosheet-shaped particles with a monoclinic crystal phase. This

unique structure was attributed to using chelating agents during the aqueous synthesis. Furthermore, FTIR and XPS confirmed the expected structure of PNFE.

A comprehensive investigation of the electrochemical performance of both electrodes revealed that the mixed-salt electrolyte strategy enables high cell voltages and enhanced cycling stability at moderate electrolyte concentrations. This circumvents the limitations of state-of-the-art water-in-salt electrolytes (WiSEs), which rely on expensive, often fluorinated salts to suppress parasitic side reactions and stabilize the electrode materials. In the newly developed mixed-salt KMC electrolyte, the high electrode potential of CuHCF is attributed to the favorable hydration behavior and ionic mobility of K^+ ions. At the same time, divalent cations such as Mg^{2+} and Ca^{2+} contribute to electrode stability through their strong interactions with water. These interactions reduce harmful side reactions involving H_2O and OH^- by binding large numbers of water molecules in their hydration shells, thereby limiting the amount of free water available in the electrolyte and within the interstitial sites of Prussian Blue analogs (PBAs).

Moreover, the hydrolysis of Mg^{2+} and Ca^{2+} lowers OH^- activity and shifts the pH toward mildly acidic conditions, which are known to stabilize PBAs and mitigate degradation reactions. The stabilizing effect of these divalent cations on CuHCF was further validated through XRD, SEM, and electrochemical analyses, supporting the proposed mechanism.

For the PNFE anode, the electrode potential was found to correlate with the charge density of the guest cation, with lower charge densities leading to more negative potentials. Although PNFE is generally less prone to degradation than CuHCF, slight stability improvements were observed when using divalent ion-based and mixed-salt electrolytes. This is likely associated with increased electrolyte viscosities, mitigating material detachment. Both electrodes are characterized by exceptionally high rate capabilities in the used aqueous electrolytes. CuHCF could retain ≈85 % of its maximum capacity of ≈65 mAh g^{-1} at 10 C, while PNFE displayed a maximum capacity of ≈148 mAh g^{-1} and ≈90 % retention at 10 C.

In addition to the empirical performance evaluation, the charge storage mechanisms of the cathode and anode were analyzed using CV and EIS measurements. CV at different scan rates

revealed that the charge transfer at the composite CuHCF cathode is mostly mass-transport limited, consistent with the intercalation mechanism. In contrast, the PNFE anode exhibited mostly surface-limited kinetics, indicating a pseudocapacitive charge storage mechanism, allowing for its superior fast charging capabilities. The EIS analysis of CuHCF confirmed the previously reported three-stage intercalation process of PBAs. For the PNFE anode, a novel EEC model was developed, revealing the presence of a previously undetected secondary single-stage redox pathway besides the well-known conjugated two-step reduction process. Moreover, the proposed mechanisms for CuHCF and PNFE were valid for both monovalent and divalent cations.

The resulting CuHCF/KMC/PNFE full cell achieved high energy densities of up to 48 Wh kg^{-1}, impressive rate capabilities, and good cycling stability. Retaining nearly 90 % of its maximum capacity at 10 C and reaching power densities of more than 10 kW kg^{-1}, it is particularly suitable for high-power applications. These results not only meet but, in several respects, surpass benchmarks from the current state-of-the-art, confirming the promising properties of the novel mixed-salt electrolyte strategy.

In the second part, this concept was extended to another LFAB comprising a Mn-rich PBA cathode, a mixed-salt CKN electrolyte, and the same PNFE anode. Besides the electrolyte optimizations, the FeMnHCF-C cathode was stabilized through Mn-substitution by Fe and using a chelating agent to control the crystallinity. Both approaches mitigate the rapid degradation of MnHCF caused by lattice distortions due to the Jahn-Teller effect on Mn^{III}. SEM, XRD, ICP-MS, and BET investigations showed significant compositional, morphological, and structural changes, which could be correlated to stability improvements in electrochemical measurements. After successful stabilization, the optimized cathode exhibits a high specific capacity of around 110 mAh g^{-1} enabled by the two-electron redox reaction, including a $Mn^{II/III}$ transition in addition to the $Fe^{II/III}$ transition observed in all PBAs.

As for CuHCF, the charge transfer kinetics of FeMnHCF-C were found to be mostly limited by mass transport. Nonetheless, the cathode features good fast-charging capabilities, retaining around 90 % of its maximum capacity at 10 C in the optimized CKN electrolyte.

After combining the FeMnHCF-C cathode and the CKN electrolyte with the PNFE anode discussed in the first part, the full cell delivered some of the highest reported energy densities (≈72 Wh kg^{-1}) for LFABs based on Na^+, K^+, Mg^{2+}, or Ca^{2+}. Moreover, most systems that achieve similar or better performance (usually 40-80 Wh kg^{-1}) rely on WiSEs, limiting their practical application. It is worth noting that aqueous Zn-ion batteries can typically reach even higher energy densities, enabled by the high specific capacity of the Zn anode.[64] However, their application remains challenging due to dendrite formation and parasitic side reactions.[304,305,306]

Within the wide range of electrochemical energy storage technologies, the developed LFABs rank among established technologies like lead-acid or Ni-Cd batteries, while surpassing them in terms of power density and sustainability. They also feature much higher energy densities than most supercapacitors, making them a potential alternative for mobile applications like public transport. To evaluate the practical applicability of the developed batteries, a conceptual scaling to a home storage unit was conducted. While aqueous batteries tend to have lower energy densities due to the use of water-based electrolytes, they offer significant advantages in terms of safety, cost, and environmental impact. The use of inexpensive salts and electrode materials enables low production costs, while the absence of flammable solvents and toxic elements ensures operational safety and ease of recycling. These characteristics make the batteries suitable for stationary storage, particularly in residential and decentralized energy systems.

The implications of this work extend well beyond laboratory innovation. As nations seek to decarbonize and decentralize their energy sectors and secure sustainable supply chains, technologies like LFABs become increasingly important. This dissertation supports a shift in battery design away from maximizing performance at all costs and towards balancing performance, sustainability, and cost. By demonstrating the validity of the mixed-salt aqueous

electrolyte approach, this work shows a potential pathway towards decentralized production of batteries in regions without access to lithium, cobalt, or other critical materials, which can reduce geopolitical dependencies. Furthermore, using benign electrolytes and stable organic/inorganic materials can facilitate recycling and reduce e-waste. The safety benefits are also critical for public and industrial applications. With the increasing adoption of energy storage in homes, hospitals, data centers, and public transportation, minimizing the risks of fire or explosion becomes an essential requirement.

While the results of this work can substantially advance the practical application of LFABs, several limitations remain, and opportunities for future work are offered. The transition from lab-scale coin cells to large-format pouch or prismatic cells will require optimization of electrode fabrication processes, current collector materials, and sealing techniques compatible with aqueous environments. These cells then need to be tested under broader operating conditions, including temperature extremes and various cycling protocols. Research efforts in this direction are currently undertaken in our group by F. Weißbach and M. B. Minhaj in their advised MSc theses. In addition, although the stability observed over 600-700 cycles is promising, real-world batteries may need to operate over several thousand cycles. In particular, further improvements to the stability of Mn-rich PBAs would allow for high-energy LFABs with more competitive cyclability. By systematically investigating the effect of synthesis parameters, such as temperature, ion-doping, chelating agents, and drying protocols, M. H. R. Vance recently commenced this work in his MSc project. Furthermore, fundamental investigations on the underlying degradation and stabilization mechanisms, e.g., in-situ XRD and EIS, could provide new insights enabling further active material and electrolyte optimizations.

In summary, this work provides a comprehensive and systematic approach to designing sustainable high-performance aqueous batteries. By combining advanced organic and inorganic electrode materials with an optimized low-cost electrolyte composition, two full-cell systems were developed that exhibit excellent electrochemical properties, outperform comparable

systems reported in the literature, and demonstrate the practical potential of LFABs for a wide range of applications. The results of this dissertation can serve as a blueprint for future developments in the field of green battery technologies and support the ongoing shift towards a sustainable and resilient energy economy.

List of Abbreviations

ACIB	Aqueous calcium-ion battery
AKIB	Aqueous potassium-ion battery
AMIB	Aqueous magnesium-ion battery
ASIB	Aqueous sodium-ion battery
ASSB	All-solid-state battery
AZIB	Aqueous zinc-ion battery
BET	Brunauer–Emmett–Teller
CCCV	Constant-current-constant-voltage
CE	Counter electrode
CKN	2.5 M $Ca(NO_3)_2$ + 1.5 M KNO_3
CoHCF	Cobalt hexacyanoferrate
CuHCF	Copper hexacyanoferrate
CV	Cyclic voltammetry
DI	De-ionized
EC	Electrochemical cell
EDA	Ethylenediamine
EDL	Electrical double layer
EDX	Energy-dispersive X-ray spectroscopy
EEC	Electrical equivalent circuit
EIS	Electrochemical impedance spectroscopy
ESW	Electrochemical stability window
FeHCF	Iron hexacyanoferrate
FeMnHCF-A	Iron-manganese hexacyanoferrate
FeMnHCF-C	Iron-manganese hexacyanoferrate with controlled crystallinity
FTIR	Fourier transform infrared spectroscopy
FWHM	Full width at half maximum
GC	Galvanostatic cycling
HER	Hydrogen evolution reaction
ICP-MS	Inductively coupled plasma mass spectrometry

IHP	Inner Helmholtz plane
IR	Infrared
ISE	Institute for Solar Energy Systems
KMC	1. 8 mol kg^{-1} KCl + 1.8 mol kg^{-1} $MgCl_2$
LCO	Lithium cobalt oxide
LFAB	Li-free aqueous battery
LIB	Li-ion battery
MnHCF	Manganese hexacyanoferrate
MnHCM	Manganese hexacyanomanganate
NCM	Lithium nickel cobalt manganese oxide
Ni-Cd	Nickel-cadmium
NiHCF	Nickel hexacyanoferrate
Ni-MH	Nickel-metal-hydride
NMP	N-Methyl-2-pyrrolidone
NTCDA	1,4,5,8-Naphthalene tetracarboxylic dianhydride
OER	Oxygen evolution reaction
OHP	Outer Helmholtz plane
PB	Prussian blue
PBA	Prussian blue analog
PC	Propylene carbonate
PDF	Powder Diffraction File
PEO	Polyethylene oxide
PHES	Pumped hydroelectric storage
PI	Polyimide
PNFE	Poly(naphthalene-four-formyl-ethylenediamine)
PTCDI	3,4,9,10-perylene tetracarboxylic diimide
PV	Photovoltaic
PVDF	Polyvinylidene flouride
PVP	Polyvinylpyrrolidone
RE	Reference electrode
SEM	Scanning electron microscopy

SHE	Standard hydrogen electrode
SOC	State-of-charge
SSA	Specific surface area
SSC	Silver-silver-chloride
SSE	Solid-state electrolyte
TGA	Thermogravimetric analysis
WE	Working electrode
WHO	World Health Organization
WiSE	Water-in-salt electrolyte
XPS	X-ray photoelectron spectroscopy
XRD	X-ray diffraction

Attached Publications

1. Identifying the Charge Storage Mechanism in Polyimide Anodes for Na-ion Aqueous Batteries by Impedance Spectroscopy.

R.L. Streng, S. Vagin, Y. Guo, B. Rieger, A.S. Bandarenka. *RSC Energy Advances* **2024**, 3, 874-882

Energy Advances

ROYAL SOCIETY OF CHEMISTRY

PAPER

View Article Online
View Journal | View Issue

Check for updates

Cite this: *Energy Adv.*, 2024, 3, 874

Identifying the charge storage mechanism in polyimide anodes for Na-ion aqueous batteries by impedance spectroscopy†

Raphael L. Streng,[a] Sergei Vagin,[bc] Yuejie Guo,[a] Bernhard Rieger[c] and Aliaksandr S. Bandarenka[*ab]

Received 19th January 2024,
Accepted 20th March 2024

DOI: 10.1039/d4ya00037d

rsc.li/energy-advances

Polyimides such as poly(naphthalene four formyl ethylenediamine) (PNFE) demonstrate promising electrochemical properties as anode materials for aqueous sodium-ion batteries. They display high specific capacities and good cyclability. Still, an accurate physical model describing the exact charge storage mechanism in these electroactive polymers needs to be explored in more detail. This work aims to address this gap through an impedance study to elucidate the mechanisms of reduction and oxidation processes of polyimide electrodes. An electrochemical impedance model is also proposed, which enables good fitting of the impedance data at all potentials. This model confirms the commonly accepted two-stage enolization reaction as the main reduction path and also unveils a previously unrecognized single-electron pathway. A complete model was identified by including this novel pathway, which enabled a better understanding of these materials.

Open Access Article. Published on 21 March 2024. Downloaded on 5/22/2025 10:14:39 AM.
This article is licensed under a Creative Commons Attribution 3.0 Unported Licence.

1. Introduction

In times of rising demand for sustainable energy storage solutions, rechargeable batteries have become crucial in transitioning towards a renewable energy economy and powering modern technologies.[1,2] Among various systems, lithium-ion batteries (LIBs) are currently dominating the market, as they offer high energy and power densities, which are essential for application in electric vehicles and mobile devices.[3,4] However, the limited supply of lithium as well as the inherent safety issues of LIBs, have motivated a recent interest in alternative battery technologies.[5–8] Recent advances in battery research include Li-free systems utilizing more abundant alkali metals such as Na,[9–11] as well as safer aqueous electrolytes.[12,13] Combining their advantages, aqueous sodium-ion batteries (ASIBs) have attracted increased attention due to their potential to complement and even replace LIBs, especially in stationary energy storage applications. The natural abundance of sodium and the intrinsic safety, high ionic conductivity, and low cost of the aqueous electrolyte can make them favorable for these systems.[14–18] However, the larger size of sodium ions and the electrochemical stability window of water limit the choice of electrode materials. Various compounds, such as Prussian blue analogs,[19,20] manganese oxides,[21–23] and polyanionic compounds[10,11,13] offer superior stability and fast charging performance as cathodes for ASIBs. However, only a few suitable anode materials for ASIBs have been reported besides the transition metal-based NASICON-type $NaTi_2(PO_4)_3$[24,25] and the Prussian blue analog manganese hexacyanomanganate.[23]

Redox-active organic materials can be a sustainable, inexpensive, and high-performance alternative to inorganic compounds that often contain scarce or polluting elements.[26,27] Polyimides (PIs) have emerged as a promising anode material for aqueous metal-ion batteries due to their low electrode potential, high cycling stability, and superior specific capacity.[28,29] In addition, they exhibit remarkable mechanical strength, thermal resistance, and chemical stability and are fully compatible with aqueous electrolytes.[24]

Whereas the exceptional electrochemical performance of PIs has been reported several times,[28–30] a more detailed examination of the underlying charge transfer processes should be further performed. Ultimately, understanding the charge storage mechanism in PIs is of great importance to unlock their full potential and accelerate their application in practical systems. Electrochemical impedance spectroscopy (EIS) is a non-destructive, non-invasive, and fast technique that can reveal charge transfer mechanisms and characterize degradation as well as mass transport processes.[31] By applying a low amplitude sinusoidal voltage or current signal over a certain

[a] Physics of Energy Conversion and Storage, Department of Physics, Technische Universität München, James-Franck-Str. 1, 85748 Garching, Germany. E-mail: bandarenka@ph.tum.de
[b] Catalysis Research Center TUM, Ernst-Otto-Fischer-Straße 1, 85748 Garching, Germany
[c] WACKER-Lehrstuhl für Makromolekulare Chemie, Department of Chemistry, Technische Universität München, Lichtenbergstraße 4, 85748 Garching, Germany
† Electronic supplementary information (ESI) available. See DOI: https://doi.org/10.1039/d4ya00037d

© 2024 The Author(s). Published by the Royal Society of Chemistry

Open Access Article. Published on 21 March 2024. Downloaded on 5/22/2025 10:14:39 AM.
This article is licensed under a Creative Commons Attribution 3.0 Unported Licence.

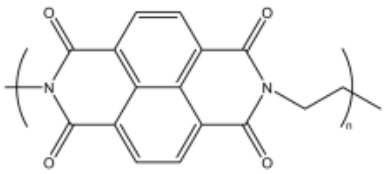


Fig. 1 Chemical structure of poly(naphthalene four formyl ethylenediamine) (PNFE).

frequency range, EIS can fully extract any information on the impedances in the cell. However, to understand the data, it is essential to interpret the spectrum with an accurate physical model, often expressed for simplicity in terms of equivalent electric circuits (EECs).[32] Thus, for each electrode, complete EECs that describe the physical processes in a meaningful way need to be created. These models can then be combined to gain information on the full battery.

This work provides new insight into the redox mechanism of the electrode material poly(naphthalene four formyl ethylenediamine) (PNFE, see Fig. 1) by subjecting it to an in-depth EIS study.

2. Experimental

2.1. Synthesis of PNFE

All utilized chemicals were purchased from commercial suppliers and utilized without additional purification unless mentioned.

Poly(naphthalene four formyl ethylenediamine) was prepared according to literature procedure with minor modification.[28] In brief, 1,4,5,8-naphthalene tetracarboxylic dianhydride (NTCDA, 2.68 g, 10 mmol) and ethylenediamine (EDA, 0.6 g, 10 mmol) were mixed with 20 ml of degassed *N*-methyl pyrrolidone (NMP) in a Schlenk flask. The flask was equipped with an air-cooled condenser and an overpressure valve on top, and the reaction mixture was heated overnight in a sand bath at a bath temperature set to 215 °C. After cooling, the dark precipitate was filtered off and washed thoroughly with NMP and subsequently with water. It was dried *in vacuo* with a stepwise increase of drying temperature (room temperature, 120 °C and 210 °C) to a constant vacuum of 0.08 mbar yielding 2.7 g (92%) of grey-brownish powder.

Elemental analysis: calcd for an infinite polyimide ($C_{16}H_8N_2O_4$), %: C 65.76, H 2.76, N 9.59; calcd for an octamer, %: C 65.10, H 3.03, N 10.52; found, %: C 65.13, H 2.91, N 10.32.

2.2. Structural characterization

The chemical structure of the obtained polymer was characterized *via* Fourier-transformed infrared (FTIR) spectroscopy using a Bruker Vertex-70 spectrometer equipped with a Platinum-ATR-accessory. To analyze the morphology of the film a field emission scanning electron microscope (SEM, JSM-7500F, JEOL) was employed. Thermogravimetric analysis (TGA) was carried out in argon using a METTLER TOLEDO TGA/DSC 2 (STARe system). A temperature range from 30 °C to 800 °C and a heating rate of 10 °C min^{-1} was chosen. X-ray photoelectron spectroscopy (XPS) spectra of the PNFE electrode were conducted using a non-monochromatized Al Kα source (1486.7 eV) on a SPECS setup (SPECS XR50 Xf-Ray source, SPECS PHOIBOS 150 hemispherical analyzer, SPECS spectrometer). The XPS spectra were fitted in the Casa XPS software (Version 2.3.24PR1.0). The binding energies were corrected by referencing the C–C peak of the C 1s spectrum to 284.8 eV.

2.3. Electrode preparation

The electrodes were prepared by the slurry casting method as follows. 80 wt% of the polyimide active material was ground with 10 wt% carbon black (MTI, USA) and 10 wt% Nafion™ binder (5 wt% in lower aliphatic alcohols and water, Sigma Aldrich, USA) in a planetary ball mill. Isopropyl alcohol and water in a 1 : 1 ratio were added under vigorous stirring to form the slurry, which was subsequently coated onto a pyrolytic graphite current collector with an active material mass loading of approximately 2.5 mg cm^{-2}. The so-prepared electrodes were dried overnight at room temperature before electrochemical measurements were performed. After drying, the electrode film thickness was determined to be 42 ± 3 μm.

2.4. Electrochemical measurements

Electrochemical measurements were conducted using a three-electrode glass cell with a constant argon flow to maintain an inert atmosphere. 8 M $NaClO_4$ was used as the electrolyte, as highly concentrated electrolytes are known to enhance electrode stability by preventing active material dissolution.[33,34] Before being run into the cell the electrolyte was purged with argon for approximately 10 minutes. The reference electrode utilized was an Ag/AgCl electrode (SSC, 3 M KCl, SI Analytics, "B 3420+"), connected to the electrolyte *via* a Luggin capillary. A platinum wire (MaTeck, Germany) was employed as the counter electrode.

CV (cyclic voltammetry) and EIS (electrochemical impedance spectroscopy) measurements were conducted using a BioLogic VSP-300 Potentiostat. To prevent any disturbances caused by the impedance of the reference electrode, a small shunt capacitor was connected between the reference electrode and an additional platinum wire, which was wrapped around the Luggin capillary and ended near it.

The cyclic voltammograms (CVs) were recorded at different scan rates ranging from 1 mV s^{-1} to 50 mV s^{-1} between 0 V *vs.* SSC and −1.1 V *vs.* SSC. Staircase electrochemical impedance spectroscopy was carried out in the same potential range in steps of 100 mV. Before recording the spectrum at each step, the potential was held for 10 minutes to ensure equilibrium conditions, which are vital for impedance measurements. A 10 mV AC amplitude was applied to the electrode with frequencies ranging from 1.00 MHz to 250 mHz. After the validity of the data was verified by Kramers–Kronig analysis, the spectra were fitted using the EIS Data Analysis 2.1 software.[35]

© 2024 The Author(s). Published by the Royal Society of Chemistry

Open Access Article. Published on 21 March 2024. Downloaded on 5/22/2025 10:14:39 AM.
This article is licensed under a Creative Commons Attribution 3.0 Unported Licence.

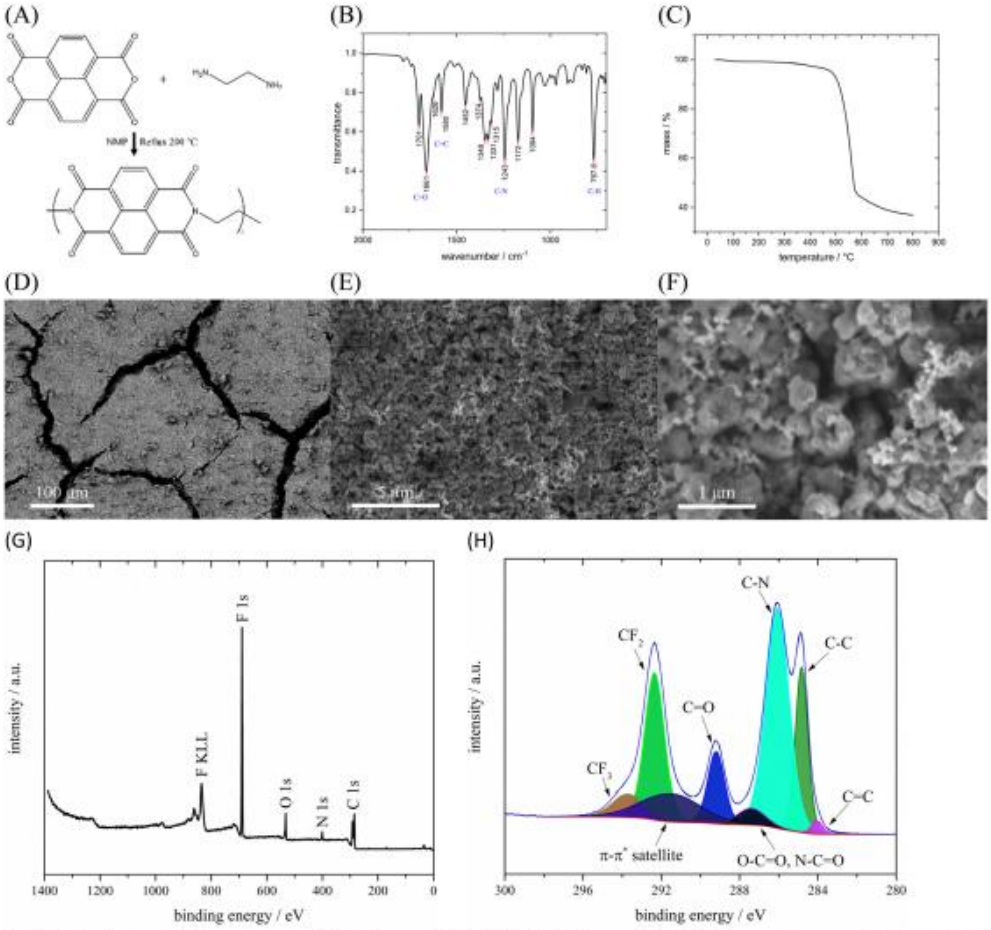


Fig. 2 (A) Synthesis route, (B) FTIR spectrum, and (C) TGA curve of PNFE. (D)–(F) SEM pictures of the PNFE slurry coated on a pyrolytic graphite sheet at different magnifications. (G) XPS survey spectrum of the PNFE slurry electrode. (H) Fitted XPS spectrum of the C 1s region of the PNFE slurry electrode.

3. Results and discussion

PNFE was synthesized using a simple one-step dehydration condensation reaction between NTCDA and EDA in NMP as shown in Fig. 2(A). The chemical structure of the as-prepared polymer was confirmed by FTIR-spectroscopy. The FTIR spectrum of the PNFE polymer is depicted in Fig. 2(B). The observed peaks are in good accordance with the expected structure of the synthesized polymer. Notably, the bands at 1701 cm^{-1} and 1661 cm^{-1} correspond to stretching vibrations of the C=O bonds in the electrochemically active carbonyl groups. Furthermore, characteristic stretching vibrations of the C=C bonds in the cyclic alkenes (1626 cm^{-1} and 1580 cm^{-1}) and various vibrations of aromatic and non-aromatic C–N bonds (1348 cm^{-1} to 1094 cm^{-1}) can be observed. The remaining spectral bands can be attributed to vibrations of C–H bonds in the polymer.

Fig. 2(C) shows the TGA curve of PNFE. The small initial mass loss is caused by the evaporation of residual water within the active material. Decomposition of the polymer can only be observed at a temperature of approximately 500 °C which confirms the excellent thermal stability of PNFE. To analyze the morphology of the PNFE electrode scanning electron microscopy (SEM) was conducted. It reveals a relatively even distribution of polymer agglomerates, which are typically less than 1 µm in size, as shown in Fig. 2(D–F). Together with the Nafion™ binder and the carbon black, the active material forms a porous film with pore sizes in the nm to µm range. To further analyze the surface structure of the PNFE electrodes, XPS

 © 2024 The Author(s). Published by the Royal Society of Chemistry

Open Access Article. Published on 21 March 2024. Downloaded on 5/22/2025 10:14:39 AM.
This article is licensed under a Creative Commons Attribution 3.0 Unported Licence.

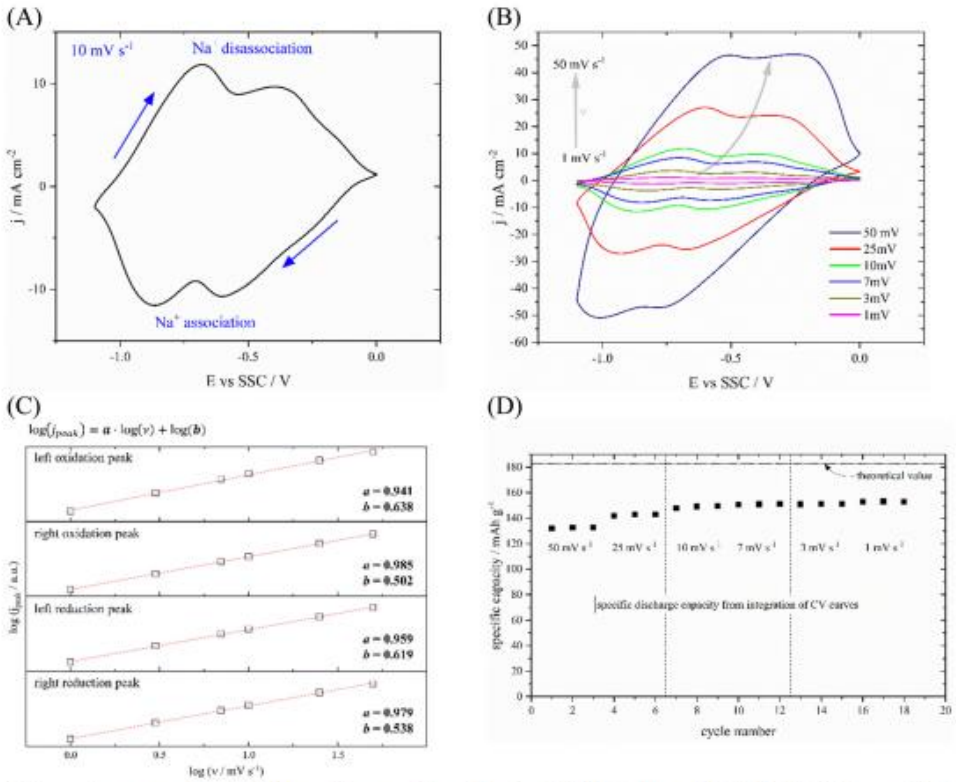


Fig. 3 (A) Cyclic voltammogram of the PNFE film coated on a pyrolytic graphite sheet in 8 M $NaClO_4$ recorded at 10 mV s^{-1}. (B) CVs recorded at different scan rates. (C) Dependence of the peak current on the scan rate for all four peaks. (D) Specific discharge capacity calculated by integrating the CV curves at different scan rates.

spectra were recorded. The survey scan depicted in Fig. 2(G) shows characteristic peaks for carbon, nitrogen, oxygen, and fluorine. Carbon and oxygen are part of the active material and the binder, whereas nitrogen and fluorine can be attributed to PNFE and Nafion™, respectively. In the C 1s spectrum (Fig. 2(H)), multiple peaks can be observed. The sharp peaks at 284.8 eV, 286.1 eV, 289.2 eV, and 292.4 eV correspond to C–C, C–N, C═O, and CF_2 bonds, respectively. The weaker peaks at 284.3, 287.4, and 293.8 are attributed to C═C, O–C═O or N–C═O, and CF_3. In addition, the extended delocalized electrons in the aromatic rings of PNFE result in a π–π^* satellite structure at 291.5 eV. These results indicate that the active material and the binder are both present at the surface of the electrode, which is necessary to ensure mechanical stability as well as electrolyte access.

The electrochemical properties as well as the rate dependence of PNFE were investigated by measuring CVs at various scan rates. A typical CV recorded at 10 mV s^{-1} is shown in Fig. 3(A). Two separate pairs of reduction and oxidation peaks can be clearly distinguished. The oxidation peaks lie at −0.68 V



Fig. 4 Reduction mechanism of PNFE. In the first step, a radical anion is formed, followed by the generation of the dianion in the second step. Further reduction (3 or 4 electrons) is possible but only occurs at much lower potentials.[58]

© 2024 The Author(s). Published by the Royal Society of Chemistry

Open Access Article. Published on 21 March 2024. Downloaded on 5/22/2025 10:14:39 AM.
This article is licensed under a Creative Commons Attribution 3.0 Unported Licence.

vs. SSC and −0.39 V *vs.* SSC respectively. The reduction peaks are close at −0.87 V *vs.* SSC and −0.61 V *vs.* SSC implying a reversible redox reaction. This double-peak structure supports the two-electron reduction mechanism which is commonly reported for PNFE and similar polyimides.[36,37] As shown in Fig. 4, the reduction leads to a two-step enolization reaction of two opposite carbonyl groups. In the first step, a radical anion is formed followed by the formation of the di-anion which allows it to adsorb two sodium ions. It should be noted that this is the generally accepted scheme for ion adsorption at carbonyl-based organic electrode materials. Since there are four carbonyl groups, one may expect further reduction by up to four electrons. Whereas this is generally possible, it only occurs at much lower potentials and thus below the hydrogen evolution reaction (HER) threshold.[38] The relatively wide expansion of the peaks in the *x*-direction suggests repulsive interactions between the two redox centers preventing the resolution of the two separate electron transfers. Therefore, a full understanding of the redox mechanism is only accessible by employing additional techniques. Here we use EIS to reveal the underlying processes.

Fig. 3(B) shows the CVs of PNFE at different scan rates between 1 and 50 mV s^{-1}. The peak-to-peak separation ΔE_{p-p} increases with increasing scan rate, which is mostly linked to the uncompensated resistance stemming from the electrolyte's ionic conductivity. However, it becomes clear that the charge transfer mechanism is highly reversible as ΔE_{p-p} drops to 59 mV at a scan rate of 1 mV s^{-1} for both pairs of peaks. By relating the peak current i_{peak} to the scan rate ν it is possible to deduce information on the processes limiting the charge transfer and, therefore, determine the current response in the CVs:

$$i_{peak} = b \cdot \nu^a \Rightarrow \log(i_{peak}) = \log(b) + a \cdot \log(\nu) \quad (1)$$

Hereby, the value of the parameter a ranges from 0.5 for fully mass transport limited processes to 1.0 for fully surface limited processes. As shown in Fig. 3(C) a lies close to 1.0 for all peaks within the investigated scan rate range implying low mass transport limitations. Due to the high concentration of the 8 M $NaClO_4$ electrolyte, the faradaic current is not impaired by the diffusion of ions toward the electrode surface. However, at higher scan rates, a slightly lower value for a can be observed, as can be expected for slurry electrodes with higher mass loadings. This is most likely caused by the diffusion of Na^+ within the film, which will be discussed in more detail in the EIS analysis.

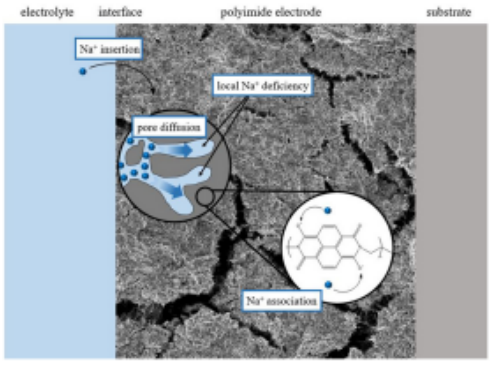


Fig. 6 Diffusion limitations arise due to local Na^+ deficiency in the pores of the slurry. Even with the highly concentrated electrolyte, the diffusion through the small pores is too slow to compensate for concentration gradients immediately.

The total transferred charge within one cycle can be calculated by integrating the CVs. Fig. 3(D) shows that a maximum specific discharge capacity of *ca.* 153 mA h g^{-1} is measured at the slowest scan rates. As indicated by the dotted line, this value is significantly lower than the theoretical specific capacity of PNFE for a two-electron charge transfer. This observation is in accordance with previous studies on various polyimides, which consistently report capacities considerably below the

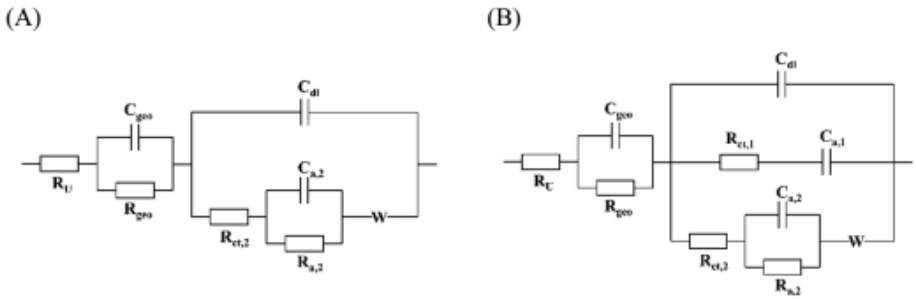


Fig. 5 (A) EEC describing a two-stage conjugated mechanism with reversible stages. It includes the electrolyte resistance (R_U), the impedances of the capacitance of the film (R_{geo}, C_{geo}), of the double layer (C_{dl}), and the two-stage mechanism ($R_{ct,2}$, $C_{a,2}$, $R_{a,2}$) as well as a Warburg element modeling diffusion of Na^+ ions inside the pores of the slurry (W). (B) The EEC used to fit the data additionally includes the impedance of the parallel single-stage mechanism ($R_{ct,1}$, $C_{a,1}$).

© 2024 The Author(s). Published by the Royal Society of Chemistry

Open Access Article. Published on 21 March 2024. Downloaded on 5/22/2025 10:14:39 AM.
This article is licensed under a Creative Commons Attribution 3.0 Unported Licence.

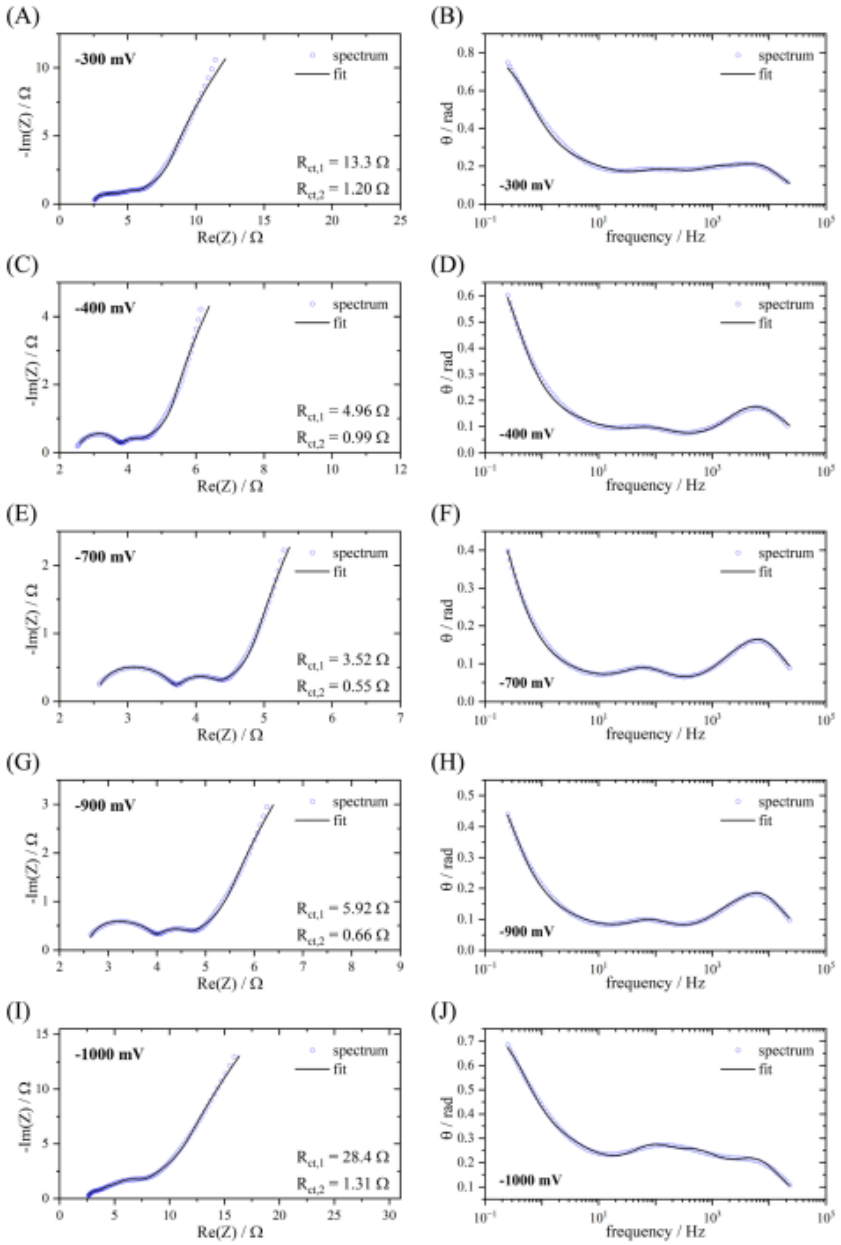


Fig. 7 Fitted EIS spectra of PNFE at different potentials *vs.* SSC. The graphs on the left show the Nyquist plots (A), (C), (E), (G) and (I). The graphs on the right show the dependence of the phase shift Θ on the frequency (B), (D), (F), (H) and (J). For fitting the EEC in Fig. 5(B) was used.

© 2024 The Author(s). Published by the Royal Society of Chemistry

Open Access Article. Published on 21 March 2024. Downloaded on 5/22/2025 10:14:39 AM.
This article is licensed under a Creative Commons Attribution 3.0 Unported Licence.

theoretically expected value.[28–30,37] This implies that the redox mechanism of PNFE is not sufficiently described by the simple two-electron transfer shown in Fig. 4.

Electrochemical impedance spectra were recorded at different potentials within the potential range in which the redox activity was observed in the CVs to obtain further insights into the mechanism. The fitting of these spectra requires a physically meaningful EEC model. Fig. 5(A) shows the equivalent circuit describing the two-stage mechanism which is depicted in Fig. 4. This circuit model can be derived from the so-called Randles circuit modeling faradaic processes controlled by diffusion and kinetics.[39] The Randles circuit consists of the electrolyte uncompensated resistance R_U, the double layer capacity C_{dl}, the charge transfer resistance R_{ct}, and a semi-infinite Warburg element W accounting for diffusion. In this case, the diffusion limitations are assumed to arise due to local sodium-ion deficiencies within the pores of the slurry, as shown in Fig. 6. Though the concentration of sodium ions in the bulk electrolyte is very high, the movement through the smaller pores is likely diffusion-limited. In addition, the delocalization of the charge over the conjugated structure of the imide molecule affects mass transport as well. To account for the two stages of the mechanism, an adsorption capacitance $C_{a,2}$ and resistance $R_{a,2}$ are added to the Randles circuit.[34] Hereby, the model reflects the fact that the reduction of the first carbonyl group determines the second step of the redox process, which unquestionably takes place after the transfer of the first electron. Thus, the two stages are conjugated, and $C_{a,2}$, and $R_{a,2}$ are connected in the circuit accordingly. The impedance linked to the contribution of the film on the graphite substrate to the overall impedance response is accounted for by C_{geo} and R_{geo}.

In other words, this model describes a conjugated two-electron transfer with reversible stages, which corresponds to the mechanism shown in Fig. 4. It should be noted that the capacitative contribution could also be modeled with constant phase elements (CPEs) instead of capacitors. However, the direct physical meaning of the model is not clear, especially when multiple CPEs are used. In the case of the PNFE electrode, the fit quality does not improve significantly when C_{dl} or C_{geo} are replaced by CPEs. Furthermore, upon fitting, the exponent of the CPEs is very close to 1.00, indicating nearly ideal capacitative behavior. The resulting EEC depicted in Fig. 5(A) can be used to fit the data with high accuracy at potentials more positively than −300 mV.

Fig. 7 shows the impedance spectra at different potentials ranging from −300 mV *vs.* SSC to −1000 mV *vs.* SSC in Nyquist plots as well as the dependence of the phase shift Θ on the frequency. At −300 mV *vs.* SSC, the processes are fairly modeled by the two-stage mechanism. However, the spectra recorded at more negative electrode potentials within the region where faradaic processes take place do not support this model. At −400 mV and below, an additional contribution can be observed, leading to a different curvature in the transition region between high and low frequencies. This effect is even more distinctive in the Θ *vs.* frequency representation, which displays a different shape at these potentials. The exact origin of this is outside the scope of this manuscript as it does not influence the fitting statistics significantly.

Simultaneously to the primary two-stage conjugated mechanism, a one-electron single-stage mechanism was found to take place. This process can be modeled by a charge transfer resistance $R_{ct,1}$ and an adsorption capacitance $C_{a,1}$[34] that are connected in parallel to the elements representing the two-stage mechanism. By including these parameters, the spectra can be fitted with extremely high accuracy for all potentials, as shown in Fig. 7. This pathway is most likely linked to the formation of the stable radical anion after reduction by a single electron. This observation indicates that a certain portion of the polymer is not further reduced after this step. Reasons for this may be polymer–polymer or polymer–substrate interactions. Due to this effect, the experimental specific capacity of PNFE is expected to be lower than the theoretical specific capacity for a two-electron charge transfer as parts of the polymer only accept one electron. Therefore, the observed capacity losses serve as an important verification of the suggested EEC.

The fitting parameters and their respective errors for all potentials are given in Table S1 (ESI†). It shows that the charge transfer resistance of the two-stage conjugated pathway is significantly lower than the charge transfer resistance of the single-stage pathway. At all potentials, $R_{ct,1}$ is 5–10 times higher than $R_{ct,2}$, with the difference getting smaller towards lower potentials. Therefore, the two-electron mechanism is determined to be dominating, whereas the single-electron mechanism is mostly suppressed. At −300 mV *vs.* SSC, the difference is the largest, which is why the spectrum can also be fitted with the simpler circuit that is depicted in Fig. 5(A). However, at lower potentials, the ratio decreases, and the contribution of the single-stage mechanism becomes significant.

4. Conclusions

In conclusion, this research contributes to elucidating the charge storage mechanism of polyimides through the integration of CV and EIS analyses. The established two-step conjugated enolization mechanism has been definitively identified as the primary process governing this electrode material. Nevertheless, this investigation has unveiled a previously unrecognized single-electron pathway manifesting at potentials below −300 mV *vs.* SSC, challenging the completeness of the conventional model. This newly identified pathway, likely associated with the stabilization of radical anions post-initial reduction, provides crucial insights into the observed disparities between experimental and theoretical specific capacities.

The introduction of the electrochemical equivalent circuit (EEC) proposed in this study enables highly accurate and minimally error-prone fitting of impedance spectra for polyimide electrodes. Moreover, the implications extend beyond this specific material, as analogous organic electrode materials relying on enolization reactions can likely be similarly modeled. Consequently, the outcomes of this research offer a potent

© 2024 The Author(s). Published by the Royal Society of Chemistry

Open Access Article. Published on 21 March 2024. Downloaded on 5/22/2025 10:14:39 AM.
This article is licensed under a Creative Commons Attribution 3.0 Unported Licence.

analytical tool for comprehending the processes within carbonyl-based electrode materials and batteries employing such electrodes.

Beyond its fundamental contributions, this work paves the way for more comprehensive EIS analyses, opening up novel avenues for monitoring degradation effects, cell aging, and various processes in a non-destructive manner. The knowledge gleaned from this study promises to be instrumental in advancing the understanding of organic electrode materials, ultimately contributing to the optimization and longevity of electrochemical systems.

Author contributions

R. S.: conceptualization, data curation, formal analysis, validation, investigation, visualization, methodology, writing – original draft, writing – review and editing. S. V.: investigation, writing – original draft, writing – review and editing. Y. G.: investigation, validation. B. R.: resources, supervision, funding acquisition. A. S. B.: conceptualization, resources, software, formal analysis, supervision, funding acquisition, writing – review and editing.

Conflicts of interest

There are no conflicts to declare.

Acknowledgements

The Authors acknowledge financial support from the Deutsche Forschungsgemeinschaft (DFG) in the framework of Germany's Excellence Strategy – EXC 2089/1-390776260, the cluster of excellence "e-conversion".

References

1 J. B. Goodenough, Electrochemical energy storage in a sustainable modern society, *Energy Environ. Sci.*, 2014, **7**, 14–18.
2 A. Kalair, N. Abas, M. S. Saleem, A. R. Kalair and N. Khan, Role of energy storage systems in energy transition from fossil fuels to renewables, *Energy Storage*, 2021, **3**, e135.
3 G. E. Blomgren, The Development and Future of Lithium Ion Batteries, *J. Electrochem. Soc.*, 2017, **164**, A5019–A5025.
4 M. Li, J. Lu, Z. Chen and K. Amine, 30 Years of Lithium-Ion Batteries, *Adv. Mater.*, 2018, e1800561.
5 D. Larcher and J.-M. Tarascon, Towards greener and more sustainable batteries for electrical energy storage, *Nat. Chem.*, 2015, **7**, 19–29.
6 E. A. Olivetti, G. Ceder, G. G. Gaustad and X. Fu, Lithium-Ion Battery Supply Chain Considerations: Analysis of Potential Bottlenecks in Critical Metals, *Joule*, 2017, **1**, 229–243.
7 Y. Wang, R. Chen, T. Chen, H. Lv, G. Zhu, L. Ma, C. Wang, Z. Jin and J. Liu, Emerging non-lithium ion batteries, *Energy Storage Mater.*, 2016, **4**, 103–129.
8 S.-W. Kim, D.-H. Seo, X. Ma, G. Ceder and K. Kang, Electrode Materials for Rechargeable Sodium-Ion Batteries: Potential Alternatives to Current Lithium-Ion Batteries, *Adv. Energy Mater.*, 2012, **2**, 710–721.
9 B. Qin, M. Wang, S. Wu, Y. Li, C. Liu, Y. Zhang and H. Fan, Carbon dots confined nanosheets assembled $NiCo_2S_4$@CDs cross-stacked architecture for enhanced sodium ion storage, *Chin. Chem. Lett.*, 2023, 108921.
10 Z.-Y. Gu, Y.-L. Heng, J.-Z. Guo, J.-M. Cao, X.-T. Wang, X.-X. Zhao, Z.-H. Sun, S.-H. Zheng, H.-J. Liang, B. Li and X.-L. Wu, Nano self-assembly of fluorophosphate cathode induced by surface energy evolution towards high-rate and stable sodium-ion batteries, *Nano Res.*, 2023, **16**, 439–448.
11 J.-Z. Guo, Z.-Y. Gu, M. Du, X.-X. Zhao, X.-T. Wang and X.-L. Wu, Emerging characterization techniques for delving polyanion-type cathode materials of sodium-ion batteries, *Mater. Today*, 2023, **66**, 221–244.
12 D. Xie, Y. Sang, D.-H. Wang, W.-Y. Diao, F.-Y. Tao, C. Liu, J.-W. Wang, H.-Z. Sun, J.-P. Zhang and X.-L. Wu, ZnF2 -Riched Inorganic/Organic Hybrid SEI: in situ-Chemical Construction and Performance-Improving Mechanism for Aqueous Zinc-ion Batteries, *Angew. Chem., Int. Ed.*, 2023, **62**, e202216934.
13 J.-L. Yang, J.-M. Cao, X.-X. Zhao, K.-Y. Zhang, S.-H. Zheng, Z.-Y. Gu and X.-L. Wu, Advanced aqueous proton batteries: working mechanism, key materials, challenges and prospects, *Energy Chem.*, 2022, **4**, 100092.
14 J.-Y. Hwang, S.-T. Myung and Y.-K. Sun, Sodium-ion batteries: present and future, *Chem. Soc. Rev.*, 2017, **46**, 3529–3614.
15 Nagmani, D. Pahari, P. Verma and S. Puravankara, Are Na-ion batteries nearing the energy storage tipping point? – Current status of non-aqueous, aqueous, and solid-sate Na-ion battery technologies for sustainable energy storage, *J. Energy Storage*, 2022, **56**, 105961.
16 F. Zhang, W. Zhang, D. Wexler and Z. Guo, Recent Progress and Future Advances on Aqueous Monovalent-Ion Batteries towards Safe and High-Power Energy Storage, *Adv. Mater.*, 2022, **34**, e2107965.
17 D. Kundu, E. Talaie, V. Duffort and L. F. Nazar, The emerging chemistry of sodium ion batteries for electrochemical energy storage, *Angew. Chem., Int. Ed.*, 2015, **54**, 3431–3448.
18 D. Bin, F. Wang, A. G. Tamirat, L. Suo, Y. Wang, C. Wang and Y. Xia, Progress in Aqueous Rechargeable Sodium-Ion Batteries, *Adv. Energy Mater.*, 2018, **8**, 1703008.
19 C. D. Wessells, R. A. Huggins and Y. Cui, Copper hexacyanoferrate battery electrodes with long cycle life and high power, *Nat. Commun.*, 2011, **2**, 550.
20 X. Lamprecht, P. Zellner, G. Yesilbas, L. Hromadko, P. Moser, P. Marzak, S. Hou, R. Haid, F. Steinberger, T. Steeger, J. M. Macak and A. S. Bandarenka, Fast-Charging Capability of Thin-Film Prussian Blue Analogue Electrodes for Aqueous Sodium-Ion Batteries, *ACS Appl. Mater. Interfaces*, 2023, **15**, 23951–23962.

© 2024 The Author(s). Published by the Royal Society of Chemistry

Open Access Article. Published on 21 March 2024. Downloaded on 5/22/2025 10:14:39 AM.
This article is licensed under a Creative Commons Attribution 3.0 Unported Licence.

21 F. Yin, Z. Liu, S. Yang, Z. Shan, Y. Zhao, Y. Feng, C. Zhang and Z. Bakenov, $Na_4Mn_9O_{18}$/Carbon Nanotube Composite as a High Electrochemical Performance Material for Aqueous Sodium-Ion Batteries, *Nanoscale Res. Lett.*, 2017, **12**, 569.
22 Y. Lu, X. Wu, Z. Li, H. Jiang, L. Liu, Q. Ban and L. Gai, Na^+/K^+-codoped amorphous manganese oxide with enhanced performance for aqueous sodium-ion battery, *J. Alloys Compd.*, 2023, **937**, 168344.
23 C. Ding, Z. Chen, C. Cao, Y. Liu and Y. Gao, Advances in Mn-Based Electrode Materials for Aqueous Sodium-Ion Batteries, *Nano-Micro Lett.*, 2023, **15**, 192.
24 T. Xu, M. Zhao, Z. Li, Z. Su, W. Ren, S. Yang and V. G. Pol, A High Rate and Long Cycling Performance NaTi 2 (PO 4) 3 Core–Shell Porous Nanosphere Anode for Aqueous Sodium-Ion Batteries, *Energy Technol.*, 2022, **10**, 2200970.
25 M. Wu, W. Ni, J. Hu and J. Ma, NASICON-Structured $NaTi_2(PO_4)_3$ for Sustainable Energy Storage, *Nano-Micro Lett.*, 2019, **11**, 44.
26 J. J. Shea and C. Luo, Organic Electrode Materials for Metal Ion Batteries, *ACS Appl. Mater. Interfaces*, 2020, **12**, 5361–5380.
27 C. Han, J. Zhu, C. Zhi and H. Li, The rise of aqueous rechargeable batteries with organic electrode materials, *J. Mater. Chem. A*, 2020, **8**, 15479–15512.
28 W. Deng, Y. Shen, J. Qian and H. Yang, A polyimide anode with high capacity and superior cyclability for aqueous Na-ion batteries, *Chem. Commun.*, 2015, **51**, 5097–5099.
29 T. Gu, M. Zhou, M. Liu, K. Wang, S. Cheng and K. Jiang, A polyimide–MWCNTs composite as high performance anode for aqueous Na-ion batteries, *RSC Adv.*, 2016, **6**, 53319–53323.
30 L. Chen, J. L. Bao, X. Dong, D. G. Truhlar, Y. Wang, C. Wang and Y. Xia, Aqueous Mg-Ion Battery Based on Polyimide Anode and Prussian Blue Cathode, *ACS Energy Lett.*, 2017, **2**, 1115–1121.
31 P. Iurilli, C. Brivio and V. Wood, On the use of electrochemical impedance spectroscopy to characterize and model the aging phenomena of lithium-ion batteries: a critical review, *J. Power Sources*, 2021, **505**, 229860.
32 M. Gaberšček, Understanding Li-based battery materials via electrochemical impedance spectroscopy, *Nat. Commun.*, 2021, **12**, 6513.
33 L. Jiang, Y. Lu, C. Zhao, L. Liu, J. Zhang, Q. Zhang, X. Shen, J. Zhao, X. Yu, H. Li, X. Huang, L. Chen and Y.-S. Hu, Building aqueous K-ion batteries for energy storage, *Nat. Energy*, 2019, **4**, 495–503.
34 X. Lamprecht, I. Evazzade, I. Ungerer, L. Hromadko, J. M. Macak, A. S. Bandarenka and V. Alexandrov, Mechanisms of Degradation of $Na_2Ni[Fe(CN)_6]$ Functional Electrodes in Aqueous Media: A Combined Theoretical and Experimental Study, *J. Phys. Chem. C*, 2023, **127**, 2204–2214.
35 A. S. Bandarenka, Development of hybrid algorithms for EIS data fitting, in *Lecture Notes on Impedance Spectroscopy. Measurement, Modeling and Applications*, ed. O. Kanoun, CRC Press, Tailor and Francis Group, London, 2013, vol. 4, pp. 29–36.
36 H. Banda, D. Damien, K. Nagarajan, M. Hariharan and M. M. Shaijumon, A polyimide based all-organic sodium ion battery, *J. Mater. Chem. A*, 2015, **3**, 10453–10458.
37 Y. Hu, H. Ding, Y. Bai, Z. Liu, S. Chen, Y. Wu, X. Yu, L. Fan and B. Lu, Rational Design of a Polyimide Cathode for a Stable and High-Rate Potassium-Ion Battery, *ACS Appl. Mater. Interfaces*, 2019, **11**, 42078–42085.
38 G. Hernández, N. Casado, R. Coste, D. Shanmukaraj, L. Rubatat, M. Armand and D. Mecerreyes, Redox-active polyimide–polyether block copolymers as electrode materials for lithium batteries, *RSC Adv.*, 2015, **5**, 17096–17103.
39 A. Lasia, *Electrochemical Impedance Spectroscopy and its Applications*, Springer New York, New York, NY, 2014.

© 2024 The Author(s). Published by the Royal Society of Chemistry

2. All-Solid-State Li-ion Batteries with Commercially Available Electrolytes: A Feasibility Review.

R. Götz*, R.L. Streng*, J. Sterzinger*, T. Steeger, M.M. Kaye, M. Vitort, A.S. Bandarenka. *InfoMat* **2024**, 6, e12627

Received: 28 May 2024 | Revised: 6 August 2024 | Accepted: 27 August 2024

DOI: 10.1002/inf2.12627

REVIEW ARTICLE

WILEY

All-solid-state Li-ion batteries with commercially available electrolytes: A feasibility review

Rainer Götz | **Raphael Streng** | **Johannes Sterzinger** | **Tim Steeger** | **Matti M. Kaye** | **Maksym Vitort** | **Aliaksandr S. Bandarenka**

Physics Department, Physics of Energy Conversion and Storage, Technical University of Munich, Garching, Germany

Correspondence
Aliaksandr S. Bandarenka, Physics Department, Physics of Energy Conversion and Storage, Technical University of Munich, James-Franck-Str. 1, 85748 Garching, Germany.
Email: bandarenka@ph.tum.de

Funding information
e-conversion funded by German Research Foundation, Grant/Award Number: EXC 2089/1-390776260

Abstract

The all-solid-state battery (ASSB) concept promises increases in energy density and safety; consequently recent research has focused on optimizing each component of an ideal fully solid battery. However, by doing so, one can also lose oversight of how significantly the individual components impact key parameters. Although this review presents a variety of materials, the included studies limit electrolyte-separator choices to those that are either fully commercial or whose ingredients are readily available; their thicknesses are predefined by the manufacturer or the studies in which they are included. However, we nevertheless discuss both electrode materials. Apart from typical materials, the list of anode materials includes energy-dense candidates, such as lithium metal, or anode-free approaches that are already used in Li-ion batteries. The cathode composition of an ASSB contains a fraction of the solid electrolyte, in addition to the active material and binders/plasticizers, to improve ionic conductivity. Apart from the general screening of reported composites, promising composite cathodes together with constant-thickness separators and metallic lithium anodes are the basis for studying theoretically achievable gravimetric energy densities. The results suggest that procurable oxide electrolytes in the forms of thick pellets (>300 μm) are unable to surpass the performance of already commercially available Li-ion batteries. All-solid-state cells are already capable of exceeding the performance of current batteries with energy densities of 250 Wh kg^{-1} by pairing composite cathodes with high mass loadings and using separators that are less than 150 μm thick, with even thinner electrolytes (20 μm) delivering more than 350 Wh kg^{-1}.

KEYWORDS

all-solid-state batteries, anode-free, composite cathodes, energy density, lithium metal

Rainer Götz, Raphael Streng, and Johannes Sterzinger contributed equally to this study.

This is an open access article under the terms of the Creative Commons Attribution License, which permits use, distribution and reproduction in any medium, provided the original work is properly cited.
© 2024 The Author(s). *InfoMat* published by UESTC and John Wiley & Sons Australia, Ltd.

1 | INTRODUCTION

While lower battery prices[1] and renewable energy costs[2] have led to the affordable large-scale grid storage of electrical energy, the mobile electric sector still struggles to compete with internal combustion engines in terms of power and energy density. The personal vehicle market prioritizes the implications of these limitations, as public acceptance is heavily influenced by vehicle comfort that are mainly ascribable to the ranges[3] and charging times[4] of electric vehicles. Even though state-of-the-art and even more upcoming Li-ion batteries attempt to overcome these concerns,[5,6] the all-solid-state battery (ASSB) concept may provide possible improvements, especially in terms of energy density[7–9] and safety owing to the use of supposedly nonflammable solid electrolytes. Janek and Zeier surveyed the prospects of solid-state batteries in detail a few years ago,[10] including their remaining problems, and recently complemented their evaluation with new trends, including composite cathodes with highly conducting solid electrolytes. Moreover, these researchers advocated diversifying the approaches and materials used as well as focusing on the main issues that hinder their broad application.[11] Kim et al. discussed more specifically how these challenges manifest themselves in oxide and sulfide electrolytes and presented possible routes for overcoming them.[12] They concluded that three points are essential: (1) the cost-effective and scalable production of highly conductive solid electrolytes that are both dense and thin (20 μm), (2) coupling solid electrolytes with suitable electrode materials, including the active material, binder, and additives, and (3) enabling current densities above 0.6 mA cm^{-2} by addressing (i) lithium-dendrite formation, (ii) interfacial electrochemical stability, and (iii) physical contact that worsens over time. In contrast, Randau et al. presented a benchmarking study that explored how various reported cells of a specific ASSB type compare in terms of selected performance parameters; for example, specific energy with respect to cell thickness and cycling stability.[13] A comparison of lithium-metal ASSBs with various electrolyte–cathode combinations links the maximum allowed cell resistance to reachable specific energies. Commonly, these reviews not only broadly screen available materials but also specify the desired parameters of all individual battery components. While providing such minimum requirements provides guidance when optimizing each battery component, ultimately leading to an ideal ASSB, it can also introduce vagueness in terms of the impact of achieving only a few target parameters or even just one.

In this review, we not only list commercially available or at least state-of-the-art materials for solid electrolyte separators but also consider theoretically reachable energy densities at available or already reported thicknesses. Consequently, isolating the electrodes represents the remaining challenge. Although various options have been presented for anodes, close attention is paid to lithium metal. Cathodes are covered more comprehensively, as their composite nature leads to problems associated with material compatibility. Furthermore, the maximum energy density is determined by the solid–electrolyte fraction. Finally, the reports assess the extent to which theoretical energy densities can arise through various pairings.

Additionally, we present measures that mitigate interfacial issues, including coatings between electrolytes and electrodes, as well as safety aspects and the upscaling potentials of the respective solid electrolytes.

2 | MATERIALS

2.1 | Separator solid electrolytes

Solid(-state) electrolytes (SEs/SSEs) are solid-ion conductors that can be classified into three categories: inorganic, polymer, and composite, with some oxides, sulfides (both inorganic), and composites listed in Table 1. Oxide electrolytes are typically rigid and have high voltage-stability windows, good ionic conductivities, and are highly stable in air.[35]

Generally, sulfides exhibit the highest ionic conductivities and deformable mechanical properties; they can be further classified into thio-LISICONs, which are derived from the Li_3PO_4 solid electrolyte by exchanging oxygen for sulfur, argyrodite Li_6PS_5X (where X = Br, Cl, I), LGPS ($Li_{10}GeP_2S_{12}$), and LGPS-type ($Li_{11-x}M_{2-x}P_{1+x}S_{12}$, where M = Ge, Sn, Si).[36,37] In comparison, halide electrolytes have the general $Li_{3+m}M_{1+n}X_6$ formula where M represents one or multiple metallic elements and X represents one or multiple halogen elements. Halides are generally less ionically conductive than sulfides; however, they are more electrochemically stable, especially when combined with oxide cathodes. Moreover, they are more compatible with lithium anodes than sulfides.[38] Composite materials combine flexibility and adaptability to volume change with the superior ionic conductivities of inorganic materials, which enables the electrolyte properties to be fine-tuned as desired.[39,40] In general, all SEs still suffer from low ionic conductivities when compared to liquid electrolytes, with only some sulfide electrolytes delivering comparable values of 10^{-2} S cm^{-1} or higher.

2.1.1 | Electrochemical stability

Figure 1 summarizes the electrochemical windows of various SSEs, which shows that most SSE/electrode

TABLE 1 Examples of various electrolytes, including their chemical compositions, as well as reported conductivities, bending strengths or moduli, and potential windows.

Family	Electrolyte group	Chemical composition	Conductivity in S/cm @RT, up to	[a]Bending strength in MPa or [b]modulus in GPa	Potential Window (V vs. Li/Li^+)	Ref.
Oxide	NASICON-type	$Li_{1+x}Al_xTi_{2-x}(PO_4)_3$ (LATP)	1.9×10^{-3}	140 MPa[a]	2.65–4.6	14,15
		$Li_{1+x}Al_xGe_{2-x}(PO_4)_3$ (LAGP)	6.2×10^{-3}	100 MPa[a]	1.85–4.9	15–17
		$Li_2O-Al_2O_3-SiO_2-P_2O_5-TiO_2-GeO_2$ (LICGC)	1×10^{-4}	140 MPa[a]	–	18
	Lithium-based perovskite	$Li_{3x}La_{(2/3-x)(1/3-2x)}TiO_3$ (LLTO)	1×10^{-3}	79 MPa[a]	2.1–3.68	19,20
	Garnet	$Li_7La_3Zr_2O_{12}$ (LLZO)	5×10^{-4}	–	0.05–3.61	21,22
		$Li_{6.65}Ga_{0.15}La_3Zr_{1.9}Sc_{0.1}O_{12}$ (Sc:LLZO)	1.8×10^{-3}	–	1.65–3.7	23,24
		$Li_{6.4}La_3Zr_{1.4}Ta_{0.6}O_{12}$ (Ta:LLZO, LLZTO)	1×10^{-3}	120 MPa[a]	–	24,25
		$Li_3PO_4 + N_2$ (LiPON)	1×10^{-6}	80 GPa[b]	0.0–4.3	26
Sulfide		$Li_{10}GeP_2S_{12}$ (LGPS)	1.2×10^{-2}	–	1.19–2.38	20,27,28
		$Li_{10}GeP_2S_{12-x}O_x$	1×10^{-2}	–	0.0–10.0	29
		Li_6PS_5Cl (LPSCl, powder)	3×10^{-3}	–	1.11–2.19	30
		Li_6PS_5Cl (LPSCl, pellet)	2×10^{-3}	42.1 GPa[b]	–	20,31,32
		$Li_{6.6}Si_{0.6}Sb_{0.4}S_5I$	2.4×10^{-2}	–	–	33
Composite		PEO + 10 wt% LLZTO	2×10^{-4}	–	0.0–4.0	34

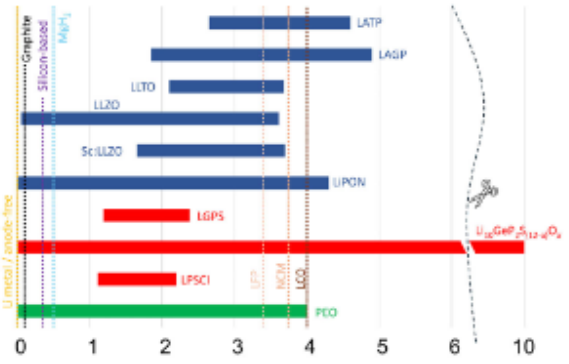


FIGURE 1 Comparing the electrochemical stability windows of the SSEs listed in Table 1. Most SSEs are thermodynamically unstable as they do not cover the potential of the specified anode material.

interfaces are thermodynamically unstable, with solid–electrolyte interphases (SEIs) formed at anode sides.[41] While such interfaces may extend the electrochemical stability window, they frequently hinder ion transport owing to their poor ionic conductivities and mixed electronic–ionic conductivity properties. Consequently, this inefficiency fails to inhibit further reactions between the electrode and SSE, resulting in significant self-discharging and polarization. Modifying the interface can enhance SSE/anode-material compatibility. Chen et al. comprehensively reviewed this topic and examined anode/SSE compatibility in detail.[42] To sustain low interfacial impedance across multiple cycles, an SSE must be thermodynamically stable with respect to the anode. This condition is satisfied when the anode potential is within the electrochemical window of the SSE; otherwise the SSE is reduced by the anode, which indicates that the anode material and the SSE are inherently incompatible.[42] The oxygen-substituted LGPS-type solid electrolyte reported by Sun et al. ($Li_{10}GeP_2S_{12-x}O_x$) deserves special attention; it not only features conductivities of around 10^{-2} S cm^{-1}, but is also electrochemically stable between −0.5 and 10 V (vs. Li/Li^+).[29]

An SSE must also be thermodynamically stable with respect to the cathode to sustain a low interfacial impedance across multiple cycles. This condition is satisfied when the cathode potential is within the electrochemical window of the SSE. Otherwise, the SSE is oxidized at the cathode.[42] In a similar manner to the anode side, Figure 1 shows that most SSE/cathode interfaces are thermodynamically unstable, leading to the formation of cathode–

electrolyte interphases (CEIs) at the cathode sides.[41] Furthermore, inherent cathode-material/SSE incompatibility leads to the formation of a space-charge layer at the SSE/cathode interface.[42]

2.1.2 | Mechanical properties

If mechanical properties are reported, they are often not determined under standardized conditions, which makes it difficult to provide fair comparisons. Of course, this is possibly due to the different flexural modes associated with the various electrolyte groups. Oxide electrolytes are stiff and brittle; hence, their maximum bending strengths prior to breakage is of interest ($\sim 10^2$–10^3 MPa). On the other hand, the flexible nature of a sulfide electrolyte is better assessed by its elastic (Young's) modulus ($\sim 10^2$ GPa) (Table 1). Ideally, a proper comparison should feature only members of the same electrolyte group and use the same testing procedure.

2.1.3 | Safety aspects

Several safety aspects associated with solid electrolytes must be considered. Firstly, the nonflammability of a solid electrolyte becomes nuanced when closely inspected.[43] Oxide electrolytes are incombustible owing to their ceramic characteristics; however, some electrolytes tend to yield at elevated temperatures when combined with lithium anodes.[44] The same cannot be said for sulfur- or polymer-containing electrolytes. Compared with the state-of-the-art liquid electrolyte (1 M $LiPF_6$ in 1:1 (v:v) EC:DMC), sulfide electrolytes do not produce flammable products during combustion; however, heating them still produces a flame, as does grinding them with $Li_{0.5}CoO_2$ (as the active cathode material) and lithium. The latter combination simulates the thermal runaway of a full cell containing two electrode materials and Li_6PS_5Cl, which exhibits a more violent reaction than that associated with the combustion of the sulfide electrolyte alone, indicative of a thermal safety risk in the event of a short circuit. However, not all sulfide electrolytes show this heightened thermal risk; for example, Li_3PS_4 does not exhibit such behavior.[30] Moreover, the sulfide-electrolyte/cathode-material combination determines the thermal-runaway risk. In addition to LCO, Li_6PS_5Cl reacts violently with the $Li_{1-x}Ni_{0.8}Co_{0.1}Mn_{0.1}O_2$ nickel-rich cathode but is stable in the presence of $LiFePO_4$.[45]

Because polymers are considered for composite-electrolyte and composite-cathode (see next section) applications, their compatibilities with other materials are highly important in relation to thermal runaway. Polyacrylonitrile (PAN) and polyvinylidene fluoride (PVDF) are considered nonflammable, whereas polyethylene oxide (PEGMA) and polyethylene glycol diacrylate (PEGMA) are flammable.[46] In addition to identifying flame retardants that thermally stabilize polymers,[47] correct pairings within composites are crucial.[44,48]

Moreover, most solid electrolytes are unstable in air owing to reactions with O_2, H_2O, or CO_2, which provides manufacturing hurdles because dry rooms and, in extreme cases, inert atmospheres, are indispensable.[49] Fabricating sulfide electrolytes is also risky; not only do electrolytes need to be protected from the aerobic atmosphere, but personnel also need to be shielded from potentially hazardous H_2S. Although H_2S concentrations are manageable in dry rooms for some production steps, others must be performed in an inert atmosphere (Ar, N); hence, odor development is unavoidable, and locally high concentrations must be registered using personal gas detectors.[43,50]

2.1.4 | Upscaling aspects

Upscaling all-solid-state-battery production and achieving desired component thicknesses requires advancements in both materials and manufacturing techniques.[33] Traditional thick pellets are not only unsuitable for large-scale production but are also undesirable in terms of energy density (see Section 3).[51,52] In this regard, considering conductivity and mechanical strength as parameters that need to be optimized is useful; here, a solid electrolyte that is either too thin or too thick favors either conductivity or mechanical strength.

In particular, oxide electrolytes, such as lithium garnets (LLZO), perovskites (LLTO), and NASICON-type (LATP) structures are typically produced in pellet form using high-temperature sintering, which is energy-intensive and hence a cost factor.[53] Emerging methods, such as ultrafast high-temperature sintering, wet-chemical deposition, and advanced film-fabrication techniques, including pulsed-laser deposition (PLD) and aerosol-deposition methods (ADMs) have been explored with the aim of creating thin, uniform solid electrolyte (SE) layers. These methods aim to ensure mechanical stability and ionic conductivity while maintaining uniform thickness across large areas. However, thin-film deposition methods are rarely scaled owing to their inherently low cost-effectiveness.[52] Optimizing thin oxide-electrolyte production involves developing high-throughput processes and precise coating methods to achieve the desired form factor and performance. Moreover, manufacturing hurdles not only include the electrolyte membrane itself but also the further processing of the as-then-prepared thin sheet.

Techniques that combine them with cathode materials, such as co-sintering at high temperatures, present challenges ascribable to chemical incompatibilities.[54]

Compared with oxide electrolytes, sulfides are malleable, which is a good feature for any production process that involves cold pressing. Composite cathodes that include sulfide electrolytes (as opposed to oxide electrolytes) can therefore omit the sintering step and save energy. The inherent flexibility of sulfide electrolytes provide another way of quickly achieving large-scale production by imitating the manufacturing processes of established lithium-ion batteries (LIBs). Treating the separator as just another layer that needs to be cast enables one to use existing machines, thereby accelerate upscaling.[37,51] Also, the production of sulfide electrolyte base materials needs to be evaluated based on their potentials to be prepared on large scales. As an example, one might examine the liquid-phase synthesis method, which is fast, inexpensive, and has the potential to be highly scalable. To that end, precursors that are less expensive than Li_2S are crucial, while environmental issues also need to be considered, which is mainly due to the use of essential organic solvents.[55]

Although sulfides are easier to work with than oxide electrolytes, from a mechanical perspective, composites are even more machinable. The polymer within a composite electrolyte functions as the matrix, which not only engenders the electrolyte itself with flexibility, but also improves electrolyte/electrode contact.[40]

In addition to good machinability, new techniques with promising upscaling potentials have emerged. The manufacturing process itself is typically also adaptable using a flexible material; for example, it can be designed such that 3D-printed batteries are possible.[52,56] Recently, Sakuú announced a battery that not only showcased more than 80% of its initial capacity after 1000 cycles but was also supposedly fully dry-printed.[57] Therefore, solid electrolytes can conceivably be manufactured at scale without the use of toxic solvents.

While all the materials presented above have garnered attention as possible solid–electrolyte candidates, here, we only compare four of them (see Figure 2), which were mainly chosen on the basis of their availabilities, ionic conductivities, and demonstrated thicknesses.

We first discuss commercially available LICGC™ AG-01 reported by Ohara[18] to have an ionic conductivity of 1×10^{-4} S cm^{-1}, which is stable toward air and water. Circular and square samples are available in thicknesses of 150 and 20 µm, respectively. In terms of mechanical stability, the sample exhibited a bending strength of 140 MPa. Although its air stability is favorable for research and low-scale production, the low ionic conductivity of this solid–electrolyte candidate renders it unsuitable for use in commercial applications. It has also been shown to be unstable when in direct contact with Li metal.[59]

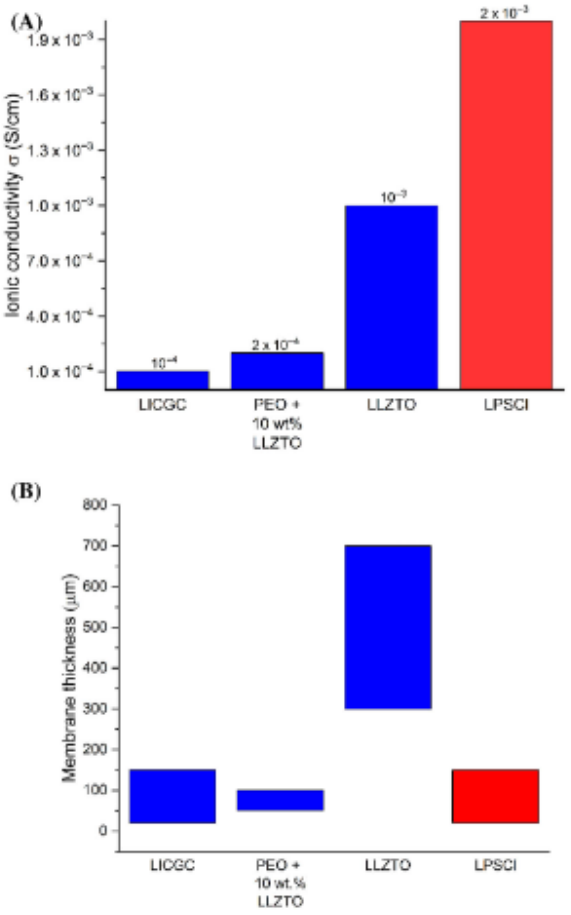


FIGURE 2 (A) Ionic conductivities of selected solid electrolytes as separators. Reported values for electrolytes in membrane forms (composite electrolytes) or as pellets/discs.[18,25,31,58] Blue: composite/oxide electrolytes; red: sulfide electrolytes. (B) Demonstrated or available electrolyte membrane thicknesses.

We next discuss LLZTO ($Li_{6.5}La_3Zr_{1.5}Ta_{0.5}O_{12}$), which has attracted attention owing to its projected ionic conductivity of more than 1×10^{-3} S cm^{-1}.[25] Unfortunately, this material is sensitive to oxidation and water[60] and is lithiophobic,[61] which is why an interlayer is required. Samples can be polished down to approximately 200–300 µm on the laboratory scale, but only 700-µm-thick pellets are commercially available.[25] The pellets exhibit flexural strengths of approximately 120 MPa. Thus, while it is mechanically strong, thinner samples are required to deliver the energy densities required for automotive applications (see Section 3).

PEO-LLZTO, which is a hybrid electrolyte composed of polyethylene oxide (PEO) mixed with LLZTO, is the third example. The ionic conductivity of this hybrid electrolyte reportedly depends on the weight percentage of LLZTO (10 or 40 wt%) and lies between 2×10^{-4} and 4×10^{-4} S cm^{-1}, with thicknesses usually below 100 µm.[62,65] This hybrid electrolyte is reported to exhibit good cycling stability, is inexpensive, and offers more applications possibilities owing to its flexibility that is ascribable to its large PEO content. Unfortunately, the mechanical strength of this hybrid is insufficient for use in large-scale applications, such as automotive batteries.[65] Because LLZTO is used, contact with air or water is detrimental, however, both these limitations can be overcome using additional polymers or other materials as additives by combining their strengths.[66]

We finally discuss the LPSCl sulfide electrolyte, which can deliver ionic conductivities of up to 2×10^{-3} S cm^{-1} for its pellets depending on the synthesis method.[31] However, owing to its brittle nature,[67] LPSCl requires a support framework, such as PVDF[68] or HNBR,[69] to fabricate thinner, flexible membranes, which decreases the ionic conductivity by up to 70%. The electrolyte is also poorly stable toward lithium[70] and requires buffer layers as a consequence.[71] The high ionic conductivity of this electrolyte facilitates its use in future applications that require fast charging.

In the next section, we discuss in more detail the use of solid electrolytes as ingredients in composite cathodes to boost ionic conductivity, as well as compatibility issues.

2.2 | Cathodes

As mentioned previously, significant improvements have been made in relation to the ionic conductivities of bulk solid electrolytes (SE) and lithium-metal-anode/SE interfaces. In a similar manner to conventional Li-ion batteries, the most commonly used cathode active materials are layered or spinel lithium transition-metal oxides ($Li_xM_yO_z$, M = Co, Ni, Mn, etc.) and olivine polyanionic compounds ($LiMPO_4$, M = Fe, Mn, Ni, Co, etc.).[72] In particular, NCM ($LiNi_xCo_yMn_zO_2$) and LCO ($LiCoO_2$) are commonly used as high-capacity cathode active materials (CAM) for LIBs and ASSBs, respectively. However, compared with conventional Li-ion batteries, the cathode structure and SE/cathode interface require several changes to enable effective charge transport between the active material and the SE separator.[69] Owing to the semiconducting nature of most cathode materials, conducting additives are required to enable electron transport; consequently, cathodes for conventional LIBs consist of active-material particles, conducting additives, and binder materials, which form a porous structure that is infiltrated by the liquid electrolyte. However, pathways for ion transport must be artificially created in an ASSB by preparing composite electrodes that contain the SE.[73,74] The mixing ratio and method are decisive for providing optimal electrode designs that enable sufficient electronic and ionic conductivities, as expressed by the tortuosity of the electrode.[75] At the same time, the proportion of active material should be as high as possible to maximize the specific capacity and energy density of the cathode.

Various reviews are dedicated to preparation strategies for ASSB cathodes with the aim of improving interfacial ionic conductivity and stability.[69,72,74–76] However, the areal capacities reported in most studies are insufficient for use in practical applications. In 2021, a break-even analysis by Kravchyk et al. found that ASSBs with Li-garnet solid electrolytes require areal capacities of at least 3.5 mAh cm^{-2} to deliver similar or even higher energy densities than conventional LIBs.[77] The thin electrodes (<1 mAh cm^{-2}) commonly employed in laboratory cells cannot fulfill this capacity requirement even for very thin (20–50-µm-thick) solid electrolytes. Therefore, this section focuses on strategies that enable composite cathodes for solid-state batteries with high areal capacities while concurrently providing high active-material utilization. Table 2 lists various composite cathodes that reportedly exceed the minimum areal capacity requirement. Notably, many of these electrodes are prepared using techniques in which the SE separator is deposited directly on top of the composite cathode, or vice versa. Although this approach leads to improved interfacial charge transfer, it may not be compatible with commercial battery-production processes; nevertheless, the underlying strategies are still worth discussing and can, in many cases, be modified to produce freestanding cathodes.

For a better overview, Figure 3 shows the areal capacities of state-of-the-art composite cathodes against their respective mass loadings. The dotted line provides guidance for the eye and corresponds to a specific capacity of about 157 mAh g^{-1}.

2.2.1 | Composite (polymer/oxide) and oxide electrolytes

Bi et al. combined the high conductivities of polymeric electrolytes with the mechanical stiffnesses of garnet-type oxide electrolytes to develop a composite cathode containing a 90%-PEO/10%-LLZTO SE. The $LiFePO_4$-based electrode displayed specific capacities of approximately 155, 142, and 118 mAh g^{-1} at LFP mass loadings

TABLE 2 High areal capacity composite cathodes and their compositions, SEs used as ion-conducting additives, specific capacities with mass loadings, and areal capacities.

Cathode composition	Solid electrolyte (SE)	Specific capacity	Areal capacity	Ref.	#
Composite (polymer/oxide) and oxide electrolytes					
LFP:CB:SE, 8:1:1	90% PEO + 10% LLZTO	118 mAh g^{-1} @ 15.2 mg cm^{-2}	1.79 mAh cm^{-2}	Bi et al.[58]	a
NCM(811):SE, 6:4 (vol.)	**PEGMA + MePrPyl TFSI + LiTFSI**	**199 mAh g^{-1} @ 83.9 mg cm^{-2}**	**16.7 mAh cm^{-2}**	**Huang et al.[78]**	**b**
NCM(811):CB:SE, 8:1:N.A.	LAGP + PEG-BATGIC	154 mAh g^{-1} @ 13 mg cm^{-2}	2.0 mAh cm^{-2}	Zhang et al.[79]	c
NCM(622):CB:PVDF:LLZTO: $LiClO_4$, 80:10:7:2:1	PDOL	140 mAh g^{-1} @ 21 mg cm^{-2}	2.94 mAh cm^{-2}	Zhang et al.[80]	d
LFP:ITO:SE, 87.7:8.8:3.5	**PEO:LiTFSI: nano-SiO_2**	**157 mAh g^{-1} @ 95 mg cm^{-2}**	**15 mAh cm^{-2}**	**Chen et al.[81]**	**e**
Sulfide electrolytes					
LAZO@LNO:SE:CNF, ~65:30:5	LPSCl	180 mAh g^{-1} @ 25 mg cm^{-2}	4.5 mAh cm^{-2}	Wang et al.[82]	f
LZO@LCO:LPSCl:VGCF, 60:35:5	**LPSCl (nano soft carbon and LLZTO interface layer)**	**120 mAh g^{-1} @ 111.1 mg cm^{-2}**	**15 mAh cm^{-2}**	**Yang et al.[83]**	**g**
NCM(811):SE:PTFE, 70:28:2	**LPSCl**	**180 mAh g^{-1} @ 71.4 mg cm^{-2}**	**13 mAh cm^{-2}**	**Liang et al.[84]**	**h**
NCM(830611):SE:CB, 70:27.5:2.5	**LPSCl**	**205 mAh g^{-1} @ 43 mg cm^{-2}**	**8.7 mAh cm^{-2}**	**Doerrer et al.[85]**	**i**
HfO_2@NMC(851005):SE:CB, 69:30:1	LPSCl	200 mAh g^{-1} @ 10.5 mg cm^{-2}	2.1 mAh cm^{-2}	Kitschc et al.[86]	j
NCM(701515):SE:CB:BR, 70:27.5:1:1.5	LPSClBr	165 mAh g^{-1} @ 8 mg cm^{-2}	1.3 mAh cm^{-2}	Kwon et al.[87]	k
Halide electrolytes					
NMC90:SE, 8:2	LIC	107 mAh g^{-1} @ 72.6 mg cm^{-2}	9.8 mAh cm^{-2}	Ma et al.[88]	l
LCO:SE, 8:2	**$Li_2In_{1/3}Sc_{1/3}Cl_4$**	**138 mAh g^{-1} @ 52.4 mg cm^{-2}**	**7.2 mAh cm^{-2}**	**Zhou et al.[89]**	**m**
NMC85:SE, 9:1	$Li_2In_{1/3}Sc_{1/3}Cl_4$	192 mAh g^{-1} @ 21.6 mg cm^{-2}	4.1 mAh cm^{-2}	Zhou et al.[89]	n
LCO:SE, 85:15	**LIC**	**131.7 mAh g^{-1} @ 48.7 mg cm^{-2}**	**6 mAh cm^{-2}**	**Wang et al.[90]**	**o**
NMC(830611):SE:CNF, 65:30:5	Li_3InCl_6	210 mAh g^{-1} @ ~14 mg cm^{-2}	3 mAh cm^{-2}	Gao et al.[91]	p

Note: Entries in bold are used in the study.

of about 6.4, 9.9, and 15.2 mg cm^{-2}, respectively. These researchers also demonstrated that these composite electrodes outperformed a conventional electrode coupled with a freestanding electrolyte, which delivered only 118 and 30 mAh g^{-1} at 6 and 10.2 mg cm^{-2}, respectively.[92] Chen et al. followed a similar approach by combining PEG, $LiN(CF_3SO_2)_2$, and a nano-SiO_2 electrolyte with an electrolyte-infused $LiFePO_4$/ITO pellet composite cathode. The resulting improved ionic and electronic properties led to a specific capacity of 157 mAh g^{-1} at a $LiFePO_4$ mass loading of 95 mg cm^{-2}, which corresponds to an exceptionally high areal capacity of 15 mAh cm^{-2}.[81] Similarly, Huang et al. reported a hybrid cathode composed of NMC(811)-rich pillars surrounded by a [LiTFSI + PEGMA + MePrPyl TFSI] polymer composite electrolyte with a volumetric CAM-to-SE ratio of 6:4. A specific capacity of 199 mAh g^{-1} at an NMC811 mass loading of 83.9 mg cm^{-2} was achieved using a novel

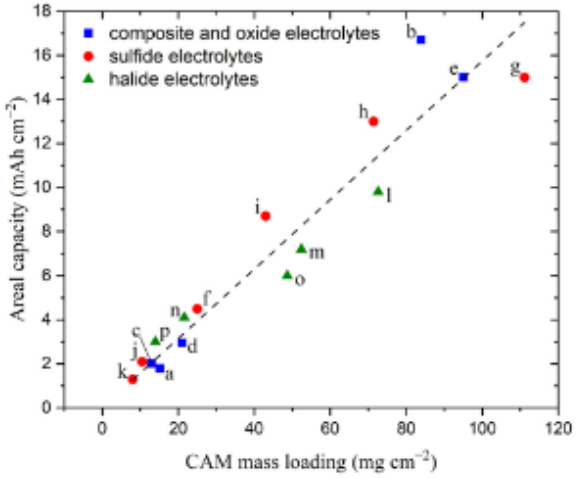


FIGURE 3 Areal capacities of the state-of-the-art all-solid-state cathodes listed in Table 1 plotted against their respective CAM mass loading. The dotted line provides guidance for the eye and corresponds to a specific capacity of about 157 mAh g^{-1}. Colors correspond to the type of solid electrolyte used: composites (polymer + oxide) and oxides (blue), sulfides (red), and halides (green).

directional freezing and polymerization process by enabling low-tortuosity ion-transport pathways. The associated areal capacity of 16.7 mAh cm^{-2} is among the highest reported values for comparable systems and well above the previously established threshold of 3.5 mAh cm^{-2}.[78]

2.2.2 | Sulfide electrolytes

Solid sulfide electrolytes exhibit exceptionally high ionic conductivities and favorable mechanical properties, making them promising candidates for all-solid-state batteries. However, pairing them with high-voltage cathodes is difficult because sulfide electrolytes suffer from narrow electrochemical stability windows, leading to their oxidation. Moreover, continuous operation results in interfacial debonding and rapid capacity loss.[90] Preventing interfacial reactions is paramount for overcoming cathode/sulfide-electrolyte compatibility issues, which is commonly accomplished by introducing interfacial buffer layers with high ionic and low electronic conductivities between the cathode and solid electrolyte.[93,94]

Wang et al. combined an LNO composite cathode with an LPSCl electrolyte using atomic layer deposition to introduce an ultrathin LAZO buffering layer. This coating reduces contact loss and side reactions, thereby enabling high-voltage operation. The resulting full cell features a specific capacity of 180 mAh g^{-1} at an LNO mass loading of 25 mg cm^{-2}, which corresponds to an areal capacity of 4.5 mAh cm^{-2}.[82]

Active-material utilization can be improved by introducing conducting additives. Kitsche et al. also followed an atomic-layer-deposition strategy and reported an NMC(851005), LPSCl, and carbon black composite cathode with a high specific capacity of 200 mAh g^{-1} and an areal capacity of 2.1 mAh cm^{-2}. The applied HfO_2 coating layer enabled high-voltage operation, further highlighting the effectiveness of the buffer layer.[86]

Based on a similar concept, Yang et al. fabricated a soft-carbon cubic-phase nano $Li_{6.4}La_3Zr_{1.4}Ta_{0.6}O_{12}$ (LLZTO) interface layer that connected a $LiZrO_2$-coated (LZO-coated) $LiCoO_2$ (LCO)/LPSCl/VGCF composite cathode to an LPSCl electrolyte. The resulting assembly exhibited improved and uniform Li^+ migration at the interfacial layer, which suppressed Li-dendrite formation. The enhanced electrochemical performance was accompanied by a specific capacity of 120 mAh g^{-1} at an LCO mass loading of 111 mg cm^{-2} and an exceptionally high areal capacity of 15 mAh cm^{-2}.[83]

Doerrer et al. used a different approach to increase cathode/sulfide-electrolyte interfacial stability that involved a single-crystal particulate NMC(830611), LPSCl, and carbon-black (70:27.5:2.5) composite cathode with superior surface interactions and interfacial contact compared to polycrystalline NMC systems; this cathode delivered one of the highest specific capacities reported to date (205 mAh g^{-1}) at an NMC mass loading of 43 mg cm^{-2}, which translates into an areal capacity of 8.7 mAh cm^{-2}.[85]

2.2.3 | Halide electrolytes

To avoid stability issues associated with the use of sulfide electrolytes, Wang et al. used Li_3InCl_6 in combination with a Li_3InCl_6-coated $LiCoO_2$ composite cathode. The high ionic conductivities of halide electrolytes and their stabilities toward high-voltage cathodes enabled them to deliver a specific capacity of 131.7 mAh g^{-1} at an LCO mass loading of 48.7 mg cm^{-2}, which corresponds to an areal capacity of 6 mAh cm^{-2}.[90]

Ma et al. achieved an even higher areal capacity of 9.8 mAh cm^{-2} with the same electrolyte. Freeze-drying resulted in small Li_3InCl_6 particles, which improved the charge-transmission capabilities of NCM90 and the solid–electrolyte–composite cathode, thereby demonstrating that high-areal-capacity systems are achievable without complicated coatings or cathode compositions.[61]

For the study discussed below, we selected composite cathodes with the highest specific and areal capacities,

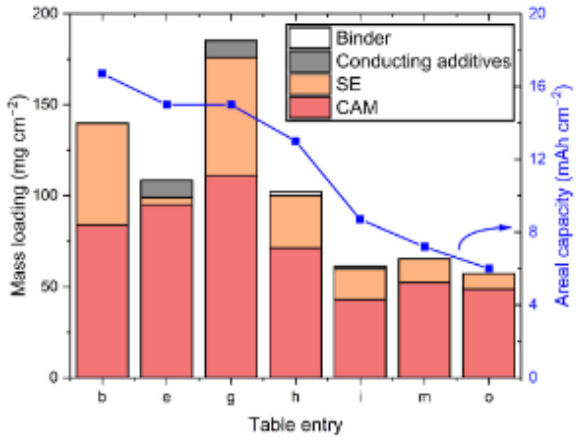


FIGURE 4 Mass loadings of the components of the selected composite cathodes listed in Table 1. The bars represent the portions of each cathode composed of the respective components, including the cathode active material (CAM), the solid electrolyte (SE), conducting additives, such as carbon or ITO, and the binder. The blue curve shows the areal capacity achieved for each cathode design.

which are indicated in bold in Table 2. A more detailed overview of each design is shown in Figure 4. The colored regions of each column represent the mass portions of each component of the composite cathode, whereas the blue line shows the areal capacity achieved by the respective design. Minimizing the portion of the cathode composed of inactive materials, such as conducting additives or binders, is beneficial for creating a high-energy-densities full battery. However, an optimized CAM/other-component ratio facilitates faster and more homogeneous ion conduction, thereby improving active material utilization. Generally, a high areal capacity at a relatively low mass loading is desirable for maximizing the specific energy of the cell. Thus, composite cathodes (b), (e), (h), and (i) appear to provide the optimal properties required for competitive ASSBs.

2.3 | Anodes

The anode within an ASSB is a critical component because it significantly influences key performance parameters, such as energy density, safety, lifespan, and fast-charging ability.[95] Current research efforts are directed toward developing novel materials and interfaces that address existing challenges and unlock the complete potential of ASSB anode materials.

Lithium metal is an important anode material for an ASSB because it has the highest theoretical capacity and lowest potential among known options.[96–98] Nevertheless, lithium-metal anodes face numerous challenges that must be addressed, which highlights the fact that ASSBs with lithium-metal anodes are far from transitioning from laboratory development to commercial applications.[99,100] Hence, in addition to lithium metal, alternative anode materials, such as insertion anodes (e.g., graphite anodes), alloy anodes (e.g., Si-based anodes), and conversion anodes (e.g., metal hydrides) have been investigated for use in ASSBs.[99] Although their theoretical capacities may not match that of lithium metal, they offer distinct advantages in terms of mitigating lithium dendrites and enhancing battery safety.[99,100] Liu et al. provide a comprehensive overview of alternative anode materials for use in all-solid-state lithium-ion batteries in their review.[99]

2.3.1 | Lithium metal

Owing to its unique characteristics, lithium metal is a prime candidate for use as an ASSB anode material. With a theoretical capacity of 3860 mAh g^{-1} and the lowest potential (−3.04 V vs. the standard hydrogen electrode) among known anode materials, it is the optimal anode material for SSB use.[96,98] Nevertheless, the substantial volume expansion experienced by lithium during charging, which averages at around 5 μm per 1 mAh cm^{-2} of plated Li,[101] is a primary obstacle that needs to be addressed. This expansion creates elevated pressure levels, which may result in the lithium metal slowly creeping through the pores of the electrolyte.[102] Such dendrite formation during cycling can lead to short circuits that ultimately result in a shorter battery lifespan.[103] In addition, lithium-metal anodes face other challenges, including capacity decay, increasing overpotential, and potential safety risks.[99] Hence, numerous approaches have been proposed to enhance the performance of lithium-metal anodes, including designing artificial solid–electrolyte interfaces, regulating the lithium-ion deposition path, and increasing the buffer layer at the electrode–electrolyte interface.[104–106] Zhang et al. provide a thorough summary of recent strategies aimed at improving Li-metal anodes.[104]

2.3.2 | Graphite

Graphite has emerged as the predominant anode material for commercial secondary lithium-ion batteries (LIBs) owing to its numerous advantages that include abundant raw-material resources, cost-effective production methods, structural stability, and environmental friendliness.[107,108] In contrast to lithium-metal anodes,

graphite anodes are typically exceptionally cycling stable in ASSBs with minimal volume changes.[109,110] Nonetheless, graphite anodes are not without certain limitations, including a comparatively modest theoretical charge capacity (372 mAh g^{-1}[111]) and thermodynamic instability when used with certain solid electrolytes, such as sulfide-based electrolytes.[112] In addition, in a similar manner to a lithium-metal anode, the deposition of lithium on the surface of a graphite anode can result in the formation of Li dendrites during charging.[112] Recent research efforts have been directed toward overcoming these limitations by reducing the size of the graphite particles to the nanometer scale and exploring the use of graphite-based composites.[99]

2.3.3 | Silicon-based anodes

Silicon-based anodes have been extensively researched owing to their high specific capacities (3580 mAh g^{-1} for $Li_{15}Si_4$), low redox potentials (0.35 V vs. Li^+/Li), the high abundance of silicon, and affordability.[99] As an alloyed anode, silicon exists in a range of alloy phases, including LiSi, $Li_{12}Si_7$, $Li_{15}Si_4$, and $Li_{22}Si_5$.[99] Unlike liquid lithium-ion batteries, the high stability of the solid electrolyte prevents the formation of a solid–electrolyte interphase (SEI) layer between the silicon anode and the electrolyte. Notably, sulfide solid electrolytes and silicon anodes are thermodynamically stable and highly compatible.[99] Moreover, the lower operating potential of silicon reduces concerns regarding lithium-dendrite formation, and unlike lithium metal, silicon is stable under ambient conditions, negating the need for a protective atmosphere; hence, making it well-suited for mass production.[99] However, silicon-based ASSB anodes face several challenges, particularly the substantial effects of volume expansion and their inherently low conductivities.[113] These limitations have been promisingly addressed in recent studies. Decreasing particle size to the nanometer scale is an effective strategy for enhancing the surface contact area and mitigating volume expansion in a Si-based anode during charging/discharging cycles.[99,114] Silicon–carbon composite materials and silicon alloy materials significantly reduce the volume expansion experienced by silicon and its electronic resistance, thereby significantly enhancing the rate capability of the silicon-based anode.[99,114]

2.3.4 | Conversion anodes

Conversion electrodes that employ the conversion reaction also exhibit promising performance as ASSB anode materials owing to their low potentials and high capacities. The electrochemical mechanism of a conversion electrode is based on the following reaction:

$$M_aX_b + (bn)Li^+ + (bn)e^- \leftrightarrow aM + bLi_nX.$$

In this context, M represents a metal or a blend of metals, X represents negatively charged nitrogen, oxygen, sulfur, halogen, or phosphorus ions, and n indicates the oxidation state of X. Conversion electrodes composed of metal oxides, hydrides, nitrides, sulfides, phosphides, fluorides, and other materials have been extensively studied for use in lithium-ion battery applications.

Nevertheless, electrode degradation is a major issue for conversion-electrode materials. Electrodes that rely on the conversion reaction chemically interact with lithium to form new phases with uncontrolled spatial distributions. Therefore, insulating compounds with low conductivities and high overpotentials are formed, which compromise electrochemical reversibility. Furthermore, challenges, such as poor kinetics, limited cycling life, and low reversibility, hinder the potential commercialization of conversion electrodes. Recently, progress toward addressing these issues has been made. Again, reducing the particle size to the nanometer scale has proven to be an effective strategy. Moreover, efforts have focused on modifying the surfaces of conversion electrodes and forming electrolyte-additives layers on the electrodes.

Metal-hydride-based conversion electrodes have demonstrated significant promise as potential ASSB anode candidates owing to their low potentials, minimal polarizations, high specific volumetric and gravimetric capacities, and cost-effectiveness. An ASSB with a metal-hydride-based anode requires an ideal solid electrolyte with excellent conductivity for both lithium and hydrogen ions.[99] Solid electrolytes that meet these criteria include $LiBH_4$ and Li_2S–P_2S_5. Among metal hydrides, MgH_2 stands out owing to its high theoretical specific capacity of 2038 mA h g^{-1}, an operating potential of 0.5 V (compared to Li/Li^+), cost-effectiveness, and natural abundance in nature, and has become a key research focus as an ASSB anode.[99] However, despite its numerous advantages, SSBs that use MgH_2 exhibit poor charge/discharge reversibilities.

2.3.5 | Anode-free ASSBs

An anode-free ASSB is a lithium-metal battery in which a lithium anode is formed during the first charging cycle. Specifically, lithium ions from the cathode are reversibly plated onto a bare current collector as lithium metal during the initial charging cycle.[111,115] This setup offers

several advantages over current lithium-based batteries, such as higher volumetric and gravimetric energy densities, better cell safety, simpler manufacturing methods, and enhanced lifespans.[111,115] However, anode-free SSBs still encounter significant challenges, including rapid capacity degradation,[111] whose primary causes include low coulombic efficiency and a gradual increase in the overpotential of the lithium-metal anode.[111] Furthermore, the substantial volume changes within an anode-free ASSB caused by lithium plating and stripping severely affect cycling stability and shorten the lifespan of the battery cell.[115] Additionally, anode-free ASSBs are subjected to non-uniform lithium-ion fluxes during lithium plating.[111] Current research is directed toward resolving these issues by developing SEs with high ionic conductivities, forming passivated layers that are kinetically inert and stable against lithium metal at the interface, and broadly modifying the electrolyte–anode interface. Huang et al. presented a comprehensive overview of recent strategies aimed at enhancing anode-free ASSBs.[111]

In recent years, various anode materials have been investigated for use in ASSBs. The main research areas are discussed above. The structure and size of the active material, use of a binder, selection of a suitable solid electrolyte, and the manufacturing process significantly affect the electrochemical properties of the anode.[99]

Graphite, lithium-metal, and anode-free ASSBs were selected for further discussion. Graphite was selected because it is the predominant anode material used in commercial secondary LIBs today and serves as a lower benchmark limit. Li metal has exceptional characteristics; hence it is the prime candidate for use as an ASSB anode material. With a theoretical capacity of 3860 mAh g^{-1} and the lowest potential (−3.04 V vs. the standard hydrogen electrode) among known anode materials, it theoretically provides the optimal ASSB-anode-material solution. Anode-free ASSBs were selected because they show promising future potential. Although still in their early stages, anode-free ASSBs offer several advantages over current lithium-based batteries, including even higher volumetric and gravimetric energy densities than those of ASSBs with lithium-metal anodes.

2.3.6 | Economic aspects

Estimating the costs associated with anode materials, such as graphite, silicon-based anodes, and conversion electrodes, presents considerable challenges, particularly when compared against the anode-production costs of current LIBs. Nevertheless, research efforts have focused on estimating the potential costs associated with producing ASSBs with lithium-metal anodes, as well as anode-free ASSBs. Heubner et al. provide preliminary cost assumptions in their study.[116]

The high reactivity of lithium components with ambient air necessitates stringent dry-room conditions for ASSBs with lithium-metal anodes, resulting in significant acquisition, operating, and maintenance costs.[116] Additionally, fabricating sufficiently thin lithium foil with acceptable purities and microstructures over large areas is extremely challenging and expensive, potentially leading to lithium foil prices in the 300–400 USD kg^{-1} range, or even up to 1000 USD kg^{-1} for films with advantageous thicknesses ($\ll$100 μm). However, currently, there are no available models or practical experiences that enable costs to be reliably compared on an industrial scale. Consequently, whether or not these costs are competitive with those associated with currently used LIB anode materials remains uncertain.[116]

Anode-free ASSBs offer substantial processing-cost advantages by eliminating active-material-related anode-manufacturing steps that contribute 12%–18% to production costs during LIB manufacturing.[117] Additionally, the removal of the anode coating reduces material consumption and simplifies cell production, further lowering costs. Moreover, the process conditions are significantly less demanding because lithium metal is absent during assembly, thereby considerably reducing acquisition, operating, and maintenance costs. However, no models or practical experiences currently exist that facilitate industrial-scale costs to be reliably compared.[116]

2.4 | Interfacial issues

Although reasonably high SSE ionic conductivities have been reported, the internal resistances of the corresponding ASSBs remain large, which is mainly ascribable to the interfacial charge-transfer resistance associated with Li ions. Dendrite formation and significant anodic volume expansion have been identified as the primary issues on the anode side. In particular, Si-based anode materials experience substantial volume expansions during charging and discharging cycles, resulting in fracturing and delamination.[99] In the case of a lithium-metal anode, volume expansion leads to higher pressure levels that can result in the lithium metal gradually infiltrating electrolyte pores.[102] Furthermore, the SSE must be thermodynamically stable with respect to the anode to maintain low interfacial impedance over multiple cycles. This stability is achieved when the anode potential falls within the electrochemical window of the

SSE; the SSE is reduced by the anode if this condition is not met, indicative of an inherent incompatibility between the anode material and the SSE.[42] Recently, Ma et al. comprehensively reviewed this topic and discussed the compatibility of the anode/electrolyte interface in detail.[110]

The cathode/electrolyte interface mainly suffers from interfacial instability and poor physical contact that arise from poor mechanical stability and charge-layer formation owing to chemical and electrochemical instability, resulting in the oxidation and decomposition of the SE. Challenges associated with these issues and their solutions are discussed thoroughly in the review articles of Jiang et al. and Lou et al.[118,119] Promising solutions involve the previously discussed introduction of protective coatings and buffer layers that enable the use of high-voltage cathodes without compromising stability. Furthermore, electrode composition and processing, structural design, and active-material morphology play essential roles. Although not as severe in cathodes as in anodes, volume expansion can harm mechanical stability, especially at low stack pressures, necessitating the use of low-volume-change CAMs and buffer layers.[120] The interested reader is referred to several dedicated reviews.[121–123]

3 | ENERGY DENSITIES OF ASSBs WITH STATE-OF-THE-ART MATERIALS

The gravimetric energy densities of hypothetical full cells were estimated using various previously introduced cathode designs to determine ASSB feasibility based on commercially available solid electrolytes. A simple cell design with copper and aluminum current collectors and a Li-metal anode was considered in these calculations. The gravimetric energy density, E_{spec}, of the battery is defined as the ratio of the total energy, E, to its total mass, M, and the total energy of the battery can be calculated as the product of the total capacity, Q, and cell voltage, V. However, because total values are usually not readily available, areal densities are preferred in these calculations; consequently, the areal capacity, q_A, and the areal mass density of each component, $m_{A,x}$, were used. For simplicity, the battery was assumed to be mass-balanced with equal anodic and cathodic areal capacities. Owing to the very low weight of the Li-metal anode (usually <5% of the cell mass), the anode mass has relatively little influence. Although anode-free cells can achieve higher energy densities, this difference is negligible. Consequently, the following equation can be used to calculate gravimetric energy density:

$$E_{spec} = \frac{q_A \cdot V}{m_A} = \frac{q_A \cdot V}{m_{A,Cath} + m_{A,Anode} + m_{A,Separ} + m_{A,CC}},$$

with the cathodic areal capacities listed in Table 2. The areal mass densities are defined as follows:

- $m_{A,Cath}$: Value taken from Table 2 divided by the active-material ratio in the cathode.
- $m_{A,Anode}$: Calculated as $\frac{q_A}{q_{spec,Li}}$ with the specific capacity of lithium, $q_{spec,Li} = 3.86$ mAh mg^{-1}.
- $m_{A,Separ}$: Calculated as $\rho \cdot d$, using the density, ρ, and the thickness, d, of the solid electrolyte separator ($\rho = 3.05$ g cm^{-3} for LICGC™,[18] $\rho = 5.26$ g cm^{-3} for LLZTO,[124] $\rho = 1.13$ g cm^{-3} for PEO,[91] $\rho = 1.64$ g cm^{-3} for LPSCl[125]).
- $m_{A,CC}$: Current collector materials: $\rho = 8.9$ mg cm^{-2} for 10 µm copper foil and $\rho = 2.7$ mg cm^{-2} for 10 µm aluminum foil.[126]

Respective cell voltages of 3.4 V (LFP), 3.75 V (NCM) and 4.0 V (LCO) were used.[127]

The resulting gravimetric energy densities of the various cathodes are plotted against CAM mass loadings in Figure 5. Only reported cathodes with areal capacities and mass loadings that lead to energy densities comparable to those of commercial LIBs are included in the graph. The colors of the lines and symbols correspond to the material classes of the separator and cathode additive, respectively. Therefore, a matching line and symbol color implies that the same or at least similar electrolytes are used for both parts of the cell. It should be noted that different materials can be combined; however, interactions that impair stability or charge transport cannot be excluded. The horizontal dotted lines indicate two thresholds: 250 Wh kg^{-1} for state-of-the-art conventional LIBs, and 360 Wh kg^{-1} for the already commercialized quasi-ASSB by WeLion currently used in NIO electric vehicles.[128]

Thin and low-density solid electrolytes are clearly key to surpassing the aforementioned thresholds. For example, cells with 700- or 300-µm-thick LLZTO electrolytes cannot deliver energy densities above ~200 Wh kg^{-1}, and a significantly thinner (~30 µm) electrolyte is required to exceed 360 Wh kg^{-1}, which may prove challenging considering the brittleness of LLZTO. Adding low-density and more-flexible PEO dramatically increases the maximum energy density to ~375 Wh kg^{-1}, even for thicker (50–100 µm) electrolytes. However, ultra-thin 20 µm LICGC™ delivers the highest specific energy among the commercially available options. Owing to their comparably low densities, LPSCl-based cells deliver even higher energy densities at similar thicknesses, which seems feasible as 35–120-µm-thick

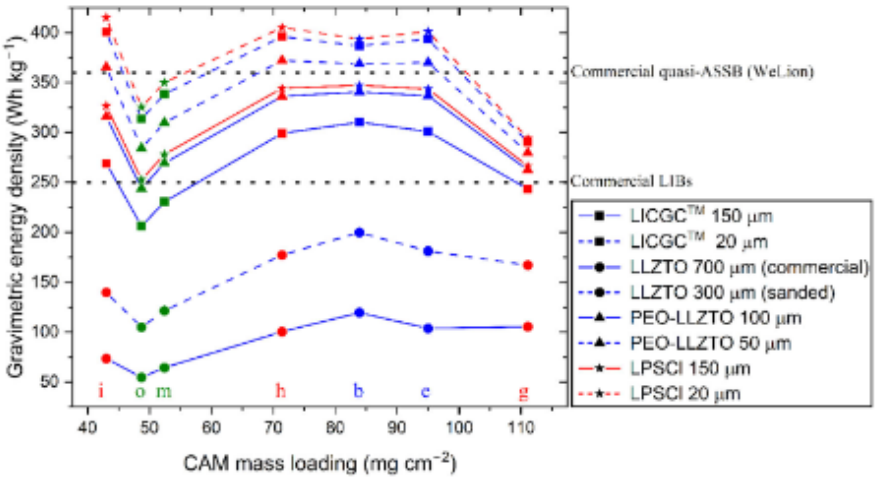


FIGURE 5 Estimated gravimetric energy densities for ASSB full cells that use Li-metal anodes, various commercially available solid-state electrolytes, and state-of-the-art cathode designs. The colors correspond to the solid electrolyte used as the separator (line color and style) and as the cathode additive (symbol color), respectively: PEO/LLZTO-composites and oxides (blue), sulfides (red), and halides (green). The letters at the bottom of the figure correspond to the entries in Table 2.

electrolyte films have already been successfully prepared in the past.[129–131]

The highest energy density was achieved using the design reported by Doerrer et al.,[85] who used monocrystalline NCM to deliver an exceptional specific capacity of 205 mAh g^{-1}, which corresponds to almost 100% active-material utilization. This strategy facilitates the use of relatively low cell mass while maintaining high areal capacity. The specific energy is expected to exceed 400 Wh kg^{-1} when combined with 20 µm LPSCl as a compatible electrolyte separator. However, it should be noted that the use of monocrystalline NCM is associated with higher material costs because it is synthesized in a more complex manner than commonly employed polycrystalline materials. A comparison of approaches that use polycrystalline CAMs reveals that mass loadings between ~70 and ~100 mg cm^{-2} appear to yield optimal performance, with values close to 400 Wh kg^{-1} also achievable within these limits. Yang et al. reported[83] that higher mass loadings lead to lower material utilization owing to the long ion-conduction pathways within the electrodes; consequently, the additional inactive mass effectively decreases the gravimetric energy density of the full battery.

Oxide-based ASSBs deliver the best performance by combining a commercially available 20 µm LICGC™ glass electrolyte with the cathode preparation strategies reported by Huang et al.[78] and Chen et al.,[12] who both suggested combining polymers with inorganic oxide materials, thereby rendering this approach as a promising option for achieving energy densities close to 400 Wh kg^{-1}. Similar results can be achieved by potentially improving the compatibility between the composite cathode and the solid electrolyte using the same separator composition (LLZTO | PEO).

To put these results into perspective, the energy densities of ASSBs used in electric vehicles can be estimated by considering the average ranges of vehicles powered by state-of-the-art LIBs. According to the International Energy Agency, BEVs have an average driving range of 350 km with a single charge, which corresponds to ~54% of the median range of gasoline-powered cars.[132] Assuming an average energy density of 250 Wh kg^{-1} for current-generation automotive batteries, ranges of 490–560 km should be feasible with ASSBs based on the results presented above. Therefore, delivering energy densities of between 450 and 500 Wh kg^{-1} is considered to be a future goal based on these estimations, as it would enable ranges similar to those of conventional combustion-engine-based vehicles.

Limitations arising from the use of conventional Li-ion batteries, particularly in electric vehicles, have prompted the industry to investigate high-energy-density ASSBs. In this regard, *QuantumScape* and *ONE* follow cost-effective, anode-free approaches to yield energy densities similar to those suggested in this study.[7,8] Optimization that affords lower prices is another key factor for commercial applications; hence, the slightly lower gravimetric energy densities can be rationalized in terms of more cost-effective production procedures. *CATL* announced a "condensed" semi-solid-state battery with an exceptional energy density of 500 Wh kg^{-1}, which

surpasses the values discussed in this review.[9] The undisclosed chemistry, however, includes non-solid components, most likely liquid interfacial layers that improve ionic-conduction pathways in the cathode. In addition to achieving competitive energy densities, other factors, such as cycling stability, safety, and production costs, play important roles in evaluating ASSB viability. High capacity retention during frequent battery charging and discharging is a key factor that determines battery performance. The reported cycling lives of batteries that employ cathode designs used to evaluate potential energy densities are shown in Figure 6. With more than 98% capacity retention after 4000 cycles at a high cycling rate of 25 C, the cathode proposed by Yang et al. demonstrated the best cycling stability. The same design maintained 94% of its initial capacity after 350 cycles at 1 C.[83] Doerrer et al. reported a capacity retention of 96% after 50 cycles at 0.5 mA cm^{-2} for their high-energy-density single-crystal cathode.[85] Similarly, Huang et al. and Wang et al. carried out relatively short stability testing for 200 cycles at 0.5 and 0.1 C, respectively, whereas Chen et al. did not report any cycling-stability data.[81] Therefore, longer cycling is required to determine how economically competitive these batteries are.

Furthermore, evaluating production expenses and costs linked to each cathode and battery design is of utmost importance when assessing the possibility of realistically implementing them in the market. While exactly quantifying material and processing costs on an industrial scale is nearly impossible, it appears likely that manufacturing methods compatible with already existing

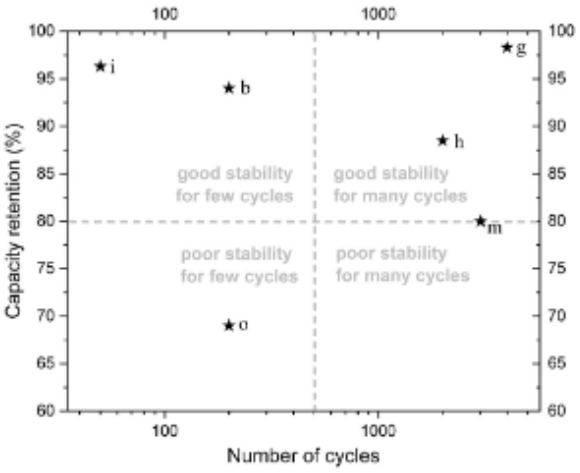


FIGURE 6 Cycling stabilities of batteries that employ the cathode designs discussed when evaluating energy densities. The letters correspond to the entries in Table 2. Chen et al. (entry c, Table 2) did not report any long-term cycling data.

machinery used to produce electrodes for conventional LIBs are the most economically viable. Although the design proposed by Wang et al. (entry b in Table 2) enables high energy densities, the directional polymer-freezing technique is significantly more intricate than established slurry-casting and calendaring methods used to produce LIBs.[90] Other approaches that lead to similar energy densities, such as those reported by Chen et al. (entry e in Table 2), Liang et al. (entry h in Table 2), and Doerrer et al. (entry i in Table 2), rely on much simpler powder-pressing methods.[81,84,85] The design reported by Chen et al. (entry e in Table 2) appears to be the most cost-efficient among those that use high-energy-density cathodes as it uses less expensive LFP instead of NCM or LCO and does not rely on additional coatings. In general, composite-cathode preparation for ASSBs is expected to be costlier than the cathode manufacturing processes used for conventional LIBs because it involves a high-temperature sintering step in most cases. The anode and electrolyte must be considered when assessing the production costs of a full ASSB. Although lithium prices are subject to large fluctuations, they affect ASSBs and LIBs equally. Consequently, the anode does not significantly affect the economic competitiveness of solid-state batteries that use Li-metal or anode-free configurations. The costs associated with the SE itself are difficult to estimate, as they depend highly on the production scale and method.

Schnell et al. performed bottom-up calculations that focused on sulfide- and oxide-based electrolytes to assess the competitiveness of ASSBs with conventional LIBs.[133] To that end, they not only addressed the developmental forecasts for ASSBs but also accounted for progress in LIB production. In addition to omitting the electrolyte filling and simplifying the formation procedure, they identified bipolar stacking (in a similar manner to fuel cell applications) as a potential way of decreasing costs per battery module compared with the classical parallel stacking configurations used in LIBs. Using this approach in combination with an NMC811 cathode and a lithium-metal anode led to predicted manufacturing costs between 132 and 86 USD kWh^{-1}, which is expected to break even with a LIB that uses a Si/C anode if the price of the LPS sulfide separator can be reduced to about 50 USD kg^{-1}. ASSBs using LLZ oxide separators only facilitate a 267 to 123 USD kWh^{-1} reduction, which is not expected to be price competitive with Si/C-anode-based LIBS, even if the LLZ price were to be reduced to 10 USD kg^{-1}. The Nissan Motor Corporation aims to reduce the price of ASSBs for electric vehicles even further, to 75 USD kWh^{-1} by 2028 and has projected projects even lower prices of 65 USD kWh^{-1} thereafter, which would make electric vehicles as cost-effective as

their gasoline-powered counterparts.[134] However, these predictions only serve as rough estimates because they depend heavily on the assumed technological learning rate. Currently, the manufacturing costs of ASSBs are significantly higher than those of LIBs, and efforts to upscale production to the industrial level are required in order to establish realistic values. Adopting current industrial methods for producing LIBs is paramount for cost-effective upscaling by making use of existing infrastructure wherever possible. However, major changes to conventional LIB-production are necessary; hence, concurrently developing the product and process is expected to yield the best results for ASSB upscaling.[133,135] To assess scalability, Zhang et al. constructed three 1-Ah ASSBs using Ohara LICGC™ powder together with PEO-LiTFSI as the polymer matrix. ASSB cells were composed of a composite electrolyte, NMC622 cathodes, and MCMB (MesoCarbon MicroBead) graphite anodes. In doing so, these researchers demonstrated the scalable production of practical ASSBs that exhibit consistent electrochemical performance with confirmed safety.[136]

4 | CONCLUSION

In this review, we discussed commercially available state-of-the-art materials for solid electrolyte separators and calculated the potential energy densities of ASSBs with respect to currently feasible material thicknesses. This approach separately calculates potential energy densities for selecting and combining different electrode materials. Although various options have been presented for the anode, we focused on promising materials, such as lithium metal and the anode-free ASSB concept. Cathodes are more thoroughly examined in this review, which addressed compatibility issues arising from their composite nature. Together, our findings revealed the highest possible theoretical energy densities for different material combinations. Additionally, we discussed interfacial measures, such as coatings between electrolytes and electrodes, as well as safety aspects and upscaling potentials.

Among the separators discussed in this review, LPSCl exhibited the highest ionic conductivity. However, manufacturing a thin membrane requires a support framework for mechanical stability and lithium compatibility, which can significantly reduce the conductivity, depending on the material used. LLZTO separators also exhibit relatively high ionic conductivities; however, they require interlayer materials to ensure good contact with lithium and to protect against the atmosphere. Furthermore, commercial LLZTO electrolytes must also be thin. The PEO-LLZTO hybrid electrolyte is highly stable with lithium and can easily be modified by incorporating additional materials in order to optimize other parameters. Ohara LICGC, which has the advantages of being commercially available and highly stable toward air and water, still has low ionic conductivity as its major drawback.

Cathodes paired with composite polymer-oxide electrolytes and sulfide electrolytes that use interfacial layers exhibit the highest areal capacities, with LPSCl, PEO, and PEGMA notable examples of such electrolytes. Halide electrolytes also exhibit relatively high areal capacities; they also enable simpler systems devoid of complicated coatings and cathode compositions owing to their high-voltage stabilities. Furthermore, composite cathodes containing the respective solid electrolytes are crucial for achieving high areal capacities regardless of the type of solid electrolyte separator used. NMC, LCO, and LFP are CAMs that can be used to fabricate high-areal-capacity composite cathodes.

Various anode materials for use in ASSBs have been investigated in recent years. Lithium metal is an essential anode material because it exhibits the highest theoretical capacity and lowest potential among known options. However, lithium-metal anodes still face many challenges that must be overcome, which highlights the fact that ASSBs with lithium-metal anodes are far from transitioning from laboratory development to commercial applications. Therefore, aside from lithium metal, alternative anode materials, such as insertion anodes (e.g., graphite anodes), alloy anodes (e.g., Si-based anodes), and conversion anodes (e.g., metal hydrides), have been investigated for ASSB use.[99] Although their theoretical capacities do not match those of lithium metal, they offer distinct benefits in mitigating lithium dendrites and enhancing battery safety. The anode-free-ASSB concept has shown significant potential for the development of next-generation ASSBs, despite being in its early stages.

Overall, our selection of various material combinations and subsequent calculations show that ASSBs with exceptional energy densities that far exceed 250 Wh kg^{-1} appear feasible using market-available thin solid-state electrolytes and state-of-the-art design strategies for high-capacity composite cathodes. In conclusion, our feasibility study showed that ASSBs with gravimetric specific energies of approximately 350 and 400 Wh kg^{-1} can be realistically produced based on the current state of research and technology.

ACKNOWLEDGMENTS

We thank the German Research Foundation (DFG) under Germany's excellence strategy—EXC 2089/1-390776260 ("e-conversion") 3.4 V (LFP). Open Access funding enabled and organized by Projekt DEAL.

CONFLICT OF INTEREST STATEMENT

The authors declare no conflict of interest.

ORCID

Rainer Götz https://orcid.org/0000-0003-1589-2550
Johannes Sterzinger https://orcid.org/0009-0004-2416-2124
Matti M. Kaye https://orcid.org/0009-0006-3831-1797
Aliaksandr S. Bandarenka https://orcid.org/0000-0002-5970-4315

REFERENCES

1. Ritchie H. *The Price of Batteries Has Declined by 97% in the Last Three Decades*; 2021. Accessed May 2024. https://ourworldindata.org/battery-price-decline
2. Roser M. *Why Did Renewables Become So Cheap So Fast?* 2020. Accessed May 2024. https://ourworldindata.org/cheap-renewables-growth
3. Lee J, Kim H. *Electric Car Range Is the most Important Factor for Korean Consumers: Study*; 2019. [Pulse]. Accessed May 2024. https://pulsenews.co.kr/view.php?year=2019&no=584972
4. Ouyang D, Ou X, Zhang Q, Dong C. Factors influencing purchase of electric vehicles in China. *Mitig Adapt Strateg Glob Change*. 2020;25(3):413-440.
5. NCM 811 Battery. Accessed May 2024. https://www.grepow.com/nmc811-battery.html
6. Samsung INR21700-50G; 2022. Accessed May 2024. https://www.batemo.com/products/batemo-cell-explorer/samsung-inr21700-50g/
7. QS Platform QuantumScape; 2021. Accessed May 2024. https://www.quantumscape.com/technology/
8. One Dual Battery; 2023. Accessed May 2024. https://one.ai/products/gemini
9. CATL Condensed Battery; 2023. Accessed May 2024. https://www.catl.com/en/news/6015.html
10. Janek J, Zeier WG. A solid future for battery development. *Nat Energy*. 2016;1(9):1-4.
11. Janek J, Zeier WG. Challenges in speeding up solid-state battery development. *Nat Energy*. 2023;8(3):230-240.
12. Kim KJ, Balaish M, Wadaguchi M, Kong L, Rupp JLM. Solid-state Li-metal batteries: challenges and horizons of oxide and sulfide solid electrolytes and their interfaces. *Adv Energy Mater*. 2021;11(1):2002689.
13. Randau S, Weber DA, Kötz O, et al. Benchmarking the performance of all-solid-state lithium batteries. *Nat Energy*. 2020;5(3):259-270.
14. Xu X, Wen Z, Yang X, Zhang J, Gu Z. High lithium ion conductivity glass-ceramics in Li_2O–Al_2O_3–TiO_2–P_2O_5 from nanoscaled glassy powders by mechanical milling. *Solid State Ion*. 2006;177(26–32):2611-2615.
15. Benabed Y, Rioux M, Rousselot S, Hautier G, Dollé M. Assessing the electrochemical stability window of NASICON-type solid electrolytes. *Front Energy Res*. 2021;9:682008.
16. Kumar B, Thomas D, Kumar J. Space-charge-mediated superionic transport in lithium ion conducting glass–ceramics. *J Electrochem Soc*. 2009;156(7):A506.
17. MSE PRO LISICON LATP Solid State Electrolyte Membrane, 300 µm thick, 12 mm diameter. Accessed May 2024. https://www.mscsupplies.com/products/latp-solid-state-electrolyte-membrane-12mm-diameter-300um-thickness?variant=31732389380154
18. LICGC™ AG-01, Ohara Corp. Accessed May :2024. https://oharacorp.com/lithium-ion-conducting-glass-ceramics-licgc/
19. Inaguma Y, Liquan C, Itoh M, et al. High ionic conductivity in lithium lanthanum titanate. *Solid State Commun*. 1993;86(10):689-693.
20. Schwietert TK, Vasileiadis A, Wagemaker M. First-principles prediction of the electrochemical stability and reaction mechanisms of solid-state electrolytes. *JACS Au*. 2021;1(9):1488-1496.
21. Murugan R, Thangadurai V, Weppner W. Fast lithium ion conduction in garnet-type $Li_7La_3Zr_2O_{12}$. *Angew Chem Int Ed Engl*. 2007;46(41):7778-7781.
22. Zhu Y, He X, Mo Y. Origin of outstanding stability in the lithium solid electrolyte materials: insights from thermodynamic analyses based on first-principles calculations. *ACS Appl Mater Interfaces*. 2015;7(42):23685-23693.
23. Buannic L, Orayech B, Del López Amo J-M, et al. Dual substitution strategy to enhance Li+ ionic conductivity in $Li_7La_3Zr_2O_{12}$ solid electrolyte. *Chem Mater*. 2017;29(4):1769-1778.
24. Benabed Y, Vanacker A, Foran G, Rousselot S, Hautier G, Dollé M. Solving the $Li_7La_3Zr_2O_{12}$ electrochemical stability window puzzle. *Mater Today Energy*. 2023;35:101320.
25. Ampcera® Ta-LLZO Garnet Ceramic Membrane Solid Electrolyte, LLZTO, 0.7 mm Thick, 14 mm Diameter. MSE Supplies. Accessed May 2024. https://www.mscsupplies.com/products/ampcera-solid-electrolyte-llzo-ceramic-membrane-garnet?variant=7228451127354
26. Bates JB, Dudney NJ, Gruzalski GR, et al. Fabrication and characterization of amorphous lithium electrolyte thin films and rechargeable thin-film batteries. *J Power Sources*. 1993;43(1–3):103-110.
27. Liang X, Wang L, Jiang Y, et al. In-channel and in-plane Li ion diffusions in the superionic conductor $Li_{10}GeP_2S_{12}$ probed by solid-state NMR. *Chem Mater*. 2015;27(16):5503-5510.
28. Mo Y, Ong SP, Ceder G. First principles study of the $Li_{10}GeP_2S_{12}$ lithium super ionic conductor material. *Chem Mater*. 2012;24(1):15-17.
29. Sun Y, Suzuki K, Hara K, et al. Oxygen substitution effects in $Li_{10}GeP_2S_{12}$ solid electrolyte. *J Power Sources*. 2016;324:798-803.
30. Wang S, Wu Y, Ma T, Chen L, Li H, Wu F. Thermal stability between sulfide solid electrolytes and oxide cathode. *ACS Nano*. 2022;16(10):16158-16176.
31. Lee JM, Park YS, Moon J-W, Hwang H. Ionic and electronic conductivities of lithium argyrodite Li_6PS_5Cl electrolytes prepared via wet milling and post-annealing. *Front Chem*. 2021;9:778057.
32. Papakyriakou M, Lu M, Liu Y, et al. Mechanical behavior of inorganic lithium-conducting solid electrolytes. *J Power Sources*. 2021;516:230672.
33. Minkiewicz J, Jones GM, Ghanizadeh S, et al. Large-scale manufacturing of solid-state electrolytes: challenges, progress, and prospects. *Open Ceram*. 2023;16:100497.
34. Zhou L, Assoud A, Zhang Q, Wu X, Nazar LF. New family of argyrodite thioantimonate lithium superionic conductors. *J Am Chem Soc*. 2019;141(48):19002-19013.
35. Reddy MV, Julien CM, Mauger A, Zaghib K. Sulfide and oxide inorganic solid electrolytes for all-solid-state Li batteries: a review. *Nanomaterials (Basel)*. 2020;10(8):1606.

36. Chen S, Xie D, Liu G, et al. Sulfide solid electrolytes for all-solid-state lithium batteries: structure, conductivity, stability and application. *Energy Storage Mater*. 2018;14:58-74.
37. Wu J, Liu S, Han F, Yao X, Wang C. Lithium/sulfide all-solid-state batteries using sulfide electrolytes. *Adv Mater*. 2021;33(6):e2000751.
38. Wang Q, Zhou Y, Wang X, et al. Designing lithium halide solid electrolytes. *Nat Commun*. 2024;15(1):1050.
39. Karabelli D, Birke KP, Weeber M. A performance and cost overview of selected solid-state electrolytes: race between polymer electrolytes and inorganic sulfide electrolytes. *Batteries*. 2021;7(1):18.
40. Dirican M, Yan C, Zhu P, Zhang X. Composite solid electrolytes for all-solid-state lithium batteries. *Mater Sci Eng R Rep*. 2019;136:27-46.
41. Fong R, Sacken U v, Dahn JR. Studies of lithium intercalation into carbons using nonaqueous electrochemical cells. *J Electrochem Soc*. 1990;137(7):2009-2013.
42. Chen X, Xie J, Zhao X, Zhu T. Electrochemical compatibility of solid-state electrolytes with cathodes and anodes for all-solid-state lithium batteries: a review. *Adv Energy Sustain Res*. 2021;2(5):2000101.
43. Bates AM, Preger Y, Torres-Castro L, Harrison KL, Harris SJ, Hewson J. Are solid-state batteries safer than lithium-ion batteries? *Joule*. 2022;6(4):742-755.
44. Li S, Zhang S-Q, Shen L, et al. Progress and perspective of ceramic/polymer composite solid electrolytes for lithium batteries. *Adv Sci (Weinh)*. 2020;7(5):1903088.
45. Kim T, Kim K, Lee S, Song G, Jung MS, Lee KT. Thermal runaway behavior of Li_6PS_5Cl solid electrolytes for $LiNi_{0.8}Co_{0.1}Mn_{0.1}O_2$ and $LiFePO_4$ in all-solid-state batteries. *Chem Mater*. 2022;34(20):9159-9171.
46. Liao Y, Xu X, Luo X, et al. Recent progress in flame-retardant polymer electrolytes for solid-state lithium metal batteries. *Batteries*. 2023;9(9):439.
47. Han L, Liao C, Mu X, et al. Flame-retardant ADP/PEO solid polymer electrolyte for dendrite-free and long-life lithium battery by generating Al, P-rich SEI layer. *Nano Lett*. 2021;21(10):4447-4453.
48. Xia Y, Fujieda T, Tatsumi K, Prosini PP, Sakai T. Thermal and electrochemical stability of cathode materials in solid polymer electrolyte. *J Power Sources*. 2001;92(1–2):234-243.
49. Zhao S, Zhu X, Jiang W, et al. Fundamental air stability in solid-state electrolytes: principles and solutions. *Mater Chem Front*. 2021;5(20):7452-7466.
50. Scharmann T, Özcelikman C, Nguyen DM, et al. Quantification of hydrogen sulfide development during the production of all-solid-state batteries with argyrodite sulfide-based separators. *ACS Appl Energy Mater*. 2024;7(3):1261-1269.
51. Lee J, Lee T, Char K, Kim KJ, Choi JW. Issues and advances in scaling up sulfide-based all-solid-state batteries. *Acc Chem Res*. 2021;54(17):3390-3402.
52. Wu J, Yuan L, Zhang W, Li Z, Xie X, Huang Y. Reducing the thickness of solid-state electrolyte membranes for high-energy lithium batteries. *Energy Environ Sci*. 2021;14(1):12-36.
53. Schnell J, Tietz F, Singer C, Hofer A, Billot N, Reinhart G. Prospects of production technologies and manufacturing costs of oxide-based all-solid-state lithium batteries. *Energy Environ Sci*. 2019;12(6):1818-1833.
54. Balaish M, Gonzalez-Rosillo JC, Kim KJ, Zhu Y, Hood ZD, Rupp JLM. Processing thin but robust electrolytes for solid-state batteries. *Nat Energy*. 2021;6(3):227-239.
55. Gamo H, Nagai A, Matsuda A. Toward scalable liquid-phase synthesis of sulfide solid electrolytes for all-solid-state batteries. *Batteries*. 2023;9(7):355.
56. Chen A, Qu C, Shi Y, Shi F. Manufacturing strategies for solid electrolyte in batteries. *Front Energy Res*. 2020;8:571440.
57. Sakuu's Dry Printed and UN38.3 *Certified Li-Metal Batteries*. Sakuu; 2024. Accessed July 23, 2024. https://www.sakuu.com/news/sakuus-dry-printed-li-metal-batteries-hit-major-mi
58. Bi Z, Mu S, Zhao N, Sun W, Huang W, Guo X. Cathode supported solid lithium batteries enabling high energy density and stable cyclability. *Energy Storage Mater*. 2021;35:512-519.
59. Hartmann P, Leichtweiss T, Busche MR, et al. Degradation of NASICON-type materials in contact with lithium metal: formation of mixed conducting interphases (MCI) on solid electrolytes. *J Phys Chem C*. 2013;117(41):21064-21074.
60. Kun R, Langer F, Delle Piane M, et al. Structural and computational assessment of the influence of wet-chemical post-processing of the Al-substituted cubic $Li_7La_3Zr_2O_{12}$. *ACS Appl Mater Interfaces*. 2018;10(43):37188-37197.
61. Luo W, Gong Y, Zhu Y, et al. Reducing interfacial resistance between garnet-structured solid-state electrolyte and Li-metal anode by a germanium layer. *Adv Mater*. 2017;29(22):1606042.
62. Chen L, Li Y, Li S-P, Fan L-Z, Nan C-W, Goodenough JB. PEO/garnet composite electrolytes for solid-state lithium batteries: from "ceramic-in-polymer" to "polymer-in-ceramic". *Nano Energy*. 2018;46:176-184.
63. Guan D, Huang Y, He M, et al. Multilayer PEO/LLZTO composite electrolyte enables high-performance solid-state Li-ion batteries. *Ionics*. 2021;27(10):4127-4134.
64. Zhang J, Zhao N, Zhang M, et al. Flexible and ion-conducting membrane electrolytes for solid-state lithium batteries: dispersion of garnet nanoparticles in insulating polyethylene oxide. *Nano Energy*. 2016;28:447-454.
65. Zhuang H, Ma W, Xie J, et al. Solvent-free synthesis of PEO/garnet composite electrolyte for high-safety all-solid-state lithium batteries. *J Alloys Compd*. 2021;860:157915.
66. Tong R-A, Chen L, Shao G, Wang H, Wang C-A. An integrated solvent-free modification and composite process of $Li_{6.4}La_3Zr_{1.4}Ta_{0.6}O_{12}$/poly(ethylene oxide) solid electrolytes: enhanced compatibility and cycle performance. *J Power Sources*. 2021;492:229672.
67. Yi J, Zhou D, Liang Y, Liu H, Ni H, Fan L-Z. Enabling high-performance all-solid-state lithium batteries with high ionic conductive sulfide-based composite solid electrolyte and ex-situ artificial SEI film. *J Energy Chem*. 2021;58:17-24.
68. Liu S, Zhou L, Han J, et al. Super long-cycling all-solid-state battery with thin Li_6PS_5Cl-based electrolyte. *Adv Energy Mater*. 2022;12(25):2200660.
69. Zhang X-D, Yue F-S, Liang J-Y, Shi J-L, Li H, Guo Y-G. Structure design of cathode electrodes for solid-state batteries: challenges and progress. *Small Struct*. 2020;1(3):202000042.

70. Cheng T, Merinov BV, Morozov S, Goddard WA. Quantum mechanics reactive dynamics study of solid Li-electrode/Li_6PS_5Cl-electrolyte interface. *ACS Energy Lett*. 2017;2(6):1454-1459.
71. Chen B, Xu C, Wang H, Zhou J. Insights into interfacial stability of Li_6PS_5Cl solid electrolytes with buffer layers. *Curr Appl Phys*. 2019;19(2):149-154.
72. Ratsoma MS, Makgopa K, Modibane KD, Raju K. Prospective cathode materials for all-solid-state batteries. In: Palaniyandy N, Abhilash KP, Nalini B, eds. *Solid State Batteries*. Springer International Publishing; 2022:83-125.
73. Zeng Z, Cheng J, Li Y, et al. Composite cathode for all-solid-state lithium batteries: progress and perspective. *Mater Today Phys*. 2023;32:101009.
74. Li Y, Zhang D, Xu X, et al. Interface engineering for composite cathodes in sulfide-based all-solid-state lithium batteries. *J Energy Chem*. 2021;60:32-60.
75. Minnmann P, Quillman L, Burkhardt S, Richter FH, Janek J. Editors' choice—quantifying the impact of charge transport bottlenecks in composite cathodes of all-solid-state batteries. *J Electrochem Soc*. 2021;168(4):40537.
76. Li L, Duan H, Li J, Zhang L, Deng Y, Chen G. Toward high performance all-solid-state lithium batteries with high-voltage cathode materials: design strategies for solid electrolytes, cathode interfaces, and composite electrodes. *Adv Energy Mater*. 2021;11(28):202003154.
77. Kravchyk KV, Okur F, Kovalenko MV. Break-even analysis of all-solid-state batteries with Li-garnet solid electrolytes. *ACS Energy Lett*. 2021;6(6):2202-2207.
78. Huang C, Leung CLA, Leung P, Grant PS. A solid-state battery cathode with a polymer composite electrolyte and low tortuosity microstructure by directional freezing and polymerization. *Adv Energy Mater*. 2021;11(1):202002387.
79. Zhang Z, Chen S, Yao X, et al. Enabling high-areal-capacity all-solid-state lithium-metal batteries by tri-layer electrolyte architectures. *Energy Storage Mater*. 2020;24:714-718.
80. Zhang G, Deng B, Liu Q, et al. Enhanced areal specific capacity and energy density of solid-state lithium battery by using porous aluminum foam. *J Energy Storage*. 2021;33:102167.
81. Chen R-J, Zhang Y-B, Liu T, et al. All-solid-state lithium battery with high capacity enabled by a new way of composite cathode design. *Solid State Ion*. 2017;310:44-49.
82. Wang L, Mukherjee A, Kuo C-Y, et al. High-energy all-solid-state lithium batteries enabled by Co-free $LiNiO_2$ cathodes with robust outside-in structures. *Nat Nanotechnol*. 2024;19(2):208-218.
83. Yang M, Wu Y, Yang K, et al. High-areal-capacity and long-cycle-life all-solid-state lithium-metal battery by mixed-conduction interface layer. *Adv Energy Mater*. 2024;14(15):2303229.
84. Liang Z, Xiao Y, Wang K, et al. Enabling stable and high areal capacity solid state battery with Ni-rich cathode via failure mechanism study. *Energy Storage Mater*. 2023;63:102987.
85. Doerrer C, Capone I, Narayanan S, et al. High energy density single-crystal NMC/Li_6PS_5Cl cathodes for all-solid-state lithium-metal batteries. *ACS Appl Mater Interfaces*. 2021;13(31):37809-37815.
86. Kitsche D, Tang Y, Ma Y, et al. High performance all-solid-state batteries with a Ni-rich NCM cathode coated by atomic layer deposition and lithium thiophosphate solid electrolyte. *ACS Appl Energy Mater*. 2021;4(7):7338-7345.
87. Kwon TY, Kim KT, Oh DY, Song YB, Jun S, Jung YS. Three-dimensional networking binders prepared in situ during wet-slurry process for all-solid-state batteries operating under low external pressure. *Energy Storage Mater*. 2022;49:219-226.
88. Ma T, Wang Z, Wu D, et al. High-areal-capacity and long-cycle-life all-solid-state battery enabled by freeze drying technology. *Energy Environ Sci*. 2023;16(5):2142-2152.
89. Zhou L, Zuo T-T, Kwok CY, et al. High areal capacity, long cycle life 4 V ceramic all-solid-state Li-ion batteries enabled by chloride solid electrolytes. *Nat Energy*. 2022;7(1):83-93.
90. Wang C, Liang J, Jiang M, et al. Interface-assisted in-situ growth of halide electrolytes eliminating interfacial challenges of all-inorganic solid-state batteries. *Nano Energy*. 2020;76:105015.
91. Gao X, Liu B, Hu B, et al. Solid-state lithium battery cathodes operating at low pressures. *Joule*. 2022;6(3):636-646.
92. Kim SY, Cha H, Kostecki R, Chen G. Composite cathode design for high-energy all-solid-state lithium batteries with long cycle life. *ACS Energy Lett*. 2023;8(1):521-528.
93. Wang C, Liang J, Zhao Y, Zheng M, Li X, Sun X. All-solid-state lithium batteries enabled by sulfide electrolytes: from fundamental research to practical engineering design. *Energy Environ Sci*. 2021;14(5):2577-2619.
94. Wu J, Shen L, Zhang Z, et al. All-solid-state lithium batteries with sulfide electrolytes and oxide cathodes. *Electrochem Energ Rev*. 2021;4(1):101-135.
95. Machín A, Morant C, Márquez F. Advancements and challenges in solid-state battery technology: an in-depth review of solid electrolytes and anode innovations. *Batteries*. 2024;10(1):29.
96. Kim S, Oguchi H, Toyama N, et al. A complex hydride lithium superionic conductor for high-energy-density all-solid-state lithium metal batteries. *Nat Commun*. 2019;10(1):1081.
97. Liu B, Zhang J-G, Xu W. Advancing lithium metal batteries. *Joule*. 2018;2(5):833-845.
98. Fuchs T, Haslam CG, Moy AC, et al. Increasing the pressure-free stripping capacity of the lithium metal anode in solid-state-batteries by carbon nanotubes. *Adv Energy Mater*. 2022;12(26):2201125.
99. Liu C, Sun J, Zheng P, et al. Recent advances of non-lithium metal anode materials for solid-state lithium-ion batteries. *J Mater Chem A*. 2022;10(32):16761-16778.
100. Cangaz S, Hippauf F, Reuter FS, et al. Enabling high-energy solid-state batteries with stable anode interphase by the use of columnar silicon anodes. *Adv Energy Mater*. 2020;10(34):2001320.
101. Deysher G, Ridley P, Ham S-Y, et al. Transport and mechanical aspects of all-solid-state lithium batteries. *Mater Today Phys*. 2022;24:100679.
102. Doux J-M, Nguyen H, Tan DHS, et al. Stack pressure considerations for room-temperature all-solid-state lithium metal batteries. *Adv Energy Mater*. 2020;10(1):1903253.
103. Krauskopf T, Richter FH, Zeier WG, Janek J. Physicochemical concepts of the lithium metal anode in solid-state batteries. *Chem Rev*. 2020;120(15):7745-7794.

104. Zhang Y, Zuo T-T, Popovic J, et al. Towards better Li metal anodes: challenges and strategies. *Mater Today*. 2020;33:56-74.
105. Cui Y, Wan J, Ye Y, Liu K, Chou L-Y. A fireproof, lightweight, polymer–polymer solid-state electrolyte for safe lithium batteries. *Nano Lett*. 2020;20(3):1686-1692.
106. Wang Y-H, Yue J, Wang W-P, et al. Constructing a stable interface between the sulfide electrolyte and the Li metal anode via a Li^+-conductive gel polymer interlayer. *Mater Chem Front*. 2021;5(14):5328-5335.
107. Li H, Li Y, Zhang L. Designing principles of advanced sulfur cathodes toward practical lithium-sulfur batteries. *SusMat*. 2022;2(1):34-64.
108. Li M, Lu J, Chen Z, Amine K. 30 years of lithium-ion batteries. *Adv Mater*. 2018;30(33):e1800561.
109. Shen L, Zhao C, Weng W, et al. In situ-formed LiF-rich multifunctional interfaces toward stable $Li_{10}GeP_2S_{12}$-based all-solid-state lithium batteries. *Adv Mater Inter*. 2022;9(24):2200822.
110. Zhang Q, Cao D, Ma Y, Natan A, Aurora P, Zhu H. Sulfide-based solid-state electrolytes: synthesis, stability, and potential for all-solid-state batteries. *Adv Mater*. 2019;31(44):e1901131.
111. Huang W-Z, Zhao C-Z, Wu P, et al. Anode-free solid-state lithium batteries: a review. *Adv Energy Mater*. 2022;12(26):2201044.
112. Zhang N, Guo D, Su Q, et al. Lithium fluoride embedded Prelithiated graphite Interface layer enables stable all-solid-state lithium ion batteries. *Batteries Supercaps*. 2024;7(4):e202300488.
113. Zhang C. Review-recent development on silicon-based anodes for high-performance lithium-ion batteries. *E3S Web Conf*. 2021;252:3004.
114. Kong X, Xi Z, Wang L, et al. Recent progress in silicon-based materials for performance-enhanced lithium-ion batteries. *Molecules*. 2023;28(5):2079.
115. Nanda S, Gupta A, Manthiram A. Anode-free full cells: a pathway to high-energy density lithium-metal batteries. *Adv Energy Mater*. 2021;11(2):202000804.
116. Heubner C, Maletti S, Auer H, et al. From lithium-metal toward anode-free solid-state batteries: current developments, issues, and challenges. *Adv Funct Mater*. 2021;31(51):202106608.
117. Duffner F, Mauler L, Wentker M, Leker J, Winter M. Large-scale automotive battery cell manufacturing: analyzing strategic and operational effects on manufacturing costs. *Int J Prod Econ*. 2021;232:107982.
118. Jiang Y, Lai A, Ma J, et al. Fundamentals of the cathode–electrolyte interface in all-solid-state lithium batteries. *ChemSusChem*. 2023;16(9):e202202156.
119. Lou S, Zhang F, Fu C, et al. Interface issues and challenges in all-solid-state batteries: lithium, sodium, and beyond. *Adv Mater*. 2021;33(6):e2000721.
120. Liu B, Pu SD, Doerrer C, et al. The effect of volume change and stack pressure on solid-state battery cathodes. *SusMat*. 2023;3(5):721-728.
121. Liang Y, Liu H, Wang G, et al. Challenges, interface engineering, and processing strategies toward practical sulfide-based all-solid-state lithium batteries. *InfoMat*. 2022;4(5):e12292.
122. Chen C, Jiang M, Zhou T, et al. Interface aspects in all-solid-state Li-based batteries reviewed. *Adv Energy Mater*. 2021;11(13):202003939.
123. Su S, Ma J, Zhao L, et al. Progress and perspective of the cathode/electrolyte interface construction in all-solid-state lithium batteries. *Carbon Energy*. 2021;3(6):866-894.
124. LLZTO. Ion Conductive Ceramic Sheet, 1 pc, (12D × 0.8 mm). MTI Corporation. Accessed June 2024. https://www.mtixtl.com/eq-llzto-rd.aspx
125. Ampcera®. *Argyrodite Li6PS5Cl Sulfide Solid Electrolyte*. MSE Supplies. Accessed June 2024. https://www.mscsupplies.com/cn-dc/products/ampcera-sulfide-solid-electrolyte-argyrodite-li6ps5cl-powder?variant=22924472614970
126. Arblaster JW. *Selected Values of the Crystallographic Properties of Elements*. ASM International; 2018.
127. Nitta N, Wu F, Lee JT, Yushin G. Li-ion battery materials: present and future. *Mater Today*. 2015;18(5):252-264.
128. Staats N. Nio Becomes The First EV Maker To Bring Semi Solid-state Batteries To The Mass Market. *TopSpeed*; 2023. Accessed May 14, 2024. https://www.topspeed.com/nio-first-evmaker-to-bring-solid-state-batteries/
129. Li S, Yang Z, Wang S-B, et al. Sulfide-based composite solid electrolyte films for all-solid-state batteries. *Commun Mater*. 2024;5(1):44.
130. Liu G, Shi J, Zhu M, et al. Ultra-thin free-standing sulfide solid electrolyte film for cell-level high energy density all-solid-state lithium batteries. *Energy Storage Mater*. 2021;38:249-254.
131. Luo S, Wang Z, Fan A, et al. A high energy and power all-solid-state lithium battery enabled by modified sulfide electrolyte film. *J Power Sources*. 2021;485:229325.
132. IEA. Evolution of average range of electric vehicles by powertrain, 2010–2021. *Charts—Data & Statistics*. IEA; 2024. Accessed July 15, 2024. https://www.iea.org/data-and-statistics/charts/evolution-of-average-range-of-electric-vehicles-by-powertrain-2010-2021
133. Schnell J, Knörzer H, Imbsweiler AJ, Reinhart G. Solid versus liquid—a bottom-up calculation model to analyze the manufacturing cost of future high-energy batteries. *Energy Tech*. 2020;8(3):201901237.
134. Global Nissan Newsroom. *Nissan Unveils Prototype Production Facility For All-Solid-State Batteries*; 2024. Accessed July 15, 2024. https://global.nissannews.com/en/releases/nissan-prototype-production-facility-for-all-solid-state-batteries
135. Singer C, Schnell J, Reinhart G. Scalable processing routes for the production of all-solid-state batteries—modeling interdependencies of product and process. *Energy Tech*. 2021;9(1):202000665.
136. Zhang N, Beutl A, Rajinovic K, Kahr J, Jahn M, Nestoridi M. Scalable preparation of practical 1Ah all-solid-state lithium-ion batteries cells and their abuse tests. *J Energy Storage*. 2023;59:106547.

AUTHOR BIOGRAPHIES



Rainer Götz obtained his MSc under the supervision of Prof. A. S. Bandarenka and is currently pursuing his PhD in the same group. With a focus on interfaces within solid-state lithium-metal batteries, Rainer is investigating ways of overcoming typical interfacial hurdles at solid/solid contacts in order to look more closely at fundamental processes. In particular, special attention is directed toward the formation of space-charge layers at those contacts, including determining how much of an impact they have under close-to-operating conditions.



Raphael Streng received his MSc in Applied and Engineering Physics from the Technical University of Munich (TUM) in 2022 and has been a PhD candidate in the Energy Conversion and Storage group at TUM. Raphael's research focuses on Li-free aqueous batteries, paying special attention to electrolyte effects on various active materials and the development of sustainable battery systems for large-scale energy storage.



Johannes Sterzinger earned his MSc in Applied & Engineering Physics at the Technical University of Munich (TUM) in 2023 and currently holds a PhD position at TUM working on optimizing functional materials for a sustainable future. As a member of the Energy Conversion & Storage group at TUM and the European ICONIC project, his research focuses on discovering innovative energy & catalyst materials at the nanoscale that contribute to a more resource-efficient, eco-friendly, and green economy.

How to cite this article: Götz R, Streng R, Sterzinger J, et al. All-solid-state Li-ion batteries with commercially available electrolytes: A feasibility review. *InfoMat*. 2024;6(12):e12627. doi:10.1002/inf2.12627

3. A Fast and Highly Stable Aqueous Calcium-Ion Battery for Sustainable Energy Storage.

R.L. Streng, S. Reiser, S. Wager, N. Pommer, A.S. Bandarenka. *ChemSusChem* **2025**, 18, e202401469

ChemSusChem | Research Article
doi.org/10.1002/cssc.202401469
Chemistry Europe
European Chemical Societies Publishing

www.chemsuschem.org

A Fast and Highly Stable Aqueous Calcium-Ion Battery for Sustainable Energy Storage

Raphael L. Streng,[a] Samuel Reiser,[a] Sabrina Wager,[a] Nykola Pommer,[a] and Aliaksandr S. Bandarenka*[a, b]

Aqueous alkali-ion batteries are gaining traction as a low-cost, sustainable alternative to conventional organic lithium-ion batteries. However, the rapid degradation of commonly used electrode materials, such as Prussian Blue Analogs and carbonyl-based organic compounds, continues to challenge the economic viability of these devices. While stability issues can be addressed by employing highly concentrated water-in-salt electrolytes, this approach often requires expensive and, in many cases, fluorinated salts. Here, we show that replacing monovalent K^+ ions with divalent Ca^{2+} ions in the electrolyte significantly enhances the stability of both a copper hexacyanoferrate cathode and a polyimide anode. These findings have direct implications for developing an optimized aqueous Ca-ion battery that demonstrates exceptional fast-charging capabilities and ultra-long cycle life and points toward applying Ca-based batteries for large-scale energy storage.

1. Introduction

Our societies' ever-rising energy demand, combined with the growing awareness of the negative implications of fossil fuel-based energy production, has led to a transition toward renewable energy sources.[1,2] However, the generation vs. consumption discrepancy of, e.g., solar or wind power still poses a significant challenge to energy supply safety and independence. Accordingly, large-scale storage is crucial for the renewable energy transition.[3–5] There is a wide range of storage technologies, among which batteries are considered one of the most efficient and flexible.[6,7] Due to their high energy density, Li-ion batteries (LIBs) dominate the battery market for electric vehicles and portable electronics and are also a popular choice for stationary storage applications.[8] However, the competition for scarce lithium resources and safety concerns related to the organic electrolyte have sparked a renewed interest in alternative systems employing safer and more available materials.[9,10] Aqueous batteries based on highly abundant salts are promising candidates to replace LIB in stationary energy storage and certain public transport applications due to their inherent safety, sustainability, and fast-charging capabilities..[11–13] At the same time, the main drawback of aqueous batteries is the relatively narrow electrochemical stability window, limiting the maximum cell voltage and, thus, the cell's energy density.[14] Therefore, for aqueous batteries to economically challenge LIBs, lowering production costs and improving cycling stability by mitigating degradation effects is paramount.[15] However, most compounds that qualify as anode or cathode active materials suffer from rapid capacity fading.[16–18] As capacity loss is usually linked to active material dissolution in water, most stabilization approaches focus on reducing the amount of free water in the electrolyte by employing so-called water-in-salt electrolytes.[19–22] Herby, the high incorporation ratio of water molecules in the ion hydration shell mitigates hydrolysis of the anode and cathode. While being very successful, this strategy relies on using high amounts of expensive, often fluorinated salts, which contradicts the aim of reducing production costs.[23] Thus, new approaches to improve the cycling stability of aqueous batteries should be investigated. In fact, stabilization measures such as electrolyte additives and protective coatings have been studied extensively.[24–28] Additionally, the effect of the electrolyte anions and alkali cations on electrode materials has been investigated in recent years.[15,29–31] However, as most research focuses on aqueous batteries using either only monovalent ions such as Li^+, Na^+, and K^+ or only divalent ions such as Mg^{2+} and Ca^{2+}, the effect of exchanging monovalent cations for divalent cations is rarely discussed. This is where our research comes in, aiming to fill this gap and provide potential solutions for the challenges of aqueous batteries.

This study investigates a model battery consisting of an organic polyimide anode, a Prussian blue analog (PBA) copper hexacyanoferrate cathode, and an aqueous potassium or calcium chloride electrolyte. This combination is selected due to the promising properties of both electrode materials.[32,33] The effect of the electrolyte cation on each electrode is tested separately before the cycling stability of the aqueous K-ion and the aqueous Ca-ion battery are compared. Finally, the Ca-ion battery's rate capability and energy density are assessed in more detail.

[a] Physics of Energy Conversion and Storage, Physik-Department, Technische Universität München, Garching, Germany
[b] Catalysis Research Center TUM, Garching, Germany
Correspondence: Aliaksandr S. Bandarenka, Physics of Energy Conversion and Storage, Physik-Department, Technische Universität München, James-Franck-Str. 1, 85748 Garching, Germany.
Email: bandarenka@ph.tum.de

Supporting Information for this article is available on the WWW under https://doi.org/10.1002/cssc.202401469

© 2024 The Author(s). ChemSusChem published by Wiley-VCH GmbH. This is an open access article under the terms of the Creative Commons Attribution License, which permits use, distribution and reproduction in any medium, provided the original work is properly cited.

© 2024 The Author(s). ChemSusChem published by Wiley-VCH GmbH

2. Materials and Methods

2.1. Material Synthesis

All chemicals for synthesis were purchased from commercial suppliers and used without further purification.

Poly(naphthalene four formyl ethylenediamine) (PNFE) was synthesized for our previous work and also used for this study without any further processing..[34] In a typical procedure, 10 mmol (2.68 g) of 1,4,5,8-naphthalene tetracarboxylic dianhydride (NTCDA) and 10 mmol (0.6 g) of ethylenediamine (EDA) were dissolved in 20 ml of degassed N-methyl pyrrolidone (NMP) in a Schlenk flask. The mixture was heated to 215 °C in a sand bath and reacted under reflux overnight. The dark precipitate was filtered, washed with NMP and subsequently with water several times. Finally, it was dried under vacuum at 0.08 mbar stepwise at three different temperatures (room temperature, 120 °C, and 210 °C). The product was a grey-brownish powder with a high yield of 92 % (2.7 g).

Elemental analysis of PNFE: Calcd. for an infinite polyimide ($C_{16}H_8N_2O_4$), %: C 65.76, H 2.76, N 9.59; calcd. for an octamer, %: C 65.10, H 3.03, N 10.52; found, %: C 65.13, H 2.91, N 10.32.

Copper hexacyanoferrate (CuHCF) was prepared by coprecipitation according to the method reported by Xu et al.[35] 1 mmol of $CuCl_2 \cdot 2H_2O$ and 1 mmol of $Na_4P_2O_7 \cdot 10\ H_2O$ were dissolved in 20 ml DI water to form solution A. Solution B was prepared by adding 1 mmol of $Na_4Fe(CN)_6 \cdot 10\ H_2O$, 0.3 g of polyvinylpyrrolidone (PVP) and 0.58 g of NaCl into 50 ml DI water. Subsequently, solution A was dropwise added to solution B under vigorous stirring at room temperature. Subsequently, the mixture was left for aging for 5 days before the precipitate was collected by centrifugation and washed 3 times with water and ethanol, respectively. The product was dried overnight at 70 °C.

2.2. Electrode Preparation

PNFE and CuHCF electrodes were prepared using the slurry casting method. For the PNFE slurry 80 wt. % polyimide active material, 10 wt. % carbon black super C-65 (MTI, USA) and 10 wt. % Nafion™ binder (5 wt. % in lower aliphatic alcohols and water, Sigma Aldrich, USA) was mixed and ground in a planetary ball mill. To form the anode slurry, water, and isopropyl alcohol in a 1 : 1 ratio were added as dispersing agents under vigorous stirring.

The CuHCF slurry was prepared using a similar procedure, mixing 80 wt % active material with 10 wt. % carbon black super C-65 and 10 wt. % polyvinylidene fluoride (PVDF, MTI, USA) in a planetary ball mill. NMP was added under vigorous stirring to form the cathode slurry.

Both slurries were cast onto a pyrolytic graphite sheet current collector. The active material mass loading was approximately 4.0 mg cm^{-2} for the CuHCF cathode and 2.0 mg cm^{-2} for the PNFE anode.

2.3. Material Characterization

The morphology of the electrode films was investigated with a field emission scanning electron microscope (SEM, JSM-7500F, JEOL). Fourier-transformed infrared (FTIR, Bruker Vertex-70) spectroscopy was used to characterize the chemical structure of PNFE, and powder x-ray diffraction (XRD) was used to analyze the crystal structure of CuHCF. Thermogravimetric analysis (TGA) was performed under an argon atmosphere using a METTLER TOLEDO TGA/DSC 2 (STARe system). The analysis was conducted over a temperature range of 30 °C to 800 °C, with a heating rate of 10 °C per minute. X-ray photoelectron spectroscopy (XPS) measurements of the PNFE electrode were obtained using a SPECS system, equipped with a non-monochromatized Al Kα source (1486.7 eV), an SPECS XR50 X-ray source, a SPECS PHOIBOS 150 hemispherical analyzer, and an SPECS spectrometer. XPS spectra were analyzed and fitted using Casa XPS software (Version 2.3.24PR1.0), with binding energies adjusted by setting the C–C peak in the C 1s spectrum to 284.8 eV.

2.4. Electrochemical Measurements

Single-electrode measurements were conducted in a three-electrode setup inside a closed glass cell with constant argon flow to ensure and maintain an inert atmosphere. The electrolyte and the glass cell were purged with argon for at least 10 minutes before the electrolyte was run into the cell. A platinum wire (MaTeck, Germany) was used as the counter electrode. The reference electrode was an Ag/AgCl electrode (SSC, 3 M KCl, SI Analytics) connected to the electrolyte via a Luggin capillary. 3 M and saturated KCl and $CaCl_2$ were employed as electrolytes.

Cyclic voltammetry (CV) and galvanostatic cycling with potential limitations (GCPL) were conducted using a BioLogic VSP-300 potentiostat. Cyclic voltammograms (CVs) were recorded at different scan rates ranging from 1 mV s^{-1} to 50 mV s^{-1} at potentials from −1.0 V to 0.0 V and from 0.3 V to 1.1 V (vs. SSC) for anode and cathode, respectively. Galvanostatic (dis−)charging was carried out at C-rates between 1 C and 300 C within the same potential ranges. The cycling stability in different electrolytes was tested by galvanostatically charging and discharging the electrodes for 100 cycles at 10 C (cathode) and 1000 cycles at 100 C (anode).

Potentiostatic electrochemical impedance spectroscopy (PEIS) was carried out at −500 mV vs. SSC for the anode and at 800 mV vs. SSC for the cathode. The potential was held for 10 minutes before recording the spectrum to ensure equilibrium conditions. The AC amplitude was set to 10 mV, and a frequency range from 1.00 MHz to 250 MHz was used. Before fitting the data, the validity was verified by Kramers-Kronig analysis.

© 2024 The Author(s). ChemSusChem published by Wiley-VCH GmbH

2.5. Full-Cell Assembly and Measurements

Due to the corrosive interaction of chlorides with most stainless steel alloys, a 3D-printed plastic cell with pyrolytic graphite foil as contacts was used for the full cell. The aqueous K-ion and Ca-ion batteries were assembled under a nitrogen atmosphere inside a glovebox to avoid dissolved oxygen in the electrolyte. A commercial BS 17–25 separator (Mativ Inc., France) for alkaline batteries soaked in the respective electrolyte was placed between the electrodes. The closed cell was fully sealed by rubber o-rings.

CV and GCPL measurements were also conducted with a Biologic VSP-300 potentiostat for the full cell. CVs were recorded at scan rates from 1 $mV s^{-1}$ to 50 mV^{-1} between cell voltages of 0.6 V, and 1.7 V. GCPL was conducted at C-rates between 300 C and 1 C in the same voltage range.

3. Results and Discussion

Organic electrode materials have attracted increased attention due to their exceptional sustainability, tunability, and compatibility with aqueous electrolytes. Several high-performance materials have been developed in recent years, including conductive polymers, carbonyl compounds, radicals, and organic frameworks.[32,36–39] Among them, polyimides are regarded as one of the most promising anode materials for aqueous batteries and have been used in various aqueous Li-ion, Na-ion, and K-ion batteries.[40,41] PNFE was synthesized in a one-step dehydration condensation reaction between NTCDA and EDA in NMP in our previous work[34] and used as an anode in this study. FTIR, TGA, and XPS analysis confirming the successful synthesis of PNFE is shown in Figure S1 (replotted from[34]). The observed FTIR pattern is in good accordance with the expected structure of PNFE. In particular, the bands at 1626 cm^{-1} and 1580 cm^{-1} can be attributed to stretching vibrations of the C=C bonds in the cyclic alkenes. Furthermore, various vibrations of aromatic and non-aromatic C–N bonds (1348 cm^{-1} to 1094 cm^{-1}) and stretching vibrations of the C–O bonds in the electrochemically active carbonyl groups (1701 cm^{-1} and 1661 cm^{-1}) can be observed. The remaining spectral bands correspond to vibrations of C–H bonds in the polymer. In the XPS survey scan, characteristic peaks for fluorine, oxygen, carbon, and nitrogen can be observed corresponding to the constituents of the Nafion binder and the active material. The fitted C 1s spectrum shows sharp peaks for the contributions from C–C, C–N, C–O, and CF_2 bonds and weaker peaks that can be attributed to C=C, N–C=O, and CF_3 bonds. The structural stability of PNFE upon ball milling was confirmed by a subsequent FTIR measurement (Figure S3). The reduction mechanism of PNFE in the presence of monovalent ions such as K^+ is shown in Figure 1(a). It involves a two-step enolization of two opposite carbonyl groups during which the charge within the aromatic rings is redistributed.[34] The remaining carbonyl groups can generally be reduced as well. However, this reduction requires potentials below the hydrogen evolution reaction (HER) threshold, making it unfeasible in aqueous batteries.

In addition to monovalent ions, polyimides have also been shown to host divalent cations such as Mg^{2+} and Ca^{2+}.[42,43] The associated mechanism is illustrated in Figure 1(b). In this process, carbonyl groups from two neighboring monomers participate in hosting a single divalent cation. Consequently, the total transferred charge is equivalent to that of monovalent ion insertion.

To compare the electrochemical behavior of PNFE in aqueous electrolytes containing either monovalent or divalent ions, CVs were recorded at 10 $mV s^{-1}$ in 3 M KCl and $CaCl_2$ solutions. The resulting voltammograms are shown in Figure 2(a) and (b). In the presence of K-ions, two reduction peaks (−0.65 V, −0.87 V vs. SSC) and two oxidation peaks (−0.23 V, −0.68 V vs. SSC) appear, which is in good accordance with the previously introduced two-step redox mechanism.

In $CaCl_2$, the shape of the CV, as well as the position of the peaks, differs significantly. The reduction peaks overlap at

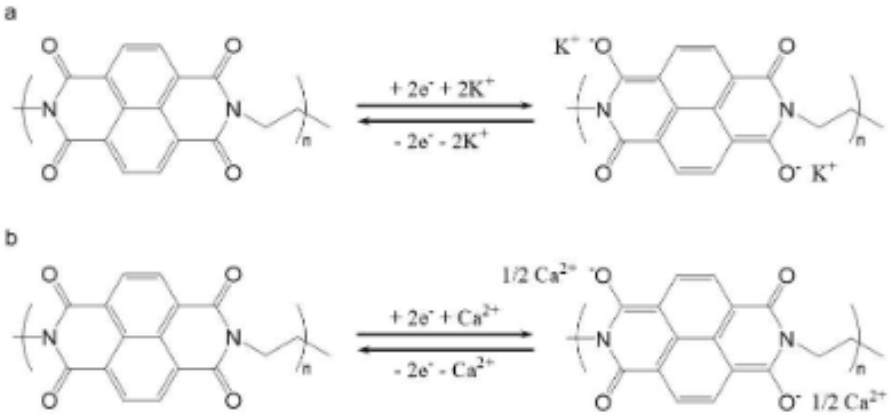


Figure 1. Reduction and oxidation mechanism of PNFE. Redox mechanism of PNFE in the presence of (a) K-ions and (b) Ca-ions.

© 2024 The Author(s). ChemSusChem published by Wiley-VCH GmbH

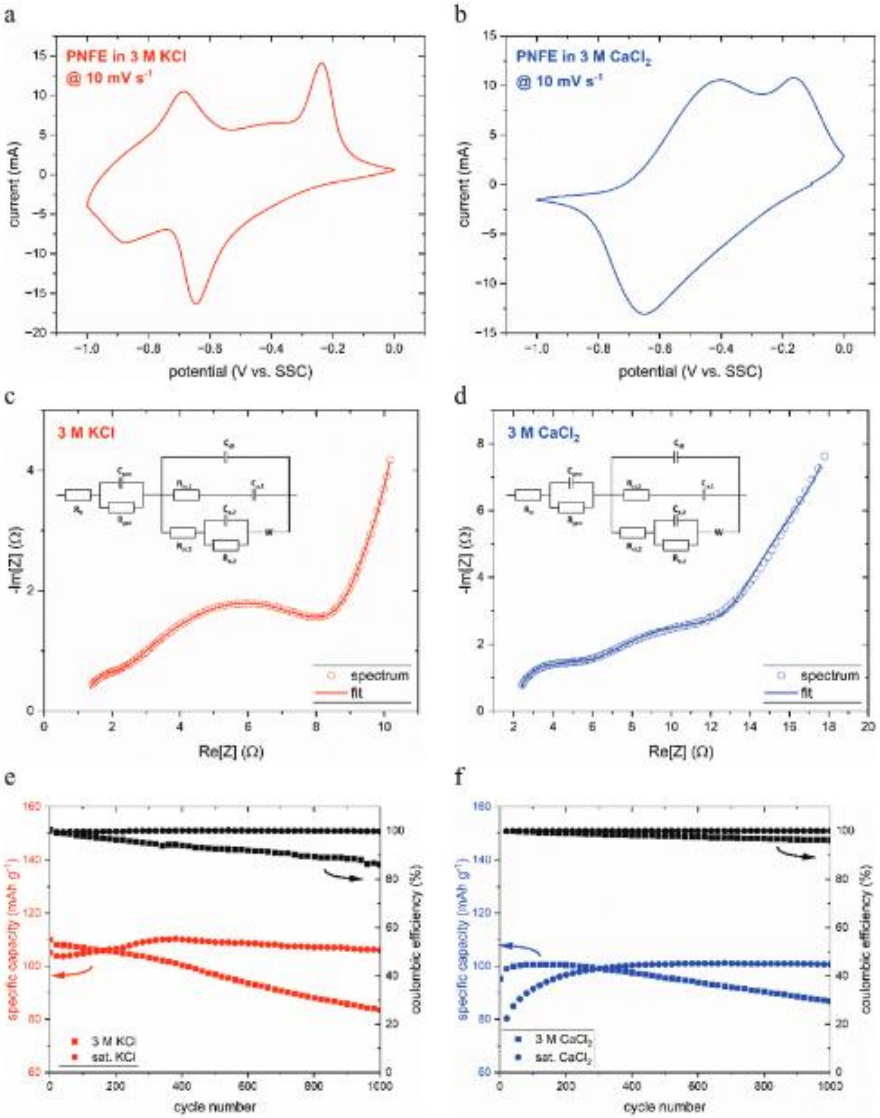


Figure 2. CV and stability measurements of PNFE electrodes in KCl and $CaCl_2$ electrolytes. (a) CV of a PNFE electrode in 3 M KCl at 10 mVs^{-1}. (b) CV of a PNFE electrode in 3 M $CaCl_2$ at 10 mVs^{-1}. (c) Fitted impedance spectrum of a PNFE electrode in 3 M KCl at −500 mV vs. SSC. (d) Fitted impedance spectrum of a PNFE electrode in 3 M $CaCl_2$ at −500 mV vs. SSC. (e) Cycling stability of PNFE in 3 M and saturated KCl recorded over 1000 cycles at 100 C. (f) Cycling stability of PNFE in 3 M and saturated $CaCl_2$.

−0.65 V vs. SSC, and the oxidation peaks are located at −0.40 and −0.15 V vs. SSC, respectively. Thus, PNFE exhibits a slightly higher half-charge potential in the presence of Ca-ions, as the higher charge density of the divalent ion facilitates the enolization process. To further analyze the influence of the cation on the reduction mechanism of PNFE, potentiostatic electrochemical impedance spectroscopy (PEIS) measurements were carried out in both electrolytes at −500 mV vs. SSC. Figures 2(c) and (d) show the fitted impedance spectra of the anode in 3 M KCl and 3 M $CaCl_2$, respectively, as well as the equivalent circuit used to fit the data. This impedance model was demonstrated to accurately describe the charge storage mechanism of PNFE in our previous work and can be used to fit the shown data accurately with a root mean square deviation of

© 2024 The Author(s). ChemSusChem published by Wiley-VCH GmbH

less than 1%.[34] It is derived from the so-called Randles circuit, including the uncompensated electrolyte resistance R_u, the double layer capacity C_{dl}, the charge transfer resistance R_{ct}, and a semi-infinite Warburg element to account for diffusion. The presence of the adsorption capacitance and resistance ($C_{a,2}$ and $R_{a,2}$) in both electrolytes indicates that the electrode material goes through a two-step reduction process regardless of the cation species supporting the reduction mechanism shown in Figure 1. In addition, a secondary single-electron reduction pathway ($R_{ct,1}$ and $C_{a,1}$) can be observed in both cases, corresponding to the reduction of only one carbonyl group per polymer unit with subsequent stabilization of the radical anion due to polymer-polymer interactions. However, in 3 M KCl and 3 M $CaCl_2$, $R_{ct,1}$ is ~15 times and ~10 times higher than $R_{ct,2}$, respectively, indicating that this pathway is significantly suppressed compared to the main two-step reduction. The parameters C_{geo} and R_{geo} account for the contribution of the film on the graphite sheet. For a more detailed discussion of the impedance model, the reader is referred to our previous work.[34] Based on the PEIS analysis, two reduction steps are detected in both electrolytes. Thus, although only one cathodic peak can be observed in the CV in the $CaCl_2$ electrolyte, it actually represents the merging of the two peaks observed in the KCl electrolyte. The overlap of the potentials of the two reduction steps can be explained by the interplay between multiple monomers involved in hosting a single Ca-ion. As multiple neighboring polymer units take part in the insertion of divalent ions, the two reduction steps can no longer be distinguished as two clearly separated peaks. The two naphthalene diimide groups participating in the adsorption of a single Ca^{2+} cation may be in different oxidation states, causing the peaks to merge. When a Ca-ion is attracted by a reduced carbonyl group, its electron-attracting nature will facilitate the reduction of adjacent carbonyl groups. Therefore, the reduction of the different polymer units becomes more conjugated, affecting the CV shape. In addition, repulsive interactions between the redox centers lead to further peak broadening. These findings demonstrate that the electrochemical behavior of PNFE can be tailored by using different cations affecting electrode potential and reversibility.

Furthermore, the influence of the electrolyte composition on the cycling stability of PNFE was investigated by repeatedly charging and discharging the electrode for 1000 cycles in both electrolytes. A high cycling rate of 100 C (36 s per (dis–)charge cycle) was chosen as PNFE exhibits an exceptionally high capacity retention of ~70% at this rate. Figures 2(e) and (f) show the specific discharge capacity of the anode in KCl and $CaCl_2$, respectively. In 3 M KCl, the initial discharge capacity is ~110 mAh g^{-1} but decays significantly, with only ~75% of the capacity remaining after 1000 cycles.

Due to the stronger interaction and, therefore, slower diffusion of Ca-ions, the initial capacity at 100 C is slightly lower in 3 M $CaCl_2$. However, the capacity retention is improved (~87% after 100 cycles), which can be attributed to the higher concentration of water-binding anions and the stronger interaction between the divalent Ca-ions and the water dipoles. Harmful interactions with the anode become less likely as the water molecules are more strongly bound to the cations.

As mentioned previously, electrode degradation is commonly associated with active material dissolution into the aqueous electrolyte. It can be mitigated by increasing the salt concentration and limiting the amount of free water. Therefore, the cycling stability was also evaluated in saturated KCl (4.7 mol kg^{-1}) and saturated $CaCl_2$ (6.7 mol kg^{-1}). PNFE exhibits exceptional cycling stability in both solutions without significant degradation after 100 cycles. In $CaCl_2$, a precycling phase with increasing capacity can be observed, which is most likely linked to slow electrolyte penetration into the pores of the slurry due to the higher viscosity of the saturated solution. It becomes clear that whereas sufficient capacity retention in PNFE anodes can be achieved in a saturated KCl electrolyte, replacing K^+ with Ca^{2+} generally impedes degradation effects. In addition to the reasons listed above, electrolyte viscosity can play a role, as the transport of dissolution products away from the electrode-electrolyte interface is needed for further dissolution.

Figure 3 shows the rate performance of PNFE in saturated $CaCl_2$. Galvanostatic cycling was carried out at C-rates ranging from 1 C to high rates of up to 300 C.

At 1 C, a maximum discharge capacity of ca 150 mAh g^{-1} with a Coulombic efficiency of ~90% can be observed. Slight losses can be explained by the parasitic HER, which is more pronounced in the large electrolyte volume of the three-electrode setup than in real-life cells that only contain minimal amounts of water. As a pyrolytic graphite sheet is used as the current collector, it should be noted that graphite can store Ca-ions with considerable capacities in non-aqueous electrolytes. However, at 0.5–1.0 V vs. Ca^{2+}/Ca the potential for calcium intercalation into graphite is far below the potentials used in the measurements above.[44] Accordingly, preliminary CV measurements of the current collector in the aqueous $CaCl_2$ electrolytes showed no capacity contributions.

At increasing C-rates, the capacity retention remains high, with a discharge capacity of 135 mAh g^{-1} at 10 C and over 100 mAh g^{-1} at 100 C. This agrees with previous studies showing that PNFE exhibits pseudocapacitive behavior with low diffusion limitations.[34,43] Even in the more viscous saturated $CaCl_2$ electrolyte, the anode demonstrates exceptional fast charging capability, allowing supercapacitor-like applications.

CuHCF, which was selected as a suitable cathode material for the aqueous battery studied in this work, was synthesized by a modified coprecipitation, as reported by Xu et al.[35] They found that the addition of the chelating agents $Na_4P_2O_7$ and PVP during the coprecipitation improved the crystallinity of the CuHCF particles. Furthermore, they observed a change in crystal structure from cubic to monoclinic when the precipitation occurs in the presence of concentrated NaCl. Highly crystalline nanosheets are formed in this configuration, as shown in the SEM pictures in Figure S2 (b) and (c). The successful synthesis of CuHCF nanosheets was further confirmed by powder XRD (Figure S2a). To assess the stability of CuHCF upon ball milling, the XRD spectrum was again recorded after this processing step (Figure S3).

© 2024 The Author(s). ChemSusChem published by Wiley-VCH GmbH

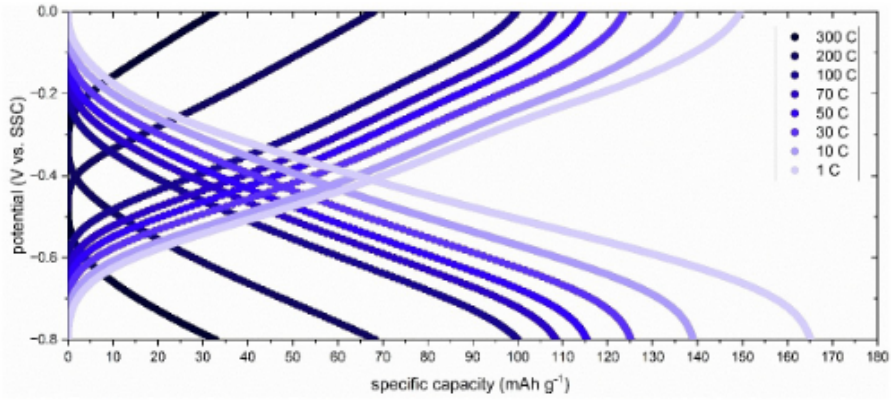


Figure 3. Rate performance of PNFE in saturated $CaCl_2$. Galvanostatic (dis−) charge curves of a PNFE electrode measured at C-rates ranging from 300 C (12 s) to 1 C (1 h) in a saturated $CaCl_2$ aqueous electrolyte.

The electrochemical behavior of CuHCF was investigated in 3 M KCl and 3 M $CaCl_2$, similar to the previous investigations on the PNFE anode. Figure 4(a) and (b) show the CVs of the cathode recorded at a scan rate of 10 mV s^{-1}. K-ions' intercalation manifests itself by a reduction peak located at 0.74 V vs. SSC, with the corresponding oxidation peak at 0.80 V vs. SSC. In the $CaCl_2$ electrolyte, the peaks are shifted towards lower potentials at ca 0.61 V and ca 0.68 V vs. SSC, respectively. In 2018, Bors et al. reported a distinct relationship between the hydration energy of alkali metal ions and the intercalation potential of various PBAs. Generally, more negative hydration energy (e.g., Li^+: −520 kJ mol^{-1}) leads to lower redox potentials if compared to more positive hydration energy (e.g., Cs^+: −276 kJ mol^{-1}). However, to our knowledge, no studies have reported a similar relation, including both monovalent and divalent cations. While the hydration energy of Ca^{2+} at −1577 kJ mol^{-1} is indeed lower than that of K^+ at −322 kJ mol^{-1}, the potential difference is relatively low, considering the large hydration energy gap.

The charge transfer mechanism of the cathode in both electrolytes was further investigated by impedance spectroscopy. To account for the redox potential shift depending on the intercalating species, the potential was set to 800 mV vs. SSC for KCl and 700 mV vs. SSC for $CaCl_2$. Figures 4(c) and (d) show the fitted spectra and the used equivalent circuit. The model cation intercalation into PBAs in aqueous media was adapted from Yun et al. and represents a three-step mechanism, including an electroactive step, a specific adsorption step, and a non-electroactive step.[45] The electroactive step of the intercalation into PBAs corresponds to the fast-proceeding oxidation of Fe^{II}. Subsequently, anions specifically adsorb on the electrode surface to compensate for the temporary excess positive charge due to slow cation de-intercalation. In the last step, the cations and anions leave the surface. In the case of thicker slurry electrodes, the model is expanded by a semi-infinite Warburg element to account for solid-state and pore diffusion. In the 3 M $CaCl_2$ electrolyte, the charge transfer resistance (R_{ct}) and the resistances representing the adsorption ($R_{a,1}$) and the non-electroactive step ($R_{a,2}$) are about 50% higher than in the 3 M KCl solution, whereas the Warburg coefficient is not influenced by the cation species. In both cases, the resistances are in the range of 0.5–2.0 Ω, and the Warburg coefficients lie at 4.5 Ω s$^{-1/2}$ (KCl) and 4.3 Ω s$^{-1/2}$ ($CaCl_2$) for an electrode with a surface area of 0.5 cm^2 and a mass loading of 3.9 mg cm^2. Generally, the diffusion of multivalent ions such as Mg^{2+} or Al^{3+} is significantly more sluggish than for monovalent ions due to their high charge density and, therefore, strong interaction with the host lattice. However, the relatively large ionic radius and lower charge density of Ca-ions likely facilitate ion diffusion leading to a similar diffusion coefficient as for K-ions.[42] However, the deintercalation and desorption are more strongly impeded in the case of Ca^{2+}, which is likely due to the temporary and locally higher charge density at the electrode surface during the oxidation process in the presence of multivalent ions. Thus, although the voltage polarization in the presence of K-ions is expected to be slightly lower, the rate capability is generally high for both systems. Particularly at high currents, where diffusion becomes a main limiting factor, the performance will not be as strongly affected by the cation species.

To evaluate the cation effect on the stability of CuHCF, the electrode was cycled at 10 C for 100 cycles in KCl and $CaCl_2$ electrolytes. Due to the more diffusion-limited processes in CuHCF compared to PNFE, a lower (dis−)charging rate was chosen. Figures 4(e) and (f) show the resulting specific capacity per cycle. Both in 3 M and saturated KCl, the cathode degrades rapidly, with only ~40% of the initial capacity remaining after 100 cycles. This strong capacity degradation can be explained by several mechanisms that have been proposed in previous studies. Generally, lattice defects caused by $Fe(CN)_6$ vacancies generated during material synthesis have been shown to result in structural instability and capacity fading.[33,46,47] Additionally, multiple groups have investigated the detrimental effect of interstitial water on PBA performance and cycling stability. For example, Song et al. and Kim et al. have reported significant

© 2024 The Author(s). ChemSusChem published by Wiley-VCH GmbH

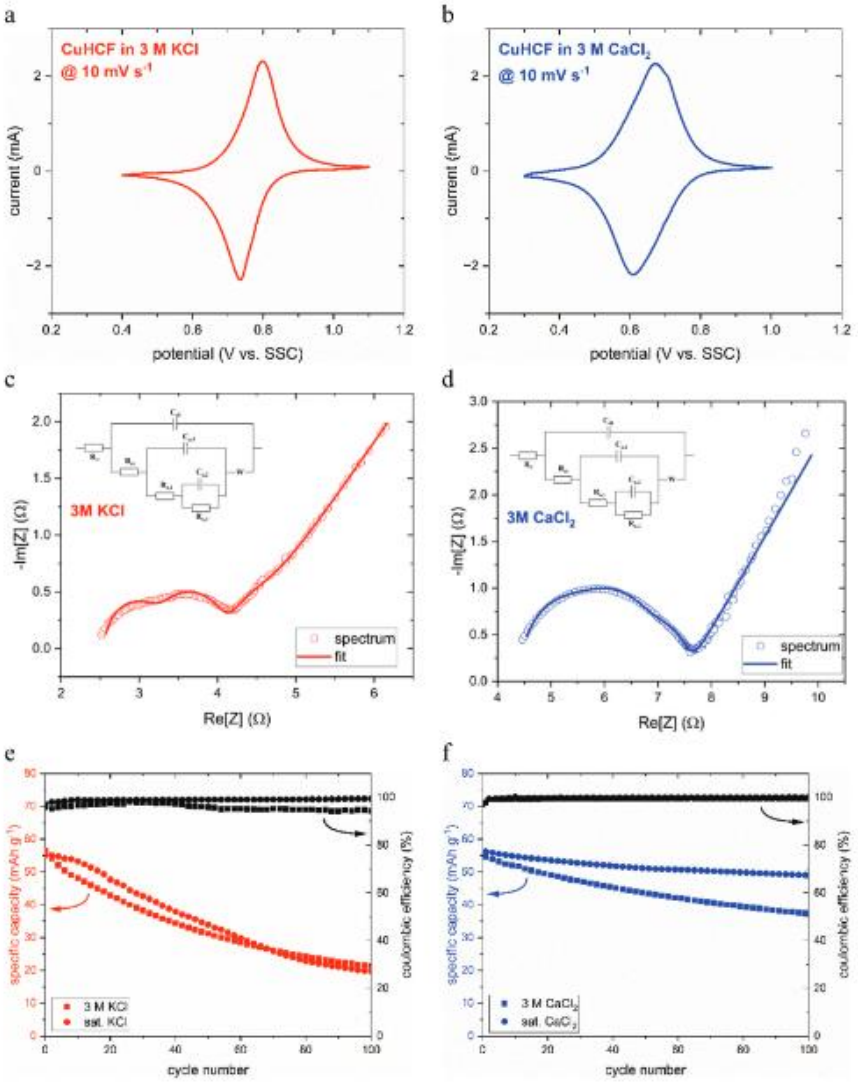


Figure 4. CV and stability measurements of CuHCF electrodes in KCl and $CaCl_2$ electrolytes. (a) CV of a CuHCF electrode in 3 M KCl at 10 mV s^{-1}. (b) CV of a CuHCF electrode in 3 M $CaCl_2$ at 10 mV s^{-1}. (c) Fitted impedance spectrum of a CuHCF electrode in 3 M KCl at 800 mV vs. SSC. (d) Fitted impedance spectrum of a CuHCF electrode in 3 M $CaCl_2$ at 700 mV vs. SSC. (e) Cycling stability of CuHCF in 3 M and saturated KCl recorded over 1000 cycles at 100 C. (f) Cycling stability of CuHCF in 3 M and saturated $CaCl_2$.

stability improvements induced by the removal of interstitial water during material synthesis for MnHCF and CuHCF, respectively.[48,49] PBAs are also known to degrade rapidly under alkaline conditions and suffer from capacity decay due to the attack on Fe-sites by OH^-.[50–52]

In 3 M $CaCl_2$, however, the capacity retention improves significantly to ~70%, which can be attributed to two main effects: First, the electrolyte pH decreases due to the reactivity of Ca-ions with OH-ions. As mentioned above, the detrimental impact of OH^--adsorption on the stability of PBAs has been demonstrated previously by multiple studies. Thus, the acidity

© 2024 The Author(s). ChemSusChem published by Wiley-VCH GmbH

of the $CaCl_2$ electrolyte can be expected to mitigate dissolution effects by minimizing the presence of harmful OH^- species. Although small, a certain concentration of OH^- is present in all aqueous electrolytes. Hence, particularly at electrodes that operate close to the oxygen evolution potential, the specific adsorption of OH-ions can lead to local pH changes and promote degradation. Furthermore, Ojwang et al. have demonstrated a two-step degradation mechanism for FeHCF that involves a redox reaction between the PBA and water in the reversible first step, inducing locally alkaline conditions. Subsequently, an irreversible structural decomposition under basic conditions occurs in the second step.[53] This effect may be mitigated in Ca-based electrolytes as OH-ions are captured by the strongly interacting Ca-ions. Second, as discussed above, the higher Cl^- concentration and the stronger hydration of Ca^{2+} decrease the amount of free water and increase viscosity, further impeding dissolution. It has been shown that the structural decomposition of PBAs can be reversed in the presence of the respective transition metal cation.[54] Thus, the viscous $CaCl_2$ electrolyte may improve the cycling stability by preventing the transport of dissolution products away from the electrode. This effect can be amplified using saturated $CaCl_2$, leading to a capacity retention of ~90%. Although cathode degradation is still observable, it is significantly suppressed and should be even less pronounced within a battery cell containing only minimal amounts of electrolyte.

Figure 5 shows the galvanostatic charge and discharge curves of the CuHCF cathode recorded at C-rates ranging from 1 C to 300 C. The electrode displays a maximum discharge capacity of ca 65 $mAh\,g^{-1}$ with a Coulombic efficiency of nearly 100% at 1 C. With capacities of ca 60 $mAh\,g^{-1}$ and ca 34 $mAh\,g^{-1}$ at 10 C and 100 C, respectively, the fast-charging capabilities of CuHCF are considerably inferior to those of PNFE at similar mass loadings. Thus, the rate capability of the full cell can be influenced by controlling the mass balancing between the anode and the cathode. An oversized cathode will increase the specific capacity at high rates, whereas balanced anode and cathode capacities are favorable for slow-charging applications.

For this study, a mass-balanced cell was assembled with an anode-to-cathode active material ratio of 1:2. Based on the previous findings regarding electrode stability, saturated $CaCl_2$ was used as the electrolyte. The galvanostatic charge and discharge curves of this battery are shown in Figure 6(a). 5 cycles were recorded at each C-rate to ensure reversibility and monitor any degradation at different C-rates. At 1 C, the voltage profile shows a sloping plateau between 0.6 V and 1.5 V. In the voltage window from 0.6 V to 1.7 V, a reversible specific capacity of ca 41 $mAh\,g^{-1}$ is observed, which amounts to ~90% of the expected value, taking into account a cathode capacity of 65 $mAh\,g^{-1}$ and an anode capacity of 150 $mAh\,g^{-1}$. The battery exhibits exceptional fast charging capabilities, showing capacity retention of ca 88% at 10 C, ca 66% at 100 C, and ca 46% at 200 C, respectively. At C-rates above 10 C, the Coulombic efficiency approaches 100%, indicating good reversibility, as shown in Figure 6(b).

The specific discharge energy per cycle, which is calculated by integrating the discharge curves, is shown in Figure 6(c). Due to increasing voltage polarization at higher currents, the specific energy exhibits a greater C-rate dependence than the specific capacity. It drops from 41 $Wh\,kg^{-1}$ at 1 C to 35 $Wh\,kg^{-1}$ at 10 C (normalized to anode and cathode active material), indicating that the battery can be almost fully charged within minutes, nevertheless. Even at 100 C, more than 60% of the maximum energy density is still reached, making this battery a viable choice for supercapacitor-like use cases, e.g., in mobile applications that require lower ranges but short charging times. This conclusion is supported by evaluating the power density of the cell, which is calculated by multiplying the specific current with the average discharge voltage at each C-rate. The specific current ranges from 41 $mA\,g^{-1}$ (1 C) to 12.3 $A\,g^{-1}$ (300 C), while the average discharge voltage lies between 1.00 V (1 C) and 0.81 V (300 C). This yields power densities between ~40 $W\,kg^{-1}$ at 1 C and up to ~10 $kW\,kg^{-1}$ at 300 C, which are, to our knowledge, among the highest reported for aqueous batteries so far.

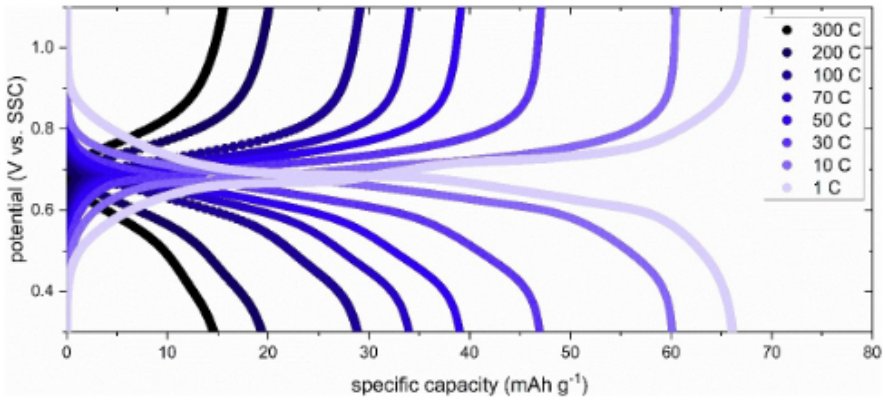


Figure 5. Rate performance of CuHCF in saturated $CaCl_2$. Galvanostatic (dis–) charge curves of a CuHCF electrode measured at C-rates ranging from 300 C (12 s) to 1 C (1 h) in a saturated $CaCl_2$ aqueous electrolyte.

© 2024 The Author(s). ChemSusChem published by Wiley-VCH GmbH

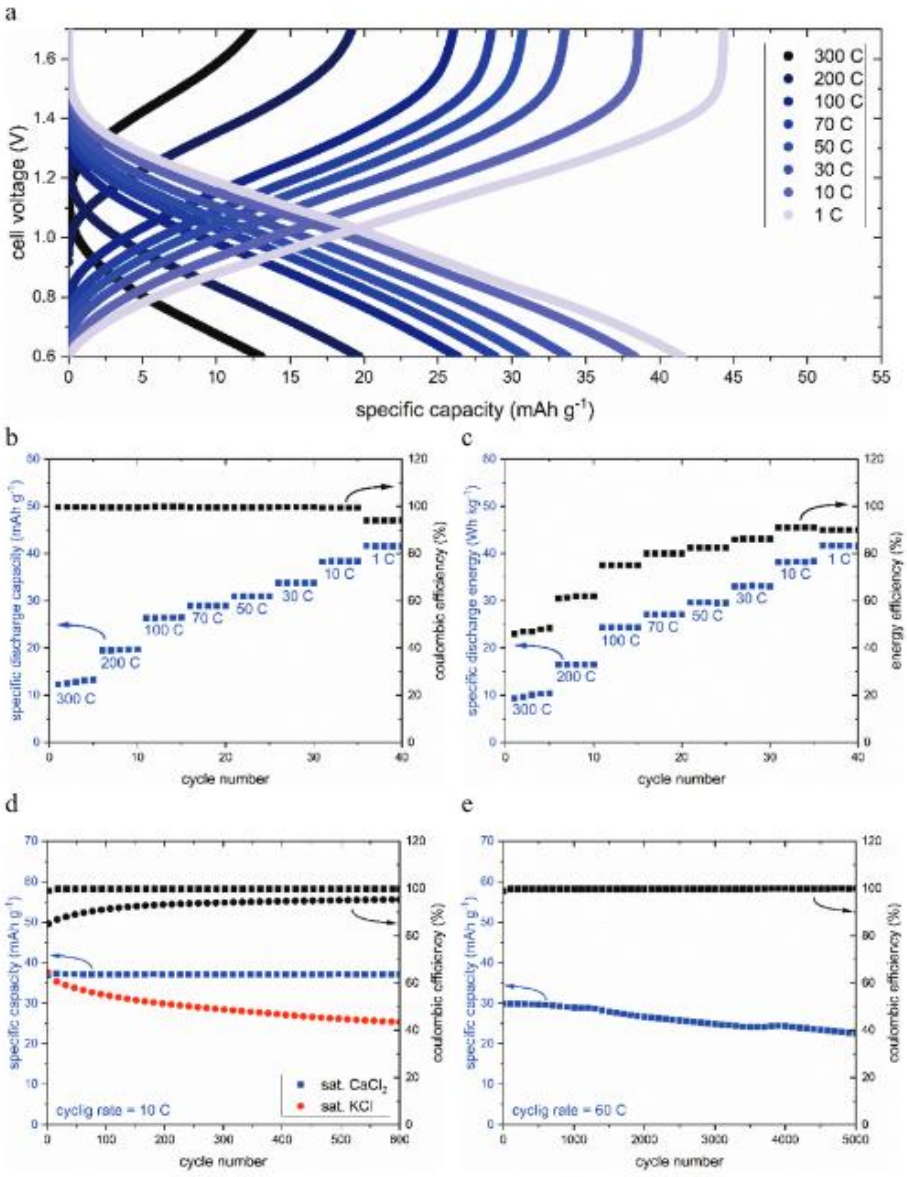


Figure 6. Performance of the CuHCF/$CaCl_2$/PNFE full cell. (a) Galvanostatic (dis−) charge curves. (b) Specific discharge capacity and Coulombic efficiency per cycle at different cycling rates. (c) Specific energy and energy efficiency per cycle. (d) Cycling stability measured over 600 cycles at 10 C. (e) Cycling stability measured over 5000 cycles at 60 C. The specific capacity and energy are normalized to anode and cathode active material.

To confirm the beneficial influence of the Ca-ion electrolyte on the cycling stability of the aqueous battery, cells containing either a saturated KCl or a saturated $CaCl_2$ electrolyte were continuously charged and discharged at an intermediate rate of 10 C for 600 cycles. While the aqueous K-ion battery only retains ~65% of its initial capacity, the aqueous Ca-ion battery maintains its capacity throughout the measurement. Furthermore, it displays a higher Coulombic efficiency due to suppressed water splitting side reactions in the concentrated $CaCl_2$ electrolyte (Figure 6(d)). The stability under long-term fast

© 2024 The Author(s). ChemSusChem published by Wiley-VCH GmbH

cycling was investigated by cycling the Ca-ion battery for 5000 cycles at 60 C. Even under these high-stress conditions, it maintained nearly 80% of its initial capacity at the end of the measurement, indicating excellent high-rate stability (Figure 6(e)). To further analyze the influence of the cation species on the characteristics of the full cell and the diffusion kinetics in the electrodes, CVs of the K-ion battery and the Ca-ion battery were recorded at different scan rates ranging from 1 $mV s^{-1}$ to 40 $mV s^{-1}$. The resulting voltammograms can be seen in Figure 7(a) and (c), respectively.

As expected from the single-electrode measurements, the reduction and oxidation peaks are found at slightly higher voltages for the K-ion battery since the electrode potential difference is larger. Although the energy density could, therefore, be maximized by using K^+ ions, the vast stability improvements with Ca^{2+} ions outweigh this drawback. For both batteries, the peak-to-peak separation increases at larger scan rates, which can be mostly attributed to the uncompensated internal resistance of the cells. However, the low peak-to-peak separation at 1 $mV s^{-1}$ indicates excellent reversibility of the charging processes, which is reflected in the aforementioned high energy efficiency at low C-rates. Relating the peak current j_{peak} to the scan rate ν, furthermore, reveals information on the diffusion kinetics in the electrodes:

$$j_{peak} = a \cdot \nu^b \quad (1)$$

For fully surface-limited processes like adsorption, the value of parameter b lies at 1.0, whereas it is 0.5 for fully mass-transport-limited processes. Figures 7(b) and (e) show the peak current of the main cathodic peak of the CV for both cells plotted against the scan rate with a fit according to equation (1). Interestingly, the value of parameter b does not change significantly when monovalent K-ions are replaced with divalent Ca-ions in the aqueous battery. Lying at ~0.8, it implies that the charging and discharging processes are partially mass-transport-limited for both cells. Since the charge storage mechanism of PNFE is quasi-capacitive and, thus, mostly surface-limited,[34,43] the mass transport limitations mainly stem from solid-state-diffusion kinetics at the CuHCF cathode. As multivalent ions typically have higher charge densities and, thus, higher polarization strengths than monovalent ions, the solid-state diffusion becomes more sluggish due to the stronger interactions between the cation and the host lattice. However, the relatively

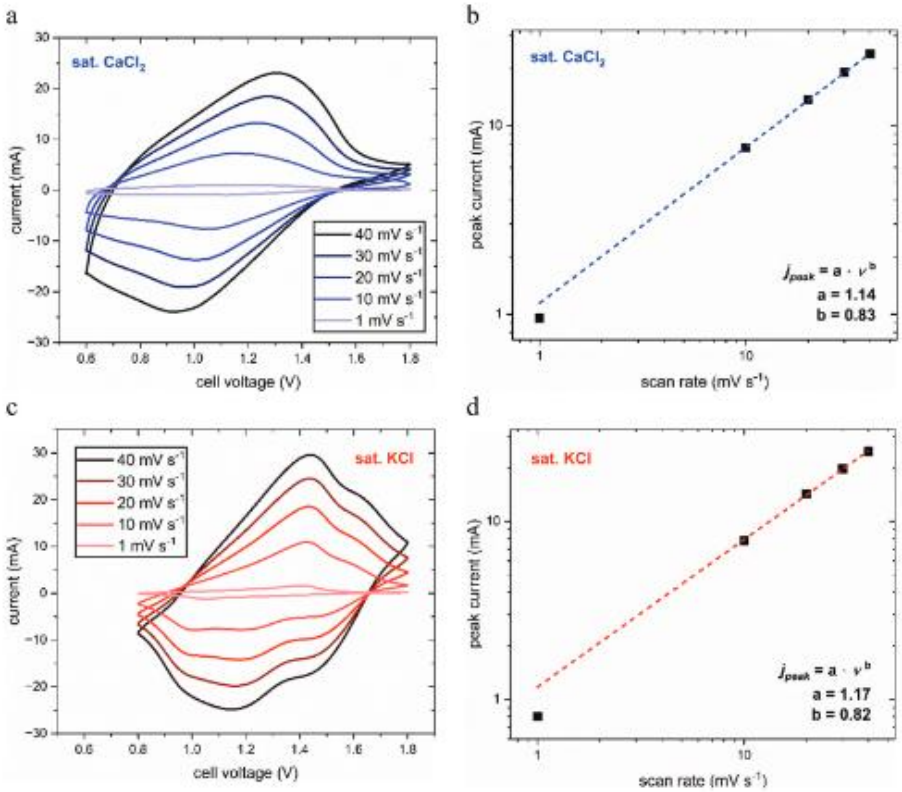


Figure 7. CVs of the sat. $CaCl_2$ and the sat. KCl full cell. (a) CVs of the Ca-ion battery at different scan rates. (b) Dependence of the reduction peak current on the scan rate for the Ca-ion battery. (c) CVs of the K-ion battery. (d) Dependence of the peak current on the scan rate for the K-ion battery.

© 2024 The Author(s). ChemSusChem published by Wiley-VCH GmbH

large ionic radius of Ca^{2+} leads to a significantly lower charge density than for other multivalent ions used in batteries, such as Al^{3+} and Mg^{2+}.[47] Consequently, the use of Ca-ions instead of K-ions does not impair the fast diffusion kinetics as severely, maintaining the high rate capability of the battery, which confirms the observations from the impedance measurements for the cathode.

The electrochemical performance of the full cell presented in this work is compared to other state-of-the-art aqueous Ca-ion batteries in Figure S4, demonstrating the superior power and energy density of this battery. Whereas an aqueous sulfur/$Ca_{0.4}MnO_2$ battery reported by Tang et al. in 2021 showed impressive energy densities of up to ~100 Wh kg^{-1}, the slow kinetics of this system severely limit its power density.[55] Energy densities similar to our work were achieved by Gheytani et al., Zhou et al., Zhang et al., and Wang et al.[36,47,56,57] In addition, several other groups have developed high-performance aqueous Ca-ion batteries which are not included in the comparison due to missing data on energy and power density.[58,59] However, power densities exceeding 10 kW kg^{-1} have not been reported for aqueous Ca-ion batteries to the best of our knowledge.

4. Conclusions

In conclusion, this work demonstrates that the cation choice affects the stability of electrode materials in aqueous batteries. Besides the influence on the redox potential and behavior, the organic polyimide anode and the copper hexacyanoferrate cathode demonstrated an elongated cycle life when using a Ca-ion-based instead of a K-ion-based electrolyte. While the degradation of the anode could already be mitigated by saturating the aqueous KCl electrolyte, such an effect could not be observed for the cathode. However, the stability of the cathode was largely improved in a 3 M $CaCl_2$ electrolyte and, more so, in a saturated $CaCl_2$ electrolyte.

Similar findings could be made for the full cell employing both previously investigated electrodes. A rapid capacity decay was observed for the aqueous K-ion battery, whereas the Ca-ion battery showed no significant degradation after 600 cycles at 10 C. Consequently, the performance of the latter cell was further analyzed, demonstrating an energy density of ~41 Wh kg^{-1} at 1 C and a maximum power density of ~10 kW kg^{-1} at 300 C. Due to these exceptional fast-charging properties, the stability was also evaluated at a fast cycling rate of 60 C. Under these conditions, the aqueous Ca-ion battery maintained a high capacity retention of nearly 80% after 5000 cycles.

Aside from the significant findings regarding the influence of the cation choice on the performance of aqueous batteries, this work helps to pave the way toward the practical implementation of aqueous batteries in large-scale energy storage. The battery proposed in this study uses only low-cost and highly available materials and promises to further advance the development of sustainable battery systems.

Author Contributions

R. Streng and A. Bandarenka proposed the concept. R. Streng, S. Reiser, S. Wager, and N. Pommer performed the experiments. R. Streng and A. Bandarenka co-wrote the manuscript. All authors participated in data analysis and manuscript discussion.

Acknowledgments

The authors thank Mr. Siegfried Schreier, Mr. Peter Schneider, and Mr. Christian Schott for their assistance in acquiring SEM, XPS, and XRD data. Furthermore, the authors acknowledge Dr. Sergei Vagin's assistance in synthesizing PNFE and acquiring the FTIR data and Dr. Anatoliy Senyshyn's assistance in fitting the XRD data.

We acknowledge Deutsche Forschungsgemeinschaft (DFG, German Research Foundation) under Germany's Excellence Strategy – EXC 2089/1 – 390776260 (e-conversion) for funding. ASB acknowledges additional financial support from TUM Innovation Network for Artificial Intelligence powered Multi-functional Material Design (ARTEMIS). Open Access funding enabled and organized by Projekt DEAL.

Conflict of Interests

The authors declare no competing financial interests.

Data Availability Statement

The data that support the findings of this study are available from the corresponding author upon reasonable request.

Keywords: Aqueous batteries · Calcium · Potassium · Polyimides

[1] B. D. Solomon, K. Krishna, *Energy Policy* **2011**, *39*(11), 7422–7431.
[2] J. Tian, L. Yu, R. Xue, et al., *Appl. Energy* **2022**, *307*, 118205.
[3] A. B. Gallo, J. R. Simões-Moreira, H. Costa, et al., *Renew. Sustain. Energy Rev.* **2016**, *65*, 800–822.
[4] P. Denholm, E. Ela, B. Kirby, et al. Role of Energy Storage with Renewable Electricity Generation, *U.S. Department of EnergyOffice of Scientific and Technical Information*, **2010**.
[5] A. Kalair, N. Abas, M. S. Saleem, et al., *Energy Storage* **2021**, *3*(1), e135.
[6] S. Passerini, D. Bresser, A. Moretti, A. Varzi, Batteries *Present and Future Energy Storage Challenges*, John Wiley & Sons, Incorporated, Newark **2020**.
[7] H. Ibrahim, A. Ilinca, J. Perron, *Renew. Sustain. Energy Rev.* **2008**, *12*(5), 1221–1250.
[8] G. Zubi, R. Dufo-López, M. Carvalho, et al., *Renew. Sustain. Energy Rev.* **2018**, *89*, 292–308.
[9] A. Luntz, *J. Phys. Chem. Lett.* **2015**, *6*(2), 300–301.
[10] Y. Gao, Z. Pan, J. Sun, et al., *Nano-Micro Lett.* **2022**, *14*(1), 94.
[11] D. Bin, F. Wang, A. G. Tamirat, et al., *Adv. Energy Mater.* **2018**, *8*(17), 1703008.
[12] Y. Liang, Y. Yao, *Nat. Rev. Mater.* **2023**, *8*(2), 109–122.
[13] J. O. G. Posada, A. J. Rennie, S. P. Villar, et al., *Renew. Sustain. Energy Rev.* **2017**, *68*, 1174–1182.
[14] H. Kim, J. Hong, K.-Y. Park, et al., *Chem. Rev.* **2014**, *114*(23), 11788–11827.

© 2024 The Author(s). ChemSusChem published by Wiley-VCH GmbH

[15] X. Lamprecht, F. Speck, P. Marzak, et al., *ACS Appl. Mater. Interfaces* **2022**, *14*(2), 3515–3525.
[16] G. Plečkaityte, M. Petruleviciene, L. Staisiūnas, et al., *J. Mater. Chem. A* **2021**, *9*(21), 12670–12683.
[17] G. Yang, Q. Li, K. Ma, et al., *J. Mater. Chem. A* **2020**, *8*(16), 8084–8095.
[18] H. Ahn, D. Kim, M. Lee, et al., *Commun. Mater.* **2023**, *4*(1), 37.
[19] T. Liang, R. Hou, Q. Dou, et al., *Adv. Funct. Mater.* **2021**, *31*(3), 2006749.
[20] Y. Shen, B. Liu, X. Liu, et al., *Energy Storage Mater.* **2021**, *34*, 461–474.
[21] L. Suo, O. Borodin, T. Gao, et al., *Science (New York, N.Y.)* **2015**, *350*(6263), 938–943.
[22] D. Xiao, L. Zhang, Z. Li, et al., *Energy Storage Mater.* **2022**, *44*, 10–28.
[23] L. Droguet, A. Grimaud, O. Fontaine, et al., *Adv. Energy Mater.* **2020**, *10*(43), 2002440.
[24] Y. Geng, L. Pan, Z. Peng, et al., *Energy Storage Mater.* **2022**, *51*, 733–755.
[25] Z. Liang, F. Tian, G. Yang, et al., *Nat. Commun.* **2023**, *14*(1), 3591.
[26] S. Jeong, B. H. Kim, Y. D. Park, et al., *J. Alloys Compd.* **2019**, *784*, 720–726.
[27] T. Liu, H. Wu, H. Wang, et al., *Nano-Micro Lett.* **2024**, *16*(1), 144.
[28] P. R. Kumar, Y. H. Jung, B. Moorthy, et al., *J. Electrochem. Soc.* **2016**, *163*(7), A1484–A1492.
[29] Y. Zhang, L. Zhao, Y. Liang, et al., *2667–1417* **2022**, *2*(1), 110–115.
[30] S. Phadke, R. Mysyk, M. Anouti, *J. Energy Chem.* **2020**, *40*, 31–38.
[31] S. Husmann, A. J. Zarbin, *Electrochim. Acta* **2018**, *283*, 1339–1350.
[32] C. Han, J. Zhu, C. Zhi, et al., *J. Mater. Chem. A* **2020**, *8*(31), 15479–15512.
[33] J. Qian, C. Wu, Y. Cao, et al., *Adv. Energy Mater.* **2018**, *8*(17), 1870079.
[34] R. L. Streng, S. Vagin, Y. Guo, et al., *Energy Adv.* **2024**, *3*(4), 874–882.
[35] Y. Xu, J. Wan, L. Huang, et al., *Energy Storage Mater.* **2020**, *33*, 432–441.
[36] C. Wang, R. Li, Y. Zhu, et al., *Adv. Energy Mater.* **2024**, *14*(1), 2470004.
[37] C. Han, J. Tong, X. Tang, et al., *ACS Appl. Mater. Interfaces* **2020**, *12*(9), 10479–10489.
[38] B. Häupler, A. Wild, U. S. Schubert, *Adv. Energy Mater.* **2015**, *5*(11), 1402034.
[39] K. Nakahara, S. Iwasa, M. Satoh, et al., *Chem. Phys. Lett.* **2002**, *359*(5–6), 351–354.
[40] T. Gu, M. Zhou, M. Liu, et al., *RSC Adv.* **2016**, *6*(58), 53319–53323.
[41] W. Deng, Y. Shen, J. Qian, et al., *Chem. Commun. (Cambridge, England)* **2015**, *51*(24), 5097–5099.
[42] S. Gheytani, Y. Liang, F. Wu, et al., *Adv. Sci. (Weinheim, Baden-Wurttemberg, Germany)* **2017**, *4*(12), 1700465.
[43] L. Chen, J. L. Bao, X. Dong, et al., *ACS Energy Lett.* **2017**, *2*(5), 1115–1121.
[44] J. Park, Z.-L. Xu, G. Yoon, et al., *Adv. Mater. (Deerfield Beach, Fla.)* **2020**, *32*(4), e1904411.
[45] J. Yun, J. Pfisterer, A. S. Bandarenka, *Energy Environ. Sci.* **2016**, *9*(3), 955–961.
[46] Y. You, X.-L. Wu, Y.-X. Yin, et al., *Energy Environ. Sci.* **2014**, *7*(5), 1643–1647.
[47] B. Xie, P. Zuo, L. Wang, et al., *Nano Energy* **2019**, *61*, 201–210.
[48] J. Song, L. Wang, Y. Lu, et al., *J. Am. Chem. Soc.* **2015**, *137*(7), 2658–2664.
[49] D. Kim, A. Choi, C. Park, et al., *J. Mater. Chem. A* **2023**, *11*(25), 13535–13542.
[50] C. D. Wessells, R. A. Huggins, Y. Cui, *Nat. Commun.* **2011**, *2*, 550.
[51] C. D. Wessells, S. V. Peddada, R. A. Huggins, et al., *Nano Lett.* **2011**, *11*(12), 5421–5425.
[52] X. Lamprecht, I. Evazzade, I. Ungerer, et al., *J. Phys. Chem. C* **2023**, *127*(5), 2204–2214.
[53] D. O. Ojwang, M. Svensson, C. Njel, et al., *ACS Appl. Mater. Interfaces* **2021**, *13*(8), 10054–10063.
[54] T. Shao, C. Li, C. Liu, et al., *J. Mater. Chem. A* **2019**, *7*(4), 1749–1755.
[55] X. Tang, D. Zhou, B. Zhang, et al., *Nat. Commun.* **2021**, *12*(1), 2857.
[56] R. Zhou, Z. Hou, Q. Liu, et al., *Adv. Funct. Mater.* **2022**, *32*(26), 2200929.
[57] S. Zhang, Y.-L. Zhu, S. Ren, et al., *J. Am. Chem. Soc.* **2023**, *145*(31), 17309–17320.
[58] R. Li, J. Yu, F. Chen, et al., *Adv. Funct. Mater.* **2023**, *33*(30), 2214304.
[59] R. Cang, C. Zhao, K. Ye, et al., *ChemSusChem* **2020**, *13*(15), 3911–3918.

Manuscript received: July 4, 2024
Revised manuscript received: October 1, 2024
Accepted manuscript online: October 23, 2024
Version of record online: November 14, 2024

© 2024 The Author(s). ChemSusChem published by Wiley-VCH GmbH

4. A Low-Cost and High-Energy Aqueous Potassium-Ion Battery.

R.L. Streng, T. Steeger, A. Senyshyn, S. Abel, P. Schneider, C. Benning, B. Miller Naranjo, D. Gryc, M.Z. Hussain, O. Lieleg, M. Elsner, A.S. Bandarenka, K. Cicvarić. *Journal of Energy Chemistry* **2025**, 106, 523-531.

Journal of Energy Chemistry 106 (2025) 523–531

Contents lists available at ScienceDirect

Journal of Energy Chemistry

journal homepage: www.elsevier.com/locate/jechem

A low-cost and high-energy aqueous potassium-ion battery ☆

Raphael L. Streng [a], Tim Steeger [a], Anatoliy Senyshyn [b], Steffen Abel [a], Peter Schneider [a], Christine Benning [d], Bernardo Miller Naranjo [e,f], David Gryc [g], Mian Zahid Hussain [g], Oliver Lieleg [e,f], Martin Elsner [d], Aliaksandr S. Bandarenka [a,c,*], Katarina Cicvarić [a,*]

[a] Physics of Energy Conversion and Storage, Physik-Department, Technische Universität München, James-Franck-Str. 1, 85748 Garching, Bavaria, Germany
[b] Heinz Maier-Leibnitz Zentrum (MLZ), Technische Universität München, Lichtenbergstr. 1, 85748 Garching, Bavaria, Germany
[c] Catalysis Research Center TUM, Ernst-Otto-Fischer-Straße 1, 85748 Garching, Bavaria, Germany
[d] Chair of Analytical Chemistry and Water Chemistry, Chemie-Department, Technische Universität München, Lichtenbergstraße 4, 85748 Garching, Bavaria, Germany
[e] Department of Materials Engineering, School of Engineering and Design, Technical University of Munich, Boltzmannstraße 15, 85748 Garching, Bavaria, Germany
[f] Center for Protein Assemblies (CPA), Munich Institute of Biomedical Engineering (MIBE), Technical University of Munich, Ernst-Otto-Fischer Straße 8, 85748 Garching, Bavaria, Germany
[g] Chair of Inorganic and Metal-Organic Chemistry, Department of Chemistry, School of Natural Sciences, Technical University of Munich (TUM), Lichtenbergstraße 4, 85748 Garching, Bavaria, Germany

ARTICLE INFO

Article history:
Received 27 December 2024
Revised 8 February 2025
Accepted 9 February 2025
Available online 13 March 2025

Keywords:
Aqueous Battery
Electrolyte
Potassium
Calcium

ABSTRACT

To address challenges related to the intermittency of renewable energy sources, aqueous potassium-ion batteries (AKIBs) are a promising and sustainable alternative to conventional systems for large-scale energy storage. To enable their practical application, maximizing energy density and longevity while minimizing production and material costs is a key goal. In this work, we propose an AKIB consisting only of abundant and cost-efficient materials, which delivers a high energy density of more than 70 Wh kg^{-1}. We combine simple strategies to stabilize the Mn-rich Prussian blue analog cathode by Fe-doping, improving the crystallinity, and tuning the electrolyte composition without employing expensive water-in-salt electrolytes. Using a mixed 2.5 M $Ca(NO_3)_2$ + 1.5 M KNO_3 electrolyte, we assemble a novel AKIB with a Fe-doped manganese hexacyanoferrate cathode and an organic poly(naphthalene-4-formyl-ethylenediamine) anode. Besides a high energy density, the full cell delivers a specific capacity of approximately 60 mA h g^{-1}, a power density of 5000 W kg^{-1}, and 80% capacity retention after 600 cycles.
© 2025 The Authors. Published by Published by Elsevier B.V. and Science Press on behalf of Science Press and Dalian Institute of Chemical Physics, Chinese Academy of Sciences. This is an open access article under the CC BY license (http://creativecommons.org/licenses/by/4.0/).

1. Introduction

The rise in global energy demand, along with the global warming and environmental pollution caused by fossil fuel, necessitates the utilization of renewable energy sources, such as solar, wind, tidal, etc. Due to the intermittent nature of these energy sources, energy storage systems are needed to maximize their usage. Lithium-ion batteries (LIBs) dominate the markets of electric vehicles and consumer electronics owing to their high energy density and cycling stability [1,2]. However, LIBs are plagued by safety risks caused by flammable and toxic organic electrolytes and high costs due to the limited and uneven distribution of lithium in the earth's crust [3,4].

Aqueous potassium-ion batteries (AKIBs) comprising non-flammable aqueous electrolytes and earth-abundant potassium emerged as a promising alternative. Further, potassium is an alkali metal with a standard redox potential of −2.936 V vs. SHE, comparable to that of lithium (−3.040 V vs. SHE) and lower than that of sodium (−2.714 V vs. SHE), enabling higher operating voltages and boosting the energy density [5]. Moreover, the weakest Lewis acidity of K^+ compared to Li^+ and Na^+ results in the smallest Stokes radius, favoring higher ionic diffusion in aqueous electrolytes and rate capability [6]. However, the practical implementation of this battery system is hampered by an insufficient cycle life and narrow thermodynamic electrochemical stability window of water (1.23 V), suppressing the operating voltage, which limits the energy density [7–10].

Prussian blue analogs (PBAs) are a promising class of cathode materials for aqueous potassium-ion batteries, generally

☆ This article is part of a special issue entitled: 'Emerging Potassium-Based Energy Storage Technologies' published in Journal of Energy Chemistry.

* Corresponding authors.
E-mail addresses: bandarenka@ph.tum.de (A.S. Bandarenka), katarina.cicvaric@tum.de (K. Cicvarić).

https://doi.org/10.1016/j.jechem.2025.02.039
2095-4956/© 2025 The Authors. Published by Published by Elsevier B.V. and Science Press on behalf of Science Press and Dalian Institute of Chemical Physics, Chinese Academy of Sciences. This is an open access article under the CC BY license (http://creativecommons.org/licenses/by/4.0/).

represented by the chemical formula $A_xM_A[M_B(CN)_6]_y\square_{1-y}\cdot zH_2O$, where A is a guest cation (Li, Na, K, Mg or Ca), M_A is a transition metal such as Fe, Mn, Co, Ni or Cu, M_B is commonly Fe, and □ denotes $M_B(CN)_6$ vacancy. The rigid 3D framework of PBAs with large interstitial sites can accommodate potassium ions, while open channels enable intercalation and deintercalation. Based on the electrochemical activity of the transition metal, the electrochemical mechanism can be divided into single-electron redox reactions represented by redox-inactive metals such as Ni, Cu, and Zn and multi-electron redox reactions represented by redox-active metals such as Fe, Mn, Co and V [10–14]. Typically, the PBAs relying on single-electron redox reactions such as $K_{0.6}Ni_{1.2}Fe(CN)_6\cdot 3.6H_2O$ [15] or $K_{0.71}Cu[Fe(CN)_6]_{0.72}\cdot 3.7H_2O$ [16] deliver low specific capacities of about 60 mA h g^{-1}, but have a long cycle life (5000–40000 cycles). Comparing, $K_2Fe[Fe(CN)_6]\cdot 2H_2O$ [17] or $K_2Co[Fe(CN)_6]$ [18] functioning through multi-electron redox reaction achieve above 100 mA h g^{-1}, but show significantly faster capacity decay (~500 cycles).

A candidate holding great promise for AKIBs is $K_2Mn[Fe(CN)_6]$, as it offers the highest theoretical capacity and operating voltage and incorporates low-cost and non-polluting elements [19,20]. Nevertheless, low cycle life induced by dissolution of Mn in aqueous electrolytes and structural instability due to Mn^{3+}-triggered Jahn–Teller distortion are major setbacks for this material [14,21]. A significant breakthrough was achieved in a full AKIB comprising Fe-doped Mn-rich PBA ($K_xFe_yMn_{1-y}[Fe(CN)_6]_w\cdot zH_2O$) and 22 mol kg^{-1} (m) potassium trifluoromethane sulfonate (KCF_3SO_3) water-in-salt electrolyte, where the suppression of detrimental phase transition was attributed to Fe substitution. In contrast, a low amount of free water in the electrolyte alleviates Mn dissolution [22]. However, as noted by the authors, the high consumption of the expensive KCF_3SO_3 salt associated with this approach limits its practical applicability. An alternative strategy for Mn dissolution mitigation in organic electrolytes was accomplished in nearly stoichiometric $K_2Mn[Fe(CN)_6]$ with a negligible amount of defects and water, synthesized with the aid of the chelating agent EDTA [21]. In our recent work, we demonstrated the use of concentrated Ca-based electrolytes as a more sustainable approach to limit PBA dissolution [23].

Herein, we introduce a full AKIB cell comprising a Fe-doped Mn-PBA cathode, a poly(naphthalene-4-formyl-ethylenediamine) (PNFE) anode, and an inexpensive 2.5 M $Ca(NO_3)_2$ + 1.5 M KNO_3 electrolyte. The enhanced capacity retention of Mn-PBA was achieved by combined effects of Fe doping, regulating the crystal growth with the aid of a chelating agent, and introducing Ca-ions as an electrolyte additive. The optimized cathode and anode materials deliver high specific capacities of 109 and 150 mA h g^{-1}, respectively, while combined in the full cell, 60 mA h g^{-1} specific capacity, an energy density above 70 Wh kg^{-1}, and a maximum power density of approximately 5000 W kg^{-1} was obtained.

2. Experimental

2.1. Material synthesis

2.1.1. Synthesis of PNFE

All chemicals for synthesis were purchased from commercial suppliers and used without further purification.

Poly(naphthalene-4-formyl-ethylenediamine) (PNFE) was synthesized in our previous work, and the anode active material used in this study originates from the same batch [24]. Initially, 10 mmol (2.68 g) of 1,4,5,8-naphthalene tetracarboxylic dianhydride (NTCDA) and 10 mmol (0.6 g) of ethylenediamine (EDA) were dissolved in 20 mL of degassed N-methyl pyrrolidone (NMP) in a Schlenk flask. The mixture was heated to 215 °C in a sand bath and refluxed overnight, causing the formation of a dark precipitate. The resulting product was filtered and thoroughly washed several times with NMP and water. Drying was performed under vacuum at 0.08 mbar in three sequential steps (room temperature, 120 and 210 °C). This process yielded a grey-brownish powder with a high yield of 92% (2.7 g).

Elemental analysis of PNFE: Calcd. for an infinite polyimide ($C_{16}H_8N_2O_4$), %: C 65.76, H 2.76, N 9.59; calcd. for an octamer, %: C 65.10, H 3.03, N 10.52; found, %: C 65.13, H 2.91, N 10.32.

2.1.2. Synthesis of MnHCF and FeMnHCF

Manganese hexacyanoferrate (MnHCF) and iron manganese hexacyanoferrate were synthesized via coprecipitation. In both cases, 200 mL of solution A, containing the transition metal salt (s), and 200 mL of solution B, containing 8 mmol of $K_3[Fe(CN)_6]$ (Sigma Aldrich, USA), were simultaneously added dropwise into 100 mL of deionized (DI) water under continuous stirring at 60 °C. For MnHCF, solution A was prepared by dissolving 8 mmol $MnSO_4$ (Sigma Aldrich, USA) in 200 mL DI water. For FeMnHCF-A, solution A contained a mixture of 1.4 mmol $FeSO_4$ (Sigma Aldrich, USA) and 2.6 mmol $MnSO_4$ (Sigma Aldrich, USA) dissolved in 200 mL of DI water.

To produce morphology-controlled FeMnHCF-C, solution A was prepared by dissolving 2.8 mmol $FeSO_4$, 5.2 mmol $MnSO_4$, and 8 mmol $C_6H_5Na_3O_7\cdot 2H_2O$ (Sigma Aldrich, USA) in 200 mL DI water. 4 mmol of $K_4[Fe(CN)_6]$ were dissolved in 200 mL of DI water to form solution B.

Once the additions were complete, the respective mixtures were left to age overnight. Following the aging process, the products were separated by centrifugation, washed two times with water and once with ethanol, and dried overnight at 70 °C.

2.2. Electrode preparation

PNFE, MnHCF, and FeMnHCF electrodes were prepared using the slurry-casting method. The PNFE slurry consisted of 80 wt. % polyimide active material, 10 wt. % carbon black super C-65 (MTI, USA) and 10 wt. % Nafion™ binder (5 wt. % in lower aliphatic alcohols and water, Sigma Aldrich, USA). These components were mixed and ground in a planetary ball mill, after which water and isopropyl alcohol in a 1:1 ratio were added as dispersing agents under vigorous stirring to form the anode slurry.

Cathode slurries were prepared similarly by combining 80 wt. % active material (MnHCF or FeMnHCF), 10 wt. % carbon black super C-65 and 10 wt. % polyvinylidene fluoride (PVDF, MTI, USA) in a planetary ball mill. NMP was added as a solvent to these cathode mixtures under vigorous stirring to produce homogeneous slurries.

Final electrode production involved casting the prepared slurries onto pyrolytic graphite sheet current collectors. The active material mass loadings were approximately 2 mg cm^{-2} for the PNFE anode and 3 mg cm^{-2} for the MnHCF, FeMnHCF-A, and FeMnHCF-C cathodes.

2.3. Material characterization

Morphological investigations of electrode films were conducted using a field emission scanning electron microscope (SEM, Zeiss Gemini NVision40). In the case of FeMnHCF-C, the average particle size was determined from these SEM images by creating a particle size distribution using the software ImageJ. Powder X-ray diffraction (XRD) measurements were conducted with a Rigaku MiniFlex 600-C X-ray diffractometer utilizing Cu-K_α radiation (λ = 1.5406 Å) and an integrated Ni-based filter to analyze the crystal structure and crystallinity of the MnHCF and FeMnHCF active material powders. For inductively coupled plasma-mass spectrometry (ICP-MS),

MnHCF, FeMnHCF-A, and FeMnHCF-C were dissolved in 65% HNO_3 and subsequently analyzed for their relative Mn and Fe contents.

Nitrogen gas sorption isotherms were recorded with a Micrometrics 3Flex analyzer under liquid nitrogen at 77 K for surface area and pore size analysis. The BET-specific surface area and pore size distribution were evaluated using the dedicated software provided by Micrometrics 3Flex. The prepared electrodes and the bare substrate were cut into small pieces, filled into the measuring tubular glass cells, and activated at 120 ℃ for 16 h under vacuum before the analysis.

Viscosity measurements were conducted on a commercial shear rheometer (MCR 302, Anton Paar GmbH, Graz, Austria) equipped with a cone-shaped measuring head (CP50-1, 79040, Anton Paar) and an air-cooled bottom plate (P-PTD 200/56/Air, Anton Paar). For each sample, the viscosity was measured over a shear rate range from 1000 to 5 s^{-1} following a logarithmic ramp. Five measuring points were captured within each decade, and three technical replicates of this measurement were conducted per sample type. All measurements were conducted at 25°C, and a solvent trap was used to prevent liquid evaporation from the samples during the measurements.

2.4. Electrochemical measurements

Electrochemical investigations of individual electrodes were performed using a three-electrode setup in a closed glass cell under constant argon flow to maintain an inert atmosphere. Before introducing the electrolytes, both the glass cell and the electrolytes were purged with argon for at least 10 min. A platinum wire (MaTeck, Germany) served as the counter electrode, and the Ag/AgCl reference electrode (SSC, 3 M KCl, SI Analytics) was connected to the electrolyte via a Luggin capillary. The electrolytes employed in this study included 5 M $Ca(NO_3)_2$, 3 M KNO_3, and a 1:1 (volume) mixture of the two, resulting in a solution containing 2.5 M $Ca(NO_3)_2$ and 1.5 M KNO_3 (CKN2515).

Electrochemical measurements were conducted with a BioLogic VSP-300 potentiostat. Cyclic voltammetry (CV) and galvanostatic cycling with potential limitations (GCPL) were employed to evaluate the performance of the electrodes. Initial stability and intercalation investigations of the cathode materials in the three electrolytes were performed via CV at a scan rate of 20 mV s^{-1} with potentials ranging from 0 to 1.5 V vs. SSC.

Further investigations of the FeMnHCF-C slurry cathode with the CKN2515 electrolyte involved CV measurements at scan rates ranging from 1 to 50 mV s^{-1} within the same potential range. Furthermore, GCPL measurements were conducted at C-rates ranging from 100 C to 1 C, within a potential range of 0 and 1.3 V vs. SSC. The PNFE slurry anode was characterized using similar methods, with CV conducted over a potential range of 0 to −0.9 V vs. SSC and GCPL measurements performed between 0 and −0.8 V vs. SSC.

2.5. Full-cell assembly and measurements

A 3D-printed plastic cell with pyrolytic graphite foil contacts was used as the full-cell casing to prevent the corrosion of stainless steel contacts. An aqueous K/Ca-ion battery was assembled using the CKN2515 electrolyte, a FeMnHCF-C slurry cathode, and a PNFE slurry anode, with a cathode to anode active material mass ratio of 1:1.4. Assembly was conducted under a nitrogen atmosphere inside a glovebox to prevent oxygen dissolution in the electrolyte. An electrolyte-soaked commercial BS 17–25 separator (Mativ Inc., France), designed for alkaline batteries, was placed between the electrodes, and the cell was sealed with rubber O-rings. For the performance evaluation, GCPL was performed using a BioLogic VSP-300 potentiostat. The cell was cycled at C-rates ranging from 100 C to 1 C within a voltage range of 0 to 2.1 V.

3. Results and discussion

The structural and morphological properties of the Mn-based PBAs were analyzed using XRD, ICP-MS, and SEM. Fig. 1 shows the results of the morphological investigation of MnHCF, FeMnHCF-A, and FeMnHCF-C via SEM. The fitted XRD patterns are displayed in Fig. S1. The XRD data of a Si reference were used for all three samples to estimate the instrumental resolution function. The XRD pattern of MnHCF exhibits narrow diffraction peaks and weak splitting with several weak reflections underneath the high-intensity ones. This indicates high-symmetry ordering. The diffraction intensities can be modeled by a parent cubic structure (*Fm*-3*m*, a = 10.504 Å) (left side of Fig. S1(a)) [25] while the symmetric splitting of reflections indicates a weak distortion, which can be modeled by a tetragonal lattice with doubled c lattice parameters (primitive, a = 10.530 Å, 20.991 Å) (right side of Fig. S1(a)). A small tetragonal distortion of 0.3% can be concluded. The SEM analysis (Fig. 1 (a)) of the MnHCF cathode reveals agglomerated, nonuniform particles of inconsistent size (up to ~7 µm). As shown in Table S1, ICP-MS indicates a Fe/Mn ratio of merely 0.83. This small share can be attributed to a high number of $Fe(CN)_6$ vacancies, which is consistent with the comparably low crystallinity revealed by the SEM and XRD analysis.

The FeMnHCF-A XRD pattern (Fig. S1(b)) reveals a series of well-isolated, broad peaks, which (similar to MnHCF) can be indexed with a parent cubic lattice (*Fm*-3*m*, a = 10.188 Å), with the exception of two sharp reflections associated with an unidentified secondary phase. For this sample, no measurable tetragonal distortion can be concluded. Similar to MnHCF, the SEM images of the FeMnHCF-A slurry mainly feature irregularly shaped particles of ranging sizes (up to ~3 µm), with the largest particles being smaller than those in the MnHCF sample. For both samples, generating a particle size distribution was not possible due to difficulties in distinguishing smaller particles. However, both samples exhibit a wide range of particle sizes and irregular shapes, suggesting low crystallinity. ICP-MS reveals a Fe/Mn ratio of 1.68 (Table S1) and, thus, a successful decrease in the density of Mn in the lattice.

The structure of FeMnHCF-C can be unambiguously associated with the structural model of the KMnHCF-type [5], which is reflected by a characteristic triplet at ca. 2θ = 25°. The best fits (Fig. S1(c)) were obtained for space group $P2_1/c$, a = 6.983 Å, b = 7.304 Å, c = 12.305 Å, β = 124.79°. The sample is characterized by high crystallinity. The peak broadening analysis revealed a weak microstrain of isotropic character, which can be attributed to local chemical inhomogeneities affecting the peak widths at high scattering angles. The high crystallinity is backed up by the SEM (Fig. 1 (c)) analysis, showing crystalline, cube-like particles of consistent size. The size consistency and crystallinity are reflected by a narrow particle size distribution (Fig. S2), yielding an average particle size of about (858 ± 96) nm. Here, the largest particles are significantly smaller compared to those in the other samples. The more uniform and regular morphology of FeMnHCF-C can be attributed to the chelating effect of the sodium citrate additive during the synthesis. By binding to the transition metal cations, the citrate anions slow down the crystallization rate, effectively reducing the density of lattice defects [20,26]. ICP-MS reveals a Fe/Mn ratio of 1.37 (Table S1). FeMnHCF-C represents a highly crystalline sample with slightly lower Fe incorporation, resulting from the citrate-aided coprecipitation procedure.

BET analysis was carried out to determine the specific surface area and pore size distribution of all three samples. The nitrogen sorption isotherms (Fig. S3(a)) indicate a drastic decrease in overall porosity in iron-doped samples. MnHCF exhibited a type-I isotherm with a calculated specific surface area (SSA) of 81 m^2 g^{-1} compared to MnFeHCF-A and MnFeHCF-C, which demonstrated

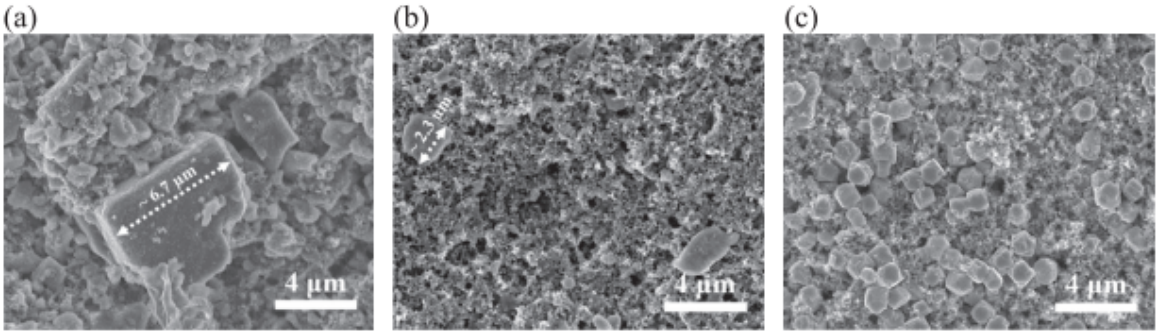


Fig. 1. Structural characterization of Mn-based PBAs. (a) SEM image of the manganese hexacyanoferrate (MnHCF) cathode. (b) SEM image of the FeMnHCF-A cathode. (c) SEM image of the FeMnHCF-C cathode.

5.6 and 2 $m^2 g^{-1}$, respectively. Under identical measurement conditions, the graphite substrate showed a negligible SSA of 0.5 $m^2 g^{-1}$. It is worth mentioning that MnFeHCF-A has a larger hysteresis between relative pressures (P/P^0) of 0.4 and 0.8 with a type-IV isotherm, indicating the presence of mesopores. The NLDFT pore size distribution (Fig. S3(b)) confirms the presence of micropores of 0.9 and 1.1 nm (<2 nm) in the MnHCF sample, whereas in the samples MnFeHCF-A and MnFeHCF-C a lower amount of broadly distributed mesopores between 6–20 nm can be observed. This indicates that the large MnHCF agglomerates observed in the SEM pictures are, in fact, porous structures with small micropores instead of regular crystals, which can be attributed to the high defect content. In contrast, the FeMnHCF-A and, particularly, the FeMnHCF-C samples consist of more evenly distributed crystalline particles, as the SEM and XRD measurements showed before. Hence, they only feature larger mesopores and, thus, a lower specific surface area.

Fig. 2 shows the 1st, 10th, and 50th CV cycles and the capacity retention per cycle over 100 cycles of MnHCF, FeMnHCF-A, and FeMnHCF-C in different electrolytes. Due to a short precycling phase linked to slow electrode wetting, which was observed in all electrodes, the "1st cycle" refers to the cycle at which the peak currents reached their maximum, and no further growth was observed. In saturated 3 M KNO_3, pure MnHCF displays a dominant pair of oxidation and reduction peaks at 0.73 V and 0.55 V vs. SSC, respectively, corresponding to the $Fe^{II/III}$ transition (Fig. 2 (a)). The additional $Mn^{II/III}$ transition is represented by another pair of peaks at 1.28 V and 0.91 V vs. SSC. The steep increase in current toward the right potential boundary is associated with the parasitic oxygen evolution side reactions, indicating that the electrode can only be reversibly cycled to potentials below ~1.30 V vs. SSC. To monitor the cycling stability, the electrode was repeatedly reduced and oxidized for 100 cycles at 20 mV s^{-1} (Fig. 2 (a) and (j)). By comparing the 1st and 10th cycles, it becomes apparent that MnHCF experiences rapid degradation in this electrolyte. Previous studies have shown that Mn-based PBAs suffer severe structural changes due to Jahn-Teller distortions at the N-coordinated Mn centers [20,27]. According to the literature, MnHCF undergoes a partly irreversible phase transition from cubic to tetragonal during the $Mn^{II/III}$ redox process, which is related to structural collapse and capacity loss [28,29]. Hence, material or electrolyte modifications are necessary to enhance the cycle life of MnHCF and enable its practical application. Doping with different transition metal ions such as Fe, Ni, or Co has been identified as an effective strategy to mitigate the detrimental effects of Jahn-Teller distortions by decreasing the Mn density in the crystal lattice [22,30,31]. In addition, this substitution has been shown to significantly change the $Mn^{II/III}$ redox mechanism, further impeding phase transitions [32]. A detailed investigation of this effect was previously reported by Jiang et al. in 2019. They showed that, while pure MnHCF undergoes two phase transitions from monoclinic to cubic and cubic to tetragonal, iron doping introduces a solid solution reaction with a single-phase transition between monoclinic and cubic with higher reversibility. Furthermore, the $Mn^{II/III}$ and the $Fe^{II/III}$ redox processes are completely independent in MnHCF. In contrast, the Fe-doped FeMnHCF exhibits activity of the $Fe^{II/III}$ redox couple over the full potential range. In addition, they showed that due to the Fe-doping, the $Mn^{II/III}$ redox reaction becomes asymmetric, significantly altering the mechanism and suppressing Jahn-Teller distortions [22]. Other groups have also reported similar results investigating the effects of Ni, Co, and Fe doping on Mn-based PBAs [30,32,33]. Accordingly, the iron-doped FeMnHCF-A shows significantly improved cycling stability, as shown in Fig. 2 (b) and (j). In addition, this modification shifts the left pair of peaks toward more negative potentials, whereas the more positive redox peaks become more pronounced, enabling a higher capacity utilization at high potentials. The CV curve of MnHCF-C features only one major oxidation and reduction peak, at 1.05 V and 0.77 V vs. SSC, respectively, showing that the electrochemical behavior of the Mn-based PBA is influenced both by the crystallinity and the composition (Fig. 2(c)). Although both FeMnHCF-A and FeMnHCF-C display significant stability improvements compared to pure MnHCF, they still suffer from severe electrode degradation and capacity loss in KNO_3, as demonstrated in Fig. 2 (j). Typically, this can be addressed by utilizing highly concentrated water-in-salt electrolytes based on highly soluble fluorinated salts such as KCF_3SO_3 or potassium bis(fluorosulfonyl)imide (KFSI) [34,35].

However, as mentioned above, this strategy is associated with high electrolyte costs as it requires high amounts of expensive salts. In our previous work, we have demonstrated the use of a low-cost saturated $CaCl_2$ electrolyte as an alternative approach to stabilize a Cu-based PBA cathode [23]. Since the divalent Ca-ions have a much higher charge density and more negative hydration energy than the monovalent K-ions, they can bind more water molecules in their hydration shell [36]. Additionally, at the same molarity, the anion concentration is doubled compared to the equivalent potassium salt, further reducing the amount of free water. As for water-in-salt electrolytes, this mitigates harmful side reactions and active material dissolution. Furthermore, the strong interaction of Ca^{2+} with OH^- can suppress the detrimental effect of the well-studied alkaline degradation pathway of PBAs, similar to what has been observed in mildly acidic electrolytes [37]. In this work, saturated $Ca(NO_3)_2$, corresponding to a concentration of 5 M, was used instead of $CaCl_2$ to avoid the oxidation of Cl^- at the

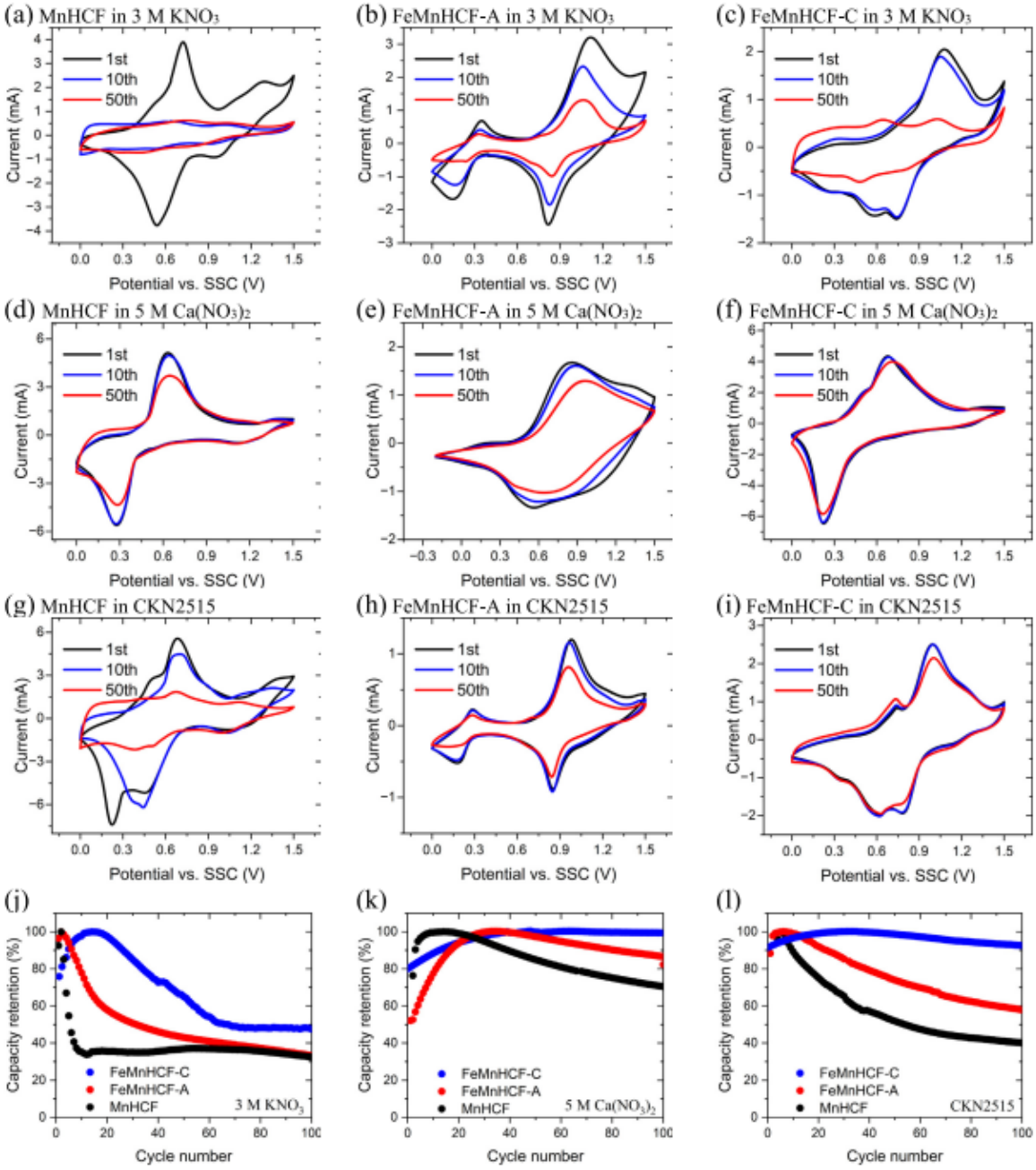


Fig. 2. Material and electrolyte optimization of Mn-based PBAs. CV curves of the 1st, 10th and 50th cycles at 20 mV s^{-1} of (a) MnHCF in 3 M KNO_3, (b) FeMnHCF-A in 3 M KNO_3, (c) FeMnHCF-C in 3 M KNO_3, (d) MnHCF in 5 M $Ca(NO_3)_2$, (e) FeMnHCF-A in 5 M $Ca(NO_3)_2$, (f) FeMnHCF-C in 5 M $Ca(NO_3)_2$, (g) MnHCF in 2.5 M $Ca(NO_3)_2$ + 1.5 M KNO_3, (h) FeMnHCF-A in 2.5 M $Ca(NO_3)_2$ + 1.5 M KNO_3, (i) FeMnHCF-C in 2.5 M $Ca(NO_3)_2$ + 1.5 M KNO_3. Cycling performance of the three electrode materials in (j) 3 M KNO_3, (k) 5 M $Ca(NO_3)_2$, (l) CKN2515.

relatively high potentials needed to charge Mn-based PBAs. As shown in Fig. 2 (d–f), all three electrodes exhibit significantly lower capacity fading in this electrolyte. Especially the CV curves of FeMnHCF-C display almost no changes within 50 cycles, demonstrating the successful stabilization of the electrode. Fig. 2 (k) shows that FeMnHCF-C retains nearly 100% of its maximum capacity after 100 cycles. It should be noted that besides the limited free water content, 5 M $Ca(NO_3)_2$ is also characterized by a higher viscosity than 3 M KNO_3, as shown in Fig. S4. This hinders the transport of dissolution products away from the electrode surface

and further impedes degradation. Previous research shows that confining the dissolved transition metal ions in close vicinity of the electrode can trigger ultrafast nucleation and restructuring of the PBA in the presence of $Fe(CN)_6$-anions [38]. Similar to the mechanism driving the electrochemical deposition of PBAs used to synthesize thin films, the active material can regrow on the electrode when the dissolution products remain close to the electrode [39]. Hence, the sluggish diffusion of dissolved transition metal ions in the bulk electrolyte has been linked to highly improved PBA cycling stability [40]. While this approach effectively enhances the long-term performance of all investigated Mn-based PBAs, it also significantly alters their reduction and oxidation potentials. For all three electrodes, the peaks are shifted in the negative direction and display an increased peak-to-peak separation, indicating lower reversibility of the redox reaction. Both effects can be considered disadvantageous, as they are detrimental to the efficiency, cell voltage, and hence energy density of the full cell.

Therefore, to combine the stabilizing influence of Ca^{2+} and the favorable (de-)intercalation potentials of the PBAs in the presence of K^+, a mixed 2.5 M $Ca(NO_3)_2$ + 1.5 M KNO_3 electrolyte, denoted as CKN2515, was prepared. This approach takes advantage of the relatively high co-solubility of $Ca(NO_3)_2$ and KNO_3, allowing the mixing of the two saturated solutions without the crystallization of either salt. While the resulting mixture features a lower viscosity than 5 M $Ca(NO_3)_2$, its viscosity is about 4 times higher than for 3 M KNO_3 (Fig. S4). The cycling performances of MnHCF, FeMnHCF-A, and FeMnHCF-C in CKN2515 are shown in Fig. 2 (g–i), respectively. The capacity retention over 100 cycles is shown in Fig. 2 (l). In the CV of MnHCF, the peaks corresponding to Ca^{2+} (de-)intercalation can be observed in the first few cycles but vanish quickly. Afterward, the reduction peak shifts to the right, resulting in a CV shape similar to that of pure KNO_3, indicating that the intercalation of K-ions is preferred over Ca-ions. While MnHCF still degrades severely, FeMnHCF-A and FeMnHCF-C display significant stability improvements, similar to 5 M $Ca(NO_3)_2$, with FeMnHCF-C being the most stable. Furthermore, the redox peak positions and shapes of the iron-doped PBAs in CKN2515 are the same as in pure KNO_3, showing that Ca^{2+} only takes a passive role in the electrolyte and is not intercalated into the crystal lattice. Hence, the mixed electrolyte preserves the stabilizing effect of the Ca-based electrolyte, as well as the advantageous redox potential and reversibility of the cathode in the K-based electrolyte. In summary, the cyclability of Mn-based PBAs was largely improved by combining Mn-substitution, the use of a chelating agent during synthesis for controlled crystallinity, and electrolyte composition tuning.

To investigate the electrochemical performance of the optimized FeMnHCF-C cathode in CKN2515, galvanostatic cycling was carried out at different C-rates ranging from 1 C to 100 C. The potential range was set to 0.0–1.3 V vs. SSC since parasitic OER currents were observed in the CVs at potentials above 1.3 V vs. SSC. The resulting charge and discharge curves are shown in Fig. 3 (a). At 1 C, the discharge profile displays a sloping plateau between 0.95 and 0.60 V vs. SSC and a reversible specific capacity of ~109 mA h g^{-1} at a coulombic efficiency of ~92%. The FeMnHCF-C electrode also exhibits excellent fast-charging capabilities, retaining ~91% of the discharge capacity from 1 C to 10 C. Moreover, it displays exceptional performance even at high rates (30 C–100 C) with a specific discharge capacity of ~60 mA h g^{-1} at 100 C and nearly 100% efficiency at all rates above 10 C.

Fig. 3 (b) shows the CV curves of FeMnHCF-C recorded at different scan rates ranging from 1 to 50 mV s^{-1}. The peak-to-peak separation between the dominant oxidation peak and the two main reduction peaks increases with increasing scan rate due to the uncompensated resistance linked to the ionic conductivity of the electrolyte. However, at 1 mV s^{-1}, it drops to ~20 and ~120 mV for the left and right peaks, respectively, indicating that the intercalation of K^+ into the PBA structure is highly reversible. Moreover, it is possible to deduce information about the process limiting the charge transfer by relating the peak current j_p to the scan rate v

$$j_p = b \cdot v^a \quad (1)$$

For surface-limited processes, parameter a approaches 1.0, while for mass-transport-limited processes it approaches 0.5. As shown in the inset in Fig. 3 (b), a is close to 0.56 (evaluated for the main oxidation peak), indicating that the charge transfer is mostly mass-transport limited, as expected for slurry electrodes of intercalation-type materials.

To maintain the superior performance of the FeMnHCF-C cathode in a full cell setup, an anode with equally high specific capacity, stability, and fast charging capabilities is required. Here, the organic redox-active material PNFE was employed as the anode, as it was previously shown to deliver extremely high-rate capabilities and exceptional cyclability [23,24,41,42]. PNFE was synthesized in a one-step dehydration condensation reaction between NTCDA and EDA in NMP, and the structure was confirmed by FTIR (Fig. S5(b)). An SEM image of the anode consisting of PNFE particles, typically between 100 and 500 nm in size, carbon black, and the Nafion binder is shown in Fig. S5(a). The electrochemical performance of the anode in the CKN2515 aqueous electrolyte was investigated by galvanostatic cycling and cyclic voltammetry. Fig. 4 (a) shows the charge and discharge profiles recorded at different C-rates ranging from 1 C to 100 C. At 1 C, PNFE displays a reversible specific capacity of ~150 mA h g^{-1}, maintaining ca. 93% at 10 C. Moreover, it shows an exceptional high-rate capability with ca. 66% capacity retention even at 100 C, closely matching the fast-charging capabilities of the cathode.

Fig. 4 (b) shows the CV curves of the anode recorded at different scan rates ranging from 1 to 50 mV s^{-1}. As shown in our previous work, PNFE undergoes a two-step redox process, corresponding to the subsequent enolization of two carbonyl groups [24]. This general mechanism remains unchanged regardless of whether monovalent or divalent cations are inserted [23]. In the anodic scan, this is reflected by two distinct oxidation peaks, whereas the reduction peaks overlap in the cathodic scan. It is worth noting that at the PNFE anode, the oxidation and reduction of the active material are compensated by Ca-ions rather than K-ions in the mixed CKN2515 electrolyte, which can easily be seen by comparing the peak shape and positions of the measurement conducted in CKN2515 with the CVs of PNFE recorded in 3 M KNO_3 and 5 M $Ca(NO_3)_2$ depicted in Fig. S5(c) and (d), respectively. By relating the peak current of the main reduction peak with the scan rate via equation (1), parameter a is found to be close to 0.9, indicating that for the anode, the charge transfer process is mainly surface-limited. These minimal diffusion limitations can be linked to the pseudo-capacitive charge storage mechanism of the polyimide [24,41,42].

Based on the promising performance of both the FeMnHCF-C cathode and the PNFE anode in the CKN2515 aqueous electrolyte, a PNFE/CKN2515/FeMnHCF-C full cell was assembled, with an anode to cathode active material mass ratio of 1:1.4. Fig. 5 (a) shows the (dis-)charge profiles of the full battery recorded at different C-rates between 1 C (62 mA g^{-1}) and 100 C (6.2 A g^{-1}). The corresponding data can be found in Table S2. Within the voltage window from 0.0 to 1.9 V at 1 C, the battery exhibits a reversible capacity of ~62 mA h g^{-1} and a sloping discharge plateau between 1.8 and 1.0 V. It also shows superior fast charging capabilities with ~85% capacity retention at 10 C and ~25% capacity retention at high rates of up to 100 C. The coulombic efficiency increases from ~94% at 1 C to above 99% at higher rates, confirming that the CKN2515 aqueous electrolyte is electrochemically stable within the operating voltage

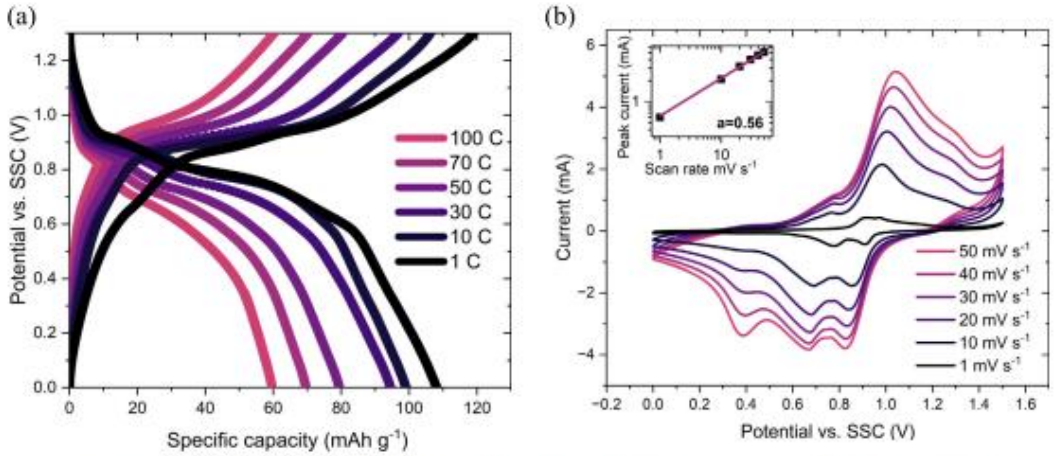


Fig. 3. Electrochemical performance of FeMnHCF-C in the 2.5 M $Ca(NO_3)_2$ + 1.5 M KNO_3 (CKN2515) electrolyte. (a) Galvanostatic (dis-)charge curves recorded at different C-rates. (b) CVs recorded at different scan rates.

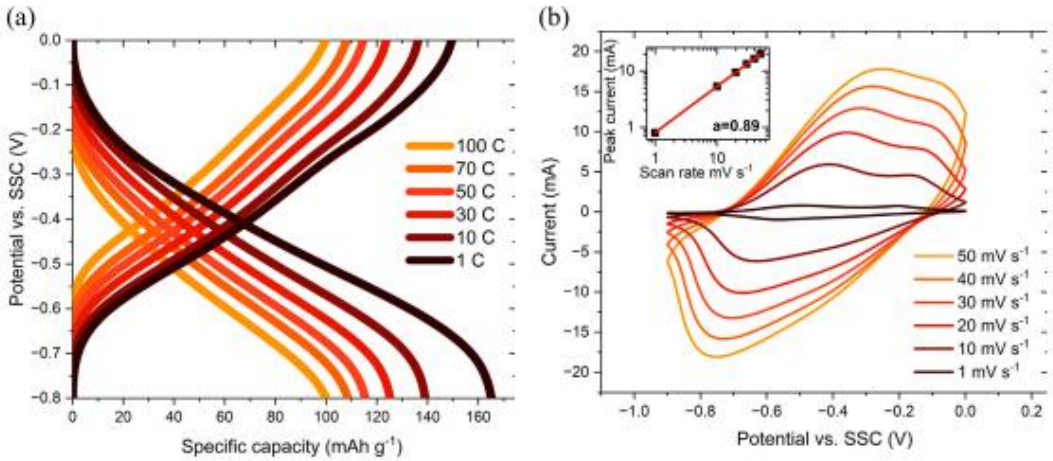


Fig. 4. Electrochemical performance of the PNFE anode in the 2.5 M $Ca(NO_3)_2$ + 1.5 M KNO_3 (CKN2515) aqueous electrolyte. (a) Galvanostatic (dis-)charge curves recorded at different C-rates. (b) CVs recorded at different scan rates.

window of the battery. The cycling stability of the full cell was assessed by continuously charging and discharging it at 10 C for 600 cycles. As shown in Fig. 5 (b) and (c), the battery retains ~80% of its maximum specific discharge capacity, which is reached after ca. 50 cycles due to the slow penetration of the electrolyte into the pores of the slurry electrodes.

The corresponding energy and power densities for each C-rate can be calculated by integrating the discharge curves and by multiplying the specific current with the average discharge voltage, respectively. At a power density of ca. 70 W kg^{-1}, the battery displays a high energy density of 72 Wh kg^{-1}, of which 12 Wh kg^{-1} can be retained even at extremely high power densities of up to ~5000 W kg^{-1}. These performance parameters are compared to state-of-the-art AKIBs reported in recent literature in Fig. 5 (d). Most notably, Jiang et al. achieved a slightly higher energy density of 80 Wh kg^{-1} with an aqueous battery based on a FeMnHCF cathode and an organic 3,4,9,10-perylene tetracarboxylic diimide (PTCDI) anode [22]. Similar high energy densities were also reported by Liang et al. in 2021 using the same anode material and a KVO_x cathode [44]. Furthermore, the designs proposed by Wang et al., Li et al., and Chen et al. are worth mentioning due to their competitive performances [34,35,43]. However, it should be noted that except for the PNFE/sat. KNO_3/FeHCF aqueous battery reported by Wang et al., all other compositions rely on highly concentrated electrolytes based on relatively expensive salts, such as 22 m KCF_3SO_3 or 30 m KFSI. While these water-in-salt electrolytes generally enable even longer cycle lives than the one shown in this work, their use is linked to largely increased material costs compared to the proposed CKN2515 electrolyte, which consists of abundant and available materials. As rightfully mentioned by Jiang et al., the economic viability of AKIBs will require employing lower-concentration electrolytes based on more cost-efficient salts [22]. Hence, modifying the FeMnHCF-C synthesis, combined with the $Ca(NO_3)_2$ electrolyte additive and the highly stable PNFE anode, can be a step toward the practical application of AKIBs for energy storage.

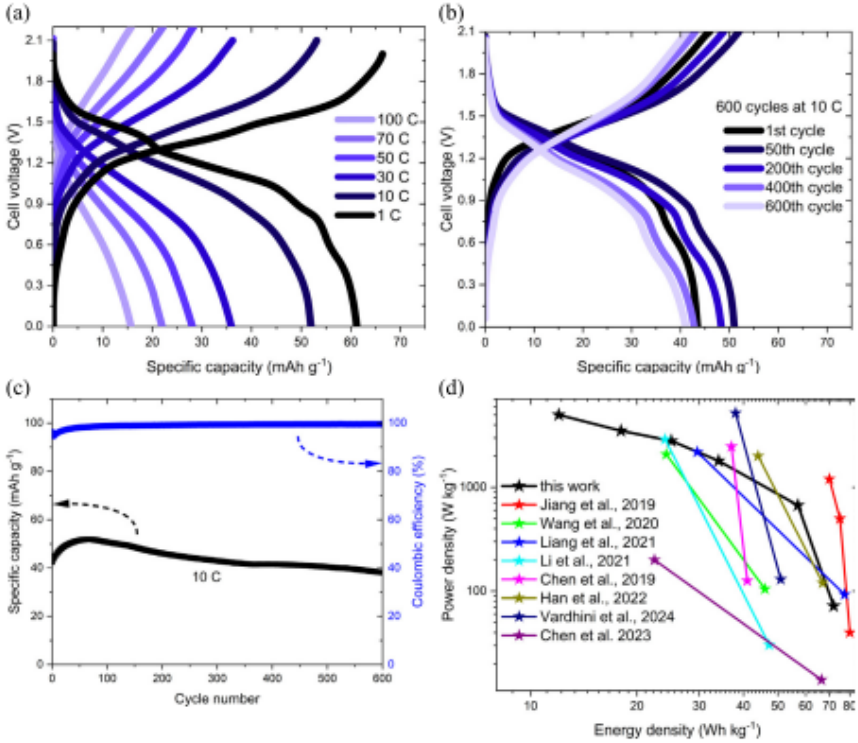


Fig. 5. Electrochemical performance of the PNFE/CKN2515/FeMnHCF-C full cell. (a) (Dis-)charge profiles recorded at different C-rates. (b) (Dis-)charge profiles of different cycles recorded at 10 C. (c) Cycling stability recorded over 600 cycles at 10 C. (d) Ragone plot comparing the performance of the battery in this work with other state-of-the-art AKIBs reported by Jiang et al. [22], Wang et al. [43], Liang et al. [44], Li et al. [35], Chen et al. [34], Han et al. [45], Vardhini et al. [46], and Chen et al. [47] The specific capacity and energy density are normalized to the combined anode and cathode active material mass.

4. Conclusions

In this study, we have developed a sustainable, high-performance aqueous potassium-ion battery (AKIB) utilizing a Fe-doped $FeMn[Fe(CN)_6]$ cathode, an organic PNFE anode, and a mixed KNO_3 + $Ca(NO_3)_2$ electrolyte. Through a series of strategic modifications, we significantly enhanced the cycle life of the Mn-based Prussian blue analog (PBA) cathode. Specifically, we investigated the synergistic effects of Fe doping, controlled crystal growth facilitated by chelating agents, and the incorporation of Ca-ions as an electrolyte additive. The optimized cathode demonstrates a high specific capacity of approximately 109 mA h g^{-1} and excellent capacity retention even at rapid charging rates of up to 100 C. Complementing this, the PNFE anode achieves a notable specific capacity of around 150 mA h g^{-1} and exceptional high-rate performance.

Combined, the PNFE/CKN2515/FeMnHCF-C full cell achieves a reversible specific capacity of ~60 mA h g^{-1}, an energy density exceeding 70 Wh kg^{-1}, and a maximum power density of approximately 5000 W kg^{-1}, based on the active materials in the anode and cathode. Remarkably, this battery delivers competitive performance compared to state-of-the-art AKIBs that utilize more expensive and less sustainable water-in-salt electrolytes like KCF_3SO_3 or KFSI. These results underscore the potential of this cost-effective and environmentally friendly system to advance the development of sustainable energy storage technologies.

Author contributions

R. Streng and A.S. Bandarenka proposed the concept. R. Streng, T. Steeger, and S. Abel carried out the electrochemical measurements. P. Schneider measured the XRD data. C. Benning carried out the ICP-MS measurements. D. Gryc performed BET measurements. B. Miller Naranjo performed the viscosity experiments. R. Streng, M. Hussain, and T. Steeger analyzed the electrochemical and BET data, respectively. A. Senyshyn evaluated the XRD patterns. R. Streng, T. Steeger, M. Hussain and K. Cicvarić co-wrote the manuscript. O. Lieleg, M. Elsner, A.S. Bandarenka, and K. Cicvarić supervised the project. A.S. Bandarenka acquired funding. All authors participated in data analysis and manuscript discussion.

CRediT authorship contribution statement

Raphael L. Streng: Writing – review & editing, Writing – original draft, Methodology, Investigation, Formal analysis, Data curation, Conceptualization. **Tim Steeger:** Writing – review & editing, Investigation, Formal analysis, Data curation. **Anatoliy Senyshyn:** Writing – review & editing, Software, Formal analysis, Data curation. **Steffen Abel:** Formal analysis, Data curation. **Peter Schneider:** Writing – review & editing, Formal analysis, Data curation. **Christine Benning:** Writing – review & editing, Formal analysis, Data curation. **Bernardo Miller Naranjo:** Writing – review & editing, Formal analysis, Data curation. **David Gryc:** Writing – review &

editing, Formal analysis, Data curation. **Mian Zahid Hussain:** Writing – review & editing, Formal analysis, Data curation. **Oliver Lieleg:** Writing – review & editing, Supervision. **Martin Elsner:** Writing – review & editing, Formal analysis. **Aliaksandr S. Bandarenka:** Writing – review & editing, Supervision, Software, Resources, Project administration, Methodology, Funding acquisition, Formal analysis, Conceptualization. **Katarina Cicvarić:** Writing – review & editing, Writing – original draft, Supervision, Methodology, Formal analysis, Conceptualization.

Declaration of competing interest

The authors declare that they have no known competing financial interests or personal relationships that could have appeared to influence the work reported in this paper.

Acknowledgments

The authors thank Mr. Siegfried Schreier for his assistance in acquiring SEM data. Furthermore, the authors acknowledge Dr. Sergei Vagin's assistance in synthesizing PNFE and acquiring the FTIR data.

We acknowledge Deutsche Forschungsgemeinschaft (DFG, German Research Foundation) under Germany's Excellence Strategy–EXC 2089/1–390776260 (e-conversion) for funding. ASB acknowledges additional financial support from TUM Innovation Network for Artificial Intelligence powered Multifunctional Material Design (ARTEMIS).

Appendix A. Supplementary material

Supplementary data to this article can be found online at https://doi.org/10.1016/j.jechem.2025.02.039.

References

[1] C.P. Grey, D.S. Hall, Nat. Commun. 11 (2020) 6279.
[2] T. Kim, W. Song, D.-Y. Son, L.K. Ono, Y. Qi, J. Mater. Chem. A 7 (2019) 2942.
[3] H. Zhang, J. Huang, X. Qian, X. Wang, W. Xu, Y. Lin, J. Power Sources 480 (2020) 228836.
[4] H. Wu, X. Zhang, Y. Wang, J. Zhou, H. Huang, J. Energy Chem. 79 (2023) 162.
[5] Y. Ma, Z. Ma, C. Xu, J. Yang, Y. Dong, X. Yang, Y. Yang, B. Xu, J. Energy Chem. 63 (2021) 288.
[6] S.H. Lee, J.H. Park, T. Kim, K. Kwak, T. Kim, S. Kang, S.M. Lee, H.S. Park, W.B. Ko, M. Choi, J. Alloys Compd. 922 (2022) 166155.
[7] M.A. Al-Abdullah, M. Rameez, R.A. Shakoor, J. Energy Storage 52 (2022) 104969.
[8] F. Wang, X. Wang, J. Li, C. Wang, D. Liu, S. Chen, L. Xing, Z. Wu, X. Wang, Electrochim. Acta 440 (2023) 141671.
[9] R. Hu, C. Chen, X. Zhang, J. Luo, H. Jiang, D. Zhou, M. Zhou, J. Power Sources 532 (2022) 231381.
[10] H. Xu, X. Li, X. Wu, Y. Yan, Z. Yang, H. Liu, J. Power Sources 556 (2023) 232519.
[11] Y. Zhai, H. Wang, J. Xu, D. Sun, W. Zhao, J. Zhang, C. Cao, Chem. Eng. J. 430 (2022) 132960.
[12] K. Yadav, A. Singh, A. Khosla, J. Energy Storage 55 (2022) 105511.
[13] W. Zhao, J. Xu, Y. Zhai, J. Zhang, C. Cao, D. Sun, J. Power Sources 533 (2022) 231382.
[14] C. Ma, C. Lin, N. Li, Y. Chen, Y. Yang, L. Tan, Z. Wang, Q. Zhang, Y. Zhu, Small 20 (2024) e2310184.
[15] C.D. Wessells, S.V. Peddada, R.A. Huggins, Y. Cui, Nano Lett. 11 (2011) 5421–5425.
[16] C.D. Wessells, R.A. Huggins, Y. Cui, Nat. Commun. 2 (2011) 550.
[17] D. Su, A. McDonagh, S.-Z. Qiao, G. Wang, Adv. Mater. 29 (2017) 1604007.
[18] X. Wei, J. Wei, Y. Song, D. Wu, X.D. Liu, H. Chen, P. Xiao, Y. Zhang, Chem. Commun. 57 (2021) 7019–7022.
[19] L. Xue, Y. Li, H. Gao, W. Zhou, X. Lü, W. Kaveevivitchai, A. Manthiram, J.B. Goodenough, J. Am. Chem. Soc. 139 (2017) 2164–2167.
[20] Y. Tang, W. Li, P. Feng, M. Zhou, K. Wang, Y. Wang, K. Zaghib, K. Jiang, Adv. Funct. Mater. 30 (2020) 1908754.
[21] L. Deng, J. Qu, X. Niu, J. Liu, J. Zhang, Y. Hong, M. Feng, J. Wang, M. Hu, L. Zeng, Q. Zhang, L. Guo, Y. Zhu, Nat. Commun. 12 (2021) 2167.
[22] L. Jiang, Y. Lu, C. Zhao, L. Liu, J. Zhang, Q. Zhang, X. Shen, J. Zhao, X. Yu, H. Li, X. Huang, L. Chen, Y.-S. Hu, Nat. Energy 4 (2019) 495–503.
[23] R.L. Streng, S. Reiser, S. Wager, N. Pommer, A.S. Bandarenka, ChemSusChem (2024) e202401469. https://doi.org/10.1002/cssc.202401469.
[24] R.L. Streng, S. Vagin, Y. Guo, B. Rieger, A.S. Bandarenka, Energy Adv. 3 (2024) 874–882.
[25] J. Peng, Y. Gao, H. Zhang, Z. Liu, W. Zhang, L. Li, Y. Qiao, W. Yang, J. Wang, S. Dou, S. Chou, Angew. Chem. Int. Ed. 61 (2022) e202205867.
[26] M. Qin, W. Ren, R. Jiang, Q. Li, X. Yao, S. Wang, Y. You, L. Mai, ACS Appl. Mater. Interfaces 13 (2021) 3999–4007.
[27] X. Ding, Q. Zhou, Z. Wang, L. Liu, Y. Wang, T. Song, F. Wu, H. Gao, J. Mater. Chem. A 12 (2024) 27598–27609.
[28] X. Bie, K. Kubota, T. Hosaka, K. Chihara, S. Komaba, J. Mater. Chem. A 5 (2017) 4325–4330.
[29] J. Song, L. Wang, Y. Lu, J. Liu, B. Guo, P. Xiao, J.-J. Lee, X.-Q. Yang, G. Henkelman, J.B. Goodenough, J. Am. Chem. Soc. 137 (2015) 2658–2664.
[30] X. Zhao, Z. Xing, C. Huang, J. Mater. Chem. A 11 (2023) 22835–22844.
[31] J. Dai, S. Tan, L. Wang, F. Ling, F. Duan, M. Ma, Y. Shao, X. Rui, Y. Yao, E. Hu, X. Wu, C. Li, Y. Yu, ACS Nano 17 (2023) 20949–20961.
[32] Y. Moritomo, S. Urase, T. Shibata, Electrochim. Acta 210 (2016) 963–969.
[33] M. Maisuradze, M. Li, M. Gaboardi, G. Aquilanti, J. Rikkert Plaisier, M. Giorgetti, Adv. Mater. Sci. Technol. 6 (2024) 2200010.
[34] H. Chen, Z. Zhang, Z. Wei, G. Chen, X. Yang, C. Wang, F. Du, Sustainable Energy Fuels 4 (2020) 128–131.
[35] Y. Li, W. Deng, Z. Zhou, C. Li, M. Zhang, X. Yuan, J. Hu, H. Chen, R. Li, J. Mater. Chem. A 9 (2021) 2822–2829.
[36] G. Hummer, L.R. Pratt, A.E. García, J. Phys. Chem. 100 (1996) 1206–1215.
[37] X. Lamprecht, F. Speck, P. Marzak, S. Cherevko, A.S. Bandarenka, ACS Appl. Mater. Interfaces 14 (2022) 3515–3525.
[38] Z. Zhao, W. Zhang, M. Liu, S.J. Yoo, N. Yue, F. Liu, X. Zhou, K. Song, J.-G. Kim, Z. Chen, X.-Y. Lang, Q. Jiang, C. Zhi, W. Zheng, Nano Lett. 23 (2023) 5307–5316.
[39] R. Yang, Z. Qian, J. Deng, J. Electrochem. Soc. 145 (1998) 2231–2236.
[40] L. Chen, W. Sun, K. Xu, Q. Dong, L. Zheng, J. Wang, D. Lu, Y. Shen, J. Zhang, F. Fu, H. Kong, J. Qin, H. Chen, ACS Energy Lett. 7 (2022) 1672–1678.
[41] W. Deng, Y. Shen, J. Qian, H. Yang, Chem. Commun. 51 (2015) 5097–5099.
[42] L. Chen, J.L. Bao, X. Dong, D.G. Truhlar, Y. Wang, C. Wang, Y. Xia, ACS Energy Lett. 2 (2017) 1115–1121.
[43] M. Wang, H. Wang, H. Zhang, X. Li, J. Energy Chem. 48 (2020) 14–20.
[44] G. Liang, Z. Gan, X. Wang, X. Jin, B. Xiong, X. Zhang, S. Chen, Y. Wang, H. He, C. Zhi, ACS Nano 15 (2021) 17717–17728.
[45] B. Han, D. Zhang, X. Liu, Z. Wang, W. Qu, S. Zhang, C. Deng, J. Mater. Chem. A 10 (2022) 13508–13518.
[46] G. Vardhini, P.S. Dilip, S.A. Kumar, S. Suriyakumar, M. Hariharan, M.M. Shaijumon, ACS Appl. Mater. Interfaces 16 (2024) 48782–48791.
[47] J. Chen, S. Lei, S. Zhang, C. Zhu, Q. Liu, C. Wang, Z. Zhang, S. Wang, Y. Shi, L. Yin, R. Wang, Adv. Funct. Mater. 33 (2023) 2201507.

5. Degradation Mechanisms of Prussian Blue Analogs and State-of-the-Art Approaches for Stability Optimization: A Review.

J. Sterzinger, R.L. Streng, S. Chen, R. Götz, W. Hu, J. Li, A.S. Bandarenka. *J. Phys. Chem. C* **2025**, 129, 7135-7153.

THE JOURNAL OF PHYSICAL CHEMISTRY C
A JOURNAL OF THE AMERICAN CHEMICAL SOCIETY
pubs.acs.org/JPCC

Open Access
This article is licensed under CC-BY 4.0

Review

Degradation Mechanisms of Prussian Blue Analogues and State-of-the-Art Approaches for Stability Optimization: A Review

Published as part of The Journal of Physical Chemistry C special issue "Degradation of Electrochemical Materials in Energy Conversion and Storage".

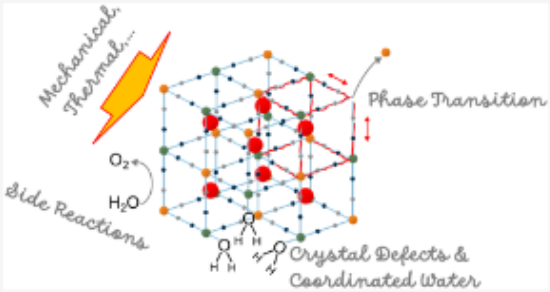
Johannes Sterzinger, Raphael Streng, Shuai Chen, Rainer Götz, Wang Hu, Jinyang Li, and Aliaksandr S. Bandarenka*

Cite This: J. Phys. Chem. C 2025, 129, 7135−7153

Read Online

ACCESS | Metrics & More | Article Recommendations

ABSTRACT: Prussian Blue Analogues (PBAs) are promising candidates for next-generation battery materials due to their open structure framework, high ionic conductivity, and compositional flexibility, enabling rapid ion transport and high power density. Despite these advantages, their practical application remains significantly hindered by long-term performance and stability challenges, primarily driven by degradation mechanisms inherent to PBAs. This review provides a comprehensive overview of recent research on the degradation processes affecting PBAs beyond Li-ion batteries, such as alkali metal-ion batteries or Zn-ion batteries. We discuss the impact of transition metal dissolution, phase transitions, the Jahn−Teller effect, crystal defects, coordinated water, side reactions, and other degradation mechanisms. We also outline various stabilization strategies developed in recent years, including advancements in PBA synthesis, postsynthesis treatments, optimization of the electrode composition, coatings, electrolyte modifications, and optimized cycling protocols. Finally, we propose future research directions to further advance the stability and durability of PBAs. We aim to inspire continued investigation and more studies of PBAs, paving the way for more efficient, sustainable, and highly stable future energy storage devices.

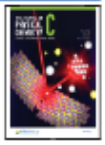


1. INTRODUCTION

Batteries have become indispensable in modern life, enabling the transition toward a sustainable energy future.[1−3] They are an essential part of technologies ranging from portable electronics to electric vehicles and large-scale energy storage systems.[4−7] In particular, with the increasing reliance on renewable energy sources such as solar and wind, which are inherently intermittent, efficient and reliable energy storage solutions are critical to balance supply and demand.[8−10] Simultaneously, the widespread adoption of electric vehicles and portable devices demands batteries that combine high energy and high power density, long service life, affordability, and sustainability.[11]

Lithium-ion batteries (LIBs) have long dominated the battery market due to their excellent performance characteristics.[12−15] However, concerns about the limited availability of lithium, the environmental impact of its extraction, the humanitarian and economic issues associated with cobalt, and the inherent safety risks of LIBs have driven the search for alternative chemistries.[16−19] Therefore, battery technologies based on more available charge carrier ions such as Na^+, K^+, Mg^{2+}, Ca^{2+}, Zn^{2+}, and Al^{3+} have attracted renewed interest. Due to the larger ionic radii of these cations compared to Li^+, though, novel or alternative intercalation materials need to be developed and investigated. In this context, Prussian Blue Analogues (PBAs), a family of transition metal hexacyanoferrates, have emerged as promising candidates for next-generation battery materials.[20,21] PBAs can be represented by the general formula $A_xM^1[M^2(CN)_6]_{1-y}\cdot zH_2O$ where A is an intercalated, usually an alkali-metal, ion. M^1 and M^2 represent transition metals. The values y and z correspond to the fraction of $M^2(CN)_6$ vacancies and zeolitic or coordinated water, respectively. M^1 and M^2 are interconnected by C≡N linkers, forming an open-framework structure with large interstitial sites that can reversibly store a wide range of cations from an

Received: February 7, 2025
Revised: March 21, 2025
Accepted: March 21, 2025
Published: April 3, 2025



ACS Publications
© 2025 The Authors. Published by American Chemical Society

https://doi.org/10.1021/acs.jpcc.5c00877
J. Phys. Chem. C 2025, 129, 7135−7153

electrolyte. These materials are particularly suited for aqueous and nonaqueous alkali-ion, alkaline-earth-ion, and Zn-ion batteries, which rely on abundant and widely distributed elements.[22−25] Their unique characteristics—such as the open-framework structure, high ionic conductivity, and compositional flexibility—enable rapid ion transport, high power densities, and the potential for cost-effective and environmentally friendly energy storage solutions.[26,27]

Despite their many advantages, the practical use of PBAs faces significant challenges, particularly because of their unsatisfactory long-term performance and stability. While various review articles have discussed the structure, applications, and electrochemical properties of PBAs, capacity fading and cycling stability are usually not discussed in detail.[20,22,28−30] Like any battery material, PBAs are subject to various degradation mechanisms that reduce their capacity, cycling stability, and overall efficiency. Structural collapse, water (de)intercalation, and transition metal dissolution are key processes leading to performance decay.[26,31−34] Environmental factors such as electrolyte composition, pH, and temperature further influence these degradation pathways, complicating the development of stable PBA-based systems.[35−37] Addressing these challenges requires a profound understanding of the degradation mechanisms that affect PBAs under real-world conditions. Advances in characterization techniques and computational modeling have provided valuable insights into the molecular-level processes driving degradation.[38−41] These studies have revealed that structural and compositional factors, including the crystallinity of the PBAs, the type of transition metals used, and the presence of coordinated water, play a critical role in determining their stability.[42−44] Additionally, strategies such as surface modifications, compositional tuning, and electrolyte optimization are being explored to mitigate degradation and enhance the longevity of PBA-based batteries.[45−47] However, there are still very few comprehensive reviews that cover all of these different degradation mechanisms and their potential interplay and the wide variety of strategies to mitigate them.

This short review provides a detailed analysis of the degradation mechanisms affecting PBAs, with a focus on their implications for energy storage applications. Figure 1 presents a schematic representation of the overall structure of PBAs, as well as a summary of their inherent degradation mechanisms and potential stabilization strategies explored in this review. By linking the degradation mechanisms to structural and environmental factors, we aim to highlight the fundamental challenges and opportunities for improving PBA stability. Furthermore, it highlights recent advancements in material design and engineering approaches that address these hurdles, offering a roadmap for the development of robust and efficient PBA-based batteries. Through these insights, we aim to contribute to the broader goal of advancing sustainable and cost-effective energy storage technologies for the future.

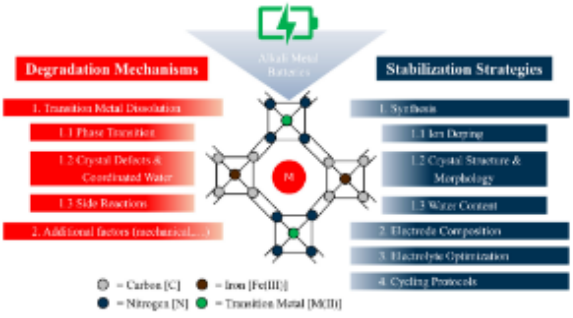


Figure 1. A schematic illustration of the general structure of PBAs, along with an overview of the PBA inherent degradation mechanisms and potential stabilization strategies discussed in this review.

2. DEGRADATION MECHANISMS

The degradation of PBA cathodes is mainly linked to the dissolution of transition metals from the lattice framework.[35] The loss of either N-coordinated or C-coordinated transition metals results in structural collapse or a reduction in available interstitial sites for cation storage, ultimately leading to a capacity decline. Various underlying mechanisms can induce transition metal dissolution including phase transitions (most prominently the Jahn−Teller effect), crystal defects, coordinated water, and side reactions. In addition to transition metal dissolution, PBA degradation is influenced by common factors that also affect other battery electrode materials, such as mechanical strain during intercalation and de-intercalation as well as thermal effects. In this section, the multiple underlying mechanisms triggering transition metal dissolution as well as common factors, such as mechanical strain during intercalation, will be thoroughly discussed.

2.1. Transition Metal Dissolution. *2.1.1. Phase Transitions.* PBAs exist in various crystal phases, including cubic, monoclinic, and tetragonal. At higher concentrations of alkali metal (A) per unit volume, rhombohedral PBAs can also form. These rhombohedral PBAs can be produced either by drying monoclinic PBAs or through direct synthesis.[48,49] Additionally, Peng et al. report a unique Cerium Hexacyanoferrate (Ce-HCF) that exhibits a hexagonal structure.[50]

During charging and discharging, the crystal phases of PBAs often change due to the intercalation and de-intercalation of alkali metal (A) ions. This process is known as the phase transition. Thereby, the phases roughly correlate with the A^+ content within the unit cell.[51] Generally, PBAs can be categorized into two distinct groups. The first group includes materials that undergo two electrochemical transitions at both transition metal centers M^1 and M^2. FeHCF, CoHCF, and MnHCF are the most prominent examples of this group. High specific capacities characterize these PBAs; however, they often suffer from poor cyclability. The second group includes materials with one inert transition metal, such as NiHCF and CuHCF, where only Fe is redox active. These materials display lower specific capacities but longer cycle lives.

FeHCF and CoHCF usually display a cubic phase in the oxidized and single-reduced state, which changes to rhombohedral upon the second reduction step.[52,53] MnHCF tends to undergo three transitions from tetragonal (oxidized) to cubic (single-reduced) and monoclinic (fully reduced).[54] Depending on the synthesis procedure, NiHCF and CuHCF assume cubic phases, which can be shifted toward monoclinic phases at higher intercalated A^+ contents.[55−57]

Phase transitions do not have to be detrimental to the stability per se, as reversible cycling is possible—even when phases change during charging or discharging.[48,49] However, observed gradual capacity drops are sometimes ascribed to specific phase transitions.[58] For example, monoclinic PBA (e.g., Na-MnHCF) becomes cubic upon the de-intercalation of one Na ion per formula unit at first but then irreversibly

https://doi.org/10.1021/acs.jpcc.5c00877
J. Phys. Chem. C 2025, 129, 7135−7153

transforms to tetragonal Na-MnMHCF with the removal of the second Na ion. In contrast, a rhombohedral version of the same PBA allows the reversible cycling between the charged (tetragonal) and the discharged (rhombohedral) state (Figure 2).[44] The decisive factor for phase transitions is how the crystal

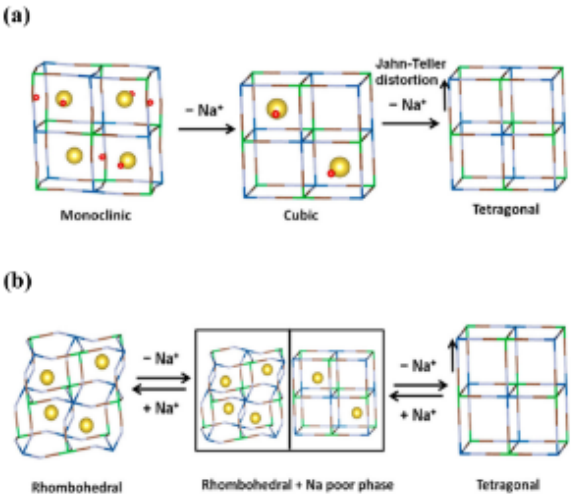


Figure 2. Structural changes of Na-MnHCF upon intercalation and de-intercalation of sodium ions. (a) The monoclinic material turns into a cubic and then a tetragonal configuration after Na^+ extraction. This process is accompanied by Jahn−Teller distortion, ultimately resulting in an irreversible degradation of the PBA. (b) In comparison, starting from a PBA with a rhombohedral phase allows reversible cycling. Adapted with permission from ref 44. Copyright 2015 American Chemical Society.

structure adjusts to the uptake and removal of the charge carrier ions. Especially for iron- and manganese-containing PBAs, there is a particular phase transition mechanism that determines the prolonged stability of the crystal structure upon repeated cycling: the so-called Jahn−Teller effect.

The Jahn−Teller effect, caused by the interaction between degenerate electronic states and symmetry-lowering vibrational modes, explains distortions in molecular systems with nonlinear geometries. This leads to a distorted d-orbital electron density and lattice deformation, driven by an intrinsic thermodynamic force.[59,60] Driven by this thermodynamic force, such systems undergo symmetry-lowering distortions. This tends to optimize the electronic energy levels, reduce Coulomb repulsion, and minimize the total electronic energy.[61−63] Typically, for general octahedral coordination compounds of PBAs containing transition metal ions, the d-orbitals can be split into the t_{2g} (triply degenerate) and e_g (doubly degenerate). The Jahn−Teller distortion and corresponding structural change can arise from the uneven occupancy of the above-mentioned orbitals (t_{2g} and e_g), related to the two types of electro states (high-spin and low-spin) based on the interaction between crystal field splitting energy (Δ) and electronic pairing energy (P).

In detail, systems with electronic configurations such as d^3, low-spin d^6, d^8, and d^{10} possess a subtle Jahn−Teller distortion due to a uniform orbital occupancy. As for the uneven orbital occupancy, the Jahn−Teller effect can be categorized into strong and weak types in most instances: the former comes from the uneven occupancy of the e_g orbitals (such as high-spin d^4, low-spin d^7, and d^9),[64] while the latter is due to the uneven occupancy of the t_{2g} orbitals (such as d^1, d^2, low-spin d^4 and d^5, high-spin d^6, and d^7).[63]

For example, $Na_xMn[Fe(CN)_6]_y{\cdot}nH_2O$ transforms from a monoclinic lattice into a cubic one during the charge−discharge process. This poses potential vulnerabilities to the lattice structure and ion transfer path.[65−67] Similar structural changes from cubic to rhombohedral in $Na_xFe[Fe(CN)_6]_y{\cdot}nH_2O$ and $Na_xCo[Fe(CN)_6]_y{\cdot}nH_2O$ had been observed as well, leading to a degradation of the cathode in some situations, especially in the case of poor crystal structures.[68,69]

Consequently, mitigating the Jahn−Teller effect is crucial to achieving an extended lifespan for PBA electrodes.

2.1.2. Crystal Defects and Coordinated Water. As mentioned previously, PBAs can be represented by the chemical formula $A_xM[Fe(CN)_6]_y{\cdot}zH_2O$ ($0 \le x \le 2$; $0 < y \le 1$), where A represents alkali metal elements (such as Li, Na, and K) and M represents transition metals (such as Fe, Mn, Ni, Co, Cu, and Zn).[20] The ideal crystal structure of PBAs is shown in Figure 3a, where CN^- ligands connect the M and Fe

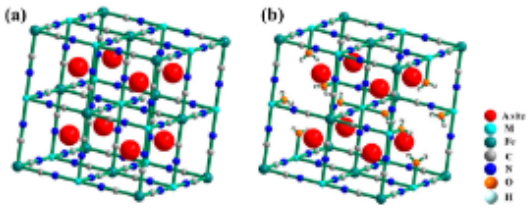


Figure 3. Schematic crystal structures of (a) the PBA framework without any defects and (b) PBA crystal structures ($NaM[Fe(CN)_6]_{0.75}{\cdot}B_{0.25}{\cdot}zH_2O$) with 25% $Fe(CN)_6$ vacancies. The vacancies are filled with H_2O. Reprinted with permission from ref 69. Copyright 2016 American Chemical Society.

ions, forming a three-dimensional framework. Samples with minimal doping or defects typically exhibit a standard cubic crystal structure.[69] However, due to imperfections in the production process, such as incomplete reactions or impurities, defects are inevitably introduced into the crystal lattice[70,71] causing lattice distortion and often resulting in a transformation of the crystal structure to monoclinic[72] or rhombohedral[73] phases.

The most common type of crystal defect in PBAs is the $Fe(CN)_6$ vacancy. A PBA with $Fe(CN)_6$ vacancies can be expressed as $A_{2-x}M[Fe(CN)_6]_y{\cdot}B_{1-y}{\cdot}zH_2O$, where B represents the $Fe(CN)_6$ vacancy. Figure 3b shows a 25% $Fe(CN)_6$ vacancy in a PBAs ($NaM[Fe(CN)_6]_{0.75}{\cdot}B_{0.25}{\cdot}zH_2O$) unit cell, and the adjacent M ions are coordinated by water molecules.[69]

The presence of $Fe(CN)_6$ vacancies in PBAs significantly impacts the structure, stability, and performance of a cathode. First, randomly distributed $Fe(CN)_6$ vacancies disrupt the three-dimensional framework constructed by cyanide CN^-, M, and Fe ions, leading to distorted and defective lattice structures. These defective lattice structures are prone to collapse during the charge−discharge processes, which involve inserting and extracting charge carrier ions. This way, the stability of the crystal structure is significantly reduced.[74]

Furthermore, $Fe(CN)_6$ vacancies also directly impact the electronic conduction pathways within the CN^-, M, and Fe ion frameworks, disrupting the continuity of the conduction network. This leads to impeded insertion reactions of charge carrier ions in certain regions of the lattice. Further, it hinders

https://doi.org/10.1021/acs.jpcc.5c00877
J. Phys. Chem. C 2025, 129, 7135−7153

the rapid diffusion of charge carrier ions, increases ohmic polarization within the cathode material, and limits the kinetics of electrochemical reactions, ultimately degrading the rate performance.[75]

Additionally, $Fe(CN)_6$ vacancies introduce coordinated water molecules into the crystal lattice, which bind to the vacant M sites, reducing the number of available binding sites for charge carrier ions and leading to a significant loss of capacity for insertion. As a result, the charge and discharge capacity is adversely affected.

Meanwhile, when water molecules occupy $Fe(CN)_6$ vacancies, the interstitial water stabilizes the structural framework by balancing the charge. From an energetic perspective, these water molecules strongly favor remaining in the vacancies and compete with charge carrier ions for more interstitial space, preventing these ions from entering the crystal lattice. This significantly reduces the capacity utilization of the PBAs.[76,77] Moreover, water molecules initially retained in the lattice may later detach from the vacancies and migrate into the electrolyte, which can result in electrochemical reactions with organic electrolytes, reducing the concentration of effective ions for transport and thereby compromising electrolyte stability. Such instability can negatively affect battery efficiency and potentially pose safety risks.[44,78,79]

2.1.3. Side Reactions. In practical applications, PBAs will inevitably come in contact with other components in the battery, potentially leading to side reactions. The main causes of these side reactions can be summarized as follows: (1) zeolitic/coordinated water in the PBA framework, (2) dissolution of transition metals, (3) formation of an unstable SEI layer, and (4) irreversible redox reactions caused by polarization overpotential.

As already described in the previous section, improper control of the synthesis process of PBAs can result in the formation of significant crystal defects and the generation of crystalline water.[80,81] This type of crystallization water typically enters the electrolyte in the form of $A(OH)_2^+$ units and further negatively affects the cycling performance of batteries.[82] In aqueous batteries, this crystalline water can hardly influence the performance due to the good compatibility of crystalline water and water-based electrolytes. However, in organic electrolyte systems, crystalline water will negatively impact the electrolyte and the electrode charge carrier ions during cycling. During the discharging process, as the lattice changes, crystallized water enters the electrolyte.[44] While charging, it undergoes reduction with the anode to generate H_2 and reacts with the electrolyte and cathode to produce CO_2.[83]

Meanwhile, as described above, an uncontrolled synthesis process can lead to numerous $Fe[CN]_6$ group vacancies in the PBA lattice.[22] The presence of these defects makes it difficult for the crystal structure to remain stable. During the process of charging and discharging, the PBA structure collapses, causing the cathode to fail while releasing a large number of $M_2[CN]_6$ groups into the electrolyte. The dissolution of transition metals not only leads to the loss of active cathode material but also allows free transition metal ions to migrate to the anode side and incorporate into the SEI. This exacerbates electrolyte decomposition and increases the battery's self-discharge effect. Therefore, even a small amount of transition metal dissolution can severely impact the battery's lifespan.[84]

During the first battery cycle, a stable solid electrolyte interface (SEI) layer forms between the electrolyte and the electrode, with its composition determined by both the cathode and the electrolyte. This SEI layer consumes part of the PBA and reduces the initial Coulombic efficiency.[85] In Na^+ cathode materials, the relatively large ionic radius of Na^+ makes achieving zero-strain electrodes nearly impossible.[56] Therefore, in PBAs, the extraction and insertion of Na^+ lead to constant lattice changes, causing SEI disruption and continuous growth. This results in decreased Coulombic efficiency during cycling and reduced cathode capacity.[85]

Generally, the electrochemical process of PBA electrodes like MnHCF and CoHCF typically exhibits two voltage plateaus, with the corresponding voltages determined by the spin states of the transition metal elements.[26,86] However, in the case of cathode structural collapse, other side reactions occur, or the operations of batteries under low temperatures can impede the kinetics of the charge carrier ion transport, thereby leading to a polarization voltage.[87] This polarization voltage, in turn, triggers more irreversible reactions, accelerating the battery's degradation process.

2.2. Other Degradation Pathways. In addition to the mechanisms discussed above, the degradation of PBAs is also influenced by common factors observed in other electrode materials, such as mechanical strain during intercalation and de-intercalation, as well as thermal behavior.[70,88] Mechanical degradation of cathode materials has emerged as a significant scientific challenge, as it can lead to localized fractures, the creation of new reactive surfaces, and increased electronic transfer resistance, ultimately causing capacity fading and battery failure.[88] Similar to the degradation mechanisms observed in oxide cathode materials, the primary causes of mechanical degradation in PBA cathode materials include inhomogeneous strain during phase transitions, volume expansion, and the generation of vacancies during ion insertion and extraction.[88]

The distinctive crystal structure of PBAs, characterized by open 3D frameworks and large interstitial voids, facilitates rapid ion intercalation with minimal volume expansion, a critical factor for high-rate and long-term battery performance.[21] For most PBAs, such as CuHCF, NiHCF, and ZnHCF, which possess a single active site, the volume expansion caused by ion intercalation is typically less than 1%, comparable to that of other electrode materials commonly used in commercial batteries.[40,88] However, as discussed above, phase transitions can lead to a more pronounced volume expansion. Notably, while offering higher specific capacities, PBAs with two active redox sites generally experience more significant volume expansion and structural distortions.[40] Phase transitions in such materials are often associated with total volume changes exceeding 2%, which can compromise the electrode cycle life. This expansion may generate high-pressure levels, potentially causing material cracking.[40]

While temperature resistance is generally not a significant concern for many PBA applications, such as aqueous sodium-ion batteries (ASIBs), due to the minimal heat generated during charging and discharging, PBAs may still experience temperature fluctuations from external conditions, which can accelerate degradation.[22] Moreover, due to their unique crystal structure, many PBAs exhibit the uncommon property of negative thermal expansion. Margadonna et al. reported that many PBAs are isotropic materials with nearly zero thermal expansion across a broad temperature range, from 4.2 to 300 K.[89] This behavior helps maintain the stability of the crystal structure within the typical temperature range encountered by PBA in applications such as in ASIBs.

https://doi.org/10.1021/acs.jpcc.5c00877
J. Phys. Chem. C 2025, 129, 7135−7153

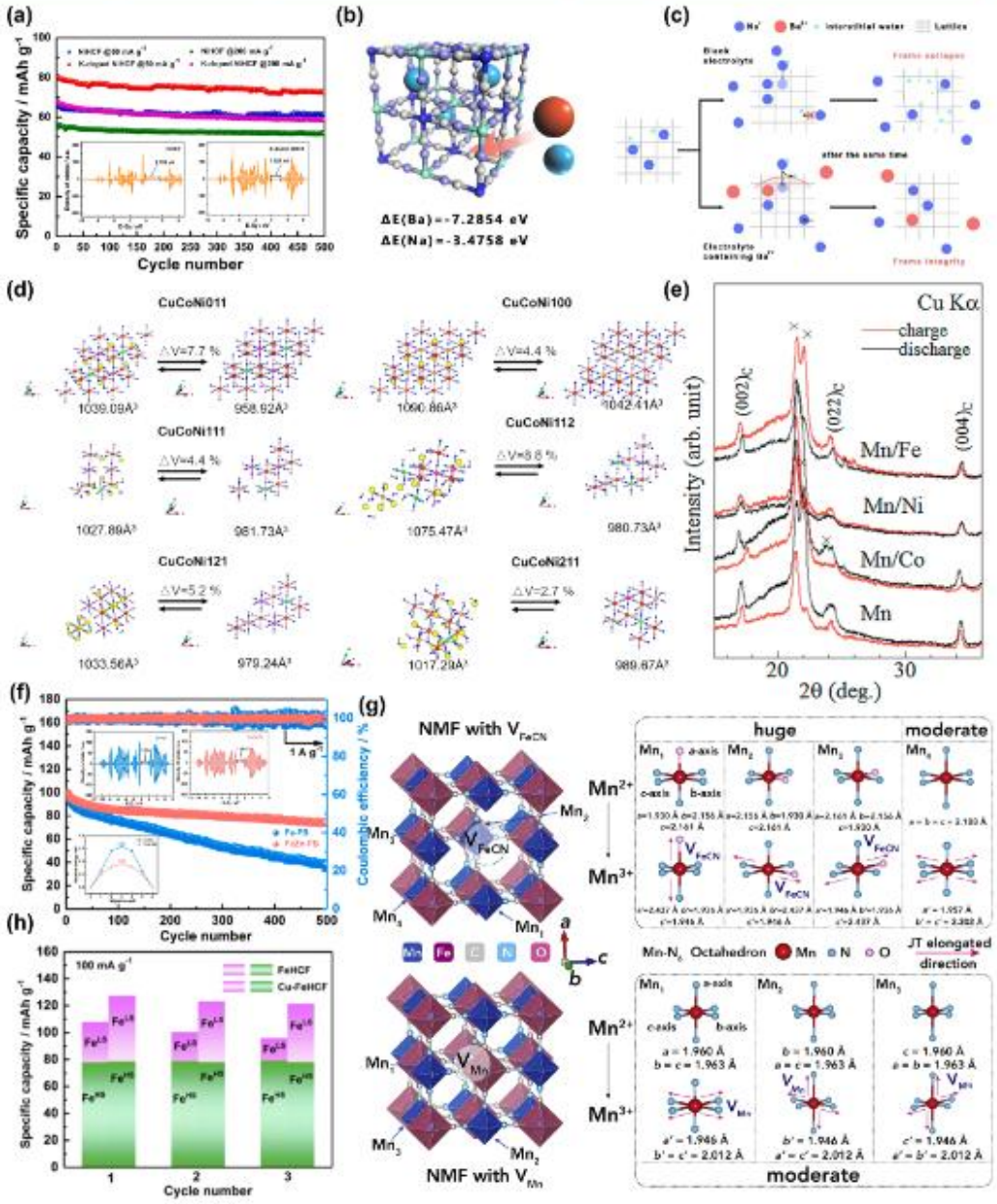


Figure 4. (a) The cycling performance under different current densities, with an inset illustrating the total density of states (TDOS) profiles for NiHCF and K-doped NiHCF.[92] Adapted with permission from ref 92. Copyright 2021 Elsevier B.V. Schematic diagram of (b) Ba^{2+} prior to the Na^{+} embedded lattice and (c) Ba^{2+} employing a waterproofing mechanism to stabilize the lattice.[93] Adapted with permission from ref 93. Copyright 2023 Elsevier B.V. (d) Geometry optimization of the primitive and fully charged state for CuCoNi with different element ratios.[96] Reprinted with permission from ref 96. Copyright 2020 John Wiley & Sons Ltd. (e) X-ray diffraction patterns of Mn-, Mn/Co-, Mn/Ni-, and Mn/Fe-HCFs in the fully discharged and charged states.[98] Reprinted with permission from ref 98. Copyright 2016 Elsevier Ltd. (f) Long cycle performance of Fe-PB and FeZn-PB at 1 A g^{-1}. The insets are the calculated density of state (DOS) patterns of Fe-PB and FeZn-PB, as well as the energy barrier profiles of Fe-PB and FeZn-PB.[101] Adapted with permission from ref 101. Copyright 2022 Elsevier B.V. (g) The cubic phase of traditional NMF with $[Fe(CN)_6]$ vacancy and EDTA-NMF with Mn vacancy shows a change in the Mn−N bond length and the bond's stretch direction during the second Na^{+} extraction.[102] Reprinted with permission from ref 102. Copyright 2020 Elsevier Inc. (h) First three charge−discharge capacity contribution diagrams of FeLS and FeHS of FeHCF and Cu−FeHCF at 100 mA g^{-1}, respectively.[107] Adapted with permission from ref 107. Copyright 2022 American Chemical Society.

A key application of PBAs is in aqueous zinc batteries.[25,90,91] Therefore, the specific degradation mechanisms of PBAs in these batteries are briefly outlined here. Aqueous zinc batteries (ZIBs) utilizing PBAs demonstrate good cyclic performance

https://doi.org/10.1021/acs.jpcc.5c00877
J. Phys. Chem. C 2025, 129, 7135−7153

and, in theory, offer high operating voltages.[25] However, reported PBA-based full cells often exhibit significant capacity degradation. The primary reasons are as follows:[25] (1) although the ionic radius of Zn^{2+} is smaller than that of Na^{+}, hydrated Zn^{2+} has a larger effective radius, which hinders its insertion and removal, and (2) PBA cathode materials undergo severe phase changes during Zn^{2+} intercalation, rendering them inactive over time. Li et al. offer a comprehensive overview of specific degradation mechanisms of PBAs in ZIBs in their review.[25]

3. STABILIZATION STRATEGIES

Current research focuses on addressing the various degradation mechanisms discussed in the previous section to develop more stable and efficient PBAs for energy storage applications. Synthesis plays a crucial role in enhancing PBA stability, with key strategies including ion doping, controlled crystal growth and morphology, and regulation of the water content within the PBAs. Additionally, postsynthesis treatments, such as drying at elevated temperatures, can further strengthen the structural integrity of PBAs. Beyond material synthesis, optimization opportunities also exist within battery cell design, particularly in electrode fabrication, electrolyte composition, and cycling protocols during operation.

3.1. Synthesis. *3.1.1. Ion Doping.* Ion doping introduces specific hetero-ions to tailor the electronic structure, lattice defects, or bonding environment of a material, thereby enhancing its physicochemical properties. In PBA materials, ion doping can help to improve charge transport efficiency, stabilize the crystal structure, and mitigate the volume and framework fluctuation during the charge and discharge processes.

Wei et al. regulated the structure of NiHCF through K-doping at sodium sites and investigated its sodium storage performance.[92] The K-doping induces a phase transition in NiHCF from cubic to monoclinic, creating additional sodium storage sites. Moreover, K-ions act as structural pillars, enhancing both the stability of the framework and the transport properties of the sodium ions and electrons. So, the K-doped NiHCF electrode achieves a high initial discharge capacity of 87.1 mAh g^{-1} at 10 mA g^{-1} and exhibits exceptional cycling stability, with only 0.016% capacity loss per cycle at 800 mA g^{-1} over 1000 cycles (Figure 4a).

The ion doping strategy can also improve structural stability through a water-repellent mechanism. Liu et al. proposed an ion-size-based doping strategy in which large Ba^{2+} ions are introduced into the sodium sites of PBAs, as shown in Figure 4b,c.[93] This approach prevents water molecules from entering the framework, thereby ensuring the stability of the material. The resulting $Na_xBa_yFe[Fe(CN)_6]$ material exhibits excellent electrochemical performance, with an initial Coulombic efficiency of ca. 99.3%, a reversible capacity of 92.2 mAh g^{-1}, and 96.6% capacity retention after 150 cycles.

Yimtrakarn et al. synthesized Ni-doped $Na_{1.40}Fe_{0.90}Ni_{0.10}[Fe(CN)_6]_{0.85}\cdot 1.3H_2O$ with a capacity as high as 148 mAh g^{-1} at 10 mA g^{-1}.[94] This enhanced PBA structure exhibits a very small capacity decay rate of 0.02% per cycle for 1000 cycles. In situ synchrotron X-ray diffraction shows a minimal (~1%) change in unit cell parameters, ensuring the high structural stability and long-term cyclability of PBA-based SIBs.

The synergistic mechanism of the doping of various ions has also been applied to enhance the comprehensive performance of PBAs since the introduction of mono-ion doping has only a limited effect. Ternary PBAs (T-PBAs), incorporating Cu and Fe ions into the manganese sites of Mn-PBAs, effectively eliminate the inherent multiphase transitions.[95] Instead of undergoing a conventional three-phase transition during charge and discharge, T-PBAs consistently maintain a cubic phase with minimal lattice distortion, significantly mitigating structural degradation. This way, the T-PBAs showcase unprecedented cycling stability at room temperature (10,000 cycles at 1 A g^{-1}, capacity retention: ca. 61.2%). When combined with commercial hard carbon, the T-PBAs-based sodium-ion battery full cell demonstrates outstanding capacity retention, maintaining ca. 76.8% of its initial capacity after 2000 cycles. Zhu et al. give an approach of multimetal (Cu, Co, Ni) doped PBA materials, in which the properties of the samples with different elemental compositions are fully studied.[96] Understanding the framework structure during charging and discharging based on in situ XRD and DFT calculations (Figure 4d) shows that the Cu element is crucial. Luo et al. deliver a novel nickel- and copper-codoped $K_2Mn[Fe(CN)_6]$ cathode with excellent reversible capacity (116.0 mAh g^{-1} at 0.01 A g^{-1}) and superior cycling stability (81.8% capacity retention over 500 cycles at 0.1 A g^{-1}) via a simple co-precipitation strategy.[97] The doping elements enhance the electrical conductivity of Mn-based PBAs by reducing the bandgap and mitigating the Jahn−Teller effect, thereby stabilizing the framework. Additionally, substituting sodium with potassium in the lattice helps fill vacancies in the PBA structure, resulting in higher average operating voltages and improved structural stability. In more general cases with Mn-HCF (Figure 4e), which were studied by Moritomo et al., the partial substitution of Fe, Co, and Ni with Mn could significantly and cooperatively suppress the Jahn−Teller distortion of Mn^{3+} and subsequently lead to an activation of Mn^{3+}/Mn^{2+} redox reaction.[98] Further high-entropy PBAs (HE-PBAs), such as $Na_2Mn_{0.2}Fe_{0.2}Co_{0.2}Ni_{0.2}Cu_{0.2}Fe(CN)_6$ with monoclinic (P21/n) symmetry, demonstrate enhanced electronic conductivity and Na-ion diffusivity.[99] The reported material exhibits a specific capacity of 94 mAh g^{-1} at 100 mA g^{-1} and excellent durability with 89% capacity retention over 500 cycles at 200 mA g^{-1} within a 0−2 V window.[99]

Vacancies and defects in PBAs can lead to adverse effects, such as structural instability, degraded electrochemical performance, and the occurrence of side reactions, all of which could be mitigated through an ion doping strategy. Xu et al. demonstrated through in situ XRD that K-doped NaKMHCF exhibits excellent structural reversibility, retaining 77.0% of its capacity after 500 cycles at 500 mA g^{-1}.[100] This performance is attributed to the reduced crystallization water content and vacancies in NaKMHCF. Transition metal doping can achieve effects similar to those of alkali metal doping. Zhang et al. investigate the Fe-PBA structure regulated by Zn-substitution, shown in Figure 4f.[101] Their analysis showed reduced bandgap, improved sodium ion migration, minimized $[Fe(CN)_6]$ vacancies, and decreased crystal water content.

Reducing vacancies and defects is commonly regarded as a general approach to optimizing PBAs. However, the strategic introduction of vacancies can also somewhat enhance the PBA performance. Shang et al. reported an innovative method for adjusting Mn vacancies (V_{Mn}) on the surface of Mn−Fe PBAs by utilizing a strong chelating agent, namely, disodium ethylenediaminetetraacetic acid.[102] As shown in Figure 4g, V_{Mn} in Mn−Fe PBAs restrains the variation of Mn−N bonds, mitigating the Jahn−Teller distortion of $Mn-N_6$ octahedra

https://doi.org/10.1021/acs.jpcc.5c00877
J. Phys. Chem. C 2025, 129, 7135−7153

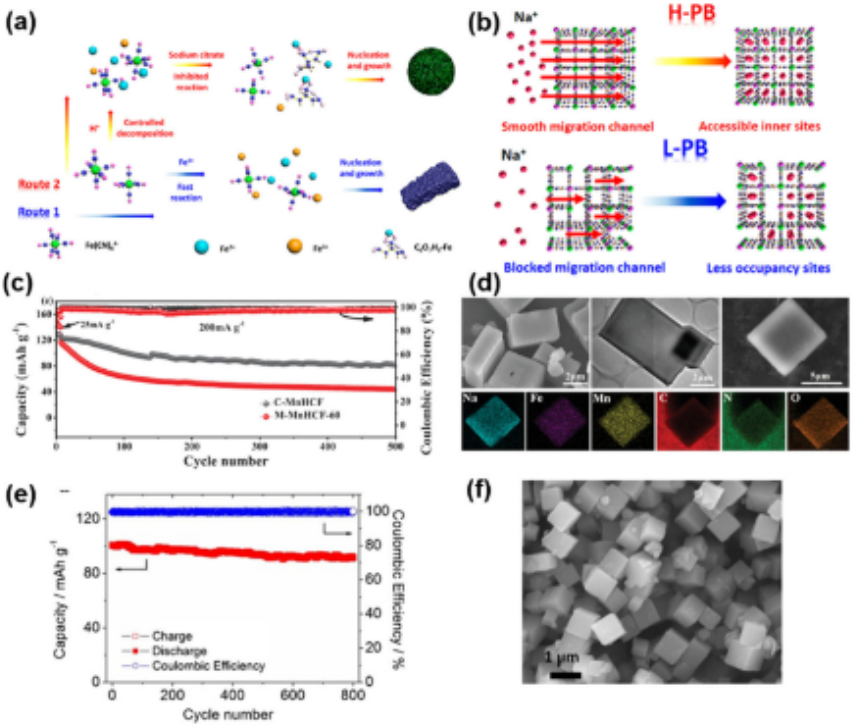


Figure 5. (a) Schematic diagram for the synthesis of Prussian blue (Route 1, the conventional co-precipitation method for L-PB; Route 2, the advanced chemical-inhibited process for H-PB).[109] Reprinted with permission from ref 109. Copyright 2021 American Chemical Society. (b) Schematic illustrations for the ion migration in high- and low-quality Prussian blue (H-PB and L-PB) materials.[109] Adapted with permission from ref 109. Copyright 2021 American Chemical Society. (c) Cycling performance at a current density of 200 mA g^{-1} of cubic and monoclinic (C-/M-)MnHCF. Adapted with permission from ref 54. Copyright 2020 WILEY-VCH Verlag GmbH & Co. KGaA, Weinheim. (d) SEM images of the M-MnHCF-60 microboxes, TEM images of a single M-MnHCF-60 particle, and EDX-elemental mapping images.[54] Adapted with permission from ref 54. Copyright 2020 WILEY-VCH Verlag GmbH & Co. KGaA, Weinheim. (e) Cycling performance of high-quality CoHCF.[110] Adapted with permission from ref 110. Copyright 2015 WILEY-VCH Verlag GmbH & Co. KGaA, Weinheim. (f) SEM picture of HQ CoHCF.[110] Adapted with permission from ref 110. Copyright 2015 WILEY-VCH Verlag GmbH & Co. KGaA, Weinheim.

and promoting highly reversible phase transitions. The Mn−Fe PBA material with the adjusted Mn vacancies (V_{Mn}) on the surface achieves outstanding long-term cycling stability and capacity retention for both the half-cell (72.3% after 2700 cycles at 0.5 A g^{-1}) and the full cell (75.5% after 550 cycles at 0.1 A g^{-1}). Furthermore, El-Hady et al. utilized a strategy of combining Mn vacancies (V_{Mn}) with the introduction of Ni to suppress the Jahn−Teller (J−T) distortion in MnHCF.[103] They prepared a Ni-doped MnHCF with V_{Mn} and low crystal water content ($K_{1.95}Na_{0.05}Ni_{0.02}Mn_{0.93}[Fe(CN)_6]_{0.05}{\cdot}0.41H_2O$), which demonstrated an 80% improvement in capacity retention after 100 cycles at 0.5 C.

Generally, two-electron redox materials ($Na_xM[Fe(CN)_6]$, where M = Co, Fe, or Mn) exhibit a theoretical capacity predicated on the reversible insertion and extraction of two sodium ions.[104] However, the insufficient redox activity of spin-iron often limits their practical capacity, leading to values significantly below the theoretical predictions. Yu et al. found that nickel doping effectively modifies the electron distribution around Fe^{2+} linked to C, enhancing the capacity via improving the redox activity of the Fe^{2+}/Fe^{3+} redox couple, as well as improving the volumetric change during the charge and discharge process.[105] Fu et al. further investigated the impact of Ni doping content on PBA capacity, finding that PBA with 3% Ni achieved a discharge capacity of 117 mA h g^{-1}, with approximately 50 mA h g^{-1} attributed to the low-spin $Fe^{2+}C_6/Fe^{3+}C_6$ redox couple.[106] The reported capacity retention is 86.3% after 90 cycles at a current density of 200 mA g^{-1}. In contrast, the non-Ni-doped PBA exhibits a capacity retention of 82.8%, while the PBA with 10% Ni achieved a capacity retention of 90.8%. The cycling performance of PBA improved with higher doping levels; however, PBA with 3% Ni exhibited the highest discharge capacity, emphasizing the trade-off between capacity and stability.

Introducing copper, an element in the same period as nickel, into PBAs can also achieve a similar effect. Chen et al. demonstrate that, while Cu doping has a small impact on the electrochemical activity of high-spin Fe (FeHS), it significantly enhances the activity of low-spin Fe (FeLS) in optimized FeHCF through a copper doping strategy.[107] After Cu doping, the capacities contributed by low-spin Fe increase from 30.0, 21.7, and 16.7 mA h g^{-1} to 48.8, 45.4, and 43.7 mA h g^{-1} for the first three cycles, respectively (Figure 4h). Moreover, Cu doping also controls the side reaction to a certain extent, resulting in better stability, with a reported 0.047% capacity decay rate for each cycle over 500 cycles.

Overall, ion doping stands out as a transformative strategy for enhancing the structural stability and the electrochemical performance of PBAs. Addressing the inherent material limitations of PBAs is achieved through the rational design

https://doi.org/10.1021/acs.jpcc.5c00877
J. Phys. Chem. C 2025, 129, 7135−7153

and selection of ion types and concentrations for doping, ranging from single-ion doping to synergistic multimetal approaches.[108] These advancements pave the way for a deeper exploration of doping mechanisms and their potential impact on the stability and other electrochemical characteristics of PBAs. Hence, ion doping plays a crucial role in the development of high-performance energy storage systems.

3.1.2. Crystal Structure and Morphology. As stated in section 2.1, structural changes and crystal defects play a significant role in PBA degradation. Hence, an effective method to stabilize PBAs is controlling the density of $Fe(CN)_6$ vacancies and the crystal structure, which can be achieved efficiently through the careful control and optimization of the synthesis reaction. Additives can be added, the pH can be changed, and the reaction kinetics can be manipulated. In addition, postsynthesis treatment is a viable option to control crystallinity and, therefore, the stability of PBAs. It should be noted that the optimal structural properties may vary depending on the specific type of PBA.[70] However, generally, higher crystallinity and fewer defects are considered favorable (Figure 5b).[26] This section aims to identify the synthesis parameters that most efficiently suppress the degradation mechanisms mentioned above for these compounds by tailoring structural parameters.

Additives. Since the synthesis of PBAs via the simple co-precipitation method often leads to irregular crystallites due to the fast reaction kinetics, chelating agents are commonly added to control the crystal formation. The most frequently employed chelating agents in the synthesis of PBAs are sodium citrate and potassium citrate.[54,69,109−112] By binding to the transition metal cations, the citrate anions effectively slow the crystallization rate and reduce the density of lattice defects (Figure 5a). Most notably, highly crystalline CuMn-PBA,[105] MnHCF (Figure 5c and 5d),[54] and CoHCF (Figure 5e and 5f)[65,110] have been reported to achieve high specific capacities while also featuring improved cyclability within the 200−800 cycle range, as shown in Figure 5c. It is also worth noting that the citrate-assisted synthesis mostly yields a cubic crystal structure, which has been shown to maintain structural stability better than monoclinic or tetragonal phases by suppressing Jahn−Teller distortions due to its high symmetry.[70] In addition, citrate salts are also commonly used to synthesize PBAs, in which only Fe-ions are redox-active, such as in NiHCF and CuHCF.[111,112] However, the influence on the cycling stability is significantly weaker in these cases. Besides citrate, different stronger chelating agents, like pyrophosphate and ethylenediaminetetraacetic acid, have recently been studied.[54,113,114] In 2021, Deng et al. reported one of the highest cycling stabilities for pure MnHCF by taking advantage of the strong chelation of ethylenediaminetetraacetic acid to Mn^{2+} (80% capacity retention after 7800 cycles).[115] This concept was also used by Shang et al. in 2020 to prepare MnHCF with unconventional Mn-vacancies, further suppressing Jahn−Teller distortions.[102] Another commonly applied strategy to achieve high crystallinity and low $Fe(CN)_6$ vacancy content is the addition of excess alkali metal cations to the co-precipitation solution.[116−118]

Reaction Conditions. Alternatively, crystal growth can be controlled by directly managing the reaction kinetics as higher crystallinity in PBAs can be achieved through a slow growth process. This involves using slow crystallization techniques to form well-ordered crystals with a lower tendency to form structural defects.[105] A unique method to artificially slow down crystal growth was developed by Duan et al. in 2021, who synthesized PB at a water−butanol interface.[77] Finally, other synthesis parameters, such as solution pH and temperature, can be regulated to achieve highly crystalline PBAs with improved cycling stability. Ensuring a specific pH during synthesis can influence the electrochemical performance and cyclability of PBAs.[105] Zuo et al. reported that a slightly acidic pH provides the most stable framework and highest cycling stability.[119] Other groups have also investigated the influence of the solution and aging temperature on various structural properties. Generally, longer aging times lead to larger and more regular crystallites, which is favorable for suppressing Jahn−Teller distortions in MnHCF or CoHCF. However, the ideal aging time varies depending on the specific PBA and the strength of the chelating agents used.[77,114] Similar results can be achieved by increasing the solution temperature.[120] Consequently, PBAs are commonly synthesized at elevated temperatures, usually ranging from 50 to 70 °C.[105,110,118,121]

3.1.3. Controlling Water Content. It should be noted that the enhanced crystallinity of PBAs, which is closely related to a reduced density of $Fe(CN)_6$ vacancies, also directly leads to a decrease in interstitial water content. As mentioned previously, recent studies investigating its impact yielded conflicting results. Some groups propose that removing water enhances performance,[71,122,44] while others argue that interstitial water contributes to better structural stability and cycling performance.[70] Notably, Ge et al. (2024) distinguished between interstitial and coordination water. Their findings show that trace amounts of coordination water are important for maintaining structural integrity and electrochemical performance.[76] Their study proved that PBAs with minimal coordination water (1.3%) exhibited superior capacity, rate capability, and cycling stability compared to completely dehydrated samples. The PBA with 1.3% water content exhibits an excellent capacity retention of 85.5% after 1200 cycles at a current density of 300 mA g^{-1}, compared with a capacity retention of 27.6% after 1200 cycles of the completely dehydrated sample. By contrast, the PBA with ~12.1%, including both interstitial and coordinated water, exhibited a capacity retention of 43.4%. These findings point toward the complexity of the influence of water in PBAs and emphasize the need for precise control of water content to optimize the performance of PBAs, e.g., in sodium-ion batteries. Several approaches have been proposed to regulate water content in PBAs, such as heat treatment[71] and chemical inhibition[122] during synthesis. Other strategies include the use of additives, pH adjustment, and manipulation of the reaction kinetics.

Additives. Since the interstitial water content is connected to defect content, incorporating excess alkali salts, such as NaCl, into the synthesis solution can aid in reducing the water content of the final product.[123] As for regulating the crystallinity, employing chelating agents is also effective. Incorporating citrate as a chelating agent during synthesis helps regulate the stoichiometry, reduce vacancies, and minimize the amount of interstitial water. In addition, by precisely controlling synthesis conditions, such as using sodium citrate and sodium supplements, sodium-rich PBAs with reduced coordinated water can be obtained.[117,124]

Reaction Kinetics and pH. Performing the synthesis at elevated temperatures (e.g., 60−80 °C) facilitates the formation of more crystalline PBAs and minimizes the incorporation of interstitial water. Synthesis approaches at higher temperatures, such as hydrothermal processing, can

https://doi.org/10.1021/acs.jpcc.5c00877
J. Phys. Chem. C 2025, 129, 7135−7153

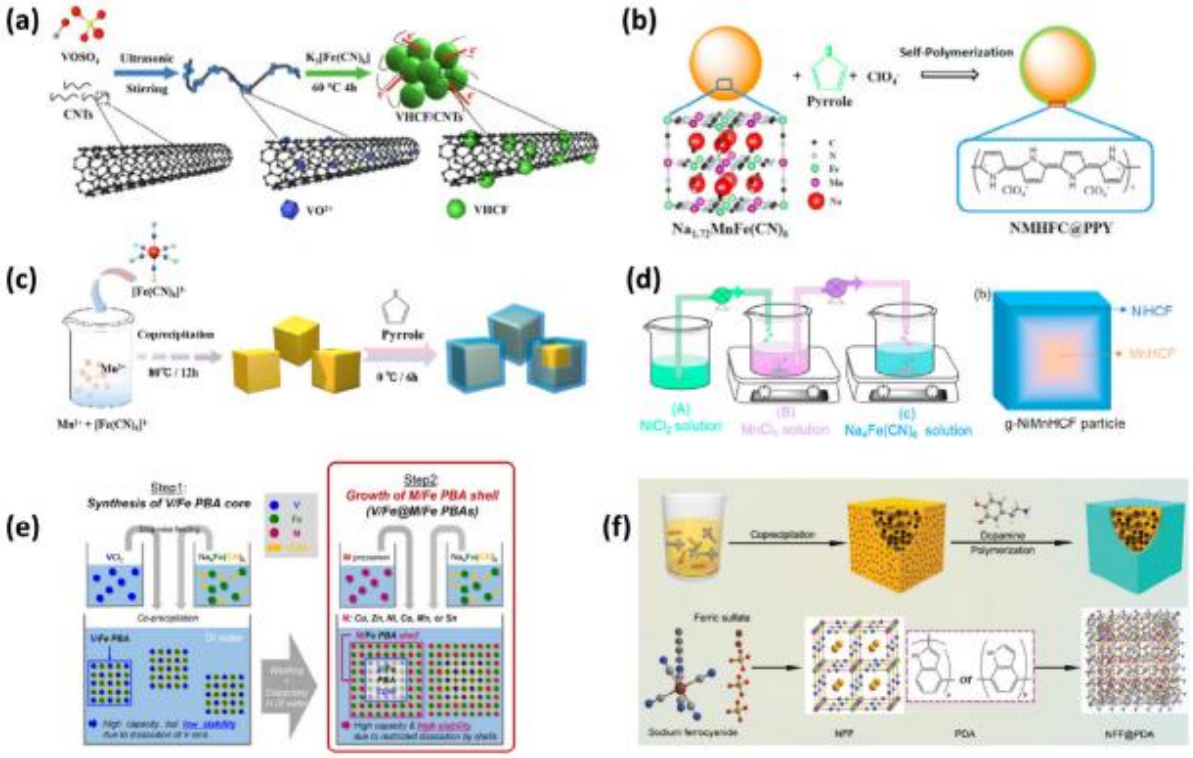


Figure 6. (a) VHCF/CNT preparation process.[130] Reprinted with permission from ref 130. Copyright 2022 Elsevier B.V. (b) Polymerization reaction between NMHFC particles and pyrrole.[58] Adapted with permission from ref 58. Copyright 2015 Elsevier Ltd. (c) Schematic depiction of KMHCF and KMHCF@PPy samples.[134] Adapted with permission from ref 134. Copyright 2022 American Chemical Society. (d) Preparation of g-NiMnHCF.[88] Adapted with permission from ref 88. Copyright 2020 American Chemical Society. (e) Synthesis procedure for core@shell-type Prussian Blue Analogue (PBA)-based cathode materials.[138] Reprinted with permission from ref 138. Copyright 2020 American Chemical Society. (f) Synthesis process for porous NFF@PDA.[140] Reprinted with permission from ref 140. Copyright 2020 WILEY-VCH Verlag GmbH & Co. KGaA, Weinheim.

significantly reduce water content compared to room-temperature synthesis.[123] Employing anhydrous solvents or carefully controlling the water content in the reaction medium to reduce water incorporation during synthesis are also effective strategies. Nonaqueous synthesis methods, such as microwave-assisted solvothermal (MW-ST) processes using nonaqueous solvents, can produce high-quality PBAs with minimal water content.[125] As already mentioned, a slow growth process results in controlled crystal growth, which can lead to fewer defects and reduced water trapping. Finally, precise regulation of pH during the reaction is of critical importance. Maintaining a specific pH during synthesis can help to obtain higher crystallinity and, therefore, reduce water trapping.[105]

Post-synthesis. After the synthesis, PBAs can be dried at elevated temperatures (e.g., 65 °C) to eliminate excess adsorbed water.[123] Washing PBAs after synthesis with low-boiling-point, water-miscible organic solvents, such as acetone, can further assist in removing residual water.[123] Notably, although these methods effectively eliminate interstitial water, the removal of coordinated water is more challenging due to its covalent bonding with Fe atoms in the crystal lattice. The selection of method and specific parameters (e.g., temperature and duration) should be carefully evaluated to prevent any alteration of the desired properties of the PBAs. For example, heating PBAs to 200 °C initiates the removal of coordinated water. However, further heating between 250 and 270 °C can achieve near-complete elimination of coordinated water.[126]

In summary, controlling the crystal growth by tuning synthesis parameters is an effective strategy to minimize defects and water content in PBAs. Highly crystalline cubic phases appear favorable for achieving long-life electrodes, particularly for materials such as MnHCF and CoHCF that degrade due to Jahn−Teller distortions during cycling. These can be achieved by utilizing chelating agents and alkali metal salts as additives during the synthesis or controlling external parameters such as the pH, temperature, and aging time. In addition, several postsynthesis treatments have been proposed to further improve the structural integrity of PBAs. These enhancements help mitigate multiple degradation mechanisms described in section 2. Higher crystallinity is linked to a lower density of defects, which are responsible for detrimental lattice distortions, as described in section 2.1.2. Furthermore, PBAs with a highly crystalline cubic structure are less prone to collapsing upon phase transitions during cycling. This is most pronounced in MnHCF and CoHCF since the highly symmetrical low-defect cubic lattice can maintain its structural stability better than other crystal phases by suppressing Jahn−Teller distortions. Furthermore, a lower water content mitigates the degradation mechanisms induced by parasitic side reactions between coordinated water and the PBA lattice,

https://doi.org/10.1021/acs.jpcc.5c00877
J. Phys. Chem. C 2025, 129, 7135−7153

which are described in sections 2.1.2 and 2.1.3. Hence, controlling the crystal structure, morphology, and water content of PBAs is an effective method to minimize capacity fading caused by phase transitions, defects, coordination of water, and side reactions.

3.2. Electrode Composition. In PBAs, their composition and structure result in various defects, particle sizes, morphologies, etc., and determine their electrochemical performances.[127] However, the interactions among electronic conductive agents, binders, and electrolytes must be considered when they are applied in practical batteries. Based on this, adjusting battery components and electrode processing and conducting necessary pretreatments of PBAs can prevent direct contact between PBAs and the electrolyte and mitigate transition metal dissolution through side reactions, thereby improving electrochemical performance.

3.2.1. Conductive Additives. PBAs themselves exhibit low electronic conductivity.[128] Thus, conductive additives are required for practical applications.[129] The most commonly used conductive materials include carbon-based substances, such as Ketjen Black (KB), carbon nanotubes (CNTs), and graphene. Given that PBAs can be synthesized through simple methods like hydrothermal synthesis or co-precipitation, research has explored directly incorporating carbon materials during the synthesis process to achieve superior electronic conductivity. Xue et al. synthesized VHCF/CNT composite cathodes with excellent conductivity by growing vanadium hexacyanoferrate on CNTs via in situ co-precipitation (Figure 6a).[130] After 100 cycles at a current density of 3200 mA/g, the capacity retention is 54%. Jiang et al. added KB during the hydrothermal synthesis of FeHCF.[131] The composite electrode exhibited excellent electronic conductivity, while reducing the crystalline water content in PBAs. After 2000 cycles, the capacity remains at 77.5 mAh/g with a capacity retention rate of 90%.

Some conductive organic polymers have also been used as additives in electrodes.[58,132] Due to their excellent chemical stability and mechanical properties, these polymers can enhance electronic conductivity while protecting PBAs and reducing the dissolution of transition metals (Figure 6b). Mukherjee et al. fabricated a type of polymer-encapsulated PBA by combining Co−Co@Ni−Fe core−shell PBA with polypyrrole.[133] The composite product showed significant improvement in both electronic and ionic conductivity. The capacity retention rate is 79% after 2000 cycles at a current density of 10 A/g. In addition, the method of applying PPR coatings has been proven to effectively suppress the dissolution of transition metal elements during cycling and mitigate the volume expansion caused by it (Figure 6c).[134]

3.2.2. Inactive Layer Coating. Introducing electrochemically inert ions is a feasible approach to maintaining the structural stability of PBAs and suppressing mechanical degradation. A core−shell PBA material can be formed by coating a highly stable, low-specific-capacity external structure onto a high-specific-capacity, low-stability internal structure, effectively protecting the internal material while providing a relatively high capacity. Due to the ultrahigh cycling stability of NiHCF and its advantage of generating almost no strain during cycling, NiHCF is frequently used to coat other PBAs with relatively poorer cycling stabilities.[135,136] Hu et al. prepared a series of $Na_xNi_yMn_{1-y}Fe(CN)_6{\cdot}nH_2O$ materials and found that, by altering the content of transition metals in the material, the charge−discharge activity and structural stability of PBAs could be adjusted (Figure 6d).[88] The assembled battery retains 93% of its capacity after 1000 cycles at a 5 C rate. Simply coating the outer layer of PBAs with NiHCF can significantly enhance chemical stability while improving structural stability and mitigating the damage caused by phase transitions during cycling.[137]

In addition, CuHCF can serve as an effective coating layer. Choi et al. utilized a two-step co-precipitation method to coat a Cu/Fe PBA layer on the exterior of a V/Fe PBA core, increasing the capacity retention of the battery from 72% to 90% over 200 cycles (Figure 6e).[138] Wang et al. prepared a FeHCF@CuHCF composite material via a hydrothermal method, which exhibited excellent cycling stability, retaining 80.6% of its initial specific capacity after 1000 cycles at a current density of 50 $mA{\cdot}g^{-1}$.[139]

3.2.3. Other Coatings. In addition to materials with high electronic conductivity, many other coating materials, such as standard polymer composites and metal compounds, can also significantly improve the interfacial properties of PBAs. In recent reports, a series of organic polymer materials such as Polydopamine (PDA), Polyaniline (PANI), and Poly(3,4-ethylenedioxythiophene) (PEDOT) have been reported for coating PBAs (Figure 6f).[140] These organic polymers generally possess excellent chemical stability and good mechanical properties, ensuring the stability of PBAs during the long cycling processes. Some inorganic metal compounds, such as MoS_2, also possess excellent chemical stability and have promising potential as coating layers for PBAs.[141]

In summary, coating is a widely used strategy to improve interfacial reactions in applying PBAs. Its primary functions include enhancing interfacial electronic conductivity by adding conductive coatings, reducing interfacial reactions by adding chemically stable layers, and maintaining the structural stability of PBAs with coatings that have good mechanical properties. These methods enable PBAs to achieve optimal capacity release and a long cycling performance in batteries. By formation of a stable, impermeable layer over the PBA, the coating prevents direct exposure to the electrolyte. This helps to inhibit unwanted side reactions, such as electrolyte decomposition or the formation of undesirable byproducts that could degrade the stability of the PBA. Furthermore, as mentioned in section 2.2, during charge and discharge cycles, PBAs can experience significant volume changes due to the insertion and extraction of ions. A coating can help mitigate these mechanical stresses by providing structural support, thereby reducing the impact of volume changes on the PBA itself.

However, the impacts of these strategies are multifaceted. While improving the cycling stability, coating inevitably leads to a reduction in the energy density. Applying coating materials such as oxides or polymers may alter the surface ion/electron transport properties. Furthermore, the volume expansion of PBAs during cycling makes the coated layers prone to cracking after repeated charge−discharge processes. Selecting optimal composition strategies for PBAs remains a critical challenge in battery applications.

3.3. Electrolyte Optimization. The cathode, anode, and electrolyte in a battery full cell form an integrated system, and their interactions collectively determine the overall battery performance. Electrolytes come into direct contact with the electrode materials as ionic conductors.[142−144] The choice of solvents, salts, and additives in the electrolyte profoundly impacts both cathode and anode materials.[145] Based on their

https://doi.org/10.1021/acs.jpcc.5c00877
J. Phys. Chem. C 2025, 129, 7135−7153

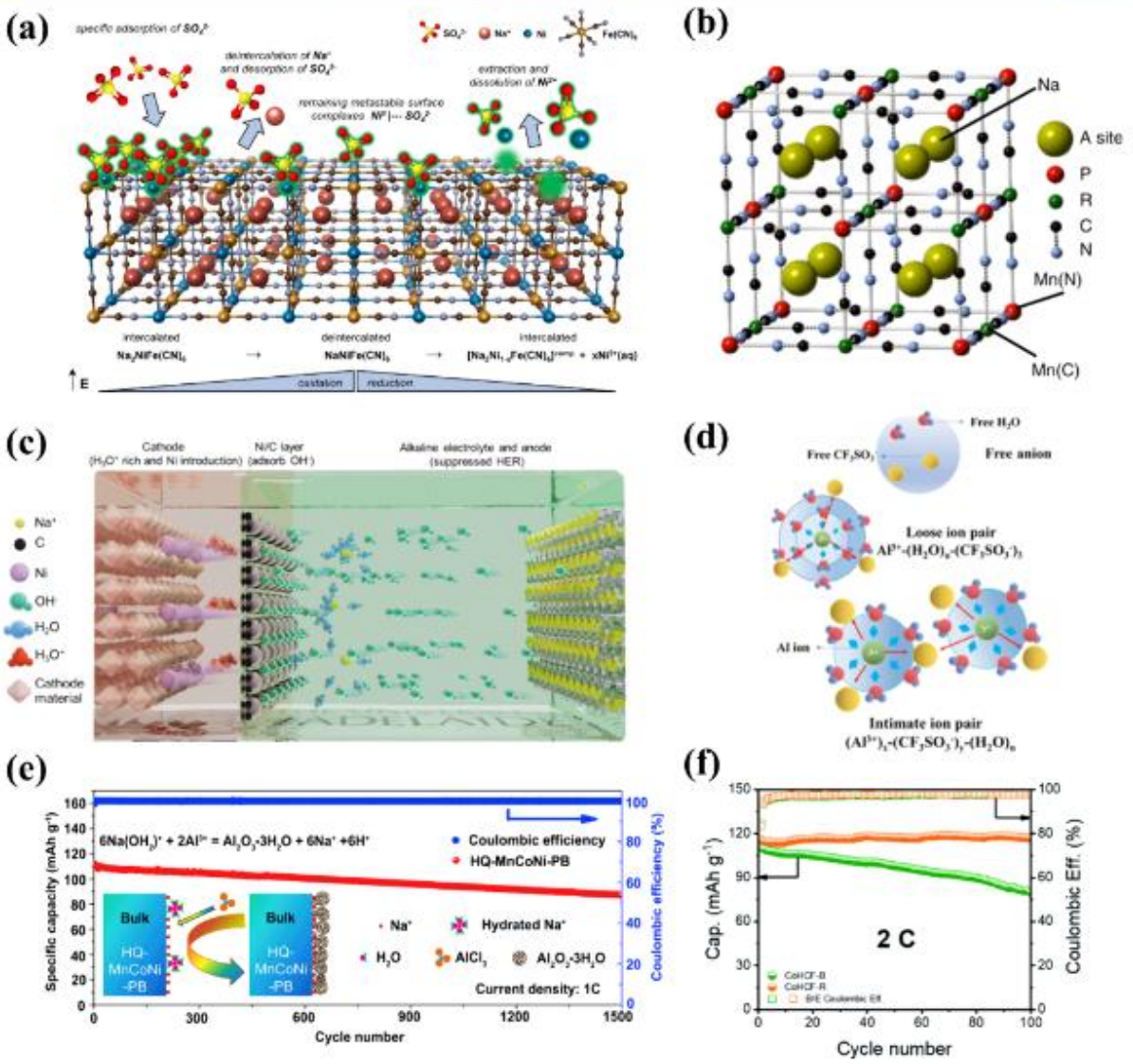


Figure 7. (a) The scheme of anion adsorption and electrode dissolution for nickel hexacyanoferrate in Na_2SO_4 at neutral pH (atoms).[35] Reprinted with permission from ref 35. Copyright 2022 American Chemical Society. (b) Unit cell of PBAs, MnHCMn, in which transition-metal cations are octahedrally coordinated to C−N ligands in a cubic framework. The interstitial A sites store the alkali cations that are electrochemically intercalated and the zeolitic water.[149] Reproduced from ref 149. Available under a CC-BY 4.0 license. Copyright 2018 Ali Firouzi et al. (c) Design concept for an alkaline aqueous battery.[152] Reproduced from ref 152. Available under a CC-BY 4.0 license. Copyright 2024 Han Wu et al. (d) The schematic diagram of the solvation structure.[153] Adapted with permission from ref 153. Copyright 2019 American Chemical Society. (e) Cycling performance of HQ-MnCoNi-PB with and without 1 wt % $AlCl_3$ electrolyte additive at 1 C; the inset is a schematic of the cell.[43] Reprinted with permission from ref 43. Copyright 2019 2019 Elsevier Ltd. (f) Cycle performances of $Na_2CoFe(CN)_6$-Na_2SO_4 and $Na_2CoFe(CN)_6$-Co-added electrolyte at current densities of 2 C.[154] Adapted with permission from ref 154. Copyright 2019 American Chemical Society.

chemical composition, alkali metal-ion battery electrolytes can be categorized into liquid electrolytes (e.g., organic solvent electrolytes, aqueous electrolytes, and ionic liquid electrolytes), glass-ceramic electrolytes, solid polymer electrolytes, and gel polymer electrolytes.[146] In sodium-ion batteries employing PBAs as cathode materials, the electrolyte significantly influences the cycling stability and electrochemical performance of the cathode.[147,148]

As shown in Figure 7a, Lamprecht et al. investigated the dissolution mechanisms of $Na_2Ni[Fe(CN)_6]$ and $Na_2Co[Fe(CN)_6]$ as model electrodes and found the nature of anions in the electrolyte markedly affects the degradation rate of the cathode material, demonstrating that optimizing the electrolyte composition can effectively mitigate the degradation of PBAs.[33,35] They demonstrated that surface Fe sites are more favorable for anion adsorption than Ni sites, following the adsorption strength trend of $SO_4^{2-} > OH^- > Cl^- > ClO_4^- > CH_3COO^- > NO_3^-$. These anion adsorption characteristics help explain the significant differences in the stability of PBA electrodes, aligning with experimental findings that indicate

https://doi.org/10.1021/acs.jpcc.5c00877
J. Phys. Chem. C 2025, 129, 7135−7153

higher stability in the presence of weakly adsorbing anions such as ClO_4^- and NO_3^- compared to strongly adsorbing anions like SO_4^{2-} and OH^-. Given the critical role of OH^- in PBA decomposition, the basic strength of the anions must also be considered. While mild acidification of the electrolyte (pH ~ 2−3) generally enhances stability by reducing OH^- activity, excessive availability and intercalation of H_3O^+ lead to rapid degradation of the Ni—[N≡C—Fe] bond. This occurs due to protonation of the N-sites within the crystal structure, an undesirable side reaction that ultimately results in electrode dissolution.

Modifying the electrolyte solvent system is another effective strategy for improving battery performance. Firouzi et al. developed a full battery system comprising a MnHCMn(II/I) anode, the copper hexacyanoferrate (CuHCF) cathode (Figure 7b), and an organic−aqueous cosolvent Na^+ electrolyte and found that the cosolvent electrolyte effectively suppressed the dissolution of PBA electrode material, markedly extending the operational lifespan of the electrodes.[149]

Meanwhile, the sodium salts primarily supply Na^+ ions in the electrolyte, directly impacting the rate of the ionic conductors and the cycling performance of the electrode.[150,151] As shown in Figure 7c, Wu et al. report an affordable alkaline electrolyte of fluorine-free sodium perchlorate ($NaClO_4$) combined with a Ni/C coating based on a Mn-based cathode ($Na_2MnFe(CN)_6$, NMF), $NaTi_2(PO_4)_3$ (NTP) anode, obviating O_2 evolution and electrode dissolution in the cathode, achieving the high-capacity retention with a high electrode loading.[152] The full cell achieves an exceptional lifespan of over 13,000 cycles, maintaining a high capacity retention of 74.3% at 10 C. Zhou et al. proposed a 5 m $Al(CF_3SO_3)_3$ water-in-salt electrolyte (Al-WISE) in Figure 7d; the high-concentration electrolyte broadened the stable electrochemical window and effectively inhibited the dissolution of PBAs during cycling, thereby significantly enhancing the long-term cycling stability of the battery.[153]

Additives, an essential component of electrolytes, are typically composed of natural or synthetic organic and inorganic compounds designed to enhance the ionic conductivity, improve the rate performance of the electrolyte, and optimize battery performance. For example, Xie et al. demonstrated that the addition of $AlCl_3$ as an electrolyte additive successfully mitigated parasitic reactions caused by residual coordination water during charge/discharge cycles. The in situ formation of an $Al_2O_3{\cdot}3H_2O$ layer not only consumed the residual water but also protected the electrode, significantly improving the cycling stability of PBAs (Figure 7e).[43]

Similarly, Shao et al. introduced 1 wt % $CoSO_4$ as an additive into a 1 M Na_2SO_4 base electrolyte in Figure 7f. They found that Co^{2+} participated in the Na^+ intercalation/de-intercalation process, effectively suppressing the structural collapse and dissolution of the PBA ($Na_2CoFe(CN)_6$) framework.[154]

In summary, the electrolyte composition plays a crucial role in the long term cycling stability of PBA electrodes. We can adjust the electrolyte by the solvent, salt, and additives, impacting the energy density and stability of the electrode. Therefore, when exploring the stable cycling performance of electrodes, selecting suitable electrolytes is also paramount. By utilization of electrolytes with higher salt concentrations, such as 8 M $NaClO_4$, the increased ion concentration reduces the relative amount of water in the system. As the ions compete with water molecules for coordination sites in the PBA structure, this results in a decrease in the amount of coordinated water in the PBA crystal, ultimately enhancing the stability of PBA cathodes. In addition, a reduced amount of water is available to dissolve transition metals. Optimizing the electrolyte can enhance the cycle life of the electrode and improve ionic conductivity, but it may also affect electrode compatibility and induce some unpredictable side reactions.

The anode should exhibit electrolyte compatibility and cycle protocol requirements comparable to those of the PBA cathode. Regarding electrolyte composition, as mentioned above, most research indicates that high electrolyte concentrations positively influence the stability of PBA cathodes. This correlation is also observed in the majority of anode materials; however, it remains a critical factor to consider in selecting an appropriate anode.

3.4. Cycling Protocols. So far, strategies to prevent degradation have been discussed only by implementing material modifications. However, just like any galvanic cells and most prominently seen for the omnipresent Li-ion batteries, there are also physically motivated recommendations on how to use such a reversible energy storage unit.[155]

First, especially at the cathode side, high voltage leads to side reactions and gas evolution, including the evolution of H_2, CO_2, and $(CN)_2$.[83] To reduce the accompanying capacity fading, the cutoff voltage, like for Li-ion batteries, needs to be limited. Noticeably above 1.23 V, water splitting within an aqueous electrolyte takes place. The complete voltage window (e.g., 2.0−4.0 V)[156] can only be used when the electrolyte is specifically designed to support it.[40,153,156]

A comparison between various charging speeds reveals another aspect: While the retention capacity decreases at higher C-rates, the Coulombic efficiency improves with increasing current.[157−161] So far, this effect has been ascribed to the reduced extent of water intercalation during the fast-charging process.[67] An additional indication that excess water plays a significant role in that sense comes from a study that uses $Fe(CF_3SO_3)_3$ as an additive in a water-in-salt electrolyte for potassium PBA cathodes.[162] This study reports a K-ion battery full cell with an energy density as high as 92 Wh kg^{-1} and retains 82.5% of the initial capacity after 6,500 cycles at 1,500 mA g^{-1}. The electrode surface thereby undergoes a modification, and iron is substituted by manganese. At the same time, the free water content drops and Mn-dissolution is diminished. In this case, $Fe(CF_3SO_3)_3$ changes the solvation structure and the stability window increases.[163] From then on, the Coulombic efficiency becomes almost independent of the C-rate.

In conclusion, stability windows set electrochemical limits beyond possible stabilization efforts due to the thermodynamic decomposition of both the electrodes and electrolytes. The water content, however small it may be, seems to affect the Coulombic efficiency of PBA electrodes. This adverse effect is more pronounced for lower currents, which leads to two possible strategies: The higher the operating C-rate, the less one must think about the water content as a degradative effect. Alternatively, additives are needed to bind the water even more, which is also necessary to utilize high potential windows, which in turn results in a high energy density. The anode should have requirements for electrolytes and cycling protocols comparable to those of the PBA cathode. Specifically, the anode must be selected to ensure compatibility with the cycling protocol requirements of the PBA cathode. If this

https://doi.org/10.1021/acs.jpcc.5c00877
J. Phys. Chem. C 2025, 129, 7135−7153

condition is not met, then the anode may induce electrolyte decomposition, leading to the formation of parasitic by-products. For instance, in aqueous electrolytes, the generation of OH^- ions can alter the pH, ultimately compromising the stability of the PBA cathode.

4. CONCLUSIONS AND PERSPECTIVES

PBAs are considered promising candidates for next-generation battery materials. However, their practical use is still significantly constrained by the long-term performance and stability challenges. Stability issues typically arise, in most cases, from the dissolution of transition metals from the lattice framework, a process known as Transition Metal Dissolution (Figure 8). Generally, Transition Metal Dissolutions can be



Figure 8. Overview of the degradation mechanisms of PBAs and reported stabilization approaches.

triggered by multiple underlying mechanisms, including phase transitions (most prominently the Jahn–Teller effect), crystal defects, coordinated water, and side reactions. Beyond Transition Metal Dissolutions, PBA degradation is also affected by common factors seen in other battery electrode materials, such as mechanical strain during intercalation and de-intercalation, as well as thermal effects.

Current research aims to address all of these different degradation mechanisms, trying to develop more stable and efficient PBAs for energy storage applications. Synthesis plays a key role in fabricating PBAs with a high stability. Ion doping during synthesis has emerged as an effective strategy to improve the structural stability and electrochemical performance of PBAs, particularly in addressing the Jahn–Teller effect. Overcoming material limitations is accomplished by employing various doping approaches with different ion types and concentrations, approaches ranging from single-ion doping to multimetal strategies. Controlling crystal growth during synthesis by adjusting synthesis parameters is another strategy to reduce defects and the water content in PBAs. Highly crystalline cubic phases are beneficial for achieving long-life electrodes, particularly for materials such as MnHCF and CoHCF, which degrade due to Jahn–Teller distortions during cycling. These highly crystalline phases can be achieved by using chelating agents and alkali metal salts as additives during synthesis or by controlling parameters such as the pH, temperature, and aging time. Additionally, postsynthesis treatments like drying at elevated temperatures can further enhance the structural integrity of PBAs.

Nevertheless, there is also potential for optimization within the battery cell design itself, particularly in electrode fabrication, electrolyte composition, and cycling protocols during operation. Coating is a common strategy to improve interfacial reactions in the application of PBAs in batteries. Its key functions include enhancing interfacial electronic conductivity with conductive coatings, reducing interfacial reactions by adding chemically stable layers, and maintaining the structural integrity of Prussian blue with coatings that exhibit good mechanical properties. The composition of the electrolyte is also critical to the long-term cycling stability of the PBA electrodes. Adjustments to the solvent, salt, and additives can significantly enhance the stability of the electrode. With respect to cycling protocols during battery operation, stability windows set electrochemical limits beyond possible stabilization efforts due to the thermodynamic decomposition of both electrodes and electrolytes. Even minimal water content appears to influence the Coulombic efficiency of PBA electrodes. Interestingly, at higher operating C-rates, the impact of the water content on degradation seems to be less significant.

However, the precise degradation mechanisms of PBAs are still not fully understood, indicating substantial opportunities for future research. Cycling stability is a critical property for next-generation batteries. Commercially established electrodes for LIBs, such as $LiFePO_4$, $LiMn_2O_4$, and graphite, exhibit outstanding cycle life, surpassing 1000 cycles with a capacity retention greater than 80%.[22] In contrast, most PBA cathodes currently display cycle lives of less than 1000 cycles.[22] Meeting or exceeding this benchmark should be a central focus in the future development of PBAs.

Another key consideration in research should be that alkali-metal batteries should serve as an environmentally friendly alternative to commercial lithium-ion batteries, which rely on not-abundant raw materials such as cobalt. Therefore, research should prioritize PBAs with abundant raw materials, e.g., CuHCF and NiHCF, rather than those with rare earth elements, e.g., InHCF. This should also be a consideration when it comes to ion doping. Additionally, the composition, including binders, should also be environmentally sustainable, avoiding materials such as highly toxic NMP, which is currently used in the lithium-ion battery industry as a binder. The focus of PBA research should be on low-cost, environmentally friendly, and widely available materials.

To gain a deeper understanding of the reaction and degradation mechanisms of PBAs, operando studies should be conducted, such as operando Mössbauer and ex-situ Mössbauer spectroscopy.[164] Furthermore, in situ XRD presents an intriguing path for future research, as it could provide deeper insights into the structural changes occurring in PBAs during cycling.

Among PBAs, MnHCF and CoHCF exhibit both high capacity and high potential; however, they also experience the most significant stability challenges. As a result, they represent a promising focus for future research on PBA degradation and the development of potential stabilization strategies. Additionally, since the impact of water content on PBA stability remains a topic of debate, future studies should quantify water content using techniques such as thermogravimetric analysis (TGA) when characterizing PBAs. Other important research areas include examining the impact of cation selection on stability, exploring ion doping to mitigate the Jahn–Teller effect, investigating the impact of various coatings, and developing novel synthesis methods to precisely control lattice water in PBAs. Moreover, additional theoretical insights, such as DFT

https://doi.org/10.1021/acs.jpcc.5c00877
J. Phys. Chem. C 2025, 129, 7135−7153

calculations, would be valuable in guiding future research directions as well as more research on the full cell level, e.g., to investigate the influence of anode materials on PBA cathode stability.

AUTHOR INFORMATION

Corresponding Author

Aliaksandr S. Bandarenka − *Physics of Energy Conversion and Storage, Technical University of Munich, Physics Department, 85748 Garching, Germany; Catalysis Research Center TUM, 85748 Garching, Germany;* orcid.org/0000-0002-5970-4315; Email: bandarenka@ph.tum.de

Authors

Johannes Sterzinger − *Physics of Energy Conversion and Storage, Technical University of Munich, Physics Department, 85748 Garching, Germany;* orcid.org/0009-0004-2416-2124

Raphael Streng − *Physics of Energy Conversion and Storage, Technical University of Munich, Physics Department, 85748 Garching, Germany*

Shuai Chen − *Physics of Energy Conversion and Storage, Technical University of Munich, Physics Department, 85748 Garching, Germany*

Rainer Götz − *Physics of Energy Conversion and Storage, Technical University of Munich, Physics Department, 85748 Garching, Germany*

Wang Hu − *Physics of Energy Conversion and Storage, Technical University of Munich, Physics Department, 85748 Garching, Germany*

Jinyang Li − *Physics of Energy Conversion and Storage, Technical University of Munich, Physics Department, 85748 Garching, Germany*

Complete contact information is available at: https://pubs.acs.org/10.1021/acs.jpcc.5c00877

Notes

The authors declare no competing financial interest.

Biographies

Johannes Sterzinger obtained his MSc in Applied & Engineering Physics from the Technical University of Munich (TUM) in 2023 and is currently pursuing a PhD at TUM. His research focuses on optimizing functional materials for a sustainable future. As part of the Energy Conversion & Storage group at TUM and the European ICONIC project, he explores innovative nanoscale energy and catalyst materials that promote a more resource-efficient, eco-friendly, and sustainable economy.

Raphael Streng earned his MSc in Applied and Engineering Physics from the Technical University of Munich (TUM) in 2022 and is currently a PhD candidate in the Energy Conversion and Storage group at TUM. His research focuses on lithium-free aqueous batteries, with a particular emphasis on electrolyte effects on active materials and the development of sustainable battery systems for large-scale energy storage.

Shuai Chen earned his Bachelor of Engineering (2020) and Master of Engineering (2024) in Materials Science from Huazhong University of Science and Technology. He is currently studying at the Technical University of Munich (TUM) in the Energy Conversion and Storage Group, focusing on all-solid-state lithium batteries, particularly sulfide/halide electrolyte synthesis and electrode−electrolyte interface research.

Rainer Götz obtained his M.Sc. degree under the supervision of Prof. Aliaksandr S. Bandarenka and investigated during his Ph.D. studies interfaces within solid-state lithium metal batteries. Besides looking for ways to overcome these typical interfacial hurdles at solid/solid contacts*, he also developed in situ techniques that enabled the recording of electrochemical impedance and EPR spectroscopy concurrently. Such methods are of interest at the interfaces of solid-state batteries, as well as for the hydrogen evolution reaction, to combine electrochemical and physical information.

Wang Hu obtained a dual master's degree from Shanghai Jiao Tong University and Kyushu University in March 2023. He is currently pursuing his PhD in the Energy Conversion and Storage group at the Technical University of Munich (TUM). His research focuses on lithium metal batteries, with particular emphasis on the interfacial behavior between the anode and electrolyte, as well as mechanisms for suppressing lithium dendrite growth.

Jinyang Li is currently pursuing a Ph.D. in the Department of Physics at the Technical University of Munich. He received his B.S. and M.S. degrees from Ocean University of China, Qingdao. His research interests focus on novel energy conversion and storage technologies.

Aliaksandr S. Bandarenka earned his Ph.D. in physical and solid-state chemistry from Belarusian State University, Minsk, Belarus, in 2005. He then pursued postdoctoral research at the University of Twente, Netherlands, until 2008 and at the Technical University of Denmark's Department of Physics until 2010. In 2010, he became a group leader at the Center for Electrochemical Sciences (CES) at Ruhr University Bochum, Germany. Currently, he is a W3 Associate Professor in the Department of Physics at TUM, Germany. His research focuses on electrocatalyst development, batteries, interfacial charge transfer, and techniques for characterizing and modifying electrified solid/liquid interfaces. Over his career, he has received notable honors, including the Hans-Jürgen Engell Award from the International Society of Electrochemistry in 2013 and the German National Ernst Haage Award in 2016.

ACKNOWLEDGMENTS

We would like to thank the German Research Foundation (DFG) under Germany's excellence strategy − EXC 2089/1 − 390776260, Germany's excellence cluster "e-conversion", and the Excellence Strategy of the Federal Government and the Länder in the context of the ARTEMIS Innovation Network.

REFERENCES

(1) Peters, I. M.; Breyer, C.; Jaffer, S. A.; Kurtz, S.; Reindl, T.; Sinton, R.; Vetter, M. The Role of Batteries in Meeting the PV Terawatt Challenge. *Joule* **2021**, *5*, 1353−1370.

(2) Kloppenburg, S.; Smale, R.; Verkade, N. Technologies of Engagement: How Battery Storage Technologies Shape Householder Participation in Energy Transitions. *Energies* **2019**, *12*, 4384.

(3) Kong, L.; Tang, C.; Peng, H.; Huang, J.; Zhang, Q. Advanced Energy Materials for Flexible Batteries in Energy Storage: A Review. *SmartMat* **2020**, *1*, No. e1007.

(4) Cairns, E. J.; Albertus, P. Batteries for Electric and Hybrid-Electric Vehicles. *Annu. Rev. Chem. Biomol. Eng.* **2010**, *1*, 299−320.

(5) Chen, X.; Shen, W.; Vo, T. T.; Cao, Z.; Kapoor, A. An Overview of Lithium-Ion Batteries for Electric Vehicles. *2012 10th International Power & Energy Conference (IPEC)* **2012**, 230−235.

(6) Liang, Y.; Zhao, C.; Yuan, H.; Chen, Y.; Zhang, W.; Huang, J.; Yu, D.; Liu, Y.; Titirici, M.; Chueh, Y.; et al. A Review of Rechargeable Batteries for Portable Electronic Devices. *InfoMat* **2019**, *1*, 6−32.

(7) Faunce, T. A.; Prest, J.; Su, D.; Hearne, S. J.; Iacopi, F. On-Grid Batteries for Large-Scale Energy Storage: Challenges and Oppor-

tunities for Policy and Technology. *MRS Energy & Sustainability* **2018**, *5*, 10.
(8) Kalair, A.; Abas, N.; Saleem, M. S.; Kalair, A. R.; Khan, N. Role of Energy Storage Systems in Energy Transition from Fossil Fuels to Renewables. *Energy Storage* **2021**, *3*, No. e135.
(9) Kittner, N.; Lill, F.; Kammen, D. M. Energy Storage Deployment and Innovation for the Clean Energy Transition. *Nature Energy* **2017**, *2*, No. 17125.
(10) Rahimi, E.; Rabiee, A.; Aghaei, J.; Muttaqi, K. M.; Esmaeel Nezhad, A. On the Management of Wind Power Intermittency. *Renewable and Sustainable Energy Reviews* **2013**, *28*, 643−653.
(11) Tarascon, J.-M. Key Challenges in Future Li-Battery Research. *Philosophical Transactions of the Royal Society A: Mathematical, Physical and Engineering Sciences* **2010**, *368*, 3227−3241.
(12) Li, M.; Lu, J.; Chen, Z.; Amine, K. 30 Years of Lithium-Ion Batteries. *Adv. Mater.* **2018**, *30*, No. 1800561.
(13) Deng, D. Li-ion Batteries: Basics, Progress, and Challenges. *Energy Science & Engineering* **2015**, *3*, 385−418.
(14) Zhao, Y.; Pohl, O.; Bhatt, A. I.; Collis, G. E.; Mahon, P. J.; Rüther, T.; Hollenkamp, A. F. A Review on Battery Market Trends, Second-Life Reuse, and Recycling. *Sustainable Chemistry* **2021**, *2*, 167−205.
(15) Götz, R.; Streng, R.; Sterzinger, J.; Steeger, T.; Kaye, M. M.; Vitort, M.; Bandarenka, A. S. All-solid-state Li-ion batteries with commercially available electrolytes: A feasibility review. *InfoMat* **2024**, *6*, No. e12627.
(16) Kulova, T. L.; Fateev, V. N.; Seregina, E. A.; Grigoriev, A. S. A Brief Review of Post-Lithium-Ion Batteries. *Int. J. Electrochem. Sci.* **2020**, *15* (8), 7242−7259.
(17) Costa, C. M.; Barbosa, J. C.; Gonçalves, R.; Castro, H.; Campo, F. J. D.; Lanceros-Méndez, S. Recycling and Environmental Issues of Lithium-Ion Batteries: Advances, Challenges and Opportunities. *Energy Storage Materials* **2021**, *37*, 433−465.
(18) Chen, Y.; Kang, Y.; Zhao, Y.; Wang, L.; Liu, J.; Li, Y.; Liang, Z.; He, X.; Li, X.; Tavajohi, N.; et al. A Review of Lithium-Ion Battery Safety Concerns: The Issues, Strategies, and Testing Standards. *Journal of Energy Chemistry* **2021**, *59*, 83−99.
(19) Calvão, F.; Mcdonald, C. E. A.; Bolay, M. Cobalt Mining and the Corporate Outsourcing of Responsibility in the Democratic Republic of Congo. *Extractive Industries and Society* **2021**, *8*, No. 100884.
(20) Wang, B.; Han, Y.; Wang, X.; Bahlawane, N.; Pan, H.; Yan, M.; Jiang, Y. Prussian Blue Analogs for Rechargeable Batteries. *iScience* **2018**, *3*, 110−133.
(21) Zhao, S.; Guo, Z.; Yan, K.; Guo, X.; Wan, S.; He, F.; Sun, B.; Wang, G. The Rise of Prussian Blue Analogs: Challenges and Opportunities for High-Performance Cathode Materials in Potassium-Ion Batteries. *Small Structures* **2021**, *2*, No. 2000054.
(22) Peng, J.; Zhang, W.; Liu, Q.; Wang, J.; Chou, S.; Liu, H.; Dou, S. Prussian Blue Analogues for Sodium-Ion Batteries: Past, Present, and Future. *Adv. Mater.* **2022**, *34*, No. 2108384.
(23) Shu, W.; Han, C.; Wang, X. Prussian Blue Analogues Cathodes for Nonaqueous Potassium-Ion Batteries: Past, Present, and Future. *Adv. Funct. Mater.* **2024**, *34*, No. 2309636.
(24) Trócoli, R.; Houdeville, R.; Frontera, C.; Vincent, S.; Garcia Lastra, J. M.; Palacín, M. R. Prussian Blue Analogues as Positive Electrodes for Mg Batteries: Insights into Mg^{2+} Intercalation. *ChemSusChem* **2024**, *17*, No. e202301224.
(25) Li, Y.; Zhao, J.; Hu, Q.; Hao, T.; Cao, H.; Huang, X.; Liu, Y.; Zhang, Y.; Lin, D.; Tang, Y.; et al. Prussian Blue Analogs Cathodes for Aqueous Zinc Ion Batteries. *Materials Today Energy* **2022**, *29*, No. 101095.
(26) Li, W.; Han, C.; Cheng, G.; Chou, S.; Liu, H.; Dou, S. Chemical Properties, Structural Properties, and Energy Storage Applications of Prussian Blue Analogues. *Small* **2019**, *15*, No. 1900470.
(27) Yi, H.; Qin, R.; Ding, S.; Wang, Y.; Li, S.; Zhao, Q.; Pan, F. Structure and Properties of Prussian Blue Analogues in Energy Storage and Conversion Applications. *Adv. Funct. Mater.* **2021**, *31*, No. 2006970.
(28) Du, G.; Pang, H. Recent Advancements in Prussian Blue Analogues: Preparation and Application in Batteries. *Energy Storage Materials* **2021**, *36*, 387−408.
(29) Xu, C.; Yang, Z.; Zhang, X.; Xia, M.; Yan, H.; Li, J.; Yu, H.; Zhang, L.; Shu, J. Prussian Blue Analogues in Aqueous Batteries and Desalination Batteries. *Nano-Micro Letters* **2021**, *13*, 166.
(30) Xie, B.; Sun, B.; Gao, T.; Ma, Y.; Yin, G.; Zuo, P. Recent Progress of Prussian Blue Analogues as Cathode Materials for Nonaqueous Sodium-Ion Batteries. *Coord. Chem. Rev.* **2022**, *460*, No. 214478.
(31) Sada, K.; Greene, S. M.; Kmiec, S.; Siegel, D. J.; Manthiram, A. Unveiling the Influence of Water Molecules on the Structural Dynamics of Prussian Blue Analogues. *Small* **2024**, *20*, No. 2406853.
(32) Shu, W.; Li, J.; Zhang, G.; Meng, J.; Wang, X.; Mai, L. Progress on Transition Metal Ions Dissolution Suppression Strategies in Prussian Blue Analogs for Aqueous Sodium-/Potassium-Ion Batteries. *Nano-Micro Letters* **2024**, *16*, 128.
(33) Lamprecht, X.; Evazzade, I.; Ungerer, L.; Hromadko, L.; Macak, J. M.; Bandarenka, A. S.; Alexandrov, V. Mechanisms of degradation of $Na_2Ni[Fe(CN)_6]$ functional electrodes in aqueous media: a combined theoretical and experimental study. *J. Phys. Chem. C* **2023**, *127*, 2204−2214.
(34) Marzak, P.; Kosian, M.; Yun, J.; Bandarenka, A. S. Intercalation of Mg^{2+} into electrodeposited Prussian Blue Analogue thin films from aqueous electrolytes. *Electrochim. Acta* **2019**, *307*, 157−163.
(35) Lamprecht, X.; Speck, F.; Marzak, P.; Cherevko, S.; Bandarenka, A. S. Electrolyte Effects on the Stabilization of Prussian Blue Analogue Electrodes in Aqueous Sodium-Ion Batteries. *ACS Appl. Mater. Interfaces* **2022**, *14*, 3515−3525.
(36) Phadke, S.; Mysyk, R.; Anouti, M. Effect of Cation (Li^+, Na^+, K^+, Rb^+, Cs^+) in Aqueous Electrolyte on the Electrochemical Redox of Prussian Blue Analogue (PBA) Cathodes. *Journal of Energy Chemistry* **2020**, *40*, 31−38.
(37) Marzak, P.; Yun, J.; Dorsel, A.; Kriele, A.; Gilles, R.; Schneider, O.; Bandarenka, A. S. Electrodeposited $Na_2Ni[Fe(CN)_6]$ thin film cathodes exposed to simulated aqueous Na-ion battery conditions. *J. Phys. Chem. C* **2018**, *122*, 8760−8768.
(38) Nordstrand, J.; Toledo-Carrillo, E.; Vafakhah, S.; Guo, L.; Yang, H. Y.; Kloo, L.; Dutta, J. Ladder Mechanisms of Ion Transport in Prussian Blue Analogues. *ACS Appl. Mater. Interfaces* **2022**, *14*, 1102−1113.
(39) Gao, Y.; Yang, H.; Wang, X.; Bai, Y.; Zhu, N.; Guo, S.; Suo, L.; Li, H.; Xu, H.; Wu, C. The Compensation Effect Mechanism of Fe−Ni Mixed Prussian Blue Analogues in Aqueous Rechargeable Aluminum-Ion Batteries. *ChemSusChem* **2020**, *13*, 732−740.
(40) Jiang, M.; Hou, Z.; Ren, L.; Zhang, Y.; Wang, J.-G. Prussian Blue and Its Analogues for Aqueous Energy Storage: From Fundamentals to Advanced Devices. *Energy Storage Materials* **2022**, *50*, 618−640.
(41) Lamprecht, X.; Marzak, P.; Wieczorek, A.; Thomsen, N.; Kim, J.; Garlyyev, B.; Liang, Y.; Bandarenka, A. S.; Yun, J. High voltage and superior cyclability of indium hexacyanoferrate cathodes for aqueous Na-ion batteries enabled by superconcentrated $NaClO_4$ electrolytes. *RSC Energy Advances* **2022**, *1*, 623−631.
(42) Li, Z.; Liu, T.; Meng, R.; Gao, L.; Zou, Y.; Peng, P.; Shao, Y.; Liang, X. Insights into the Structure Stability of Prussian Blue for Aqueous Zinc Ion Batteries. *Energy & Environmental Materials* **2021**, *4*, 111−116.
(43) Xie, B.; Zuo, P.; Wang, L.; Wang, J.; Huo, H.; He, M.; Shu, J.; Li, H.; Lou, S.; Yin, G. Achieving Long-Life Prussian Blue Analogue Cathode for Na-Ion Batteries via Triple-Cation Lattice Substitution and Coordinated Water Capture. *Nano Energy* **2019**, *61*, 201−210.
(44) Song, J.; Wang, L.; Lu, Y.; Liu, J.; Guo, B.; Xiao, P.; Lee, J.-J.; Yang, X.-Q.; Henkelman, G.; Goodenough, J. B. Removal of Interstitial H_2O in Hexacyanometallates for a Superior Cathode of a Sodium-Ion Battery. *J. Am. Chem. Soc.* **2015**, *137*, 2658−2664.

https://doi.org/10.1021/acs.jpcc.5c00877
J. Phys. Chem. C 2025, 129, 7135−7153

(45) Ge, J.; Fan, L.; Rao, A. M.; Zhou, J.; Lu, B. Surface-Substituted Prussian Blue Analogue Cathode for Sustainable Potassium-Ion Batteries. *Nature Sustainability* **2022**, *5*, 225−234.
(46) Pan, T.-Y.; Ruqia; Wu, C.-Y.; Ni, C.-S.; Gull, S.; Haider, A.; Chen, H.-Y. Improvement in Cycling Stability of Prussian Blue Analog-Based Aqueous Sodium-Ion Batteries by Ligand Substitution and Electrolyte Optimization. *Electrochim. Acta* **2022**, *427*, No. 140778.
(47) Jeong, H.; Jo, C. Structure-Controlled Prussian Blue Analog as a Cathode Material for Long-Life Seawater Batteries. *ECS Meeting Abstracts* **2023**, *MA2023-02*, 688−688.
(48) Wang, L.; Lu, Y.; Liu, J.; Xu, M.; Cheng, J.; Zhang, D.; Goodenough, J. B. A superior low-cost cathode for a Na-ion battery. *Angewandte Chemie Int. Ed.* **2013**, *52* (7), 1964−1967.
(49) Wang, L.; Song, J.; Qiao, R.; Wray, L. A.; Hossain, M. A.; Chuang, Y. D.; Goodenough, J. B. Rhombohedral Prussian white as cathode for rechargeable sodium-ion batteries. *J. Am. Chem. Soc.* **2015**, *137* (7), 2548−2554.
(50) Peng, J.; Li, C.; Yin, J.; Wang, J.; Yu, Y.; Shen, Y.; Huang, Y. Novel cerium hexacyanoferrate (II) as cathode material for sodium-ion batteries. *ACS Applied Energy Materials* **2019**, *2* (1), 187−191.
(51) Song, J.; Wang, L.; Lu, Y.; Liu, J.; Guo, B.; Xiao, P.; Goodenough, J. B. Removal of interstitial H_2O in hexacyanometallates for a superior cathode of a sodium-ion battery. *J. Am. Chem. Soc.* **2015**, *137* (7), 2658−2664.
(52) Berrettoni, M.; Giorgetti, M.; Zamponi, S.; Conti, P.; Ranganathan, D.; Zanotto, A.; Saladino, M. L.; Caponetti, E. Synthesis and Characterization of Nanostructured Cobalt Hexacyanoferrate. *J. Phys. Chem. C* **2010**, *114*, 6401−6407.
(53) You, Y.; Yu, X.; Yin, Y.; Nam, K.-W.; Guo, Y.-G. Sodium Iron Hexacyanoferrate with High Na Content as a Na-Rich Cathode Material for Na-Ion Batteries. *Nano Research* **2015**, *8*, 117−128.
(54) Tang, Y.; Li, W.; Feng, P.; Zhou, M.; Wang, K.; Wang, Y.; Zaghib, K.; Jiang, K. High-Performance Manganese Hexacyanoferrate with Cubic Structure as Superior Cathode Material for Sodium-Ion Batteries. *Adv. Funct. Mater.* **2020**, *30*, No. 1908754.
(55) Zhou, A.; Cheng, W.; Wang, W.; Zhao, Q.; Xie, J.; Zhang, W.; Gao, H.; Xue, L.; Li, J. Hexacyanoferrate-Type Prussian Blue Analogs: Principles and Advances Toward High-Performance Sodium and Potassium Ion Batteries. *Adv. Energy Mater.* **2021**, *11*, No. 2000943.
(56) Wessells, C. D.; Huggins, R. A.; Cui, Y. Copper Hexacyanoferrate Battery Electrodes with Long Cycle Life and High Power. *Nat. Commun.* **2011**, *2*, 550.
(57) Wessells, C. D.; Peddada, S. V.; Huggins, R. A.; Cui, Y. Nickel Hexacyanoferrate Nanoparticle Electrodes For Aqueous Sodium and Potassium Ion Batteries. *Nano Lett.* **2011**, *11*, 5421−5425.
(58) Li, W. J.; Chou, S. L.; Wang, J. Z.; Wang, J. L.; Gu, Q. F.; Liu, H. K.; Dou, S. X. Multifunctional conducting polymer coated $Na_{1+x}MnFe(CN)_6$ cathode for sodium-ion batteries with superior performance via a facile and one-step chemistry approach. *Nano Energy* **2015**, *13*, 200−207.
(59) Jahn, H. A.; Teller, E. Stability of Polyatomic Molecules in Degenerate Electronic States - I—Orbital Degeneracy. *Proceedings of the Royal Society of London. Series A - Mathematical and Physical Sciences* **1937**, *161*, 220−235.
(60) Qian, J.; Wu, C.; Cao, Y.; Ma, Z.; Huang, Y.; Ai, X.; Yang, H. Prussian Blue Cathode Materials for Sodium-Ion Batteries and Other Ion Batteries. *Adv. Energy Mater.* **2018**, *8*, No. 1702619.
(61) Senn, P. A Simple Quantum Mechanical Model That Illustrates the Jahn-Teller Effect. *J. Chem. Educ.* **1992**, *69*, 819.
(62) Zheng, Y.; Xie, H.; Li, J.; Hui, K. S.; Yu, Z.; Xu, H.; Dinh, D. A.; Ye, Z.; Zha, C.; Hui, K. N. Insights into the Jahn-Teller Effect in Layered Oxide Cathode Materials for Potassium-Ion Batteries. *Adv. Energy Mater.* **2024**, *14*, No. 2400461.
(63) Kim, W. J.; Smeaton, M. A.; Jia, C.; Goodge, B. H.; Cho, B.-G.; Lee, K.; Osada, M.; Jost, D.; Ievlev, A. V.; Moritz, B.; et al. Publisher Correction: Geometric Frustration of Jahn−Teller Order in the Infinite-Layer Lattice. *Nature* **2023**, *620*, E12−E12.
(64) Yaghoobnejad Asl, H.; Manthiram, A. Proton-Induced Disproportionation of Jahn−Teller-Active Transition-Metal Ions in Oxides Due to Electronically Driven Lattice Instability. *J. Am. Chem. Soc.* **2020**, *142*, 21122−21130.
(65) Peng, F.; Yu, L.; Gao, P.; Liao, X.-Z.; Wen, J.; He, Y.; Tan, G.; Ren, Y.; Ma, Z.-F. Highly Crystalline Sodium Manganese Ferrocyanide Microcubes for Advanced Sodium Ion Battery Cathodes. *Journal of Materials Chemistry A* **2019**, *7*, 22248−22256.
(66) Gebert, F.; Cortie, D. L.; Bouwer, J. C.; Wang, W.; Yan, Z.; Dou, S.; Chou, S. Epitaxial Nickel Ferrocyanide Stabilizes Jahn−Teller Distortions of Manganese Ferrocyanide for Sodium-Ion Batteries. *Angew. Chem., Int. Ed.* **2021**, *60*, 18519−18526.
(67) Xiao, Y.; Xiao, J.; Zhao, H.; Li, J.; Zhang, G.; Zhang, D.; Guo, X.; Gao, H.; Wang, Y.; Chen, J.; et al. Prussian Blue Analogues for Sodium-Ion Battery Cathodes: A Review of Mechanistic Insights, Current Challenges, and Future Pathways. *Small* **2024**, *20*, No. 2401957.
(68) You, Y.; Wu, X.-L.; Yin, Y.-X.; Guo, Y.-G. High-quality Prussian Blue Crystals as Superior Cathode Materials for Room-Temperature Sodium-Ion Batteries. *Energy Environ. Sci.* **2014**, *7*, 1643−1647.
(69) Wu, X.; Wu, C.; Wei, C.; Hu, L.; Qian, J.; Cao, Y.; Ai, X.; Wang, J.; Yang, H. Highly Crystallized $Na_2CoFe(CN)_6$ with Suppressed Lattice Defects as Superior Cathode Material for Sodium-Ion Batteries. *ACS Appl. Mater. Interfaces* **2016**, *8*, 5393−5399.
(70) Liu, X.; Cao, Y.; Sun, J. Defect Engineering in Prussian Blue Analogs for High-Performance Sodium-Ion Batteries. *Adv. Energy Mater.* **2022**, *12*, No. 2202532.
(71) Wang, W.; Gang, Y.; Peng, J.; Hu, Z.; Yan, Z.; Lai, W.; Zhu, Y.; Appadoo, D.; Ye, M.; Cao, Y.; et al. Effect of Eliminating Water in Prussian Blue Cathode for Sodium-Ion Batteries. *Adv. Funct. Mater.* **2022**, *32*, No. 2111727.
(72) Shen, L.; Jiang, Y.; Liu, Y.; Ma, J.; Sun, T.; Zhu, N. High-Stability Monoclinic Nickel Hexacyanoferrate Cathode Materials for Ultrafast Aqueous Sodium Ion Battery. *Chemical Engineering Journal* **2020**, *388*, No. 124228.
(73) Yuan, X.; Ma, F.; Chen, X.; Sun, R.; Chen, Y.; Fu, L.; Zhu, Y.; Liu, L.; Yu, F.; Wang, J.; et al. Aqueous Zinc−Sodium Hybrid Battery Based on High Crystallinity Sodium−Iron Hexacyanoferrate. *Materials Today Energy* **2021**, *20*, No. 100660.
(74) Wang, Q.; Wang, W.; Xing, Z.; Wu, Y.; Gao, X.; Nie, C.; Cui, R.; Ju, Z. Sodium Salt Assisted Room-Temperature Synthesis of Prussian Blue Analogues as High-Performance Cathodes for Sodium-Ion Batteries. *Appl. Surf. Sci.* **2024**, *669*, No. 160499.
(75) Zhang, H.; Gao, Y.; Peng, J.; Fan, Y.; Zhao, L.; Li, L.; Xiao, Y.; Pang, W. K.; Wang, J.; Chou, S. Prussian Blue Analogues with Optimized Crystal Plane Orientation and Low Crystal Defects toward 450 Wh kg^{-1} Alkali-Ion Batteries. *Angew. Chem., Int. Ed.* **2023**, *62*, No. e202303953.
(76) Ge, L.; Song, Y.; Niu, P.; Li, B.; Zhou, L.; Feng, W.; Ma, C.; Li, X.; Kong, D.; Yan, Z.; et al. Elaborating the Crystal Water of Prussian Blue for Outstanding Performance of Sodium Ion Batteries. *ACS Nano* **2024**, *18*, 3542−3552.
(77) Duan, C.; Meng, Y.; Wang, Y.; Zhang, Z.; Ge, Y.; Li, X.; Guo, Y.; Xiao, D. High-Crystallinity and High-Rate Prussian Blue Analogues Synthesized at the Oil−Water Interface. *Inorganic Chemistry Frontiers* **2021**, *8*, 2008−2016.
(78) Guo, X.; Wang, Z.; Deng, Z.; Li, X.; Wang, B.; Chen, X.; Ong, S. P. Water Contributes to Higher Energy Density and Cycling Stability of Prussian Blue Analogue Cathodes for Aqueous Sodium-Ion Batteries. *Chem. Mater.* **2019**, *31*, 5933−5942.
(79) Nielsen, I.; Ulander, A.; Juranyi, F.; Larsen, S. R.; Karlsson, M.; Brant, W. R.; Andersson, M. S. Impact of Sodium on the Water Dynamics in Prussian Blue Analogues. *Chem. Mater.* **2024**, *36*, 11246−11253.
(80) Herren, F.; Fischer, P.; Ludi, A.; Haelg, W. Neutron Diffraction Study of Prussian Blue, $Fe_4[Fe(CN)_6]_3.xH_2O$. Location of Water Molecules and Long-Range Magnetic Order. *Inorg. Chem.* **1980**, *19*, 956−959.

https://doi.org/10.1021/acs.jpcc.5c00877
J. Phys. Chem. C 2025, 129, 7135−7153

(81) Kareis, C. M.; Lapidus, S. H.; Her, J.-H.; Stephens, P. W.; Miller, J. S. Non-Prussian Blue Structures and Magnetic Ordering of $Na_2Mn^{II}[Mn^{II}(CN)_6]$ and $Na_2Mn^{II}[Mn^{II}(CN)_6]\cdot 2H_2O$. *J. Am. Chem. Soc.* **2012**, *134*, 2246−2254.
(82) Xiao, P.; Song, J.; Wang, L.; Goodenough, J. B.; Henkelman, G. Theoretical Study of the Structural Evolution of a $Na_2FeMn(CN)_6$ Cathode upon Na Intercalation. *Chem. Mater.* **2015**, *27*, 3763−3768.
(83) Ma, Y.; Ma, Y.; Dreyer, S. L.; Wang, Q.; Wang, K.; Goonetilleke, D.; Omar, A.; Mikhailova, D.; Hahn, H.; Breitung, B.; et al. High-Entropy Metal-Organic Frameworks for Highly Reversible Sodium Storage. *Adv. Mater.* **2021**, *33*, No. 2101342.
(84) Vetter, J.; Novák, P.; Wagner, M. R.; Veit, C.; Möller, K.-C.; Besenhard, J. O.; Winter, M.; Wohlfahrt-Mehrens, M.; Vogler, C.; Hammouche, A. Ageing Mechanisms in Lithium-Ion Batteries. *J. Power Sources* **2005**, *147*, 269−281.
(85) You, Y.; Wu, X.-L.; Yin, Y.-X.; Guo, Y.-G. A Zero-Strain Insertion Cathode Material of Nickel Ferricyanide for Sodium-Ion Batteries. *Journal of Materials Chemistry A* **2013**, *1*, No. 14061.
(86) Li, W.-J.; Chou, S.-L.; Wang, J.-Z.; Kang, Y.-M.; Wang, J.-L.; Liu, Y.; Gu, Q.-F.; Liu, H.-K.; Dou, S.-X. Facile Method To Synthesize Na-Enriched $Na_{1+x}FeFe(CN)_6$ Frameworks as Cathode with Superior Electrochemical Performance for Sodium-Ion Batteries. *Chem. Mater.* **2015**, *27*, 1997−2003.
(87) Huang, Y.; Xie, M.; Wang, Z.; Jiang, Y.; Yao, Y.; Li, S.; Li, Z.; Li, L.; Wu, F.; Chen, R. A Chemical Precipitation Method Preparing Hollow-Core-Shell Heterostructures Based on the Prussian Blue Analogs as Cathode for Sodium-Ion Batteries. *Small* **2018**, *14*, No. 1801246.
(88) Hu, P.; Peng, W.; Wang, B.; Xiao, D.; Ahuja, U.; Réthoré, J.; Aifantis, K. E. Concentration-Gradient Prussian Blue Cathodes for Na-Ion Batteries. *ACS Energy Letters* **2020**, *5*, 100−108.
(89) Margadonna, S.; Prassides, K.; Fitch, A. N. Zero Thermal Expansion in a Prussian Blue Analogue. *J. Am. Chem. Soc.* **2004**, *126*, 15390−15391.
(90) Li, M.; Maisuradze, M.; Sciacca, R.; Hasa, I.; Giorgetti, M. A Structural Perspective on Prussian Blue Analogues for Aqueous Zinc-Ion Batteries. *Batteries & Supercaps* **2023**, *6*, No. e202300340.
(91) Liu, J.; Shen, Z.; Lu, C.-Z. Research Progress of Prussian Blue and Its Analogues for Cathodes of Aqueous Zinc Ion Batteries. *Journal of Materials Chemistry A* **2024**, *12*, 2647−2672.
(92) Wei, C.; Fu, X.-Y.; Zhang, L.-L.; Liu, J.; Sun, P.-P.; Gao, L.; Chang, K.-J.; Yang, X.-L. Structural Regulated Nickel Hexacyanoferrate with Superior Sodium Storage Performance by K-Doping. *Chemical Engineering Journal* **2021**, *421*, No. 127760.
(93) Liu, X.; Gong, H.; Han, C.; Cao, Y.; Li, Y.; Sun, J. Barium Ions Act as Defenders to Prevent Water from Entering Prussian Blue Lattice for Sodium-Ion Battery. *Energy Storage Materials* **2023**, *57*, 118−124.
(94) Yimtrakarn, T.; Lo, Y.; Kongcharoenkitkul, J.; Lee, J.; Kaveevivitchai, W. High Capacity and Fast Kinetics Enabled by Metal-Doping in Prussian Blue Analogue Cathodes for Sodium-Ion Batteries. *Chemistry - An Asian Journal* **2024**, *19*, No. e202301145.
(95) Wang, Y.; Jiang, N.; Liu, J.; Sun, S.; Wang, X.; Yang, J.; Yang, C.; Liu, Y. Ultralong Lifespan Zero-Cobalt/Nickel Prussian Blue Analogs Cathode Realized by Solid Solution Reaction Sodium Storage Mechanism. *Adv. Funct. Mater.* **2024**, *34*, No. 2406809.
(96) Zhu, Y.; Zhang, Z.; Bao, J.; Zeng, S.; Nie, W.; Chen, P.; Zhou, Y.; Xu, Y. Multi-metal Doped High Capacity and Stable Prussian Blue Analogue for Sodium Ion Batteries. *International Journal of Energy Research* **2020**, *44*, 9205−9212.
(97) Luo, Y.; Shen, J.; Yao, Y.; Dai, J.; Ling, F.; Li, L.; Jiang, Y.; Wu, X.; Rui, X.; Yu, Y. Inhibiting the Jahn−Teller Effect of Manganese Hexacyanoferrate via Ni and Cu Codoping for Advanced Sodium-Ion Batteries. *Adv. Mater.* **2024**, *36*, No. 2405458.
(98) Moritomo, Y.; Urase, S.; Shibata, T. Enhanced Battery Performance in Manganese Hexacyanoferrate by Partial Substitution. *Electrochim. Acta* **2016**, *210*, 963−969.
(99) Naskar, P.; Mondal, P.; Biswas, B.; Laha, S.; Banerjee, A. Investigating the Impact of Copper and Zinc Doping in High-Entropy Prussian Blue Analogues for Na-Ion Batteries: From Material Analysis to Device Fabrication. *Energy Technology* **2024**, *13*, No. 2401733.
(100) Xu, L.; Liu, Y.; Chen, M.; Wu, W.; Qiu, S.; Wu, H.; Zheng, M.; Zhang, X.; Wu, X. Suppressing Vacancies and Crystal Water of Sodium Manganese Iron-Based Prussian Blue Analogue by Potassium Doping for Advanced Sodium-Ion Batteries. *Chem. Eng. Sci.* **2025**, *302*, No. 120848.
(101) Zhang, L.-L.; Chen, Z.-Y.; Fu, X.-Y.; Yan, B.; Tao, H.-C.; Yang, X.-L. Effect of Zn-Substitution Induced Structural Regulation on Sodium Storage Performance of Fe-Based Prussian Blue. *Chemical Engineering Journal* **2022**, *433*, No. 133739.
(102) Shang, Y.; Li, X.; Song, J.; Huang, S.; Yang, Z.; Xu, Z. J.; Yang, H. Y. Unconventional Mn Vacancies in Mn−Fe Prussian Blue Analogs: Suppressing Jahn-Teller Distortion for Ultrastable Sodium Storage. *Chem.* **2020**, *6*, 1804−1818.
(103) El-Hady, D. A.; Lyu, Y.; Zhan, S.; Yang, J.; Wang, Y.; Yang, F.; Zhao, Q.; Gu, M.; Shao, M. Vacancy and Composition Engineering of Manganese Hexacyanoferrate for Sodium-Ion Storage. *ACS Applied Energy Materials* **2022**, *5*, 8547−8553.
(104) Zeng, Y.; Xu, J.; Wang, Y.; Li, S.; Luan, D.; Lou, X. W. Formation of CuMn Prussian Blue Analog Double-Shelled Nanoboxes Toward Long-Life Zn-ion Batteries. *Angew. Chem., Int. Ed.* **2022**, *61*, No. e202212031.
(105) Yu, S.; Li, Y.; Lu, Y.; Xu, B.; Wang, Q.; Yan, M.; Jiang, Y. A Promising Cathode Material of Sodium Iron−Nickel Hexacyanoferrate for Sodium Ion Batteries. *J. Power Sources* **2015**, *275*, 45−49.
(106) Fu, H.; Liu, C.; Zhang, C.; Ma, W.; Wang, K.; Li, Z.; Lu, X.; Cao, G. Enhanced Storage of Sodium Ions in Prussian Blue Cathode Material through Nickel Doping. *Journal of Materials Chemistry A* **2017**, *5*, 9604−9610.
(107) Chen, Z.-Y.; Fu, X.-Y.; Zhang, L.-L.; Yan, B.; Yang, X.-L. High-Performance Fe-Based Prussian Blue Cathode Material for Enhancing the Activity of Low-Spin Fe by Cu Doping. *ACS Appl. Mater. Interfaces* **2022**, *14*, 5506−5513.
(108) Kumar, K.; Kundu, R. Doping Engineering in Electrode Material for Boosting the Performance of Sodium Ion Batteries. *ACS Applied Materials & Interfaces* **2024**, *16*, 37346−37362.
(109) Qin, M.; Ren, W.; Jiang, R.; Li, Q.; Yao, X.; Wang, S.; You, Y.; Mai, L. Highly Crystallized Prussian Blue with Enhanced Kinetics for Highly Efficient Sodium Storage. *ACS Appl. Mater. Interfaces* **2021**, *13*, 3999−4007.
(110) Wu, X.; Sun, M.; Guo, S.; Qian, J.; Liu, Y.; Cao, Y.; Ai, X.; Yang, H. Vacancy-Free Prussian Blue Nanocrystals with High Capacity and Superior Cyclability for Aqueous Sodium-Ion Batteries. *ChemNanoMat* **2015**, *1*, 188−193.
(111) Rehman, R.; Peng, J.; Yi, H.; Shen, Y.; Yin, J.; Li, C.; Fang, C.; Li, Q.; Han, J. Highly Crystalline Nickel Hexacyanoferrate as a Long-Life Cathode Material for Sodium-Ion Batteries. *RSC Adv.* **2020**, *10*, 27033−27041.
(112) Shi, L.; Bi, X.; Newcomer, E.; Hall, D. M.; Gorski, C. A.; Galal, A.; Logan, B. E. Co-Precipitation Synthesis Control for Sodium Ion Adsorption Capacity and Cycle Life of Copper Hexacyanoferrate Electrodes in Battery Electrode Deionization. *Chemical Engineering Journal* **2022**, *435*, No. 135001.
(113) Shu, W.; Huang, M.; Geng, L.; Qiao, F.; Wang, X. Highly Crystalline Prussian Blue for Kinetics Enhanced Potassium Storage. *Small* **2023**, *19*, No. 2207080.
(114) Xu, Y.; Wan, J.; Huang, L.; Xu, J.; Ou, M.; Liu, Y.; Sun, X.; Li, S.; Fang, C.; Li, Q.; et al. Dual Redox-Active Copper Hexacyanoferrate Nanosheets as Cathode Materials for Advanced Sodium-Ion Batteries. *Energy Storage Materials* **2020**, *33*, 432−441.
(115) Deng, L.; Qu, J.; Niu, X.; Liu, J.; Zhang, J.; Hong, Y.; Feng, M.; Wang, J.; Hu, M.; Zeng, L.; et al. Defect-Free Potassium Manganese Hexacyanoferrate Cathode Material for High-Performance Potassium-Ion Batteries. *Nat. Commun.* **2021**, *12*, 2167.
(116) Lee, H.-W.; Wang, R. Y.; Pasta, M.; Woo Lee, S.; Liu, N.; Cui, Y. Manganese Hexacyanomanganate Open Framework as a High-Capacity Positive Electrode Material for Sodium-Ion Batteries. *Nat. Commun.* **2014**, *5*, 5280.

https://doi.org/10.1021/acs.jpcc.5c00877
J. Phys. Chem. C 2025, 129, 7135−7153

(117) Kjeldgaard, S.; Dugulan, I.; Mamakhel, A.; Wagemaker, M.; Iversen, B. B.; Bentien, A. Strategies for Synthesis of Prussian Blue Analogues. *Royal Society Open Science* **2021**, *8*, No. 201779.
(118) Jiang, L.; Lu, Y.; Zhao, C.; Liu, L.; Zhang, J.; Zhang, Q.; Shen, X.; Zhao, J.; Yu, X.; Li, H.; et al. Building Aqueous K-Ion Batteries for Energy Storage. *Nature Energy* **2019**, *4*, 495−503.
(119) Zuo, D.; Wang, C.; Wu, J.; Qiu, H.; Zhang, J.; Han, J.; Liu, X. Effect of Co-Precipitation pH on the Electrochemical Properties of Prussian Blue Electrode Materials for Sodium-Ion Batteries. *Solid State Ionics* **2019**, *336*, 120−128.
(120) Park, S.; Kim, J.; Yi, S.; Chun, S. Coprecipitation Temperature Effects of Morphology-Controlled Nickel Hexacyanoferrate on the Electrochemical Performance in Aqueous Sodium-Ion Batteries. *ChemSusChem* **2021**, *14*, 1082−1093.
(121) Zakaria, M. B.; Chikyow, T. Recent Advances in Prussian Blue and Prussian Blue Analogues: Synthesis and Thermal Treatments. *Coord. Chem. Rev.* **2017**, *352*, 328−345.
(122) Chen, R.; Huang, Y.; Xie, M.; Wang, Z.; Ye, Y.; Li, L.; Wu, F. Chemical Inhibition Method to Synthesize Highly Crystalline Prussian Blue Analogs for Sodium-Ion Battery Cathodes. *ACS Appl. Mater. Interfaces* **2016**, *8*, 31669−31676.
(123) Camacho, P. S.; Wernert, R.; Duttine, M.; Wattiaux, A.; Rudola, A.; Balaya, P.; Fauth, F.; Berthelot, R.; Monconduit, L.; Carlier, D.; et al. Impact of Synthesis Conditions in Na-Rich Prussian Blue Analogues. *ACS Appl. Mater. Interfaces* **2021**, *13*, 42682−42692.
(124) Wang, W.; Gang, Y.; Hu, Z.; Yan, Z.; Li, W.; Li, Y.; Gu, Q.-F.; Wang, Z.; Chou, S.-L.; Liu, H.-K.; et al. Reversible Structural Evolution of Sodium-Rich Rhombohedral Prussian Blue for Sodium-Ion Batteries. *Nat. Commun.* **2020**, *11*, 980.
(125) Geng, W.; Zhang, Z.; Yang, Z.; Tang, H.; He, G. Non-Aqueous Synthesis of High-Quality Prussian Blue Analogues for Na-Ion Batteries. *Chem. Commun.* **2022**, *58*, 4472−4475.
(126) Zhang, R.; Liu, Y.; Liu, H.; Zhong, Y.; Zhang, Y.; Wu, Z.; Wang, X. Y-Tube Assisted Coprecipitation Synthesis of Iron-Based Prussian Blue Analogues Cathode Materials for Sodium-Ion Batteries. *RSC Adv.* **2024**, *14*, 12096−12106.
(127) Xu, C.; Yang, Z.; Zhang, X.; Xia, M.; Yan, H.; Li, J.; Yu, H.; Zhang, L.; Shu, J. Correction to: Prussian Blue Analogues in Aqueous Batteries and Desalination Batteries. *Nano-Micro Letters* **2021**, *13*, 187.
(128) Syed Mohd Fadzil, S. A. F.; Woo, H. J.; Azzahari, A. D.; Winie, T.; Kufian, M. Z. Sodium-Rich Prussian Blue Analogue Coated by Poly(3,4-Ethylenedioxythiophene) Polystyrene Sulfonate as Superior Cathode for Sodium-Ion Batteries. *Materials Today Chemistry* **2023**, *30*, No. 101540.
(129) Wu, X.; Ru, Y.; Bai, Y.; Zhang, G.; Shi, Y.; Pang, H. PBA Composites and Their Derivatives in Energy and Environmental Applications. *Coord. Chem. Rev.* **2022**, *451*, No. 214260.
(130) Xue, Y.; Shen, X.; Zhou, H.; Cao, J.; Pu, J.; Ji, Z.; Kong, L.; Yuan, A. Vanadium Hexacyanoferrate Nanoparticles Connected by Cross-Linked Carbon Nanotubes Conductive Networks for Aqueous Zinc-Ion Batteries. *Chemical Engineering Journal* **2022**, *448*, No. 137657.
(131) Jiang, Y.; Yu, S.; Wang, B.; Li, Y.; Sun, W.; Lu, Y.; Yan, M.; Song, B.; Dou, S. Prussian Blue@C Composite as an Ultrahigh-Rate and Long-Life Sodium-Ion Battery Cathode. *Adv. Funct. Mater.* **2016**, *26*, 5315−5321.
(132) Ruan, Y.; Chen, L.; Cui, L.; An, Q. PPy-Modified Prussian Blue Cathode Materials for Low-Cost and Cycling-Stable Aqueous Zinc-Based Hybrid Battery. *Coatings* **2022**, *12*, 779.
(133) Mukherjee, P.; Vishwanath, R. S.; Borenstein, A.; Zidki, T. Compositing Redox-Rich Co−Co@Ni−Fe PBA Nanocubes into Cauliflower-like Conducting Polypyrrole as an Electrode Material in Supercapacitors. *Materials Chemistry Frontiers* **2023**, *7*, 1110−1119.
(134) Chen, M.; Li, X.; Yan, Y.; Yang, Y.; Xu, Q.; Liu, H.; Xia, Y. Polypyrrole-Coated $K_2Mn[Fe(CN)_6]$ Stabilizing Its Interfaces and Inhibiting Irreversible Phase Transition during the Zinc Storage Process in Aqueous Batteries. *ACS Appl. Mater. Interfaces* **2022**, *14*, 1092−1101.
(135) Ye, L.; Fu, H.; Ji, J.; Wu, Z.; Ren, H.; Zhang, Y.; Shi, M.; Yang, J. Bilayer Mn-Based Prussian Blue Cathode with High Redox Activity for Boosting Stable Cycling in Aqueous Sodium-Ion Half/Full Batteries. *J. Colloid Interface Sci.* **2025**, *684*, 635−646.
(136) Zuo, D.; Wang, C.; Han, J.; Han, Q.; Hu, Y.; Wu, J.; Qiu, H.; Zhang, Q.; Liu, X. One-Step Synthesis of Novel Core-Shell Bimetallic Hexacyanoferrate for High Performance Sodium-Storage Cathode. *Journal of Materials Science & Technology* **2022**, *114*, 180−190.
(137) Sun, J.; Ye, H.; Oh, J. A. S.; Sun, Y.; Plewa, A.; Wang, Y.; Wu, T.; Zeng, K.; Lu, L. Alleviating Mechanical Degradation of Hexacyanoferrate via Strain Locking during Na^+ Insertion/Extraction for Full Sodium Ion Battery. *Nano Research* **2022**, *15*, 2123−2129.
(138) Choi, T.-U.; Baek, G.; Lee, S. G.; Lee, J.-H. Hierarchically Designed Cathodes Composed of Vanadium Hexacyanoferrate@Copper Hexacyanoferrate with Enhanced Cycling Stability. *ACS Appl. Mater. Interfaces* **2020**, *12*, 24817−24826.
(139) Wang, Z.; Huang, Y.; Luo, R.; Wu, F.; Li, L.; Xie, M.; Huang, J.; Chen, R. Ion-Exchange Synthesis of High-Energy-Density Prussian Blue Analogues for Sodium Ion Battery Cathodes with Fast Kinetics and Long Durability. *J. Power Sources* **2019**, *436*, No. 226868.
(140) Liu, Y.; He, D.; Cheng, Y.; Li, L.; Lu, Z.; Liang, R.; Fan, Y.; Qiao, Y.; Chou, S. A Heterostructure Coupling of Bioinspired, Adhesive Polydopamine, and Porous Prussian Blue Nanocubics as Cathode for High-Performance Sodium-Ion Battery. *Small* **2020**, *16*, No. 1906946.
(141) Morant-Giner, M.; Sanchis-Gual, R.; Romero, J.; Alberola, A.; García-Cruz, L.; Agouram, S.; Galbiati, M.; Padial, N. M.; Waerenborgh, J. C.; Martí-Gastaldo, C.; et al. Prussian Blue@MoS2Layer Composites as Highly Efficient Cathodes for Sodium- and Potassium-Ion Batteries. *Adv. Funct. Mater.* **2018**, *28*, No. 1706125.
(142) Delmas, C. Sodium and Sodium-Ion Batteries: 50 Years of Research. *Adv. Energy Mater.* **2018**, *8*, No. 1703137.
(143) Sirengo, K.; Babu, A.; Brennan, B.; Pillai, S. C. Ionic Liquid Electrolytes for Sodium-Ion Batteries to Control Thermal Runaway. *Journal of Energy Chemistry* **2023**, *81*, 321−338.
(144) Huang, Y.; Zhao, L.; Li, L.; Xie, M.; Wu, F.; Chen, R. Electrolytes and Electrolyte/Electrode Interfaces in Sodium-Ion Batteries: From Scientific Research to Practical Application. *Adv. Mater.* **2019**, *31*, No. 1808393.
(145) Dreyer, S. L.; Maddar, F. M.; Kondrakov, A.; Janek, J.; Hasa, I.; Brezesinski, T. Elucidating Gas Evolution of Prussian White Cathodes for Sodium-ion Battery Application: The Effect of Electrolyte and Moisture. *Batteries & Supercaps* **2024**, *7* (4), No. e202300595.
(146) Aslfattahi, N.; Samylingam, L.; Kiai, M. S.; Kadirgama, K.; Kulish, V.; Schmirler, M.; Said, Z. State-of-the-Art Review on Electrolytes for Sodium-Ion Batteries: Potential Recent Progress and Technical Challenges. *Journal of Energy Storage* **2023**, *72*, No. 108781.
(147) Ojwang, D. O.; Häggström, L.; Ericsson, T.; Mogensen, R.; Brant, W. R. Guest Water Hinders Sodium-Ion Diffusion in Low-Defect Berlin Green Cathode Material. *Dalton Transactions* **2022**, *51*, 14712−14720.
(148) Maddar, F. M.; Walker, D.; Chamberlain, T. W.; Compton, J.; Menon, A. S.; Copley, M.; Hasa, I. Understanding Dehydration of Prussian White: From Material to Aqueous Processed Composite Electrodes for Sodium-Ion Battery Application. *Journal of Materials Chemistry A* **2023**, *11*, 15778−15791.
(149) Firouzi, A.; Qiao, R.; Motallebi, S.; Valencia, C. W.; Israel, H. S.; Fujimoto, M.; Wray, L. A.; Chuang, Y.-D.; Yang, W.; Wessells, C. D. Monovalent Manganese Based Anodes and Co-Solvent Electrolyte for Stable Low-Cost High-Rate Sodium-Ion Batteries. *Nat. Commun.* **2018**, *9*, 861.
(150) Gao, T.; Wang, B.; Wang, L.; Liu, G.; Wang, F.; Luo, H.; Wang, D. $LiAlCl_4$-$3SO_2$ as a High Conductive, Non-Flammable and Inorganic Non-Aqueous Liquid Electrolyte for Lithium Ion Batteries. *Electrochim. Acta* **2018**, *286*, 77−85.

https://doi.org/10.1021/acs.jpcc.5c00877
J. Phys. Chem. C 2025, 129, 7135−7153

(151) Darjazi, H.; Falco, M.; Colò, F.; Balducci, L.; Piana, G.; Bella, F.; Meligrana, G.; Nobili, F.; Elia, G. A.; Gerbaldi, C. Electrolytes for Sodium Ion Batteries: The Current Transition from Liquid to Solid and Hybrid Systems. *Adv. Mater.* **2024**, *36*, No. 2313572.
(152) Wu, H.; Hao, J.; Jiang, Y.; Jiao, Y.; Liu, J.; Xu, X.; Davey, K.; Wang, C.; Qiao, S.-Z. Alkaline-Based Aqueous Sodium-Ion Batteries for Large-Scale Energy Storage. *Nat. Commun.* **2024**, *15*, 575.
(153) Zhou, A.; Jiang, L.; Yue, J.; Tong, Y.; Zhang, Q.; Lin, Z.; Liu, B.; Wu, C.; Suo, L.; Hu, Y.-S.; et al. Water-in-Salt Electrolyte Promotes High-Capacity $FeFe(CN)_6$ Cathode for Aqueous Al-Ion Battery. *ACS Appl. Mater. Interfaces* **2019**, *11*, 41356−41362.
(154) Shao, T.; Li, C.; Liu, C.; Deng, W.; Wang, W.; Xue, M.; Li, R. Electrolyte Regulation Enhances the Stability of Prussian Blue Analogues in Aqueous Na-Ion Storage. *Journal of Materials Chemistry A* **2019**, *7*, 1749−1755.
(155) Zhang, S. S. Challenges and Strategies for Fast Charge of Li-Ion Batteries. *ChemElectroChem.* **2020**, *7*, 3569−3577.
(156) Yan, X.; Yang, Y.; Liu, E.; Sun, L.; Wang, H.; Liao, X.-Z.; He, Y.; Ma, Z.-F. Improved Cycling Performance of Prussian Blue Cathode for Sodium Ion Batteries by Controlling Operation Voltage Range. *Electrochim. Acta* **2017**, *225*, 235−242.
(157) Zhang, Z.; Avdeev, M.; Chen, H.; Yin, W.; Kan, W. H.; He, G. Lithiated Prussian Blue Analogues as Positive Electrode Active Materials for Stable Non-Aqueous Lithium-Ion Batteries. *Nat. Commun.* **2022**, *13*, 7790.
(158) Yang, S.; Feng, X.; Min, X.; Ma, B.; Liu, Y.; Mi, R.; Wu, X.; Wang, W.; Huang, Z.; Fang, M. Multi-Metal Substituted Fe-Based Prussian Blue as High-Capacity Cathode Material for Potassium Ion Batteries. *Chem. Phys. Lett.* **2024**, *852*, No. 141522.
(159) Naskar, P.; Debnath, S.; Maiti, A.; Biswas, B.; Banerjee, A. Low-Cost and Scalable Ni-Prussian Blue Analogue//Functionalized Carbon Based Na-Ion Systems for All Climate Operations. *ChemPhysChem* **2023**, *24*, No. e202200588.
(160) Wang, Y.; Li, Q.; Hong, H.; Yang, S.; Zhang, R.; Wang, X.; Jin, X.; Xiong, B.; Bai, S.; Zhi, C. Lean-Water Hydrogel Electrolyte for Zinc Ion Batteries. *Nat. Commun.* **2023**, *14*, 3890.
(161) Wu, J.; Zheng, Y.; Zhang, P.; Rao, X.; Zhang, Z.; Wu, J.-M.; Wen, W. A Rocking-Chair Rechargeable Seawater Battery. *Research* **2024**, *7*, No. 0461.
(162) Ge, J.; Fan, L.; Rao, A. M.; Zhou, J.; Lu, B. Surface-Substituted Prussian Blue Analogue Cathode for Sustainable Potassium-Ion Batteries. *Nature Sustainability* **2022**, *5*, 225−234.
(163) Schkeryantz, L. A.; Zheng, J.; McCulloch, W. D.; Qin, L.; Zhang, S.; Moore, C. E.; Wu, Y. Designing Potassium Battery Salts through a Solvent-in-Anion Concept for Concentrated Electrolytes and Mimicking Solvation Structures. *Chem. Mater.* **2020**, *32*, 10423−10434.
(164) Wang, Z.; Sougrati, M. T.; He, Y.; Le Pham, P. N.; Xu, W.; Iadecola, A.; Ge, R.; Zhou, W.; Zheng, Q.; Li, X.; et al. Sodium Storage and Capacity Retention Behavior Derived from High-Spin/Low-Spin Fe Redox Reaction in Monoclinic Prussian Blue Based on Operando Mössbauer Characterization. *Nano Energy* **2023**, *109*, No. 108256.

https://doi.org/10.1021/acs.jpcc.5c00877
J. Phys. Chem. C 2025, 129, 7135−7153

6. Controlling the Morphology and Electrochemical Properties of Electrodeposited Nickel Hexacyanoferrate Thin Films.

T. Steeger,* R.L. Streng,* A. Senyshyn, V. Dyadkin, X. Lamprecht, R. List, A. S. Bandarenka. *ChemElectroChem* **2025**, 12, 2500073.

ChemElectroChem | Research Article doi.org/10.1002/celc.202500073 | Chemistry Europe

www.chemelectrochem.org

Controlling the Morphology and Electrochemical Properties of Electrodeposited Nickel Hexacyanoferrate

Tim Steeger, Raphael L. Streng, Anatoliy Senyshyn, Vadim Dyadkin, Xaver Lamprecht, Roman List, and Aliaksandr S. Bandarenka*

In recent years, Prussian blue analogs (PBAs) have gained significant attention due to their broad applicability. The synthesis routines of this material class have been shown to allow for great tunability by varying the corresponding parameters. The control of crystal phase, defect, and water content, as well as electrochemical properties, have been studied extensively for the state-of-the-art coprecipitation method. In turn, electrochemical deposition, which is particularly suited for thin-film production, remains mainly underexplored. This study investigates the effects of synthesis temperature, scan rate, precursor concentration, and supporting electrolyte pH on nickel hexacyanoferrate (NiHCF) films electrodeposited onto a high surface area carbon-based substrate via cyclic voltammetry. Electrochemical analysis and morphological characterization reveal that higher deposition temperatures increase cation-specific capacity, influence NiHCF coverage, and promote larger, more crystalline structures. Scan rate, precursor concentration, and pH variations further demonstrate the correlation between deposition parameters, crystallite size, and NiHCF structure. These findings highlight the tunability of electrodeposited PBAs for tailored electrochemical performance and morphology.

1. Introduction

The material class of Prussian blue analogs (PBAs) has attracted increasing attention in recent years due to their suitability for a wide range of applications ranging from gas storage and capture[1–3] to water desalination,[4,5] medicine,[6,7] and energy storage.[8,9] Their compatibility with aqueous, organic, and even solid-state electrolytes and their open-framework structure make them promising candidates, particularly as cathodes for novel electrochemical energy storage systems beyond Li-ion batteries (LIBs).[10–12] Besides their large interstitial sites that allow PBAs to accommodate large cations,[13–15] they feature a unique open-channel structure that enables fast cation transport and superior fast-charging capabilities.[16,17] Hence, they have been successfully implemented as cathode materials in aqueous and organic Na-, K-, Mg-, Ca-, Zn-, and Al-ion batteries, underlining their exceptional versatility.[10,18–24]

PBAs can be represented by the general formula $A_xM_A[M_B(CN)_6]_y\square_{1-y} \cdot zH_2O$, where A is the guest cation, M_A is the N-coordinated transition metal (e.g., Mn, Fe, Co, Ni or Cu), M_B is the C-coordinated transition metal (commonly Fe), and □ denotes an $M_B(CN)_6$ vacancy.[8] Conventionally, PBAs are synthesized by coprecipitation from M_A- and $M_B(CN)_6$-salt precursors in an aqueous solution.[25–27] Hereby, the resulting crystal phase, defect and water content, and electrochemical performance can be effectively tuned by varying specific synthesis parameters, such as temperature, additives, solution pH, and precursor concentration.[28–30] Notably, investigations on the effects of coprecipitation temperature on nickel hexacyanoferrate (NiHCF) morphology and performance by Park et al. showed that higher temperatures lead to larger particles with higher specific capacities. In contrast, lower temperatures lead to smaller particles with enhanced rate capability.[31]

Besides the coprecipitation approach, PBAs can be prepared by a facile single-step electrochemical deposition on top of a conductive substrate.[32–36] While this method is less common due to its limited scalability toward high mass loadings and areal capacities, it can be a powerful tool for synthesizing PBA thin films with exceptional fast-charging capabilities for supercapacitor-like hybrid batteries.[16,17] Furthermore, the large variety of non-battery applications of PBAs includes analytic systems such as bio and electrochemical sensors with a wide range of requirements beyond cation storage capacity.[38–40] As for the coprecipitation method, multiple electrodeposition parameters can be tuned to achieve specific morphologies and electrochemical properties. In 2017, Ma et al. showed significant morphology changes between nickel hexacyanoferrate thin films deposited on carbon cloth (CC) substrates by cyclic voltammetry (CV),

T. Steeger, R. L. Streng, X. Lamprecht, R. List, A. S. Bandarenka
Physics of Energy Conversion and Storage, Physik-Department
Technische Universität München
James-Franck-Str. 1, 85748 Garching, Germany
E-mail: bandarenka@ph.tum.de

A. Senyshyn
Heinz Maier-Leibnitz Zentrum (MLZ)
Technische Universität München
Lichtenbergstr. 1, 85748 Garching, Bavaria, Germany

V. Dyadkin
Swiss-Norwegian Beamlines
ESRF–The European Synchrotron
Avenue des Martyrs 71, 38042 Grenoble Cedex 9, France

Supporting information for this article is available on the WWW under https://doi.org/10.1002/celc.202500073

© 2025 The Author(s). ChemElectroChem published by Wiley-VCH GmbH. This is an open access article under the terms of the Creative Commons Attribution License, which permits use, distribution and reproduction in any medium, provided the original work is properly cited.

© 2025 The Author(s). ChemElectroChem published by Wiley-VCH GmbH

pulsed electrodeposition (UPED), or potentiostatic methods.[41] Further modifications could be achieved by varying the deposition potential and pulse time for the UPED method, enabling the optimization toward high specific capacitances as required for supercapacitor applications. Yet, the effect of other parameters, such as temperature and precursor concentration, on the morphology of electrodeposited PBA films requires further investigation to enhance the tunability of these electrodes to the specific requirements of each use case.

This work investigates the influence of deposition temperature, scan rate, concentration of the $NiCl_2$ and $K_3Fe(CN)_6$ precursor solutions, and supporting electrolyte pH on the structure, morphology, and Na-ion storage capacity of NiHCF films deposited on a carbon cloth substrate via cyclic voltammetry. The effects of each parameter variation are analyzed in detail by combining electrochemical methods, scanning electron microscopy (SEM), X-ray diffraction (XRD), and quartz crystal microbalance (QCM) measurements. To the best of our knowledge, this is the first study systematically investigating these effects on the electrodeposition method. Although less common than the coprecipitation method, this synthesis process enables the controlled in situ growth of PBA films for model systems and other applications. The findings of this work have direct implications for the design of high-performance PBA functional electrodes and demonstrate the exceptional versatility of the electrodeposition approach.

2. Results and Discussion

CC is a high-specific surface-area conductive substrate that is cost-effective and lightweight and exhibits mechanical and chemical stability in aqueous solutions. Electrochemically activated CC (CCEA) exhibits enhanced wettability, improving the homogeneity and adhesion of NiHCF, and is therefore used as a substrate in this work.[42]

Figure 1 shows the electrodeposition process of NiHCF on a CCEA substrate. The standard deposition procedure involves cycling CCEA in the precursor solution at a scan rate of 50 mV s^{-1} until no further growth of the peak current is observed. This is followed by four cycles at 10 mV s^{-1} to ensure more accurate CV acquisition. Figure 1A shows the CV curves recorded during the initial cycles of the growth period at 50 mV s^{-1}. The CV shape exhibits the peak structure characteristics of NiHCF, corresponding to the Fe^{II}/Fe^{III} transition, which can be described by the following simplified reaction

$$NaNi[Fe^{III}(CN)_6](s) + Na^+(aq) + e^- \Leftrightarrow Na_2Ni[Fe^{II}(CN)_6](s) \quad (1)$$

In reality, this process involves at least three steps.[43] Increasing peak currents reflect the growth of active NiHCF on the CCEA surface. The electrodeposition is reflected by a small reduction peak on the left, only discernible in the initial cycles. It corresponds to the reduction of $[Fe^{III}(CN)_6]^{3-}$, which is accompanied by the formation of NiHCF and can be modeled as

$$2Na^+(aq) + Ni^{2+}(aq) + [Fe^{III}(CN)_6]^{3-}(aq) + e^- \Rightarrow Na_2Ni[Fe(CN)_6](s) \quad (2)$$

Figure 1B shows the evolution of the areal charge with time during the electrodeposition procedure. The growth of NiHCF on the substrate surface corresponds to a capacity increase reflected by the rising charge oscillation amplitude. Transitioning to the slower 10 mV s^{-1} cycling speed results in a jump in capacity due to a reduction in diffusion limitations.

To evaluate the influence of the electrodeposition temperature on the NiHCF growth behavior, **Figure 2** depicts the electrochemical results obtained from electrodepositions performed with temperatures ranging from 25 to 90 °C. Figure 2A shows the areal capacity per cycle during the electrodeposition at 50 mV s^{-1}. The growth rate shows no clear trend during the initial 10–30 cycles, likely due to minor substrate inconsistencies and

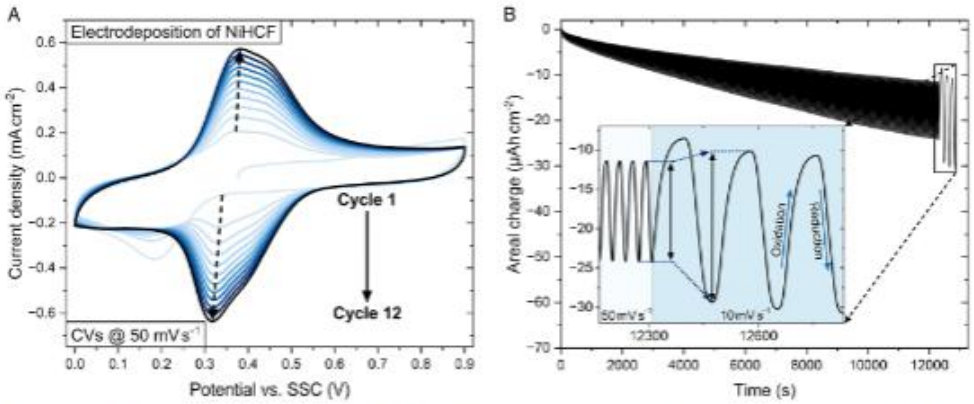


Figure 1. Electrodeposition of NiHCF onto a CC substrate at 25 °C deposition temperature using standard concentration and scan rate. A) Initial CV cycles during the 50 mV s^{-1} growth period. B) Evolution of the areal charge with time during the 50 mV s^{-1} growth period and subsequent 10 mV s^{-1} cycling period for more precise data acquisition.

© 2025 The Author(s). ChemElectroChem published by Wiley-VCH GmbH

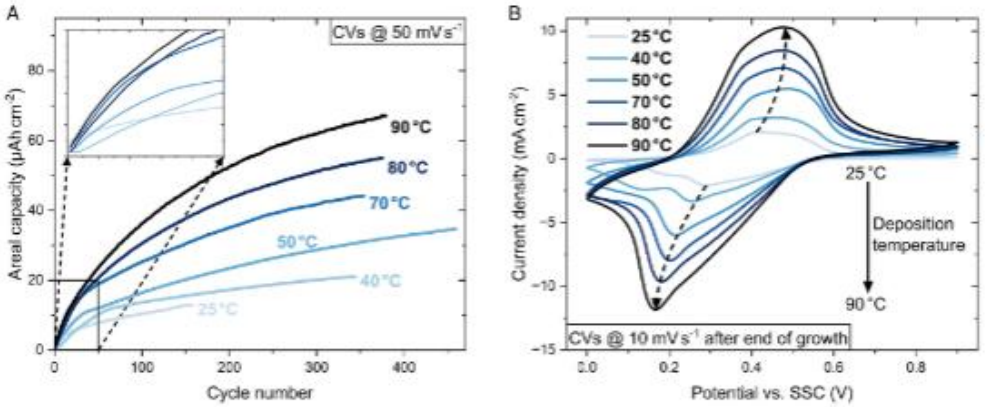


Figure 2. Electrodeposition behavior of NiHCF on CCEA substrates for different deposition temperatures. A) Evolution of the areal capacity per cycle for the 50 mV s^{-1} growth period. B) CV cycles at 10 mV s^{-1} following the completion of the NiHCF growth at 50 mV s^{-1}.

incomplete precursor mixing. Across all temperatures, growth begins rapidly, flattens over time, and exhibits consistent deposition durations, particularly at higher temperatures. Overall, higher deposition temperatures result in increased growth rates and final areal capacities. The 10 mV s^{-1} CV cycles recorded after no further growth was detected at 50 mV s^{-1} are depicted in Figure 2B. For all temperatures, they exhibit similar shapes and growing peak current densities with rising deposition temperature, reflecting gradually increasing final areal capacities.

For morphological and structural investigations of NiHCF, the samples electrodeposited at different temperatures were analyzed by SEM and XRD after careful rinsing and drying. **Figure 3** shows selected SEM images for each deposition temperature. 25 °C electrodepositions mainly result in closed NiHCF thin films, which constitute fused, cube-shaped crystallites. Cracks and regions with detaching battery films suggest an average film thickness of ≈200 nm (see Figure S1A, Supporting Information). Despite primarily homogeneous coverage, individual crystallites are visible in some areas. Between 25 and 40 °C, coverage transitions toward predominantly single crystallites. At higher deposition temperatures, individual crystallites dominate, except at 70 °C, where the morphology reverts to continuous thin-film coverage with fewer crystallites than at 25 °C. This behavior was consistently observed across multiple 70 °C samples. The estimated average film thickness of ≈400 nm (see Figure S1B, Supporting Information) at 70 °C represents a significant increase over the 25 °C baseline, likely due to a larger average size of crystallites forming the film. Accordingly, while 25 and 70 °C may represent a temperature optimum for inducing continuous coverage among the investigated temperatures, these films consist of merged individual primary particles. Despite temperature variations, all samples exhibit a cubic crystallite shape. However, the average crystallite size appears to increase with higher deposition temperatures. For a more detailed investigation, particle size distributions (Figure S2, Supporting Information) of individual crystallites were created for all temperatures except 70 °C due to insufficient coverage with individual crystallites.

Figure 4A shows the resulting Lorentz distributions approximating these particle size distributions, yielding average particle sizes as presented in Figure 4B. Here, a clear trend of increasing particle size with rising temperature, ranging from about (81 ± 8) nm at 25 °C to (340 ± 56) nm at 90 °C, is observed. The most pronounced increment occurs between 25 and 50 °C. The increase is more gradual between 50 and 80 °C, which coincides with the formation of continuous battery films observed for 70 °C depositions. Additionally, higher deposition temperatures result in more significant variance in particle size, reflected by broader distributions.

Figure 5A shows the XRD patterns of these samples with varying deposition temperatures together with the pattern of the bare CCEA support. For all samples containing NiHCF, a series of weak, sharp Bragg reflections were detected on top of the broad diffraction signal from the CCEA support. Subtracting the CCEA background yields a series of small reflections extending to a larger momentum transfer, as depicted in Figure 5B. The systematic absence of reflections (especially regarding the strong 220 reflection expected at 11.6° 2θ) indicates that the lattice symmetry is lower than cubic.[44] Therefore, data analysis was performed using a monoclinic structure model (P21/n space group), resulting in a pseudocubic lattice (cubic: ICDD PDF-5+ database, PDF# 01-070-1662, 2025; monoclinic: ICDD PDF-5+ database, PDF# 01-090-9209, 2025).[44] All samples exhibit similar XRD patterns, showing that the more continuous films produced at 25 and 70 °C share the same underlying structure as the other temperatures.

The pseudocubic (200) and (400) reflections (observed at 8.1 and 16.2° 2θ) are particularly well suited for a single profile decomposition. This involved fitting both reflections for each deposition temperature, as also shown in Figure 5B, and yields the respective peak position and width, as depicted in **Figure 6A,B**. The systematic shift in peak positions toward lower

© 2025 The Author(s). ChemElectroChem published by Wiley-VCH GmbH

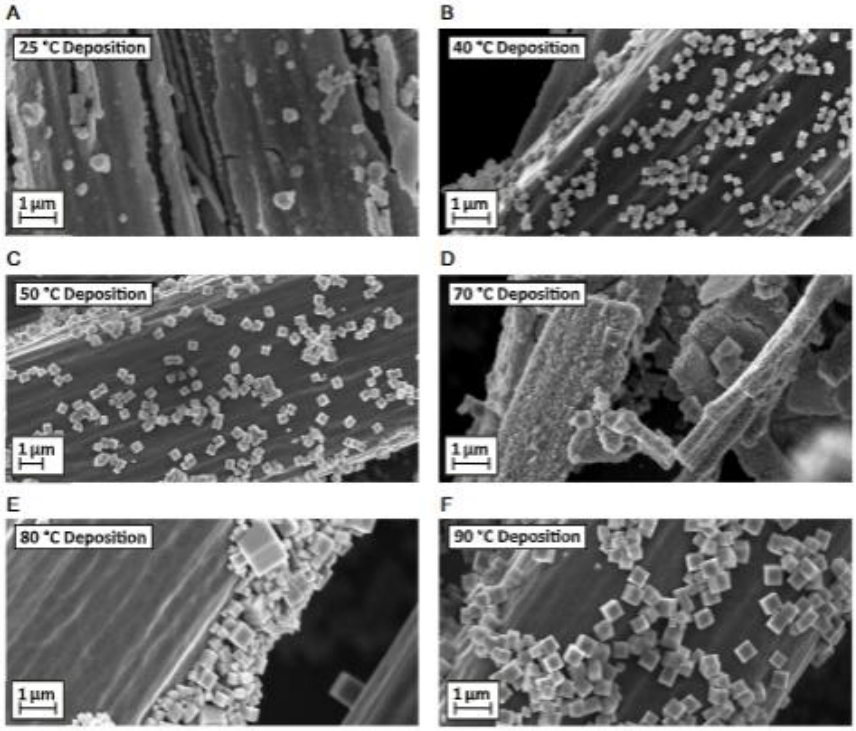


Figure 3. SEM images of NiHCF deposited onto CCEA substrates at different deposition temperatures. A) 25 °C electrodeposition. B) 40 °C electrodeposition. C) 50 °C electrodeposition. D) 70 °C electrodeposition. E) 80 °C electrodeposition. F) 90 °C electrodeposition.

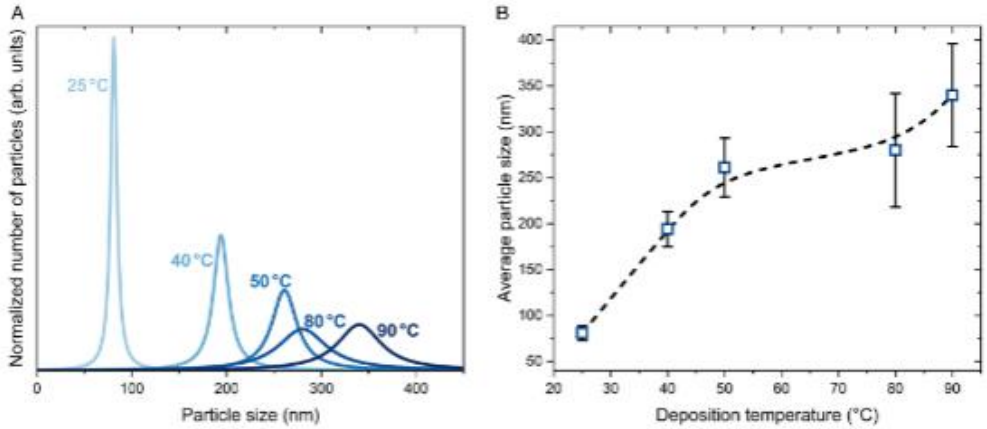


Figure 4. Particle size analysis of NiHCF crystallites deposited onto CCEA substrates at different deposition temperatures. A) Particle size distributions of NiHCF crystallites obtained from SEM images. B) Corresponding average particle size. The dashed line provides guidance for the eye.

angles with rising deposition temperature corresponds to an increase in the symmetry of the pseudocubic lattice. A substantial reduction in peak widths can be observed between the 25 and 50 °C samples, along with a nearly unchanged FWHM for samples with temperatures ranging from 50 to 90 °C. Nevertheless, for all temperatures, the FWHM is higher than the resolution of the diffractometer. The width of characteristic Bragg reflections can be considered a measure of crystallinity/mosaicity, indicating higher

© 2025 The Author(s). ChemElectroChem published by Wiley-VCH GmbH

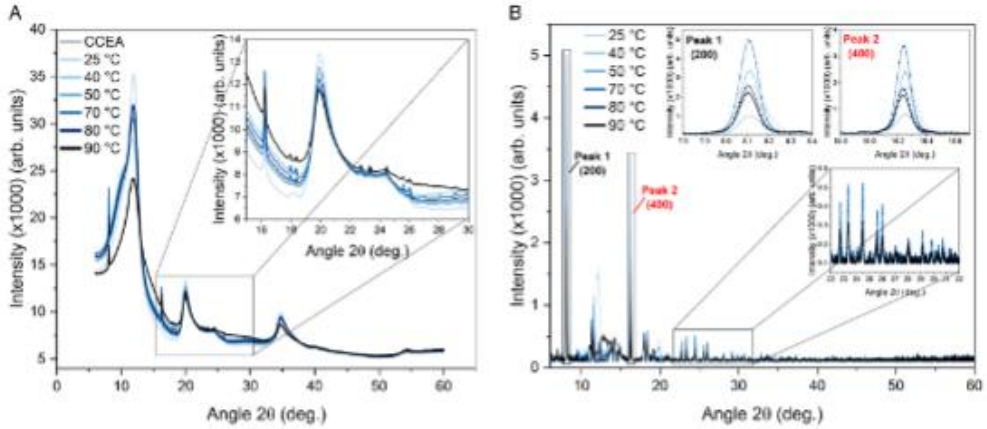


Figure 5. Diffraction patterns of NiHCF samples deposited onto CCEA substrates at different deposition temperatures. A) Unaltered diffraction patterns, including the bare CCEA substrate. B) Diffraction patterns of samples with different deposition temperatures with subtracted CCEA background together with single profile decompositions of the pseudocubic (200) and (400) reflections (marked as peak 1 and peak 2).

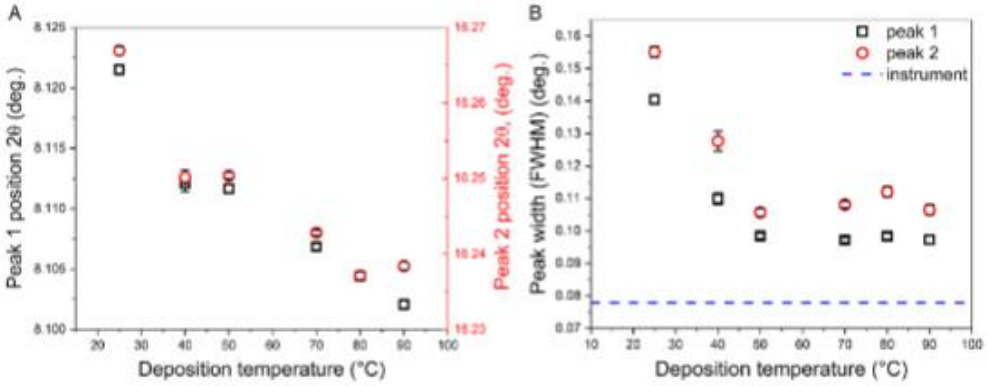


Figure 6. Peak parameters resulting from the single profile decomposition of the pseudocubic (200) and (400) reflections (marked as peak 1 and peak 2) for NiHCF samples deposited at different deposition temperatures. A) Positions of peak 1 and peak 2. B) Full width at half maximum (FWHM) of peak 1 and peak 2.

crystallinity for increased deposition temperatures. This observation coincides with the increased crystallite size found for elevated deposition temperatures.

The best results of the full profile decomposition in accordance with the monoclinic structure model are listed in Table S1, Supporting Information. Figure S3A, Supporting Information, shows the representative fit of the full profile decomposition for the 80 °C sample. The resulting lattice parameters *a*, *b*, and *c* and the corresponding monoclinic angle β and cell volume are depicted in Figure S3B–F, Supporting Information for all deposition temperatures. In agreement with the single profile decomposition results, the cell volume increases with rising deposition temperature, while the separate parameters of the monoclinic lattice display more complex behavior: The lattice parameters and *c* increase with rising temperature, while *b* decreases. The monoclinic angle displays a well-defined minimum for 40 and 50 °C depositions. To quantify the distortion of the monoclinic lattice with respect to the cubic metrics, a distortion parameter was introduced

$$\Delta = |a - \bar{l}| + \left|b - \frac{\bar{l}}{\sqrt{2}}\right| + \left|c - \frac{\bar{l}}{\sqrt{2}}\right|, \quad \text{with } \bar{l} = \frac{1}{3}\left(a + \sqrt{2}b + \sqrt{2}c\right) \tag{3}$$

Samples with 50, 70, and 80 °C depositions display significantly lower values of lattice distortion, as shown in Figure S3G, Supporting Information, indicating metric proximity to the cubic lattice. It stands to reason that these samples exhibit a higher degree of intercalation, as sodium-ion intercalation is typically associated with a transition between the cubic and monoclinic phases.[45] However, it is unclear why this occurs at these

© 2025 The Author(s). ChemElectroChem published by Wiley-VCH GmbH

particular temperatures since the electrodepositions consistently concluded in a fully intercalated state. The analysis of the sample peak broadening yields Figure S3H, Supporting Information, and reveals the presence of larger microstrains in the 25 and 40 °C samples, which can be directly related to the relatively low chemical homogeneity of these samples (in agreement with the single profile decomposition). The significant jump between 25 and 40 °C, along with the substantially increased microstrain for the 40 °C sample, can most likely be related to the transition toward single-crystallite coverage observed during the SEM analysis.

Together with the growth behavior, the trends observed with the SEM and XRD analysis can be explained by the higher mobility of ions in the precursor solution associated with rising deposition temperatures, which inhibits the formation of concentration gradients in the electrodeposition electrolyte. This influences supersaturation levels, which dictate nucleation and growth processes during the electrodeposition.[46–48] Enhanced mobility ensures uniform ion distribution, promoting more consistent nucleation and the growth of larger, higher-quality crystallites. At higher temperatures, atoms and ions possess greater kinetic energy, enabling them to move more freely and rearrange into well-ordered, thermodynamically stable crystalline structures. This enhanced atomic mobility promotes crystal growth over nucleation. While elevated temperatures can initially increase nucleation, at a certain threshold, nucleation rates decrease as atoms preferentially incorporate into existing crystallites rather than forming new nuclei. This shift favors the development of larger crystals instead of numerous smaller ones.

Previous studies on the precipitation of PBAs suggest that crystal formation follows a multistep growth process. Initially, small primary particles form and aggregate to reduce surface energy. These aggregates further minimize porosity and defect content, which promotes the growth of larger particles. At higher temperatures, surface energy is reduced, facilitating the dissolution of smaller crystallites and the redeposition of their material onto larger ones, a process driven by the thermodynamic stability of larger crystallites due to their lower surface-to-volume ratio. Additionally, elevated temperatures enhance diffusion, accelerating the transport of atoms or ions to crystallite surfaces and ensuring a continuous supply of material for growth. This increased atomic mobility also allows for defect reduction within the crystal lattice, leading to larger, higher-quality crystallites.[31,49] In addition, the nucleation and growth rates also directly depend on the temperature. The XRD analysis indicates increased crystallinity and chemical homogeneity for rising deposition temperatures, which is associated with a lower defect content and larger crystallite size. Since water, in addition to occupying interstitial sites, coordinates to exposed transition metal sites at vacancies, a defect-reduced crystal structure typically coincides with a lower content of water, which is promoted by favored dehydration at higher temperatures.[31,50,51] Accordingly, bigger crystallites can be associated with increased specific capacities due to the reduced share of inactive vacancies and water in the structure.

Electrochemical QCM measurements were conducted to confirm the correlation between deposition temperature and specific capacity. They allow for the simultaneous, in-operando determination of NiHCF mass and capacity. **Figure 7A** shows the respective areal charge and mass loading oscillations, exhibiting growing amplitudes as the NiHCF grows on the substrate surface during a 25 °C electrodeposition with standard parameters. The initial growth stage involving 15 CV cycles at a scan rate of 50 mV s^{-1} is followed by a 10 mV s^{-1} period, allowing for more accurate capacity and mass determination. The specific capacity for each temperature is calculated as the weighted average based on the fraction of areal capacity measured during the oxidation and the respective QCM mass change from three 10 mV s^{-1} cycles, with the mass derived from the quartz crystal's resonance frequency shift. The capacity estimation is performed during oxidation, as this process typically exhibits more reversible values due to the underlying reduction mechanism during the electrodeposition. Figure 7B depicts the resulting specific capacity of

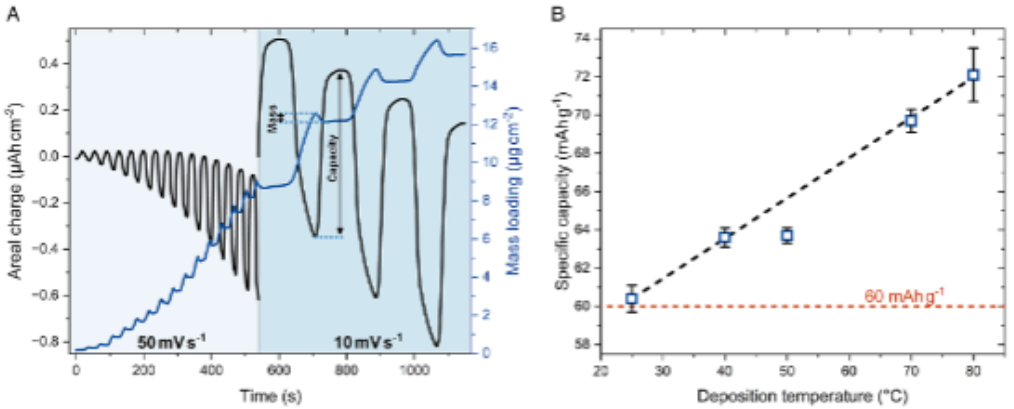


Figure 7. Specific capacity determination for the electrodeposition of NiHCF on QCM chips at different deposition temperatures. A) Areal charge and mass loading during the electrodeposition procedure at 25 °C. The mass loading reflects the data retrieved from the QCM system. B) Specific capacity of NiHCF for different deposition temperatures. The respective values correspond to the specific capacity determined during the oxidation of the more accurate 10 mV s^{-1} cycling stage. The dashed line provides guidance for the eye.

© 2025 The Author(s). ChemElectroChem published by Wiley-VCH GmbH

NiHCF for electrodeposition temperatures ranging from 25 to 80 °C. Temperatures higher than 80 °C were avoided due to the limited temperature resistance of the QCM system. The specific capacity shows a clear, linearly increasing trend with rising temperature, growing from about 60 mAh g^{-1} at 25 °C to ≈72 mAh g^{-1} at 80 °C. Based on this trend, it is reasonable to assume that 90 °C electrodepositions yield even higher specific capacities. These results confirm the relationship between higher deposition temperatures and improved specific capacity due to a lower defect and water content. Although the water content is not measured directly, the increased specific capacity indicates that more interstitial sites are available for Na-intercalation at higher synthesis temperatures, coinciding with a reduced amount of interstitial water blocking these sites.[51]

As demonstrated, temperature control significantly impacts the electrochemical properties and morphology of electrodeposited NiHCF by influencing the crystallite nucleation and growth behavior. A similar effect is expected from related deposition parameters that affect concentration gradients near the electrode surface and alter supersaturation levels. Key factors in this regard include the deposition scan rate and the concentration of the precursor solution. To investigate the influence of the electrodeposition scan rate, concentration, and pH value, electrodepositions of NiHCF were performed on CCEA substrates. At the same time, the deposition temperature was fixed at 90 °C to maintain superior growth behavior. **Figure 8**A shows representative SEM images resulting from electrodepositions with scan rates ranging from 10 to 200 mV s^{-1} and a constant precursor solution concentration of 0.25 M Na_2SO_4 (pH = 7), 1 mM $NiCl_2$, and 1 mM $K_3[Fe(CN)_6]$. Scan rates of 50 (see Figure 3F), 75, and 100 mV s^{-1} result in similar coverage dominated by individual crystallites, with occasional continuous thin films constituting fused crystallites. Electrodepositions at 10 and 200 mV s^{-1} produce fragmented coverage, with fewer individual crystallites and more clusters and fragments of continuous thin films. Besides the 10 mV s^{-1} samples, continuous thin film formation appears to be more pronounced for higher scan rates, while the overall coverage decreases. Despite these differences, the fundamental cube-shaped crystallite structure remains unchanged across all scan rates. However, varying scan rates appear to affect crystallite sizes, prompting further analysis via particle size distributions (Figure S4, Supporting Information). Figure 8B depicts the resulting Lorentz distributions approximating these particle size distributions. A similar coverage was observed for the 10 and 200 mV s^{-1} samples, corresponding to a large average particle size and high variance. 50 and

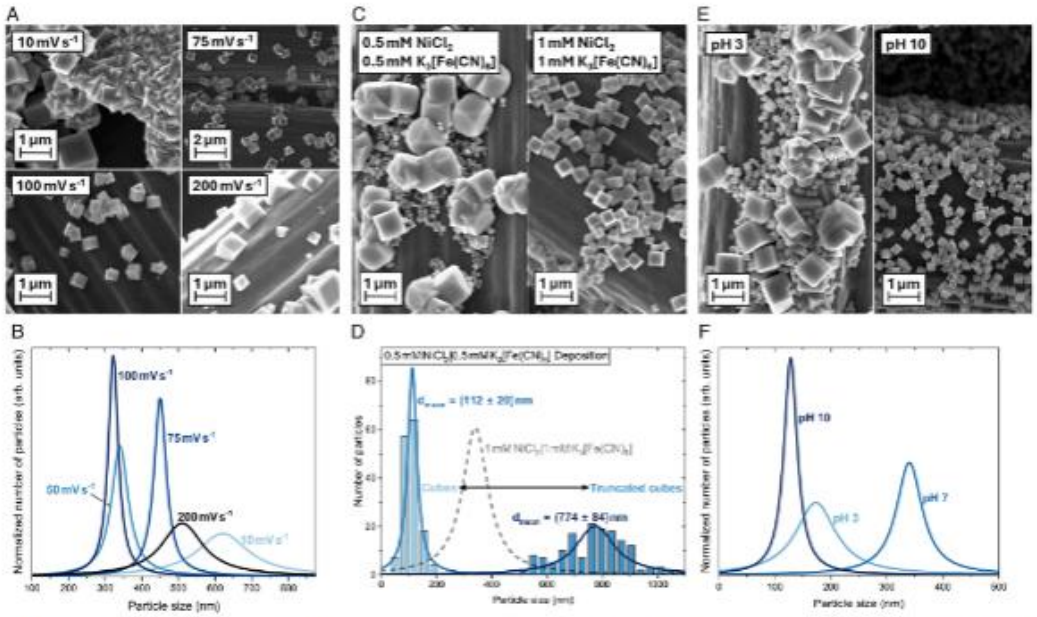


Figure 8. SEM images and particle size analysis for NiHCF deposited onto CCEA substrates at 90 °C with different deposition scan rates, precursor solution concentrations, and pH values. A) SEM images of NiHCF electrodeposited at various scan rates with a constant precursor solution concentration (1 mM $NiCl_2$, 1 mM $K_3[Fe(CN)_6]$) and a supporting electrolyte pH of 7. B) Corresponding particle size distributions of NiHCF crystallites. Evaluated for 300 individual particles and approximated with Lorentz distributions. C) SEM images of NiHCF electrodeposited at a scan rate of 50 mV s^{-1} with different precursor solution concentrations and a supporting electrolyte pH of 7. D) Corresponding particle size distributions of NiHCF crystallites. E) SEM images of NiHCF electrodeposited at a scan rate of 50 mV s^{-1} for different precursor solution pH values with a constant precursor solution concentration (1 mM $NiCl_2$, 1 mM $K_3[Fe(CN)_6]$). F) Corresponding particle size distributions of NiHCF crystallites. Evaluated for 300 individual particles and approximated with Lorentz distributions.

© 2025 The Author(s). ChemElectroChem published by Wiley-VCH GmbH

100 mV s^{-1} depositions yield the lowest particle sizes, while 75 mV s^{-1} results in medium-sized particles. Overall, both lower and higher scan rates lead to larger average particle sizes. The observed trend likely results from varying concentration gradients similar to those noted in the previous investigation. Low scan rates provide more time for ion diffusion, which reduces concentration gradients. In contrast, high scan rates involve briefer periods of negative overpotentials that fulfill the supersaturation criterion for electrodeposition.[46] This reduces ion depletion per cycle and also leads to lower concentration gradients. Consequently, both low and high scan rates favor more crystalline growth, resulting in larger average crystallite sizes. This suggests the average particle size tunability based on the deposition scan rate, allowing for control over crystallite size and potentially impacting the electrochemical characteristics of electrodeposited NiHCF.

To illustrate the effect of the precursor concentration, Figure 8C compares an SEM image of the 50 mV s^{-1} sample deposited at 90 °C using the standard concentration with a sample where the $NiCl_2$ and $K_3[Fe(CN)_6]$ concentration was reduced to 0.5 mM. The lower precursor concentration leads to the formation of truncated cubes, which primarily occur in clusters. The truncated cubes are significantly larger (over 1 µm) than the standard cubic crystallites, smaller versions of which are also present on this sample's surface. Figure 8D shows the associated particle size distribution and corresponding Lorentz distribution compared to the sample with the standard concentration. The cube-shaped crystallites present on the low-concentration sample exhibit a significantly smaller average size than the size obtained from the standard deposition at 90 °C. The truncated cubes observed in this sample have the largest average crystallite size recorded across all samples presented in this study. These truncated cubes likely result from the ongoing growth of standard cubes enabled by the unique nucleation and crystal growth conditions occurring at lower concentrations. This is likely due to the fact that, after initial nucleation, the growth of existing crystallites is thermodynamically favored at lower concentrations. Once these crystallites reach their maximum size, new crystallites begin to form but remain small due to the eventual depletion of the precursor solution. The presence of both structures suggests that low concentrations offer a viable pathway to significantly modify NiHCF morphology, producing two distinct crystallite sizes and morphologies within the same sample.

To investigate the influence of the supporting electrolyte pH, electrodepositions at 50 mV s^{-1} and 90 °C were conducted using a precursor concentration of 1 mM $NiCl_2$ and 1 mM $K_3[Fe(CN)_6]$ while adjusting the pH of the 0.25 M Na_2SO_4 supporting electrolyte to 3 and 10. Figure 8E shows selected SEM images of the resulting NiHCF crystallites. Lower pH leads to a wider range of particle sizes and promotes crystallite agglomeration, whereas higher pH values result in more uniformly sized and well-separated crystallites. The respective particle size was again analyzed by creating particle size distributions (Figure S5, Supporting Information) and approximated using Lorentz distributions, which are depicted in Figure 8F. The distribution for pH 7 represents the standard 90 °C sample (see Figure S2E, S4B, Supporting Information). Similar to the effect of the scan rate, both low and high pH values yield smaller average particle sizes than the pH 7 sample. Furthermore, as evident from the SEM images themselves, the pH 3 sample exhibits a wider range of particle sizes, while pH 10 produces the sharpest distribution. This trend is influenced by differences in nucleation kinetics and the pH-dependent hydrolysis and decomposition of $[Fe(CN)_6]^{3-}$.[52,53] Higher pH promotes more uniform crystallite growth, while neutral pH provides optimal conditions for achieving the largest average crystallite sizes.

It should be noted that the exact role of each individual parameter is difficult to isolate since it is specific to the respective parameter combination. However, clear trends emerge. Deposition temperature has the most significant effect on capacity and particle size, with higher temperatures promoting larger crystallites and fewer defects. The precursor concentration significantly influences morphology, with lower concentrations favoring the formation of truncated cubes. Among the conditions investigated, electrodepositions at 90 °C, 50 mV s^{-1}, 1 mM $NiCl_2$, and 1 mM $K_3[Fe(CN)_6]$ resulted in the highest areal capacity at the end of the deposition and a high specific capacity.

Furthermore, it is worth mentioning that truly continuous thin films like the one observed for the standard deposition at 25 °C, as commonly reported in the literature, only form for very specific parameter combinations (like 25 and 70 °C for the given parameters). Based on the results of this study, achieving continuous NiHCF films with both high specific capacities and sufficiently high thickness for applications requiring high areal capacities appears unlikely. Therefore, further investigations of the specific parameters that trigger either continuous or single-crystallite growth should be conducted in the future.

3. Conclusion

This study demonstrates the tunability of PBA films prepared via electrodeposition by systematically varying key synthesis parameters. Notably, the electrolyte temperature during deposition was found to significantly influence film growth dynamics and electrochemical performance. Higher deposition temperatures accelerated film growth and increased achievable areal capacities. SEM and XRD analysis further revealed that elevated temperatures lead to the formation of larger, more separated crystallites, indicative of higher chemical homogeneity, a lower defect content, and improved cation storage capacity. Electrochemical QCM measurements confirmed this enhancement, showing that the specific capacity of NiHCF increased from 60 to 72 mAh g^{-1} when the deposition temperature was raised from 25 to 80 °C.

Beyond temperature effects, further investigations into scan rate, precursor concentration, and supporting electrolyte pH also revealed prominent morphological changes, reinforcing the versatility of electrodeposited PBA electrodes. Notably, both high (200 mV s^{-1}) and low (10 mV s^{-1}) scan rates promoted the growth of larger crystallites, while a decrease in concentration introduced an additional crystal morphology in the form of truncated cubes. These findings highlight the potential for tailoring the morphology and electrochemical properties of NiHCF and other PBAs through controlled electrodeposition. By optimizing synthesis

© 2025 The Author(s). ChemElectroChem published by Wiley-VCH GmbH

conditions, this approach can pave the way for the development of high-performance PBA-based materials for energy storage and a wide range of other applications.

4. Experimental Section

Material Synthesis

All chemicals for substrate preparation and NiHCF electrodeposition were purchased from commercial suppliers and used without further purification.

Material Synthesis: Substrate Preparation

Carbon cloth (CC, Plain Carbon Cloth 1071 HCB, Fuel Cell Store, USA) served as the primary substrate for the electrodeposition of NiHCF. Each sample was subjected to sequential 10 min ultrasonication in acetone, ethanol, and DI water, with water rinses between each step. After this cleaning, the samples were left to dry. To improve the wettability of the otherwise hydrophobic substrate, CC samples were electrochemically activated (electrochemical oxidative exfoliation) based on a procedure proposed by Ye et al.[54] Electrochemical activation involves the oxidation of CC in a 0.1 M Na_2SO_4 (Grüssing, Germany) and 2 M KOH (Thermo Fisher Scientific, USA) solution using a two-electrode configuration with CC as the positive electrode and glassy carbon as the counter electrode. The oxidation was performed at about 10 V for 2 min using an HP/Agilent E3616A 60 W DC power supply (Keysight Technologies, USA). During this process, substantial gas evolution at both electrodes was observed. SO_4^{2-} ions were chosen due to their superior exfoliation properties for graphitic samples.[55] Electrochemically activated carbon cloth substrates will be denoted as CCEA.

Material Synthesis: Electrodeposition of NiHCF

The electrodeposition of NiHCF was either conducted on CCEA or QCM200 quartz crystal microbalance (QCM, Stanford Research Systems, USA) gold substrates (titanium/gold crystals). All electrodepositions were performed using a three-electrode setup in a closed glass cell under constant argon flow to maintain an inert atmosphere. The electrochemical methods were applied via a VSP-300 (BioLogic, France) potentiostat using a platinum wire counter electrode (MaTeck, Germany) and an Ag/AgCl reference electrode (SSC, 3 M KCl, SI Analytics, Germany) connected to the electrolyte via a Luggin capillary.

CCEA samples were placed in a custom-made acrylic glass holder to ensure uniform electrical contact with all CC fibers while exposing ≈1.77 cm^2 of CC surface area to the electrolyte on both sides. The electrodeposition of NiHCF involved CV cycling between 0.0 V and 0.9 V versus SSC in a 0.25 M Na_2SO_4-based precursor solution prepared as outlined below. To investigate the influence of temperature, a scan rate of 50 mV s^{-1} was used, followed by four 10 mV s^{-1} cycles after the NiHCF growth had seized. Precursor temperatures ranging from 25 to 90 °C were studied. For each electrodeposition, 90 mL of 0.25 M Na_2SO_4 containing 1 mM $NiCl_2$ (Alfa Aesar, USA) was added to the main cell after argon purging. This solution was then indirectly heated to the target temperature using an HD-4 heating circulator (Julabo, Germany). Meanwhile, 10 mL of 0.25 M Na_2SO_4 containing 1 mM $K_3[Fe(CN)_6]$ (Sigma–Aldrich, USA) was purged of oxygen in a preconditioning cell. Once the 90 mL Ni^{2+}-containing solution reached the desired temperature, the remaining 10 mL $Fe(CN)_6^{3-}$-containing solution was added to the main cell, and CV cycling was initiated. This method prevents premature NiHCF coprecipitation and ensures stable temperatures and proper precursor mixing once the solutions are combined. Cycling concluded at 0.0 V versus SSC, and the precursor solutions were immediately removed to prevent degradation. Finally, the cell was rinsed with DI water, and the samples were retrieved, carefully washed with DI water, dried, and stored for further evaluation. For QCM samples, cycling follows a standardized protocol of 15 cycles at 50 mV s^{-1} followed by four cycles at 10 mV s^{-1} to ensure proper thin film growth and accurate measurement values. The temperature was reduced to a range from 25 to 80 °C due to the limited temperature resistance of the QCM system.

To investigate the influence of the scan rate, NiHCF electrodepositions were performed on CCEA substrates using a precursor solution concentration of 0.25 M Na_2SO_4, 1 mM $NiCl_2$, and 1 mM $K_3[Fe(CN)_6]$ at a fixed temperature of 90 °C, with scan rates ranging from 10 to 200 mV s^{-1}. The effect of the precursor concentration was examined similarly, maintaining a scan rate of 50 mV s^{-1} and a temperature of 90 °C while reducing the $NiCl_2$ and $K_3[Fe(CN)_6]$ concentrations to 0.5 mM. The influence of the supporting electrolyte pH was determined by adjusting the pH value of the 0.25 M Na_2SO_4 (before the addition of $NiCl_2$ and $K_3[Fe(CN)_6]$) to pH 3 using H_2SO_4 (Sigma–Aldrich, USA) and pH 10 using NaOH (Grüssing, Germany), while utilizing a scan rate of 50 mV s^{-1}, a temperature of 90 °C and precursor concentrations of 1 mM $NiCl_2$, and 1 mM $K_3[Fe(CN)_6]$.

Material Characterization

The resulting NiHCF morphology was investigated using a Gemini NVision40 field emission scanning electron microscope (Zeiss, Germany). Distributions were created from the corresponding SEM images using ImageJ software to analyze the average particle size.

For XRD, the samples were first pulverized in a hydraulic press. A small portion of each powder was then structurally characterized using powder diffraction and synchrotron radiation. The samples were filled into 0.5 mm glass capillaries and mounted on a capillary spinner. Structural studies were performed at the Swiss-Norwegian beamline BM1A (ESRF, Grenoble, France) with a photon energy of 17.792 keV, $\lambda = 0.725912$ Å.[56] The calibration of the setup was performed with the LaB_6 SRM 660c standard. The 2D diffraction data from a Pilatus 2M detector were reduced using the SNBL Toolbox program package.[56]

Electrochemical characterization data was obtained from the electrodeposition process, primarily focusing on the more precise 10 mV s^{-1} cycling period following the main growth phase.

Acknowledgements

The authors thank Mr. Siegfried Schreier for his assistance in acquiring SEM data. We acknowledge Deutsche Forschungsgemeinschaft (DFG, German Research Foundation) under Germany's Excellence Strategy – EXC 2089/1 – 390776260 (e-conversion) for funding. A.S.B. acknowledges additional financial support from TUM Innovation Network for Artificial Intelligence powered Multifunctional Material Design (ARTEMIS).

Open Access funding enabled and organized by Projekt DEAL.

Conflict of Interest

The authors declare no conflict of interest.

© 2025 The Author(s). ChemElectroChem published by Wiley-VCH GmbH

Author Contributions

Tim Steeger: conceptualization (equal); data curation (equal); formal analysis (equal); investigation (equal); writing—original draft (lead); writing—review and editing (lead). **Raphael L. Streng**: conceptualization (equal); data curation (equal); formal analysis (equal); investigation (equal); writing—original draft (lead); writing—review and editing (lead). **Anatoliy Senyshyn**: formal analysis (equal); investigation (equal); software (lead); writing—original draft (supporting); writing—review and editing (equal). **Vadim Dyadkin**: data curation (equal); formal analysis (supporting); investigation (supporting); writing—original draft (supporting); writing—review and editing (supporting). **Xaver Lamprecht**: conceptualization (equal); formal analysis (supporting); investigation (supporting); methodology (equal); writing—original draft (supporting); writing—review and editing (supporting). **Roman List**: data curation (supporting); formal analysis (supporting); writing—original draft (supporting); writing—review and editing (supporting). **Aliaksandr Bandarenka**: conceptualization (equal); formal analysis (supporting); writing—original draft (supporting); writing—review and editing (supporting); Funding and supervision (leading). **Tim Steeger** and **Raphael L. Streng** contributed equally to this work.

Keywords: batteries · electrochemical depositions · electron microscopy · nickel hexacyanoferrate · Prussian blue analogs · supercapacitor · X-ray diffraction

[1] S. S. Kaye, J. R. Long, *Catal. Today* **2007**, *120*, 311.
[2] P. K. Thallapally, R. K. Motkuri, C. A. Fernandez, B. P. McGrail, G. S. Behrooz, *Inorg. Chem.* **2010**, *49*, 4909.
[3] L. E. A. Reguera, C. P. Krap, J. Balmaseda, E. Reguera, *J. Phys. Chem. C* **2008**, *112*, 15893.
[4] C. Xu, Z. Yang, X. Zhang, M. Xia, H. Yan, J. Li, H. Yu, L. Zhang, J. Shu, *Nano-Micro Lett.* **2021**, *13*, 1.
[5] E. Sebti, M. M. Besli, M. Metzger, S. Hellstrom, M. J. Schultz-Neu, J. Alvarado, J. Christensen, M. Doeff, S. Kuppan, C. V. Subban, *Desalination* **2020**, *487*, 114479.
[6] C. R. Patra, *Nanomedicine* **2016**, *11*, 569.
[7] P. Wang, S. Sun, G. Bai, R. Zhang, F. Liang, Y. Zhang, *Acta Biomater.* **2024**, *176*, 77.
[8] W. J. Li, C. Han, G. Cheng, S. L. Chou, H. K. Liu, S. X. Dou, *Small* **2019**, *15*, 1900470.
[9] X. Song, S. Song, D. Wang, H. Zhang, *Small Methods* **2021**, *5*, 2001000.
[10] J. Peng, W. Zhang, Q. Liu, J. Wang, S. Chou, H. Liu, S. Dou, *Adv. Mater.* **2022**, *34*, 2108384.
[11] B. Wang, Y. Han, X. Wang, N. Bahlawane, H. Pan, M. Yan, Y. Jiang, *iScience* **2018**, *3*, 110.
[12] P. Marzak, J. Yun, A. Dorsel, A. Kriele, R. Gilles, O. Schneider, A. S. Bandarenka, *J. Phys. Chem. C* **2018**, *122*, 8760.
[13] S. Phadke, R. Mysyk, M. Anouti, *J. Energy Chem.* **2020**, *40*, 31.
[14] Z. Wei, W. Zhao, J. Hu, T. Deng, N. Zhang, *Chem. Commun.* **2024**, *60*, 396.
[15] X. Lamprecht, F. Speck, P. Marzak, S. Cherevko, A. S. Bandarenka, *ACS Appl. Mater. Interfaces* **2022**, *14*, 3515.
[16] X. Lamprecht, P. Zellner, G. Yesilbas, L. Hromadko, P. Moser, P. Marzak, S. Hou, R. Haid, F. Steinberger, T. Steeger, J. M. Macak, *ACS Appl. Mater. Interfaces* **2023**, *15*, 23951.
[17] D. Liu, R. Huang, Y. Zhang, W. Li, S. Xi, P. Lv, C. Yu, H. Y. Yang, D. Yan, Y. Bai, *Adv. Funct. Mater.* **2024**, *35*, 2418096.
[18] Y. Yang, J. Zhou, L. Wang, Z. Jiao, M. Xiao, Q. A. Huang, M. Liu, Q. Shao, X. Sun, J. Zhang, *Nano Energy* **2022**, *99*, 107424.
[19] B. Xie, B. Sun, T. Gao, Y. Ma, G. Yin, P. Zuo, *Coord. Chem. Rev.* **2022**, *460*, 214478.
[20] J. Ge, L. Fan, A. M. Rao, J. Zhou, B. Lu, *Nat. Sustainability* **2022**, *5*, 225.
[21] R. Trócoli, R. Houdeville, C. Frontera, S. Vincent, J. M. García Lastra, M. R. Palacín, *ChemSusChem* **2024**, *17*, e202301224.
[22] R. L. Streng, S. Reiser, S. Wager, N. Pommer, A. S. Bandarenka, *ChemSusChem* **2024**, *18*, e202401469.
[23] Y. Zeng, X. F. Lu, S. L. Zhang, D. Luan, S. Li, X. W. Lou, *Angew. Chem. Int. Ed.* **2021**, *60*, 22189.
[24] Z. Li, K. Xiang, W. Xing, W. C. Carter, Y. M. Chiang, *Adv. Energy Mater.* **2015**, *5*, 1401410.
[25] C. D. Wessells, R. A. Huggins, Y. Cui, *Nat. Commun.* **2011**, *2*, 550.
[26] C. D. Wessells, S. V. Peddada, R. A. Huggins, Y. Cui, *Nano Lett.* **2011**, *11*, 5421.
[27] Y. Tang, W. Li, P. Feng, M. Zhou, K. Wang, Y. Wang, K. Zaghib, K. Jiang, *Adv. Funct. Mater.* **2020**, *30*, 1908754.
[28] S. Kjeldgaard, I. Dugulan, A. Mamakhel, M. Wagemaker, B. B. Iversen, A. Bentien, *R. Soc. Open Sci.* **2021**, *8*, 201779.
[29] M. B. Zakaria, T. Chikyow, *Coord. Chem. Rev.* **2017**, *352*, 328.
[30] G. Du, H. Pang, *Energy Storage Mater.* **2021**, *36*, 387.
[31] S. Park, J. Kim, S. H. Yi, S. E. Chun, *ChemSusChem* **2021**, *14*, 1082.
[32] B. Yuan, F. Sun, C. Li, W. Huang, Y. Lin, *Electrochim. Acta* **2019**, *313*, 91.
[33] R. Yang, Z. Qian, J. Deng, *J. Electrochem. Soc.* **1998**, *145*, 2231.
[34] V. D. Neff, *J. Electrochem. Soc.* **1978**, *125*, 886.
[35] K. Itaya, H. Akahoshi, S. Toshima, *J. Electrochem. Soc.* **1982**, *129*, 1498.
[36] K. Itaya, I. Uchida, V. D. Neff, *Acc. Chem. Res.* **1986**, *19*, 162.
[37] Y. Lin, L. Zhang, Y. Xiong, T. Wei, Z. Fan, *Energy Environ. Mater.* **2020**, *3*, 323.
[38] A. A. Karyakin, *Curr. Opin. Electrochem.* **2017**, *5*, 92.
[39] S. Ying, C. Chen, J. Wang, C. Lu, T. Liu, Y. Kong, F. Y. Yi, *ChemPlusChem* **2021**, *86*, 1608.
[40] A. A. Karyakin, *Electroanalysis* **2001**, *13*, 813.
[41] X. Ma, X. Du, X. Li, X. Hao, A. D. Jagadale, A. Abudula, G. Guan, *J. Alloys Compd.* **2017**, *695*, 294.
[42] A. Tóth, K. László, in *Novel Carbon Adsorbents*, Elsevier, Amsterdam **2012**, pp. 147–171.
[43] J. Yun, J. Pfisterer, A. S. Bandarenka, *Energy Environ. Sci.* **2016**, *9*, 955.
[44] L. Shen, Y. Jiang, Y. Liu, J. Ma, T. Sun, N. Zhu, *Chem. Eng. J.* **2020**, *388*, 124228.
[45] H. Yi, R. Qin, S. Ding, Y. Wang, S. Li, Q. Zhao, F. Pan, *Adv. Funct. Mater.* **2021**, *31*, 2006970.
[46] A. Milchev, *Russ. J. Electrochem.* **2008**, *44*, 619.
[47] A. Milchev, *ChemTexts* **2016**, *2*, 4.
[48] R. Scharifker, J. Mostany, in *Encyclopedia of Electrochemistry: Online*, Wiley-VCH, Weinheim **2007**.
[49] M. Hu, N. L. K. Torad, Y.-D. Chiang, K. C.-W. Wu, Y. Yamauchi, *CrystEngComm* **2012**, *14*, 3387.
[50] K. Hurlbutt, S. Wheeler, I. Capone, M. Pasta, *Joule* **2018**, *2*, 1950.
[51] G. P. Demopoulos, *Hydrometallurgy* **2009**, *96*, 199.
[52] P. L. Domingo, B. García, J. M. Leal, *Can. J. Chem.* **1990**, *68*, 228.
[53] J. Luo, A. Sam, B. Hu, C. DeBruler, X. Wei, W. Wang, T. L. Liu, *Nano Energy* **2017**, *42*, 215.
[54] Y. Ye, *Nanoscale* **2016**, *8*, 10406.
[55] K. Parvez, Z. S. Wu, R. Li, X. Liu, R. Graf, X. Feng, *J. Am. Chem. Soc.* **2014**, *136*, 6083.
[56] V. Dyadkin, P. Pattison, V. Dmitriev, D. Chernyshov, *J. Synchrotron Radiat.* **2016**, *23*, 825.

Manuscript received: February 19, 2025
Revised manuscript received: March 24, 2025
Version of record online:

© 2025 The Author(s). ChemElectroChem published by Wiley-VCH GmbH

7. Sustainable High-Performance Aqueous Batteries Enabled by Optimizing Electrolyte Composition.

R.L. Streng, S. Reiser, A. Senyshyn, S. Wager, J. Sterzinger, P. Schneider, D. Gryc, M.Z. Hussain, A.S. Bandarenka. *Advanced Science* **2025**, 12, 2417587.

RESEARCH ARTICLE

ADVANCED SCIENCE Open Access

www.advancedscience.com

Sustainable High-Performance Aqueous Batteries Enabled by Optimizing Electrolyte Composition

*Raphael L. Streng, Samuel Reiser, Anatoliy Senyshyn, Sabrina Wager, Johannes Sterzinger, Peter Schneider, David Gryc, Mian Zahid Hussain, and Aliaksandr S. Bandarenka**

Lithium-free aqueous batteries (LFABs) offer a sustainable alternative to lithium-ion batteries for large-scale energy storage, addressing issues like material scarcity and flammability. However, their economic viability is limited by low energy density and cycle life due to the narrow electrochemical stability window of water and active material dissolution. High-concentration water-in-salt electrolytes typically used to tackle these issues are expensive and potentially hazardous. This work presents a novel, cost-efficient electrolyte design using safe salts at lower concentrations. The influence of different cation species on the copper hexacyanoferrate cathode and polyimide anode is systematically explored, optimizing the electrolyte for improved cell voltage and cycling stability. The resulting battery, with a 1.8 mol kg^{-1} $MgCl_2$ + 1.8 mol kg^{-1} KCl aqueous electrolyte, achieves a competitive energy density of 48 Wh kg^{-1} and 95% efficiency. It also shows 70% capacity retention even at extremely high (dis-)charge rates of 50 C and a maximum specific power of over 10000 W kg^{-1}, indicating its strong potential for supercapacitor applications. Utilizing exclusively inexpensive and safe salts, this work significantly advances the practical application of low-cost LFABs for large-scale energy storage.

1. Introduction

The ongoing transition from fossil fuels toward renewable energy sources and the electrification of the transport sector necessitate novel energy storage solutions.[1–4] Especially in mobile applications and large-scale stationary storage, batteries have taken a central role in the last decades.[5] Lithium-ion batteries (LIB) are predominant in battery electric vehicles (BEV) and mobile devices within the wide range of battery systems.[6] While their unmatched energy density justifies their leading position in the market, their inherent safety concerns and the scarcity of lithium motivate an increasing interest in beyond-lithium-ion batteries.[7,8] Cell chemistries based on, e.g., sodium, potassium, magnesium, or calcium, can be a more sustainable and cost-efficient alternative to conventional LIBs. These metals are up to three orders of magnitude more abundant in the earth's crust than lithium, making them easily accessible in most parts of the world.[9] In addition, safety concerns related to flammability and toxicity can be overcome by using aqueous instead of organic electrolytes. Therefore, lithium-free aqueous batteries (LFAB) have recently received growing attention.[10,11] While the narrow electrochemical stability of water limits their cell voltage and, thus, energy density, they offer advantageous properties for large-scale energy storage. In addition, the high ionic conductivity of aqueous electrolytes enables ultrahigh power densities, making them a viable choice for applications requiring fast-charging capabilities.[12,13] These include fast-response stationary storage devices for grid stabilization and applications in the transport sector. Whereas personal vehicles optimized for long-range rely on LIBs, public transport can significantly benefit from high-power-density

R. L. Streng, S. Reiser, S. Wager, J. Sterzinger, P. Schneider, A. S. Bandarenka
Physics of Energy Conversion and Storage
Department of Physics
Technische Universität München (TUM)
James-Franck-Str. 1, 85748 Garching, Germany
E-mail: bandarenka@ph.tum.de

The ORCID identification number(s) for the author(s) of this article can be found under https://doi.org/10.1002/advs.202417587

© 2025 The Author(s). Advanced Science published by Wiley-VCH GmbH. This is an open access article under the terms of the Creative Commons Attribution License, which permits use, distribution and reproduction in any medium, provided the original work is properly cited.

DOI: 10.1002/advs.202417587

A. Senyshyn
Heinz Maier-Leibnitz Zentrum (MLZ)
Technische Universität München
Lichtenbergstr. 1, 85748 Garching, Germany

D. Gryc, M. Z. Hussain
Chair of Inorganic and Metal-Organic Chemistry
Department of Chemistry
School of Natural Sciences
TUM, Lichtenbergstraße 4, 85748 Garching, Bavaria, Germany

A. S. Bandarenka
Catalysis Research Center
TUM
Ernst-Otto-Fischer-Straße 1, 85748 Garching, Germany

systems.[14,15] Multiple companies have developed buses using supercapacitors (SCs) that can be charged quickly during normal operation.[16,17] In this sector, aqueous battery-SC-hybrid systems can be a promising alternative, offering higher energy densities than SCs and better fast-charging capabilities than LIBs.

However, LFABs have not been successfully implemented into the market so far, as their economic viability remains doubtful due to considerably lower energy densities compared to state-of-the-art LIBs.[18,19] Thus, the narrow electrochemical stability window of water and the limited cell voltage can be regarded as the main drawback of aqueous batteries.[20] In addition, rapid capacity degradation due to active material dissolution has been identified as one of the main challenges to the practical application of LFABs.[21,22] A commonly used strategy to address these issues is the use of highly concentrated water-in-salt electrolytes (WiSE). By minimizing the amount of "free water" through molecular crowding, water-splitting side reactions and electrode material hydrolysis can be mitigated effectively.[23] Since the original WiSE, 21 mol kg^{-1} LiTFSI, was proposed by Suo et al. in 2015, multiple alternative water-in-salt systems have been identified.[24] In particular, $KN(SO_2F)_2$ (KFSI) and KSO_3CF_3 (KOTf) are frequently used due to their exceptional solubilities. In 2019, Jiang et al. reported a high energy density aqueous battery based on 22 M KOTf,[25] and in 2020, a 62 mol kg^{-1} aqueous KFSI/KOTf electrolyte was developed by Ko et al.[26] Although effective, this approach depends on costly and toxic fluorinated salts, which raise the per-Wh cost and increase safety risks for the battery. Hence, WiSEs based on more available salts have been the subject of extensive research in recent years. The most promising candidates include potassium acetate (KAc)[27] and $NaClO_4$,[28] which come at significantly lower prices than the systems mentioned above. However, the high basic strength of acetates limits their compatibility with certain commonly used electrode materials, such as Prussian blue analogs (PBAs).[29] At the same time, the strongly oxidative nature of perchlorates is linked to potentially significant safety risks, especially at concentrations close to the solubility limit. In addition, various organic and inorganic nonionic additives, such as sugar or metal oxides, have been demonstrated to show great potential as molecular crowding agents for aqueous electrolytes, suppressing side reactions and degradation.[30,31]

In this work, we present a novel approach to tuning important electrode properties by systematically investigating the effect of the cation on the redox potential and the cycling stability of a copper hexacyanoferrate (CuHCF) cathode and a polyimide anode. Namely, sodium, potassium, magnesium, and calcium ions were used as they represent the most abundant alkali and alkaline earth metals in the earth's crust and are, thus, the most promising candidates for designing low-cost and sustainable batteries.[9] Based on these findings, we propose a relatively low-concentration mixed-salt electrolyte enabling an optimized cell voltage and battery cycle life. Using only highly abundant KCl and $MgCl_2$ in the electrolyte, the model cell achieves a competitive energy density and a remarkable fast-charging capability and power density, representing a significant step toward a practical and cost-efficient design for aqueous batteries.

2. Results and Discussion

Prussian blue analogs (PBAs) are among the most promising active cathode materials for aqueous batteries. Their open-channel structure and large interstitial sites enable exceptional fast-charging capabilities, allowing them to host even large cations such as Na^+ and K^+.[32,33] Furthermore, the facile synthesis, compositional and electrochemical tunability, and the abundance of commonly used precursor materials make them a particularly interesting group of materials for grid-scale energy storage. One of the most investigated PBAs is copper hexacyanoferrate (CuHCF), which offers a high electrode potential close to the oxygen evolution threshold and has been shown to host a multitude of monovalent and multivalent cations.[34–36] As shown in our previous work, the charge-storage mechanism of CuHCF features at least three distinct stages. Based on impedance spectroscopy measurements, these stages are detectable for the intercalation of monovalent and divalent cations. For a more detailed analysis of the intercalation mechanism, the reader is referred to our previous studies.[37] Generally, CuHCF is synthesized via a simple coprecipitation reaction from two aqueous solutions containing Cu ions and $Fe(CN)_6$ ions, respectively. However, this synthesis route leads to irregular particles with low crystallinity and high amounts of interstitial water, impairing the specific capacity.[38] Hence, chelating agents like sodium citrate or sodium pyrophosphate have been established as a reliable method to minimize vacancies and water content.[39,40] In this work, CuHCF was synthesized according to the method reported by Xu et al., which used sodium pyrophosphate and polyvinyl pyrrolidone as chelating additives.[41] In their work, Xu et al. found that the so-prepared highly crystalline CuHCF features a lower water content with increased Na-storage capabilities compared to the conventional simple coprecipitation method. The fitted X-ray diffraction (XRD) pattern of the resulting particles is shown in Figure S1 (Supporting Information). Interestingly, this synthesis modification leads to a change from the typical cubic crystal structure of PBAs to a monoclinic structure with lattice parameters $a = 11.22$ Å, $b = 7.30$ Å, and $c = 6.95$ Å, which is depicted in **Figure 1**A,B shows a scanning electron microscopy (SEM) picture of the cathode used in this work, consisting of sheet-shaped CuHCF crystals in the 200–800 nm size range. The pore structure of the cathode was analyzed using Brunauer–Emmett–Teller (BET) analysis (Figure S3A, Supporting Information). The N_2 adsorption exhibits a Type II isotherm, which indicates the nonporous (or macroporous) nature of the sample. A minimal uptake at $p/p_s < 0.2$ suggests weak interactions between N_2 molecules and the surface, confirming the absence of micro/mesopores. In the mid-pressure range ($p/p_s = 0.2$–0.8), multilayer adsorption dominates, followed by a steep rise in adsorption at $p/p_s > 0.9$, which is attributed to N_2 condensation in macropores or on the external surface of the material. The BET specific surface area (SSA) of the CuHCF cathode was calculated to be 1.9 $m^2 g^{-1}$, which is extremely low, further confirming the macroporous nature or low accessible surface area. The graphite substrate, which makes up the larger part of the overall cathode mass, showed a negligible SSA of 0.5 $m^2 g^{-1}$ under the same measurement conditions.

Besides PBAs, redox-active organic compounds have gained recent interest, particularly as anode materials for LFABs, owing to their sustainability and electrochemical tunability.[42–44]

© 2025 The Author(s). Advanced Science published by Wiley-VCH GmbH

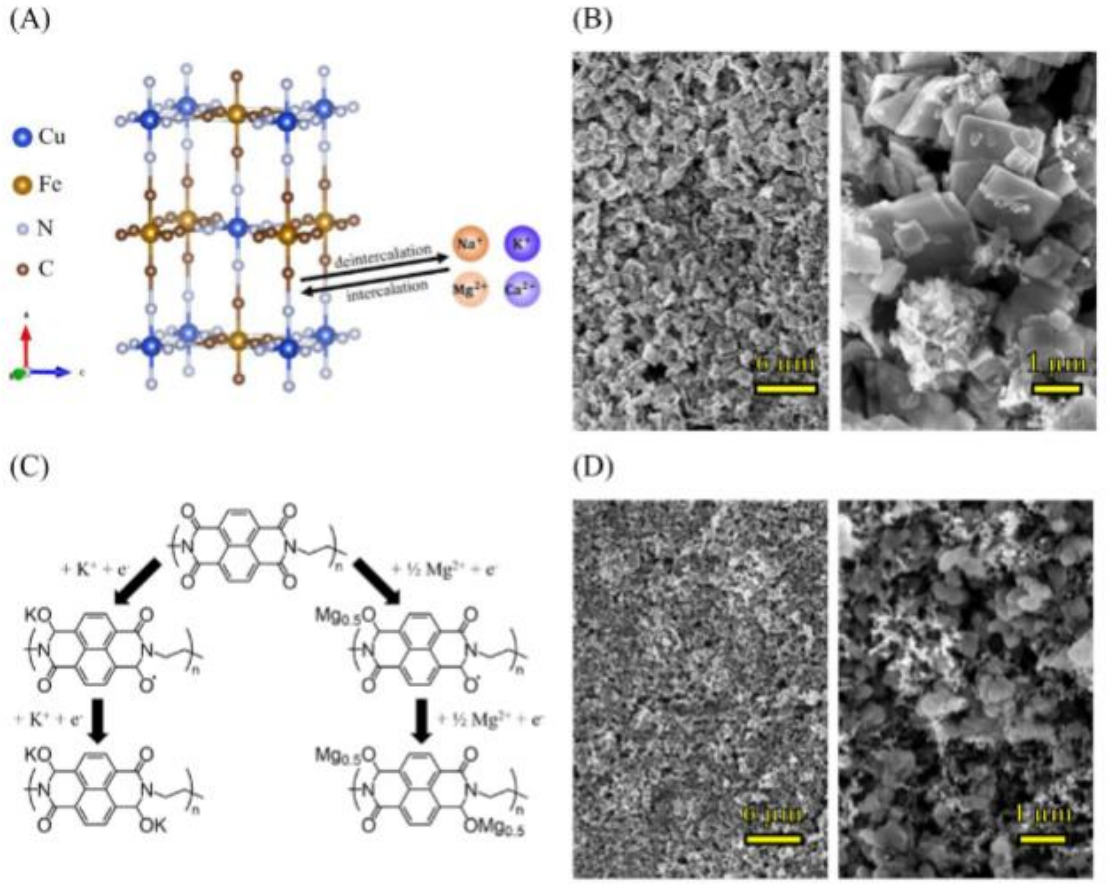


Figure 1. Charge storage mechanisms and structures of the anode and cathode. A) Intercalation mechanism and crystal structure of CuHCF. B) SEM images of the CuHCF cathode. C) Enolization mechanism and chemical structure of PNFE. D) SEM images of the PNFE anode.

Especially, materials based on perylene diimide and naphthalene diimide (NDI) have been successfully implemented as anodes for various monovalent and multivalent ion aqueous batteries.[25,45] Our previous work investigated the charge storage mechanism and exceptional electrochemical performance of poly(naphthalene four formyl ethylenediamine) (PNFE), an NDI-derived redox-active polymer.[46] Through an enolization process shown in Figure 1A, the polyimide can store various monovalent and divalent ions such as Na^+, K^+, and Mg^{2+}. This material was selected as the anode for this work because it offers superior cation storage capacity and fast-charging capabilities. PNFE, synthesized for our previous study, is formed in a one-step dehydration condensation reaction between 1,4,5,8-naphthalene tetracarboxylic dianhydride and ethylene diamine. Figure S2A (Supporting Information) shows the Fourier-transform infrared (FTIR) spectrum of the as-prepared polymer, confirming the successful synthesis as the observed peaks are in good accordance with the expected chemical structure. Stretching vibrations of the electrochemically active carbonyl groups correspond to the bands observed at 1700 and 1661 cm^{-1}. The other peaks can be assigned to vibrations of C=C bonds in the cyclic alkenes (1580 cm^{-1}), various vibrations of aromatic and nonaromatic C—N bonds (1347 to 1094 cm^{-1}), and vibrations of C—H bonds (1452, 1374, 1031, and 768 cm^{-1}), respectively. An X-ray photoelectron spectroscopy (XPS) survey scan and the fitted C1s spectrum of the electrode slurry coated onto a pyrolytic graphite sheet replotted from our previous work are shown in Figure S2B,C (Supporting Information).[46] Characteristic peaks for F, O, N, and C can be observed, confirming the presence of both the active material and the Nafion binder at the electrode surface. In the C1s spectrum, peaks related to C=C, C—C, C—N, N—C=O, C=O, CF_2, and CF_3 bonds, as well as a π–π^* satellite, are found. Figure 1D (Supporting Information) shows an SEM picture of the anode, revealing a porous structure with particle sizes around 100 nm and pores mostly in the micrometer range. This was confirmed by BET analysis (Figure S3B, Supporting Information). Like the cathode, the N_2 adsorption of the PNFE anode exhibits a Type II isotherm, indicating a microporous nature. It

© 2025 The Author(s). Advanced Science published by Wiley-VCH GmbH

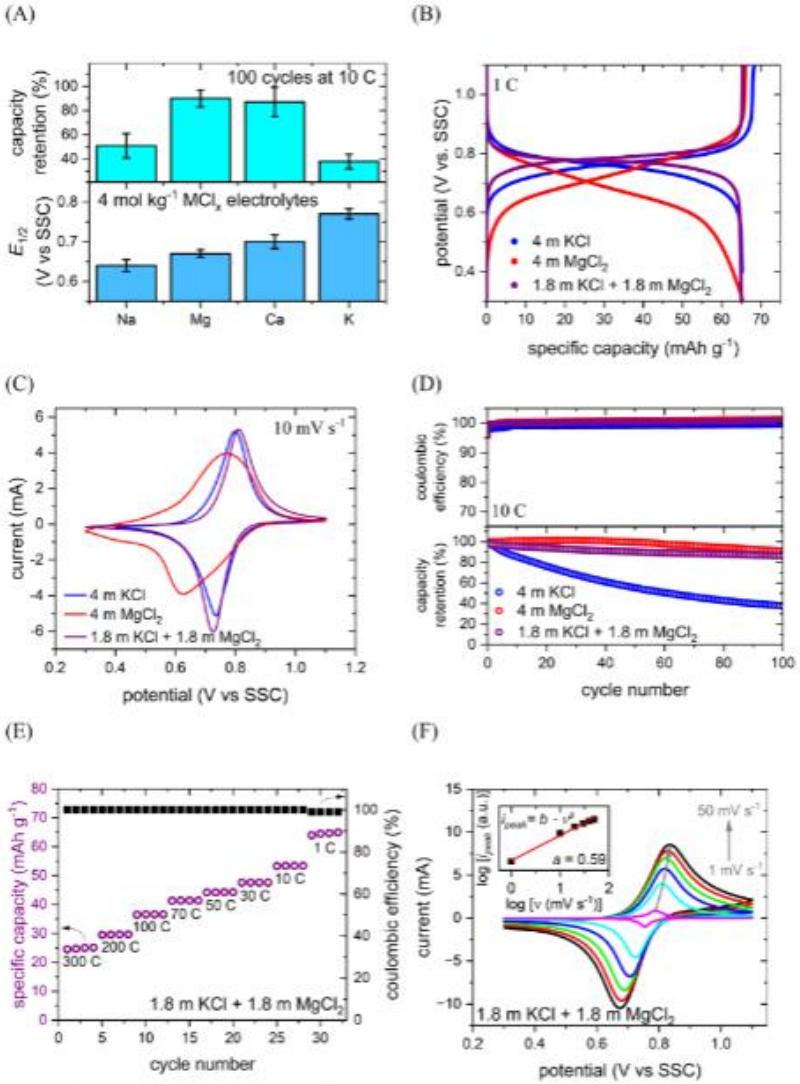


Figure 2. Electrochemical performance of CuHCF. A) Summary of the electrode potential and cycling stability in different 4 mol kg^{-1} MCl$_x$ (M = Na, K, Mg, Ca) aqueous electrolytes. Data presented as mean ± SD, n = 5. B) Galvanostatic (dis-)charge curves, C) CVs, and D) cycling stability in KCl, MgCl$_2$, and 1.8 mol kg^{-1} KCl + 1.8 mol kg^{-1} MgCl$_2$. E) Specific discharge capacity in 1.8 mol kg^{-1} KCl + 1.8 м MgCl$_2$. F) CVs at different scan rates in 1.8 mol kg^{-1} KCl + 1.8 mol kg^{-1} MgCl$_2$.

shows a similar behavior as the cathode with a specific area of 1.5 m^2 g^{-1}.

As mentioned above, both electrode materials can host a large variety of alkali metal and alkaline earth metal cations, of which Na^+, K^+, Mg^{2+}, and Ca^{2+} can be regarded as the most interesting for designing sustainable battery systems. Hence, the influence of the cation species on important electrode properties was investigated by cyclic voltammetry and galvanostatic cycling in 4 mol kg^{-1} MCl$_x$ (M = Na, K, Mg, Ca) aqueous electrolytes. **Figure 2** shows the influence of the electrolyte composition on the electrochemical performance of the CuHCF cathode. A high electrode potential and minimal active material degradation are favorable for cathode materials. Thus, the half charge potential $E_{1/2}$ of the cathode in the respective electrolyte was evaluated as the mid-point between the cathodic and the anodic peak in the cyclic voltammograms (CVs). The cycling stability was assessed by charging and discharging the electrode for 100 cycles at 10 C.

© 2025 The Author(s). Advanced Science published by Wiley-VCH GmbH

In Figure 2A, the results of both investigations are summarized. As shown in the lower half of the graph, the cathode potential is strongly dependent on the cation choice as it increases by more than 100 mV following the trend $Na^+ < Mg^{2+} < Ca^{2+} < K^+$. Previous studies have shown a strong correlation between the hydration energy of alkali metal cations and the intercalation potential of PBAs.[47,48] The smaller hydration shell of K^+ facilitates the intercalation, thus raising the reduction potential compared to Na^+. According to this trend, the significantly more negative hydration energy and larger hydration shells of divalent Mg and Ca ions should lead to lower electrode potentials. However, the intercalation of Mg^{2+} and Ca^{2+} occurs, in fact, at a more positive potential than for Na^+, which is in accordance with previous literature.[49,50] Mizuno et al., who reported similar intercalation potentials for Na^+ and Mg^{2+} at NiHCF, attributed this effect to the partial dehydration of Mg^{2+} upon intercalation. They found that Mg^{2+} intercalation at the PBA surface is blocked in an organic propylene carbonate (PC) electrolyte. As the PC molecule is too large to co-intercalate, the divalent ions must be completely desolvated during the charge transfer. However, this leads to strong coulombic repulsion of the bare Mg-ions at the PBA surface. In aqueous electrolytes, in contrast, Mg^{2+} is only partially dehydrated at the interface enabling Mg-intercalation in these systems. This significantly lowers the energy demand for intercalation compared to complete dehydration, thus promoting the reduction of the PBA.[50] Based on these results, aqueous electrolytes using potassium salts lead to the most positive electrode potentials for CuHCF, enabling the highest energy densities.

However, the stability measurements shown in the upper half of Figure 2A reveal that the cathode active material suffers from severe degradation in both 4 mol kg^{-1} NaCl and 4 mol kg^{-1} KCl, with only ≈40% of the capacity remaining after 100 cycles at 10 C. This capacity loss may be linked to multiple degradation mechanisms for CuHCF and PBAs that have been suggested and investigated in the past. In summary, three main processes have been identified as the main drivers of PBA degradation upon cycling:

1) $Fe(CN)_6$ vacancies introduced during synthesis causing lattice defects have been shown to promote the collapse of the crystal structure during (de)intercalation of cations.[51,52] However, this appears unlikely as the governing degradation mechanism for the CuHCF nanosheets as they are characterized by high crystallinity and few defects.[41]
2) Besides $Fe(CN)_6$ vacancies, interstitial or zeolitic water inclusions can form during the synthesis in aqueous media, which also contribute to the degradation of the PBA structure.[53] Interstitial water occupying the alkali metal sites can lead to capacity decay through hydrolysis of the PBA framework or block the ion channels, impeding solid-state diffusion.[54] Although the use of sodium pyrophosphate as a chelating agent should help minimize the water content in the structure, a certain amount of interstitial H_2O is always present in PBAs.
3) Finally, the detrimental effect of OH^- species at the electrode surface has been identified as one of the main drivers for electrode degradation for PBAs.[29] Naturally, the concentration of OH^- in neutral electrolytes such as NaCl and KCl is relatively low. However, a certain amount of H_3O^+ and OH^- is generally present in any aqueous solution. At operating potentials close to or even beyond the oxygen evolution onset, specific adsorption of OH^- on the electrode surface can induce locally increased pH values, promoting the well-understood alkaline degradation pathway for PBAs. As CuHCF is cycled to potentials well above 1.23 V versus SHE, this effect can contribute substantially to electrode degradation.

The latter two mechanisms are likely responsible for the relatively rapid capacity loss of CuHCF in aqueous KCl and NaCl electrolytes. However, as shown in Figure 2A, only a minimal capacity decay can be observed in electrolytes based on Mg^{2+} or Ca^{2+}, indicating that the divalent cations suppress these processes. While the interstitial water content in CuHCF is initially the same for all investigated systems, the higher charge density ions may capture residual water, impeding its negative effects. A similar observation has previously been reported by Xie et al., who achieved significantly enhanced cycle life for a PBA cathode by using $AlCl_3$ as an electrolyte additive. They demonstrated that the Al^{3+} ions could bind with interstitial water molecules, removing them from the alkali metal sites and suppressing detrimental side reactions.[55] A similar effect can also be assumed for Ca^{2+} and particularly Mg^{2+}, which are characterized by high charge densities and, thus, strong interactions with water. Furthermore, smaller divalent ions feature a high reactivity with OH ions, decreasing their activity in aqueous solutions by undergoing a hydrolysis reaction with water:[56,57]

$$M(H_2O)_n^{2+} \rightarrow MOH(H_2O)_{n-1}^{+} + H^+ \ (\text{with} M = Mg, Ca) \quad (1)$$

Consequently, the presence of Mg^{2+} or Ca^{2+} can additionally suppress the alkaline degradation pathway, as OH^- species adsorbing at the electrode surface or forming even within the crystal structure from interstitial water are captured. It should also be noted that molecular crowding of the electrolyte has been demonstrated as an effective strategy to improve the cycling stability of PBAs.[21,26] Due to their much more negative hydration enthalpy, Mg^{2+} and Ca^{2+} form larger and more strongly bound hydration shells in water, than Na^+ and K^+. For example, Mg^{2+} typically coordinates with six water molecules in its primary hydration shell, forming an octahedral structure. The Mg—O bond distance in this configuration is ≈2.1 Å. The high charge density of Mg^{2+} leads to a well-ordered and stable hydration shell. This strong interaction also influences the second hydration shell, contributing to the overall stability of the hydrated ion complex.[58,59] In contrast, K^+ ions form a relatively unstable first coordination sphere with a coordination number between 6 and 8 and a K—O distance of ≈2.8 Å. K^+ ions typically do not form a second coordination sphere.[60] Therefore, the strong hydration of multivalent ions decreasing the free water content in the electrolyte likely also contributes to the stabilization of the cathode.

To further analyze the degradation process, the structural changes to the CuHCF cathode after cycling were investigated using SEM and XRD. Figure S5A (Supporting Information) shows the XRD patterns of the fully reduced CuHCF cathode recorded before and after cycling in KCl and $MgCl_2$.

The initial XRD pattern of the cathode before cycling corresponds to the expected superimposing of CuHCF and the graphite-based substrate. However, after cycling in either electrolyte, most characteristic reflections of the monoclinic CuHCF structure disappear, leaving the substrate-dominated pattern.

© 2025 The Author(s). Advanced Science published by Wiley-VCH GmbH

Only the monoclinic (011) (pseudo-cubic (200)) reflection at 17.7° 2θ remains visible, corresponding to a pseudo-cubic cell volume of ≈1000 Å^3 for all samples (Figure S5B, Supporting Information). The reflection FWHM and its position remain nearly unaffected by electrochemical treatment, revealing the coherent scattering domain to be preserved along with the stable chemical composition.

However, the absence of other characteristic peaks suggests extreme abnormal broadening at higher diffraction angles, likely due to high microstrain caused by an inhomogeneous distribution of intercalates in the active material. In addition, two new peaks of unclear origin emerge in the highly degraded KCl sample, indicating further structural changes. More systematic operando characterizations monitoring the structure evolution of CuHCF during cycling will be needed to obtain more detailed insights into the fading mechanisms.

SEM analysis of the cathode after cycling in 4 mol kg^{-1} KCl reveals significant morphological changes to the CuHCF nanosheets (Figure S5D, Supporting Information). While the overall shape of the particles remains unaltered, etched holes and pores can be observed on the active material, suggesting severe transition metal dissolution consistent with the electrochemical results. In contrast, as shown in Figure S5B (Supporting Information), this effect is not seen after cycling the cathode in 4 mol kg^{-1} $MgCl_2$, indicating that the material dissolution is suppressed in this electrolyte.

Based on these findings, a stabilization mechanism in the aqueous Mg-ion electrolyte can be proposed. Prior studies have shown that the capacity fading of PBAs is closely associated with water incorporation into the structure and the interaction between free water in the electrolyte and the active material.[53,54,47] Hydrolysis and specific adsorption of hydroxide ions (OH^-) are known to promote transition metal dissolution, ultimately leading to structural degradation and capacity loss. Therefore, the interaction between cations and water plays a critical role in the electrochemical stability of PBA electrodes. Multivalent ions, due to their higher charge density, form larger hydration shells and exhibit stronger interactions with water molecules and OH^- anions compared to monovalent ions of similar ionic radius. As a result, water molecules and hydroxide species are more likely to coordinate with the electrolyte cations rather than interact with the PBA framework. This reduces the extent of hydrolytic degradation at the electrode surface. Experimental evidence from the XRD and SEM analyses supports this mechanism. In the KCl electrolyte, capacity fading correlates with pronounced structural changes and active material dissolution. The XRD patterns show the disappearance of characteristic peaks after cycling, along with the emergence of new peaks indicative of phase transformation. SEM images further reveal significant morphological degradation and material loss. In contrast, these changes are absent in the $MgCl_2$-based electrolyte. This suggests that the lower concentration of free water and reactive OH^- species in the $MgCl_2$ electrolyte effectively suppresses the degradation process, thereby enhancing electrode stability.

In summary, CuHCF displays the highest and, thus, most favorable intercalation potential in the presence of K-ions. However, the cycling stability in the 4 mol kg^{-1} KCl electrolyte is insufficient and can be largely improved by using divalent-ion-based electrolytes such as $MgCl_2$ and $CaCl_2$. As the stabilization is linked to the interaction between the divalent cations and the aqueous environment, it should also be achieved when using, e.g., $MgCl_2$ as an electrolyte additive for KCl. Hence, the performance of the cathode was further investigated in a mixed 1.8 mol kg^{-1} KCl + 1.8 mol kg^{-1} $MgCl_2$ aqueous electrolyte. Figure 2B shows a representative charge and discharge cycle of CuHCF in 4 mol kg^{-1} KCl, 4 mol kg^{-1} м $MgCl_2$, and the mixed electrolyte. In the Mg-based electrolyte, the plateaus during intercalation and deintercalation are significantly more sloped than in 4 mol kg^{-1} KCl. Furthermore, as already discussed above, the average discharge potential in $MgCl_2$ is lower and thus less favorable. However, when using a bi-salt electrolyte containing both K^+ and Mg^{2+}, the profile closely resembles the pure KCl electrolyte, indicating that the reduction is facilitated by the presence of K^+. That is further confirmed when analyzing the CVs of CuHCF in the three aforementioned electrolytes. As shown in Figure 2C, the peak positions and shapes in the mixed electrolyte closely match the curve for 4 mol kg^{-1} KCl. In 4 mol kg^{-1} $MgCl_2$, however, the cathode displays significantly broader peaks and a higher peak-to-peak separation due to the more sluggish charge transfer and diffusion kinetics of the Mg^{2+} ions. That implies that adding $MgCl_2$ to the K-based electrolyte does not significantly influence the charge transfer kinetics and electrode potential. As K^+ features a much smaller hydration shell, its intercalation should be favored over the intercalation of Mg^{2+}. However, energy-dispersive X-ray spectrometry (EDX) analysis shows the presence of both K and Mg in a CuHCF cathode reduced in the mixed electrolyte (Figure S6, Supporting Information). Hence, although the ion transfer kinetics are the same as in the pure KCl electrolyte, both Mg^{2+} and K^+ intercalate into the electrode in the mixed electrolyte, since the reduction and oxidation peaks, representing their respective (de-)intercalation potentials, overlap. Therefore, the mixed electrolyte is capable of combining the beneficial properties of both pure electrolytes. While the electrode potential itself is not affected by the additional Mg-ions, the electrolyte modification improves other important electrode properties. At 1 C, the coulombic efficiency is increased from ≈95% to ≈99% compared to the pure KCl electrolyte due to the water-binding effect of Mg^{2+} and the acidification of the electrolyte by the Lewis acid.

Figure 2D displays the capacity retention of the CuHCF electrode over 100 cycles at 10 C in the single salt and mixed electrolytes. As discussed above, the cycling stability is largely improved when Mg^{2+} is intercalated instead of K^+. A similar effect is observed in the mixed electrolyte as the capacity retention increases from ≈40% in KCl to over 90% in the bi-salt electrolyte. This proves that the stabilization through water- and OH^--capturing can be achieved by using an Mg salt as an additive to an alkali-ion-based electrolyte. As evidenced by the EDX results, both Mg and K intercalate into the PBA structure. Therefore, the effects of Mg ions on interstitial water and OH^- species also occur in the mixed electrolyte, and the same stabilization mechanism as in the pure $MgCl_2$ electrolyte can be expected. Using mixed electrolytes enables a longer cycle life for CuHCF while maintaining the flat discharge profile and high electrode potential associated with the K-ion-based electrolyte.

To evaluate the performance of the cathode in the 1.8 mol kg^{-1} KCl + 1.8 mol kg^{-1} $MgCl_2$ mixed electrolyte in more detail, galvanostatic cycling was carried out at different rates ranging from

© 2025 The Author(s). Advanced Science published by Wiley-VCH GmbH

1 C (65 mA g^{-1}) to 300 C (19.5 A g^{-1}). Figure 2E shows the specific capacity and coulombic efficiency for each cycle. At 1 C, the electrode displays a maximum discharge capacity of 65 mAh g^{-1}, of which ≈85% can be retained at 10 C and ≈40% can be retained at an ultrahigh rate of 300 C. The maximum specific capacity exceeds the values commonly reported for CuHCF cathodes prepared by the conventional coprecipitation method, which can be linked to the low vacancy and water content and the change in crystal structure achieved by the synthesis procedure using sodium pyrophosphate as a chelating agent.[18,41] The high crystallinity and large interstitial sites further facilitate fast ion transport kinetics, enabling a relatively high rate capability. The reaction kinetics were further analyzed by recording CVs at scan rates between 1 and 50 mV s^{-1}. The peak current i_{peak} can be related to the scan rate v by the empirical formula $i_{peak} = b \cdot v^a$ with the parameter a indicating the rate-limiting process. For purely mass-transport-limited kinetics, as commonly observed in intercalation-type electrode materials a approaches 0.5. For purely surface-limited kinetics, such as for capacitive charge storage in supercapacitors, a approaches 1.0. As shown in Figure 2F, the parameter a lies at 0.59 for CuHCF in the mixed electrolyte, indicating mostly mass transport limited kinetics.

CV and galvanostatic cycling with potential limitations (GCPL) measurements were carried out on PNFE to investigate the influence of the electrolyte composition on the electrochemical performance of the anode. **Figure 3A** shows an overview of the cation effects on the most important electrode properties. Similarly to the cathode, significant changes in electrode potential and stability can be observed when varying the cationic species in the electrolyte. PNFE displays the most negative and, thus, most favorable half-charge potential in the presence of K^+. As this electrolyte also enables the highest cathode potential, a K-based battery should deliver the highest cell voltage and energy density among the investigated systems. Comparing all cations, the anode potential follows the $K^+ < Na^+ < Mg^{2+}/Ca^{2+}$ trend with no discernible difference between Ca^{2+} and Mg^{2+}. As the charge storage mechanism of PNFE does not feature intercalation into a crystal lattice, the hydration energy of the cation does not seem to play a role in determining the redox potential. However, it is closely linked with the charge density of the inserted ion. The high charge density of Mg^{2+} and Ca^{2+} facilitates the enolization process, yielding more positive potentials, while the low charge density of the monovalent Na^+ and K^+ results in more negative potentials.

As for the cathode, the electrolyte composition also affects the cycling stability of the anode. Since PNFE exhibits high fast-charging capabilities, the electrode was cycled at a C-rate of 100 C for 1000 cycles to assess the degradation. Generally, only small capacity losses can be observed in all electrolytes, but they are slightly higher in solutions based on K^+ and Na^+. This capacity fading is most likely related to material detachment from the electrode, as there are no known degradation mechanisms for polyimides. To confirm this hypothesis, SEM images of the PNFE anode were taken before and after cycling in the KCl electrolyte. As shown in Figure S7 (Supporting Information), the anode displays significantly enlarged cracks on the surface and detached flakes in multiple areas. Furthermore, the detached solid material was observed floating in the electrolyte at the bottom of the cell. Due to the larger cation hydration shell and higher anion concentration, solutions of $MgCl_2$ and $CaCl_2$ are more viscous than KCl and NaCl at the same concentration (Figure S4, Supporting Information), inhibiting the transport of dissolution products away from the electrode. However, it should be noted that for all electrolytes, this effect would be less pronounced in realistic cell setups containing significantly smaller volumes of electrolyte. Hence, it can be assumed that the cycle life of the full battery using the two mentioned electrode materials will mostly depend on the cathode stability.

A 1.8 mol kg^{-1} KCl + 1.8 mol kg^{-1} $MgCl_2$ was identified to yield optimal cycling stability and electrode potential for the CuHCF cathode. Therefore, the electrochemical performance of PNFE was also analyzed in this electrolyte. Figure 3B shows the charge and discharge curves of the anode in pure KCl, pure $MgCl_2$, and the mixed electrolyte recorded at 1 C. The (dis-)charge profiles for the Mg-based and the bi-salt electrolytes are almost identical, indicating that Mg^+ insertion is preferred over K^+. Although the lower average reduction and oxidation potentials in the presence of K^+ are favorable for achieving higher full-cell voltages, the plateaus are less sloped in the presence of Mg^{2+}. As shown in Figure 3C, the CV of PNFE in KCl displays a significant potential difference between the first and second electron transfer and a large peak-to-peak separation for the first redox step. In contrast, the two reduction and oxidation peaks overlap in the Mg-based and mixed electrolytes. As demonstrated in our previous work, the underlying charge transfer mechanism of PNFE does not change when divalent ions are inserted instead of monovalent ions.[46] However, as multiple polymer units are involved in the storage of a single Mg^{2+} ion, the oxidation and reduction peaks can no longer be clearly distinguished since interactions between the redox active centers lead to further peak broadening and overlapping. When using a bi-salt electrolyte, the general CV shape is not affected, but the peak-to-peak separation decreases due to the enhanced electrolyte conductivity enabled by the higher mobility of K^+. Figure 3D shows the capacity retention of PNFE per cycle in 4 mol kg^{-1} KCl, 4 mol kg^{-1} $MgCl_2$, and 1.8 mol kg^{-1} KCl + 1.8 mol kg^{-1} $MgCl_2$ recorded at 100 C over 1000 cycles. Although relatively slow, a continuous capacity decay accompanied by a decrease in coulombic efficiency can be observed in the pure KCl electrolyte. In $MgCl_2$ and the bi-salt electrolyte, the anode remains stable after the initial cycles, displaying no significant capacity fading and high coulombic efficiencies. The capacity growth occurring during the first cycles in pure $MgCl_2$ can be linked to delayed electrode wetting due to the high viscosity of this electrolyte.

To investigate the electrochemical performance of the PNFE anode in the mixed electrolyte, GCPL, and CV measurements were carried out at different C-rates and scan rates, respectively. In Figure 3E, the specific capacities per cycle for different charging and discharging rates ranging from 1 C (150 mA g^{-1}) to 300 C (45 A g^{-1}) are displayed. At 1 C, the anode exhibits a maximum discharge capacity of 148 mAh g^{-1}, of which ≈85% are retained at 10 C and ≈60% are retained at 300 C. While the coulombic efficiency decreases slightly at lower rates due to parasitic HER, this effect is more pronounced in the flooded cell setup compared to a realistic battery assembly with minimal electrolyte volume. To understand the exceptional rate capability of PNFE, the peak current of CVs recorded at different scan rates is evaluated in Figure 3F. For the anode, the value of param-

© 2025 The Author(s). Advanced Science published by Wiley-VCH GmbH

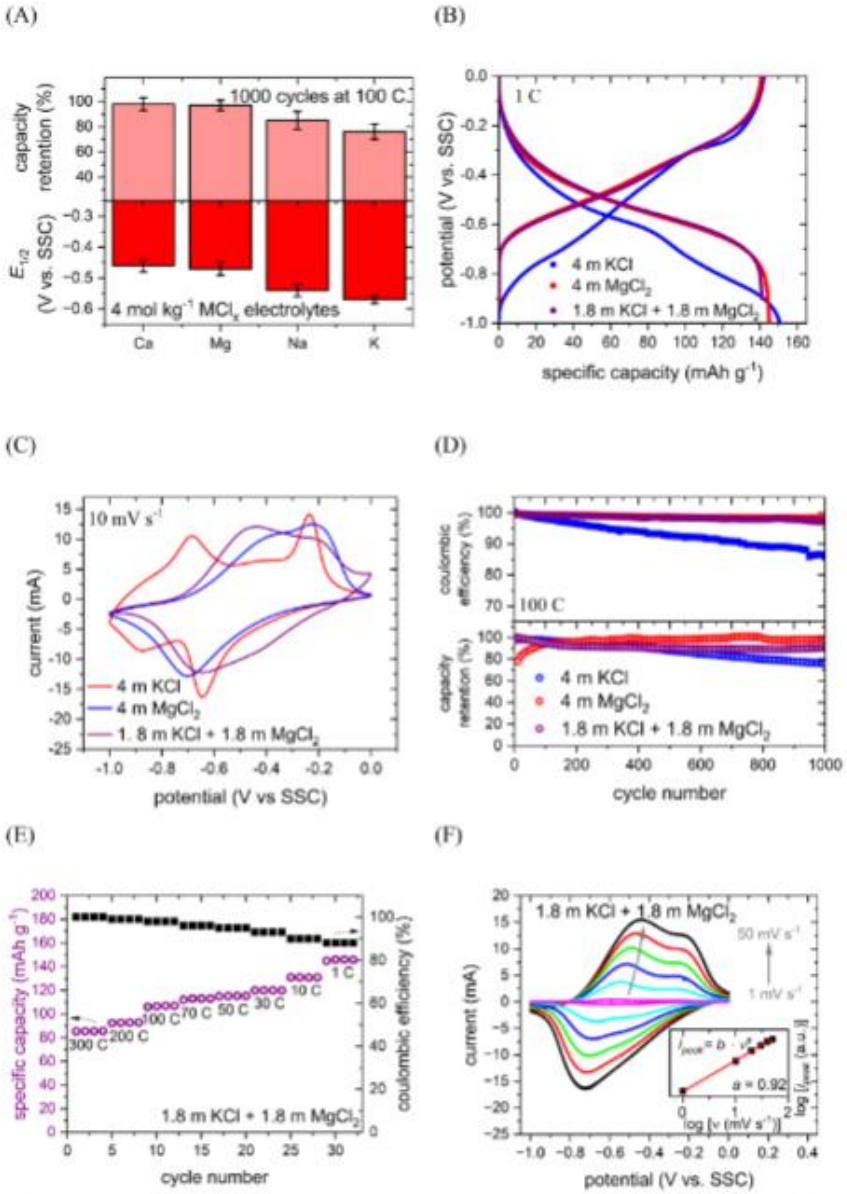


Figure 3. Electrochemical performance of PNFE. A) Summary of the electrode potential and cycling stability in different 4 mol kg^{-1} MCl$_x$ (M = Na, K, Mg, Ca) aqueous electrolytes. Data presented as mean ± SD, $n = 5$. B) Galvanostatic (dis-)charge curves, C) CVs, and D) cycling stability in KCl, MgCl$_2$, and 1.8 mol kg^{-1} KCl + 1.8 mol kg^{-1} MgCl$_2$. E) Specific discharge capacity in 1.8 mol kg^{-1} KCl + 1.8 mol kg^{-1} MgCl$_2$. F) CVs at different scan rates in 1.8 mol kg^{-1} KCl + 1.8 mol kg^{-1} MgCl$_2$.

eter a, introduced previously when studying the cathode, lies at 0.92, indicating that the kinetics are mostly surface-limited. This reflects the pseudo-capacitive nature of the charge storage mechanism of PNFE, which translates to fast charge transfer kinetics.

Both electrodes exhibited promising electrochemical performance in the mixed electrolyte and were thus combined into a model aqueous battery. **Figure 4A** shows the combined CV of the PNFE anode and the CuHCF cathode in the bi-salt electrolyte.

Considering the redox-active potential regions of the single electrodes, the battery should be able to operate at cell voltages between 0.8 and 1.7 V. Furthermore, no parasitic HER or OER currents can be observed in the CVs, indicating that the electrolyte stability window is sufficient for this material combina-

© 2025 The Author(s). Advanced Science published by Wiley-VCH GmbH

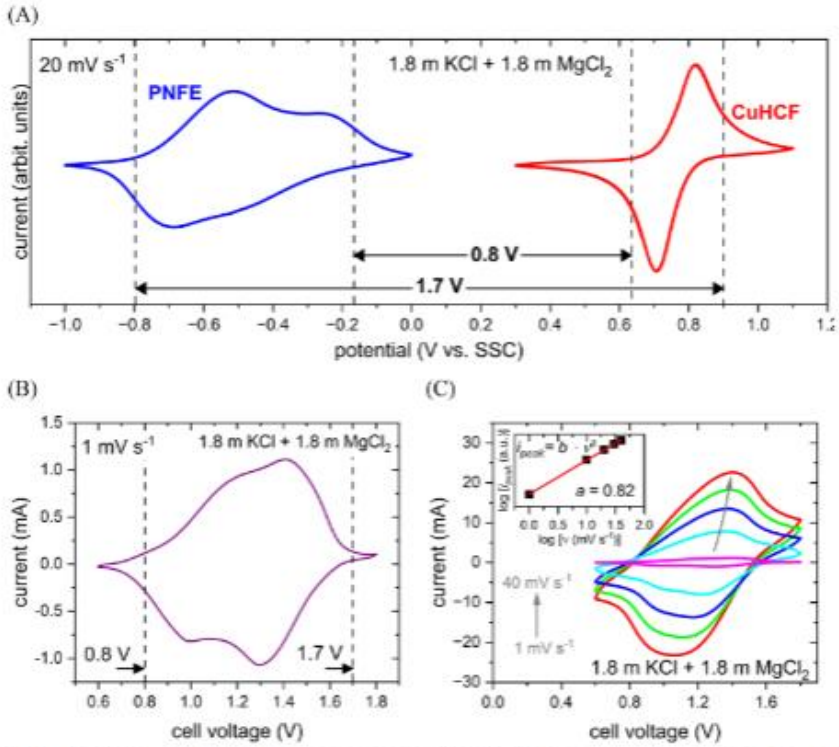


Figure 4. CV analysis of the PNFE/1.8 mol kg^{-1} KCl + 1.8 mol kg^{-1} $MgCl_2$/CuHCF full cell. A) CVs of anode and cathode in the bi-salt electrolyte. B) CV of the full cell at 1 mV s^{-1}. C) CVs of the full cell at different scan rates. Inset: peak current versus scan rate.

tion. A CV of the full cell recorded at 1 mV s^{-1} is depicted in Figure 4B, confirming that the battery displays highly reversible charge and discharge peaks within the expected voltage range. Two oxidation peaks at 1.17 and 1.42 V and two reduction peaks at 1.01 and 1.30 V are recorded, reflecting the behavior of the anode and cathode. To analyze the charge transfer kinetics of the full cell, CVs were recorded at different scan rates ranging from 1 to 40 mV s^{-1} (Figure 4C). For the full cell, parameter *a*, extracted from the dependence of the peak current on the scan rate, yields 0.82, lying between the anode and cathode values and indicating a partially mass-transport-limited process. As the anode exhibits almost no diffusion limitations, the kinetics of the full cell are probably limited by the cathode. Hence, the preferential intercalation of K^+ over Mg^{2+} into CuHCF enables enhanced rate capabilities as divalent ions feature higher charge densities and, thus, interact more strongly with the host lattice. This allows for the control of the fast-charging capability of the full cell by tuning the capacity ratio of the electrodes since an oversized cathode will improve the high-rate performance. In contrast, balanced cathode and anode capacities enable higher energy densities at low rates. For this study, a ratio between anode and cathode active material of 1:2 was chosen to achieve nearly equal electrode capacities.

Figure 5A shows the charge and discharge profiles of the CuHCF/1.8 mol kg^{-1} KCl + 1.8 mol kg^{-1} $MgCl_2$/PNFE aqueous battery recorded at C-rates between 1 C (42 mAh g^{-1}) and 300 C (12.6 A g^{-1}). To ensure stable operating conditions and monitor any rate-dependent degradation, multiple cycles were recorded at each C-rate. At a discharge rate of 1 C, the voltage curve features a sloping plateau between 1.6 and 0.8 V, with an average discharge voltage of 1.22 V. Within the 0.6–1.7 V range, the cell achieves a reversible capacity of 42 mAh g^{-1}, corresponding to ≈90% of the theoretical value calculated from the specific capacities of the anode (148 mAh g^{-1}) and cathode (65 mAh g^{-1}). The battery demonstrates strong fast-charging capability, retaining ≈90% of its capacity at 10 C, 57% at 100 C, and 30% at 300 C. This can be attributed to the low charge density and hydration energy of K^+ enabling fast diffusion kinetics at the cathode, which can be considered the rate-limiting process within the battery. As shown in Figure 5B, coulombic efficiencies exceed 95% across all C-rates, affirming the cell's high reversibility.

By integrating the discharge profile, the specific discharge energy for each cycle and C-rate is evaluated with regard to the combined active material mass of the anode and cathode and displayed in Figure 5C. Due to increased voltage polarization at higher rates, the specific energy shows a stronger dependence on the rate than the specific capacity. However, the specific energy declines only slightly from 48 Wh kg^{-1} at 1 C to 43 Wh kg^{-1} at 10 C, indicating the battery can achieve fast-charging times of 5–10 min with minimal energy loss. At 10 C, the cell also demonstrates

© 2025 The Author(s). Advanced Science published by Wiley-VCH GmbH

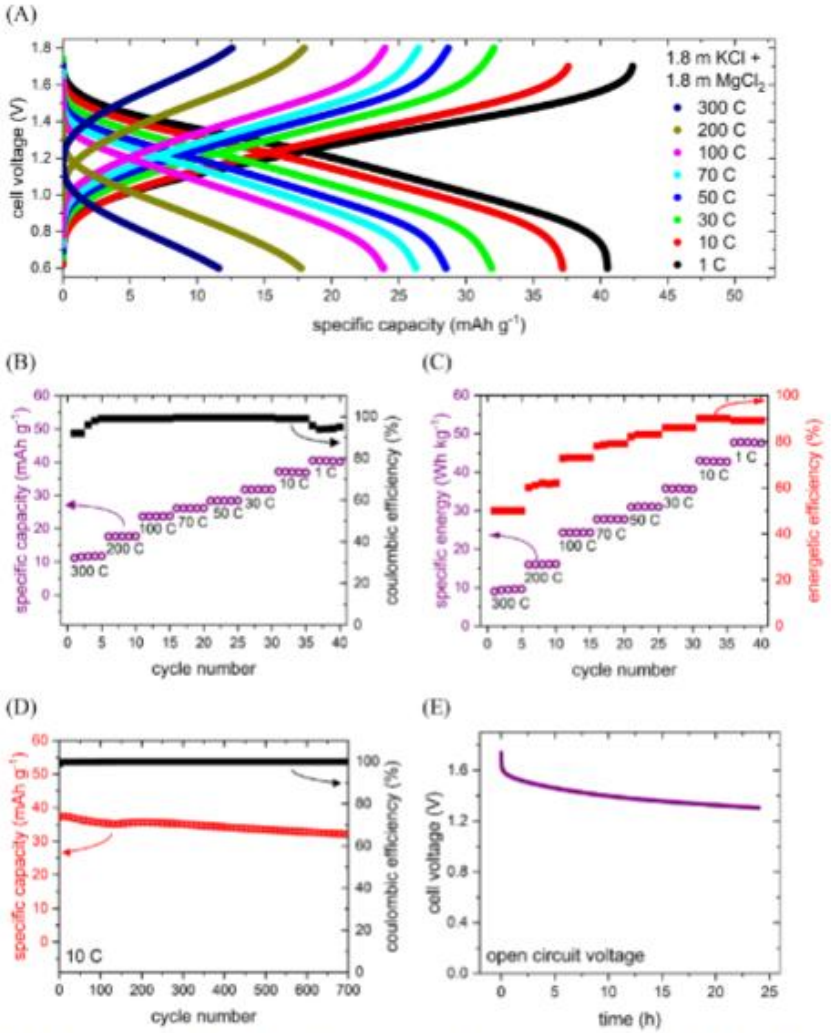


Figure 5. Electrochemical performance of the PNFE/1.8 mol kg^{-1} KCl + 1.8 mol kg^{-1} $MgCl_2$/CuHCF full cell. A) (Dis-)charge curves of the full cell at different current densities. B) Specific capacity and C) specific energy for each cycle during a rate capability test. D) Cycling stability. (E) Open-circuit voltage. (Energy densities are normalized to the combined anode and cathode active material mass).

its highest energetic efficiency of 90%. While voltage polarization reduces efficiency at higher rates, coulombic losses from parasitic HER and OER contribute to minor efficiency decreases at lower rates. It should be noted that besides OER, Cl-oxidation can contribute to parasitic currents at the cathode in electrolytes containing Cl^--anions. However, due to its significantly higher onset potential, this reaction most likely plays a minor role compared to the OER. Consequently, this cell is suitable for applications requiring moderate energy densities but fast-charging capabilities, such as public transportation or grid stabilization, and can even operate effectively at high rates of 100, 200, and 300 C. To further support this conclusion, the power density can be calculated by multiplying the specific discharge current by the average discharge voltage at each rate. The specific currents span from 42 mAh g^{-1} (1 C) to 12.6 A g^{-1} (300 C), while the average discharge voltages range from 1.22 V (1 C) to 0.85 V (300 C). This results in power densities between 51.2 W kg^{-1} and 10.7 kW kg^{-1}, representing some of the highest values reported for aqueous batteries to date.

To assess the cycling stability, the CuHCF/1.8 mol kg^{-1} KCl + 1.8 mol kg^{-1} $MgCl_2$/PNFE aqueous battery was charged and discharged repeatedly at 10 C. Figure 5D shows the specific capacity and coulombic efficiency for each cycle. The cell exhibits good cycle performance, retaining ≈90% of its initial capacity after 700 cycles while also maintaining high coulombic efficiency of nearly 100% throughout the entire measurement. To confirm the suc-

© 2025 The Author(s). Advanced Science published by Wiley-VCH GmbH

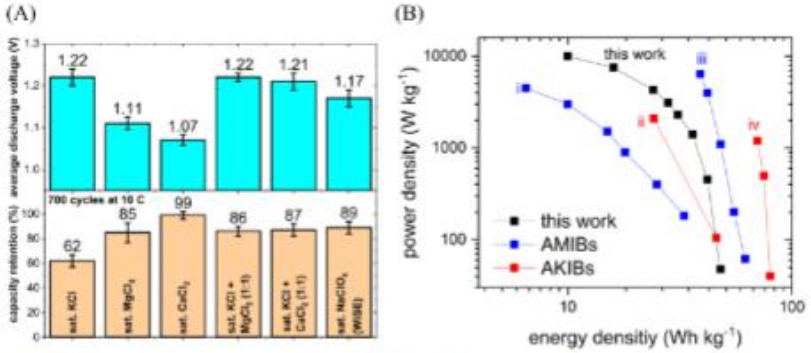


Figure 6. A) Comparison of the cell voltage and cycling stability of PNFE//CuHCF batteries with different electrolytes. Data presented as mean ± SD, $n = 5$. B) Comparison of the aqueous battery performance in this work with AKIBs and AMIBs reported by i) Chen et al.[45] ii) Wang et al.,[61] iii) Wang et al.,[62] and Jiang et al.[25]

cessful suppression of water-splitting side reactions in the battery based on the bi-salt electrolyte, the cell was initially charged to a voltage of 1.7 V, and then the cell voltage was recorded for 24 h under open-circuit conditions (Figure 5E). After an initial drop to ≈1.5 V, the open-circuit voltage (OCV) remains relatively stable, indicating that the cell exhibits no significant self-discharge.

To further demonstrate the superior properties of the aqueous battery based on the bi-salt electrolyte, multiple cells using the same electrode materials were assembled with various electrolytes. Subsequently, the average discharge voltage and cycling stability were assessed for at least five cells for each combination.

An overview of the results is given in **Figure 6A**. As expected from the single-electrode measurements, the battery featuring saturated (4.6 mol kg^{-1}) KCl suffers from significant capacity fading while providing a relatively high cell voltage. In contrast, the cells using electrolytes based on divalent Ca^{2+} and Mg^{2+} deliver substantially lower cell voltages but show improved capacity retention. Especially when using saturated (6.7 mol kg^{-1}) $CaCl_2$, the battery exhibits almost no capacity loss over 700 cycles due to the high concentration and viscosity of this electrolyte. For a more detailed analysis of this highly stable configuration, the reader is referred to our previous work.[37] However, as higher cell voltages are desirable for maximizing energy density, the use of mixed electrolytes containing K-ions together with divalent species proves to be a promising strategy for optimizing battery performance. Both the cells based on 1.8 KCl + 1.8 mol kg^{-1} $MgCl_2$ and 2 mol kg^{-1} KCl + 2 mol kg^{-1} $CaCl_2$ show better capacity retention than the K-ion battery and higher cell voltages than the Mg- and Ca-ion systems. In addition, a reference cell containing a commonly used $NaClO_4$ water-in-salt electrolyte displays similar capacity retention and a slightly lower cell voltage, confirming that the bi-salt electrolyte approach yields competitive results compared to the more expensive WiSE strategy. To confirm this conclusion, a comparison between the optimized battery proposed in this work and state-of-the-art aqueous K-ion (AKIB) and Mg-ion batteries (AMIB) reported in the literature is shown in Figure 6B. Whereas the batteries developed by Wang et al. and Jiang et al. exhibit higher energy densities, they rely on fluorinated $Mg(TFSI)_2$ and KCF_3SO_3 salts, respectively.[25,62] It should be noted that while Jian et al. work with very high concentrations to enable stable cycling of the Mn-PBA cathode, Wang et al. use a relatively dilute electrolyte. However, the used $Li_3V_2(PO_4)_3$ cathode material features both lithium and vanadium, raising the expected cost of this configuration. Nevertheless, the superior energy densities of these systems render them suitable for applications requiring lighter cell weight. The energy density of the cell in our work exceeds the values typically reported for aqueous batteries based on F-free dilute electrolytes, such as the AKIB and AMIB reported by Chen et al. and Wang et al., respectively.[45,61] In addition, power densities of more than 10 kW kg^{-1} are superior to all of the designs mentioned above and have, to the best of our knowledge, rarely been reported for aqueous batteries so far.

3. Conclusions

This study demonstrates that the choice of cation strongly influences key electrode properties, such as redox potential and cycling stability. Among the cations examined, potassium ions generally provide the highest electrode potential at the CuHCF cathode, but the cycling stability in a 4 mol kg^{-1} KCl electrolyte remains inadequate. At the same concentration, divalent cations like Mg^{2+} and Ca^{2+} significantly improve cycling performance, albeit at the cost of reducing the intercalation potential. However, we show that combining monovalent K^+ with divalent ions optimizes both stability and electrode potential. Similar trends were observed for the PNFE anode, where K^+ results in the lowest insertion potential, while Ca^{2+} and Mg^{2+} lead to the longest cycle life.

Building on these insights, we developed a full aqueous battery using the specified electrode materials and a 1.8 mol kg^{-1} KCl + 1.8 mol kg^{-1} $MgCl_2$. This battery achieves a competitive energy density of 48 Wh kg^{-1} at 1 C, with an energy efficiency of 95%, and a power density exceeding 10 kW kg^{-1} at 300 C. It also demonstrates excellent fast-charging capabilities, retaining 70% of its capacity at a high rate of 50 C, making it suitable for supercapacitor-like applications, such as applications in the public transport sector. By utilizing abundant, low-cost salts in a safe and environmentally friendly electrolyte, we believe that our work represents a significant step toward the practical application of aqueous beyond-lithium-ion batteries.

© 2025 The Author(s). Advanced Science published by Wiley-VCH GmbH

4. Experimental Section

Material Synthesis: All chemicals were purchased from commercial suppliers and used without further purification.

PNFE was synthesized for a previous work and used without further processing. For detailed synthesis information, the reader is referred to a previous publication.[46] In short, 10 mmol of 1,4,5,8-naphthalene tetracarboxylic dianhydride (NTCDA) and 10 mmol of ethylenediamine (EDA) were dissolved in 20 mL of degassed N-methyl pyrrolidone (NMP) in a Schlenk flask. The mixture was heated to 215 °C in a sand bath and refluxed overnight. The resulting dark precipitate was filtered and washed several times with NMP and water. It was then dried under vacuum at 0.08 mbar, progressively increasing the temperature from room temperature to 120 °C and finally to 210 °C. The final product was a gray-brown powder with a high yield of 92% (2.7 g).

Elemental Analysis of PNFE: Calcd. for an infinite polymer ($C_{16}H_8N_2O_4$). %: C 65.76, H 2.76, N 9.59; calcd. for an octamer, %: C 65.10, H 3.03, N 10.52; found, %: C 65.13, H 2.91, N 10.32.

Copper hexacyanoferrate (CuHCF) was prepared by coprecipitation from two solutions according to the method reported by Xu et al.[41] To prepare solution A, 1 mmol of $CuCl_2 \cdot 2\ H_2O$ and 1 mmol of $Na_4P_2O_7 \cdot 10\ H_2O$ were dissolved in 20 mL of deionized (DI) water. For solution B, 1 mmol of $Na_4Fe(CN)_6 \cdot 10\ H_2O$, 0.3 g of polyvinylpyrrolidone (PVP), and 0.58 g of NaCl were mixed into 50 mL of DI water. Solution A was then gradually added to solution B, while vigorously stirring at room temperature. The mixture was left to age for 5 d, after which the precipitate was separated by centrifugation and washed three times each with water and ethanol. Finally, the product was dried overnight at 70 °C.

Electrode Preparation: As reported in a previous work, PNFE and CuHCF electrodes were fabricated using the slurry casting method.[37] For the PNFE slurry, a mixture consisting of 80 wt% polyimide as the active material, 10 wt% carbon black super C-65 (MTI, USA), and 10 wt% Nafion binder (5 wt% in lower aliphatic alcohols and water, Sigma Aldrich, USA) was ground using a planetary ball mill. Water and isopropyl alcohol in a 1:1 ratio were added as dispersing agents, and the mixture was stirred vigorously to form the anode slurry.

The CuHCF slurry was prepared similarly, using 80 wt% active material, 10 wt% carbon black super C-65, and 10 wt% polyvinylidene fluoride (PVDF, MTI, USA), also ground in a planetary ball mill. NMP was added during stirring to create the cathode slurry.

Both slurries were cast onto pyrolytic graphite sheet current collectors. The mass loading of the active material was ≈3.5 mg cm^{-2} for the CuHCF cathode and 2.0 mg cm^{-2} for the PNFE anode.

Material Characterization: The PNFE anode was characterized by field emission SEM (JSM-7500F, JEOL). FTIR (Bruker Vertex-70) spectroscopy and XPS (Al Kα source, SPECS XR50 Xf-Ray, SPECS PHOIBOS 150 hemispherical analyzer, SPECS spectrometer). SEM and powder XRD (Rigaku MiniFlex 600-C) were used to analyze the structure of the CuHCF cathode.

The viscosities of the electrolytes were measured at 25 °C with a commercial shear rheometer (MCR 302, Anton Paar GmbH, Graz, Austria) equipped with a cone-shaped measuring head (CP50-1, 79040, Anton Paar) and an air-cooled bottom plate (P-PTD 200/56/Air, Anton Paar).

Scanning electron microscopy – energy-dispersive X-ray spectrometry (SEM-EDX, JSM-IT200, JEOL) was conducted to analyze the elemental composition of CuHCF after being reduced in the mixed electrolyte.

Nitrogen gas sorption isotherms were measured using a Micromeritics 3Flex analyzer under liquid nitrogen at 77 K to determine surface area and pore size distribution. The BET specific surface area and pore size distribution were analyzed with the dedicated software provided by Micromeritics. Prior to measurement, the prepared electrodes and bare substrate were cut into small pieces, placed in a tubular glass measuring cells, and activated under vacuum at 120 °C for 16 h to remove any residual moisture or contaminants.

Electrochemical Measurements: Single-electrode measurements were performed using a three-electrode setup within a sealed glass cell, maintained under a constant argon flow to ensure an inert atmosphere. Both the electrolyte and the glass cell were purged with argon for at least 10 minutes before introducing the electrolyte into the cell. A platinum wire (MaTeck, Germany) served as the counter electrode, while an Ag/AgCl electrode (SSC, 3 M KCl, SI Analytics), connected to the electrolyte through a Luggin capillary, was used as the reference electrode. 4 mol kg^{-1} (4 m) NaCl, KCl, $MgCl_2$, and $CaCl_2$ were used as single-salt electrolytes. A saturated mixture of 1.8 mol kg^{-1} KCl and 1.8 mol kg^{-1} $MgCl_2$ was prepared as a bi-salt electrolyte.

A BioLogic VSP-300 potentiostat was used to conduct CV and GCPL. CVs were recorded at different scan rates ranging from 1 to 50 mV s^{-1} at potentials from −1.0 to 0.0 V and from 0.3 to 1.1 V (vs SSC) for anode and cathode, respectively. Galvanostatic (dis-)charging was carried out at C-rates between 1 and 300 C within the same potential ranges. By galvanostatically charging and discharging the electrodes for 100 cycles at 10 C (cathode) and for 1000 cycles at 100 C (anode), the cycling stability in different electrolytes was tested.

Full-Cell Assembly and Measurements: To address the corrosive effects of chlorides on most stainless steel alloys, a 3D-printed plastic cell with pyrolytic graphite foil as contacts was used for the full-cell assembly. The aqueous bi-salt battery was constructed in a nitrogen-filled glovebox to prevent oxygen from dissolving into the electrolyte. A commercial alkaline battery separator, pre-soaked in a 1.8 mol kg^{-1} KCl + 1.8 mol kg^{-1} $MgCl_2$ electrolyte, was placed between the electrodes. The cell was fully sealed with rubber O-rings to ensure a closed environment.

For the full-cell, CV, GCPL, and OCV measurements were performed using a Biologic VSP-300 potentiostat. CVs were measured at scan rates ranging from 1 to 40 mV s^{-1}, with cell voltages between 0.6 and 1.8 V. GCPL was carried out at C-rates from 300 to 30 C over the same voltage range. For the 10 and 1 C rates, the upper voltage limit was slightly reduced to 1.7 V to prevent side reactions. The OCV was monitored for 24 h after fully charging the battery with a constant voltage hold at 1.7 V.

Statistical Analysis: All statistical values are expressed as mean ± SD (standard deviation) with the number of samples *n* given in the figure captions. Statistical analysis was carried out using Origin 2023 software.

Supporting Information

Supporting Information is available from the Wiley Online Library or from the author.

Acknowledgements

The authors acknowledge Mr. Siegfried Schreier for his assistance in acquiring SEM pictures and Dr. Sergei Vagin for his assistance in synthesizing PNFE and acquiring the FTIR spectra. The authors thank Deutsche Forschungsgemeinschaft (DFG, German Research Foundation) under Germany's Excellence Strategy – EXC 2089/1 – 390776260 (e-conversion) for funding. A.S.B. acknowledges additional financial support from TUMInnovation Network for Artificial Intelligence-Powered Multifunctional Material Design (ARTEMIS).

Open access funding enabled and organized by Projekt DEAL.

Conflict of Interest

The authors declare no conflict of interest.

Author Contributions

R.S. and A.B. proposed the concept and co-wrote the manuscript. R.S., S.R., S.W., J.S., P.S., and D.G. performed the experiments. R.S., A.S., J.S., and M.H. analyzed the data. All authors contributed to data analysis and manuscript conceptualization.

Data Availability Statement

The data that support the findings of this study are available from the corresponding author upon reasonable request.

© 2025 The Author(s). Advanced Science published by Wiley-VCH GmbH

Keywords

aqueous batteries, electrolytes, fast charging, magnesium, potassium

Received: March 1, 2025
Revised: April 17, 2025
Published online:

[1] A. Kalair, N. Abas, M. S. Saleem, A. R. Kalair, N. Khan, *Energy Storage* **2021**, *3*, 135.
[2] M. Arbabzadeh, R. Sioshansi, J. X. Johnson, G. A. Keoleian, *Nat. Commun.* **2019**, *10*, 3413.
[3] M. Jafari, A. Botterud, A. Sakti, *Renewable Sustainable Energy Rev.* **2022**, *158*, 112077.
[4] B. P. Roberts, C. Sandberg, *Proc. IEEE* **2011**, *99*, 1139.
[5] N. Kittner, F. Lill, D. M. Kammen, *Nat. Energy* **2017**, *2*, 17125.
[6] J. Wen, D. Zhao, C. Zhang, *Renewable Energy* **2020**, *162*, 1629.
[7] Y. Gao, Z. Pan, J. Sun, Z. Liu, J. Wang, *Nano-Micro Lett.* **2022**, *14*, 94.
[8] A. Luntz, *J. Phys. Chem. Lett.* **2015**, *6*, 300.
[9] A. A. Yaroshevsky, *Geochem. Int.* **2006**, *44*, 48.
[10] J. O. G. Posada, A. J. R. Rennie, S. P. Villar, V. L. Martins, J. Marinaccio, A. Barnes, C. F. Glover, D. A. Worsley, P. J. Hall, *Renewable Sustainable Energy Rev.* **2017**, *68*, 1174.
[11] Y. Liang, Y. Yao, *Nat. Rev. Mater.* **2023**, *8*, 109.
[12] D. Chao, C. Ye, F. Xie, W. Zhou, Q. Zhang, Q. Gu, K. Davey, L. Gu, S.-Z. Qiao, *Adv. Mater.* **2020**, *32*, 2001894.
[13] F. Zhang, W. Zhang, D. Wexler, Z. Guo, *Adv. Mater.* **2022**, *34*, 2107965.
[14] G. Navarro, J. Torres, M. Blanco, J. Nájera, M. Santos-Herran, M. Lafoz, *Energies* **2021**, *14*, 3060.
[15] T. P. Sumangala, M. S. Sreekanth, A. Rahaman, in *Handbook of Nanocomposite Supercapacitor Materials III: Selection*, Springer Nature, New York **2021**, pp. 367–393.
[16] L. Buzzoni, G. Pede, in *Proc. Electrical Systems Aircraft, Railway and Ship Propulsion (ESARS)*, IEEE, Piscataway, NJ **2012**, pp. 1–5.
[17] Chariot Motors, Ultracapacitor | Chariot e-Bus | Chariot Motors | Electric Bus, **2023**, available at https://chariot-electricbus.com/cmproduct/12m-ultracapacitor-chariot-e-bus/.
[18] M. Pasta, C. D. Wessells, N. Liu, J. Nelson, M. T. McDowell, R. A. Huggins, M. F. Toney, Y. Cui, *Nat. Commun.* **2014**, *5*, 3007.
[19] H. Ahn, D. Kim, M. Lee, K. W. Nam, *Commun. Mater.* **2023**, *4*, 37.
[20] Z. Pan, X. Liu, J. Yang, X. Li, Z. Liu, X. J. Loh, J. Wang, *Adv. Energy Mater.* **2021**, *11*, 2100608.
[21] X. Lamprecht, F. Speck, P. Marzak, S. Cherevko, A. S. Bandarenka, *ACS Appl. Mater. Interfaces* **2022**, *14*, 3515.
[22] H. Zhang, X. Liu, H. Li, I. Hasa, S. Passerini, *Angew. Chem., Int. Ed.* **2021**, *60*, 598.
[23] T. Liang, R. Hou, Q. Dou, H. Zhang, X. Yan, *Adv. Funct. Mater.* **2021**, *31*, 2006749.
[24] L. Suo, O. Borodin, T. Gao, M. Olguin, J. Ho, X. Fan, C. Luo, C. Wang, K. Xu, *Science* **2015**, *350*, 938.
[25] L. Jiang, Y. Lu, C. Zhao, L. Liu, J. Zhang, Q. Zhang, X. Shen, J. Zhao, X. Yu, H. Li, X. Huang, L. Chen, Y.-S. Hu, *Nat. Energy* **2019**, *4*, 495.
[26] S. Ko, Y. Yamada, A. Yamada, *Electrochem. Commun.* **2020**, *116*, 106764.
[27] M. R. Lukatskaya, J. I. Feldblyum, D. G. Mackanic, F. Lissel, D. L. Michels, Y. Cui, Z. Bao, *Energy Environ. Sci.* **2018**, *11*, 2876.
[28] R. Sakamoto, M. Yamashita, K. Nakamoto, Y. Zhou, N. Yoshimoto, K. Fujii, T. Yamaguchi, A. Kitajou, S. Okada, *Phys. Chem. Chem. Phys.* **2020**, *22*, 26452.
[29] X. Lamprecht, I. Evazzade, I. Ungerer, L. Hromadko, J. M. Macak, A. S. Bandarenka, V. Alexandrov, *J. Phys. Chem. C* **2023**, *127*, 2204.
[30] H. Bi, X. Wang, H. Liu, Y. He, W. Wang, W. Deng, X. Ma, Y. Wang, W. Rao, Y. Chai, H. Ma, R. Li, J. Chen, Y. Wang, M. Xue, *Adv. Mater.* **2020**, *32*, 2000074.
[31] R. Deng, J. Chen, F. Chu, M. Qian, Z. He, A. W. Robertson, J. Maier, F. Wu, *Adv. Mater.* **2024**, *36*, 2311153.
[32] K. Hurlbutt, S. Wheeler, I. Capone, M. Pasta, *Joule* **2018**, *2*, 1950.
[33] J. Qian, C. Wu, Y. Cao, Z. Ma, Y. Huang, X. Ai, H. Yang, *Adv. Energy Mater.* **2018**, *8*, 1870079.
[34] X. Li, A. Wu, C. Gao, Z. Li, S. W. Lee, *Mater. Today Energy* **2023**, *31*, 101205.
[35] R. Trócoli, F. La Mantia, *ChemSusChem* **2015**, *8*, 481.
[36] C. D. Wessells, R. A. Huggins, Y. Cui, *Nat. Commun.* **2011**, *2*, 550.
[37] R. L. Streng, S. Reiser, S. Wager, N. Pommer, A. S. Bandarenka, *ChemSusChem* **2025**, *18*, 202401469.
[38] X. Wu, Z. Jian, Z. Li, X. Ji, *Electrochem. Commun.* **2017**, *77*, 54.
[39] S. Fan, Y. Liu, Y. Gao, Y. Liu, Y. Qiao, L. Li, S. L. Chou, *Sustainable Mater.* **2023**, *3*, 749.
[40] S. Park, J. Kim, S. H. Yi, S. E. Chun, *ChemSusChem* **2021**, *14*, 1082.
[41] Y. Xu, J. Wan, L. Huang, J. Xu, M. Ou, Y. Liu, X. Sun, S. Li, C. Fang, Q. Li, J. Han, Y. Huang, Y. Zhao, *Energy Storage Mater.* **2020**, *33*, 432.
[42] X. Dong, H. Yu, Y. Ma, J. L. Bao, D. G. Truhlar, Y. Wang, Y. Xia, *Chem.-Eur. J.* **2017**, *23*, 2560.
[43] C. Han, J. Zhu, C. Zhi, H. Li, *J. Mater. Chem. A* **2020**, *8*, 15479.
[44] K. Holguin, M. Mohammadiroudbari, K. Qin, C. Luo, *J. Mater. Chem. A* **2021**, *9*, 19083.
[45] L. Chen, J. L. Bao, X. Dong, D. G. Truhlar, Y. Wang, C. Wang, Y. Xia, *ACS Energy Lett.* **2017**, *2*, 1115.
[46] R. L. Streng, S. Vagin, Y. Guo, B. Rieger, A. S. Bandarenka, *Energy Adv.* **2024**, *3*, 874.
[47] X. Lamprecht, P. Marzak, A. Wieczorek, N. Thomsen, J. Kim, B. Garlyyev, Y. Liang, A. S. Bandarenka, J. Yun, *Energy Adv.* **2022**, *1*, 623.
[48] R. Bors, J. Yun, P. Marzak, J. Fichtner, D. Scieszka, A. S. Bandarenka, *ACS Omega* **2018**, *3*, 5111.
[49] P. Marzak, M. Kosiahn, J. Yun, A. S. Bandarenka, *Electrochim. Acta* **2019**, *307*, 157.
[50] Y. Mizuno, M. Okubo, E. Hosono, T. Kudo, H. Zhou, K. Oh-Ishi, *J. Phys. Chem. C* **2013**, *117*, 10877.
[51] X. Wu, Y. Luo, M. Sun, J. Qian, Y. Cao, X. Ai, H. Yang, *Nano Energy* **2015**, *13*, 117.
[52] K. Zhu, Z. Li, T. Jin, L. Jiao, *J. Mater. Chem. A* **2020**, *8*, 21103.
[53] W. Wang, Y. Gang, J. Peng, Z. Hu, Z. Yan, W. Lai, Y. Zhu, D. Appadoo, M. Ye, Y. Cao, Q.-F. Gu, H.-K. Liu, S.-X. Dou, S.-L. Chou, *Adv. Funct. Mater.* **2022**, *32*, 2111727.
[54] Y. Gao, X. Wu, L. Wang, Y. Zhu, G. Sun, Y. Tang, M. Yan, Y. Jiang, *Adv. Funct. Mater.* **2024**, *34*, 2314860.
[55] B. Xie, P. Zuo, L. Wang, J. Wang, H. Huo, M. He, J. Shu, H. Li, S. Lou, G. Yin, *Nano Energy* **2019**, *61*, 201.
[56] M. Peschke, A. T. Blades, P. Kebarle, *Int. J. Mass Spectrom.* **1999**, *185*, 685.
[57] P. L. Brown, S. E. Drummond, D. A. Palmer, *J. Chem. Soc., Dalton Trans.* **1996**, 3071.
[58] W. Li, Z. Sun, *J. Phys. Chem. Lett.* **2025**, *16*, 503.
[59] A. Bhattacharjee, A. B. Pribil, B. R. Randolf, B. M. Rode, T. S. Hofer, *Chem. Phys. Lett.* **2012**, *536*, 39.
[60] P. R. Smirnov, *Russ. J. Gen. Chem.* **2020**, *90*, 1693.
[61] M. Wang, H. Wang, H. Zhang, X. Li, *J. Energy Chem.* **2020**, *48*, 14.
[62] F. Wang, X. Fan, T. Gao, W. Sun, Z. Ma, C. Yang, F. Han, K. Xu, C. Wang, *ACS Cent. Sci.* **2017**, *3*, 1121.

© 2025 The Author(s). Advanced Science published by Wiley-VCH GmbH

References

[1] P.P. Groumpos. A Critical Historical and Scientific Overview of all Industrial Revolutions. *IFAC-PapersOnLine* 2021, 54(13), 134-139.

[2] N. Sá, F. Martins, C. Felgueiras, N. Caetano. New Trends in Energy Production and Utilization. *Energy Procedia* 2017, 107, 7-14.

[3] N. Abas, A. Kalair, N. Khan. Review of Fossil Fuels and Future Energy Technologies. *Futures* 2015, 69, 31-49.

[4] F. Martins, C. Felgueiras, M. Smitkova, N. Caetano. Analysis of Fossil Fuel Energy Consumption and Environmental Impacts in European Countries. *Energies* 2019, 12(6), 964.

[5] M. Höök, X. Tang. Depletion of fossil fuels and anthropogenic climate change—a review. *Energy Policy* 2013, 52, 797-809.

[6] IPCC 2021, V. Masson-Delmotte, P. Zhai, A. Pirani, S. L. Connors, C. Péan, S. Berger, N. Caud, Y. Chen, L. Goldfarb, M. I. Gomis, M. Huang, K. Leitzell, E. Lonnoy, J. B. R. Matthews, T. K. Maycock, T. Waterfield, O. Yelekçi, R. Yu, B. Zhou (eds.). Climate change 2021: the physical science basis. Contribution of Working Group I to the Sixth Assessment Report of the Intergovernmental Panel on Climate Change. *Cambridge University Press* 2021.

[7] E. Maibach, T. Myers, A. Leiserowitz. Climate scientists need to set the record straight: There is a scientific consensus that human-caused climate change is happening. *Earth's Future* 2014, 2 (5), 295–298.

[8] J. Cook, D. Nuccitelli, S.A. Green, M. Richardson, B. Winkler, R. Painting, R. Way, P. Jacobs, A. Skuce. Quantifying the consensus on anthropogenic global warming in the scientific literature. *Environ. Res. Lett.* 2013, 8, 024024.

[9] C. Bellard, C. Bertelsmeier, P. Leadley, W. Thuiller, F. Courchamp. Impacts of climate change on the future of biodiversity. *Ecol. Lett.* 2012, 15 (4), 365–377.

[10] R.S.J. Tol. Estimating global impacts from climate change. *Global Environmental Change* 2005, 15 (3), 195–224.

[11] J.G. Pausas, J.E. Keeley. Wildfires and global change. *Front. Ecol. Environ.* 2021, 19 (7), 387–395.

[12] B. Clarke, F. Otto, R. Stuart-Smith, L. Harrington. Extreme weather impacts of climate change: an attribution perspective. *Environmental Research: Climate* 2022, 1 (1), 012001.

[13] J. Laherrère, C. A. S. Hall, R. Bentley. How Much Oil Remains for the World to Produce? Comparing Assessment Methods, and Separating Fact from Fiction. *Curr. Res. Environ. Sustain.* 2022, *4*, 100174.

[14] D. O'Rourke, S. Connolly. Just Oil? The Distribution of Environmental and Social Impacts of Oil Production and Consumption. *Annu. Rev. Energy Environ.* 2003, 28, 587-617.

[15] A.O. Adeola, A.S. Akingboye, O.T. Ore, O.A. Oluwajana, A.H. Adewole, D.B. Olawade, A.C. Ogunyele. Crude oil exploration in Africa: socio-economic implications, environmental impacts, and mitigation strategies. *Environ. Syst. Decis.* 2022, 42, 26–50.

[16] C. M. C. Inacio Jr, L. Kristoufek, S. A. David. Assessing the Impact of the Russia–Ukraine War on Energy Prices: A Dynamic Cross-Correlation Analysis. *Physica A: Stat. Mech. Appl.* 2023, 626, 129084.

[17] H. Wang, X. Zhang, Y. Li. Economic impact of crude oil supply disruption on social welfare losses and strategic petroleum reserves. *Resour. Policy* 2022, 77, 102689.

[18] F. P. Perera. Multiple Threats to Child Health from Fossil Fuel Combustion: Impacts of Air Pollution and Climate Change. *Environ. Health Perspect.* 2017, 125, 141-148.

[19] J. Lelieveld, A. Haines, R. Burnett, C. Tonne, K. Klingmüller, T. Münzel, A. Pozzer. Air Pollution Deaths Attributable to Fossil Fuels: Observational and Modelling Study. *BMJ* 2023, 383.

[20] World Health Organization (WHO). Air Pollution. *World Health Organization*. Available online: https://www.who.int/health-topics/air-pollution#tab=tab_1 (accessed on March 25, 2025)

[21] S. Seddighi, E. J. Anthony, H. Seddighi, F. Johnsson. The Interplay Between Energy Technologies and Human Health: Implications for Energy Transition. *Energy Rep.* 2023, 9, 5592-5611.

[22] G. R. Timilsina. Are Renewable Energy Technologies Cost Competitive for Electricity Generation? *Renewable Energy* 2021, 180, 658-672.

[23] Energy Charts. Installed Power in Germany. Available online: https://www.energy-charts.info/charts/installed_power/chart.htm?c=DE (accessed on March 25, 2025).

[24] A. Kalair, N. Abas, M. S. Saleem, A. R. Kalair, N. Khan. Role of Energy Storage Systems in Energy Transition from Fossil Fuels to Renewables. *Energy Storage* 2020, 3, e135.

[25] S. Zhou, Y. Wang, Y. Zhou, L. E. Clarke, J. A. Edmonds. Roles of Wind and Solar Energy in China's Power Sector: Implications of Intermittency Constraints. *Appl. Energy* 2018, 213, 22-30.

[26] Energy Charts**.** Power Generation in Germany, Week 12, 2025. *Fraunhofer ISE*. Available online: https://www.energy-charts.info/charts/power/chart.htm?c=DE&year=2025&week=12&legendItems=3x0vfvg. (accessed on March 26, 2025).

[27] A. P. Jha, A. Mahajan, S. K. Singh, P. Kumar. Renewable Energy Proliferation for Sustainable Development: Role of Cross-Border Electricity Trade. *Renewable Energy* 2022, 201, 1189-1199.

[28] M. McPherson, N. Johnson, M. Strubegger. The Role of Electricity Storage and Hydrogen Technologies in Enabling Global Low-Carbon Energy Transitions. *Appl. Energy* 2018, 216, 649-661.

[29] C.-J. Yang. Pumped Hydroelectric Storage. *Storing Energy: With Special Reference to Renewable Energy Sources* 2016, 25-38.

[30] G. W. Crabtree, L. Trahey. Q&A: The United States Senate Hearing on Grid-Scale Energy Storage. *Electrochem. Soc. Interface* 2019, 28, 18.

[31] A. Blakers, M. Stocks, B. Lu, C. Cheng. A Review of Pumped Hydro Energy Storage. *Prog. Energy* 2021, 3, 022003.

[32] Energy Charts. Simulated Power Generation in Germany. Available online: https://www.energy-charts.info/charts/power_simulated/chart.htm?l=en&c=DE&solar=215&wind_onshore=115&wind_offshore=30&load=750&legendItems=1waw3. (accessed on March 26, 2025).

[33] J. Figgener, P. Stenzel, K.-P. Kairies, J. Linßen, D. Haberschusz, O. Wessels, G. Angenendt, M. Robinius, D. Stolten, D. U. Sauer. The Development of Stationary Battery Storage Systems in Germany – A Market Review. *J. Energy Storage* 2020, 29, 101153.

[34] A. Zeh, M. Müller, M. Naumann, H. C. Hesse, A. Jossen, R. Witzmann. Fundamentals of Using Battery Energy Storage Systems to Provide Primary Control Reserves in Germany. *Batteries* 2016, 2, 29.

[35] K.-P. Kairies, J. Figgener, D. Haberschusz, O. Wessels, B. Tepe, D. U. Sauer. Market and Technology Development of PV Home Storage Systems in Germany. *J. Energy Storage* 2019, 23, 416-424.

[36] M. Broussely, G. Pistoia, Eds. *Industrial Applications of Batteries: From Cars to Aerospace and Energy Storage.* Elsevier, 2007.

[37] R. Korthauer, Ed. *Lithium-Ion Batteries: Basics and Applications.* Springer, 2018.

[38] X. Hao, et al. Plug-in Electric Vehicles in China and the USA: A Technology and Market Comparison. *Mitig. Adapt. Strateg. Glob. Change* 2020, 25, 329-353.

[39] M. Khaleel, et al. Electric Vehicles in China, Europe, and the United States: Current Trend and Market Comparison. *Int. J. Electr. Eng. Sustain.* 2024, 1-20.

[40] F. Mohammadi, M. Saif. A Comprehensive Overview of Electric Vehicle Batteries Market. *e-Prime Adv. Electr. Eng. Electron. Energy* 2023, 3, 100127.

[41] G. E. Blomgren. The Development and Future of Lithium-Ion Batteries. *J. Electrochem. Soc.* 2017, 164, A5019.

[42] M. Li, J. Lu, Z. Chen, K. Amine. 30 Years of Lithium-Ion Batteries. *Adv. Mater.* 2018, 30, 1800561.

[43] F. M. N. U. Khan, M. G. Rasul, A. S. M. Sayem, N. Mandal. Maximizing Energy Density of Lithium-Ion Batteries for Electric Vehicles: A Critical Review. *Energy Rep.* 2023, 9 (Suppl. 11), 11-21.

[44] T. Kim, W. Song, D.-Y. Son, L. K. Ono, Y. Qi. Lithium-Ion Batteries: Outlook on Present, Future, and Hybridized Technologies. *J. Mater. Chem. A* 2019, 7, 17030-17057.

[45] T. Chen, Y. Jin, H. Lv, A. Yang, M. Liu, B. Chen, Y. Xie, Q. Chen. Applications of Lithium-Ion Batteries in Grid-Scale Energy Storage Systems. *Trans. Tianjin Univ.* 2020, 26, 208-217.

[46] Y. Chen, Y. Kang, Y. Zhao, L. Wang, J. Liu, Y. Li, Z. Liang, X. He, X. Li, N. Tavajohi, B. Li. A Review of Lithium-Ion Battery Safety Concerns: The Issues, Strategies, and Testing Standards. *J. Energy Chem.* 2021, 59, 83-99.

[47] X. Sun, Z. Liu, F. Zhao, H. Hao. Global Competition in the Lithium-Ion Battery Supply

Chain: A Novel Perspective for Criticality Analysis. *Environ. Sci. Technol.* 2021, 55, 18.

[48] W. Huang, X. Feng, X. Han, W. Zhang, F. Jiang. Questions and Answers Relating to Lithium-Ion Battery Safety Issues. *Cell Rep. Phys. Sci.* 2021, 2, 100295.

[49] L. Kong, C. Li, J. Jiang, M. G. Pecht. Li-Ion Battery Fire Hazards and Safety Strategies. *Energies* 2018, 11, 2191.

[50] A. Alessia, A. Becci, M. Villen-Guzman, C. Vereda-Alonso, F. Beolchini. Challenges for Sustainable Lithium Supply: A Critical Review. *J. Clean. Prod.* 2021, 300, 126954.

[51] X.-Q. Wang, M. Qin, N.-C. Moldovan, C.-W. Su. Bubble Behaviors in Lithium Price and the Contagion Effect: An Industry Chain Perspective. *Resour. Policy* 2023, 83, 103725.

[52] X. Sun, M. Ouyang, H. Hao. Surging Lithium Price Will Not Impede the Electric Vehicle Boom. *Joule* 2022, 6, 1738-1742.

[53] T. Coughlin. Impact of COVID-19 on the Consumer Electronics Market. *IEEE Consum. Electron. Mag.* 2020, 10, 58-59.

[54] F. Maisel, C. Neef, F. Marscheider-Weidemann, N. F. Nissen. A Forecast on Future Raw Material Demand and Recycling Potential of Lithium-Ion Batteries in Electric Vehicles. *Resour. Conserv. Recycl.* 2023, 192, 106920.

[55] Statista. Battery-Grade Lithium Carbonate Price. Available online: https://www.statista.com/statistics/606350/battery-grade-lithium-carbonate-price/ (accessed on March 27, 2025).

[56] Statista. World Production of Lithium. Available online: https://www.statista.com/statistics/606684/world-production-of-lithium/ (accessed on March 27, 2025).

[57] Z. Zhu, T. Jiang, M. Ali, Y. Meng, Y. Jin, Y. Cui, W. Chen. Rechargeable Batteries for Grid-Scale Energy Storage. *Chem. Rev.* 2022, 122, 22, 13528-13575.

[58] K. Santos-Pereira, J. D. F. Pereira, L. S. Veras, D. L. S. Cosme, D. Q. Oliveira, O. R. Saavedra. The Requirements and Constraints of Storage Technology in Isolated Microgrids: A Comparative Analysis of Lithium-Ion vs. Lead-Acid Batteries. *Energy Syst.* 2021, 1-24.

[59] L. Wang, T. Wang, L. Peng, Y. Wang, M. Zhang, J. Zhou, M. Chen, et al. The Promises, Challenges, and Pathways to Room-Temperature Sodium-Sulfur Batteries. *Nat. Sci. Rev.* 2022, 9, 3, nwab050.

[60] D. Bin, F. Wang, A. G. Tamirat, L. Suo, Y. Wang, C. Wang, Y. Xia. Progress in Aqueous Rechargeable Sodium-Ion Batteries. *Adv. Energy Mater.* 2018, 8, 17, 1703008.

[61] X. Zhang, T. Xiong, B. He, S. Feng, X. Wang, L. Wei, L. Mai. Recent Advances and Perspectives in Aqueous Potassium-Ion Batteries. *Energy Environ. Sci.* 2022, 15, 9, 3750-3774.

[62] M. Li, Y. Ding, Y. Sun, Y. Ren, J. Yang, B. Yin, H. Li, S. Zhang, T. Ma. Emerging Rechargeable Aqueous Magnesium Ion Battery. *Mater. Rep. Energy* 2022, 2, 4, 100161.

[63] M. E. Arroyo-de Dompablo, A. Ponrouch, P. Johansson, M. R. Palacín. Achievements, Challenges, and Prospects of Calcium Batteries. *Chem. Rev.* 2019, 120, 14, 6331-6357.

[64] B. Tang, L. Shan, S. Liang, J. Zhou. Issues and Opportunities Facing Aqueous Zinc-Ion Batteries. *Energy Environ. Sci.* 2019, 12, 11, 3288-3304.

[65] A. A. Yaroshevsky. Abundances of Chemical Elements in the Earth's Crust. *Geochem. Int.* 2006, 44, 48–55.

[66] J. O. G. Posada, A. J. R. Rennie, S. P. Villar, V. L. Martins, J. Marinaccio, A. Barnes, C. F. Glover, D. A. Worsley, P. J. Hall. Aqueous Batteries as Grid Scale Energy Storage Solutions. *Renew. Sustain. Energy Rev.* 2017, 68, 1174-1182.

[67] H. Ahn, D. Kim, M. Lee, K. W. Nam. Challenges and Possibilities for Aqueous Battery Systems. *Commun. Mater.* 2023, 4 (1), 37.

[68] J. Yi, Y. Xia. Advanced Aqueous Batteries: Status and Challenges. *MRS Energy Sustain.* 2022, 9 (2), 106-128.

[69] T. M. Gür. Review of Electrical Energy Storage Technologies, Materials and Systems: Challenges and Prospects for Large-Scale Grid Storage. *Energy Environ. Sci.* 2018, *11*(10), 2696-2767.

[70] Y. Zhang, C.-g. Zhou, J. Yang, S.-c. Xue, H.-l. Gao, X.-h. Yan, Q.-y. Huo, S.-w. Wang, Y. Cao, J. Yan, K.-z. Gao, L.-x. Wang. Advances and Challenges in Improvement of the Electrochemical Performance for Lead-Acid Batteries: A Comprehensive Review. *J. Power Sources* 2022, 520, 230800.

[71] N. Vangapally, T. R. Penki, Y. Elias, S. Muduli, S. Maddukuri, S. Luski, D. Aurbach, S. K. Martha. Lead-Acid Batteries and Lead–Carbon Hybrid Systems: A Review. *J. Power Sources* 2023, 579, 233312.

[72] M. Huang, X. Wang, X. Liu, L. Mai. Fast Ionic Storage in Aqueous Rechargeable Batteries: From Fundamentals to Applications. *Adv. Mater.* 2022, 34 (9), 2105611.

[73] W. Tang, Y. Zhu, Y. Hou, L. Liu, Y. Wu, K. P. Loh, K. Zhu. Aqueous Rechargeable Lithium Batteries as an Energy Storage System of Superfast Charging. *Energy Environ. Sci.* 2013, 6 (7), 2093-2104.

[74] M. Huang, X. Wang, X. Liu, L. Mai. Fast Ionic Storage in Aqueous Rechargeable Batteries: From Fundamentals to Applications. *Adv. Mater.* 2022, 34 (9), 2105611.

[75] M. E. Şahin, F. Blaabjerg, A. Sangwongwanich. A Comprehensive Review on Supercapacitor Applications and Developments. *Energies* 2022, 15 (3), 674.

[76] M. B. F. Ahsan, S. Mekhilef, T. K. Soon, M. B. Mubin, P. Shrivastava, M. Seyedmahmoudian. Lithium-Ion Battery and Supercapacitor-Based Hybrid Energy Storage System for Electric Vehicle Applications: A Review. *Int. J. Energy Res.* 2022, 46 (14), 19826-19854.

[77] Chariot Electric Bus. Available online: https://chariot-electricbus.com/ (accessed on Mar. 30, 2025).

[78] Aowei. Available online: http://www.aowei.com/en/program/productinfo-105.html (accessed on Mar. 30, 2025).

[79] H. Yi, R. Qin, S. Ding, Y. Wang, S. Li, Q. Zhao, F. Pan. Structure and Properties of Prussian Blue Analogues in Energy Storage and Conversion Applications. *Adv. Funct. Mater.* 2021, 31 (6), 2006970.

[80] J. Peng, W. Zhang, Q. Liu, J. Wang, S. Chou, H. Liu, S. Dou. Prussian Blue Analogues for Sodium-Ion batteries: Past, Present, and Future. *Advanced Materials* 2022 34(15), 2108384.

[81] F. Ma, Q. Li, T. Wang, H. Zhang, G. Wu. Energy Storage Materials Derived from Prussian Blue Analogues. *Sci. Bull.* 2017, 62 (5), 358-368.

[82] B. Wang, Y. Han, X. Wang, N. Bahlawane, H. Pan, M. Yan, Y. Jiang. Prussian Blue Analogs for Rechargeable Batteries. *iScience* 2018, 3, 110-133.

[83] W. J. Li, C. Han, G. Cheng, S. L. Chou, H. K. Liu, S. X. Dou. Chemical Properties, Structural Properties, and Energy Storage Applications of Prussian Blue Analogues. *Small* 2019, 15 (32), 1900470.

[84] J. Cattermull, M. Pasta, A. L. Goodwin. Structural Complexity in Prussian Blue Analogues. *Mater. Horiz.* 2021, 8 (12), 3178-3186.

[85] M. J. Piernas Muñoz, E. Castillo Martínez. Prussian Blue and Its Analogues: Structure, Characterization, and Applications. *Prussian Blue Based Batteries* 2018, 9-22.

[86] C. D. Wessells, S. V. Peddada, R. A. Huggins, Y. Cui. Nickel Hexacyanoferrate Nanoparticle Electrodes for Aqueous Sodium and Potassium Ion Batteries. *Nano Lett.* 2011, 11 (12), 5421-5425.

[87] C. D. Wessells, R. A. Huggins, Y. Cui. Copper Hexacyanoferrate Battery Electrodes with Long Cycle Life and High Power. *Nat. Commun.* 2011, 2 (1), 550.

[88] R. Trócoli, F. La Mantia. An Aqueous Zinc-Ion Battery Based on Copper Hexacyanoferrate. *ChemSusChem* 2015, 8 (3), 481-485.

[89] Y. Ling, B. He, L. Han, W. Gong, C. Chang, Q. Zhang. Two-Electron Redox Chemistry Enables Potassium-Free Copper Hexacyanoferrate as High-Capacity Cathode for Aqueous Mg-Ion Battery. *InfoMat* 2024, 6 (6), e12549.

[90] Md. Adil, S. Sau, P. Dammala, S. Mitra. Comprehensive Study of Sodium Copper Hexacyanoferrate as a Sodium-Rich Low-Cost Positive Electrode for Sodium-Ion Batteries. *Energy Fuels* 2022, 36 (14), 7816-7828.

[91] L. Shen, Y. Jiang, Y. Liu, J. Ma, T. Sun, N. Zhu. High-Stability Monoclinic Nickel Hexacyanoferrate Cathode Materials for Ultrafast Aqueous Sodium Ion Battery. *Chem. Eng. J.* 2020, 388, 124228.

[92] Y. Xu, J. Wan, L. Huang, J. Xu, M. Ou, Y. Liu, X. Sun, et al. Dual Redox-Active Copper Hexacyanoferrate Nanosheets as Cathode Materials for Advanced Sodium-Ion Batteries. *Energy Storage Mater.* 2020, 33, 432-441.

[93] M. Ciabocco, M. Berrettoni, S. Zamponi, R. Spinosi, P. Conti. An Overview on the Facile and Reversible Cations Intercalation in Nickel-Hexacyanoferrate Open Framework. *Int. J. Electrochem. Sci.* 2018, 13 (6), 5535-5551.

[94] B. Wang, S. Liu, W. Sun, Y. Tang, H. Pan, M. Yan, Y. Jiang. Intercalation Pseudocapacitance Boosting Ultrafast Sodium Storage in Prussian Blue Analogs. *ChemSusChem* 2019, 12 (11), 2415-2420.

[95] T. Yuan, Y. Chen, X. Gao, R. Xu, Z. Zhang, X. Chen, L. Cui. Research Progress of Prussian Blue and Its Analogs as High-Performance Cathode Nanomaterials for Sodium-Ion Batteries. *Small Methods* 2024, 8 (8), 2301372.

[96] Y. A. Kumar, S. S. Sana, T. Ramachandran, M. A. Assiri, S. S. Rao, S. C. Kim. From Lab to Field: Prussian Blue Frameworks as Sustainable Cathode Materials. *Dalton Trans.* 2024, 53 (26), 10770-10804.

[97] Z. Shen, S. Guo, C. Liu, Y. Sun, Z. Chen, J. Tu, X. Zhao. Na-rich Prussian white cathodes for long-life sodium-ion batteries. *ACS Sustainable Chemistry & Engineering*, 2018, 6(12), 16121-16129.

[98] C. Zhang, Y. Xu, M. Zhou, L. Liang, H. Dong, M. Wu, Y. Lei. Potassium Prussian Blue Nanoparticles: A Low-Cost Cathode Material for Potassium-Ion Batteries. *Adv. Funct. Mater.* **2017**, 27 (4), 1604307.

[99] M. Takachi, T. Matsuda, Y. Moritomo. Cobalt Hexacyanoferrate as Cathode Material for Na^+ Secondary Battery. *Appl. Phys. Express* 2013, 6 (2), 025802.

[100] Y. Tang, W. Li, P. Feng, M. Zhou, K. Wang, Y. Wang, K. Jiang. High-Performance Manganese Hexacyanoferrate with Cubic Structure as Superior Cathode Material for Sodium-Ion Batteries. *Adv. Funct. Mater.* 2020, 30 (10), 1908754.

[101] F. Calvão, C. E. A. McDonald, M. Bolay. Cobalt Mining and the Corporate Outsourcing of Responsibility in the Democratic Republic of Congo. *Extr. Ind. Soc.* 2021, 8 (4), 100884.

[102] C. Banza Lubaba Nkulu, L. Casas, V. Haufroid, T. De Putter, N. D. Saenen, T. Kayembe-Kitenge, P. M. Obadia, D. K. Wa Mukoma, J.-M. L. Ilunga, T. S. Nawrot, O. L. Numbi, E. Smolders, B. Nemery. Sustainability of Artisanal Mining of Cobalt in DR Congo. *Nat. Sustain.* 2018, 1, 495–504.

[103] M. Li, R. Sciacca, M. Maisuradze, G. Aquilanti, J. Plaisier, M. Berrettoni, M. Giorgetti. Electrochemical Performance of Manganese Hexacyanoferrate Cathode Material in Aqueous Zn-Ion Battery. *Electrochim. Acta* 2021, 400, 139414.

[104] L. Deng, J. Qu, X. Niu, J. Liu, J. Zhang, Y. Hong, Y. Zhu. Defect-Free Potassium Manganese Hexacyanoferrate Cathode Material for High-Performance Potassium-Ion Batteries. *Nat. Commun.* 2021, 12 (1), 2167.

[105] K. Nakamoto, R. Sakamoto, M. Ito, A. Kitajou, S. Okada. Effect of Concentrated Electrolyte on Aqueous Sodium-Ion Battery with Sodium Manganese Hexacyanoferrate Cathode. *Electrochemistry* 2017, 85 (4), 179-185.

[106] T. Cao, F. Zhang, M. Chen, T. Shao, Z. Li, Q. Xu, D. Cheng, H. Liu, Y. Xia. Cubic Manganese Potassium Hexacyanoferrate Regulated by Controlling of the Water and Defects as a High-Capacity and Stable Cathode Material for Rechargeable Aqueous Zinc-Ion Batteries. *ACS Appl. Mater. Interfaces* 2021, 13 (23), 26864-26871.

[107] W. Shu, J. Li, G. Zhang, J. Meng, X. Wang, L. Mai. Progress on Transition Metal Ions Dissolution Suppression Strategies in Prussian Blue Analogs for Aqueous Sodium-/Potassium-Ion Batteries. *Nano-Micro Lett.* 2024, 16 (1), 128.

[108] L. Jiang, Y. Lu, C. Zhao, L. Liu, J. Zhang, Q. Zhang, X. Shen, J. Zhao, X. Yu, H. Li, X. Huang, L. Chen, Y.-S. Hu. Building Aqueous K-Ion Batteries for Energy Storage. *Nat. Energy* 2019, 4, 495–503.

[109] D. Abd El-Hady, Y. Lyu, S. Zhan, J. Yang, Y. Wang, F. Yang, Q. Zhao, M. Gu, M. Shao. Vacancy and Composition Engineering of Manganese Hexacyanoferrate for Sodium-Ion Storage. *ACS Appl. Energy Mater.* 2022, 5 (7), 6524–6533.

[110] S. Gou, X. Zhang, Y. Xu, J. Tang, Y. Ji, M. Imran, L. Pan, J. Li, B.-T. Liu. Inhibiting Dissolution Strategy Achieving High-Performance Sodium Titanium Phosphate Hybrid Anode in Seawater-Based Dual-Ion Battery. *J. Colloid Interface Sci.* 2024, 675, 429–437.

[111] T.-F. Hung, W.-H. Lan, Y.-W. Yeh, W.-S. Chang, C.-C. Yang, J.-C. Lin. Hydrothermal Synthesis of Sodium Titanium Phosphate Nanoparticles as Efficient Anode Materials for Aqueous Sodium-Ion Batteries. *ACS Sustainable Chem. Eng.* 2016, 4 (12), 7074–7079.

[112] D. Wang, X. Bie, Q. Fu, D. Dixon, N. Bramnik, Y.-S. Hu, F. Fauth, et al. Sodium Vanadium Titanium Phosphate Electrode for Symmetric Sodium-Ion Batteries with High Power and Long Lifespan. *Nat. Commun.* 2017, 8 (1), 15888.

[113] C. Han, J. Zhu, C. Zhi, H. Li. The Rise of Aqueous Rechargeable Batteries with Organic Electrode Materials. *J. Mater. Chem. A* 2020, 8 (31), 15479-15512.

[114] S. Yuan, X. Huang, T. Kong, L. Yan, Y. Wang. Organic Electrode Materials for Energy Storage and Conversion: Mechanism, Characteristics, and Applications. *Acc. Chem. Res.* 2024, 57 (10), 1550-1563.

[115] J. Huang, X. Dong, Z. Guo, Y. Wang. Progress of Organic Electrodes in Aqueous Electrolyte for Energy Storage and Conversion. *Angew. Chem.* 2020, 132 (42), 18478-18489.

[116] J. J. Shea, C. Luo. Organic Electrode Materials for Metal Ion Batteries. *ACS Appl. Mater. Interfaces* 2020, 12 (5), 5361-5380.

[117] H. Qin, Z. P. Song, H. Zhan, Y. H. Zhou. Aqueous Rechargeable Alkali-Ion Batteries with Polyimide Anode. *J. Power Sources* 2014, 249, 367-372.

[118] A. Nimkar, G. Bergman, E. Ballas, N. Tubul, N. Levi, F. Malchik, I. Kukurayeve, M. S. Chae, D. Sharon, M. Levi, N. Shpigel. Polyimide Compounds for Post-Lithium Energy Storage Applications. *Angew. Chem.* 2023, 135 (50), e202306904.

[119] A. L. Lubis, F. Baskoro, T. H. Lin, H. Q. Wong, G. S. Liou, H. J. Yen. Redox-Active High-Performance Polyimides as Versatile Electrode Materials for Organic Lithium-and Sodium-Ion Batteries. *ACS Appl. Mater. Interfaces* 2023, 16 (37), 48722-48735.

[120] L. Chen, J. L. Bao, X. Dong, D. G. Truhlar, Y. Wang, C. Wang, Y. Xia. Aqueous Mg-Ion Battery Based on Polyimide Anode and Prussian Blue Cathode. *ACS Energy Lett.* 2017, 2 (5), 1115-1121.

[121] S. Gheytani, Y. Liang, F. Wu, Y. Jing, H. Dong, K. K. Rao, X. Chi, F. Fang, Y. Yao. An Aqueous Ca-Ion Battery. *Adv. Sci.* 2017, 4 (12), 1700465.

[122] Y. Hu, H. Ding, Y. Bai, Z. Liu, S. Chen, Y. Wu, X. Yu, L. Fan, B. Lu. Rational Design of a Polyimide Cathode for a Stable and High-Rate Potassium-Ion Battery. *ACS Appl. Mater. Interfaces* 2019, 11 (45), 42078-42085.

[123] W. Deng, Y. Shen, J. Qian, H. Yang. A Polyimide Anode with High Capacity and Superior Cyclability for Aqueous Na-Ion Batteries. *Chem. Commun.* 2015, 51 (24), 5097-5099.

[124] H. Chen, Z. Zhang, Z. Wei, G. Chen, X. Yang, C. Wang, F. Du. Use of a Water-in-Salt Electrolyte to Avoid Organic Material Dissolution and Enhance the Kinetics of Aqueous Potassium Ion Batteries. *Sustainable Energy Fuels* 2020, 4 (1), 128-131.

[125] M. Wang, H. Wang, H. Zhang, X. Li. Aqueous K-Ion Battery Incorporating Environment-Friendly Organic Compound and Berlin Green. *J. Energy Chem.* 2020, 48, 14-20.

[126] T. Jin, X. Ji, P. F. Wang, K. Zhu, J. Zhang, L. Cao, L. Chen, C. Cui, T. Deng, S. Liu, N. Piao. High-Energy Aqueous Sodium-Ion Batteries. *Angew. Chem. Int. Ed.* 2021, 60(21), 11943-11948.

[127] C. H. Hamann, W. Vielstich. Elektrochemie, 4th ed. Wiley-VCH 2005.

[128] T. B. Reddy, D. Linden (editors). Linden's handbook of batteries, 2nd ed. McGraw-Hill 2011.

[129] C. Daniel, J. O. Besenhard (editors). Handbook of battery materials, 2nd ed. Wiley-VCH 2011.

[130] H. Helmholtz. Ueber Einige Gesetze Der Vertheilung Elektrischer Ströme in Körperlichen Leitern Mit Anwendung Auf Die Thierisch-Elektrischen Versuche. *Ann. Phys.* 1853, 165 (6), 211–233.

[131] M. Gouy. Sur La Constitution de La Charge Électrique à La Surface d'un Électrolyte. *J. Phys. Théor. Appl.* 1910, 9 (1), 457–468.

[132] D. L. Chapman. A Contribution to the Theory of Electrocapillarity. *Philos. Mag.* 1913, 25 (148), 475–481.

[133] O. Stern. Zur Theorie Der Elektrolytischen Doppelschicht. *Z. Elektrochem. Angew. Phys. Chem.* 1924, 30 (21–22), 508–516.

[134] D. C. Grahame. The Electrical Double Layer and the Theory of Electrocapillarity. *Chem. Rev.* 1947, 41 (3), 441–501.

[135] J. O'm. Bockris, M. A. V. Devanathan, K. Müllen. On the Structure of Charged Interfaces. *Proc. R. Soc. Lond. A Math. Phys. Sci.* 1963, 274 (1356), 55–79.

[136] Y. Liu, M. Y. Su, Z. Y. Gu, K. Y. Zhang, X. T. Wang, M. Du, J. Z. Guo, X. L. Wu. Advanced Lithium Primary Batteries: Key Materials, Research Progresses and Challenges. *Chem. Rec.* 2022, 22 (10), e202200081.

[137] Y. Liang, C. Z. Zhao, H. Yuan, Y. Chen, W. Zhang, J. Q. Huang, D. Yu, Y. Liu, M. M. Titirici, Y. L. Chueh, H. Yu. A Review of Rechargeable Batteries for Portable Electronic Devices. *InfoMat* 2019, 1 (1), 6–32.

[138] R. A. Powers. Advances and Trends in Primary and Small Secondary Batteries. *IEEE Aerosp. Electron. Syst. Mag.* 2002, 9 (4), 32–36.

[139] J. Thakur, P. Phogat, R. Jha, S. Singh. Non-Rechargeable Batteries: A Review of Primary Battery Technology and Future Trends. *Phys. Chem. Chem. Phys.* 2025, 27, 4045-4077.

[140] F. Cheng, J. Liang, Z. Tao, J. Chen. Functional Materials for Rechargeable Batteries. *Adv. Mater.* 2011, 23 (15), 1695–1715.

[141] M. Fichtner, K. Edström, E. Ayerbe, M. Berecibar, A. Bhowmik, I. E. Castelli, S. Clark, R. Dominko, M. Erakca, A. A. Franco, A. Grimaud. Rechargeable Batteries of the Future—The State of the Art from a BATTERY 2030+ Perspective. *Adv. Energy Mater.* 2022, 12 (17), 2102904.

[142] P. Zhu, D. Gastol, J. Marshall, R. Sommerville, V. Goodship, E. Kendrick. A Review of Current Collectors for Lithium-Ion Batteries. *J. Power Sources* 2021, 485, 229321.

[143] M. S. Yazici, D. Krassowski, J. Prakash. Flexible Graphite as Battery Anode and Current Collector. *J. Power Sources* 2005, 141 (1), 171–176.

[144] A. Ponrouch, D. Monti, A. Boschin, B. Steen, P. Johansson, M. R. Palacín. Non-Aqueous Electrolytes for Sodium-Ion Batteries. *J. Mater. Chem. A* 2015, 3 (1), 22–42.

[145] Y. Li, X. Wang, S. Dong, X. Chen, G. Cui. Recent Advances in Non-Aqueous Electrolyte for Rechargeable Li–O_2 Batteries. *Adv. Energy Mater.* 2016, 6 (18), 1600751.

[146] D. Ouyang, K. Wang, J. Guan, Z. Wang. Liquid Non-Aqueous Electrolytes for High-Voltage and High-Safety Lithium-Ion Cells: A Review. *J. Power Sources* 2024, 607, 234550.

[147] K. Deng, Q. Zeng, D. Wang, Z. Liu, G. Wang, Z. Qiu, Y. Zhang, M. Xiao, Y. Meng. Nonflammable Organic Electrolytes for High-Safety Lithium-Ion Batteries. *Energy Storage Mater.* 2020, 32, 425–447.

[148] A. Guerfi, M. Dontigny, P. Charest, M. Petitclerc, M. Lagacé, A. Vijh, K. Zaghib. Improved Electrolytes for Li-Ion Batteries: Mixtures of Ionic Liquid and Organic Electrolyte with Enhanced Safety and Electrochemical Performance. *J. Power Sources* 2010, 195 (3), 845–852.

[149] B. Flamme, G. R. Garcia, M. Weil, M. Haddad, P. Phansavath, V. Ratovelomanana-Vidal, A. Chagnes. Guidelines to Design Organic Electrolytes for Lithium-Ion Batteries: Environmental Impact, Physicochemical and Electrochemical Properties. *Green Chem.* 2017, 19 (8), 1828–1849.

[150] Y. Sasaki. Organic Electrolytes of Secondary Lithium Batteries. *Electrochemistry* 2008, 76 (1), 2–15.

[151] S. A. Forsyth, J. M. Pringle, D. R. MacFarlane. Ionic Liquids—An Overview. *Aust. J. Chem.* 2004, 57 (2), 113–119.

[152] A. Balducci. Ionic Liquids in Lithium-Ion Batteries. *Ionic Liquids II* 2018, 375, 1–27.

[153] M. Galiński, A. Lewandowski, I. Stępniak. Ionic Liquids as Electrolytes. *Electrochim. Acta* 2006, 51 (26), 5567–5580.

[154] R. Götz, R. Streng, J. Sterzinger, T. Steeger, M. M. Kaye, M. Vitort, A. S. Bandarenka. All-Solid-State Li-Ion Batteries with Commercially Available Electrolytes: A Feasibility Review. *InfoMat* 2024, 6.

[155] R. C. Agrawal, G. P. Pandey. Solid Polymer Electrolytes: Materials Designing and All-Solid-State Battery Applications: An Overview. *J. Phys. D Appl. Phys.* 2008, 41 (22), 223001.

[156] M. Shoji, E. J. Cheng, T. Kimura, K. Kanamura. Recent Progress for All Solid State Battery Using Sulfide and Oxide Solid Electrolytes. *J. Phys. D Appl. Phys.* 2019, *52* (10), 103001.

[157] Q. Zhang, D. Cao, Y. Ma, A. Natan, P. Aurora, H. Zhu. Sulfide-Based Solid-State Electrolytes: Synthesis, Stability, and Potential for All-Solid-State Batteries. *Adv. Mater.* 2019, 31 (44), 1901131.

[158] A. Banerjee, X. Wang, C. Fang, E. A. Wu, Y. S. Meng. Interfaces and Interphases in All-Solid-State Batteries with Inorganic Solid Electrolytes. *Chem. Rev.* 2020, 120 (14), 6878–6933.

[159] H. D. Lim, J. H. Park, H. J. Shin, J. Jeong, J. T. Kim, K. W. Nam, H. G. Jung, K. Y. Chung. A Review of Challenges and Issues Concerning Interfaces for All-Solid-State Batteries. *Energy Storage Mater.* 2020, 25, 224–250.

[160] S. Chen, M. Zhang, P. Zou, B. Sun, S. Tao. Historical Development and Novel Concepts on Electrolytes for Aqueous Rechargeable Batteries. *Energy Environ. Sci.* 2022, 15 (5), 1805–1839.

[161] C. Chakkaravarthy, A. A. Waheed, H. V. K. Udupa. Zinc—Air Alkaline Batteries—A Review. *J. Power Sources* 1981, 6 (3), 203–228.

[162] J. Islam, R. Anwar, M. Shareef, H. M. Zabed, J. N. Sahu, X. Qi, M. U. Khandaker, A. Ragauskas, I. Boukhris, M. R. Rahman, F. I. Chowdhury. Rechargeable Metal–Metal Alkaline Batteries: Recent Advances, Current Issues and Future Research Strategies. *J. Power Sources* 2023, 563, 232777.

[163] F. Beck, P. Rüetschi. Rechargeable Batteries with Aqueous Electrolytes. *Electrochim. Acta* 2000, 45 (15–16), 2467–2482.

[164] J. O'M. Bockris, A. K. N. Reddy. *Modern Electrochemistry, Volume 1: Ionics*. Plenum Press, 1970.

[165] R. A. Robinson, R. H. Stokes. *Electrolyte Solutions: The Measurement and Interpretation of Conductance, Chemical Potential and Diffusion in Solutions of Simple Electrolytes*, 2nd ed.; Butterworths Scientific Publications: London, 1959.

[166] M. Peschke, A. T. Blades, P. Kebarle. Formation, Acidity and Charge Reduction of the Hydrates of Doubly Charged Ions M^{2+} (Be^{2+}, Mg^{2+}, Ca^{2+}, Zn^{2+}). *Int. J. Mass Spectrom.* 1999, 185–187, 685–699.

[167] J. Larcin. *Chemical and Electrochemical Studies of Leclanché Cells* (Doctoral Dissertation, Middlesex Polytechnic), 1991.

[168] H. Bi, X. Wang, H. Liu, Y. He, W. Wang, W. Deng, X. Ma, Y. Wang, W. Rao, Y. Chai, et al. A Universal Approach to Aqueous Energy Storage via Ultralow-Cost Electrolyte with Super-Concentrated Sugar as Hydrogen-Bond-Regulated Solute. *Adv. Mater.* 2020, 32 (16), e2000074.

[169] R. Deng, J. Chen, F. Chu, M. Qian, Z. He, A. W. Robertson, J. Maier, F. Wu. "Soggy-Sand" Chemistry for High-Voltage Aqueous Zinc-Ion Batteries. *Adv. Mater.* 2024, 36 (11), e2311153.

[170] L. Wang, J. Wang, L. Wang, M. Zhang, R. Wang, C. Zhan. A Critical Review on Nickel-Based Cathodes in Rechargeable Batteries. *Int. J. Miner. Metall. Mater.* 2022, 29 (5), 925–941.

[171] A. Chen, P. K. Sen. Advancement in Battery Technology: A State-of-the-Art Review. *IEEE Ind. Appl. Soc. Annu. Meet.* 2016, 1–10.

[172] S. K. Dhar, S. R. Ovshinsky, P. R. Gifford, D. A. Corrigan, M. A. Fetcenko, S. Venkatesan. Nickel/Metal Hydride Technology for Consumer and Electric Vehicle Batteries—A Review and Up-Date. *J. Power Sources* 1997, 65 (1–2), 1–7.

[173] T. Sakai, I. Uehara, H. Ishikawa. R&D on Metal Hydride Materials and Ni–MH Batteries in Japan. *J. Alloys Compd.* 1999, *293*, 762–769.

[174] M. E. Şahin, F. Blaabjerg, A. Sangwongwanich. A Comprehensive Review on Supercapacitor Applications and Developments. *Energies* 2022, 15 (3), 674.

[175] W. Raza, F. Ali, N. Raza, Y. Luo, K. H. Kim, J. Yang, S. Kumar, A. Mehmood, E. E. Kwon. Recent Advancements in Supercapacitor Technology. *Nano Energy* 2018, 52, 441–473.

[176] U. Lucia. Overview on Fuel Cells. *Renew. Sustain. Energy Rev.* 2014, 30, 164–169

[177] Y. Wang, D. F. R. Diaz, K. S. Chen, Z. Wang, X. C. Adroher. Materials, Technological Status, and Fundamentals of PEM Fuel Cells – A Review. *Mater. Today* 2020, 32, 178–203.

[178] T. Horiba. Lithium-Ion Battery Systems. *Proc. IEEE* 2014, *102* (6), 939–950.

[179] G. Wang, M. Yu, X. Feng. Carbon Materials for Ion-Intercalation Involved Rechargeable Battery Technologies. *Chem. Soc. Rev.* 2021, 50 (4), 2388–2443.

[180] M. B. Armand. Intercalation Electrodes. In *Materials for Advanced Batteries*; Springer US: Boston, MA, 1980; pp. 145–161.

[181] S. H. Yu, X. Feng, N. Zhang, J. Seok, H. D. Abruña. Understanding Conversion-Type Electrodes for Lithium Rechargeable Batteries. *Acc. Chem. Res.* 2018, 51 (2), 273–281.

[182] J. Cabana, L. Monconduit, D. Larcher, M. R. Palacín. Beyond Intercalation-Based Li-Ion Batteries: The State of the Art and Challenges of Electrode Materials Reacting through Conversion Reactions. *Adv. Mater.* 2010, 22 (35), E170–E192.

[183] I. Sultana, M. M. Rahman, Y. Chen, A. M. Glushenkov. Potassium-Ion Battery Anode Materials Operating through the Alloying–Dealloying Reaction Mechanism. *Adv. Funct. Mater.* 2018, 28 (5), 1703857.

[184] M. Lübke, D. Howard, C. F. Armer, A. J. Gardecka, A. Lowe, M. V. Reddy, Z. Liu, J. A. Darr. High Energy Lithium Ion Battery Electrode Materials; Enhanced Charge Storage via Both Alloying and Insertion Processes. *Electrochim. Acta* 2017, 231, 247–254.

[185] J. P. Zheng. The Limitations of Energy Density of Battery/Double-Layer Capacitor Asymmetric Cells. *J. Electrochem. Soc.* 2003, 150 (4), A484.

[186] S. Sahoo, R. Kumar, E. Joanni, R. K. Singh, J. J. Shim. Advances in Pseudocapacitive and Battery-Like Electrode Materials for High Performance Supercapacitors. *J. Mater. Chem. A* 2022, 10 (25), 13190–13240.

[187] Y. Jiang, J. Liu. Definitions of Pseudocapacitive Materials: A Brief Review. *Energy Environ. Mater.* 2019, 2 (1), 30–37.

[188] A. Z. Weber, M. M. Mench, J. P. Meyers, P. N. Ross, J. T. Gostick, Q. Liu. Redox Flow Batteries: A Review. *J. Appl. Electrochem.* 2011, 41, 1137–1164.

[189] W. R. McKinnon, R. R. Haering. Physical Mechanisms of Intercalation. *Mod. Aspects Electrochem.* 1983, 15, 235–304.

[190] M. Noel, R. Santhanam. Electrochemistry of Graphite Intercalation Compounds. *J. Power Sources* 1998, 72 (1), 53–65.

[191] Y. Liu. Some Consideration on the Langmuir Isotherm Equation. *Colloids Surf. A Physicochem. Eng. Asp.* 2006, 274 (1–3), 34–36.

[192] L. Xiao, Y. Yuan, W. Ding, Y. Wang, L. P. Lv. Activation of Carbonyl Groups in Polyimide-Based Covalent Organic Framework with Multiwalled Carbon Nanotubes toward Boosted Pseudocapacitance. *Langmuir* 2024, 40 (47), 25220–25228.

[193] T. Zhou, Y. Yuan, L. Xiao, W. Ding, Y. Wang, L. P. Lv. Boosting of Redox-Active Polyimide Porous Organic Polymers with Multi-Walled Carbon Nanotubes towards Pseudocapacitive Energy Storage. *Nanomaterials* 2024, 14 (17), 1388.

[194] M. H. Gharahcheshmeh, K. U. A. Chowdhury. Fabrication Methods, Pseudocapacitance Characteristics, and Integration of Conjugated Conducting Polymers in Electrochemical Energy Storage Devices. *Energy Adv.* 2024, in press.

[195] R. B. Choudhary, S. Ansari, M. Majumder. Recent Advances on Redox Active Composites of Metal-Organic Framework and Conducting Polymers as Pseudocapacitor Electrode Material. *Renew. Sustain. Energy Rev.* 2021, 145, 110854.

[196] I. E. Rauda, V. Augustyn, B. Dunn, S. H. Tolbert. Enhancing Pseudocapacitive Charge Storage in Polymer Templated Mesoporous Materials. *Acc. Chem. Res.* 2013, 46 (5), 1113–1124.

[197] Y. Wang, Y. Song, Y. Xia. Electrochemical Capacitors: Mechanism, Materials, Systems, Characterization and Applications. *Chem. Soc. Rev.* 2016, 45 (21), 5925–5950.

[198] A. Szymczyk, C. Labbez, P. Fievet, A. Vidonne, A. Foissy, J. Pagetti. Contribution of Convection, Diffusion and Migration to Electrolyte Transport through Nanofiltration Membranes. *Adv. Colloid Interface Sci.* 2003, 103 (1), 77–94.

[199] R. Gundlapalli, S. Jayanti. Effect of Electrolyte Convection Velocity in the Electrode on the Performance of Vanadium Redox Flow Battery Cells with Serpentine Flow Fields. *J. Energy Storage* 2020, 30, 101516.

[200] M. W. Verbrugge. Convective Diffusion to a Rotating Disk. *J. Electrochem. Soc.* 1992, 139 (12), 3529.

[201] Y. Choo, D. M. Halat, I. Villaluenga, K. Timachova, N. P. Balsara. Diffusion and Migration in Polymer Electrolytes. *Prog. Polym. Sci.* 2020, 103, 101220.

[202] H. Mehrer. 1.1 Fick's Laws, Flux of Particles, Isotropic and Anisotropic Diffusion: 1 General Introduction. *Diffusion in Solid Metals and Alloys* 1990, 1–2.

[203] J. S. Newman. *Electrochemical Systems*, 2nd ed.; Prentice Hall: Englewood Cliffs, NJ, 1991.

[204] J. S. Newman, C. W. Tobias. Theoretical Analysis of Current Distribution in Porous Electrodes. *J. Electrochem. Soc.* 1962, 109 (12), 1183.

[205] A. Ševčík. Oscillographic Polarography with Periodical Triangular Voltage. *Collect. Czech. Chem. Commun.* 1948, 13, 349–377.

[206] T. Berzins, P. Delahay. Oscillographic Polarographic Waves for the Reversible Deposition of Metals on Solid Electrodes. *J. Am. Chem. Soc.* 1953, 75 (3), 555–559.

[207] P. T. Kissinger, W. R. Heineman. Cyclic Voltammetry. *J. Chem. Educ.* 1983, 60 (9), 702.

[208] A. Lasia. *Electrochemical Impedance Spectroscopy and Its Applications*; Springer: New York, NY, 2014.

[209] A. Ch. Lazanas, M. I. Prodromidis. Electrochemical Impedance Spectroscopy─A Tutorial. *ACS Meas. Sci. Au* 2023, 3 (3), 291–311.

[210] S. Wang, J. Zhang, O. Gharbi, et al. Electrochemical Impedance Spectroscopy. *Nat. Rev. Methods Primers* 2021, 1, 41.

[211] M. E. Orazem, B. Tribollet. *Electrochemical Impedance Spectroscopy*; John Wiley & Sons, Inc.: Hoboken, NJ, 2008.

[212] J. E. B. Randles. Kinetics of rapid electrode reactions. *Discussions of the Faraday Society* 1947, 1, 11-19.

[213] K. D. Vernon-Parry. Scanning Electron Microscopy: An Introduction. *III-Vs Rev.* 2000, 13 (4), 40–44.

[214] J. I. Goldstein, D. E. Newbury, J. R. Michael, N. W. Ritchie, J. H. J. Scott, D. C. Joy. *Scanning Electron Microscopy and X-Ray Microanalysis*, 4th ed.; Springer: Cham, 2017.

[215] L. Reimer. *Scanning Electron Microscopy: Physics of Image Formation and Microanalysis*. *Meas. Sci. Technol.* 2000, 11 (12), 1826.

[216] A. Ul-Hamid. A Beginners' Guide to Scanning Electron Microscopy. In *Vol. 1*, pp. 309–359; Springer International Publishing: Cham, 2018.

[217] A. M. Donald. The Use of Environmental Scanning Electron Microscopy for Imaging Wet and Insulating Materials. *Nat. Mater.* 2003, 2 (8), 511–516.

[218] B. E. Warren. *X-Ray Diffraction*. Courier Corporation, 1990.

[219] A. A. Bunaciu, E. G. Udriștioiu, H. Y. Aboul-Enein. X-Ray Diffraction: Instrumentation and Applications. *Crit. Rev. Anal. Chem.* 2015, 45 (4), 289–299.

[220] L. D. Whittig, W. R. Allardice. X-Ray Diffraction Techniques. *Methods of Soil Analysis: Part 1 Physical and Mineralogical Methods* 1986, 5, 331–362.

[221] A. K. Chatterjee. X-Ray Diffraction. In *Handbook of Analytical Techniques in Concrete Science and Technology*; 2000, pp. 275–332.

[222] B. E. Warren. X-Ray Diffraction Methods. *J. Appl. Phys.* 1941, 12 (5), 375–384.

[223] International Centre for Diffraction Data (ICDD). PDF Database Search. Available online: https://www.icdd.com/pdfsearch/ (accessed on April 25, 2025).

[224] N. Jaggi, D. R. Vij. Fourier Transform Infrared Spectroscopy. In *Handbook of Applied Solid State Spectroscopy*; Springer US: Boston, MA, 2006; pp. 411–450.

[225] B. C. Smith. *Fundamentals of Fourier Transform Infrared Spectroscopy*. CRC Press, 2011.

[226] J. M. Hollander, W. L. Jolly. X-Ray Photoelectron Spectroscopy. *Acc. Chem. Res.* 1970, 3 (6), 193–200.

[227] J. Chastain, R. C. King Jr. *Handbook of X-Ray Photoelectron Spectroscopy*. Perkin-Elmer Corporation, 1992, 40 (221), 25.

[228] R. S. Houk, J. J. Thompson. Inductively Coupled Plasma Mass Spectrometry. *Mass Spectrom. Rev.* 1988, 7 (4), 425–461.

[229] S. C. Wilschefski, M. R. Baxter. Inductively Coupled Plasma Mass Spectrometry: Introduction to Analytical Aspects. *Clin. Biochem. Rev.* 2019, 40 (3), 115.

[230] S. Brunauer, P. H. Emmett, E. Teller. Adsorption of Gases in Multimolecular Layers. *J. Am. Chem. Soc.* 1938, 60 (2), 309–319.

[231] P. Sinha, A. Datar, C. Jeong, X. Deng, Y. G. Chung, L. C. Lin. Surface Area Determination of Porous Materials Using the Brunauer–Emmett–Teller (BET) Method: Limitations and Improvements. *J. Phys. Chem. C* 2019, 123 (33), 20195–20209.

[232] H. A. Barnes, J. F. Hutton, K. Walters. *An Introduction to Rheology*, Vol. 3; Elsevier, 1989.

[233] J. Krägel, S. R. Derkatch. Interfacial Shear Rheology. *Curr. Opin. Colloid Interface Sci.* 2010, 15 (4), 246–255.

[234] A. S. Bandarenka. Development of Hybrid Algorithms for EIS Data Fitting. *Lect. Notes Impedance Spectrosc. Meas. Model. Appl.* 2013, 4, 29–36.

[235] K. Momma, F. Izumi. VESTA 3 for Three-Dimensional Visualization of Crystal, Volumetric and Morphology Data. *J. Appl. Crystallogr.* 2011, 44, 1272–1276.

[236] H. L. Boström, I. E. Collings, D. Daisenberger, C. J. Ridley, N. P. Funnell, A. B. Cairns. Probing the Influence of Defects, Hydration, and Composition on Prussian Blue Analogues with Pressure. *J. Am. Chem. Soc.* 2021, 143 (9), 3544–3554.

[237] Y. Huang, W. Mu, X. Bi, Z. Hou, X. Lei, Q. Wang, S. Luo. Progress in Defect Engineering of High-Performance Prussian Blue Analogues as Cathode Materials for Sodium-Ion Batteries. *J. Energy Storage* 2025, 111, 115435.

[238] Y. Wang, Z. Sun, J. Zhu, F. Ye, J. Zhu, R. Li, G. Chang. A Highly Efficient Chelating Agent Assisted the Synthesis of Prussian Blue Analogues as a Cathode Material for Sodium Ion Batteries. *Colloids Surf. A Physicochem. Eng. Asp.* 2025, 716, 136690.

[239] X. Long, J. Wang, L. Zhao, H. Zhao, K. Wang, F. Gao. Effect of Chelating Agent on Crystal Structure and Sodium Storage Performance of Fe-Based Prussian Blue. *Energy Storage Sci. Technol.* 2020, 9 (1), 57.

[240] H.-W. Lee, R. Y. Wang, M. Pasta, S. W. Lee, N. Liu, Y. Cui. Manganese Hexacyanomanganate Open Framework as a High-Capacity Positive Electrode Material for Sodium-Ion Batteries. *Nat. Commun.* 2014, 5, 5280.

[241] S. Kjeldgaard, I. Dugulan, A. Mamakhel, M. Wagemaker, B. B. Iversen, A. Bentien. Strategies for Synthesis of Prussian Blue Analogues. *R. Soc. Open Sci.* 2021, 8, 201779.

[242] A. Zhou, W. Cheng, W. Wang, Q. Zhao, J. Xie, W. Zhang, H. Gao, L. Xue, J. Li. Hexacyanoferrate-Type Prussian Blue Analogs: Principles and Advances Toward High-Performance Sodium and Potassium Ion Batteries. *Adv. Energy Mater.* 2021, 11, 2000943.

[243] R. L. Streng, S. Reiser, A. Senyshyn, S. Wager, J. Sterzinger, P. Schneider, D. Gryc, M. Z. Hussain, A. S. Bandarenka. Sustainable High-Performance Aqueous Batteries Enabled by Optimizing Electrolyte Composition. *Adv. Sci.* 2025, 12, 2417587.

[244] A. Ramgobin, G. Fontaine, S. Bourbigot. Investigation of the Thermal Stability and Fire Behavior of High Performance Polymer: A Case Study of Polyimide. *Fire Saf. J.* 2021, 120, 103060.

[245] L. Li, C. Guan, A. Zhang, D. Chen, Z. Qing. Thermal Stabilities and the Thermal Degradation Kinetics of Polyimides. *Polym. Degrad. Stab.* 2004, 84 (3), 369–373.

[246] R. L. Streng, S. Vagin, Y. Guo, B. Rieger, A. S. Bandarenka. Identifying the Charge Storage Mechanism in Polyimide Anodes for Na-Ion Aqueous Batteries by Impedance Spectroscopy. *RSC Energy Adv.* 2024, 3, 874–882.

[247] X. Lamprecht, P. Marzak, A. Wieczorek, N. Thomsen, J. Kim, B. Garlyyev, Y. Liang, A. S. Bandarenka, J. Yun. High Voltage and Superior Cyclability of Indium Hexacyanoferrate Cathodes for Aqueous Na-Ion Batteries Enabled by Superconcentrated $NaClO_4$ Electrolytes. *Energy Adv.* 2022, 1 (9), 623–631.

[248] R. Bors, J. Yun, P. Marzak, J. Fichtner, D. Scieszka, A. S. Bandarenka. Chromium(II) Hexacyanoferrate-Based Thin Films as a Material for Aqueous Alkali Metal Cation Batteries. *ACS Omega* 2018, 3 (5), 5111–5115.

[249] S. Phadke, R. Mysyk, M. Anouti. Effect of Cation (Li^+, Na^+, K^+, Rb^+, Cs^+) in Aqueous Electrolyte on the Electrochemical Redox of Prussian Blue Analogue (PBA) Cathodes. *J. Energy Chem.* 2020, 40, 31–38.

[250] P. Marzak, M. Kosiahn, J. Yun, A. S. Bandarenka. Intercalation of Mg^{2+} into Electrodeposited Prussian Blue Analogue Thin Films from Aqueous Electrolytes. *Electrochim. Acta* 2019, 307, 157–163.

[251] Y. Mizuno, M. Okubo, E. Hosono, T. Kudo, H. Zhou, K. Oh-Ishi. Suppressed Activation Energy for Interfacial Charge Transfer of a Prussian Blue Analog Thin Film Electrode with Hydrated Ions (Li^+, Na^+, and Mg^{2+}). *J. Phys. Chem. C* 2013, 117 (21), 10877–10882

[252] X. Wu, Y. Luo, M. Sun, J. Qian, Y. Cao, X. Ai, H. Yang. Low-Defect Prussian Blue Nanocubes as High Capacity and Long Life Cathodes for Aqueous Na-Ion Batteries. *Nano Energy* 2015, 13, 117–123.

[253] K. Zhu, Z. Li, T. Jin, L. Jiao. Low Defects Potassium Cobalt Hexacyanoferrate as a Superior Cathode for Aqueous Potassium Ion Batteries. *J. Mater. Chem. A* 2020, 8, 21103–21109.

[254] J. Sterzinger, R.L. Streng, S. Chen, R. Götz, W. Hu, J. Li, A.S. Bandarenka. Degradation mechanisms of prussian blue analogs and state-of-the-art approaches for stability optimization: A review. *J. Phys. Chem. C* 2025, 129, 7135-7153.

[255] Y. Gao, X. Wu, L. Wang, Y. Zhu, G. Sun, Y. Tang, M. Yan, Y. Jiang. Structurally Stable, Low H_2O Prussian Blue Analogs Toward High Performance Sodium Storage. *Adv. Funct. Mater.* 2024, 34 (22), 2314860.

[256] W. Wang, Y. Gang, J. Peng, Z. Hu, Z. Yan, W. Lai, Y. Zhu, D. Appadoo, M. Ye, Y. Cao, Q.-F. Gu, H.-K. Liu, S.-X. Dou, S.-L. Chou. Effect of Eliminating Water in Prussian Blue Cathode for Sodium-Ion Batteries. *Adv. Funct. Mater.* 2022, 32 (25), 2111727.

[257] X. Lamprecht, I. Evazzade, I. Ungerer, L. Hromadko, J. M. Macak, A. S. Bandarenka, V. Alexandrov. Mechanisms of Degradation of $Na_2Ni[Fe(CN)_6]$ Functional Electrodes in Aqueous Media: A Combined Theoretical and Experimental Study. *J. Phys. Chem. C* 2023, 127 (5), 2204–2214.

[258] W. Li, Z. Sun. Second Hydration Shell of Mg^{2+}: Competition Between Ion–Water Interaction and Hydrogen Bonding Interaction. *J. Phys. Chem. Lett.* 2025, 16 (2), 503–509.

[259] A. Bhattacharjee, A. B. Pribil, B. R. Randolf, B. M. Rode, T. S. Hofer. Hydration of Mg^{2+} and Its Influence on the Water Hydrogen Bonding Network via Ab Initio QMCF MD. *Chem. Phys. Lett.* 2012, 536, 39–44.

[260] P. R. Smirnov. Structure of the Nearest Environment of Na^+, K^+, Rb^+, and Cs^+ Ions in Oxygen-Containing Solvents. *Russ. J. Gen. Chem.* 2020, 90, 1693–1702.

[261] B. Xie, P. Zuo, L. Wang, J. Wang, H. Huo, M. He, J. Shu, H. Li, S. Lou, G. Yin. Achieving Long-Life Prussian Blue Analogue Cathode for Na-Ion Batteries via Triple-Cation Lattice Substitution and Coordinated Water Capture. *Nano Energy* 2019, 61, 201–210.

[262] P. L. Brown, S. E. Drummond, D. A. Palmer. Hydrolysis of Magnesium(II) at Elevated Temperatures. *J. Chem. Soc., Dalton Trans.* 1996, 3071–3075.

[263] J. Yun, J. Pfisterer, A. S. Bandarenka. How Simple Are the Models of Na Intercalation in Aqueous Media? *Energy Environ. Sci.* 2016, 9 (3), 955–961.

[264] R.L. Streng, S. Reiser, S. Wager, N. Pommer, A.S. Bandarenka. A fast and highly stable aqueous calcium-ion battery for sustainable energy storage. *ChemSusChem* 2025, 18, e202401469.

[265] G. Hernández, N. Casado, R. Coste, D. Shanmukaraj, L. Rubatat, M. Armand, D. Mecerreyes. Redox-Active Polyimide–Polyether Block Copolymers as Electrode Materials for Lithium Batteries. *RSC Adv.* 2015, 5, 17096–17103.

[266] N. W. Maxakato, S. S. Gwebu, G. H. Mhlongo, Eds. *Voltammetry*; IntechOpen, 2019.

[267] F. Marken, A. Neudeck, A. M. Bond. Cyclic Voltammetry. In *Electroanalytical Methods: Guide to Experiments and Applications*, 2010, pp. 57–106.

[268] N. Elgrishi, K. J. Rountree, B. D. McCarthy, E. S. Rountree, T. T. Eisenhart, J. L. Dempsey. A Practical Beginner's Guide to Cyclic Voltammetry. *J. Chem. Educ.* 2018, 95 (2), 197–206.

[269] G. Jones, S. K. Talley. The Viscosity of Aqueous Solutions as a Function of the Concentration. *J. Am. Chem. Soc.* 1933, 55 (2), 624–642.

[270] G. Jones, M. Dole. The Viscosity of Aqueous Solutions of Strong Electrolytes with Special Reference to Barium Chloride. *J. Am. Chem. Soc.* 1929, 51 (10), 2950–2964.

[271] R.L. Streng, S. Vagin, Y. Guo, B. Rieger, A.S. Bandarenka. Identifying the charge storage mechanism in polyimide anodes for Na-ion aqueous batteries by impedance spectroscopy. *RSC Energy Advances* 2024, 3, 874-882.

[272] F. Wang, X. Fan, T. Gao, W. Sun, Z. Ma, C. Yang, F. Han, K. Xu, C. Wang. High-Voltage Aqueous Magnesium Ion Batteries. *ACS Cent. Sci.* 2017, 3 (10), 1121–1128.

[273] L. Chen, J. L. Bao, X. Dong, D. G. Truhlar, Y. Wang, C. Wang, Y. Xia. Aqueous Mg-Ion Battery Based on Polyimide Anode and Prussian Blue Cathode. *ACS Energy Lett.* 2017, *2* (5), 1115–1121.

[274] M. Wang, H. Wang, H. Zhang, X. Li. Aqueous K-Ion Battery Incorporating Environment-Friendly Organic Compound and Berlin Green. *J. Energy Chem.* 2020, 48, 14–20.

[275] P. K. Jha, S. Kochrekar, A. Jadhav, R. Lassfolk, M. Salomäki, E. Mäkilä, C. Kvarnström. Wide Electrochemical Stability Window of $NaClO_4$ Water-in-Salt Electrolyte Elevates the Supercapacitive Performance of Poly(3,4-ethylenedioxythiophene). *Energy Storage Mater.* 2024, 72, 103758.

[276] J. Park, J. Lee, W. Kim. Water-in-Salt Electrolyte Enables Ultrafast Supercapacitors for AC Line Filtering. *ACS Energy Lett.* 2021, 6 (2), 495–501.

[277] M. Pang, S. Jiang, J. Zhao, S. Zhang, R. Wang, N. Li, R. Liu, Q. Pan, W. Qu, B. Xing. "Water-in-Salt" Electrolyte Enhanced High Voltage Aqueous Supercapacitor with Carbon Electrodes Derived from Biomass Waste-Ground Grain Hulls. *RSC Adv.* 2020, 10, 35545–35556.

[278] Y. Zhang, J. Xu, Z. Li, Y. Wang, S. Wang, X. Dong, Y. Wang. All-Climate Aqueous Na-Ion Batteries Using "Water-in-Salt" Electrolyte. *Sci. Bull. (Beijing)* 2022, 67 (2), 161–170.

[279] H. A. Jahn, E. Teller. Stability of Polyatomic Molecules in Degenerate Electronic States – I: Orbital Degeneracy. *Proc. R. Soc. Lond. A Math. Phys. Sci.* 1937, 161, 220–235.

[280] P. Senn. A Simple Quantum Mechanical Model That Illustrates the Jahn-Teller Effect. *J. Chem. Educ.* 1992, 69, 819.

[281] W. J. Kim, M. A. Smeaton, C. Jia, B. H. Goodge, B.-G. Cho, K. Lee, M. Osada, D. Jost, A. V. Ievlev, B. Moritz, L. F. Kourkoutis, T. P. Devereaux, H. Y. Hwang. Publisher Correction: Geometric Frustration of Jahn–Teller Order in the Infinite-Layer Lattice. *Nature* 2023, 620, E12.

[282] Y. Zheng, H. Xie, J. Li, K. S. Hui, Z. Yu, H. Xu, D. A. Dinh, Z. Ye, C. Zha, K. N. Hui. Insights into the Jahn-Teller Effect in Layered Oxide Cathode Materials for Potassium-Ion Batteries. *Adv. Energy Mater.* 2024, 14, 2400461.

[283] J. Song, L. Wang, Y. Lu, J. Liu, B. Guo, P. Xiao, J.-J. Lee, X.-Q. Yang, G. Henkelman, J. B. Goodenough. Removal of Interstitial H_2O in Hexacyanometallates for a Superior Cathode of a Sodium-Ion Battery. *J. Am. Chem. Soc.* 2015, 137, 2658–2664.

[284] J. Peng, Y. Gao, H. Zhang, Z. Liu, W. Zhang, L. Li, Y. Qiao, W. Yang, J. Wang, S. Dou, S. Chou. Ball Milling Solid-State Synthesis of Highly Crystalline Prussian Blue Analogue $Na_{2-x}MnFe(CN)_6$ Cathodes for All-Climate Sodium-Ion Batteries. *Angew. Chem. Int. Ed.* 2022, 61, e202205867.

[285] R. L. Streng, T. Steeger, A. Senyshyn, S. Abel, P. Schneider, C. Benning, B. Miller Naranjo, D. Gryc, M. Z. Hussain, O. Lieleg, M. Elsner, A. S. Bandarenka, K. Cicvarić. A Low-Cost and High-Energy Aqueous Potassium-Ion Battery. *J. Energy Chem.* 2025, 106, 523–531.

[286] M. Qin, W. Ren, R. Jiang, Q. Li, X. Yao, S. Wang, Y. You, L. Mai. Highly Crystallized Prussian Blue with Enhanced Kinetics for Highly Efficient Sodium Storage. *ACS Appl. Energy Mater.* 2021, 4 (1), 769–777.

[287] J. Song, L. Wang, Y. Lu, J. Liu, B. Guo, P. Xiao, J. J. Lee, X. Q. Yang, G. Henkelman, J. B. Goodenough. Removal of Interstitial H_2O in Hexacyanometallates for a Superior Cathode of a Sodium-Ion Battery. *J. Am. Chem. Soc.* 2015, 137 (7), 2658–2664.

[288] X. Bie, K. Kubota, T. Hosaka, K. Chihara, S. Komaba. A Novel K-Ion Battery: Hexacyanoferrate(II)/Graphite Cell. *J. Mater. Chem. A* 2017, 5 (9), 4325–4330.

[289] X. Ding, Q. Zhou, Z. Wang, L. Liu, Y. Wang, T. Song, F. Wu, H. Gao. An Ultra-Stable Mn-Based Prussian Blue Compound Effectively Suppresses Jahn–Teller Distortion as a Superior Cathode Material for Sodium-Ion Batteries. *J. Mater. Chem. A* 2024, 12 (40), 27598–27609.

[290] X. Zhao, Z. Xing, C. Huang. Investigation of High-Entropy Prussian Blue Analog as Cathode Material for Aqueous Sodium-Ion Batteries. *J. Mater. Chem. A* 2023, 11 (42), 22835–22844.

[291] J. Dai, S. Tan, L. Wang, F. Ling, F. Duan, M. Ma, Y. Shao, X. Rui, Y. Yao, E. Hu, X. Wu. High-Voltage Potassium Hexacyanoferrate Cathode via High-Entropy and Potassium Incorporation for Stable Sodium-Ion Batteries. *ACS Nano* 2023, 17 (21), 20949–20961.

[292] Z. Zhao, W. Zhang, M. Liu, S. J. Yoo, N. Yue, F. Liu, X. Zhou, K. Song, J. G. Kim, Z. Chen, X. Y. Lang. Ultrafast Nucleation Reverses Dissolution of Transition Metal Ions for Robust Aqueous Batteries. *Nano Lett.* 2023, 23 (11), 5307–5316.

[293] T. Steeger,* R. L. Streng,* A. Senyshyn, V. Dyadkin, X. Lamprecht, R. List, A. S. Bandarenka. Controlling the Morphology and Electrochemical Properties of Electrodeposited Nickel Hexacyanoferrate Thin Films. *ChemElectroChem* 2025, 12, 2500073.

[294] L. Chen, W. Sun, K. Xu, Q. Dong, L. Zheng, J. Wang, D. Lu, Y. Shen, J. Zhang, F. Fu, H. Kong. How Prussian Blue Analogues Can Be Stable in Concentrated Aqueous Electrolytes. *ACS Energy Lett.* 2022, 7 (5), 1672–1678.

[295] G. Liang, Z. Gan, X. Wang, X. Jin, B. Xiong, X. Zhang, S. Chen, Y. Wang, H. He, C. Zhi. Reconstructing Vanadium Oxide with Anisotropic Pathways for a Durable and Fast Aqueous K-Ion Battery. *ACS Nano* 2021, 15 (11), 17717–17728.

[296] Y. Li, W. Deng, Z. Zhou, C. Li, M. Zhang, X. Yuan, J. Hu, H. Chen, R. Li. An Ultra-Long Life Aqueous Full K-Ion Battery. *J. Mater. Chem. A* 2021, 9 (5), 2822–2829.

[297] B. Han, D. Zhang, X. Liu, Z. Wang, W. Qu, S. Zhang, C. Deng. Ordered Assembly of Potassium Cobalt Hexacyanoferrate Hollow Multivoid Nanocuboid Arrays for High-Performance Aqueous K-Ion Batteries Towards All-Climate Energy Storage. *J. Mater. Chem. A* 2022, 10 (25), 13508–13518.

[298] G. Vardhini, P. S. Dilip, S. A. Kumar, S. Suriyakumar, M. Hariharan, M. M. Shaijumon. Polyimide-Based Aqueous Potassium Energy Storage Systems Using Concentrated WiSE Electrolyte. *ACS Appl. Mater. Interfaces* 2024, 16 (37), 48782–48791.

[299] J. Chen, S. Lei, S. Zhang, C. Zhu, Q. Liu, C. Wang, Z. Zhang, S. Wang, Y. Shi, L. Yin, R. Wang. Dilute Aqueous Hybrid Electrolyte with Regulated Core-Shell-Solvation Structure Endows Safe and Low-Cost Potassium-Ion Energy Storage Devices. *Adv. Funct. Mater.* 2023, 33 (19), 2215027.

[300] F. J. Günter, N. Wassiliadis. State of the Art of Lithium-Ion Pouch Cells in Automotive Applications: Cell Teardown and Characterization. *J. Electrochem. Soc.* 2022, 169 (3), 030515.

[301] BYD Company Limited. Battery-Box Premium HVS/HVM – Technische Daten und Produktbeschreibung. Solarspeicher24. Available online: https://solarspeicher24.de/pdf/9885710_1049185.pdf (accessed on May 19, 2025).

[302] Huawei Technologies Co., Ltd. Huawei Luna ESS Datasheet. pvXchange GmbH. Available online:

https://www.pvxchange.com/mediafiles/pvxchange/attachments/Datenblatt%20Huawei%20Luna%20ESS.pdf (accessed on May 19, 2025).

[303] Statistisches Bundesamt (Destatis). Stromverbrauch der privaten Haushalte nach Haushaltsgrößenklassen. Verfügbar online: https://www.destatis.de/DE/Themen/Gesellschaft-Umwelt/Umwelt/UGR/private-haushalte/Tabellen/stromverbrauch-haushalte.html (accessed on May 19, 2025).

[304] J. Hao, B. Li, X. Li, X. Zeng, S. Zhang, F. Yang, S. Liu, D. Li, C. Wu, Z. Guo. An In-Depth Study of Zn Metal Surface Chemistry for Advanced Aqueous Zn-Ion Batteries. *Adv. Mater.* 2020, 32 (34), 2003021.

[305] L. Yuan, J. Hao, C. C. Kao, C. Wu, H. K. Liu, S. X. Dou, S. Z. Qiao. Regulation Methods for the Zn/Electrolyte Interphase and the Effectiveness Evaluation in Aqueous Zn-Ion Batteries. *Energy Environ. Sci.* 2021, 14 (11), 5669–5689.

[306] H. Jia, Z. Wang, B. Tawiah, Y. Wang, C. Y. Chan, B. Fei, F. Pan. Recent Advances in Zinc Anodes for High-Performance Aqueous Zn-Ion Batteries. *Nano Energy* 2020, 70, 104523.